ROSALY M. C. LOPES JOHN R. SPENCER

Io After *Galileo*

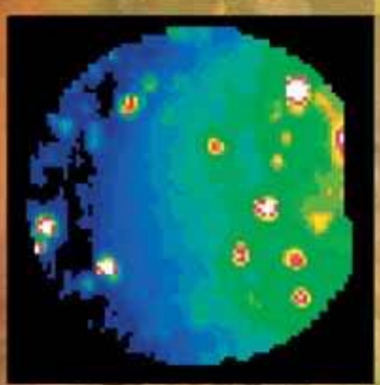

A New View of Jupiter's Volcanic Moon

Springer

PRAXIS

Io After *Galileo*

A New View of Jupiter's Volcanic Moon

Rosaly M. C. Lopes and John R. Spencer

Io After *Galileo*

A New View of Jupiter's Volcanic Moon

Springer

Published in association with
Praxis Publishing
Chichester, UK

PRAXIS

Dr Rosaly M. C. Lopes
Jet Propulsion Laboratory/NASA
Pasadena
California
USA

Dr John R. Spencer
Department of Space Studies
Southwest Research Institute
Boulder
Colorado
USA

SPRINGER–PRAXIS BOOKS IN ASTRONOMY AND PLANETARY SCIENCES
SUBJECT *ADVISORY EDITORS*: Philippe Blondel, C.Geol., F.G.S., Ph.D., M.Sc., Senior Scientist, Department of Physics, University of Bath, UK; John Mason, B.Sc., M.Sc., Ph.D.

ISBN 3-540-34681-3 Springer Berlin Heidelberg New York

Springer is part of Springer-Science + Business Media (springer.com)
Bibliographic information published by Die Deutsche Bibliothek
Die Deutsche Bibliothek lists this publication in the Deutsche Nationalbibliografie; detailed bibliographic data are available from the Internet at http://dnb.ddb.de

Library of Congress Control Number: 2006928061

Cover design: Jim Wilkie
Project management: Originator Publishing Services, Gt Yarmouth, Norfolk, UK

Printed on acid-free paper

Contents

To our late colleagues Damon Simmonelli and Bill Sinton,
who greatly contributed to our understanding of Io.
We miss their scientific insight, humor, and friendship.

Preface

This book is a community effort that grew largely out of the informal Io workshops that have happened since the early 1990s. In the first few years, the purpose of the workshops was to determine which *Galileo* observations would be key to further our understanding of this exotic moon. Since *Galileo*'s main antenna did not open, the number of observations taken by the spacecraft was exceedingly small compared with other missions; it was therefore imperative to decide which observations would be the highest priority. We can make an analogy between a tourist with a point and shoot camera, taking pictures at a high rate to decide later which are the best, and Ansel Adams, spending many hours or even days deciding how best to take a single shot.

The competition for resources on *Galileo* was fierce, but those of us in charge of Io observations for *Galileo*'s instruments decided at an early stage that much could be gained from collaboration. Thus, the workshops evolved into the planning of collaborative observations and dividing resources between us in a mostly peaceful manner. By the time we began acquiring *Galileo* Io data, in 1995 for fields and particles and 1996 for remote sensing, a *Galileo* Io working group was already well established, paving the way for collaborative research. As the years passed, the workshops became more aligned with data analysis and, finally, we started discussing key questions such as how hot Io's magma really is, and what key future observations we will need to answer the many unsolved mysteries that Io continuously threw our way. When the *Galileo* mission ended in 2003, we felt the time was right for a book reviewing the state of knowledge after *Galileo*. Hopefully, it will serve as a guide for future work, be it in the form of new space missions, telescopic observations, data analysis, or modeling.

We would like to thank all the people who participated in these workshops over the years and, in particular, all those who took on the task of organizing them. We thank Clive Horwood from Praxis for inviting us to take on this book project,

Neil Shuttlewood and his team for editing and pre-press book production, and Jim Wilkie for the cover design.

Many of the authors in this book reviewed one anothers chapters, but we are also deeply appreciative of the help from other reviewers: Robin Canup, Lazlo Kezthelyi, Susan Kieffer, Margaret Kivelson, Jack Lissauer, Ellis Miner, Jeff Moore, Neil Murphy, Jani Radebaugh, Julie Rathbun, Bill Smythe, Tilman Spohn, David Stevenson, Nick Thomas, and Bill Ward. Others who provided invaluable assistance include Daniel Beuchert, Mark Boryta, Lou Glaze, Benedicte Larignon, Michelle McMillan, Dennis L. Matson, Chris Moore, Stan Peale, Carl B. Pilcher, William Sheehan, Laurence Trafton, Philip Varghese, Glenn J. Veeder, Andrew Walker, and Ju Zhang. Many of the authors are supported by NASA research grants and we acknowledge the support from NASA's Planetary Geology and Geophysics Program, the Jovian System Data Analysis Program, and the Outer Planets Research Program. We also wish to thank the Center for Adaptive Optics and Science and Technology Center (STC), the National Science Foundation, and the Hubble Space Telescope Archive Program. Most importantly, we thank the *Galileo* Flight Team, whose enormous dedication and ingenuity enabled us to have a successful mission despite numerous problems. We also thank our fellow science team members, principal investigators, project managers, and the *Galileo* Project Scientist, Torrence Johnson. *Galileo* increased our knowledge of the Jupiter system by orders of magnitude and we are deeply grateful to all who contributed.

Rosaly M. C. Lopes,
Jet Propulsion Laboratory, Pasadena, California
John R. Spencer,
Southwest Research Institute, Boulder, Colorado

Figures

Tables

Abbreviations and acronyms

ADONIS	Adaptive Optics Near-Infrared System
AKR	Auroral Kilometric Radiation
AMU	Atomic Mass Unit
AO	Adaptive Optics
AU	Astronomical Unit
CAI	Calcium–Aluminium Inclusion
CFB	Continental Flood Basalt
CFD	Computational Fluid Dynamics
COS	Cosmic Originas Spectrograph
DDS	Dust Detector Subsystem
DSMC	Direct Simulation Monte Carlo
EPD	Energetic Particles Detector
ESO	European Southern Observatory
EUV	Extreme UltraViolet
FOS	Faint Object Spectrograph
FWHM	Full Width at Half-Maximum
GEM	*Galileo* Europa mission
GHRS	Goddard High-Resolution Spectrograph
GMM	*Galileo* Millennium Mission
GSMT	Giant Segmented Mirror Telescope
HIC	Heavy Ion Counter
HST	Hubble Space Telescope
IRIS	InfraRed Imaging Spectrograph
IRTF	InfraRed Telescope Facility
ISO	International Space Observatory
ISS	Imaging Science Subsystem
IUE	International Ultraviolet Explorer
JOI	Jupiter Orbit Insertion

JPL	Jet Propulsion Laboratory
JWST	James Webb Space Telescope
KH	Kelvin–Helmholtz
LBT	Large Binocular Telescope
LGA	Low-Gain Antenna
LTE	Local Thermodynamic Equilibrium
MAG	MAGnetometer
MMSN	Minimum-Mass Sub-Nebula
MMT	Multi-Mirror Telescope
NIMS	Near-Infrared Mapping Spectrometer
OSIRIS	OH-Suppressing InfraRed Imaging Spectrograph
OWL	OverWhelmingly Large Telescope
PLS	PLasma detector Subsystem
PPR	PhotoPolarimeter and Radiometer
PMS	Pre-Main-Sequence
PWS	Plasma Wave Subsystem
SB	Stochastic–Ballistic
SPIFFI	SPectrograph for Infrared Faint Field Imaging
SSI	Ssolid-State Imaging system
STIS	Space Telescope Imaging Spectrograph
SZA	Solar Zenith Angle
TEXES	Texas Echelon Cross Echelle Spectrograph
TMT	Thirty Meter Telescope
UVS	UltraViolet Spectrometer
VIMS	Visible–Infrared Mapping Spectrometer
VLT	Very Large Telescope

Contributors

Chapter 1
Alfred S. McEwen
University of Arizona

Chapter 2
Dale P. Cruikshank
NASA Ames Research Center

Robert M. Nelson
Jet Propulsion Laboratory

Chapter 3
Jason E. Perry
University of Arizona

Rosaly M. C. Lopes
Jet Propulsion Laboratory

John R. Spencer
Southwest Research Institute, Boulder

Claudia J. Alexander
Jet Propulsion Laboratory

Chapter 4
William B. McKinnon
Washington University in St. Louis

Chapter 5
William B. Moore
University of California, Los Angeles

Gerald Schubert
University of California, Los Angeles

John D. Anderson
Jet Propulsion Laboratory

John R. Spencer
Southwest Research Institute, Boulder

Chapter 6
Elizabeth P. Turtle
Johns Hopkins University Applied Physics Laboratory

Windy L. Jaeger
U.S. Geological Survey, Flagstaff

Paul M. Schenk
Lunar and Planetary Institute

Chapter 7
David A. Williams
Arizona State University

Robert R. Howell
University of Wyoming

Chapter 8
Paul E. Geissler
U.S. Geological Survey, Flagstaff

David B. Goldstein
University of Texas, Austin

Chapter 9
Robert W. Carlson
Jet Propulsion Laboratory

Jeffrey S. Kargel
University of Arizona

Sylvain Douté
Laboratoire de Planétologie de Grenoble

Laurence A. Soderblom
U.S. Geological Survey, Flagstaff

J. Brad Dalton
NASA Ames Research Center

Chapter 10
Emmanuel Lellouch
Observatoire de Meudon

Melissa A. McGrath
NASA Marshall Space Flight Center

Kandis Lea Jessup
Southwest Research Institute, Boulder

Chapter 11
Nicholas M. Schneider
University of Colorado

Fran Bagenal
University of Colorado

Chapter 12
Franck Marchis
University of California, Berkeley

John R. Spencer
Southwest Research Institute, Boulder

Rosaly M. C. Lopes
Jet Propulsion Laboratory

2

A history of the exploration of Io

Dale P. Cruikshank and Robert M. Nelson

"On the 7th day of January in the present year, 1610, in the first hour of the following night, when I was viewing the constellations of the heavens through a telescope, the planet Jupiter presented itself to my view, and as I had prepared for myself a very excellent instrument, I noticed a circumstance which I had never been able to notice before, namely that three little stars, small but very bright, were near the planet; and although I believed them to belong to the number of the fixed stars, yet they made me somewhat wonder, because they seemed to be arranged exactly in a straight line, parallel to the ecliptic, and to be brighter than the rest of the stars, equal to them in magnitude ... When on January 8th, led by some fatality, I turned again to look at the same part of the heavens, I found a very different state of things, for there were three little stars all west of Jupiter, and nearer together than on the previous night ..."

Galileo Galilei, *Siderius Nuncius*, March 1610
Translation by E. S. Carlos (Shapley and Howarth, 1929)

2.1 THE DISCOVERY AND EARLY OBSERVATIONS OF THE GALILEAN SATELLITES

2.1.1 From Medician Star to a world of its own

The history of the exploration of Io logically begins with Galileo's discovery of this and the other three large Jovian satellites in 1610, communicated in his *Siderius Nuncius* in March of that year. There is credible evidence for the assertion that the Bavarian astronomer Simon Marius (Mayr) independently found the satellites at about the same time, and perhaps 5 weeks earlier (Johnson, 1931; Pagnini, 1931), but his failure to communicate the discovery and the absence of a clear confirmation of the earlier dates gives Galileo the credit for the first detection. Marius never claimed

priority in discovery over Galileo, but his suggested names for the four satellites have survived the centuries, despite some scholars' contrary expectations (Lynn, 1903), and thus we have Io, Europa, Ganymede, and Callisto, after various lovers of Jupiter.

The discovery observations were followed by determinations of the periods of the orbits around Jupiter; Io's synodic period is 42.477 hours, a value close to that determined by Galileo himself. The proportionality between the periods and distances of the satellites from Jupiter not only validated Kepler's laws of planetary motion (the third law was published in 1619), but it afforded a practical means to determine, by telescopic observations of the eclipses and transits, the longitude of an observer on Earth. Then, in 1675, Ole Roemer determined from observations of eclipses and transits that the events seen near opposition occur earlier than average, while those seen far from opposition occur later. He connected the observed differences in timing of the eclipse events to the differing distance of Jupiter from Earth, and correctly deduced that light propagates at a finite velocity, requiring some 16 minutes 26.6 seconds to cross one diameter of the Earth's orbit. The radius of the Earth's orbit (the Astronomical Unit, AU) was not known reliably until somewhat later, but when Roemer's time is used with the modern value of the AU, the resulting velocity of light ($\sim$303,300 km/sec) is within 2% of the value known today.

The motions of the four Galilean satellites attracted the attention of a number of observers and mathematicians in the 17th and 18th centuries. Both Galileo and Mayr prepared tables of the motions of the satellites, followed by G. B. Hodierna in 1656, and in 1668 by J. D. Cassini. Other improved empirical tables followed, and then Pierre-Simon Laplace published his mathematical theory of the orbits in 1788. With this work the importance of the resonant periods of Io, Europa, and Ganymede were recognized. The orbital period of Europa is twice that of Io, and Ganymede's period is twice that of Europa. This succession of 2 : 1 ratios of the orbital periods is known as a Laplace resonance. Dissipation of tidal energy through the 2 : 1 Io–Europa resonance is a direct cause of the continuously active volcanoes on Io that is discussed elsewhere in this chapter and book, while the 2 : 1 Europa–Ganymede resonance serves to keep the interior of Europa in a partially liquid state.

The unusual nature of Io as a physical body began to emerge as soon as telescopes became good enough to resolve the disk and attention turned to aspects of planetary satellites beyond their orbits and dynamics. In 1892, while measuring the diameters of the Galilean satellites with a visual micrometer, W. H. Pickering noticed that Io was distinctly elliptical in outline. He watched the elongated image slowly change orientation and concluded that Io has the form of an ellipsoid, a shape that he also saw in the other three large satellites (Dobbins and Sheehan, 2004). Other observers also noted anomalous appearances of Io. For example, when Io transits Jupiter's disk both the satellite and its shadow can clearly be seen against the planet's multi-hued clouds. Observing with the Lick Observatory 12-inch refractor[1] in 1890, E. E. Barnard (1891a)

[1] Barnard was denied regular use of the 36-inch refractor until August 1892; he discovered Amalthea, Jupiter's fifth satellite (and the first one since Galileo) just 1 month later on 9 September 1892 (Cruikshank, 1982).

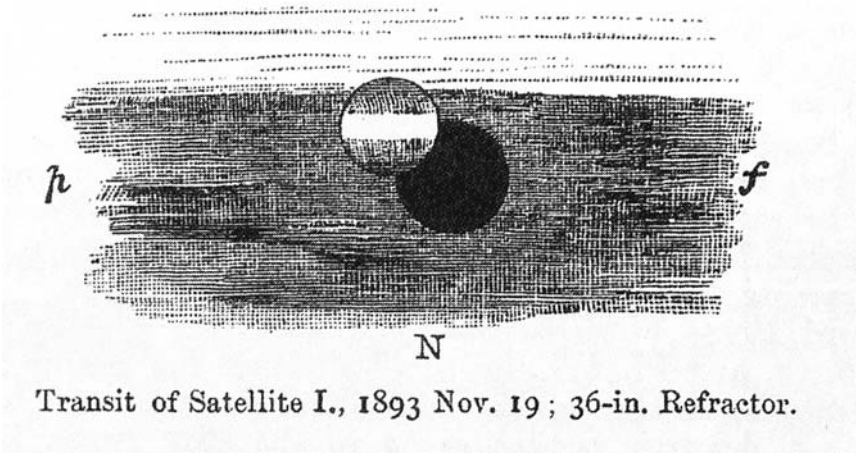

Figure 2.1. Appearance of Io against the disk of Jupiter during the transit of 19 November 1893. Observed by E. E. Barnard with the Lick Observatory 36-inch refractor, and clearly showing the dark polar regions and bright equatorial band of Io (Barnard, 1894).

noted that in transit Io often appeared as a dark or dusky spot, and on September 8 of that year it appeared to him "... elongated in a direction nearly perpendicular to the belts of Jupiter." At higher powers and with perfect definition the satellite appeared distinctly double, the components clearly separated. Barnard's colleague and double-star expert, S. W. Burnham, verified the appearance of Io in transit as a double object. Barnard suggested that Io has a white belt on its surface, parallel to those of Jupiter, or that it is actually double; he was "... strongly inclined to favor the theory of actual duplicity." The idea of a double Io eventually disappeared upon closer scrutiny with larger telescopes and the clear circularity of the shadow when projected on Jupiter's clouds. The odd apparent shape of Io was later attributed to the distribution of light and dark material on the surface, and to distorted images produced in telescopes whose tubes confined air of nonuniform temperature. In modern images of Io the color differences across the surface are clearly visible. In high-definition photographs of Io in transit against a blue–white region of Jupiter (e.g., Minton, 1973), the red–brown polar caps of the satellite are clearly discernable by their color contrast to the equatorial regions and to the background of Jupiter's clouds. Barnard (1891b) had noted that "... if a bright belt existed on the satellite, it would have the effect of apparently cutting it into two parts, since the belt would be lost in the bright surface of Jupiter. The satellite would, therefore, appear as two dusky dots, which, through irradiation, would appear small and round." (Figure 2.1.)

While Pickering adhered to his assertion of the egg shapes of the Galilean satellites for his entire career (Dobbins and Sheehan, 2004), Barnard reached the correct conclusion and moved on (Sheehan, 1995). He later used the Lick Observatory 36-inch telescope to measure the diameters of all the planets and satellites with a visual micrometer and reported the diameter of Io as 1.048 arcsec (Barnard, 1897), corresponding to 3,950 km, about 8.5% larger than the presently accepted mean

diameter of 3,642 km. Barnard's measurements followed those of an early visitor to Lick Observatory. Albert Michelson (1891) used the 12-inch Lick refractor (stopped down to 6 inches) in a very early application of his interferometric technique, later used to measure the diameters of stars. Michelson's diameter for Io was 1.02 arcsec, or about 3,844 km.

In order to refine the orbits of all four Galilean satellites, visual photometric observations of the eclipses of the Galilean satellites began in 1878 (Pickering, 1907). The observer determined the time of the midpoint of the disappearances into, and reappearances from, Jupiter's shadow, by plotting the changing brightness until the satellite became invisible (disappearances) or regained full brightness (reappearances). These observations formed the basis for the *Tables of the Four Great Satellites of Jupiter* (Sampson, 1910).

Additional interest attaches to the eclipse curves, particularly on the disappearance of the satellites into the shadow, because while the timing depends on a satellite's orbit, the exact shape of the curve depends upon the diameter of the satellite, the geographic distribution of its surface brightness (albedo), and refractive layers in Jupiter's upper atmosphere (Harris, 1961). The occasional observation of an enduring brightness "tail" at about stellar magnitude 14 of a satellite entering Jupiter's shadow was taken as evidence for a refracting layer in Jupiter's atmosphere (Harris, 1961, and G. P. Kuiper's appendix III to that article). We return below to other aspects of eclipse phenomena.

The overall color of Io attracted early attention. Kuiper (1973) notes that Hertzsprung discovered the unusually orange color in 1911, although W. H. Pickering had remarked on it in 1893 (Dobbins and Sheehan, 2004). The earliest photoelectric photometry (Stebbins, 1927; Stebbins and Jacobsen, 1928) confirmed the dramatic color difference (in B–V)[2] of Io in comparison with the other three Galilean satellites, and gave the first quantitative information on the rotational brightness variations as well as the change in brightness with solar phase angle (the solar phase function). It also established with clarity the synchronous rotation and revolution of these satellites by the repeatability of the brightness curves with orbital position. The solar phase function, in turn, enabled early calculations of the photometric properties of the surfaces, using scattering theories derived by Minnaert (1941), van de Hulst (1957), and others.

2.2 WHAT IS THE NATURE OF IO?

2.2.1 A paradigm emerges

At this point in the story, we introduce a theme to which we will return along the way. This is the theme of the changing paradigm of our understanding of Io as new ideas

[2] The letters U, V, B refer to a color filter system that astronomers use to measure the brightness of an astronomical source at three different colors, or bands, of the spectrum, ultraviolet (U), blue (B), and visual (V). The wavelengths of the bands are $U = 0.35\ \mu m$, $B = 0.435\ \mu m$, and $V = 0.555\ \mu m$. The differences in intensity of the light transmitted at each of these wavelengths provides a measure of temperature of an incandescent source (a star) and of the spectrum of a planetary object that shines by reflected sunlight. The spectrum of a planetary object is an important indicator of its composition.

and new data have been brought to bear on this object as an individual body, and as a member of the set of four Galilean satellites.

With information about the approximate sizes of the Galilean satellites and estimates of their masses from orbital dynamics, early values for their mean densities were calculated. The venerable astronomy textbook by Russell, Dugan, and Stewart (1945) listed the mean densities as 2.7, 2.9, 2.2, and 1.3 g/cm^3, for Io, Europa, Ganymede, and Callisto, respectively.[3] These or similar early values for the densities, together with the emerging information on the density and composition of Jupiter, were the starting point for speculation on the compositions of the Galilean satellites. Jeffreys (1923) noted that the densities are too low for metal and rock, and suggested that the satellites are made primarily of liquefied gases of the same sort constituting Jupiter, a view reached also (and apparently independently) by Tammann (1931 [quoted in Wildt, 1969]). The early values of the densities of the four satellites, while indicative of the presence of volatile material, were not accurate enough to reveal the striking trend of the high density of Io (3.53 g/cm^3) compared with the low value for Callisto (1.85 g/cm^3) that we know today (see below).

Considerations of the physical make-up of the Galilean satellites arose primarily in connection with calculations of the compositions of the four giant planets. At the same time, an increasing interest in the compositions of the rocky planets (including asteroids), and particularly the Moon, arose on the part of geochemists (e.g., Brown, 1949; Urey, 1952; Suess and Urey, 1956). Interest in the Moon was energized by the approaching era in which humans would have the ability to send probes there and to other planets. Thus, an intense interest arose in the geosciences community in the study of the planets, a subject formerly reserved for the field of astronomy. World War II had advanced the field of rocketry from a series of back yard science experiments to major government enterprises both in the United States and the Soviet Union. The primary motivation for rocket development concerned the intercontinental ballistic missile, but scientists had the cosmos in view.

Nobel Laureate Harold Urey was one of the early founders of planetary science. His interest in geochemistry led him to a closer examination of the planets in the context of two broad chemical classes; the four inner planets with properties generally similar to those of the Earth, and the four gas giants with their profoundly different chemical character. The outer planets all have atmospheres and low-density interiors which are chemically reduced,[4] while the inner planets have crusts of silicate rocks and oxidized atmospheres. The Moon's properties are similar to those of Earth, and by extension it might be reasonably assumed that the moons of the outer planets mimic the properties of their parent bodies. Thus, a paradigm emerged which held that objects in the outer Solar System were chemically reducing, most likely as a

[3] The earlier 1926 edition of Russell, Dugan, and Stewart listed the densities as 2.9, 2.9, 2.2, and 0.6 g/cm^3 for Io through Callisto, respectively. They suggested that the first two are composed of rock, like the Moon, and the outer two may be composed largely of ice or solid carbon dioxide.

[4] Wildt (1932) had identified bands in the spectra of Jupiter and Saturn (discovered in 1905 by V. M. Slipher) as methane and ammonia, the simplest reduced molecules of carbon and nitrogen. Herzberg (1952) identified molecular hydrogen in the atmosphere of Uranus and Neptune, and by implication, in the atmospheres of Jupiter and Saturn.

consequence of their greater distance from the Sun which made them cooler and permitted the retention of the lighter molecular weight reducing gases.

The interpretation of the many unusual observations of Io that began after the end of World War II was strongly influenced by the pre-space age paradigm which held that Io, as a body in the outer Solar System, had to be *reducing* in nature. At the same time, the cosmochemical models suggested that water ice would be a major rock on the surfaces of outer Solar System bodies of Io's size (e.g., Urey, 1952).

2.2.2 New technology enables new observations

Harris and Kuiper (Harris, 1961) conducted the next extensive broadband photometric study of Io and the other satellites with greatly improved photoelectric detectors and the McDonald Observatory 82-inch telescope in 1951–1954. They transformed the Stebbins and Jacobsen measurements to the *UBV* system, and corroborated the significant brightness and color variations seen as Io rotates, deriving the mean opposition magnitude $V_o = 4.80$, and variations of 0.18 mag in *B–V* and 0.5 mag in *U–B* colors.

Another extensive photometric study was undertaken by Morrison *et al.* (1974; see also the review in Morrison and Morrison, 1977) in the *UBVY* system (intermediate filter bandwidth) resulting in further refinement of the solar phase function and colors.

Just as detectors were improving throughout the 1950s and 1960s, so were interference filters that permitted higher throughput and narrower photometric passbands. Johnson and McCord (1971) used a photometer with 24 narrow-band filters to define the spectral reflectances of the Galilean satellites with higher spectral resolution than had previously been accomplished, finding a broad absorption in Io's reflectance of between 500 and 600 nm. With the higher spectral resolution afforded by the 24 filters, Johnson (1971) noted the steep red slope in Io's reflectance between 300 and 400 nm, and combined his own photometry with earlier work to derive phase integrals and Bond albedos of all the Galilean satellites.

The strong color and the absorption at 500–600 nm were corroborated in subsequent spectrophotometry with a series of narrower filters by Wamsteker (1972), and in an unpublished paper by Wisniewski and Andersson (1973).[5] In the Wisnewski and Andersson work, a silicon vidicon detector was applied to a prism spectrometer to give 500 spectral channels from 400 nm to 1.0 μm. In Figure 2.2 we reproduce the two spectra of Io from the unpublished manuscript.

The long wavelength limit of the early photometry and spectroscopy was imposed

[5] The unpublished paper (see references) was approved and accepted for publication by G. P. Kuiper for the *Communications of the Lunar and Planetary Laboratory*, which he edited. The proofs are dated December 1973, the month in which Kuiper died. Following Kuiper's death, the *Communications* ceased publication, and several manuscripts that were in publication were abandoned. Wisniewski sent a copy of the proofs to Cruikshank on 24 June 1975, lamenting that the paper, which included spectra of all four Galilean satellites and Titan, remained unpublished. Both Wisniewski and Andersson have since passed away.

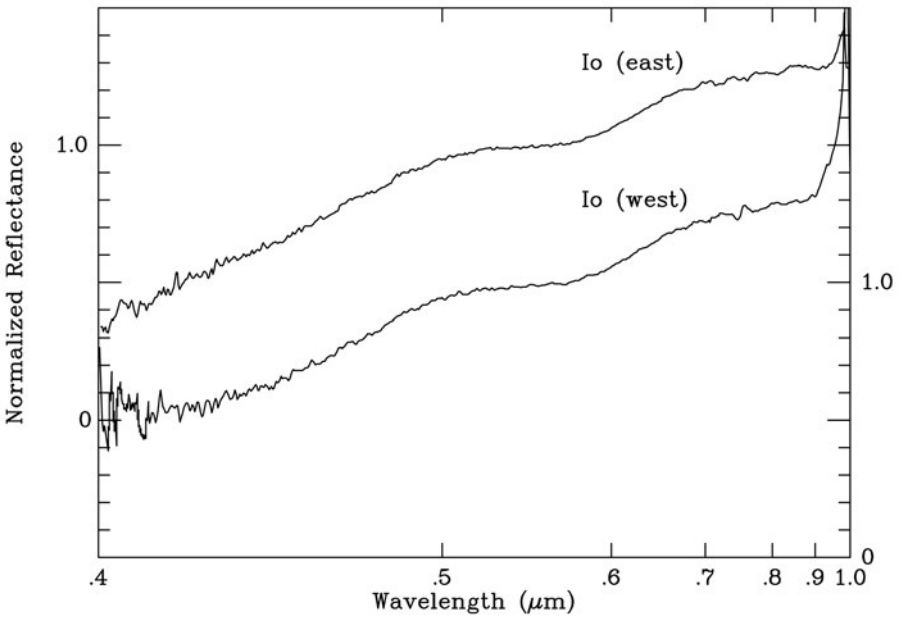

Figure 2.2. Normalized spectra of Io at western and eastern elongations in 1973, ratioed to a solar-type star (Wisniewski and Andersson, 1973, unpublished). These spectra confirm the broad absorption, 500–600 nm, first noted by Johnson and McCord (1971). The scale on the left abscissa refers to Io (east), and that on the right refers to the plot for Io (west). Reproduced courtesy of the Lunar and Planetary Laboratory, University of Arizona.

by the limitations on the photo detectors and photographic emulsions, which extended to ~1.2 μm. Photoconductor detectors developed during the war and declassified in 1945 were quickly adapted to astronomical work (Kuiper *et al.*, 1947) and the modern era of infrared astronomy was born.[6] Johnson and McCord (1971) extended the spectral reflectance observations of all four satellites longward in wavelength to 2.5 μm with an additional set of filters, showing that Io's reflectance remains high and nearly constant from ~0.7 to 2.5 μm. This property is in strong contrast to the reflectances of the other three satellites, as had been noted in the first studies with infrared detectors and prism spectrometers accomplished by Kuiper (1957) and Moroz (1966). Those earliest observations by Kuiper and Moroz led each investigator to propose independently that H_2O ice is a major constituent of the surfaces of Europa and Ganymede; Kuiper (1957) published his conclusion that the reflectances are consistent with H_2O ice only briefly and without any figures in an abstract, while Moroz (1966) published the first spectra (Figure 2.3).

[6] Earlier infrared observations of the Moon, planets, and a few astronomical sources had been possible with detectors sensitive at wavelengths beyond ~10 μm, but these had insufficient sensitivity to detect fainter sources or to obtain spectra of any but the brightest objects in the sky.

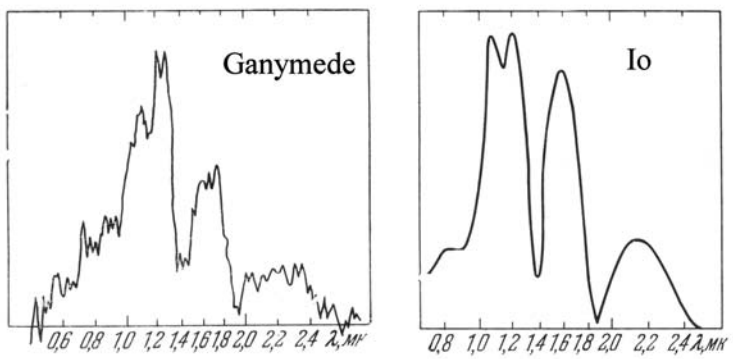

Figure 2.3. Spectra of Io and Ganymede (0.7–2.5 μm) obtained on 15 October 1964 by V. I. Moroz (1966) with a scanning prism spectrometer. The *y*-axis is brightness.The Ganymede spectrum is the record of a single scan through the spectrum, while the Io spectrum is the average of four. These spectra are not ratioed to the solar spectrum: the greater relative heights of the 1.6- and 2.2-μm peaks in the Io spectrum, where H_2O ice is absorbing, relative to those on Ganymede, indicate the absence of H_2O ice on Io.

Kuiper (1973) eventually published his spectra of the Galilean satellites in a review he wrote after the publication of two papers in which high-quality spectra clearly showed individual bands of H_2O ice on Europa and Ganymede (Pilcher *et al.*, 1973; Fink *et al.*, 1973).

The first near-infrared observations of the Galilean satellites beyond 2.5 μm were reported by Gillett *et al.* (1970), who found that the reflectance of Io at 3.5 and 4.9 μm is significantly higher than that of the other three. Although Io was clearly different from the others, the authors demurred, noting that, "The interpretation of the apparent absorption feature in the 3–5.4-μm spectrum of satellites J II–J IV coupled with the absence of absorption of like magnitude in the spectrum of J I, which retains its extremely high albedo, is beyond the scope of this paper." Lee (1972) also observed the satellites in the near-infrared out to 3.6 μm and also noted the large difference between Io and the others. Lee worked at the University of Arizona's Lunar and Planetary Laboratory, and was aware of the laboratory studies of sulfur and its compounds then in progress by G. T. Sill (1973) at the same institution. Lee concluded that the high albedo at 3.4 μm ". . . is compatible with a sulfur compound. The drop in the curves for Europa and Ganymede confirms earlier conclusions that H_2O ice is present on these satellites [Kuiper, 1957] . . ."

Note that at this point the H_2O ice bands on Europa and Ganymede had not been clearly resolved, and arguments for its presence on these two bodies (and its absence on Io) were based on the relative shapes of the reflectance curves rather than the detection of specific bands.

Other post-war improvements in detectors and filters included those suited to thermal measurements of astronomical sources in the 8–14-μm spectral region (the 10-μm, or N band), corresponding in wavelength to a transparent "window" in the Earth's atmosphere. Using the Palomar mountain Hale 5-m telescope, then the largest

in the world, Murray *et al.* (1964) set out to measure the brightness temperatures of the Galilean satellites. They detected thermal emission from Ganymede and Callisto, but could not detect Io or Europa because of their lower temperatures ($<$135 K and $<$141 K, respectively); those lower temperatures are a consequence of their high albedos in the visual region of the spectrum where relatively more sunlight is reflected. Io was eventually detected in the 10-μm band (e.g., Gillett *et al.*, 1970), and then Morrison *et al.* (1972) measured its flux in the 20-μm band, a more difficult task because of the lesser transparency of the Earth's atmosphere at that wavelength. The 20-μm (Q) band is closer to the black-body flux peak for an object of Io's temperature, but Io's 20-μm brightness temperature (127$\pm$3 K) found by Morrison *et al.* (1972) is less than the predicted black-body equilibrium temperature; the authors suggested that Io's emissivity might be less than unity. (In Section 2.3.5 we discuss the detection of anomalously *high* thermal emission from Io at shorter wavelengths.)

Further progress in studying the thermal properties of Io and the other Galilean satellites was achieved with infrared measurements during the eclipses, when sunlight is quickly cut off and the surfaces rapidly cool, and when the surfaces warm after the restoration of sunlight (Morrison and Cruikshank, 1973; Hansen, 1973). It was seen from these studies that a thin (few millimeters) layer of highly insulating, low-density material overlaying a thicker, denser material (ice or rock) could approximately explain Io's (and the other satellites') changes in temperature during eclipses. This behavior shows that Io's surface has a significant thermal inertia, which is a measure of the degree of departure of the actual surface temperature from the temperature of a gray body in instantaneous equilibrium with the insolation. Thermal inertia is related to the surface microstructure, insulating properties, and layering of different materials of different densities and textures. The thermal studies could not clearly distinguish between rocky material and ices, in part because of a lack of laboratory data on the thermal properties of such materials in a vacuum.

2.2.3 Io eclipse phenomena at optical wavelengths

Because the eclipse disappearance and reappearance events for Io as seen from Earth all occur very close to Jupiter (less than one Jupiter radius, or $<$20 arcsec), scattered light from the planet affects the accuracy of the brightness estimates of Io, and generally more so than for the other satellites, whose eclipse phenomena mostly occur at larger angular distances. The eclipse curves for Io in the visual photometry by Pickering (1907) and others show increased scatter in the points, particularly around maximum brightness, compared with the curves for the other satellites. In several Io reappearance curves, there appears to be an overshoot in brightness, such that the satellite's brightness appears too high when it first emerges from the shadow, and then after a few minutes dims a bit and remains constant. These irregularities in the eclipse curves might logically be attributed to the increased scatter in the data because of the interference of the light from Jupiter itself.

An anomalous brightening of Io by about 10 per cent for 10–20 minutes following its emergence from Jupiter's shadow was first observed with a photoelectric photometer by Binder and Cruikshank (1964), who proposed that an atmospheric component

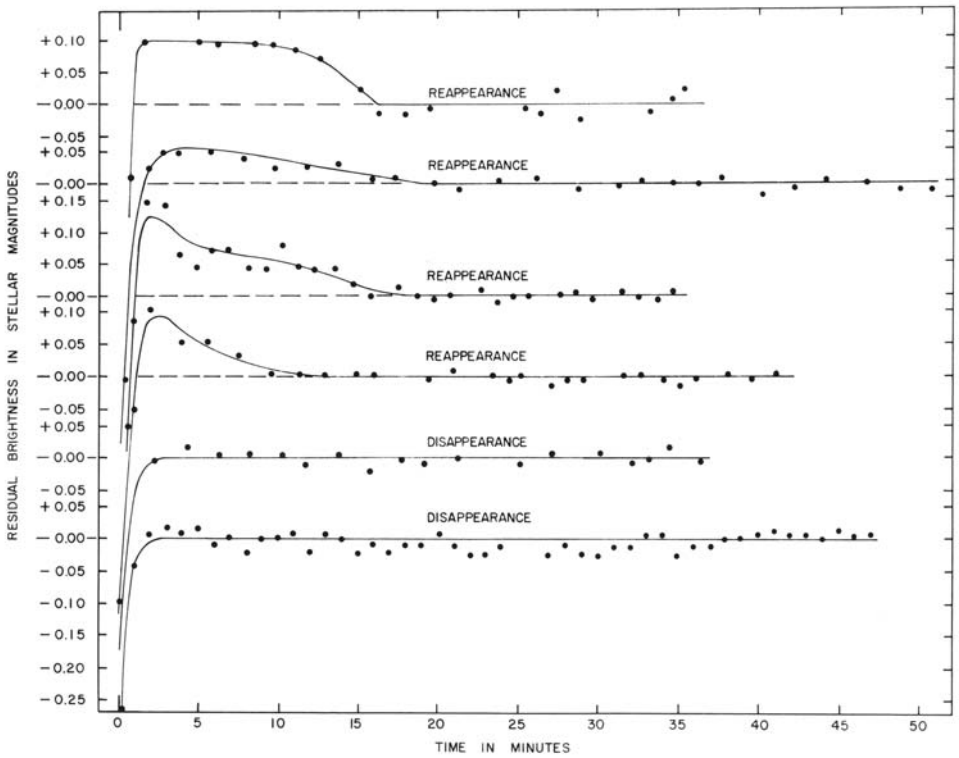

Figure 2.4. Photometry of Io eclipse reappearances and disappearances in 1962 and 1963 (Binder and Cruikshank, 1964), showing the reported post-eclipse anomalous brightening in the top four traces. No brightening effect was seen at similar geometries at the disappearance events. Reproduced courtesy Elsevier.

condenses on the surface of Io during the eclipse, and then evaporates a few minutes after the restoration of sunlight (Figure 2.4). Their 1964 paper predated the discovery of volcanic SO_2 gas constituting Io's thin and variable atmosphere, and Kuiper (1949) had placed upper limits of 200 and 40 cm-atm of gaseous methane and ammonia, respectively, for all the satellites from his spectroscopic observations. Subsequently, the anomalous brightenings have been seen by some observers (e.g., Johnson, 1971), while others found no anomaly at other eclipse reappearances. Nelson *et al.* (1993) reviewed much of the earlier literature and report observations of 14 eclipse reappearances from 1981–1989, finding modest anomalous brightenings of a few per cent at some events.

Later observations from space offer an improved situation *vis-à-vis* the scattered light from Jupiter. Observations of a few eclipse events by *Voyager* (Veverka *et al.*, 1981), *Galileo* (Buratti *et al.*, 1995; Simonelli *et al.*, 1998), and the Hubble Space Telescope (HST) (Secosky and Potter, 1994) have shown no global brightenings, although certain regions of the disk may have changed in brightness.

After the discovery of SO_2 frost on Io's surface (see Section 2.4.1) and with the knowledge that Io's atmosphere of gaseous SO_2 is variable in density on both spatial and temporal scales because of the active volcanoes, Fanale *et al.* (1981) calculated that any eclipse condensations are necessarily sporadic. The fully saturated atmosphere contains sufficient SO_2 to cause condensation of an optically thick layer only in some locations and at some times. They also found that the rapid evaporation time of $\sim$15 minutes is in agreement with the amount of SO_2 that would be returned to the atmosphere when sunlight was restored at the end of the eclipse. Scattering calculations indicate that a layer several millimeters thick is needed to achieve the required optical thickness, and such a layer would probably not evaporate in 15 minutes. Nelson *et al.* (1993) therefore concluded that the condensation/sublimation scenario is only marginally possible.

As a modern sequel to the saga of Io's anomalous eclipse behavior, when the *Cassini–Huygens* spacecraft flew by Jupiter in December, 2000, en route to Saturn, the Visible–Infrared Mapping Spectrometer (VIMS) instrument detected an apparent variation of the strengths of absorption bands of SO_2 ice in Io's spectrum from observations made before and after an eclipse. Bellucci *et al.* (2004) interpreted the changed band strength and an observed change in continuum brightness level as the condensation of atmospheric SO_2 gas as frost on Io's surface during the $\sim$2.5-hour eclipse. Subsequent time-resolved spectra of Io were obtained for five eclipse reappearances in 2004 (Cruikshank *et al.*, 2006), and at none of those events was there any observed change in the strengths of the several absorption bands of SO_2 ice in Io's spectrum.

Thus, the anomalous post-eclipse brightening of Io's surface remains unresolved. While the nominal atmospheric abundance of SO_2 gas is insufficient to condense into an optically thick surface layer during eclipse, it is marginally possible that local and temporal gross enhancements of SO_2 gas are sufficient to do so, at least in specific regions of the satellite's surface. Observing with the HST, McGrath *et al.* (2000) found enhanced SO_2 gas concentration above the Pele volcanic region, but the calculated abundance is less than that required for short-term condensation of a layer of sufficient optical thickness to produce the eclipse effect.

A response of Io's far-ultraviolet emission from the atmosphere during and after eclipse has been found by several investigators. Saur and Strobel (2004) have modeled the variation of the electrodynamic interactions of Io's atmosphere and ionosphere with the magnetosphere as an eclipse takes place, and predict that a delay in the plasma interaction when sunlight is restored after an eclipse can result in a post-eclipse brightening in the emission at far-ultraviolet wavelengths. Their model shows that the eclipse behavior at these wavelengths can clarify the relative contributions to Io's atmosphere of volcanic gases and gases derived from the sublimation of surface frost.

Although the post-eclipse brightening of Io and its interpretation are still disputed, the report by Binder and Cruikshank in 1964 called attention to the possibility that Io is not the atmospherically and geologically dead object that its small size and distance from the Sun would suggest. Accordingly, over the years Io has offered a number of surprises that continue to the present day.

2.2.4 Other reports of unusual behavior

A report by Kalinyak (1965) of unidentified and non-solar absorption lines in the visible-region spectra of Io, Europa, and Ganymede proved to be anomalous. Those data were obtained in 1963 with one of the early image tubes that electronically intensified the incident light, while apparently introducing flaws that were interpreted as absorption lines. Binder and Cruikshank (1966) obtained spectra in the same spectral region as Kalinyak's data with higher resolution, using conventional photographic techniques, and could not corroborate the features that had been reported. In the spectra by Binder and Cruikshank, one can see that the Na-D lines in the spectrum of Io are slightly less dark than the Na-D lines in the other satellites, although this was unnoticed at the time. Brown (1974) later discovered emission cores in the Io Na-D lines, leading to the characterization of Io's sodium cloud. We return to this discovery in Section 2.3.2.

A newspaper report in *Pravda* (7 January 1966) told of the discovery of atmospheres on the Galilean satellites at the Astrophysical Institute in Kazakhstan, but gave no details. We have been unable to find any further information or follow-up on this report.

Somewhat earlier, Jeans (1925, p. 348) mentioned in his book on the dynamical theory of gases that "An atmosphere has been observed on Titan", and that there are "suspected atmospheres on two of Jupiter's satellites". In his paper reporting the spectroscopic discovery of methane on Titan, Kuiper (1944) noted his puzzlement at Jeans' statement, and was unable to discover the source of those remarks.

2.3 THE *PIONEER* MISSIONS

2.3.1 A new view of Io

Observations of the Jovian satellites from space-based platforms began in the early 1970s with the launch of the *Pioneer 10* and *11* spacecraft to the outer Solar System. These spacecraft, each with mass of 258 kg, passed Jupiter in 1973 and 1974. The 25-kg instrument packages on each spacecraft included three remote-sensing instruments (an ultraviolet photometer, and imaging photopolarimeter, and an infrared radiometer), each providing important information about Jupiter and its atmosphere. The remote-sensing information about Io was limited to rather low spatial resolution, due in part to the fact that the spacecraft were spin-stabilized. However, the *Pioneer in situ* instruments provided important new results on the Io environment that had a significant impact on efforts to understand the nature of its interior, surface, and atmosphere. The *Pioneer 10* and *11* probes found that Jupiter has intense belts of charged particles, similar to the terrestrial Van Allen radiation belts, and that they are created by the Jovian magnetic field. The intensity of this radiation was found to be particularly high at Io's distance from Jupiter where atomic particles continuously impact the satellite's surface (Simpson *et al.*, 1974, 1975; Van Allen *et al.*, 1974, 1975;

Trainor *et al.*, 1974, 1975; Fillius and McIlwain, 1974; Fillius *et al.*, 1975). These discoveries spurred the development of a series of models involving radiation-induced modification of Io's surface and ejection of significant amounts of material from the surface into the Jovian magnetosphere.

The *Pioneer* results provided improved masses of the Galilean satellites by analysis of the slight gravitational deflection in the trajectory of each spacecraft as it passed each member of the Jovian system. Io was found to have a significantly higher density than the other Galilean satellites, and the trend of decreasing density of these bodies with increasing distance from Jupiter became clear (Anderson *et al.*, 1974). The values now in use are: Io 3.53, Europa 2.99, Ganymede 1.94, and Callisto 1.85 g/cm^3. Pollack and Reynolds (1974) explained the density trend quite elegantly by showing that the satellites formed rapidly during Jupiter's initial contraction phase when the planet was orders of magnitude more luminous than at present. Io's higher density shows that it is depleted in volatile components in comparison with the other Galilean satellites; this result served as an important input to, and constraint on, subsequent Io paradigm development.

We previously mentioned that Kuiper in 1957 and Moroz (1966, 1967) reported that the infrared spectra of Ganymede and Callisto were similar to the rings of Saturn, and therefore suggested that their surfaces were dominated by water ice. Both Kuiper and Moroz found that Io was different; instead of a drop in near-infrared reflectance toward 2.5 μm, the albedo remained high and fairly constant. A decade later, spectra of much improved quality clearly established that Io differs from the other Galilean satellites by a very high infrared spectral geometric albedo, and that it does not show any trace of absorption bands due to water ice of the kind found on the other Galilean satellites (Pilcher *et al.*, 1973; Fink *et al.*, 1973). The fact that Io was lacking the slightest trace of water, while water (as ice) dominated the surface of its companions, strongly influenced the pre-*Voyager* paradigm, which predicted that all small bodies in the outer Solar System would have surfaces dominated by water ice.

In 1971, Io passed in front of the star Beta Scorpii as seen from Earth; measurement of the attenuation of light from the star revealed a very low upper limit to Io's atmosphere (Smith and Smith, 1972; Bartholdi and Owen, 1972) and also permitted its diameter to be measured with high precision. The result (3,656±5 km, Taylor, 1972) is in remarkably good agreement with the currently accepted mean diameter (3,642±5 km). Later, when *Pioneer 10* passed behind Io in 1973, the attenuation of a radio signal from the spacecraft established that Io has an ionosphere, implying a very thin atmosphere with pressure about 10^{-7} bar (Kliore *et al.*, 1974, 1975).

In another great achievement, the *Pioneer* ultraviolet photometer detected a torus of hydrogen ions filling Io's orbit around Jupiter (Carlson and Judge, 1974).

The *Pioneer* missions triggered an era of intense interest in the outer planets, driven in part by the excitement generated by the *Pioneer* results, but also by a rare alignment of the outer planets which was to occur in the late 1970s. This configuration of the planets, which occurs at intervals of 150–175 years, would permit a spacecraft to fly past each giant planet in succession, using each planet's gravitational field to accelerate the spacecraft toward the next planetary rendezvous. This gravity-assist

trajectory permitted the launch of a much larger spacecraft for the same size rocket than would otherwise be possible. NASA proposed and the United States Congress approved two *Voyager* missions to the outer Solar System to be launched in 1977. The *Voyager* spacecraft each had a mass of 815 kg and 11 scientific investigations which included four remote-sensing instruments.

2.3.2 Io and Jupiter's magnetosphere

Radio bursts from Jupiter had been observed for several years at decametric wavelengths leading up to the report by Bigg (1964) that these burst are linked to Io's orbital position. This was the first indication of the electrodynamic connection between Io and the Jovian magnetosphere. The observations were followed by theoretical investigations by Piddington and Drake (1968), Goldreich and Lynden-Bell (1969), and others.

The first observations that drew a close connection between the Jovian magnetosphere and the physical properties of Io itself were the high-resolution optical spectroscopic studies by Brown (1974) and Brown and Chaffee (1974) in which emission in the sodium-D lines was discovered (Figure 2.5). While it was soon found that the emission comes from a large volume of space surrounding Io, it also emerged that Io's surface is the source of atoms which are ejected from the surface and then excited by the Sun through resonant scattering (Matson *et al.*, 1974). Potassium emission was soon found (Trafton 1975), and the third neutral species, oxygen, was detected spectroscopically by Brown (1981). These neutral atoms form a cloud around Io extended along part of the satellite's orbit, and from this cloud the atoms are ionized and swept away by Jupiter's rotating magnetic field. It was at first thought that the neutrals were largely sputtered from the surface by incident magnetospheric particles, however the later discovery of high-temperature silicate volcanoes on Io opened the possibility that some material is ejected directly into space through that mechanism.

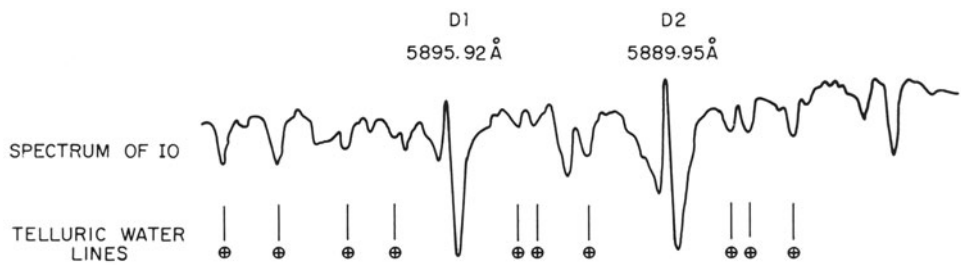

Figure 2.5. Narrow emission components are seen in the Na-D lines in this high-resolution spectrum of Io by Brown (1974), obtained with an echelle spectrograph.

2.3.3 Io week, November 1974

With the discovery of sodium emission on Io and the *Pioneer 10* occultation results, the pace of discoveries had risen to a level that merited a concerted effort on the part of observers worldwide. There was a growing feeling in the planetary science community that Io and its interaction with the circum-Jovian environment were responsible for a range of unique phenomena. Accordingly, Robert A. Brown, then at Harvard University, organized an international "Io week" for the period 6–16 November 1974. Radio astronomers, optical, and infrared observers from 16 countries on 6 continents responded, and most participated in making new observations. Brown then convened a one-day workshop at Harvard "... to discuss recent Io observations in the context of the current 'information explosion' in the study of the Galilean satellites." At least 10 presentations reported on radio, optical, and infrared measurements, together with modeling studies. This brief meeting focused attention on the unique properties and behavior of Io as perceived some 4 years before the first *Voyager* encounter. Odd as Io seemed at the time, the discovery of active volcanism in 1979 still came as a great surprise.

2.3.4 A new model for the composition of Io – the evaporite hypothesis

Io's distinctive spectral geometric albedo at visual wavelengths, along with the absence of water absorption features in the infrared spectrum formed the principal body of evidence from which the composition of Io's surface could be modeled or constrained. The absence of a thick atmosphere and its position within the Jovian magnetosphere suggested that charged particles bombard Io's surface, sputter material from the surface to the magnetosphere, and alter the chemical properties of the surface. Species found in the magnetosphere, sodium, potassium, and later sulfur, were also expected to dominate the compounds on the surface. This integrated body of evidence permitted synthesis of the post-*Pioneer*, pre-*Voyager* models of Io's surface.

One proposed explanation of Io's strong ultraviolet absorption shortward of 400–500 nm was the presence of elemental sulfur S_8 on its surface because laboratory reflectance spectra were found to have approximately similar absorption properties shortward of 500 nm (Wamsteker, 1972; Kuiper, 1973; Wamsteker *et al.*, 1974). Other materials with high infrared reflectivity were needed in addition to sulfur to match Io's reflectance properties, and suitable candidates were sought in the laboratory. In an effort to provide an integrated explanation of the available evidence, Fanale *et al.* (1974) proposed that Io's surface was an evaporate deposit consisting principally of sulfur, and halite (NaCl). They noted that Io's spectrum is similar to a leach product from the Orgueil meteorite, and pointed out the consistency of the evaporite deposit hypothesis with the absence of spectral features due to water in Io's infrared spectrum. They noted furthermore that halite, when irradiated while at low temperatures exhibits an absorption band at about 560 nm as a consequence of the formation of a metastable color center. This radiation-induced absorption feature at 560 nm could explain the spectral feature seen at that location in Io's spectrum (such a feature

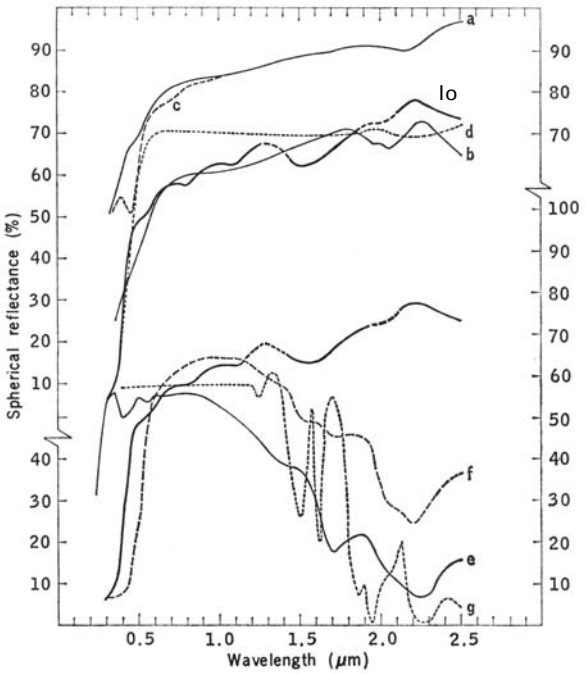

Figure 2.6. Comparison of Io's spectral geometric albedo and laboratory spectra of halite (a), a leach product from the Orgueil meteorite (b), and selensulfur (d) (after Fanale *et al.*, 1974). The evaporite model was a principal foundation of the pre-*Voyager* paradigm for Io. It addressed Io's spectral features, and the relationship between Io's surface and its magnetosphere by positing that Io's surface was composed of evaporite materials.

is not found in laboratory spectra of elemental sulfur, S_8). The comparison between Io's spectral geometric albedo and the laboratory spectra of the hypothesized surface materials is shown in Figure 2.6 (after Fanale *et al.*, 1974).

A consensus developed within the planetary science community around the evaporite hypothesis and it serves as the best example of the pre-*Voyager* paradigm. The evaporate hypothesis was explored in greater detail by many investigators using various combinations of elemental sulfur, many different salts, and other evaporite materials. Nash and Fanale (1977), after a lengthy study of the reflection spectrum of S_8 in mixtures with various combinations of candidate materials, including an attempt to simulate Io's radiation environment, found a best match to Io's spectrum to be a mixture of "... a fine-grained particulate mixture of free sulfur (55 vol%), dehydrated bloedite [$Na_2Mg(SO_4)_2 \bullet H_2O$] (30 vol%), ferric sulfate [$Fe_2(SO_4)_3 \bullet xH_2O$)] (15 vol%), and trace amounts of hematite [Fe_2O_3]". These authors acknowledged that many other combinations of materials could also be candidates for Io's surface but, given the suite of materials they explored, this was the best combination of materials that fit the set of diverse data available at the time.

2.3.5 Late developments – setting the stage for *Voyager*

Despite the consensus around the evaporite hypothesis as the pre-*Voyager* paradigm, there were continuing developments prior to *Voyager* which were harbingers of the many changes in the paradigm which the *Voyager* results were about to establish. Several groups undertaking observations in the thermal-infrared reported that although Io emits too little radiation at 20 μm, it exhibits anomalously high infrared brightness temperatures in the 3–5-μm spectral region, implying the occurrence of events of very high temperatures on the surface (Morrison and Cruikshank, 1973; Hansen, 1975). Reports of episodes of high flux at various infrared wavelengths continued until the eve of the *Voyager* encounter (Witteborn *et al.*, 1979). (See Chapter 7 for further historical details.)

In continued studies of circum-Jovian space, Kupo *et al.* (1976) reported the first emission lines from the plasma torus when they detected the forbidden lines of singly ionized SII at 671.6 and 673.1 nm. Subsequently, additional lines of ionized S and O were observed from the ground, from the International Ultraviolet Explorer satellite, and from *Voyager*. Monochromatic images taken with filters isolating the plasma emission lines showed the torus in Io's orbit, with a tilt of some 9.6 degrees imposed by the inclination of Jupiter's magnetic equator to the satellite's orbital plane (Pilcher, 1980). Brown (1976) demonstrated the utility of the collisionally excited emissions in the plasma for determining the electron density, and the ion and electron temperatures in the torus. These observations added strong support to the spectroscopic argument that sulfur was a principal constituent of Io's surface. Any model which was to explain Io's surface surely had to include elemental sulfur as a major component or else go to great lengths to explain its absence.

There were further investigations into Io's surface composition that invoked elemental sulfur S_8 as the principal cause of an absorption feature at 400–500 nm. While the evidence for sulfur on Io's surface was quite strong, the spectrum of S_8 measured in the laboratory, even considering the effect of varying temperature and particle size, was not a convincing match to Io's spectral geometric albedo. The spectrum of sulfur increased far too sharply with wavelength from 400–500 nm to fit Io's spectrum well.

Nelson and Hapke (1978) measured Io's spectrum from 320–350 nm using a spectrometer which provided five times the resolution of the narrowband filter measurements which had previously constituted the best spectral data on Io. They found a previously unknown spectral absorption band beginning shortward of 330 nm (consistent with the OAO-2 report of a very low albedo at 280 nm by Caldwell (1975)). In addition, they called attention to the existence of many allotropic forms of elemental sulfur, of which the most common allotrope, cyclooctal sulfur S_8, is just one. They noted that other short chain allotropes and long chain polymers of sulfur, alone or in combination, would better match Io's spectrum in the near-ultraviolet, visible, and near-infrared spectral range. They noted furthermore that these other allotropes were easily formed by melting and quenching, or by irradiation, and once formed they were metastable at low temperatures. Nelson and Hapke (1978) suggested, "These allotropes of sulfur could be made naturally on Io by a number

of processes. One way is by melting yellow sulfur as would be expected to occur in the vicinity of a volcanic fumarole or hot spring followed by sudden quenching to produce red sulfur.''

Continued infrared telescope observations extended understanding of Io's spectrum deeper into the infrared. In 1978, a particularly distinctive set of absorption features between 3.3 and 4.07 μm, unique to Io, was reported by Cruikshank *et al.* (1978) and Pollack *et al.* (1978). Both groups compared their spectrum of Io to a wide range of eligible candidate materials, particularly those materials whose presence is consistent with the evaporite hypothesis, but were unable to find a suitable candidate to match the 4.07-μm feature. Elemental sulfur, regardless of allotropic form, does not have features at these wavelengths; instead it is highly reflective throughout this region. Therefore, a material which causes the strong 4.07-μm and related absorption features, if it could be identified, could, when combined with sulfur in one or more allotropic forms, explain most of Io's spectrum. However, laboratory spectra of a large suite of evaporite materials did not produce a match for Io's infrared spectrum.

An especially prescient dynamical study of Io appeared early in 1979, as *Voyager 1* was approaching the Jupiter system for its March fly-by. Peale *et al.* (1979) noted that while Io's eccentricity as an object in free orbit was quite small, its forced eccentricity due to the presence of the other Galilean satellites is quite large; large enough that extensive tidal heating would be expected. They concluded that Io's core could be molten and that it would have a crust that was quite thin. This tidal heating effect might explain the previous infrared observations of anomalously high temperature and episodic thermal outbursts. Peale *et al.* (1979) also noted, ''. . . one might speculate that widespread surface volcanism would occur leading to extensive differentiation and outgassing.'' This conjecture based on dynamical calculations was the final and most compelling concept presaging what *Voyager* was about to find.

2.4 THE *VOYAGERS* ARRIVE AT JUPITER

2.4.1 Volcanoes on a distant world

While the evidence which led to the development of the evaporite hypothesis was accumulated at a measured pace on a timescale of decades, the *Voyagers* provided massive amounts of data in a highly compressed time frame. Thus, the previously existing models, which were developed over the course of a decade, were refined essentially overnight. New models were rapidly developed as diverse data sets arriving nearly simultaneously from the spacecraft were studied and integrated.

As *Voyager 1* approached the Jovian system, on-board particle detectors began to detect anomalously high concentrations of sulfur, sodium, and oxygen prior to the entry of the spacecraft into the magnetosphere. Krimigis *et al.* (1979), reported, ''. . . it is probable that the sulfur, sodium and possibly oxygen originate at Io.'' This view was consistent with sputtering as a mechanism for removal of material from Io's surface. As *Voyager* approached Io itself, images of the surface revealed no impact craters whatsoever. This striking absence of impact craters stood in stark contrast to the

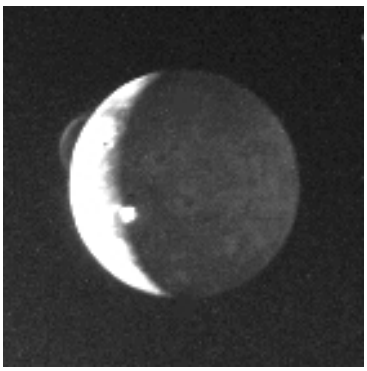

Figure 2.7. Io volcanoes: the discovery image. This figure shows two volcanoes. The image was the one in which Linda Morabito, a JPL navigation engineer, discovered the active volcanism. She was fitting the limb of Io against background field stars in order to refine *Voyager*'s trajectory, and noticed the plume on the edge of the image (from Morabito *et al*., 1979).

surfaces of the Moon, Mercury, Mars and its moons, Phobos and Deimos, where telescopic and spacecraft images had revealed ancient, heavily cratered landscapes. Because there is no plausible mechanism that could shield Io from impacts, the youth of Io's surface and the recent covering of impact craters quickly after formation emerged as an inescapable conclusion.

The reason for Io's youthful surface became clear when *Voyager* images revealed towering plumes ejected from vents on the satellite's surface as stunning expressions of a profoundly active volcanic world (Figure 2.7, from Morabito *et al*., 1979). And stunned indeed were planetary scientists, to a person. Active volcanism on Io stands as perhaps the most compelling finding of the *Voyager* fly-by of the Jovian system. In all, there were nine active plumes seen at the time of the *Voyager 1* fly-by (Strom *et al*., 1979), and hot regions on Io's surface associated with the volcanoes were discovered (Hanel *et al*., 1979). Previously undetected ionized species of sulfur and oxygen were found in the torridal ring of ionized material that orbits Jupiter at Io's approximate distance (Broadfoot *et al*., 1979), as material sputtered from Io's surface is transported to the torus, where ultimately it escapes to the broader Jovian environment.

Images of Io taken at several wavelengths showed that the colors of the surface materials were consistent with allotropic forms of sulfur (Smith *et al*., 1979). While allotropic sulfur was generally agreed to as one of Io's surface components, *Voyager* results provided important evidence for identification of the other principal material present, condensed sulfur dioxide. The *Voyager* infrared radiometer reported a significant presence of SO_2 gas measured against the background of the hot spot, the abundance was high enough to suggest that the gas was in equilibrium with material on the surface (Pearl *et al*., 1979). The detection of SO_2 as a gas was the first evidence of a neutral atmosphere (though patchy in its distribution) on Io, and it caused several groups to measure the reflectance spectrum of SO_2 frost in the laboratory. These efforts quickly revealed that SO_2 was an excellent match for the

previously unidentified absorptions in Io's infrared spectrum at 4.07 μm and shorter wavelengths (Fanale *et al.*, 1979; Smythe *et al.*, 1979). Hapke (1979) independently suggested that SO_2 frost might be present based on the spectral properties of the gas. Nash and Nelson (1978) reported that the 4.07-μm features could also be explained by SO_2 gas adsorbed on the other surface materials. SO_2, as a frost or as an adsorbate, was clearly the previously unidentified substance that, along with sulfur allotropes, covered the vast preponderance of Io's surface.

The distribution of the two main surface constituents to specific locales on Io's surface could not be established from *Voyager* images because the absorption features of condensed SO_2 lay beyond the wavelength limits of the spacecraft's cameras working in the visible region, and were too short for the operational spectral range of the infrared spectrometer. However, within a year of the fly-bys, Nash *et al.* (1980) had measured the reflection spectrum of SO_2 frost in the laboratory and found another band at 330 nm, where Nelson and Hapke (1978) had previously reported a feature from ground-based data. Nelson *et al.* (1980) using the International Ultraviolet Explorer spacecraft, which observed Io from Earth orbit, were able to confirm the existence of the 330-nm band and demonstrate that its strength correlates with Io's sub-Earth longitude in the same sense as does the 4.07-μm SO_2 feature reported by Cruikshank *et al.* (1978) and Pollack *et al.* (1978). Therefore, they concluded that the SO_2 frost was asymmetrically distributed in longitude on Io's surface with the frost being almost absent between Io longitudes 250–323° and most abundant between longitudes 72–137°. From features in Io's spectrum at wavelengths beyond the range of the *Voyager* cameras, they found the reflective regions on Io where the concentration of SO_2 is greatest. Continued observations of Io's infrared SO_2 bands by Howell *et al.* (1984) with ground-based telescopes demonstrated that the sulfur dioxide concentrations had not changed in position in the approximate 8 years since the feature was first observed (in November 1976) by Cruikshank *et al.* (1978). In a study summarizing the photometric results of the *Voyager* imaging system, Soderblom *et al.* (1980) concluded that the data were consistent with an Io surface composition consisting of mixtures of sulfur dioxide frost and allotropes of elemental sulfur.

2.4.2 Mountains of sulfur or silicate?

The tidal heating mechanism discovered by Peale *et al.* (1979), combined with *Voyager* confirmation that sulfur was ubiquitous on Io's surface, caused considerable re-appraisal of models of thermal evolution of planetary sized bodies. If Io had been subjected to the heating it currently experiences throughout its history, it surely would be the most evolved planetary body in the Solar System. Both the sulfur and SO_2 currently escaping from Io have molecular weight of 64, suggesting that volatiles of lower molecular weight (such as water, MW = 18) were lost long ago. Calculated resurfacing rates suggested that Io surface materials had been recycled many times over its existence (Johnson *et al.*, 1979). Thus, Io was analogous to a smelter that had been running for all of geologic time. While the post-*Voyager* consensus of a sulfur and SO_2 frost surface for Io took hold (see the review by Sill and Clark, 1982), the

processes which led to that surface composition state were subject to intense discussion. This combination of knowledge and speculation framed the context for the development of the revised paradigm.

Sagan (1979) elaborated on the earlier suggestion that mixtures of sulfur allotropes could easily be produced in Io's thermal environment and might explain Io's coloration by noting that a very peculiar viscosity property of molten sulfur might create diagnostic landforms on Io's surface. Solid sulfur melts at ~392 K and, as heating continues, the viscosity decreases with increasing temperature until the melt reaches 432 K. Remarkably, above this temperature the viscosity of the melt *increases* by a factor of 10^4 as the principally S_8 cyclooctal ring breaks and long chain polymers of sulfur form. Sagan therefore suggested that much of Io's surface morphology could be explained by sulfur masses which formed volcanic edifices around the hot spots. He argued that the effluent from the sulfur volcanoes flowed down the slopes sluggishly at temperatures higher than 432 K and then, as the high-temperature sulfur crosses the viscosity threshold rapid outflows of sulfur would overflow and flood the downstream landscape with the short chain sulfur allotropes imparting the orange to yellow color characteristic of the lower temperature. The Sagan model suggested that the surface would be characterized by sulfur volcanoes with flanks covered with sulfur flows displaying the characteristic coloration and viscosity flow pattern of this material. An alternative model emerged concurrently with that of Sagan. Carr *et al.* (1979) argued, based on the properties of silicate magmas, that sulfur flows are unlikely to be the dominant form of Io volcanism. They suggested that while sulfur magmas might conceivably be produced from elemental sulfur separating from a sulfur-rich silicate magma, any flows thus produced could not explain major expressions of Io topography. They noted that the rugged topography of Io in many cases included nearly vertical sheer walls. While silicate materials have the strength to support such vertical relief, sulfur might not. Clow and Carr (1980) later reported that at the temperatures indicated by infrared observations of Io, sulfur would become ductile and therefore unable to support the steep walls seen in various places on the satellite. Sulfur could not be the foundation of Io's topography.

In broad outline, the immediate post-*Voyager* paradigm had been defined. Io's surface morphology was shaped principally by silicate material but sulfur and SO_2 coated the silicate surface, making these materials the only ones that were spectrally sensible from remote-sensing instruments.

2.4.3 Post-paradigm developments and modifications

The *Voyager* images gave the first views of Io at close range (Figure 2.8). The absence of craters established that Io has the youngest surface of all bodies so far viewed in the Solar System. Geologists have classified the surface units into three types: mountains, plains, and vent regions. The mountains have heights of up to 9 km and extend laterally for several hundreds of km; many mountains are volcanic but some are products of motion of the lithosphere. The plains are lacking in extensive vertical relief and resemble the regions of low-viscosity sulfur flows. The vent regions encompass

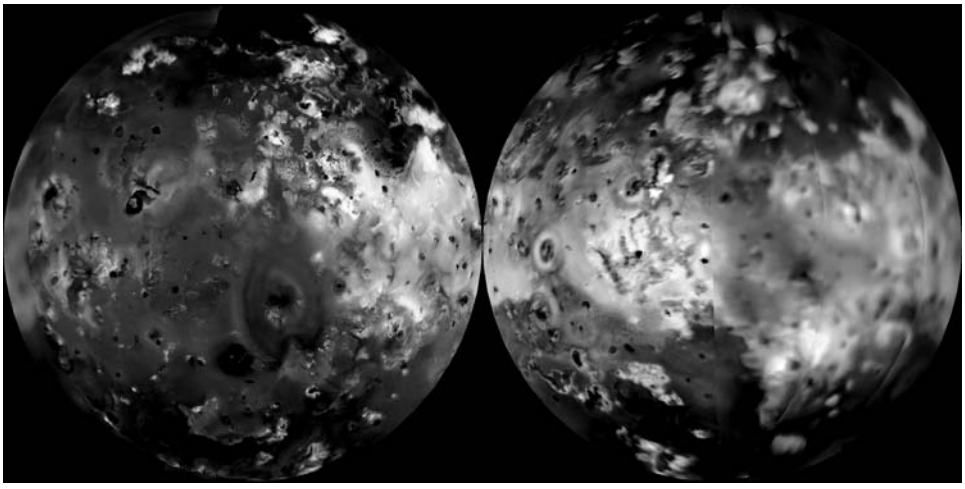

Figure 2.8. Mosaic of two hemispheres of Io from *Voyager* images. The *Voyager* images established that Io was devoid of impact craters and that Io's surface was the youngest in the Solar System. The detection of active volcanism caused a major shift in thinking regarding Io as a member of the outer Solar System of bodies (source: NASA Planetary Photojournal, image PIA00318.) (See also color section.)

crater-like depressions, dark circular features, and volcanic sources with radial flow patterns and bright halos. More detail is given in the review by Nash *et al.* (1986).

The role of silicate volcanism continued to be explored in the post-*Voyager* period using images from both spacecraft fly-bys, and continuing ground-based observations in the thermal-infrared. *Voyager 1* observed nine active plumes and 4 months later, *Voyager 2* observed eight of the nine as still active (Strom and Schneider, 1982). The images also permitted classification of the plumes into two categories. One group was comprised of three of the nine plumes observed by *Voyager 1*. This group was large, had distinct associated deposits consistent with the color of allotropic forms of sulfur, and appeared to be short-lived (a few days per eruption). The other group was characterized by plumes that were smaller in size, had distinct associated deposits which more closely resembled SO_2, and appeared to be continuous or very long-lived (McEwen and Soderblom, 1983).

2.4.4 The *Voyager* synthesis – sulfur or silicate volcanism?

The *Voyager* images of Io's volcanic surface provided morphological evidence which constrained the debate regarding the nature of the satellite's volcanism. While sulfur was one of the two materials which dominated Io's surface, the surface landform was silicate in nature. While sulfur could cover the outermost layers, elemental sulfur alone could not support the topography that the *Voyager* cameras observed. The underlying material was most likely silicate. A major question remained regarding silicate volcanism. Was the silicate volcanism occurring in the current epoch?

This question persisted as perhaps the major open issue following the first post-*Voyager* analyses. The answer to this question traces its origin to pre-*Voyager* observations in the thermal-infrared. Evidence for short episodes of high-temperature thermal activity had been presented in the literature (Section 2.2.2, see also Chapter 7) but was largely ignored because thermal anomalies of such large size were not expected on bodies as small as Io. However, the evidence continued to accumulate (Witteborn *et al.*, 1979). Between the two *Voyager* encounters Sinton (1980) reported a thermal outburst from his ground-based observations at a time when the Surt region on Io was visible from Earth. When *Voyager 2* flew by Io, it found that the Surt region had changed significantly during the time spanning the two fly-bys. Sinton *et al.* (1983) later summarized a series of observations noting eight outbursts, of which four could only be explained by temperatures having reached at least 700 K, consistent with the boiling point of sulfur in a vacuum (715 K).

Over the next few years various observers (Johnson *et al.*, 1984; Howell and McGinn, 1985) reported on continued monitoring efforts from ground-based observatories. Goguen and Sinton (1985) analyzed the polarization of infrared radiation from Io's hot spots and found that the emitter had an index of refraction that was closer to silicate than to elemental sulfur. Soon thereafter observers reported a thermal emission event that could only be interpreted as having originated from a flow that was 900 K, well above the boiling point of sulfur. They argued that this had to be a different material, perhaps giving evidence of silicate volcanism (Johnson *et al.*, 1988). Observations of high-temperature emissions continued over the next few years with still higher temperatures being reported. In their summary of this observation and reanalysis of earlier observations, Blaney *et al.* (1995) identified an event consistent with a flow temperature exceeding 1,200 K, and noted "... that the whole suite of Io's currently observed thermal anomalies was produced by multiple, high-eruptive-rate silicate flows within the past century". Thus, the case for silicate volcanism as the dominant mechanism at work in Io's hot crust was soundly established.

The post-*Voyager* synthesis gives us a view of Jupiter's strange moon in which silicate magmas, melted deep in Io by tidal heating, continue their slow recycling processes beneath a thin crust of sulfur and SO_2 frost. As they are ejected from Io's volcanic vents, sulfur and sulfur dioxide are continuously redistributed over the entirety of Io, burying older topography and creating new structures in a multicolored patchwork of flows, circles, and arcs. Here and there the bright pastel colors of Io are punctuated by a few molten, black silicate lakes distributed around the surface.

2.5 SUMMARY AND CONCLUSIONS

From the time of its discovery in 1610 to the mid-1800s, Io was a distinguished, but not a unique member of the set of four Galilean satellites, having utility as a means of determining the mass of Jupiter, finding geographic longitude of observers on Earth, and measuring the velocity of light. These merits, while not at all insignificant, are shared with the other three large moons, and do not capture the utterly unique

characteristics of Io that began to emerge as the techniques of increasingly modern astronomy were applied to it toward the end of the 19th and throughout the 20th centuries. The pace of discovery accelerated through these times, as photometry, spectroscopy, radiometry, and ultimately close-up spacecraft scrutiny revealed the extraordinary properties and behavior of the most volcanically active body in the Solar System.

Since the first indications of Io's unusual behavior emerged in the early 1960s, the framework of our understanding of this unique world has been restructured several times, built on the most reliable available information and most informed speculation. This example is not uncommon in planetary science, astronomy, and indeed in all of science, but in the case of Io the journey has taken us to a quite unexpectedly compelling world whose secrets and their implications continue to emerge.

We began this chapter with the discoveries of Galileo, the scientist, and we end it with the discoveries of the *Voyager* spacecraft. In the next chapter, Jason Perry reviews the discoveries of *Galileo*, the spacecraft. The scientist contributed immeasurably to our understanding of the Solar System as a whole, and spacecraft from *Pioneer* to *Galileo* have revealed both the charms and the secrets of one of its most fascinating worlds.

2.6 REFERENCES

Anderson, J. D., Null, G. W., and Wong, S. K. 1974. Gravitational parameters of the Jupiter system from the Doppler tracking of Pioneer 10. *Science*, **183**, 322–323.

Barnard, E. E. 1891a. Jupiter and his satellites. *Mon. Not. Royal Astron. Soc.*, **51**(9), 543–549.

Barnard, E. E. 1891b. On the phenomena of the transits of the first satellite of Jupiter. *Mon. Not. Royal Astron. Soc.,* **51**(9), 557–558.

Barnard, E. E. 1894. On the dark poles and bright equatorial belt of the first satellite of Jupiter. *Mon. Not. Royal Astron. Soc.*, **54**, 134–136.

Barnard, E. E. 1897. A micrometrical determination of the dimensions of the planets and satellites of the Solar System made with the 36-inch refractor of the Lick Observatory. *Popular Astronomy*, **5**, 285–302.

Bartholdi, P. and Owen, F. 1972. The occultation of beta Scorpii by Jupiter and Io, II: Io. *Astron. J.*, **77**, 60–65.

Bellucci, G., D'Aversa, E., Formisano, V., Cruikshank, D. P., Nelson, R. M., Matson, D., and Brown, R. H. 2004. Cassini/VIMS observation of an Io post-eclipse brightening event. *Icarus*, **172**, 141–148.

Bigg, E. K. 1964. Influence of the satellite Io on Jupiter's decametric emission. *Nature*, **203**, 1008–1010.

Binder, A. B. and Cruikshank, D. P. 1964. Evidence for an atmosphere on Io. *Icarus*, **3**, 299–305.

Binder, A. B. and Cruikshank, D. P. 1966. On the spectra of the Galilean satellites of Jupiter. *Astrophys. J.*, **144**, 1240–1241.

Blaney, D., Johnson, T. V., Matson, D. L., and Veeder, G. J. 1995. Volcanic eruptions on Io: Heat flow, resurfacing, and lava composition. *Icarus*, **113**, 220–225.

Broadfoot, A. L., Belton, M. J. S., Takacs, P. Z., Sandel, B. R., Shemansky, D. E., Holberg, J. B., Ajello, J. M., Atreya, S. K., Donahue, T. M., Moos, H. W., Bertaux,

et al. 1979. Extreme ultraviolet observations from *Voyager* encounter with Jupiter. *Science*, **204**, 979–982.

Brown, H. 1949. A table of relative abundances of nuclear species. *Rev. Modern Phys*., **21**, 625–634.

Brown, R. A. 1974. Optical line emission from Io. In: A. Woszczyk and C. Iwaniszewska (eds), *Exploration of the Planetary System* (IAU Symposium 65). Reidel, Dordrecht, pp. 527–531.

Brown, R. A. 1976. A model of Jupiter's sulfur nebula. *Astrophys. J*., **206**, L179–L183.

Brown, R. A. 1981. The Jupiter hot plasma torus: Observed electron temperature and energy flows. *Astrophys. J*., **244**, 1072–1080.

Brown, R. A. and Chaffee, F. H. 1974. High-resolution spectra of sodium emission from Io. *Astrophys. J. Let*., **187**, L125–L126.

Buratti, B. J., Mosher, J. A., and Terrile, R. J. 1995. First observational evidence for condensation of Io's SO_2 atmosphere on the nightside. *Icarus*, **118**, 418–422.

Caldwell, J. 1975. Ultraviolet observations of small bodies in the Solar System by OAO-2. *Icarus*, **25**, 384–396.

Carlson, R. W. and Judge, D. L. 1974. Pioneer 10 ultraviolet photometer observations at Jupiter encounter. *J. Geophys. Res*., **79**, 3623–3633.

Carr, M. H., Masursky, H., Strom, R. G., and Terrile, R. J. 1979. Volcanic features of Io. *Nature*, **280**, 729–733.

Clow, G. D. and Carr, M. H. 1980. Stability of sulfur slopes on Io. *Icarus*, **44**, 268–279.

Cruikshank, D. P. 1982. Barnard's satellite of Jupiter. *Sky & Telescope*, **64**, 220–224.

Cruikshank, D. P., Jones, T., and Pilcher, C. B. 1978. Absorption bands in the spectrum of Io. *Astrophys J. Let*., **225**, L89–L92.

Cruikshank, D. P., Emery, J. P., Kornei, K. A., Bellucci, G., Brown, R. H., Formisano, V., d'Aversa, E. 2006. Io: Time-resolved, near-infrared spectroscopy (1.9–4.2 μm) of eclipse reappearances. *Icarus* (submitted).

Dobbins, T. and Sheehan, W. 2004. The story of Jupiter's egg moons. *Sky & Telescope*, **107**(1), 114–120.

Fanale, F. P., Johnson, T. V., and Matson, D. L. 1974. Io: A surface evaporate deposit. *Science*, **186**, 922–924.

Fanale, F. P., Brown, R. H., Cruikshank, D. P., and Clark, R. N. 1979. Significance of absorption features in Io's IR reflectance spectrum. *Nature*, **280**, 761–763.

Fanale, F. P., Banerdt, W. B., and Cruikshank, D. P. 1981. Io: Could SO_2 condensation/sublimation cause the sometimes reported post-eclipse brightening? *Geophys. Res. Lett*., **8**, 625–628.

Fillius, R. W. and McIlwain, C. E. 1974. Measurements of the Jovian radiation belts. *J. Geophys. Res*., **79**, 3589–3599.

Fillius, R. W., McIlwain, C. E., and Mogro-Campo, A. 1975. Radiation belts of Jupiter: A second look. *Science*, **188**, 465–476.

Fink, U., Dekkers, N. H., and Larson, H. P. 1973. Infrared spectra of the Galilean satellites of Jupiter. *Astrophys. J. Let*., **179**, L155–L159.

Gillett, F. C., Merrill, K. M., and Stein, W. A. 1970. Albedo and thermal emission of Jovian satellites I–IV. *Astrophysical Let*., **6**, 247–249.

Goguen, J. D. and Sinton, W. M. 1985. Characterization of Io's volcanic activity by infrared polarimetry. *Science*, **230**, 65–69.

Goldreich, P. and Lynden-Bell, D. 1969. Io, a Jovian unipolar inductor. *Astrophys. J*., **156**, 59–78.

Hanel, R., Conrath, B., Flasar, M., Kunde, V., Lowman, P., Maguire, W., Pearl, J., Pirraglia, J., Samuelson, R., Gautier, D. *et al.* 1979. Infrared observations of the Jovian system from Voyager 1. *Science*, **204**, 972–976.

Hansen, O. L., 1973. Ten-micron eclipse observations of Io, Europa, and Ganymede. *Icarus*, **18**, 237–246.

Hansen, O. L. 1975. Infrared albedos and rotation curves of the Galilean satellites. *Icarus*, **26**, 24–29.

Hapke, B. W. 1979. Io's surface and environs: A magmatic volatile model. *Geophysical Res. Let.*, **6**, 779–802.

Harris, D. L. 1961. Photometry and colorimetry of planets and satellites. In: G. P. Kuiper and B. M. Middlehurst (eds), *Planets and Satellites*. University of Chicago Press, Chicago, pp. 272–342.

Herzberg, G. 1952. Spectroscopic evidence of molecular hydrogen in the atmospheres of Uranus and Neptune. *Astrophys. J.*, **115**, 337–340.

Howell, R. R., Cruikshank, D. P., and Fanale, F. P. 1984. Sulfur dioxide on Io: Spatial distribution and physical state. *Icarus*, **57**, 83–92.

Howell, R. R. and McGinn, M. T., 1985. Infrared speckle observations of Io: An eruption in the Loki region. *Science*, **230**, 63–65.

Jeans, J. 1925. *Dynamical Theory of Gases* (4th Edition). Cambridge University Press, Cambridge, UK.

Jeffreys, H. 1923. The constitution of the four outer planets. *Mon. Notices Roy. Astron. Soc.*, **83**, 350–354.

Johnson, J. H. 1931. The discovery of the first four satellites of Jupiter. *J. Brit. Astron. Assn.*, **41**, 164–171.

Johnson, T. V. 1971. Galilean satellites: Narrowband photometry 0.30 to 1.10 microns. *Icarus*, **14**, 94–111.

Johnson, T. V. and McCord, T. B. 1971. Spectral geometric albedos of the Galilean satellites. *Astrophys. J.*, **169**, 589–593.

Johnson, T. V., Cook, A. F., Sagan, C., and Soderblom, L. A. 1979. Volcanic resurfacing rates and implications for volatiles on Io. *Nature*, **280**, 746–750.

Johnson, T. V., Morrison, D., Matson, D. L., Veeder, G. J., Brown, R. H., and Nelson, R. M. 1984. Volcanic hotspots on Io: Stability and longitudinal distribution. *Science*, **226**, 134–137.

Johnson, T. V., Veeder, G. J., Matson, D. L., Brown, R. H., Nelson, R. M., and Morrison, D. 1988. Io: Evidence for silicate volcanism in 1986. *Science*, **242**, 1280–1283.

Kalinyak, A. A. 1965. Data on the spectra of the Galilean satellites of Jupiter. *Astronomicheskii Zhurnal*, **42**, 1067–1069 (translation in *Soviet Astron. AJ.*, **9**, 824–825, 1966).

Kliore, A. J., Caine, D. L., Fjeldbo, G., Seidel, B. L., and Rasool, S. I. 1974. Preliminary results on the atmospheres of Jupiter and Io from the Pioneer 10 S-band occultation experiment. *Science*, **183**, 323.

Kliore, A. J., Fjeldbo, G., Seidel, B., Sweetman, D., Sesplaukis, T., and Woiceshyn, P. 1975, Atmosphere of Io from Pioneer 10 radio occultation measurements. *Icarus*, **24**, 407–410.

Krimigis, S. A., Armstrong, T. P., Axford, W. I., Bostrom, C. O., Fan, C.Y., Gloeckler, G., Lanzerotti, L. J., Keath, E. P., Zwickl, R. D., Carbary, J. F., *et al.* 1979. Low-energy charged particle environment at Jupiter: A first look. *Science*, **204**, 998–1003.

Kuiper, G. P. 1944. Titan, a satellite with an atmosphere. *Astrophys. J.*, **100**, 374–383.

Kuiper, G. P. 1949. Survey of planetary atmospheres. In: G. P. Kuiper (ed.), *The Atmospheres of the Earth and Planets*. Chicago University Press, Chicago, pp. 304–345.

Kuiper, G. P. 1957. Infrared observations of planets and satellites. *Astron. J.*, **62**, 295 (abstract).

Kuiper, G. P. 1973. Comments on the Galilean satellites. *Comm. Lunar. Planet. Lab.*, **10**, 28–34.

Kuiper, G. P., Wilson, W., and Cashman, R. J. 1947. An infrared stellar spectrometer. *Astrophys. J.*, **106**, 243–250.

Kupo, I., Mekler, Y., and Eviatar, A. 1976. Detection of ionized sulfur in the Jovian magnetosphere. *Astrophys. J. Let.*, **205**, L51–L53.

Lee, T. 1972. Spectral albedos of the Galilean satellites. *Comm. Lunar Planet. Lab.*, **9**(168), 179–180.

Lynn, W. T. 1903. Simon Marius and the satellites of Jupiter. *Observatory*, **26**, 254–256.

Matson, D. L., Johnson, T. V., and Fanale, F. P. 1974. Sodium-D line emission from Io: Sputtering and resonant scattering hypothesis. *Astrophys. J. Let.*, **192**, L43–L46.

McEwen, A. S. and Soderblom, L. A. 1983. Two classes of volcanic plumes on Io. *Icarus*, **55**, 191–198.

McGrath, M. A., Belton, M. J. S., Spencer, J. R., and Sartoretti, P. 2000. Spatially resolved spectroscopy of Io's Pele plume and SO_2 atmosphere. *Icarus*, **146**, 476–493.

Michelson, A. A. (1891). Measurement of Jupiter's Satellites by Interference. *Pub. Astron. Soc. Pacific*, **3**, 274–278.

Minnaert, M. 1941. The reciprocity principle in lunar photometry. *Astrophys. J.*, **93**, 403–410.

Minton, R. B. 1973. The red polar caps of Io. *Comm. Lunar Planet. Lab.*, **10**, 35–39.

Morabito, L. A., Synnott, S. P., Kupferman, P. N., and Collins, S. A. 1979. Discovery of currently active extraterrestrial volcanism. *Science*, **204**, 972.

Moroz, V. I. 1966. Infrared spectroscopy of the Moon and Galilean Satellites. *Soviet Astron.-A. J.*, **9**, 999–1006 (original article appeared in 1965).

Moroz, V. I. 1967. *Fisika Planet*. Nauka, Moscow, 496 pp. (translated in *Physics of the Planets*, 1969, p. 389, NASA TT F-515).

Morrison, D. and Cruikshank, D. P. 1973. Thermal properties of the Galilean satellites. *Icarus*, **18**, 224–236.

Morrison, D., Cruikshank, D. P., and Murphy, R. E. 1972. Temperatures of Titan and the Galilean satellites at 20 microns. *Astrophys. J. Let.*, **173**, L143–L146.

Morrison, D. and Morrison, N. D. 1977. Photometry of the Galilean Satellites. In: J. A. Burns (ed.), *Planetary Satellites*. University of Arizona Press, Tucson, pp. 363–378.

Morrison, D., Morrison, N. D., and Lazarewicz, A. 1974. Four-color photometry of the Galilean satellites. *Icarus*, **23**, 399–416.

Murray, B. C., Wildey, R. L., and Westphal, J. A. 1964. Observations of Jupiter and the Galilean satellites at 10 microns. *Astrophys. J.*, **139**, 986–993.

Nash, D. B. and Fanale, F. P. 1977. Io's surface composition based on reflectance spectra of sulfur/salt mixtures and proton irradiation experiments. *Icarus*, **31**, 40–80.

Nash. D. B., Fanale, F. P., and Nelson, R. M. 1980. SO_2 frost: UV–visible reflectivity and Io's surface coverage. *Geophys. Res. Let.*, **7**, 665–668.

Nash, D. B. and Nelson, R. M. 1978. Spectral evidence for sublimates and adsorbates on Io. *Nature*, **280**, 763–766.

Nash, D. B., Carr, M. H., Gradie, J., Hunten, D. M., and Yoder, C. F. 1986. Io. In: J. Burns and M. S. Matthews (eds.), *Satellites*. University of Arizona Press, Tucson, pp. 629–688.

Nelson, R. M. and Hapke, B. W. 1978. Spectral reflectivities of the Galilean satellites and Titan 0.32-0.86 micrometers. *Icarus*, **36**, 304–329.

Nelson, R. M., Lane, A. L., Matson, D. L., Fanale, F. P., Nash, D. B., and Johnson, T. V. 1980. Io: Longitudinal distribution of sulfur dioxide frost. *Science*, **210**, 784–786.

Nelson, R. M., Lane, A. L., Morrill, M. E., Wallis, B. D., Gibson, J., Smythe, W. D., Horn, L. J. and Buratti, B., 1993. The brightness of Jupiter's satellite Io following emergence from eclipse: Selected observations, 1981–1989. *Icarus*, **101**, 223–233.

Pagnini, P. 1931. Galileo and Simon Mayer. *J. Brit. Astron. Assn.*, **41**, 415–422.

Peale, S., Cassen, P., and Reynolds, R. 1979. Melting of Io by tidal dissipation. *Science*, **203**, 892–894.

Pearl, J. S., Hanel, R., Kunde, V., Maguire, W., Fox, K., Gupta, S., Ponnamperuma, C., and Raulin, F. 1979. Identification of gaseous SO_2 and new upper limits for other gases on Io. *Nature*, **280**, 755–758.

Pickering, E. C. 1907. Harvard Ann. 52 (part 1). *Eclipse of Jupiter's Satellites, 1878–1903*.

Piddington, J. H. and Drake, J. F. 1968. Electrodynamic effects of Jupiter's satellite Io. *Nature*, **217**, 935–937.

Pilcher, C. B., 1980. Images of Jupiter's sulfur ring. *Science*, **207**, 181–183.

Pilcher, C. B., Ridgeway, S. T., and McCord, T. B. 1973. Galilean Satellites: Identification of water frost. *Science*, **178**, 1087–1089.

Pollack, J. B. and Reynolds, R. T. 1974. Implications of Jupiter's early contraction history for the composition of the Galilean satellites. *Icarus*, **21**, 248–253.

Pollack, J. B., Witteborn, F. C., Erickson, E. F., Strecker, D. W., Baldwin, B. J., and Bunch, T. E., 1978. Near-infrared spectra of the Galilean satellites: Observations and compositional implications. *Icarus*, **36**, 271–303.

Russell, H. N., Dugan, R. S., and Stewart, J. Q. 1945. *Astronomy* (Vol. 1). Ginn & Co., New York, 371 pp.

Sagan, C. 1979. Sulfur flows on Io. *Nature*, **280**, 750–753.

Sampson, R. A. 1910. *Tables of the Four Great Satellites of Jupiter*. W. Wesley & Son, London.

Saur, J. and Strobel, D. F. 2004. Relative contributions of sublimation and volcanoes to Io's atmosphere inferred from its plasma interaction during solar eclipse. *Icarus*, **171**, 411–420.

Secosky, J. J. and Potter, M. 1994. A Hubble Space Telescope study of post-eclipse brightening and albedo changes on Io. *Icarus*, **111**, 73–78.

Shapley, H. and Howarth, H. E. 1929. *A Source Book in Astronomy*. McGraw-Hill, New York.

Sheehan, W. 1995. *The Immortal Fire Within: The Life and Work of Edward Emerson Barnard*. Cambridge University Press, Cambridge, UK, 443 pp.

Sill, G. T. 1973. Reflection spectra of solids of planetary interest. *Comm. Lunar Planet. Lab.*, **10**(184), 1–7.

Sill, G. T. and Clark, R. N. 1982. Composition of the surfaces of the Galilean satellites. In: D. Morrison (ed.), *Satellites of Jupiter*. University of Arizona Press, Tucson, pp. 174–212.

Simonelli, D. P., Veverka, J., Senske, D. A., Fanale, F. P., Schubert, G., and Belton, M. J. S. 1998. Galileo search for SO_2 frost condensation on Io's nightside. *Icarus*, **135**, 166–174.

Simpson, J. H., Hamilton, D. C., McKibben, R. B., Mogro-Campo, A., Pyle, K. R., and Tuzzolino, A. J. 1974. The protons and electrons trapped in the Jovian dipole magnetic field and their interaction with Io. *J. Geophys. Res.*, **79**, 3522–3544.

Simpson, J. H., Hamilton, D. C., Lents, G. A., McKibben, R. B., Perkins, M., Pyle, K. R., and Tuzzolino, A. J. 1975. Jupiter revisited: First results from the University of Chicago charged particle experiment on Pioneer 11. *Science*, **188**, 455–458.

Sinton, W. M. 1980. Io's 5 micron variability. *Astrophys. J. Lett.*, **235**, L49–L51.

Sinton, W. M., Lindwall, D., Cheigh, F., and Tittemore, W. C. 1983. Io: The near-infrared monitoring program, 1979–1981. *Icarus*, **54**, 133–157.

Smith, B. A. and Smith, S. A. 1972. Upper limits for an atmosphere on Io. *Icarus*, **17**, 218–222.

Smith, B. A. and 21 coauthors. 1979. The Jupiter system through the eyes of Voyager 1. *Science*, **204**, 951–972.

Smythe, W. D., Nelson, R. M., and Nash, D. B. 1979. Spectral evidence for SO_2 frost or adsorbate on Io's surface. *Nature*, **280**, 766.

Soderblom, L. A., Johnson, T. V., Morrison, D., Danielson, G. E., Smith, B., Veverka, J., Cook, A., Sagan, C., Kupferman, P., Pieri, D., *et al.* 1980. Spectrophotometry of Io: Preliminary Voyager 1 results. *Geophys. Res. Let.*, **7**, 963–966.

Stebbins, J. 1927. The light variations of the satellites of Jupiter and their applications to measures of the solar constant. *Lick Obs. Bull.*, **13**, 1–11.

Stebbins, J. and Jacobson, T. S. 1928. Further photometric measures of Jupiter's satellites and Uranus, with tests for the solar constant. *Lick Obs. Bull.*, **13**, 180–195.

Strom, R. G., Terrile, R. G., Masursky, H., and Hansen, C. 1979. Volcanic eruption plumes on Io. *Nature*, **280**, 733–736.

Strom, R. G. and Schneider, N. M. 1982. Volcanic eruptions on Io. In: D. Morrison (ed.), *Satellites of Jupiter*. University of Arizona Press, Tucson, pp. 598–633.

Suess, H. E. and Urey, H. C. 1956. Abundances of the elements. *Rev. Mod. Phys.*, **28**, 53–74.

Tammann, G. 1931. Die Anderungen der chemischen Zusammensetzung in der Erde. *Handbuch der Experimental Physik*, **25**(part 2), 3–28 (quoted in Wildt, 1969).

Taylor, G. E. 1972. The determination of the diameter of Io from its occultation of β-Scorpii on May 14, 1971. *Icarus*, **17**, 202–208.

Trafton, L. 1975. Detection of a potassium cloud near Io. *Nature*, **258**, 690–692.

Trainor, J. H., McDonald, F. B., Teegarden, B. J., Webber, W. R., and Roelof, E. C. 1974. Energetic particles in the Jovian magnetosphere. *J. Geophys. Res.*, **79**, 3600–3613.

Trainor, J. H., McDonald, F. B., Stilwell, D. E., and Teegarden, B. J. 1975. Jovian protons and electrons, Pioneer 11 results. *Science*, **188**, 463–465.

Urey, H. C. 1952. *The Planets, Their Origin and Development*. Yale University Press, New Haven, 245 pp.

Van Allen, J. A., Baker, D. N., Randall, B. A., and Sentman, D. D. 1974. The magnetosphere of Jupiter as observed with Pioneer 10. Instruments and principal findings. *J. Geophys. Res.*, **79**, 3559–3577.

Van Allen, J. A., Randall, B. A., Baker, D. N., Goetz, C., Sentman, D. D., Thompson, M. F., and Flint, H. R. 1975. Pioneer 11 observations of energetic particles in the Jovian magnetosphere. *Science*, **188**, 459–462.

van de Hulst, H. 1957. *Light Scattering by Small Particles*. Wiley, New York, 470pp.

Veverka, J., Simonelli, D., Thomas, P., Morrison, D., and Johnson, T. V., 1981. Voyager search for post-eclipse brightening on Io. *Icarus*, **47**, 60–74.

Wamsteker, W. 1972. Narrow-band photometry of the Galilean satellites. *Comm. Lunar Planet. Lab.*, **9**(167), 171–177.

Wamsteker, W., Kros, R. L., and Fountain, J. A. 1974. On the surface composition of Io. *Icarus*, **23**, 417–424.

Wildt, R. 1932. Absorptionsspektren und Atmosphären der großen Planeten. Nachrichten der Gesselschaft de Wissenschaften zu Göttigen. *Mathematisch–Physikalische Klasse, Heft*, **22**, 87–96.

Wildt, R. 1969. The outer planets: Some early history. *J. Atmos. Sci.*, **26**, 795–797.

Wisniewski, W. and Andersson, L. 1973. Observations with a 500-channel spectrometer: Low-resolution spectra of the Galilean satellites and Titan. Scheduled for *Comm. Lunar Planet. Lab.*, but unpublished.

Witteborn, F. C., Bregman, J. D., and Pollack, J. B. 1979. Io: An intense brightening near 5 microns. *Science*, **203**, 643–646.

3

A summary of the *Galileo* mission and its observations of Io

Jason Perry, Rosaly M. C. Lopes, John R. Spencer, and Claudia Alexander

3.1 *GALILEO* ERA: 1995–2003

Even before the arrival of the two *Voyager* spacecraft at Jupiter in 1979, planning began at the Jet Propulsion Laboratory (JPL) for the Jupiter Orbiter with Probe. The mission received Congressional approval in 1977 and was renamed *Galileo* in 1978. The launch of *Galileo*, originally planned for 1982, was repeatedly delayed through the 1980s, first due to development problems with the Space Shuttle, then due to issues with the upper stage motor, and finally due to the Space Shuttle *Challenger* disaster. With a firm political commitment to launch *Galileo* from the Space Shuttle, the launch would have to wait until 18 October 1989. Due to safety recommendations following the *Challenger* disaster, *Galileo* was forced to use a lower powered upper stage than originally planned, requiring it to spiral out to Jupiter, using gravity assists at Venus and Earth to boost it on its way (Harland, 2000).

As one of NASA's unmanned Flagship-class missions, *Galileo* was heavily instrumented, with five remote-sensing instruments and six fields and particles instruments (Table 3.1), plus celestial mechanics and radio propagation experiments. The five imaging instruments covered a wide range of wavelengths, from the extreme ultraviolet to the mid-infrared. Among the objectives for the remote-sensing instruments were characterization of Io's surface morphology, geology, and physical state; investigation of the surface mineralogy and distribution of compositional units; investigation of the extent and characteristics of volcanic activity, and studies of the atmosphere and its relation to volcanic plumes.

The imaging system on *Galileo*, known as the solid-state imaging system (SSI), was comprised of a charge-coupled device with an 800×800-pixel array on a narrow-angle Cassegrain telescope (Belton *et al.*, 1992). The SSI camera had eight filter positions ranging from a violet filter centered at 418 nm to a 1MC filter with a bandpass centered at 990 nm (McEwen *et al.*, 1998a). The near-infrared mapping spectrometer (NIMS) instrument was a scanning instrument capable of taking a

Table 3.1. *Galileo* science instrument payload.

Device	Institution	Principal investigator	Primary measurements
Atmosphere structure instrument (ASI)	Ames Research Center	A. Seiff	Pressure, temperature, and density
Nephelometer (NEP)	Ames Research Center	B. Ragent	Cloud particle size, shape, and number density
Helium abundance detector (HAD)	University of Bonn	Ulf von Zahn	He/H_2 ratio to ~0.1%
Net flux radiometer (NFR)	Ames Research Center	R. Boese	Net planetary and solar fluxes, cloud locations, water and ammonia abundance
Neutral mass spectrometer (NMS)	Goddard Space Flight Center	H. Niemann	Composition in 1–150 AMU range
Lightning and radio emissions detector (LRD)	Bell Laboratories Max-Planck Institute	L. Lanzerotti K. Rinnert	Existence and characteristics of lightning
Energetic particle instrument (EPI)	University of Kiel, Ames Research Center	H. Fischer J. Mihalov	Energetic particle distribution from 5 Jupiter radii to entry
Solid-state imaging (SSI)	National Optical Astronomy Observatories	M. Belton	Map Galilean satellites at roughly 1-km resolution, and monitor atmospheric circulation
Near-infrared mapping spectrometer (NIMS)	JPL	R. Carlson	Surface composition, atmospheric composition and temperature
Ultraviolet spectrometer (UVS)	University of Colorado	C. Hord I. Stewart	Gases and aerosols in Jovian atmosphere, auroral emissions, satellite atmospheric airglow
Extreme-ultraviolet spectrometer (EUV)	University of Colorado	C. Hord K. Simmons	S, O ion emissions of the Io torus, and atomic and molecular H auroral and airglow emissions
Photopolarimeter and radiometer (PPR)	Goddard Institute for Space Studies	J. Hansen	Distribution and character of atmospheric particles; surface temperatures of the satellites
Magnetometer (MAG)	University of California	M. Kivelson	Monitor magnetic field for strength and changes
Energetic particles detector (EPD)	Johns Hopkins Applied Physics Laboratory	D. Williams	High-energy electrons, protons, and heavy ions in the magnetosphere and processes affecting these populations
Plasma detector subsystem (PLS)	University of Iowa	L. Frank	Composition, energy, and 3-D distribution of low- to medium-energy electrons and ions
Plasma wave subsystem (PWS)	University of Iowa	D. Gurnett	Electromagnetic waves and wave–particle interactions
Dust detector subsystem (DDS)	Max Planck Institut für Kernphysik	E. Grun H. Krueger	Mass, velocity, and charge of dust particles
Heavy ion counter (HIC)	California Institute of Technology	T. Garrard E. Stone	Composition, and energy of low-energy ions in the environment
Celestial mechanics	JPL	J. Anderson	Masses and internal structures of Jupiter and its satellites
Radio propagation	Stanford University	H. T. Howard	Atmospheric structure and objects' radii

408-wavelength spectrum in the range 0.7–5.2 μm, therefore measuring both reflected sunlight and thermal emission (Carlson *et al*., 1992). NIMS formed spectra using 17 detectors in combination with a moving grating. The 17 wavelengths (spaced across the wavelength range) obtained for each grating position were acquired simultaneously. During the *Galileo* nominal mission, and the *Galileo* Europa mission (GEM), two of the NIMS detectors stopped working, and the sensitivity of the first two detectors was considerably reduced. Prior to the first NIMS observations in the Io fly-by I24, grating motion ceased, probably from radiation damage to the electronics. Therefore, the observations during the Io fly-bys obtained only 13 wavelengths (though acquiring 24 samples of each instead of 1), in the rage 1.0–4.7 μm. The reduced number of wavelengths was suitable for temperature determination and band ratio mapping (for SO_2) but the instrument's ability to search for unknown surface compounds was compromised.

The photopolarimeter and radiometer (PPR) instrument (Russell *et al*., 1992) conducted three separate types of measurements in one instrument: photometry, polarimetry, and radiometry. The radiometry experiment was most useful for Io, measuring thermal emission at much longer wavelengths (visible–100 μm), and thus detecting colder temperatures than NIMS. This allows for more effective estimation of the total heat flow from Io's interior as well as measurements of the thermal emission from the sunlit surface. PPR's low spatial resolution limited its usefulness for Io studies until the close fly-bys in 1999 and onward. In addition *Galileo's* ultraviolet spectrometer (UVS) obtained spectra of Io in the 2,100–3,200-Å region, though radiation noise near Jupiter did not permit useful observations from ranges less than about 500,000 km.

The six *in situ* instruments (Russell *et al*., 1992; see Table 3.1) consisted of a magnetometer (MAG), an energetic particles detector (EPD), a plasma detector subsystem (PLS), a plasma wave subsystem (PWS), a dust detector subsystem (DDS), and a heavy ion counter (HIC). The MAG monitored magnetic fields of the environment for overall strength and the smaller changes related to the dynamics of the system such as the presence of large-scale waves. The particle energy spectrum in its totality was covered by three instruments: an EPD, which measured the energetic end of the particle energy range, from 20–890 keV – exact range being dependent upon the MeV per nucleon measured; a PLS, which measured the medium- to low-energy range of the particle spectrum, from 1 eV to 50 keV; and an HIC, which measured energetic heavy particles from 6–200 MeV per nucleon. These instruments gathered information on the velocity and density of the plasma, and also served as mass spectrometers. The EPD measured, among other things, elemental species of Helium through Iron from 10 keV per nucleon to 15 MeV per nucleon, the PLS measured masses largely in a range from 1–18 atomic mass units (AMU), and the HIC measured typically 6–18 MeV per nucleon: oxygen, sodium, carbon, sulfur, etc. The PWS acted as a radio receiver, picking up electric and magnetic signals in the range 5 Hz to 5 MHz on the electric antenna, and 5 Hz to 160 kHz on the magnetic antenna. The DDS detected the impacts of mass 10^{-19} to 10^{-9} kg. The PWS detected plasma waves and other radio signals in the environment such as the characteristic signal of plasma losing energy while gyrating around field lines (gyrofrequencies), the

characteristic signal of large-scale oscillations of the plasma in the field (plasma frequencies), and other characteristic motions of plasma. The fields and particles instruments worked together to investigate the environment of Io with more synergy than common with remote-sensing instruments. This was because magnetic field measurements as well as particle density measurements were required to properly determine selected characteristic parameters of the plasma activity, not only at Io but throughout the magnetosphere. The investigation of Io's interaction with Jupiter's magnetosphere was one of the major objectives of the *Galileo* mission. Among the questions these fields and particles instruments aimed to answer were: Did Io generate its own magnetic field? How significant was Io's influence on the magnetosphere of Jupiter?

The mission plan for *Galileo* called for 11 orbits of Jupiter following orbit insertion on 7 December 1995. During each orbit except the 5th, when *Galileo* and Jupiter were in solar conjunction, *Galileo* would fly-by one of the Galilean satellites: 4 fly-bys of Ganymede, 3 fly-bys of Callisto, and 3 fly-bys of Europa (Table 3.2). *Galileo*'s only close approach of Io would take place shortly before orbit insertion, otherwise it would stay well outside the orbit of Io to prevent encountering dangerous radiation. During the mission, thousands of images of Io were expected, including a number of movies showing variability within Io's volcanic plumes. Unfortunately, *Galileo*'s high-gain antenna failed to deploy. The antenna was designed to fold up like an umbrella to allow the spacecraft to be stowed in the Space Shuttle's cargo bay, and then unfurl during cruise to Jupiter. However, during deployment, one of the pins that made up the structural framework of the antenna became stuck. Due to this malfunction, the low-gain antenna (LGA) would have to be used for the duration of the mission, dramatically reducing the size of the data set returned by *Galileo*. Instead of returning data at an impressive rate of 134 kilobits per second with the high-gain antenna, *Galileo* was expected to achieve only 10 bits per second with the LGA. Thankfully, improved compression algorithms and data management on the spacecraft and upgrades to the Deep Space Network on Earth allowed the effective information flow from *Galileo* through the LGA to increase by a factor of 100. While, this still meant that the data set from *Galileo* of Io would be much smaller than expected (preventing the much-anticipated plume movies), the bandwidth was adequate for most science objectives to be accomplished.

3.2 JOI AND "THE LOST IO FLY-BY"

The only Io fly-by during the nominal *Galileo* mission took place shortly before Jupiter orbit insertion (JOI). The fly-by occurred at an altitude of 897 km over 8.5° south latitude, 101.1° west longitude (Anderson *et al*., 1996). This in-bound fly-by would allow for remote-sensing observations of the anti-Jovian hemisphere, as well as investigations of Io's possible magnetic field and interactions between Io and Jupiter's magnetic field. Then, with just 2 months to go until arrival at Jupiter, the planned

Table 3.2. *Galileo* orbits and Io activities.

Orbit	Fly-by satellite	Date of main fly-by in orbit	Closest approach distance to Io (km)	Notable Io activities
J0	Io	12/7/1995	897	Close fly-by: fields and particles observations, no remote sensing. Gravitational detection of Io's core
G1	Ganymede	6/27/1996	697,000	Distant observations of surface changes since *Voyager*, NIMS dayside and nightside maps, high-phase imaging, first eclipse images
G2	Ganymede	9/6/1996	441,000	Color imaging of anti-Jupiter hemisphere, NIMS maps
C3	Callisto	11/4/1996	244,000	Topography of anti-Jupiter hemisphere, high-phase imaging of the sodium cloud
E4	Europa	12/19/1996	321,000	Global color imaging
5	None			
E6	Europa	2/20/1997	401,000	Eclipse imaging
G7	Ganymede	4/5/1997	531,000	NIMS observations of Loki
G8	Ganymede	5/7/1997	956,000	Eclipse imaging, auroral emissions
C9	Callisto	6/25/1997	607,000	Discovery of Pillan eruption
C10	Callisto	9/17/1997	319,000	Dark Pillan deposits first seen
E11	Europa	11/6/1997	780,000	SSI plume inventory
E12	Europa	12/16/1997	485,000	NIMS spectral maps
13	None		438,000	
E14	Europa	3/29/1998	252,000	Multi-spectral color of anti-Jupiter hemisphere
E15	Europa	5/31/1998	312,000	Best UVS observation, color eclipse imaging
E16	Europa	7/21/1998	702,000	NIMS spectral maps
E17	Europa	9/26/1998	800,000	
E18	Europa	11/22/1998	996,000	
E19	Europa	2/1/1999	856,000	
C20	Callisto	5/5/1999	789,000	NIMS spectral maps
C21	Callisto	6/30/1999	127,000	Best SSI resolution yet on the anti-Jupiter hemisphere
C22	Callisto	8/14/1999	737,000	Distant plume monitoring, NIMS maps
C23	Callisto	9/16/1999	448,000	
I24	Io	10/11/1999	611	First close-up remote sensing
I25	Io	11/26/1999	301	Tvashtar eruption images (SSI, NIMS)
E26	Europa	1/03/2000	340,000	Color imaging of Loki–Daedaldus region, NIMS maps
I27	Io	2/22/2000	198	Trouble-free fly-by, high-resolution remote sensing
G28	Ganymede	5/20/2000	379,000	
G29	Ganymede	12/28/2000	963,000	Distant imaging: Tvashtar plume, NIMS maps
C30	Callisto	5/25/2001	342,000	NIMS dayside, nightside maps
I31	Io	8/6/2001	194	Discovery of Thor eruption (NIMS and SSI), high-resolution remote sensing
I32	Io	10/16/2001	184	Trouble-free fly-by, high-resolution remote sensing
I33	Io	1/17/2002	102	Almost all remote sensing lost
A34	Amalthea	11/7/2002	45,800	Trailing hemisphere observations scrapped due to budget constraints
J35	Jupiter	9/21/2003	impact	

science observations at Io had to be drastically curtailed as a result of a serious tape recorder anomaly. Following the first image of the Jupiter system, the commanded tape recorder rewind failed. Telemetry showed the recorder was running but the tape was not moving. The tape recorder was the key to the LGA mission for storage of high-rate data, including the Probe data, remote sensing, and high-rate fields and particles data.

Investigation suggested that the tape was sticking to one of the heads and was slipping on the capstan. A spacecraft test on 20 October 1995 moved the tape forward for a few seconds and a comprehensive program was begun to characterize tape motion and derive a set of operating rules to minimize the chance of subsequent sticking. It was believed that the motor would always have sufficient authority in the forward direction to break the tape free. After JOI, flight software was augmented to directly control some of the recorder functions and to detect a stuck tape and stop the recorder in that event. These precautions worked well for the next 6 years, until April 2002 when the tape stuck again.

As the tape recorder investigation proceeded, project leaders had to make a painful decision regarding science observations inbound to Jupiter. Only the slowest tape speed had been demonstrated to be safe and would be sufficient to capture the one-time only Probe data acquisition as the Orbiter overflew the descending Probe. Unique fields and particles data at Io, and in the Io torus, were also benign and those observations were added to the revised science plan at little risk. Unfortunately, inbound remote sensing of Jupiter, Europa, and Io, and other high-rate data had to be eliminated from the arrival sequence. This change would maximize the chances of securing the Probe data and preserving the recorder for its now virtually essential role in *Galileo*'s orbital tour.

The magnetometer and plasma measurements during the fly-by were preserved in this adjusted science data acquisition plan, however, at a lower resolution than desired. As a result, the magnetometer measurements at JOI were inconclusive regarding the presence of an internal field, and at odds with the results of the plasma instrument (Kivelson *et al.*, 1996). The question of whether Io had an internally generated magnetic field, or whether the magnetic signal could be entirely explained by currents driven in its extended ionosphere had to wait for the acquisition of additional data. Studies of the torus using plasma waves generated in the region had to be abandoned because of the tape recorder restrictions. Sufficient data were acquired that questions of charge exchange and ion pickup between the ionosphere and the torus could be addressed in the ensuing months (Huddleston *et al.*, 1998). The intensity of current along the Io auroral footprint field lines was a surprise. Intense electron beams were found to be streaming along the Io flux tube, the cylindrical volume created by the magnetic field lines that connect Io with Jupiter. The electron beams were found to be aligned with the magnetic field and moving both up and down the field lines. Analysis showed that the electrons were accelerated in the region of Io's flux tube just above Jupiter's ionosphere and form the downward current portion of the current system associated with Io's interaction with Jupiter's co-rotating plasma. This current system is illustrated in Figure 3.1.

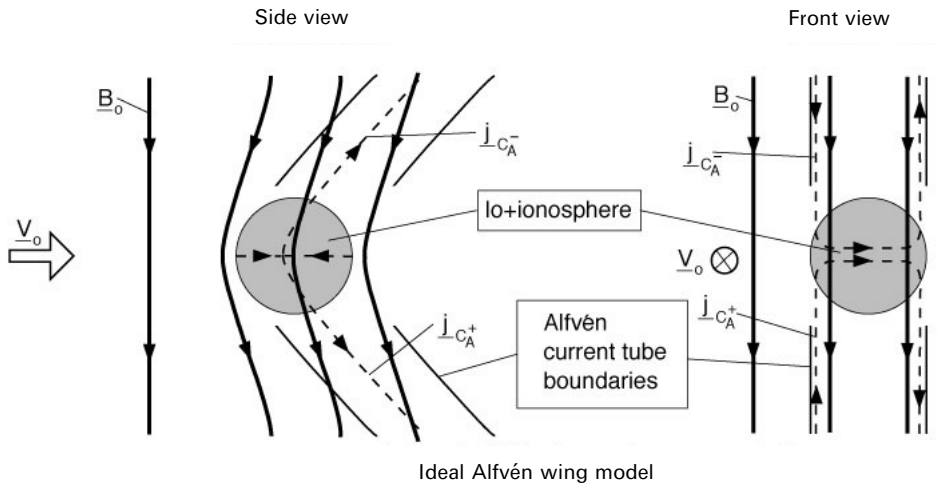

Figure 3.1. Side view and the front view of the ideal Alfvén wing model applied to Io. In the side view, Jupiter is located behind Io, in the front view Jupiter is to the far left. Magnetic field lines are bold with arrows, current flow lines are dashed with arrows, the boundaries of the current tubes are solid. Currents leaving the near-field region are connected along Alfvén characteristics to the Alfvén current tubes closing in the far-field region (after Saur *et al.*, 2004).

3.3 IO OBSERVATIONS IN THE *GALILEO* NOMINAL MISSION

Despite never coming closer than 244,000 km to Io during the nominal mission following orbit insertion, the various remote-sensing instruments on *Galileo* observed Io during almost every orbit, monitoring Io's active volcanic vents and searching for surface changes. Figure 3.2 shows a map of Io using false color images taken during the first two orbits of the *Galileo* mission. Numerous surface changes were observed between *Voyager* and *Galileo* imaging, particularly at Prometheus (new lava flow), Ra Patera (new white and yellow deposits), Euboea Fluctus (new red deposits), and Surt and Aten Paterae (*Voyager 2* plume deposits faded). Despite extensive activity observed from Earth between the *Voyager* fly-bys and the *Galileo* mission, no major surface changes were observed at Loki, Io's most energetic hot spot. As the mission progressed, some remarkable surface changes were detected, such as the change following the Pillan eruption described below.

Early *Galileo* images revealed new active volcanic centers (e.g., McEwen *et al.*, 1997, 1998a; Lopes-Gautier *et al.*, 1997, 1999), including Zamama, Gish Bar, Pillan, and Culann. *Galileo* also detected hot spots for the first time at Marduk and Prometheus, where *Voyager* had detected plumes. During the first ten orbits of *Galileo*, NIMS and SSI detected a total of 41 previously unknown hot spots (Lopes-Gautier *et al.*, 1999). The SSI was able to detect thermal emission from hot spots displaying high temperatures (>700 K) when observing Io in eclipse using its 1-μm filter, while NIMS was able to detect hot spots during both day-

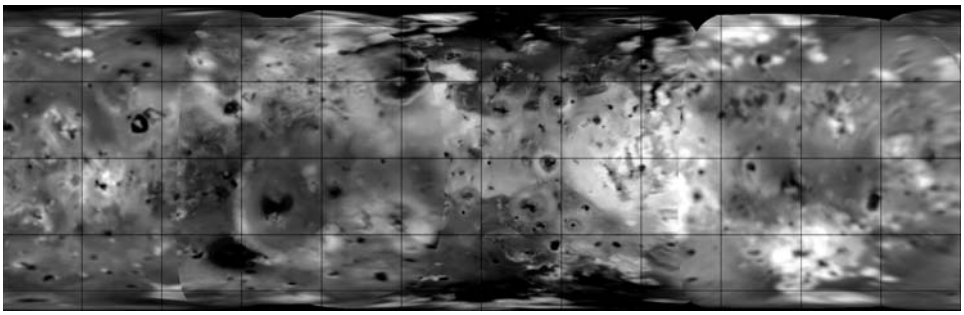

Figure 3.2. Color mosaic of images taken during the 1st and 2nd orbits during the *Galileo* nominal mission. A grid was overlain with 30° by 30° spacing. Numerous changes were observed between *Voyager* and *Galileo* but the overall pattern of volcanic centers and overall color variation was still recognizable, indicating that surface changes were limited to the area around volcanic centers that repeatedly erupted (NASA press release image PIA00585). (See also color section.)

time and night-time or eclipse observations and could detect temperatures down to about 200 K. Numerous other "suspect" spots were seen by both NIMS and SSI. Notably, SSI detected numerous bright spots at 1 μm near the sub-Jovian point of Io, however it is unclear whether those spots were active volcanic vents, local gas emissions, or something else (McEwen *et al.*, 1998a). In addition to thermal emission, SSI observations of Io in eclipse also revealed aurora produced by interactions between Io's atmosphere and plumes and the magnetospheric plasma (Geissler *et al.*, 1999).

A number of high-phase observations were also obtained during these first two orbits, allowing for imaging of Io's plume activity. A plume was found at Ra Patera during the first orbit, despite the lack of a hot spot detection by SSI (McEwen *et al.*, 1998a). Subsequent observations during the mission (by SSI, NIMS, and PPR) failed to detect a hot spot at Ra Patera until it was seen by PPR in 2001 (Rathbun *et al.*, 2004). Ra Patera was of considerable interest to investigators as, from *Voyager* images, it had caused much debate as to the nature of its flows, which were possibly sulfur (e.g., Sagan, 1979; Pieri *et al.*, 1984). By the end of the nominal mission, *Galileo* had acquired several high-phase, plume-monitoring observations. In addition, eclipse observations revealed a plume over Acala Fluctus, unseen in illuminated observations. This suggested that the Acala plume contained very little dust (McEwen *et al.*, 1998a). The high-phase observations during orbit 11, taken from distances greater than 780,000 km, revealed plumes at Zamama, Prometheus, Marduk, Pillan, and Kanehekili (Keszthelyi *et al.*, 2001).

Extensive morphological studies of volcanic features were possible during the nominal mission. Images of Io obtained during orbits 3–8 generally had higher spatial resolution than those taken during orbits 1–2, allowing for improved morphologic study of volcanic features as well as the mountains first seen in *Voyager* images. In addition, images and spectra obtained during the later portion of the *Galileo* nominal mission allowed for study of variability in Io's volcanic activity and searches for

surface changes between orbits (McEwen *et al.*, 1998a). In addition, very high phase angle images taken during the 3rd orbit showed the sodium cloud that surrounds Io (Burger *et al.*, 1999). The highest resolution images of the nominal mission were obtained during orbit 3 at distances as close as 244,000 km and have a maximum resolution of 2.5 km per pixel. These images revealed a number of mountains and other topographic features on Io's anti-Jovian hemisphere (Carr *et al.*, 1998).

The NIMS instrument was used for mapping the distribution of sulfur dioxide frost on Io, and searching for new species. Sulfur dioxide frost is ubiquitous on Io, and its spectral signature dominated the NIMS wavelength range. The only non-SO_2 component detected by NIMS during the nominal mission was the absorption feature at 3.15 μm (Carlson *et al.*, 1997), which had been previously suggested (Salama *et al.*, 1990). However, NIMS was extremely useful for studies of the global distribution of SO_2 from observations obtained during the nominal mission (Carlson *et al.*, 1997; Douté *et al.*, 2001; see also Chapter 9).

During orbits 9 and 10, SSI images were obtained at moderate-phase angle to search for surface changes, since prior orbits, and to examine mountain morphology near the terminator. The SSI also obtained eclipse observations. These observations, seen in Figure 3.3, reveal a major new eruption at the volcanic center Pillan Patera. Activity was seen by *Galileo* instruments prior to orbit 9, including a NIMS hot spot during orbits 2 and 4 (Lopes-Gautier *et al.*, 1999) and changes in caldera floor albedo from orbit to orbit (McEwen *et al.*, 1998a), but the activity was characterized as minor. However, activity at Pillan became more dramatic during late June and early July 1997 near the perijove of orbit 9. Mid-phase observations of Io by *Galileo* SSI during orbit 9 and distant observations from the Hubble Space Telescope revealed a 200 km tall plume over Pillan Patera. In addition, eclipse observations taken by *Galileo* using the clear and 1MC filter on SSI revealed a very bright spot at Pillan Patera, indicating an extremely vigorous eruption was taking place. An observation was also obtained by NIMS, closely following the SSI observation. Temperature estimates for the hot spot using both data sets indicated lava temperatures exceeding 1,700 K, higher than present-day basalt flows on Earth (McEwen *et al.*, 1998b; Davies *et al.*, 2001). This high temperature suggested an unusual composition for the lava, perhaps similar to terrestrial komatiites: ultramafic (or high-magnesium) lavas common on early Earth (Williams *et al.*, 2001; see also Chapter 7).

3.4 IO OBSERVATIONS DURING THE *GALILEO* EUROPA MISSION

Thanks in part to the amazing discoveries on Europa, NASA approved an extended mission for *Galileo* through January 2000 called the *Galileo* Europa mission (GEM). The extended mission tacked on 13 additional fly-bys to the end of the nominal mission. The first 8 orbits, 12 through 19, focused on Europa with continued distant observations of Io. The next 4 orbits, 20 through 23, were designed to reduce the perijove distance using repeated fly-bys of Callisto. This sequence included the closest approach to Io up until that point in the mission – a 140,000 km distant encounter on orbit 21. With a reduced perijove, *Galileo* was

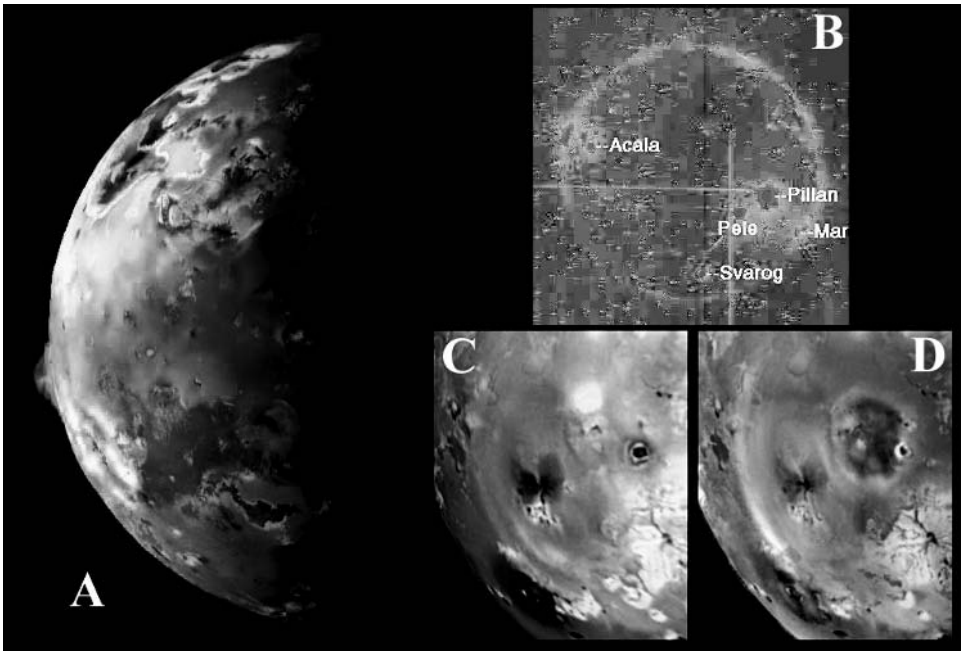

Figure 3.3. Several views of the summer 1997 eruption of Pillan Patera. North is up in all panels. (A) Shows a moderate phase angle image taken during orbit 9 (C9), showing the plume over Pillan at the limb. This observation was taken from a distance of 600,000 km and has a resolution of 6 km per pixel. (B) Shows an eclipse observation from orbit 9 showing the intensity of the Pillan eruption at the time. That observation was taken from a distance of 1.46 million kilometers and has a resolution of 14.6 km per pixel. The image has been color-coded for intensity, with red being the most intense signal. Both (C) and (D) show the aftermath of the Pillan eruption, with a new dark deposit surrounding Pillan Patera in (D). Pele and the ring that surrounds it can be seen to the south-east of Pillan. (C) Was taken during orbit 7 in April 1997 from a distance of 563,000 km, and has a resolution of 5.63 km per pixel. (D) Was taken during orbit 9 in September 1997 from a distance of 506,000 km, and has a resolution of 5.06 km per pixel (NASA press release images PIA00703, PIA01635, PIA00744). (See also color section.)

then set up to perform two close fly-bys of Io and an additional fly-by of Europa. The first Io fly-by was planned to be at 611 km (I24), and the other at 301 km, over the southern pole, and in the extended wake (I25). The question of the presence of an internally generated magnetic field could be resolved at last with a measurement over the pole. With the altitudes that were achievable, new questions arose about the possibility of actually flying through a plume.

Due to a focus on Europa, and spacecraft problems during some orbits during the Europa and Callisto phases of the GEM, SSI images of Io were only returned during orbits 14, 15, 21, and 22. During orbit 14, a clear filter image at 2.6 km per pixel was obtained by SSI showing the region surrounding Pillan (Keszthelyi *et al.*, 2001). The Pillan observation revealed the full extent of the eruption at Pillan providing the best

context view of Pillan's new lava flows. The color mosaic, shown in Figure 3.4(A) (see color section), was the highest thus far of the anti-Jovian hemisphere, showing small, previously unseen calderas with green floors, nicknamed "golf courses" and later named Chaac and Haokah Paterae (Geissler *et al.*, 1999). During orbit 15 in May 1999, three-color, high-phase observations with resolutions between 12.7 and 14 km per pixel were obtained to examine the strange photometric behavior of Io's surface materials and to search for surface changes around Kanehekili on the sub-Jovian hemisphere (Simonelli *et al.*, 2001). In addition, a four-filter, three-color eclipse observation, shown in Figure 3.3(B), was obtained to examine the interaction between the Io flux tube and Io's atmosphere and plumes (Geissler *et al.*, 1999). NIMS spectra were also obtained during orbits 12, 14, 15, 16, 20, 21, and 22. NIMS observations during this phase of the mission continued to detect hot spots, including Haokah, Susanoo, Wayland, and Girru, which had been tentatively identified from ground-based observations (Lopes *et al.*, 2001). Global or part-global observations obtained by NIMS during both the *Galileo* nominal mission and GEM linked the distribution of SO_2 to the locations of major plumes observed by SSI. Douté *et al.*'s results (2001) suggested that most of the SO_2 gas from the plumes (located mostly in the equatorial regions) flows toward colder surfaces at higher latitudes. The GEM observations also allowed the UVS to obtain its best ultraviolet observations of Io on orbit 15, providing constraints on Io's atmosphere (Hendrix *et al.*, 1999).

During orbit 21 in late June 1999, *Galileo* made its closest remote-sensing observations yet of Io, as a prelude to the Io fly-bys later that year. This fly-by allowed for an opportunity to capture a full-disk, three-color mosaic at 1.3 km per pixel, more than twice the resolution of the previous, highest resolution color observation of Io by *Galileo* during orbit 14. This mosaic, shown in Figure 3.4(C), shows the anti-Jovian hemisphere features in great detail. From the images the Amirani and Maui plumes, discovered by *Voyager*, were found to have the same vent and were in fact produced from different regions of the same, very large flow field. Other SSI results included the detection of a new plume at Masubi during orbit 21 and a dark, oval-shaped plume deposit observed during orbit 22, in August 1999, over a different location from one observed during orbit 15, indicating multiple plume sites along the long, Masubi flow field (Keszthelyi *et al.*, 2001).

3.4.1 I24

After 4 years of observing Io from a distance, *Galileo* was set to fly by Io on 11 October 1999 during orbit 24 (also known as I24). Observations from this encounter are highlighted in Figure 3.5. The fly-by was an equatorial pass, with close approach occurring near the dawn terminator north of Pillan Patera. The spacecraft came within 500 km of Io's surface. As *Galileo* receded from Io following its closest approach, a low-phase view of Io's anti-Jovian hemisphere was visible. The remote-sensing observations were designed to examine active volcanic centers, like Pillan, Prometheus, Zamama, and Amirani, to examine mountainous terrain near Dorian Montes, Tohil Mons, and Hi′iaka Patera, to examine compositional

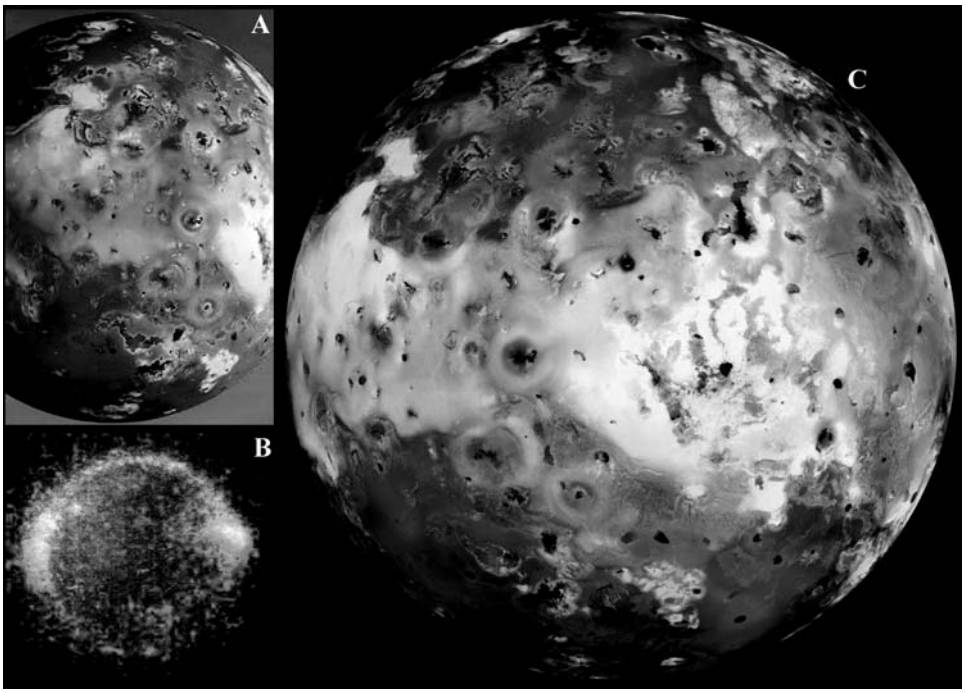

Figure 3.4. Imaging highlights from the Europa and perijove reduction phases of the GEM. (A) A mosaic of two, three-color frames showing the anti-Jovian hemisphere, taken during orbit 14 from a distance of 290,000 km with a resolution of 2.9 km per pixel. (B) A three-color observation of Io during eclipse. The faint red glows represent emissions from atomic oxygen and green glows from atomic sodium, while the bright blue emissions near the equator are likely due to electron impacts on SO_2. Image (B) was taken during orbit 15 from a distance of 1.4 million km and has a resolution of 14 km per pixel. (C) A large, three-color, 16-frame mosaic taken during orbit 21. This mosaic represents the highest resolution view of Io by *Galileo* prior to the Io targeted encounters later in the mission. The images in this mosaic were taken from a distance of 130,000 km and have a resolution of 1.3 km per pixel (NASA press release images PIA01604, PIA01637, PIA02309). (See also color section.)

variations across the surface of Io, and to understand the thermal emission and heat flow coming from the anti-Jovian hemisphere.

The fly-by was not without its problems. A few hours before closest approach, *Galileo* went into safe mode (i.e., an anomaly caused the on-board computer to place the spacecraft into a default "safe" mode, canceling the science observation sequence), preventing observations for a few hours before close approach, but recovering in time to obtain unique, high-resolution nightside data on Loki and Pele. The SSI data acquired during this fly-by also had numerous problems (McEwen, 2001). Many of the images taken by SSI were in summation mode, with half the resolution of full-frame images. Unfortunately, these images came back garbled due to a failure in the camera electronics. An algorithm was found to unscramble the images, but some

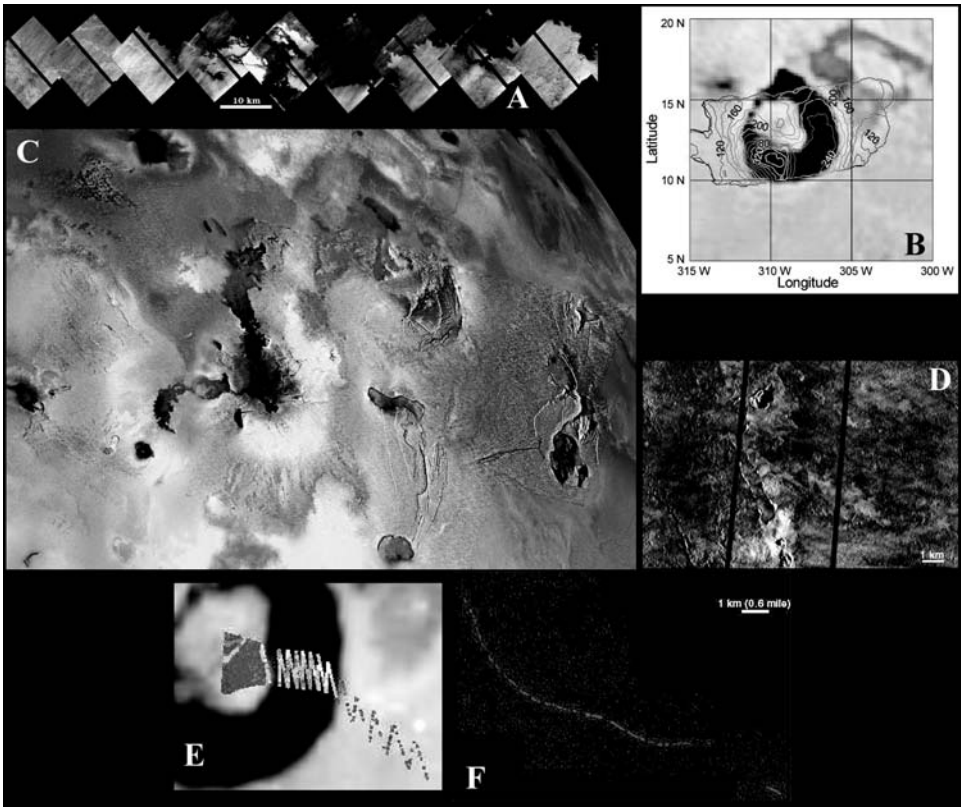

Figure 3.5. Highlights from the I24 fly-by of Io. (A) The ZAMAMA01 observation from I24. (B) Temperature map of Loki Patera taken by the PPR instrument. (C) AMSKIGI01 observation merged with color from orbit 21. (D) Portion of the PILLAN01 observation showing pits and rafted plates within the Pillan flow field. (E) NIMS observation of Loki Patera from shortly before the closest approach. (F) PELE_01 observation with a string of hot spots marking the margin of the Pele lava lake (NASA press release images PIA02537, PIA02524, PIA02526, PIA02536, PIA02514, PIA02511). (See also color section.)

artifacts, like a dark, vertical central stripe, remain. At the ends of many mosaics, partial full-resolution frames were also obtained, which were not scrambled (Keszthelyi *et al.*, 2001). NIMS also encountered problems on this fly-by. NIMS observations were designed to search for compositional variations as well as look at the high-resolution structure of volcanic hot spots. Unfortunately, the instrument's grating, which had been losing effectiveness through the GEM, became stuck in one position, allowing for spectra from only 13 wavelengths to be obtained. Luckily, the wavelengths were widely spaced within the NIMS full spectral range, but the spectral resolution achieved by only having 17 wavelengths available over a range of more than 4 μm would not be enough to resolve any but the broadest of spectral

features (Lopes-Gautier *et al*., 2000; Lopes *et al*., 2001). The spectral resolution would be enough, however, to search for hot spots, determine temperatures, and map the SO_2 distribution.

The SSI team obtained 12 clear-filter mosaic sequences for I24, many suffering from the problems associated with the summation mode. These observations are discussed in further detail in Keszthelyi *et al*. (2001) and Turtle *et al*. (2001). In addition to SSI imaging, both NIMS and PPR obtained critical, high-resolution data during the I24 fly-by, despite the NIMS grating problem. NIMS regional observations revealed 16 hot spots, 3 not previously seen. In addition, high-resolution data of Loki (shown in Figure 3.5(E)), Prometheus, and Amirani revealed a high-resolution structure to the hot spots (including multiple hot spots in the same flow field) not previously resolved (Lopes *et al*., 2001). A correlation was also found between red plume deposits and enhanced concentrations of SO_2 (Lopes-Gautier *et al*., 2000). PPR obtained high spatial resolution observations of temperatures on the floors of Loki (shown in Figure 3.5(B)) and Pele, as well as the flow fields of Pillan (Spencer *et al*., 2000; Rathbun *et al*., 2004).

I24 also enabled plasma wave studies of radio emissions at Io akin to terrestrial Auroral Kilometric Radiation (AKR) (Gurnett *et al*., 2001). Such emissions are a response to changing energetic particle distribution functions in the region, which were also studied by the EPD instrument. Behaviors of distribution functions are in turn related to the dynamics of particle responses to changing electric and magnetic field conditions. PLS investigators suggested that the spacecraft went through a "stealth plume" – a cloud of material over Pele at an altitude of 600 km (Frank and Paterson, 2000). Taken together these measurements were a first attempt at characterizing the complex relationships and dynamics in the Jovian inner magnetosphere driven by Io surface conditions.

3.4.2 I25

Following the problems encountered during the I24 fly-by, SSI observations for the I25 fly-by were quickly replanned to eliminate the offending summation mode images. Because full-mode images take up around four times as much memory as summation mode images, fewer images had to be planned. The I25 fly-by, on 26 November 1999, was a south polar pass, at an altitude of 300 km, designed to investigate the magnetic signature found by the magnetometer during the Io fly-by during JOI as well as to examine polar terrain that had not been observed thus far by *Galileo*. Unfortunately, the spacecraft went into safe mode less than 5 hours before the I25 closest approach. With a 34 minute one-way-light-time, the JPL engineering team had a total of three and a half hours to respond in order to recover science observations during the encounter. The team created a bare-bones sequence in which many instruments were not able to participate. One particularly important instrument that was not recovered was the magnetometer. The recovery process completed 4 minutes before the new sequence went active. All images with pixel scales less than 150 m per pixel were lost as well as any other data taken before and shortly after closest approach (Turtle *et al*., 2001). Despite losing the highest resolution images, the images that were

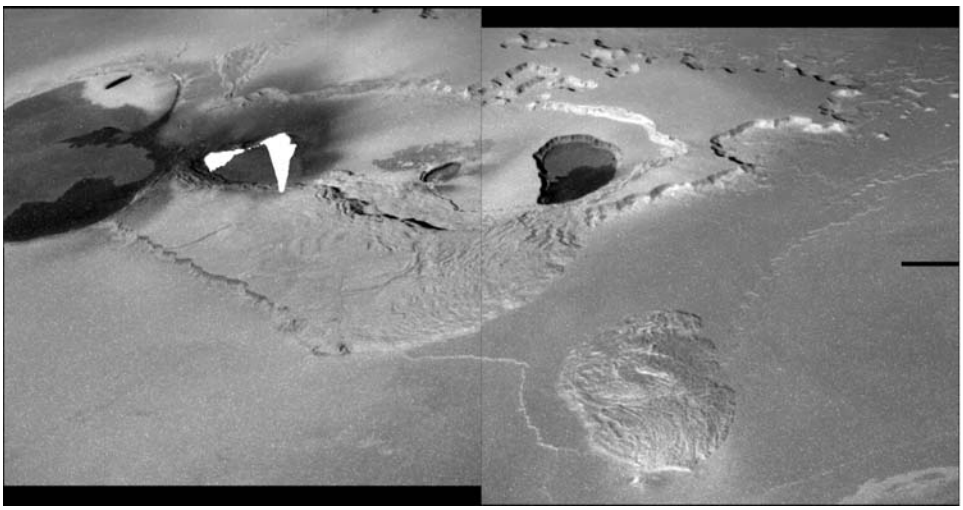

Figure 3.6. Two-frame mosaic from the GIANTS01 observations from I25. This observation shows Tvashtar Paterae at 180 m per pixel. The bright features seen in the left image are due to saturation of the detector (and subsequent bleeding) caused by a brilliant thermal emission source. Based on the morphology of the saturation, the source was interpreted as a vigorous lava curtain, with lava flow on the surface away from the curtain (McEwen *et al.*, 2000).

taken had much higher quality than those of the I24 summation mode images and were much more useful for geologic interpretation. SSI images included mosaics of Zal Patera and Montes, Hi′iaka Patera and Montes, Tvashtar Paterae, and Emakong Patera.

One of the biggest surprises of the Io fly-bys was the major eruption at Tvashtar Paterae. An SSI mosaic was planned over Tvashtar Paterae. This observation, a two-frame mosaic with a resolution of 183 m per pixel (Figure 3.6), was designed to study a group of calderas at high northern latitudes that are much larger than the average Ionian calderas nearer the equator. Unexpectedly, one of the nested calderas within Tvashtar Paterae erupted during the I25 fly-by. Intense thermal emission from a long fire fountain saturated the SSI detector (McEwen *et al.*, 2000). The eruption was also seen in observations taken by NIMS as well as by ground-based observers (Lopes-Gautier *et al.*, 2000; Howell *et al.*, 2001). Ground-based observers measured the temperature at between 1,300 K and 1,900 K, while NIMS and SSI placed constraints of 1,060 K and at least 1,300 K (Lopes *et al.*, 2001; Milazzo *et al.*, 2005).

Like SSI, NIMS and PPR data were limited to lower resolution data over the sunlit anti-Jovian hemisphere. Regional observations by NIMS detected three new hot spots at Cuchi, Chaac, and Seth Paterae (Lopes *et al.*, 2001). PPR obtained part of a high-quality global map of night-time thermal emission on approach, before being interrupted by the safing of the spacecraft (Spencer *et al.*, 2000a).

The fields and particles instruments also suffered significant observation losses, including the magnetometer measurements and plasma measurements in the Io exosphere. However, an important set of measurements conducted by PWS

showed for the first time the presence of very large electron densities of up to $6.8 \times 10^4\,\mathrm{cm}^{-3}$ in an extended plasma wake of Io, and over the southern polar region of Io (Gurnett *et al.*, 2001). The enhanced electron densities over the southern polar region had a nearly rectangular profile, the edges of which coincided with the boundaries of the Io flux tube, apparently due to the diffusion of plasma outward away from Io along the flux tube. These measurements shed light on the flux interchange mechanism that drives plasma from the vicinity of Io down the magnetotail of Jupiter.

3.5 IO OBSERVATIONS DURING THE *GALILEO* MILLENNIUM MISSION

The original plan for the GEM called for only two fly-bys of Io, I24 and I25, with the expectation that the spacecraft would have significant problems following two passes through the Io plasma torus. However, the spacecraft survived intact, even though several instruments were not functioning optimally. So an additional Io fly-by was approved for orbit 27 (I27) on 22 February 2000 as well as two additional fly-bys of Ganymede in May and December 2000 as part of a new extended mission called the *Galileo* millennium mission (GMM). These were followed by three final Io fly-bys (I31–I33) in 2001–2002. GMM took advantage of the opportunity in late 2000 to study the magnetosphere of Jupiter with two spacecraft, *Galileo* in the magnetosphere of Jupiter, and *Cassini* while on the way to its historic encounter with Saturn, passing by on the dayside. Among other things, *Cassini* was able to monitor solar wind conditions for comparison with *Galileo*'s magnetospheric observations, to look for the influence of the solar wind on the magnetosphere.

Among the priorities for Io investigations were more measurements to determine the nature of any intrinsic magnetic field of Io. In GMM, Io polar fly-bys would be performed in order to detect the differences an intrinsic magnetic field would introduce between the equatorial magnetic field and the polar magnetic field. I31 provided the first close pass of the north polar region, I32 would pass over the south pole (where observations were lost in I25). Extensive remote-sensing observations were also planned, with the intention of tripling the high-resolution data ($<$200 m per pixel) coverage for Io. After I33, the spacecraft would be on a ballistic trajectory for a Jupiter impact on the 35th orbit. Imaging would be turned off for A34 and J35.

The *Galileo* Millennium Mission (GMM) provided key opportunities for the fields and particles instruments. The collective studies of a body of encounters with Io, including studies of the extended corona, would provide an understanding of the patchy nature of the atmosphere; the composition, properties, and dynamics of the Io flux tube and its interaction with the atmosphere of Jupiter; the interaction of the atmosphere with the torus; and the mechanics of how Iogenic plasma spreads throughout the Jovian magnetosphere. The Io encounters in GMM were performed at a range of local times and geometries with respect to the Io wake. The coordinated study of Jupiter's magnetosphere with *Cassini* showed two main results. First, there seem to be globally correlated dynamic events in the magnetosphere and the signature

of these events can be seen in a number of data sets: energetic particle events, injection events, changes in hectometric, narrowband kilometric, and trapped continuum radiation. It is as if the magnetotail undergoes a global reconfiguration from time to time (Vasyliunas *et al*., 1997; Krupp *et al*., 2001a, b, 2004). Second, this set of events does not seem to be correlated with solar wind variations at Jupiter (Kurth *et al*., 2002). The absence of a correlation with solar wind suggests that the magnetosphere may exhibit a systematic response to the presence of Iogenic plasma.

3.5.1 I27

The I27 fly-by was an equatorial pass with a similar geometry to the I24 fly-by. *Galileo* also came much closer to Io on this pass, flying within 200 km of the surface. Unlike the previous two fly-bys, where problems due to the various instruments or due to "safing" events occurred on the spacecraft, this fly-by went without a glitch and all planned data was obtained. This encounter also provided a fly-through of the Io torus. Intense ion cyclotron wave activity on this and other encounters provided measurements to confirm the extensive nature of the charged particle pickup activity in the region, a level of activity that results in the spread of Iogenic material, an order of magnitude beyond the 2-Io radii originally supposed.

SSI took a number of observation sequences, including repeat observations of Pele, Prometheus, Tohil Mons, Tvashtar Paterae, Amirani, and Zal Patera. Additional observations were planned for a cliff near Isum Patera, Chaac Patera and its surrounding region, Shamshu Patera and Mons, and near Telegonus Mensae. NIMS and PPR, like SSI, were able to acquire all of their planned data. Much of the NIMS and PPR data were designed to provide ride-along coverage with SSI, allowing for correlation between the data sets. Among the highlights for NIMS include a high-resolution observation of Pele, shown in Figure 3.7(B), finding a correlation between dark material and thermal emissions in the Chaac–Camaxtli region, the discovery of four new hot spots in regional observations, and the study of the detailed thermal structure of the Amirani and Prometheus flow fields (Lopes *et al*., 2001). NIMS data from I24–I27 were also used to map the SO_2 distribution around Prometheus. Douté *et al*. (2002) used the SO_2 distribution to infer the migration of the Prometheus plume over Io's surface, a concept first proposed by Kieffer *et al*. (2000). PPR, in addition to providing ride-along data with SSI, observed its first global night-time map, covering the trailing hemisphere, shown in Figure 3.7(C), to look for sites of low-temperature thermal emission and to determine background surface temperatures. It also obtained high-resolution observations of Loki, showing dramatic changes since I24, and regional maps of dayside thermal emission (Spencer *et al*., 2000a; Rathbun *et al*., 2004).

3.5.2 G29–I31

During orbit 29 in late December 2000, *Galileo* and *Cassini* obtained complimentary coverage of Io, with *Cassini* providing better spectral and temporal coverage thanks to its more sophisticated imaging system and higher bandwidth and *Galileo* providing

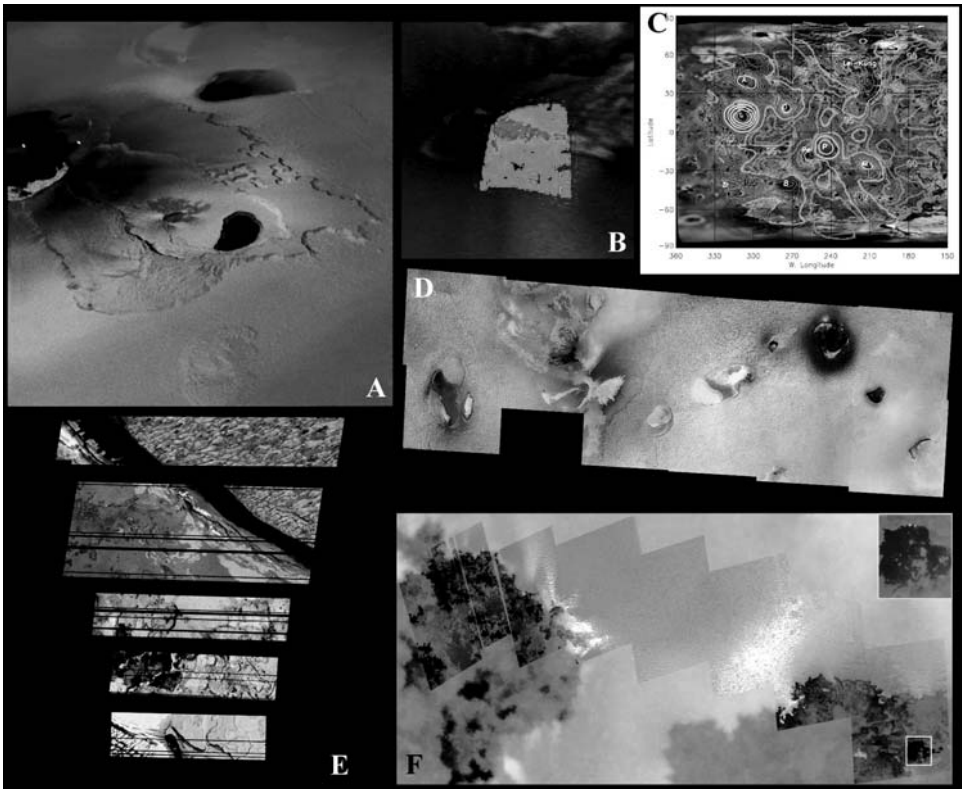

Figure 3.7. Highlights from the I27 fly-by. (A) False-color view of Tvashtar Paterae from the TVASHT01 observation. (B) NIMS observation of the Pele caldera overlain on a false-color image from *Voyager 1*. (C) Map of night-time temperatures of Io's trailing hemisphere taken by the PPR instrument. (D) CAMAXT01 observation merged with color from orbit 21. (E) Partial frames from the CHAAC01 observation. Frames showing the north-east margin of Chaac Patera are seen at the top while frames showing the floor and the south-west margin are seen at the bottom. (F) PROMTH01 observation. A dark flow with two spots of incandescent lava is highlighted to the right (NASA press release images PIA02550, PIA02560, PIA02548, PIA02566, PIA02551, PIA02564). (See also color section.)

better spatial coverage since it observed Io from a much closer distance. *Cassini* observations, shown in Figure 3.8(A), revealed a new plume at Tvashtar Paterae, one of the few found over a polar region (Porco *et al*., 2003). Low-phase *Galileo* color observations, with resolutions between 11 and 17 km per pixel (shown in Figure 3.8(B)), revealed a red plume deposit, similar to that seen around Pele, surrounding Tvashtar, forming a ring 1,440 km across (Turtle *et al*., 2004).

Following orbit 29, the spacecraft continued to perform well, except for an anomaly that cropped up, starting in orbit 28, which caused the loss of a number of SSI images. A further extension mission was granted, including a fly-by of *Callisto* in May 2001, three fly-bys of Io in August and October 2001 and January 2002, and a

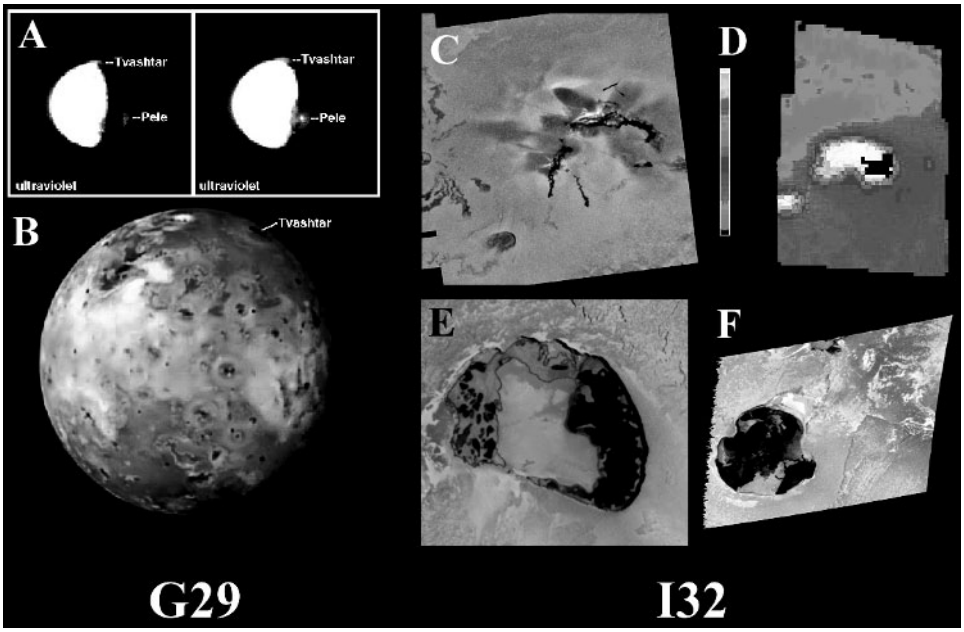

Figure 3.8. Highlights from orbit 29 and I32. Both (A) and (B) highlight a new eruption at Tvashtar observed during late 2000. The two figures in (A), enhanced images from the *Cassini* spacecraft, show a 385 km tall plume over Tvashtar as well as the plume over Pele. As seen in (B) from *Galileo*, both plumes have formed large red ring deposits. Panels (C–F) show highlights from the I32 fly-by. Both (C) and (D) show a new eruption at Thor, first seen by NIMS during I31 and in distant observations from the same orbit. Image (C) is taken from the TERMIN02 observation while (D) is a 13–16 km per pixel observation from NIMS. (E) Color observation of Tupan Patera, from the observation TUPAN_01. (F) Frame from the observation GSHBAR01, revealing fresh lava flows on its surface. (See also color section.)

fly-by of Amalthea in November 2002. Following the Amalthea fly-by, *Galileo* would then be put on a collision course with Jupiter, to prevent contamination of Europa from potential microbial stowaways on *Galileo*. Observations during the first orbit of this new extension mission, orbit 30, were designed to look at the anti-Jovian and leading hemispheres at low-phase to search for changes, examine the new Tvashtar plume deposit found during Orbit 29, and to characterize the volcanic features seen near 50° west longitude which had not been well observed by *Galileo* (or *Voyager* for that matter). Unfortunately, the SSI anomaly that started in orbit 28 occurred again during orbit 30, causing the loss of all orbit 30 images of Io.

I31 was a north polar fly-by of Io that took place on 6 August 2001. Closest approach occurred at a distance of 194 km above the surface of Io near 78° north latitude, 172° west longitude. Magnetometer measurements were performed and the results were particularly important, as they demonstrated that there is no internally generated magnetic field at Io. At a fly-by altitude of only 194 km, the spacecraft

trajectory took it directly over Tvashtar, which had been recently active. Images and spectra showed that Tvashtar was probably quiescent at the time of *Galileo*'s overflight. Nevertheless, detections by the PLS instrument of tenuous gases in the area indicated that another plume was active, and represent the first *in situ* detection of its kind of emissions from an active region not on Earth.

Imaging plans called for high-resolution observations of the I25 Tvashtar eruption site and other features (Turtle *et al.*, 2004). Unfortunately, despite commands designed to fix the SSI anomaly seen since orbit 28, the problem appeared again, causing the loss of all SSI images except the low-resolution observations. These observations, combined with those taken by NIMS, revealed a major new eruption at a volcano later named Thor. SSI observations at 18 km per pixel prior to the encounter revealed a 500 km tall plume over Thor, the tallest plume ever seen at Io in reflected sunlight (Turtle *et al.*, 2004). It quickly became clear that this was the plume whose gases were sampled by the PLS instrument. Low-resolution images of Thor during this fly-by revealed a new dark deposit surrounded by a white plume deposit, where no major activity or dark material was seen previously (Geissler *et al.*, 2004). NIMS regional observations revealed a strong thermal emission source at Thor during I31 (Lopes *et al.*, 2004) which pinpointed the location of the erupting plume. NIMS observations also revealed nine additional, previously undetected hot spots. Despite not seeing a plume or new plume deposit in the polar regions of Io during much of the *Galileo* mission (save perhaps one possible north polar detection in 1997), SSI low-resolution observations also revealed a new red ring plume deposit around Dazhbog Patera and additional red plume deposits at Surt, in addition to the deposits surrounding Tvashtar first seen on orbit 29 (Geissler *et al.*, 2004). This brought the total of plume deposits north of 40° north latitude to four in only a matter of a few months, where maybe only one had been seen during the rest of the mission. PPR obtained global and regional maps of nightside thermal emission from the volcanoes and passive surface, and its best-ever map of daytime thermal emission and surface temperatures (Rathbun *et al.*, 2004).

3.5.3 I32

The I32 encounter was a south polar fly-by of Io that took place on 16 October 2001. Closest approach occurred at a distance of 184 km above the surface of Io near 79° south latitude, 223° west longitude. Once again, this encounter provided a look at the anti-Jovian hemisphere of Io. The anomaly that caused the loss of high-resolution SSI images during I31 did not happen this time. Thus, all planned SSI observations for this fly-by were successfully obtained. Among the highlights of this fly-by was the chance to retarget observations to the location of the eruption at Thor, seen during the previous encounter. SSI obtained images at 335 m per pixel near the terminator in the northern hemisphere, which included Thor. The frame showing Thor, shown in Figure 3.8(D), shows two separate dark lava flows covering brightened flows from previous eruptions. Surrounding the dark flows is a dark pyroclastic deposit, similar to the one seen at Pillan and Pele (Turtle *et al.*, 2004). NIMS also captured a high-resolution observation, at 13–16 km per pixel, of the newly discovered

hot spot, shown in Figure 3.8(D), revealing continued activity at Thor along with a newly detected hot spot to the south-west of Thor, suggesting the presence of multiple vents for the same internal source region (Lopes *et al*., 2004).

NIMS obtained several observations in conjunction with SSI observations as well as several regional coverage observations, including a night-time observation of the southern portion of Loki Patera having a broader spatial coverage than the observation during I24. The highest thermal emission was seen along the south-western edge of Loki Patera, a region known to be the starting point of repeated eruptions at Loki. NIMS data showed that several other Ionian paterae, including Tupan and Emakong, are likely to be persistent lava lakes, a result that has important implications for the resurfacing of Io (Lopes *et al*., 2004), which may be primarily due to plume deposits rather than lava flows (Geissler *et al*., 2004). During I32, PPR again obtained global and regional maps of night-time thermal emission (Rathbun *et al*., 2004).

Further magnetometer measurements obtained during this fly-by confirmed that there is no internally generated magnetic field at Io. This encounter also included a first-time penetration of a peculiar region near Io known as the Io ramp. The ramp is a transition region from the relatively cold plasma of magnetospheric origin to the more energetic plasma of Io torus origin. Density and energy of plasma increase sharply in this transition. *Galileo* was able to obtain a nearly 2-hour sample in this region.

3.6 THE END OF THE *GALILEO* MISSION

The I33 fly-by, on 17 January 2002, was *Galileo*'s closest encounter with Io, with an altitude of only 102 km. This fly-by was also the only one to provide a high-resolution view of Io's Jupiter-facing hemisphere. Unfortunately, a "safing" event occurred shortly before the encounter and all Io data for the fly-by was lost except for some small maps of night-time thermal emissions from PPR. Additional observations were planned for orbit 34, in November 2002, when *Galileo* would come within 50,000 km of Io. This fly-by would have provided *Galileo*'s best look in daylight at prominent volcanic centers like Loki, Pillan, Ra Patera, and Pele. However, due to budget constraints, no remote-sensing observations of Io were performed during orbit 34.

The I33 encounter provided a rare opportunity to sample another peculiar region near Io known as the Io ribbon. The ribbon, as seen from the ground, is a tenuous energetic region located between the cold and warm plasma torii (Figure 3.9). Unfortunately, 5 minutes into this recording, the spacecraft went into "safing event", and this measurement was lost. The A34 and J35 sequences were designed to obtain the measurements that would establish the flux tube interchange mechanism as the controling mechanism for large-scale movement of plasma from Io to other regions of the Jovian magnetosphere. In this mechanism, flux tubes, heavily mass loaded with Iogenic plasma would be moved out by centrifugal force and replaced with comparatively empty flux tubes moving inward. Evidence for this process was sought in the *Voyager* data, but these efforts were generally unsuccessful. Extensive observations of the inner magnetosphere by *Galileo* early in the mission were the first

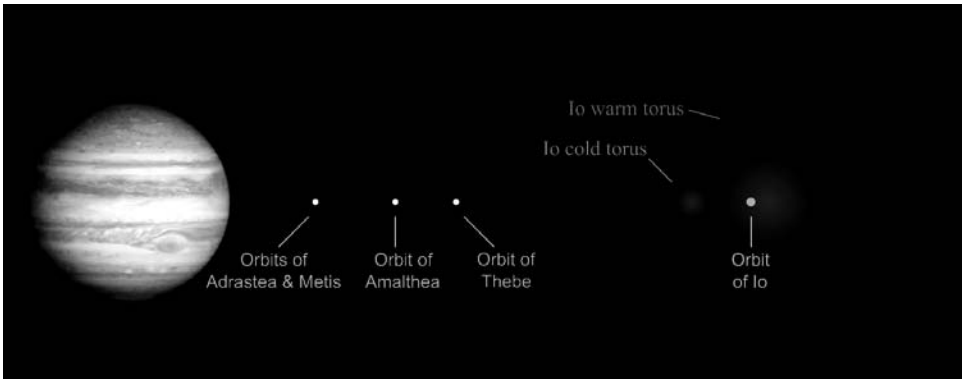

Figure 3.9. This figure illustrates both the warm and cold torus of Io. The *Galileo* spacecraft was able to sample the cold torus on the 34th orbit of Jupiter just before its final trajectory loop around Jupiter on J35. Courtesy Windows to the Universe *www.windows.ucar.edu* A34 Interactive Graphic. (See also color section.)

evidence that this process worked at Jupiter. Additional measurements during GMM, including those on A34, helped to establish the viability of this mechanism. The A34 trajectory provided the first penetration to the cold torus of Io, and *Galileo* obtained the first *in situ* measurements of that region.

Following perijove on orbit 34, *Galileo* was on a collision course, and on 23 September 2003, *Galileo* followed its atmospheric probe into Jupiter's atmosphere, ending the *Galileo* mission. Despite numerous problems with the antenna and tape recorder before the start of the primary mission, and radiation-related problems during the extended mission, *Galileo* provided critical insights into the geology and inner workings of Io. Whereas *Voyager* provided a first look at world known until then as a point in a telescope or a spectrometer plot, *Galileo* brought Io up close and personal, allowing researchers to examine the fine-scale geology, chemistry, and physics of this fascinating world.

3.7 REFERENCES

Anderson, J. D., Sjogren, W. L., and Schubert, G. 1996. Galileo gravity results and the internal structure of Io. *Science*, **272**, 709–712.

Belton, M. J. S., Klaasen, K. P., Clary, M. C., Anderson, J. L., Anger, C. D., Carr, M. H., Chapman, C. R., Davies, M. E., Greeley, R., Anderson, D. *et al*. 1992. The Galileo solid-state imaging experiment. *Space Sci. Rev*., **60**, 413–455.

Burger, M. H., Schneider, N. M., and Wilson, J. K. 1999. Galileo's close-up view of the Io sodium jet. *Geophys. Res. Lett*., **26**, 3333–3336.

Carlson, R. W., Weissman, P. R., Smythe, W. D., and Mahoney, J. C. 1992. The Near-Infrared Mapping Spectrometer Experiment on Galileo. *Space Science Reviews*, **60**, 457–502.

Carlson, R., Smythe, W., Lopes-Gautier, R., *et al*. 1997. The distribution of sulfur dioxide and other infrared absorbers on the surface of Io in 1997. *Geophys. Res. Lett*., **24**(20), 2474–2482.

Carr, M. H., McEwen, A. S., Howard, K. A., Chuang, F. C., Thomas, P., Schuster, P., Oberst, J., Keukum, G., Schubert, G., and the Galileo Imaging Team. 1998. Mountains and calderas on Io: Possible implications for lithosphere structure and magma generation. *Icarus*, **1935**, 146–165.

Davies, A. G., Keszthelyi, L. P., Williams, D. A., Phillips, C. B., McEwen, A. S., Lopes, R. M. C., Smythe, W. D., Kamp, L. W., Soderblom, L. A., and Carlson, R. W. 2001. Thermal signature, eruption style, and eruption evolution at Pele and Pillan on Io. *Journal of Geophys. Res*., **106**, 33079–33103.

Douté, S., Lopes-Gautier, R., Carlson, R., Schmitt, B., Soderblom, L., and the Galileo NIMS Team. 2001. Mapping the SO_2 frost on Io by the modeling of NIMS hyperspectral images. *Icarus*, **149**, 107–132.

Doute; S., Lopes, R., Kamp, L. W., and Carlson, R. 2002. Dynamics and evolution of SO_2 Gas condensation around Prometheus-like volcanic plumes on Io as seen by the Near-Infrared Mapping Spectrometer. *Icarus*, **158**, 460–482.

Douté, S., Lopes, R., Kamp, L. W., Carlson, R. W., Schmitt, B., and the Galileo NIMS Team. 2004. Geology and activity around volcanoes on Io from the analysis of NIMS spectral images. *Icarus*, **169**(1), 175–196.

Frank, L. A. and Paterson, W. R. 2000. Return to Io by the Galileo spacecraft – Plasma observations. *Journal of Geophys. Res.,* **105**, 25363–25378.

Geissler, P. E., McEwen, A. S., Ip, W., Belton, J. S., Johnson, T. V., Smythe, W. H., and Ingersoll, A. P. 1999. Galileo imaging of atmospheric emissions from Io. *Science*, **285**, 870–874.

Geissler, P., McEwen, A. S., Phillips, C. B., Keszthelyi, L. P., and Spencer, J. 2004. Surface changes on Io during the Galileo mission. *Icarus*, **169**, 2964.

Gurnett, D. A., Persoon, A. M., Kurth, W. S., Roux, A., and Bolton, S. J. 2001. Electron densities near Io from Galileo plasma wave observations. *Journal of Geophys. Res*., **106**, 26225–26232.

Harland, D. M. 2000. *Jupiter Odyssey: The Story of NASA's Galileo Mission*. Springer, London.

Hendrix, A. R., Stewart, A. I. F., Simmons, K. E., and Tobiska, W. K. 1999. Galileo ultraviolet spectrometer observations of Io: Spatial and temporal variations in sulfur dioxide gas and frost. *EOS*, **80**, F623.

Howell, R. R., Spencer, J. R., Goguen, J. D., Marchis, F., Prangé, R., Fusco, T., Blaney, D. L., Veeder, G. J., Rathbun, J. A., Orton, G. S., *et al*. 2001. Ground-based observations of volcanism on Io in 1999 and early 2000. *Journal of Geophys. Res*., **106**, 33129–33139.

Huddleston, D. E., Strangeway, R. J., Warnecke, J., Russell, C. T., and Kivelson, M. G. 1998. Ion cyclotron waves in the Io torus: Wave dispersion, free energy analysis, and SO2+ source rate estimates. *Journal of Geophysical Research-Planets*, **103**, 19887–19899.

Keszthelyi, L., McEwen, A. S., Phillips, C. B., Milazzo, M., Geissler, P., Turtle, E. P., Radebaugh, J., Williams, D. A., Simonelli, D. P., Breneman, H. H., *et al*. 2001. Imaging of volcanic activity on Jupiter's moon Io by Galileo during the Galileo Europa Mission and the Galileo Millennium Mission. *Journal of Geophys. Res*., **106**, 33025–33052.

Kieffer, S. W., Lopen-Gautier, R., McEwen, A., Smythe, W., Keszthelyi, L., and Carlson, R. 2000. Prometheus: Io's wandering plume. *Science*, **288**, 1204–1208.

Kivelson, M. G., Khurana, K. K., Walker, R. J., Linker, J. A., Russell, C. T., Southwood, D. J., and Polanskey, C. 1996. A magnetic signature at Io: Initial report from the Galileo magnetometer. *Science*, **273**, 337–340.

Krupp, N., Vasyliunas, V. M., Woch, J., Lagg, A., Khurana, K. K., Kivelson, M. G., Mauk, B. H., Roelof, E. C., Williams, D. J., Krimigis, S. M. *et al.* 2004. Dynamics of the Jovian Magnetosphere. In: F. Bagenal, T. Dowling, and W. McKinnon (eds.), *Jupiter: The Planet, Satellites, and Magnetosphere*. Cambridge University Press, Cambridge, UK, pp. 617–638.

Krupp, N., Lagg, A., Wilken, B., Woch, J., Livi, S., Roelof, E. C., and Williams, D. J. 2001. Global flows of energetic ions in Jupiter's equatorial plane – First-order approximation. *Journal of Geophys. Res. A. Space Physics*, **106**, 26017–26032.

Krupp, N., Woch, J., Lagg, A., Roelof, E. C., Williams, D. J., Livi, S., and Wilken, B. 2001. Local time asymmetry of energetic ion anisotropies in the Jovian magnetosphere. *Planetary and Space Science*, **49**, 283–289.

Kurth, W. S., Gurnett, D. A., Hospodarsky, G. B., Farrell, W. M., Roux, A., Dougherty, M. K., Joy, S. P., Kivelson, M. G., Walker, R. J., Crary, F. J., *et al.* 2002. The dusk flank of Jupiter's magnetosphere. *Nature*, **415**, 991–994.

Lopes, R. M. C., Kamp, L. W., Douté, S., Smythe, W. D., Carlson, R. W., McEwen, A. S., Geissler, P. E., Kieffer, S. W., Leader, F. E., Davies, A. G. *et al.* 2001. Io in the near infrared: Near-Infrared Mapping Spectrometer (NIMS) results from the Galileo flybys in 1999 and 2000. *Journal of Geophys. Res.*, **106**, 33053–33078.

Lopes, R. M. C., Kamp, L. W., Smythe, W. D., Mouginis-Mark, P., Kargel, J., Radebaugh, J., Turtle, E. P., Perry, J., Williams, D. A., Carlson, R. W., *et al.* 2004. Lava lakes on Io: Observations of Io's volcanic activity from Galileo NIMS during the 2001 fly-bys. *Icarus*, **169**, 140–174.

Lopes-Gautier, R., Davies, A. G., Carlson, R., Smythe, W., Kamp, L., Soderblom, L., Leader, F. E., Mehlman, R., and the Galileo NIMS Team. 1997. Hot Spots on Io: Initial results from Galileo's Near Infrared Mapping Spectrometer. *Geophys. Res. Lett.*, **24**(20), 2439–2442.

Lopes-Gautier, R., McEwen, A. S., Smythe, W. B., Geissler, P. E., Kamp, L., Davies, A. G., Spencer, J. R., Keszthelyi, L., Carlson, R., Leader, F. E., *et al.* 1999. Active volcanism on Io: Global distribution and variations in activity. *Icarus*, **140**, 243–264.

Lopes-Gautier, R., Douté, S., Smythe, W. D., Kamp, L. W., Carlson, R. W., Davies, A. G., Leader, F. E., McEwen, A. S., Geissler, P. E., Kieffer, S. W. *et al.* 2000. A close-up look at Io from Galileo's Near-Infrared Mapping Spectrometer. *Science*, **288**, 1201–1204.

McEwen, A. S. 2001. Introduction to the special section: Geology and geophysics of Io. *Journal of Geophys. Res.*, **106**, 32959–32961.

McEwen, A. S., Simonelli, D. P., Senske, D. R., Klassen, K. P., Keszthelyi, L., Johnson, T. V., Geissler, P. E., Carr, M. H., and Belton, M. J. S. 1997. High-temperature hot spots on Io as seen by the Galileo solid state imaging (SSI) experiment. *Geophys. Res. Lett.*, **24**(20), 2443–2446.

McEwen, A. S., Keszthelyi, L., Geissler, P., Simonelli, D. P., Carr, M. H., Johnson, T. V., Klaasen, K. P., Breneman, H., Jones, T. J., Kaufman, J. M., *et al.* 1998a. Active volcanism on Io as seen by Galileo SSI. *Icarus*, **135**, 181–219.

McEwen, A. S., Keszthelyi, L., Spencer, J. R., Schubert, G., Matson, D. L., Lopes-Gautier, R., Klassen, K. P., Head, J. W., Geissler, P., Fagents, S. *et al.* 1998b. High temperature silicate volcanism on Jupiter's moon Io. *Science*, **281**, 181–219.

McEwen, A. S., Belton, M. J. S., Breneman, H. H., Fagents, S. A., Geissler, P., Greeley, R., Head, J. W., Hoppa, G., Jaeger, W. L., Johnson, T. V. *et al.* 2000. Galileo at Io: Results from high-resolution imaging. *Science*, **288**, 1193–1198.

Milazzo, M. P., Keszthelyi, L. P., Radebaugh, J., Davies, A. G., Turtle, E. P., Geissler, P. E., Klaasen, K. P., Rathbun, J. A., and McEwen, A. S. 2005. Volcanic activity at Tvashtar Catena, Io. *Icarus*, **179**, 235–251.

Pieri, D. C., Baloga, S. M., Nelson, R. M., and Sagan, C. 1984. Sulfur flows on Ra Patera, Io. *Icarus*, **60**, 685–700.

Porco, C. C., and 23 colleagues. 2003. Cassini imaging of Jupiter's atmosphere, satellites, and rings. *Science*, **299**, 1541–1547.

Rathbun, J. A., Spencer, J. R., Tamppari, L. K., Martin, T. Z., Barnard, L., and Travis, L. D. 2004. Mapping of Io's thermal radiation by the Galileo photopolarimeter–radiometer (PPR) instrument. *Icarus*, **169**, 127–139.

Russell, E. E., Brown, F. G., Chandos, R. A., Fincher, W. C., Kubel, L. F., Lacis, A. A., and Travis, L. D. 1992. Galileo photopolarimeter/radiometer experiment. *Space Sci. Rev.*, **60**, 531–563.

Sagan, C. 1979. Sulphur flows on Io. *Nature*, **280**, 750–753.

Salama, F., Allamandola, L. J., Witteborn, F. C., Cruikshank, D. P., Sandford, S. A., and Bregman, J. D. 1990. The 2.5–5.0 μm spectra of Io: Evidence for H_2S and H_2O frozen in SO_2. *Icarus*, **83**, 66–82.

Saur, J., Neubauer, F. M., Connerney, J. E. P., Zarka, P., and Kivelson, M. G. 2004. Plasma interaction of Io with its plasma torus. In: F. Bagenal, T. Dowling, and W. McKinnon (eds.), *Jupiter: The Planet, Satellites, and Magnetosphere*. Cambridge University Press, Cambridge, UK, pp. 537–560.

Simonelli, D. P., Dodd, C., and Veverka, J. 2001. Regolith variations on Io: Implications for bolometric albedos. *Journal of Geophys. Res.*, **106**, 33241–33252.

Spencer, J. R., Rathbun, J. A., Travis, L. D., Tamppari, L. K., Barnard, L., Martin, T. Z., and McEwen, A. S. 2000a. Io's thermal emission from the Galileo photopolarimeter–radiometer. *Science*, **288**, 1198–1201.

Spencer, J. R., Jessup, K. L., McGrath, M. A., Ballester, G. E., and Yelle, R. 2000b. Discovery of gaseous S_2 in Io's Pele plume. *Science*, **288**, 1208–1210.

Turtle, E. P., Jaeger, W. L., Keszthelyi, L. P., McEwen, A. S., Milazzo, M., Moore, J., Phillips, C. B., Radebaugh, J., Simonelli, D. P., Chuang, F., *et al.* 2001. Mountains on Io: High-resolution Galileo observations, initial interpretations, and formation models. *Journal of Geophys. Res.*, **106**, 33175–33199.

Turtle, E. P., Keszthelyi, L., McEwen, A. S., Radebaugh, J., Milazzo, M., Simonelli, D. P., Geissler, P., Williams, D. A., Perry, J., Jaeger, W. L., *et al.* 2004. The final Galileo SSI observations of Io: Orbits G28–I33. *Icarus*, **169**, 3–28.

Vasyliunas, V. M., Frank, L. A., Ackerson, K. L., and Paterson, W. R. 1997. Geometry of the plasma sheet in the midnight-to-dawn sector of the Jovian magnetosphere: plasma observations with the Galileo spacecraft. In: *Geophysical Research Letters* (vol. 24). American Geophysical Union, Washington, D.C., pp. 869–872.

Williams, D. A., Davies, A. G., Keszthelyi, L. P., and Greeley, R. 2001. The summer 1997 eruption at Pillan on Io: Implications for ultrabasic lava flow emplacement. *Journal of Geophys. Res.*, **106**, 33105–33119.

4

Formation and early evolution of Io

William B. McKinnon

The Galilean satellites – Io, Europa, Ganymede, and Callisto – form a relatively closely spaced, coplanar, prograde set of bodies of similar mass orbiting in Jupiter's equatorial plane. As such they must have formed from a dissipative disk of gas and/or dust in orbit around Jupiter. The heavily cratered surface of Callisto, the outermost moon, implies that this formation took place early in Solar System history. Beyond these fundamental facts there is little universal agreement. Nevertheless, spurred by new *Galileo* results for Jupiter and its satellites, progress has been made in detailing possible satellite formation and evolution scenarios. The leading model for the formation of the Galilean satellites posits inflow of gas and solids across a tidal gap in the solar nebula, once Jupiter has itself formed in the "core accretion" model of giant planet formation. This leads to a relatively low-mass ("gas-starved"), circum-Jovian accretion disk, in which Io and the other satellites accrete slowly while the gap exists, and are not lost due to gas drag or tidal torques. The composition of Io, aside from any late accreting ice, is predicted to be essentially solar. Tidal decay of Ganymede's orbit in the proto-satellite nebula could have allowed it to capture Europa and then Io into the Laplace resonance. Such an outside-in formation sequence, if true, would reverse the long-standing view that the Laplace resonance was formed from the inside-out later in Solar System history, and implies that the strong tidal heating of Io could be primordial.

4.1 FORMATION OF JUPITER AND THE GALILEAN SATELLITES

Any model for the formation of Io and the other Galilean satellites must start with the formation of Jupiter. The leading model for giant planet formation in our Solar System is the two-stage *core accretion–gas capture* model: formation of a massive ice–rock–gas core by coagulation of planetesimals in the solar nebula followed by an accelerating gravitational capture of a massive gas and dust envelope from the solar

nebula (Mizuno, 1980; Stevenson, 1982; Bodenheimer and Pollack, 1986; Pollack *et al*., 1996; Inaba *et al*., 2003; Alibert *et al*., 2005a; Hubickyj *et al*., 2005; Klahr and Bodenheimer, 2006; Lissauer and Stevenson, 2006). The alternative gravitational instability model proposes that the solar nebula was sufficiently gravitationally unstable that a massive clump or subcondensation collapses directly, forming a giant gaseous proto-planet (Cameron, 1978; Boss, 2002; Mayer *et al*., 2004; Durisen *et al*., 2006). But, what do these different models for giant planet formation predict for satellite formation? In this chapter I follow the path posed by this question. I first review previous (pre-*Galileo*) work on giant planet satellite formation (Section 4.1.1), pausing long enough to update constraints on Io's time of formation (Section 4.1.2). The major focus of present research is on accretion disk models, and these are discussed in detail in Section 4.2. The implications for Io's composition and initial thermal state, especially in the case of slow-inflow, "gas-starved" accretion disks, are taken up in Section 4.3. Finally, I summarize how these new results may change our view of Io's long-term evolution (Section 4.4), and offer some concluding remarks (Section 4.5).

4.1.1 Classes of satellite-forming disks

As reviewed by Pollack *et al*. (1991), giant-planet satellite formation models have traditionally broken down into four classes (cf. Lunine *et al*., 2004). In the *accretion disk* model, a circum-Jovian disk forms as solar nebula gas and entrained solid particles (dust to boulders) flow through the Roche lobes to feed the growing Jupiter during the rapid (runaway) gas-capture phase of the core accretion model (Coradini *et al*., 1989; Pollack *et al*., 1996; cf. Bate *et al*., 2003; D'Angelo *et al*., 2003a; Papaloizou and Nelson, 2005). In the *spinout disk* model, a circum-Jovian disk forms after gas capture terminates and the distended, hot Jupiter cools and contracts, stranding material in orbit in order to conserve angular momentum (Korycansky *et al*., 1991; Magni and Coradini, 2004). A *blowout* or impact-generated circum-Jovian disk is also conceivable, but the requisite super-giant impact must not have perturbed Jupiter's obliquity (3°) by much, which is unlikely a priori (Canup and Ward, 2002). Finally, collisions of solid bodies within Jupiter's Hill sphere could have formed a gas-free *co-accretion* disk (Safronov *et al*., 1986).

The accretion disk model was conceived in terms of the runaway growth of Jupiter. Jupiter's proto-planetary envelope is greatly distended as this phase initiates, but as the nebular gas supply reaches some maximum value the proto-planet contracts and gas accretes hydrodynamically into the collapsing proto-Jupiter (Lissauer and Stevenson, 2006). The runaway persists as long as there is gas in the vicinity of proto-Jupiter's orbit, but may last no longer than $\sim 10^4$ to 10^5 yr (Hubickyj *et al*., 2005). Any circum-Jovian disk left after the end of this hydrodynamic phase should be better thought of as a spinout disk. Such a spinout disk is seen explicitly in the final thermal contraction phase of Magni and Coradini's (2004) 3-D numerical hydrodynamical model of Jupiter's formation by core accretion–gas capture (their fig. 15). An actual accretion disk, and one that can form satellites, requires late-inflowing gas containing sufficient angular momentum

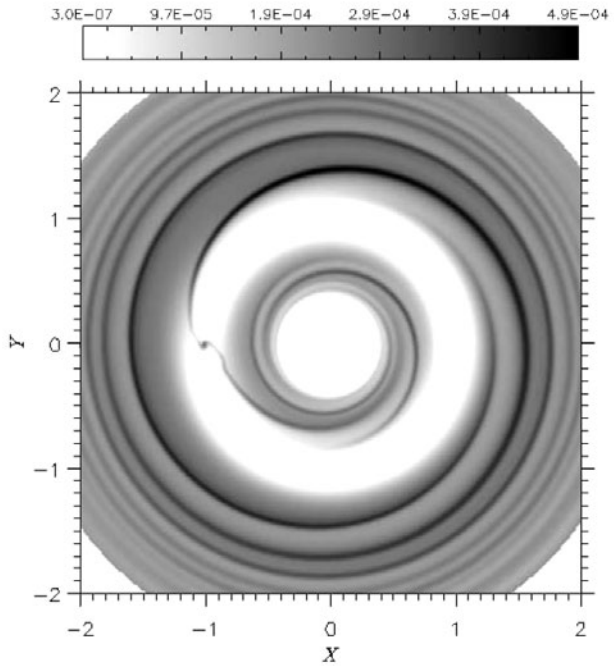

Figure 4.1. Global surface density around a 1 M_J planet orbiting a 1 M_{Sun} (solar mass) star at 5.2 AU and embedded within a low-mass disk (equivalent to 0.01 M_{Sun} within 20 AU) (modified from D'Angelo *et al.*, 2003a). In this numerical simulation, kinematic disk viscosity ν does not follow the α-model prescription, but is instead a constant 10^{15} cm^2 s^{-1} (dynamically cold); the equivalent Shakura–Sunyaev α is near 10^{-2}. Scale bar indicates surface density, with 10^{-4} corresponding to 33 g cm^{-2}.

for a centrifugal force balance at orbital distances compatible with satellite formation, and after proto-Jupiter has contracted to a scale of less than a few R_J (1 R_J = the current Jovian radius).

In this regard, it is now recognized that Jupiter's accretion probably did not terminate cleanly. Even if Jupiter opens a gap in the solar nebula around its orbital position, either through tidal torques or by simply drawing down the available nebular gas, inflow of solar nebula gas and dust across the gap continues, and potentially at a much reduced rate (Lubow *et al.*, 1999; Bryden *et al.*, 1999; Bate *et al.*, 2003; D'Angelo *et al.*, 2003a,b) (Figure 4.1). A low-mass accretion disk forms around Jupiter, and should last as long as the solar nebula exists to feed it (Stevenson, 2001; Canup and Ward, 2002; D'Angelo *et al.*, 2003a; Alibert *et al.*, 2005b). This is the genesis of the gas-starved disk model for the formation of the Galilean satellites (Canup and Ward, 2002, 2006) – the modern version of the accretion disk model. This model self-consistently solves or resolves a number of long-standing satellite formation issues (Stevenson *et al.*, 1986), and is discussed in detail in the next section.

The alternative, satellite formation model of Mosqueira and Estrada (2003a,b) is either a spinout or accretion disk model, depending on how one views the timing of

their disk creation, but the important point is that they argue for a more massive circum-Jovian disk than do Canup and Ward (2002) (or Alibert *et al.* (2005b)), one closer to the classic minimum-mass (Jovian) sub-nebula (MMSN), wherein the rock + ice in the Galilean satellites is augmented by enough H and He gas to match solar composition (for a total of $\sim 0.02\, M_J$, where M_J is the mass of Jupiter (Lunine and Stevenson, 1982)).[1] Such a relatively massive accretion disk could in principle be created *after* proto-Jupiter contracted for a sufficient continuing inflow of solar nebula gas and dust; this is also discussed below.

It is less clear what the gravitational instability model for giant planet formation (Boss, 2002) implies for satellites. This model does not naturally account for the cores of the giant planets (particularly, that of Saturn), much less the architecture of the rest of the Solar System (Lissauer, 1993), nor is it obvious that giant gaseous proto-planets are even sufficiently long-lived to cool and contract to become bodies like Jupiter and Saturn (Lissauer and Stevenson, 2006). Still, enormous progress in numerical simulations of nebular gravitational instabilities is being made (Durisen *et al.*, 2006), so this path to giant planethood remains in play (especially in relation to extrasolar giant planets; Bodenheimer and Lin, 2002). If Jupiter formed this way, it would have formed early (within $\sim 10^3$ yr to reach the giant gaseous proto-planet stage (Mayer *et al.*, 2004)) and during its Kelvin–Helmholtz cooling phase might have created a spinout disk. Given that the solar nebula would still exist at this time, subsequent formation of an accretion disk is likely as well, and may be more relevant to satellite creation. The properties of such an accretion disk are, however, obscure at present, as no model of giant gaseous proto-planet formation has ever been taken in a self-consistent manner to this late stage.

For completeness I note that the coaccretion model for the Galilean satellites has been recently revived by Estrada and Mosqueira (2006). The principal difficulties with the coaccretion model are: (1) an adequate supply of solid bodies after the solar nebula has dispersed (given that most local solids have presumably already accreted into the giant planets), and (2) the mean angular momentum of collisionally captured material is low ($\sim$ zero). Estrada and Mosqueira (2006) acknowledge that these difficulties remain, and given that there is no obvious or natural explanation for the compositional gradient among the Galilean satellites in the coaccretion model, I do not consider it further.

4.1.2 When did Io form?

I end this section by discussing the absolute time frame for Io's formation. The models of Coradini *et al.* (1989), Canup and Ward (2002, 2006), Mosqueira and Estrada (2003a,b), and Alibert *et al.* (2005b) all peg the formation of the Galilean satellites to the end of Jupiter's hydrodynamic collapse phase. In the models of Canup and Ward (2002, 2006) and Alibert *et al.* (2005b) satellite accretion is protracted, and lasts as long as the solar nebula exists. Naturally, Jupiter (and Saturn) must form while the

[1] Mosqueira and Estrada (2003b) ultimately argue for a circum-Jovian nebula depleted in gas, perhaps by an order of magnitude.

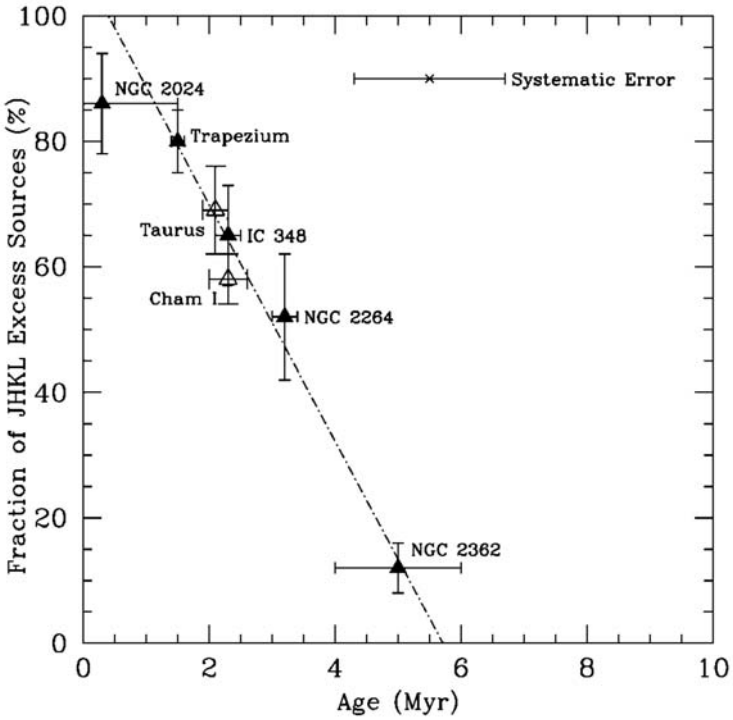

Figure 4.2. *JHKL* excess/disk fraction as a function of mean proto-stellar cluster age (from Haisch *et al.*, 2001). Disk ages depend on the spread of source ages from a single set of pre-main-sequence (PMS) model tracks. The systematic error from different PMS model tracks is indicated. The oldest cluster, at 30 Myr (not shown), had a single detected disk, for an excess fraction of $3 \pm 3\%$. The dot–dashed line is a least-squares fit to the data taken by Haisch *et al.* (2001) (filled triangles).

solar nebula exists in order for both to acquire their massive H–He envelopes. Based on the observations of young stars and disks, the lifetime of the solar nebula is generally taken to lie between a few to 10 Myr (Hubickyj *et al.*, 2005; Lissauer and Stevenson, 2006; Meyer *et al.*, 2006). Observations of infrared excesses in clusters of young stellar objects indicate that nearly all ($\geq$80%) form with optically thick circumstellar disks, and that the average lifetime of these disks is $\sim$3 Myr (Figure 4.2). Some of these "primordial" dust disks can apparently last appreciably longer, however (Hillenbrand, 2006). The observations in Figure 4.2, from Haisch *et al.* (2001), are based on near-infrared excesses (*L*-band is 3.4 μm) and are thus sensitive to hot dust close to the stars in question (within $\sim$0.1 AU). Nonetheless, the number of young stellar objects sampled is large, and age uncertainties are reduced by using stellar cluster averages. Results such as these validate earlier indicators of circumstellar disk lifetimes (Strom *et al.*, 1993), but with greatly increased confidence.

Survey results at N-band (10.3 μm), sensitive to warm (~300 K) dust in the terrestrial planet zone (~0.3–3 AU), yield similar results to Figure 4.2 (Mamajek *et al.*, 2004). Such results are now being augmented with observations from the *Spitzer Space Telescope* as well, which offers even greater sensitivity and wavelength coverage in the mid-infrared. All of these observations are consistent with a dispersion in disk lifetimes for young Sun-like stars between 1–10 Myr (Dullemond *et al.*, 2006; Hillenbrand, 2006). That is, Figure 4.2 should be thought of as a *cumulative* distribution; what we are most interested in is the underlying differential distribution of primordial disk lifetimes. The least-squares fit in Figure 4.2 corresponds to a uniform distribution of lifetimes between ~0 and 6 Myr. The "true" distribution may be more complicated, with a longer lived tail.

Direct measurement of gas abundance in primordial disks is more difficult than for dust, but observations to date are at least consistent with the above disk lifetime picture (Meyer *et al.*, 2006), and it is, of course, gas that dominates the mass of primordial disks and that is necessary to form the great bulk of gas giants such as Jupiter and Saturn (Meyer *et al.*, 2006; Hillenbrand, 2006). This observational situation will no doubt improve in the near future. Optically thick, hot and warm dust has, however, long been taken as a proxy for coexisting gas, especially as there is a close correlation of T Tauri ultraviolet excesses, a signature of disk accretion onto the central star, and optically thick hot dust infrared emission (Takeuchi *et al.*, 2005; Dullemond *et al.*, 2006; Hillenbrand, 2006; Lada *et al.*, 2006).

A final note on the stellar ages discussed here: zero is set at the stellar "birthline", as shown in the Hertzsprung–Russell luminosity–temperature diagram, where the proto-star begins its initial gravitational collapse (e.g., Sackmann *et al.*, 1993; Palla and Stahler, 1999). For the range of disk lifetimes discussed above, the formation of Jupiter, and that of Io and the other Galilean satellites, all take place while the Sun is still a PMS star, before hydrogen ignition.

4.2 THE CIRCUM-JOVIAN ACCRETION DISK

As discussed above, Io and Galilean satellites most likely formed in a circum-Jovian accretion disk supplied by inflow from the solar nebula after Jupiter formed (Coradini *et al.* 1989; Canup and Ward, 2002; Alibert *et al.*, 2005b; cf. Mosqueira and Estrada, 2003a). Figure 4.3 illustrates several key aspects of this picture. Solids and gas are delivered to circum-planetary orbit with a range of specific angular momenta such that they achieve orbit in the satellite-forming region, out to r_C (Canup and Ward, 2002). Because the gas in closer orbits moves faster than more distant gas, shear exists, and if there is viscous coupling in the gas, shear turbulence and dissipation. This causes mass to flow toward Jupiter, and angular momentum and some mass to flow outward. The model of Canup and Ward (2002) follows the classic accretion disk model of Lyden-Bell and Pringle (1974), except that the disk, or proto-Jovian nebula, is in steady-state. Mass is continuously fed into it from the solar nebula (at $\dot{M}_{\rm disk}$), and through viscous spreading both inward and outward, achieves a steady-state distribution of surface density and temperature. Commonly, kinematic disk viscosity (ν) is parameterized by

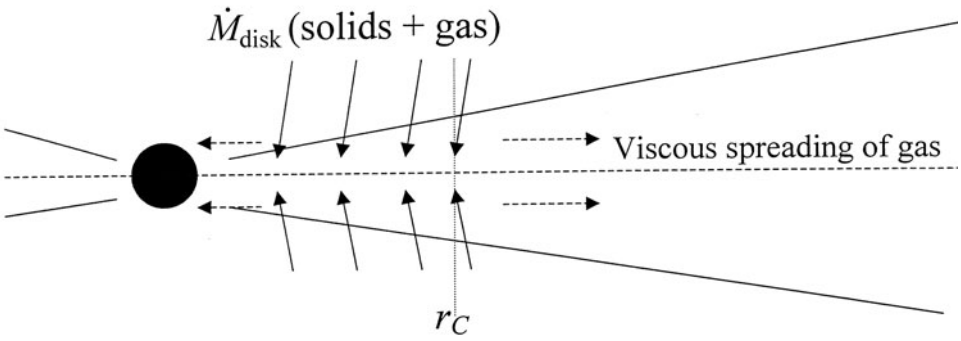

Figure 4.3. Schematic of circum-Jovian accretion disk model. $\dot{M}_{\rm disk}$ is the flux of gas and solids from the solar nebula, which achieves centrifugal balance over the region of satellite formation ($0 \leq r \leq r_C$). Nominally, the disk spreads viscously inward and outward, and is both accreted by Jupiter and stripped by other processes beyond some outer radius (modified from Canup and Ward, 2002).

the Shakura–Sunyaev "α model", according to $\nu = \alpha c H \approx \alpha c^2/\Omega$, where c is the isothermal sound speed at the nebular midplane, H is the nebular scale height, and Ω is the Keplerian orbital frequency. The α model is intended to represent turbulent viscosity (molecular viscosity being unimportant by many orders of magnitude), where the source and strength of the turbulence are all folded into the dimensionless α parameter. Modeling of accretion disks around stars has long suggested α values in the range between 10^{-4} and 10^{-2} (e.g., Hartmann *et al.*, 1998; Stone *et al.*, 2000; Dullemond *et al.*, 2006), but the appropriate values for circum-planetary disks are much less constrained. Potential sources of turbulence include thermal convection when the disk is optically thick, mechanical instabilities driven by infall from the solar nebula, and magnetorotational instabilities when the disk is thin enough that galactic cosmic rays partially ionize the gas (this requires surface densities $\leq 10^2\,\mathrm{g\,cm^{-2}}$ (Dullemond *et al.*, 2006)).

Temperatures in the proto-Jovian nebula are set by the energy balance between heating due to proto-Jupiter's luminosity, the potential energy of infalling matter, viscous dissipation within the disk and illumination from the background solar nebula, and radiative cooling from the disk photosphere (Coradini *et al.*, 1989; Canup and Ward, 2002). Viscous dissipation proves to be dominant in the energy balance and in determining disk surface density, so the choice of α and $\dot{M}_{\rm disk}$ is crucial. Figure 4.4 illustrates the disk surface density and temperature profile for the "nominal" steady-state model of Canup and Ward (2002). For this model $\alpha = 5 \times 10^{-3}$, the disk opacity K is $10^{-4}\,\mathrm{cm^2\,g^{-1}}$ (i.e., H–He gas opacity only), and the infall rate is $2 \times 10^{-7}\,M_{\rm J}\,\mathrm{yr^{-1}}$. This is an example of a "gas-starved" nebula. The surface density σ, when integrated to its outer truncation radius, contains much less mass than the MMSN, whose surface density follows a function similar to:

$$\sigma = 1.2 \times 10^6 (5.9\,R_{\rm J}/r)\,\mathrm{g\,cm^{-2}} \tag{4.1}$$

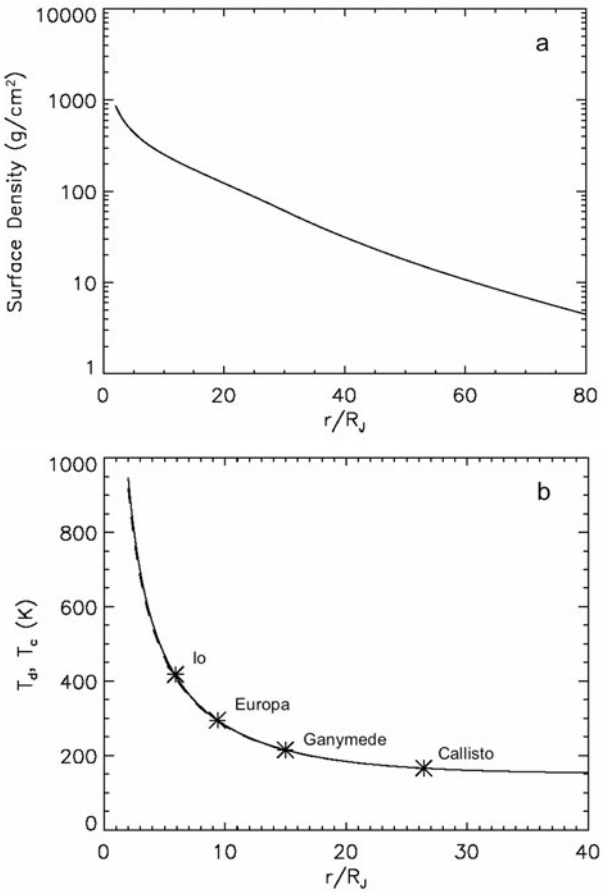

Figure 4.4. Steady-state (a) surface density σ, and (b) temperatures for a slow-inflow ($2 \times 10^{-7}\ M_J\ yr^{-1}$), low-opacity ($10^{-4}\ cm^2\ g^{-1}$) circum-Jovian accretion disk (modified from Canup and Ward, 2002). The disk is optically thin, so the disk surface temperature (T_d, dashed) and midplane temperature (T_c, solid line) are equal. The present positions of Io and the other Galilean satellites are indicated.

(e.g., Mosqueira and Estrada, 2003a), where r is radial distance. A MMSN ($\sim 2 \times 10^{-2}\ M_J$) is processed through the gas-starved disk in Figure 4.4 every 10^5 yr, however, so as long as the condensable solids can accrete along the way, and be retained in orbit, Io and the Galilean satellites can form on this timescale. This is the deeper meaning of the MMSN, not simply the instantaneous mass distribution, but the minimum mass that has passed through the disk in its lifetime (cf. Lissauer, 1993). I note that at this stage in Solar System history the solar nebula is probably several million years old, so the ratio of gas to solids in the infalling material is likely to be *non-solar*. If so, the MMSN, when seen as integrated through time, could be larger or smaller than its nominal value.

4.2.1 Advantages of the gas-starved disk scenario

The gas-starved disk model solves a number of long-standing timescale issues with the proto-Jovian nebula (Stevenson *et al.*, 1986; Canup and Ward, 2002):

(1) In the MMSN, the Kelvin–Helmholtz cooling time of the disk, $\sim 10^3\,\sigma K$ yr, is several $\times 10^4$ yr at minimum and much longer than the Safronov accretion time of the Galilean satellites (of order 10–10^3 yr; cf. Shoberg, 1982). This leads to problems of rock-rich satellite survival (see below). For the gas-starved disk, the cooling times are $\ll 10^3$ yr, so the extent of condensation is essentially set by the steady-state temperature (Figure 4.4(b)).
(2) In the MMSN the gas drag timescale for small bodies in the solid-rich, disk midplane to drift inward and be accreted by Jupiter is short, $\sim 10^3 \times (R_s/1\,\mathrm{km})$ yr, where R_s is the body radius (Stevenson *et al.*, 1986), and the orbital decay time for individual large satellites is little better, $\sim 10^3 \times (R_s/2{,}000\,\mathrm{km})$ yr (Canup and Ward, 2002). In the slowly cooling MMSN, early (rock-rich) and later generations of planetesimals could be lost, although Mosqueira and Estrada (2003a) argue that gas drag actually assists the accretional growth of small bodies and allows them to reach sizes where gas drag induced drift is not important. In the gas-starved disk, gas drag timescales are much increased, and the peril mitigated.
(3) Large satellites' orbits also migrate inward because of angular momentum transfer by disk tidal torques (type I decay), or if they are sufficiently massive as to open a gap in the circum-Jovian disk, inward migration follows the viscous spreading of the disk (type II decay). Type I decay in the MMSN is rapid, $\sim 10^2$ yr for a Galilean satellite (Canup and Ward, 2002). Type II decay is slower, $\sim 10^4 \times (10^{-3}/\alpha)$ yr, but the ability of even Ganymede to open a gap is marginal unless α is low ($<10^{-3}$) (Canup and Ward, 2002). Thus, unless the MMSN disk viscosity is sufficiently low, it is unlikely that early rock-rich satellites could have survived long enough for ice condensation and accretion. In contrast, for the gas-starved disk Type I decay times are greatly increased (by $\sim$3 orders of magnitude), so satellites can potentially survive over much of the gas-starved disk lifetime, and type II decay need not be invoked.

If the gas + solids inflow rate is markedly increased over that in Figure 4.4, to $\sim 10^{-4}\,M_J\,\mathrm{yr}^{-1}$, the steady-state disk surface densities increase, but for α in the 10^{-4} to 10^{-1} range, disk temperatures are much too high for water ice condensation in the region of the Galilean satellites, and even silicate condensation in the Io region becomes problematic (Coradini *et al.*, 1989; Canup and Ward, 2002, their fig. 4). Temperatures are even higher if grains contribute to the opacity, as opposed to gas opacity only. Such a fast-inflow accretion disk corresponds to Jupiter at the time of runaway gas accretion or immediately thereafter (Section 4.1) (Coradini *et al.*, 1989; Mosqueira and Estrada, 2003a; Bate *et al.*, 2003; D'Angelo *et al.*, 2003a). To condense and accrete the Galilean satellites, such a thick, hot disk must first cool (Coradini *et al.*, 1989; Mosqueira and Estrada, 2003a), which returns us to the epoch of slow (and diminishing) inflow from the solar nebula.

To create (or maintain) a circum-Jovian accretion disk with a mass comparable to the MMSN requires a low α, so that the disk does not spread viscously too rapidly and accrete onto Jupiter. If the disk is to have "reasonable" temperature structure (i.e., one that predicts ice condensation near Ganymede or Callisto's formation region), then α must be very low, $\sim 10^{-6}$ or less (essentially inviscid) (Lunine and Stevenson, 1982; Canup and Ward, 2002). Mosqueira and Estrada (2003a) in fact use such a MMSN model with an assumed temperature profile to "predict" α values in the 10^{-6} to 10^{-5} range in the Io to Ganymede region, with the temperatures maintained against radiative losses to space by very weak viscous dissipation.

Such a very low viscosity MMSN would necessarily be long-lived, with a viscous lifetime of 10^6 to 10^7 yr. From points (2) and (3) above, any satellites then formed would almost certainly have been lost to Jupiter via gas drag or type I decay. In this case the only hope for Io and the other Galilean satellites would be gap opening and type II decay, which would proceed on the same extended viscous timescales. This is the scenario advocated by Mosqueira and Estrada (2003b). Canup and Ward (2002) counter that the presence of Galilean-sized satellites themselves generates, through density–wave interactions, an effective $\alpha \gg 10^{-6}$, and thus a correspondingly more rapid type II orbital decay. Mosqueira and Estrada (2003b) maintain, in a complex argument, that density waves launched by Ganymede may "clear" the sub-nebula inside its orbit, thus stranding all three inner satellites, Io, Europa, and Ganymede (though how viscous evolution of the inner disk and type II decay are avoided in this case is unspecified).

On balance, the above physical arguments strongly indicate a preference for the gas-starved accretion disk origin for Io and the Galilean satellites, as opposed to formation in a more massive, MMSN. There seems little doubt that an accretion disk forms about Jupiter after it opens a gap in the solar nebula (e.g., D'Angelo *et al.*, 2003a,b). Jupiter's final growth is likely processed through such a disk, but ultimately, the inflow must abate as the solar nebula "reservoir" is depleted by: (1) growth of Jupiter and Saturn; (2) viscous accretion of the inner solar nebula onto the Sun; and (3) photoevaporation or other "T Tauri" loss processes. Io and the other Galilean satellites must have formed in this waning stage of *solar* nebula evolution.

The partially differentiated structure of Callisto also provides an independent argument for prolonged accretion ($>$ a few $\times 10^5$ yr) of the Galilean satellites, which is consistent with the gas-starved disk model (Canup and Ward, 2002), and discussed in Section 4.3.2. Mosqueira and Estrada (2003a) prefer to argue an independent accretion scenario for outermost Callisto. Given that Ganymede and Callisto are so similar in orbit, density, and mass, however, it would seem more economical, if not preferable, to seek a common origin for both, and indeed for all four Galilean satellites.

4.2.2 Time-varying disk models

Strictly speaking, the model of Mosqueira and Estrada (2003a,b), like that of Lunine and Stevenson (1982) before it, is not an accretion disk model at all, but a static, passive disk. The model of Canup and Ward (2002) is a true accretion disk, but

because its parameter space is explored in terms of a constant inflow from the solar nebula, the model is stationary or steady-state. Inflow from the solar nebula onto the circum-Jovian disk must have declined with time, however, and ultimately stopped when the solar nebula itself vanished. The consequences of such a time-evolving inflow have been recently explored by Alibert *et al.* (2005b) and Canup and Ward (2006). Alibert *et al.* (2005b) begin by assuming that the declining inflow, $\dot{M}_{\rm disk}$, is given by:

$$\dot{M}_{\rm disk} = \dot{M}_{\rm disk,0}(1 - t/\tau) \tag{4.2}$$

where $\dot{M}_{\rm disk,0} = 9 \times 10^{-7}\, M_{\rm J}\,{\rm yr}^{-1}$, $\tau = 5.6 \times 10^5\,{\rm yr}$, and the choice of $t = 0$ is arbitrary. Figure 4.5(a, b) shows the surface densities and temperatures obtained in their disk as a function of time, for a "fiducial" constant α of 2×10^{-4}. Alibert *et al.* (2005b) chose this relatively low α to satisfy some very simplified satellite decay and compositional arguments, but for the purposes of this review these calculations can simply be taken as an interesting counterpoint to those in Figure 4.4.

The model of Alibert *et al.* (2005b) is a "gas-starved" disk model, as can be seen by comparing (4.1) with Figure 4.5(a). A key physical difference, however, between this model and that of Canup and Ward (2002, 2006) is that in Alibert *et al.* (2005b) the inflow accretes to the outer boundary of the disk, here at 150 $R_{\rm J}$ (0.2 × the Hill radius), is viscously processed, and ultimately accreted by Jupiter. Thus, Io and the other Galilean satellites are presumed to accrete and migrate inward over rather great distances. Details of satellite accretion and survival are not developed in Alibert *et al.* (2005b), though, and it is not obvious why a more extended regular satellite system would not form from such an extended disk, reaching out to the prograde irregular satellites.[2] In contrast, in Canup and Ward (2002, 2006), infalling material is delivered to the inner part of the circum-Jovian accretion disk (Figure 4.3), where the solids locally accumulate into larger bodies, and it is the solid-depleted residual gas that spreads viscously into the extended disk. At the time of writing, unfortunately, the pattern of inflow near Jupiter is not well resolved (D'Angelo *et al.*, 2002, 2003a,b; Bate *et al.*, 2003), and both quasi-vertical infall (Figure 4.3) and quasi-Keplerian midplane inflow may turn out to be important for satellite-forming accretion disks.

The temperature evolution in Figure 4.5(b) is worth comment. By $t = 0.4$ Myr, about one MMSN (0.02 $M_{\rm J}$) worth of infalling matter remains to be accreted, and one may suppose that Io and the Galilean satellites more or less formed from this final solar bequest. Yet at 0.4 Myr temperatures everywhere in the disk exceed the condensation temperature of water ice (~175 K in the outer disk), which may make accreting sufficient ice in the satellites difficult. The high temperatures are a consequence of using high, interstellar dust based opacities for the disk ($K \geq 1\,{\rm cm}^2\,{\rm g}^{-1}$ (Alibert *et al.*, 2005a)). Coagulation almost certainly reduces the contribution of grain opacity in the proto-Jovian nebula, however (Podolak, 2003). The temperatures reached after infall ends (at 0.56 Myr in this model; after which the disk is "allowed" to viscously expand outward while it continues to accrete to Jupiter),

[2] This criticism applies with even more force to the model of Mousis and Gautier (2004), which provides neither sufficient mass to build the Galilean satellites nor a mechanism for them to migrate to their present positions.

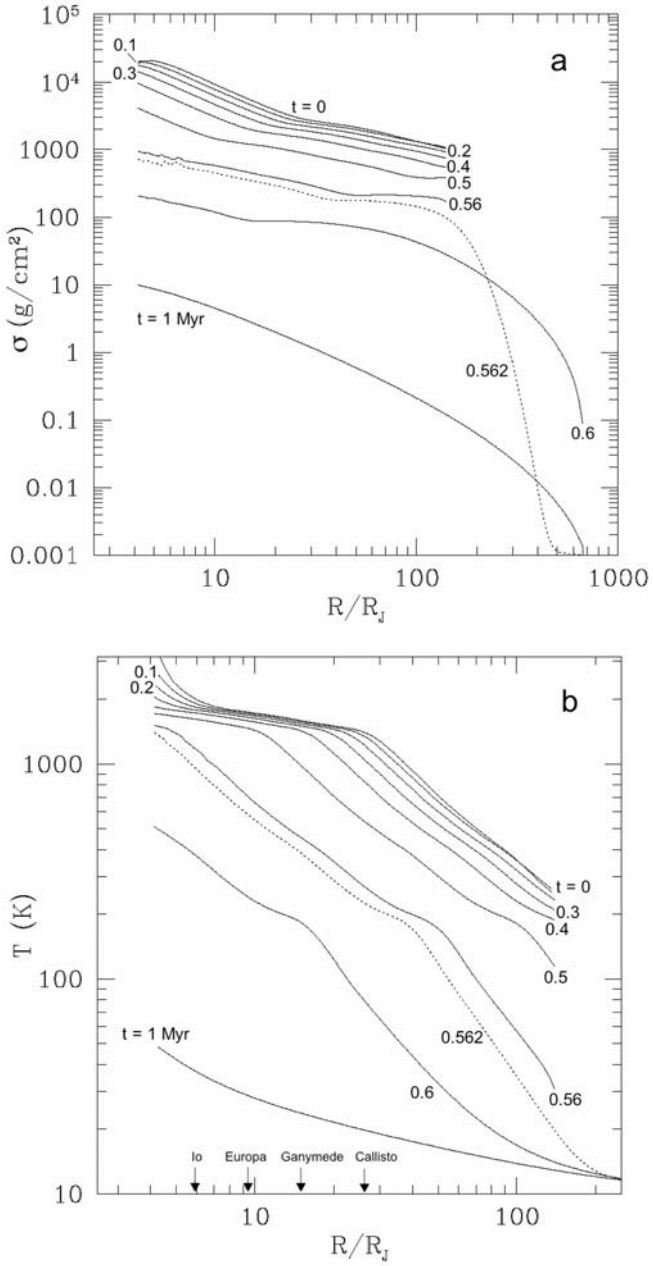

Figure 4.5. (a) Surface densities and (b) midplane temperatures for a declining inflow ($< 10^{-6}\, M_J\, \mathrm{yr}^{-1}$), high-opacity ($\geq 1\, \mathrm{cm}^2\, \mathrm{g}^{-1}$), circum-Jovian accretion disk (modified from Alibert *et al.*, 2005b). In both panels, the dotted line refers to 2,000 yr after 0.56 Myr (the epoch at which outward diffusion of the disk begins). The present positions of Io and the other Galilean satellites are indicated.

are in contrast rather low (<50 K). This model neglects the early luminosity of Jupiter, which is important for Io, and is set in the context of a very cold solar nebular background. These points are returned to below.

The gas-starved accretion disk model of Canup and Ward (2002, 2006), and the related model of Alibert *et al.* (2005b), are clear advances; they illuminate a path forward in understanding the accretion of Io and the Galilean satellites. Important matters requiring further rigorous attention are the inflow rate to the circum-Jovian disk, its strength, time history, and specific angular momentum (the latter especially, as it determines the radial scale of disk), the origin of disk viscosity, and the myriad details of disk structure and satellitesimal formation and aggregation. The latter is a focus of the most recent work by Canup and Ward (2006), in which multiple generations of satellites are formed, and it is only the final set of large satellites of Jupiter that survive type I orbital decay, as the modeled solar nebula inflow rate declines exponentially.

4.3 ACCRETION OF IO

4.3.1 Composition

I turn now specifically to the composition of the building blocks that originally made up Io. I do this in the context of the gas-starved accretion disk models above. A fundamental inference is that the solids that ultimately built Io were fed into the circum-Jovian accretion disk from solar orbit. Thus, their initial chemistry is one characteristic of planetesimals near the orbit of proto-Jupiter, as opposed to materials from the terrestrial planet zone, the inner asteroid belt, or the more distant comets (e.g., Schubert *et al.*, 2004). Logically, the closest analogs to, or survivors from, this primordial planetesimal population are the dark, reddish asteroids of the outer asteroid belt and Trojan clouds, specifically the P- and D-type asteroids (Gradie *et al.*, 1989). In detail, not much is known about these asteroid types.[3] Based on remote sensing it is presumed that they are largely similar to the C-type asteroids of the main asteroid belt and grossly chemically and mineralogically similar to the carbonaceous chondrites that are thought to come from the C-types, but more primitive (see below).

Only one meteorite has been proposed as possibly coming from a P- or D-type asteroid, the Tagish Lake carbonaceous chondrite, which fell in Canada in 2000 (Brown *et al.*, 2000). Hiroi *et al.* (2001) proposed the link based on spectral similarities in the visible and near-infrared, and analysis of the fireball trajectory indicates an aphelion of 3.3 ± 0.4 AU (Brown *et al.*, 2000), compatible with origin on a P-type parent body at least. Tagish Lake is a breccia at all scales; its major component is a fine-grained, opaque matrix of phyllosilicates, sulfides, and magnetite, surrounding aggregates of olivine, pyroxene, other minerals and inclusions (Zolensky *et al.*, 2002).

[3] Indeed, the D-type asteroids may have largely been dynamically injected into cis-Jovian orbits at a later epoch in Solar System history (Morbidelli *et al.*, 2005; H. Levison, pers. commun., 2006).

Low-temperature aqueous alteration is pervasive but incomplete, and the carbon abundance is high (~4 wt%; Brown *et al.*, 2000), with "record levels" of preserved interstellar materials (Zolensky *et al.*, 2002). All of these characteristics are consistent with an origin far from the Sun.

The mineralogy of Tagish Lake is also consistent with what is inferred spectrally for P- and D-type asteroid surfaces. Although historically the red visible–near-infrared spectral slope of these asteroids has been ascribed to some "ultracarbonaceous" material (e.g., Gradie *et al.*, 1989), Cruikshank *et al.* (2001) and Emery and Brown (2004) have shown that anhydrous mafic silicates such as pyroxene, in combination with a neutral absorber such as carbon black, better reproduce the major spectral features. The 3-μm hydration feature, characteristic of phyllosilicates, is not seen in absorption for these asteroid types, and this has long been interpreted as implying that the surfaces of P- and D-type asteroids are dominated by anhydrous as opposed to hydrous and hydrated silicates (Jones *et al.*, 1990; Lebofsky *et al.*, 1990; Rivkin *et al.*, 2002). Cruikshank *et al.* (2001) and Emery and Brown (2004) are careful to point out that up to 10–40 wt% phyllosilicates may be present on these asteroid surfaces (depending on the asteroid), but be spectrally undetectable (the neutral absorber suppresses the 3-μm band). In this interpretation of P- and D-type asteroids, anhydrous nebular condensates and interstellar materials are accreted together with water and other ices at Jupiter's distance from the Sun, but water ice melting and aqueous alteration were limited in extent (Jones *et al.*, 1990; Lebofsky *et al.*, 1990).

A key aspect of primitive carbonaceous chondrite mineralogies, such as those represented by Tagish Lake, is that in terms of refractory solids, metal, and silicates, the elemental abundances are essentially solar (Brown *et al.*, 2000; Lodders, 2003). As meter-scale and smaller boulders of such composition follow the gas inflow into the circum-Jovian accretion disk (Canup and Ward, 2002, 2006), they should encounter shocked regions (Lubow *et al.*, 1999; D'Angelo *et al.*, 2002, 2003a). The effects of these shocks on the entrained solids has not been studied, but heating and mechanical disruption are possible outcomes. Accreting onto the circum-Jovian disk at or near the position of Io in the model of Canup and Ward (2002) would subject the solids to temperatures sufficient to vaporize any ices and dehydrate most hydrated silicates (e.g., serpentine breaks down above 250–300 K at midplane pressures near Io's position in the model in Figure 4.4 (Fegley, 1999)). Most organics would also be lost (Nakano *et al.*, 2003), along with associated volatile sulfur compounds.[4] If much higher temperatures are encountered, as in the model of Alibert *et al.* (2005b) or calculations of D'Angelo *et al.* (2003a), then all (or nearly all) of the solar nebula solids should vaporize and subsequently recondense as the circum-Jovian nebula cools.

What solids should condense from a hot circum-Jovian nebula can be judged from the classic papers of Prinn and Fegley (1981, 1989), in which thermochemical equilibrium calculations in a solar-composition gas were combined with kinetic or rate considerations. Further elucidation of gas–grain reactions can be found in Fegley

[4] A "pristine" frozen sample of Tagish Lake gave off a sulfurous odor when allowed to warm to room temperature (Zolensky *et al.*, 2002).

(1999). It turns out that even the gas-starved disks exemplified by Figures 4.4 and 4.5 are denser, higher pressure disks than classic solar nebula models (e.g., Lewis, 1974), meaning that pressures are higher at a given temperature (by up to two orders of magnitude). (They are, of course, lower pressure environments than the minimum mass giant planet sub-nebulae examined in detail in Prinn and Fegley (1981, 1989).) In this circumstance, the corrosion of Fe alloy to troilite (FeS) in the presence of sub-nebular H_2S gas remains facile at the FeS stability temperature of $\approx$710 K (Fegely, 1999). Oxidation of remaining iron to magnetite (Fe_3O_4) at $\approx$370 K is also kinetically favored. What is likely to be kinetically inhibited, and in contrast to the MMSN prediction in Prinn and Fegley (1989), is the hydration of mafic silicates to form minerals such as serpentine at still lower temperatures (see Fegley, 1999, figs. 2 and 3).

The implications for Io's bulk composition are clear. Refractory oxides, metal and silicates, whether delivered directly from solar orbit or condensed from a hot circum-Jovian disk, should have existed in *essentially solar proportions*. The sulfur abundance, as sulfide, should also have been solar, or nearly so (especially as the volatile sulfur species in Tagish Lake, for example, are likely to have been products of aqueous alteration in its parent body, and such heliocentric parent body alteration could have taken place well after Jupiter and its satellites formed).[5] Much of Io's iron metal may have accreted as magnetite – an oxide – although it should be recognized that much if not all of the magnetite in Tagish Lake (and other carbonaceous chondrites) is a product of low-temperature aqueous alteration as well (Zolensky *et al*., 2002), and so might not have yet formed within solar-orbiting planetesimals near Jupiter at the time of Io's accretion. Such early aqueous alteration would depend on early ice melting, which could have been driven by heating due to decay of ^{26}Al and ^{60}Fe (e.g., Grimm and McSween, 1989).

In contrast, Io is likely to have been initially carbon-depleted compared with solar abundances, owing to elevated temperatures in the Io-forming region, although retention of some refractory organics and/or graphite is likely (Prinn and Fegley, 1989; Nakano *et al*., 2003; Lodders, 2003, 2004). It would also be a challenge for Io to acquire much bulk water. Even if the gas-starved disk model of Canup and Ward (2002) in Figure 4.4 is adopted (as a cool end member), infalling icy (or merely "wet") planetesimals should be heated and lose much of their water before accretion into the growing satellite. This dehydration may have been less than 100% effective, however, especially for larger solar planetesimals that may have been directly captured by gas drag into the circum-Jovian disk (Canup and Ward, 2002; McKinnon and Leith, 1995). If Io had accreted from completely hydrated silicates, it would upon differentiation have formed an ice shell of comparable thickness to Europa's (McKinnon and Zolensky, 2003). This seems an unlikely prospect for Io, but there is the question of ice accretion in the cooling sub-nebula model of Alibert *et al*. (2005b). From

[5] I note that the solar sulfur abundance of primitive carbonaceous chondrites (Lodders, 2003) is in itself fatal to the diffusive drawdown argument of Pasek *et al*. (2005), for depleting nebular H_2S in the region of the main asteroid belt.

Figure 4.5(b), there is at least the possibility of a thin ice veneer forming on Io at late times in the circum-Jovian disk.

The black-body temperature (T_e) of a flat disk (adequate for the argument that follows) in equilibrium with proto-Jupiter's luminosity (L_{PJ}) is given, following Chiang and Goldreich (1997), by:

$$T_e \approx \left(\frac{2}{3\pi}\right)^{1/4} \left(\frac{R_{PJ}}{a}\right)^{3/4} T_{PJ} \tag{4.3}$$

where R_{PJ} and T_{PJ} are the proto-Jovian radius and black-body temperature, respectively, and a is Io's distance from the planet. T_{PJ} can be simply scaled from $(L_{PJ}/L_{Sun})^{1/4}(R_{Sun}/R_{PJ})^{1/2}T_{Sun}$, where L_{Sun}, R_{Sun}, and T_{Sun} are the Sun's present luminosity, radius, and effective temperature, respectively. For $a = 5.9\,R_J$, $R_{PJ} = 1.6\,R_J$, and $L_{PJ} = 10^{-6}\,L_{Sun}$ (the baseline model in Hubickyj *et al.* (2005)), $T_e \approx 115$ K, too low to prevent ice condensation *at the midplane* unless the disk is substantially optically thick. If proto-Jupiter's luminosity following envelope collapse is, however, $\sim 10^{-5}\,L_{Sun}$ (Burrows *et al.*, 1997; Fortney *et al.*, 2005), then $T_e \approx 200$ K, and water-ice condensation may be prevented at Io's position. Pending resolution of the issue of Jupiter's early luminosity, the question of minor ice accretion onto Io remains open. A late, final "frosting" of ice in the Io region could also account for the inferred but otherwise enigmatic iciness of Amalthea (Takato *et al.*, 2004; Anderson *et al.*, 2005).

Regardless, this calculation also makes clear that the long-held idea that Jupiter's early luminosity is responsible for the compositional gradient of the Galilean satellites (Kuiper, 1952; Pollack and Reynolds, 1974) may not be correct. Viscous dissipation is probably more important than Jovian insolation in determining disk radial temperature structure. Figures 4.4 and 4.5 illustrate this point. An additional luminosity source is the boundary layer between the circum-Jovian disk and proto-Jupiter (Papaloizou and Nelson, 2005), as close-in orbiting material "brakes" from Keplerian velocity to the slower equatorial rotation speed of proto-Jupiter. This luminosity, $\approx \dot{M}_{disk} M_J / 2R_{PJ}$, is of order $10^{-5} L_{Sun}$ for slow inflow/accretion rates of $10^{-7}\,M_J\,yr^{-1}$ (i.e., Figure 4.4), but how important this geometrically confined luminosity source is for the rest of the disk is not obvious.

In this overall context, it is also worth noting that the temperature of the Io-forming region of the circum-Jovian disk probably cannot be supported by the background solar nebula radiation bath either. While classic analytical solar nebula models (e.g., Lewis, 1974) propose temperatures near 150 K, close to the present-day solar insolation temperature at Jupiter ($\sim$120 K), modern accretion disk models obtain lower temperatures near 5 AU (see, e.g., Wood, 2000). An extreme example is the solar nebula model of Hersant *et al.* (2001), where midplane temperatures evolve with time and drop below 20 K at 5 AU after 5 Myr of viscous evolution, and the effect of a comparable nebular boundary condition can be seen in Figure 4.5(b) (cf. Bell *et al.*, 1997).

Sophisticated proto-planetary disk models, which incorporate heating by dissipation *and* the central star (missing in Hersant *et al.*, 2001), dust evolution, and vertical

and radial radiative transport, support a more nuanced view (D'Alessio *et al.*, 1999, 2001). The latter models, for 0.5–$M_{\rm Sun}$ T Tauri stars, consistently show midplane temperatures near ~60 K at Jupiter's present position, even for very low accretion rates onto the star. While similar models for a 1–$M_{\rm Sun}$ T Tauri star would no doubt lead to modestly higher temperatures, the position of the circum-Jovian accretion disk within the solar nebula is also important. Nestled deep within the gap in the solar nebula opened by Jupiter, the satellite-forming disk would find itself plunged into shadow; no direct solar radiation would reach the disk (D'Angelo *et al.*, 2003a), and the background solar nebula would no longer fill 4π steradians. The circum-Jovian disk would be exposed to space (or whatever the birth environment of the Sun was) and to ionizing cosmic radiation. Its outer boundary would almost certainly have been colder than 150 K (cf. Canup and Ward, 2002; Figure 4.4(b)), and this may ultimately play an important role in the formulation of a realistic, time-dependent, thermochemical accretion disk model for Io and the Galilean satellites.

4.3.2 Thermal state

Io should have accreted solid material more or less as fast as solids were supplied to its "feeding zone" within the proto-Jovian nebula, either by infall or condensation. In other words, and as discussed in Section 4.2.1, sweep-up for small bodies is rapid, and faster than overall sub-nebular evolution times in either the gas-starved (Canup and Ward, 2002, 2006) or MMSN models (Mosqueira and Estrada, 2003a). In the context of the gas-starved sub-nebula, accretion times would be long enough (set by the declining infall rate) and accreting bodies small enough (possibly m-scale) that accretional heating may be severely limited by radiative losses to space (Stevenson *et al.*, 1986). This can in principle provide the necessary cold or lukewarm start to Callisto, consistent with its present inferred state of partial differentiation (Schubert *et al.*, 2004), but obviously also implies limited accretional heating for Io as well. It also goes without saying, in the gas-starved model, that there is insufficient sub-nebular gas to form an optically thick, convective envelope about Io (Lunine and Stevenson, 1982) as it accretes.

The characteristic length scale for thermal conduction in an accreting satellite is κ/u, where κ is the thermal diffusivity of the accreted material ($10^{-6}\,\mathrm{m^2\,s^{-1}}$ is typical for solid rock) and u is the radial growth rate (McKinnon, 2002). For Io, and assuming a constant rate of *mass* accretion:

$$\frac{\kappa}{u} \sim 0.5\,\mathrm{m} \times \left(\frac{\kappa}{10^{-7}\,\mathrm{m^2\,s^{-1}}}\right) \times \left(\frac{\tau_{\rm Io}}{10^5\,\mathrm{yr}}\right) \tag{4.4}$$

where $\tau_{\rm Io}$ is Io's accretion time and a reduced $\kappa \sim 10^{-7}\,\mathrm{m^2\,s^{-1}}$ is assumed appropriate for *porous* rock + metal. Heat buried greater than this depth is *not* in good conductive communication with the accreting surface, and cannot be efficiently radiated to space as Io accretes. This estimate implies that for Io to remain cool it must accrete m-sized satellitesimals on timescales $\gg 10^5$ yr or that the accreting particles are $\ll 1$ m in scale.

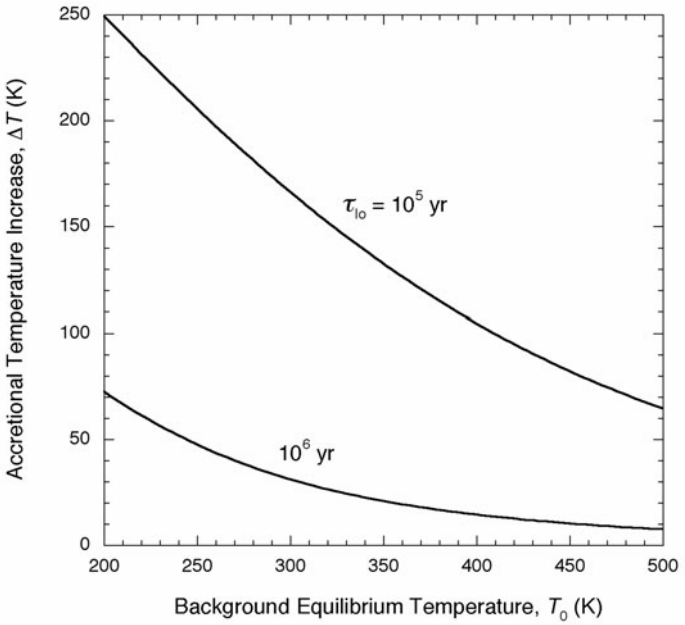

Figure 4.6. Temperature increase for Io in the limit of small satellitesimal accretion (4.5), as a function of background radiative equilibrium temperature. The contribution of satellitesimal encounter velocity is ignored, and mass accretion rate is assumed constant over the accretion time τ_{Io}.

How cool might this be? Following Stevenson *et al.* (1986):

$$T(R) = \left[\frac{1}{4\pi R^2 \sigma_{\mathrm{SB}}} \left(\frac{GM(R)}{R} + \frac{\langle v \rangle^2}{2} \right) \frac{dm}{dt} + T_0^4 \right]^{1/4} \tag{4.5}$$

where $T(R)$ is the accretional temperature profile, $M(R)$ the mass contained within a radius R, G the gravitational constant, σ_{SB} the Stefan–Boltzmann constant, $\langle v \rangle$ the mean encounter velocity, dm/dt the mass accretion rate of the satellite, and T_0 the background radiative equilibrium temperature (which for an optically thin nebula is not necessarily the nebular gas temperature). Figure 4.6 shows $\Delta T = T(R) - T_0$ as a function of T_0 for Io for accretion times of 10^5 and 10^6 yr. Note that for $dm/dt =$ constant and $\langle v \rangle = 0$ the accretional temperature increase is constant throughout the satellite. These modest to miniscule temperature increases are the smallest possible for Io. For accretion times $\leq 10^5$ yr, accretional energy dominates the background term in (4.5) over the T_0 range illustrated (e.g., for a fiducial τ_{Io} of 10^5 yr, Io's initial interior temperature is $\sim$500 K).

If Io accreted from bodies that were larger than the limit implied by (4.4), which need be no greater than 10–100 m in diameter, then some satellitesimal kinetic energy must be trapped as heat. The fraction trapped in a symmetrically accreting uniform satellite, as a function of depth, is $hGM(R)/R$, where $0 \leq h \leq 1$ and I have again

neglected the mean encounter velocity[6] (e.g., Schubert *et al.*, 1981; Stevenson *et al.*, 1986). For a characteristic rock + metal STP heat capacity of $920\,\mathrm{J\,kg^{-1}\,K^{-1}}$ (Kirk and Stevenson, 1987), accretional temperature increases in Io's outer layers could have reached $\approx 350\,\mathrm{K} \times (h/0.1)$. The factor h is empirical, and can in principle be determined by detailed calculation, but an upper limit near 0.1 is obtained by requiring ice melting in Callisto to be restricted to that body's outer layers (Schubert *et al.*, 1981).

Although the total gravitational potential energy of Io's assembly is more than adequate to melt it, its prolonged accretion in the gas-starved circum-Jovian nebula and a likely bias toward smaller satellitesimals probably limited its initial interior temperatures to $\leq$800–900 K (assuming accretional conditions similar to those illustrated in Figure 4.4 and some buried heat). While non-trivial (e.g., serpentine breaks down at pressure in this temperature range; McKinnon and Zolensky (2003)), such temperatures fall short of the Fe–FeS eutectic melting temperature ($\approx$1,250 K), at which point downward percolation of iron sulfide melt occurs, and formation of a metallic core begins.

The presence and characteristics of Io's core deserve some comment here. The density and moment of inertia determined by *Galileo* imply the existence of a substantial metallic core within Io (see the detailed review by Schubert *et al.*, 2004). Internal structural models can further constrain the properties of this core, and the surrounding mantle, subject to unavoidable assumptions of composition, chemistry, and temperature. For example, by modeling Io as a pure olivine mantle surrounding a solid Fe–FeS core, Sohl *et al.* (2002) find Io's bulk Fe/Si ratio to lie between 1 and 1.25 for solid mantles and between 1.25 and 1.5 for partially molten ones. Kuskov and Kronrod (2001) found, by basing mantle chemistries on chondritic meteorites and assuming plausible but uniform core densities, that Io's Fe/Si ratio probably lies within the 0.8–1.2 range, and that Io overall is most compatible with an L- or LL-chondrite composition. Obviously, these two works do not agree in detail on the important point of iron content. Subtle (and not so subtle) differences in modeling assumptions underlie this difference, but both conclude that Io's Fe/Si ratio is less than the solar value of $\approx$1.7 (Lodders, 2003).

There is, however, no obvious way to fractionate iron from rock in the context of the gas-starved accretion disk model, given the continuous input of solar-composition "feedstock". Temperature is obviously important for strongly tidally heated Io, and if one allows for a molten core and a full solar abundance of S, then it is *possible* to construct internal models of Io with higher, if not solar Fe/Si (McKinnon and Desai, 2003). In this case Io's core would be relatively large ($\sim$1,000 km in radius) and S (and possibly O) rich. Such a large, fluid interior would serve to maximize tidal flexing and dissipation in the (mostly) solid mantle, for a given orbital eccentricity (e.g., Cassen *et al.*, 1982). While such a model cannot be proven by gravity data alone, it is cosmochemically compatible with the oxidation state of Io's mantle (similar to that of the

[6] Mostly for convenience, but this neglect is justifiable when the eccentricities of the accreting satellitesimal swarm are low, which obtains for very small bodies orbiting in the presence of nebular gas.

Earth's upper mantle (Zolotov and Fegley, 2000), and consistent with the early argument of Lewis (1982) that Io could not have directly formed from a metal-bearing (as distinct from sulfide-bearing) chondritic assemblage, such as L- or LL-chondrites (McKinnon, 2004)).

I end this section with a note on Io's rotational history. Peale (1977) estimated that Io would have been despun by tides raised by Jupiter from an initially rapid rotation to its present synchronous period of 1.77 d in only $\sim 5000 \times (Q/100)$ yr, where Q is the specific dissipation factor. Even with modern parameter values (density, moment of inertia, etc.), this timescale is so short for plausible Q values that it is likely that Io accreted in synchronous lock. The despinning time goes as a^6, however, so if proto-Io first formed in a more distant orbit and migrated inward (discussed in the next section), it may have despun while it was migrating and accreting.

4.4 EARLY EVOLUTION OF IO

It is fitting, in this penultimate section, to briefly discuss one of the more interesting applications of the slow-inflow accretion disk model for the formation of Io and the Galilean satellites. Io's special place in the geophysical pantheon is owed to the tidal heating that follows from the satellite's resonant orbital configuration with Europa and Ganymede – the Laplace resonance. A subject of much research, the Laplace relation has long been thought to have been a by-product of the outward tidal evolution of Jupiter's satellites. As discussed in the comprehensive review of Peale (1999), Io post-formation should evolve outward under the action of Jovian tides more rapidly than Europa, and both more rapidly than Ganymede. As Io does so, it first captures Europa into the 2 : 1 mean-motion resonance, and then the coevolving pair capture Ganymede into the 2 : 1 with Europa.

Difficulties with the required extent of orbital evolution by gravitational tides alone as well as with maintaining Io's present volcanic power prompted Greenberg (1982, 1987) to offer that Io, Europa, and Ganymede were actually evolving out of a deep, primordial resonance. There was never a concrete mechanism to account for such a primordial resonance, however, until now. Simply put, assembly of the satellites in a slow-inflow, gas-starved disk predicts inward type I migration as the satellites grow to larger and larger sizes (Canup and Ward, 2002, 2006). Ganymede is by far the most massive of the three, and as type I drift is proportional to satellite mass and nebula surface density, Ganymede can in principle migrate faster. Peale and Lee (2002) demonstrated numerically that in doing so Ganymede can capture Europa into the 2 : 1 mean-motion resonance, and then the pair can migrate fast enough to capture Io as well (Figure 4.7). Given Io's greater mass than Europa, and the arguably greater disk surface density closer to Jupiter, Io's capture into the 2 : 1 with Europa depends on it not evolving faster than Europa after Europa is captured into resonance with Ganymede. Thus, Io can run, but it cannot hide.

Io's eccentricity in Figure 4.7, as well as that of Europa, are well above current values. They are due to tidal interactions with the spiral density waves launched in the

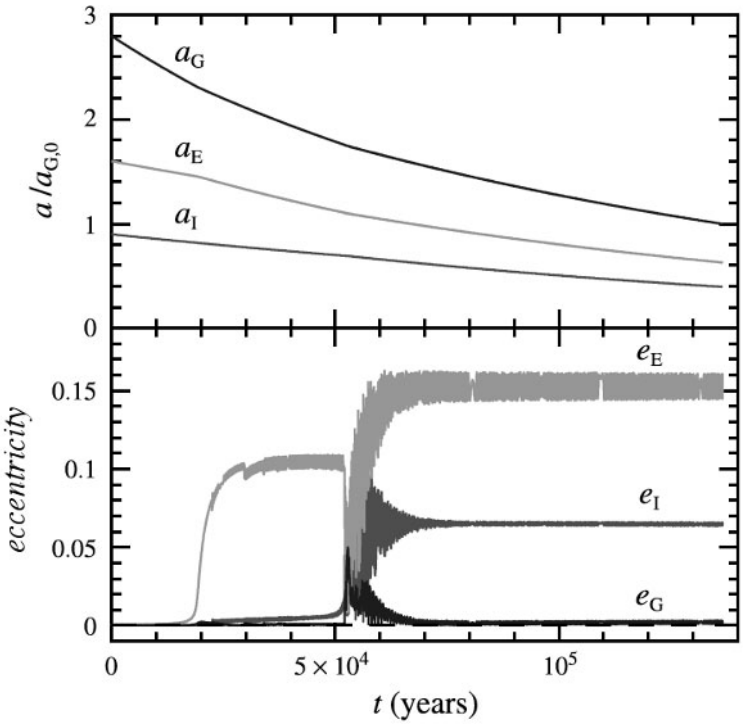

Figure 4.7. Nebula-induced evolution of the Galilean satellites into the Laplace resonance. The semimajor axes of Io (a_I), Europa (a_E), and Ganymede (a_G) are normalized to Ganymede's current distance from Jupiter, $a_{G,0}$. e_I, e_E, and e_G are the eccentricities of Io, Europa, and Ganymede, respectively. Inward migration and eccentricity-damping timescales are imposed; and the initial orbits are circular and coplanar. After circum-Jovian nebula dispersal, eccentricities are damped by solid-body tides within each satellite (modified from Peale, 2003).

circum-Jovian disk by the satellites. As the disk dissipates (i.e., as infall from the solar nebula abates), these eccentricities should begin to decline due to tidal dissipation within the satellites. Peale and Lee (2002) show that the entire system (Io–Europa–Ganymede) naturally relaxes to its current Laplace configuration.

To some, the model of Peale and Lee (2002) may be distressing, in that it removes an attractive solution to the Ganymede–Callisto dichotomy from the playing field (see, e.g., Showman and Malhotra, 1997). Yet this primordial, outside-in assembly of the Laplace resonance is both elegant and comprehensive in its predictions. One of the latter is that Io's history of high internal temperatures and extreme volcanism is likely to have begun very early (Peale, 2003). As an illustration, the decay of Io's primordial $e_I \approx 0.063$ in Figure 4.7 to the present-day value of 0.004 would imply dissipation within Io and a minimum temperature increase of $GM_J e_I^2/2C_P a_I \approx 600$ K. This estimate is a minimum because it (1) assumes Io at its present semimajor axis,

whereas Io, Europa and Ganymede have almost certainly tidally evolved outward over Solar System history (Peale, 1999); and (2) neglects any torque from Jupiter that would have acted to retard the eccentricity decay. A heat impulse of this magnitude, when added to Io's likely warm initial accretional state (Section 4.3), implies that eutectic melting and core formation started soon after the circum-Jovian nebula disappeared and accretion ended (within a few Myr). With this, Io entered the realm of enhanced tidal flexing and dissipation, which is fortunate, as both are necessary to explain its prodigious volcanic output (e.g., Schubert *et al.*, 1981).

4.5 CONCLUSION

Our understanding of the origin of Io and the Galilean satellites has evolved from early, nebulous discussions (e.g., Pollack and Fanale, 1982) into modern, quantitative analyses of accretion disk models around Jupiter (e.g., Canup and Ward, 2006). Much of this work is driven by vigorous advances in understanding star and giant-planet formation, a part of the new field of extrasolar planets. While many details remain to be worked out, it seems clear that formation of Jupiter in the core accretion–gas capture model inevitably ends with an accretion disk around the planet, and as Jupiter at some point must stop accreting gas and solids, that circum-Jovian disk must become one of the slow-inflow, gas-starved variety. Alternative models for satellite formation have and are being proposed (Mosqueira and Estrada, 2003a,b; Estrada and Mosqueira, 2006), but these have not yet been tied to models of Jupiter's formation in a direct or compelling way or necessarily account for the physical or compositional characteristics of the satellites themselves.

In fairness, the gas-starved circum-Jovian disk models to date rely on assumptions of mass and angular momentum inflow from the solar nebula that have not been robustly established. This will probably require the next generation of 3-D and thermohydrodynamic giant-planet formation models, ones that can resolve circum-Jovian disk structure within the inner 10% of Jupiter's Hill sphere ($\sim 75\, R_J$). Regardless, the slow-inflow accretion disk in principle allows satellites to grow over a protracted length of time ($>10^5$ to 10^6 yr), and in low-gas-density environment. This slows losses to Jupiter by gas drag and disk tidal torques, and provides for a cool to warm start, thus protecting Callisto from extensive melting. The latter is an important Galileo-derived constraint.

If sufficient mass is processed through the circum-Jovian accretion disk, then multiple generations of satellites may be formed and lost (Canup and Ward, 2006). The Galilean satellites then are the last generation, formed more or less from the inflow of the last MMSN worth of solar matter. Even at this late stage, the non-volatile solids that accreted to form Io and the others should be essentially solar in composition. The thermal environment at Io's formation distance is determined mostly by the subnebula itself, and should have been hot enough to largely devolatilize any small, accreting satellitesimals. At the very end of the circum-Jovian disk's lifetime, however, temperatures in the disk must inevitably fall, and late accretion of hydrated rock, or even minor ice, is not precluded.

Io traveled a great deal in its youth. It probably began accreting well outside its present position, and continued accreting while migrating inward due to disk tidal torques. The migration would have sped up once Io was captured into the Laplace resonance with Europa and Ganymede, which had been migrating inward as well, and more rapidly (Peale and Lee, 2002). Their joint orbital decay probably brought Io much closer to Jupiter than it is today while the circum-Jovian disk evanesced. Subsequently the weaker action of Jovian tidal torques slowly pushed all three satellites back outward, to their present positions, over Solar System history.

The combination of subnebular heating of inflowing solar solids, the potential energy of accretion onto Io, and tidal heating from the subnebular epoch probably pushed Io past the threshold for core formation. Once such a relatively deformable, dissipative internal structure was created, the conditions for vigorous volcanism from long-term tidal heating were assured. This early heating would have been more than sufficient to drive any and all accreted water out of Io, but the oxidation of rock and metal by water, with loss of hydrogen, was likely very important in establishing Io's overall chemical and oxidation state (e.g., Lewis, 1982).

Further work on satellite formation in a gas-starved accretion disk is likely to prove fruitful. This is, perhaps, one of the more subtle results of the *Galileo* mission. Sufficient new information, and attention, has led, perhaps for the first time, to a quantitative, believable model for satellite formation around gas giant planets.

4.6 REFERENCES

Alibert, Y., C. Mordasini, W. Benz, and C. Winisdoerffer. 2005a. Models of giant planet formation with migration and disc evolution. *Astron. Astrophys.*, **434**, 343–353.

Alibert, Y., O. Mousis, and W. Benz. 2005b. Modeling the Jovian subnebula. I: Thermodynamical conditions and migration of proto-satellites. *Astron. Astrophys.*, **439**, 1205–1213.

Anderson, J. D., T. V. Johnson, G. Schubert, S. Asmar, R. A. Jacobson, D. Johnson, E. L. Lau, G. Lewis, W. B. Moore, A. Taylor, *et al.* 2005. Almathea's density is less than that of water. *Science*, **308**, 1291–1293.

Bate, M. R., S. H. Lubow, G. I. Ogilvie, and K. A. Miller. 2003. Three-dimensional calculations of high- and low-mass planets embedded in protoplanetary disks. *Mon. Not. Roy. Astron. Soc.*, **341**, 213–229.

Bell, K. R., P. M. Cassen, H. H. Klahr, and Th. Henning. 1997. The structure and appearance of protostellar accretion disks: Limits on disk flaring. *Astrophys. J.*, **486**, 372–387.

Bodenheimer, P. and D. N. C. Lin. 2002. Implications of extrasolar planets for understanding planet formation. *Annu. Rev. Earth Planet. Sci.*, **30**, 113–148.

Bodenheimer, P. and J. B. Pollack. 1986. Calculations of the accretion and evolution of giant planets: The effects of solid cores. *Icarus*, **67**, 391–408.

Boss, A. P. 2002. Formation of gas and ice giant planets. *Earth Planet. Sci. Lett.*, **202**, 513–523.

Brown, P. G., A. R. Hildebrand, M. E. Zolensky, M. Grady, R. N. Clayton, T. K. Mayeda, E. Tagliaferri, R. Spalding, N. D. MacRae, E. L. Hoffman, *et al.* 2000. The fall, recovery,

orbit, and composition of the Tagish Lake meteorite: A new type of carbonaceous chondrite. *Science*, **290**, 320–325.

Bryden, G., X. Chen, D. N. C. Lin, R. P. Nelson, and J. C. B. Papaloizou. 1999. Tidally induced gap formation in protostellar disks: Gap clearing and suppression of protoplanetary growth. *Astrophys. J.*, **514**, 344–367.

Burrows, A., M. Marley, W. B. Hubbard, J. I. Lunine, T. Guillot, D. Saumon, R. Freedman, D. Sudarsky, and C. Sharp. 1997. A nongrey theory of extrasolar planets and brown dwarfs. *Astrophys. J.*, **491**, 856–875.

Cameron, A. G. W. 1978. Physics of the primitive solar accretion disk. *Moon Planets*, **18**, 5–40.

Canup, R. M. and W. R. Ward. 2002. Formation of the Galilean satellites: Conditions of accretion. *Astron. J.*, **124**, 3404–3423.

Canup, R. M. and W. R. Ward. 2006. Formation of large satellites around gas planets. *Nature*, **441**, 834–839.

Cassen, P. M., S. J. Peale, and R. T. Reynolds. 1982. Structure and thermal evolution of the Galilean satellites. In: D. Morrison (ed.), *Satellites of Jupiter*. University of Arizona Press, Tucson, AZ, pp. 93–128.

Chiang, E. L. and P. Goldreich. 1997. Spectral energy distributions of T Tauri stars with passive circumstellar disks. *Astrophys. J.*, **490**, 368–376.

Coradini, A., P. Cerroni, G. Magni, and C. Federico. 1989. Formation of the satellites of the outer solar system: Sources of their atmospheres. In: S. K. Atreya, J. B. Pollack, and M. S. Matthews (eds), *Origin and Evolution of Planetary and Satellite Atmospheres*. University of Arizona Press, Tucson, AZ, pp. 723–762.

Coradini, A. and G. Magni. 1997. The formation of Jupiter's satellites: Relation of present appearance with past history. In: C. Barbieri, J. H. Rahe, T. V. Johnson, and A. M. Sohus (eds), *The Three Galileos: The Man, the Spacecraft, the Telescope*. Kluwer Academic Publishers, the Netherlands, pp. 177–190.

Cruikshank, D. P., C. M. Dalle Ore, T. L. Roush, T. R. Geballe, and T. C. Owen. 2001. Constraints on the composition of Trojan asteroid 624 Hektor. *Icarus*, **153**, 348–360.

D'Alessio, P., N. Calvet, L. Hartmann, S. Lizano, and J. Canto. 1999. Accretion disks around young objects. II: Tests of well-mixed models with ISM dust. *Astrophys. J.*, **527**, 893–909.

D'Alessio, P., N. Calvet, and L. Hartmann. 2001. Accretion disks around young objects. III: Grain growth. *Astrophys. J.*, **553**, 321–334.

D'Angelo, G., T. Henning, and W. Kley. 2002. Nested-grid calculations of disk–planet interaction. *Astron. Astrophys.*, **385**, 647–670.

D'Angelo, G., T. Henning, and W. Kley. 2003a. Thermohydrodynamics of circumstellar disks with high-mass planets. *Astrophys. J.*, **599**, 548–576.

D'Angelo, G., W. Kley, and T. Henning. 2003b. Orbital migration and mass accretion of protoplanets in three-dimensional global computations with nested grids. *Astrophys. J.*, **586**, 540–561.

Dullemond, C. P., D. Hollenbach, I. Kamp, and P. D'Alessio. 2006. Models of the structure and evolution of protoplanetary disks. In: B. Reipurth, D. Jewitt, and K. Keil (eds), *Protostars and Planets V*. University of Arizona Press, Tucson, AZ, in press.

Durisen, R. H., A. P. Boss, L. Mayer, A. F. Nelson, T. Quinn, and W. K. M. Rice. 2006. Gravitational instabilities in gaseous protoplanetary disks and implications for giant planet formation. In: B. Reipurth, D. Jewitt, and K. Keil (eds), *Protostars and Planets V*. University of Arizona Press, Tucson, AZ, in press.

Emery, J. P. and R. H. Brown. 2004. The surface composition of Trojan asteroids: Constraints set by scattering theory. *Icarus*, **170**, 131–152.

Estrada, P. R. and I. Mosqueira. 2006. A gas-poor planetesimal capture model for the formation of giant planet satellite systems. *Icarus*, **181**, 486–509.

Fegley, B. 1999. Kinetics of gas–grain reactions in the solar nebula. *Space Sci. Rev.*, **92**, 177–200.

Fortney, J. J., M. S. Marley, O. Hubickyj, P. Bodenheimer, and J. J. Lissauer. 2005. Young Jupiter's are faint: New models of the early evolution of giant planets. *Astron. Nachr.*, **326**, 925–929.

Gautier, D., F. Hersant, O. Mousis, and J. I. Lunine. 2001. Enrichments on volatiles in Jupiter: A new interpretation of the Galileo measurements. *Astrophys. J.*, **550**, L227–L230.

Gradie, J. C., C. R. Chapman, and E. F. Tedesco. 1989. Distribution of taxonomic classes and the compositional structure of the asteroid belt. In: R. P. Binzel, T. Gehrels, and M. S. Matthews (eds), *Asteroids II*. University of Arizona Press, Tucson, AZ, pp. 316–335.

Greenberg, R. 1982. Orbital evolution of the Galilean satellites. In: D. Morrison (ed.), *Satellites of Jupiter*. University of Arizona Press, Tucson, AZ, pp. 65–92.

Greenberg, R. 1987. Galilean satellites: Evolutionary paths in deep resonance. *Icarus*, **70**, 334–347.

Grimm, R. E. and H. Y. McSween. 1989. Water and the thermal evolution of carbonaceous chondrite parent bodies. *Icarus*, **82**, 244–280.

Haisch, K. E., E. A. Lada, and C. J. Lada. 2001. Disk frequencies and lifetimes in young clusters. *Astrophys. J.*, **553**, L153–L156.

Hartmann, L., N. Calvet, E. Gullbring, and P. D'Alessio. 1998. Accretion and the evolution of T Tauri disks. *Astrophys. J.*, **495**, 385–400.

Hersant, F., D. Gautier, and J.-M. Huré. 2001. A two-dimensional model for the primordial nebula constrained by D/H measurements in the Solar System: Implications for the formation of giant planets. *Astrophys. J.*, **554**, 391–407.

Hillenbrand, L. A. 2006. Observational constraints on dust disk lifetimes: Implications for planet formation. In: M. Livio (ed.), *A Decade of Discovery: Planets Around Other Stars* (STScI Symposium Series 19). Cambridge University Press, Cambridge, UK, in press.

Hiroi, T., M. E. Zolensky, and C. M. Pieters. 2001. The Tagish Lake meteorite: A possible sample from a D-type asteroid. *Science*, **293**, 2234–2236.

Hubickyj, O., P. Bodenheimer, and J. J. Lissauer. 2005. Accretion of the gaseous envelope of Jupiter around a 5–10 Earth-mass core. *Icarus*, **179**, 415–431.

Inaba, S., G. W. Wetherill, and M. Ikoma. 2003. Formation of gas giant planets: Core accretion models with fragmentation and planetary envelope. *Icarus*, **166**, 46–62.

Jones, T. D., L. A. Lebofsky, J. S. Lewis, and M. S. Marley. 1990. The composition and origin of the C, P, and D asteroids: Water as a tracer of thermal evolution in the outer belt. *Icarus*, **88**, 172–192.

Kirk, R. L. and D. J. Stevenson. 1987. Thermal evolution of a differentiated Ganymede and implications for surface features. *Icarus*, **69**, 91–134.

Klahr, H. and P. Bodenheimer. 2006. Formation of giant planets by concurrent accretion of solids and gas inside an anticyclonic vortex. *Astrophys. J.*, **639**, 432–440.

Korycansky, D. G., J. B. Pollack, and P. Bodenheimer. 1991. Numerical models of giant planet formation with rotation. *Icarus*, **92**, 234–251.

Kuiper, G. P. 1952. Planetary atmospheres and their origins. In: G. P. Kuiper (ed.), *The Atmospheres of the Earth and Planets* (Revised Ed.). University of Chicago Press, Chicago, IL.

Kuskov, O. L. and V. A. Kronrod. 2001. L- and LL-chondritic models of the chemical composition of Io. *Solar System Res.*, **35**, 198–208.

Lada, C. J., A. A. Muench, K. L. Luhman, L. Allen, L. Hartmann, T. Megeath, P. Myers, G. Fazio, K. Wood, J. Muzerolle, *et al.* 2006. SPITZER observations of IC 348: The disk population at 23 million years. *Astron. J.*, **131**, 1574–1607.

Lebofsky, L. A., T. D. Jones, P. D. Owensby, M. A. Feierberg, and G. J. Consolmagno. 1990. The nature of low albedo asteroids from 3-μm spectrophotometry. *Icarus*, **83**, 12–26.

Lewis, J. S. 1974. The temperature gradient in the solar nebula. *Science*, **186**, 440–443.

Lewis, J. S. 1982. Io: Geochemistry of sulfur. *Icarus*, **50**, 105–114.

Lissauer, J. J. 1993. Planet formation. *Annu. Rev. Astron. Astrophys.*, **31**, 129–174.

Lissauer, J. J. and D. J. Stevenson. 2006. Formation of giant planets. In: B. Reipurth, D. Jewitt, and K. Keil (eds), *Protostars and Planets V*. University of Arizona Press, Tucson, AZ, in press.

Lodders, K. 2003. Solar System abundances and condensation temperatures of the elements. *Astrophys. J.*, **591**, 1220–1247.

Lodders, K. 2004. Jupiter formed with more tar than ice. *Astrophys. J.*, **611**, 587–597.

Lubow, S. H., M. Seibert, and P. Artymowicz. 1999. Disk accretion onto high-mass planets. *Astrophys. J.*, **526**, 1001–1012.

Lunine, J. I. and D. J. Stevenson. 1982. Formation of the Galilean satellites in a gaseous nebula. *Icarus*, **52**, 14–39.

Lunine, J. I., A. Coradini, D. Gautier, T. C. Owen, and G. Wuchterl. 2004. The origin of Jupiter. In: F. Bagenal, T. E. Dowling, and W. B. McKinnon (eds), *Jupiter: The Planet, Satellites and Magnetosphere*. Cambridge University Press, Cambridge, UK, pp. 19–34.

Lyden-Bell, D. and J. E. Pringle. 1974. The evolution of viscous disks and the origin of the nebula variables. *Mon. Not. Roy. Astron. Soc.*, **168**, 603–637.

Magni, G. and A. Coradini. 2004. Formation of Jupiter by nucleated instability. *Planet. Space. Sci.*, **52**, 343–360.

Malhotra, R. 1991. Tidal origin of the Laplace resonance and the resurfacing of Ganymede. *Icarus*, **94**, 399–412.

Mamajek, E. E., M. R. Meyer, P. H. Hinz, W. F. Hoffman, M. Cohen, and J. L. Hora. 2004. Constraining the lifetime of circumstellar disks in the terrestrial planet zone: A mid-IR survey of the 30-Myr-old Tucana–Horologium Association. *Astrophys. J.*, **612**, 496–510.

Mayer, L., T. Quinn, J. Wadsley, and J. Staedel. 2004. The evolution of gravitationally unstable protoplanetary disks: Fragmentation and possible giant planet formation. *Astrophys. J.*, **609**, 1045–1064.

McKinnon, W. B. 2002. On the initial thermal evolution of Kuiper Belt Objects. *Proc. Asteroids, Comets, Meteors (ACM 2002), ESA SP-500*, 29–38.

McKinnon, W. B. 2004. On the oxidation states of the Galilean satellites: Implications for internal structures, ocean chemistry, and magnetic fields. *Lunar Planet. Sci. XXXV*, #2137.

McKinnon, W. B. and S. S. Desai. 2003. Internal structures of the Galilean satellites: What can we really tell? *Lunar Planet. Sci. Conf. XXXIV*, #2104.

McKinnon, W. B. and A. C. Leith. 1995. Gas drag and the orbital evolution of a captured Triton. *Icarus*, **118**, 392–413.

McKinnon, W. B. and M. E. Zolensky. 2003. Sulfate content of Europa's ocean and shell: Evolutionary considerations and geological and astrobiological implications. *Astrobiology*, **3**, 879–897.

Meyer, M. R., D. E. Backman, A. J. Weinberger, and M. C. Wyatt. 2006. Evolution of circumstellar disks around normal stars: Placing our Solar System in context. In:

B. Reipurth, D. Jewitt, and K. Keil (eds), *Protostars and Planets V*. University of Arizona Press, Tucson, AZ.

Mizuno, H. 1980. Formation of the giant planets. *Prog. Theor. Phys.*, **64**, 544–557.

Morbidelli, A., H. F. Levison, K. Tsiganis, and R. Gomes, 2005. Chaotic capture of Jupiter's Trojan asteroids in the early Solar System. *Nature*, **435**, 462–465.

Mosqueira, I. and P. R. Estrada. 2003a. Formation of the regular satellites of giant planets in an extended gaseous nebula. I: Subnebula model and accretion of satellites. *Icarus*, **163**, 198–231.

Mosqueira, I. and P. R. Estrada. 2003b. Formation of the regular satellites of giant planets in an extended gaseous nebula. II: Satellite migration and survival. *Icarus*, **163**, 232–255.

Mousis, O. and D. Gautier. 2004. Constraints on the presence of volatiles in Ganymede and Callisto from an evolutionary turbulent model of the Jovian subnebula. *Planet Space Sci.*, **52**, 361–370.

Ojakangas, G. W. and D. J. Stevenson. 1986. Episodic volcanism of tidally heated satellites with application to Io. *Icarus*, **66**, 341–358.

Nakano, H., A. Kouchi, S. Tachibana, A. Tsuchiyama. 2003. Evaporation of interstellar organic materials in the solar nebula. *Astrophys. J.*, **592**, 1252–1262.

Palla, F. and S. W. Stahler. 1999. Star formation in the Orion nebula cluster. *Astrophys. J.*, **525**, 772–783.

Papaloizou, J. C. B. and R. P. Nelson. 2005. Models of accreting gas giant protoplanets in protostellar disks. *Astron. Astrophys.*, **433**, 247–265.

Pasek, M. A., J. A. Milsom, F. J. Ciesla, D. S. Lauretta, C. M. Sharp, and J. I. Lunine. 2005. Sulfur chemistry with time-varying oxygen abundance during Solar System formation. *Icarus*, **175**, 1–14.

Peale, S. J. 1977. Rotation histories of the natural satellites. In: J. A. Burns (ed.), *Planetary Satellites*. University of Arizona Press, Tucson, AZ, pp. 87–111.

Peale, S. J. 1986. Orbital resonances, unusual configurations and exotic rotation states among planetary satellites. In: J. A. Burns and M. S. Matthews (eds), *Satellites*. University of Arizona Press, Tucson, AZ, pp. 159–223.

Peale, S. J. 1999. Origin and evolution of the natural satellites. *Annu. Rev. Astron. Astrophys.*, **37**, 533–602.

Peale, S. J. 2003. Tidally induced volcanism. *Celest. Mech. Dyn. Astron.*, **87**, 129–155.

Peale, S. J. and M. H. Lee. 2002. A primordial origin of the Laplace relation among the Galilean satellites. *Science*, **298**, 593–597.

Podolak, M. 2003. The contribution of small grains to the opacity of protoplanetary atmospheres. *Icarus*, **165**, 428–437.

Pollack, J. B. and F. Fanale. 1982. Origin and evolution of the Jupiter satellite system. In: D. Morrison (ed.), *Satellites of Jupiter*. University of Arizona Press, Tucson, AZ, pp. 872–891.

Pollack, J. B. and R. T. Reynolds. 1974. Implications of Jupiter's early contraction history for the composition of the Galilean satellites. *Icarus*, **21**, 248–253.

Pollack J. B., Lunine, J. I., and W. C. Tittemore. 1991. Origin of the Uranian satellites. In: J. T. Bergstralh, E. D. Miner, and M. S. Matthews (eds), *Uranus*. University of Arizona Press, Tucson, AZ, pp. 469–512.

Pollack, J. B., O. Hubickyj, P. Bodenheimer, J. J. Lissauer, M. Podolak, and Y. Greenzweig. 1996. Formation of the giant planets by concurrent accretion of solids and gases. *Icarus*, **124**, 62–85.

Prinn, R. G. and B. Fegley. 1981. Kinetic inhibition of CO and N_2 reduction in circumplanetary nebulae: Implications for satellite composition. *Astrophys. J.*, **249**, 308–317.

Prinn, R. G. and B. Fegley. 1989. Solar nebula chemistry: Origin of planetary, satellite, and cometary volatiles. In: S. K. Atreya, J. B. Pollack, and M. S. Matthews (eds), *Origin and Evolution of Planetary and Satellite Atmospheres*. University of Arizona Press, Tucson, AZ, pp. 8–136.

Rivkin, A. S., E. S. Howell, F. Vilas, and L. A. Lebofsky. 2002. Hydrated minerals on asteroids. In: W. F. Bottke, A. Cellino, P. Paolicchi, and R. P. Binzel (eds), *Asteroids III*. University of Arizona Press, Tucson, AZ, pp. 235–253.

Sackmann, I.-J., A. I. Boothroyd, and K. E. Kraemer. 1993. Our Sun. III. Present and future. *Astrophys. J.*, **418**, 457–468.

Safronov, V. S., G. V. Pechernikova, E. L. Ruskol, and A. V. Vitiazev. 1986. Protosatellite swarms. In: J. A. Burns and M. S. Matthews (eds), *Satellites*. University of Arizona Press, Tucson, AZ, pp. 86–116.

Schubert, G., D. J. Stevenson, and K. Ellsworth. 1981. Internal structures of the Galilean satellites. *Icarus*, **47**, 46–59.

Schubert, G., J. D. Anderson, T. Spohn, and W. B. McKinnon. 2004. Interior composition, structure and dynamics of the Galilean satellites. In: F. Bagenal, T. E. Dowling, and W. B. McKinnon (eds), *Jupiter – The Planet, Satellites and Magnetosphere*. Cambridge University Press, Cambridge, U.K., pp. 281–306.

Shoberg, T. G. 1982. Collisional accretion times of the terrestrial planets, M.A. Thesis, Washington University, St. Louis, MO.

Showman, A. P. and R. Malhotra. 1997. Tidal evolution into the Laplace resonance and the resurfacing of Ganymede. *Icarus*, **127**, 93–111.

Sohl, F., T. Spohn, D. Breuer, and K. Nagel. 2002. Implications from Galileo observations on the interior structure and chemistry of the Galilean satellites. *Icarus*, **157**, 104–119.

Stevenson, D. J. 1982. Formation of the giant planets. *Planet. Space Sci.*, **30**, 755–764.

Stevenson, D. J. 2001. Jupiter and its moons. *Science*, **294**, 71–72.

Stevenson, D. J., A. W. Harris, and J. I. Lunine. 1986. Origins of satellites. In: J. A. Burns and M. S. Matthews (eds), *Satellites*. University of Arizona Press, Tucson, AZ, pp. 39–88.

Stone, J. M., C. F. Gammie, S. A. Balbus, and J. F. Hawley. 2000. Transport processes in protostellar disks. In: V. Mannings, A. P. Boss, and S. S. Russell (eds), *Protostars and Planets IV*. University of Arizona Press, Tucson, AZ, pp. 589–613.

Strom, S. E., S. Edwards, and M. F. Skrutskie. 1993. Evolutionary time scales for circumstellar disks associated with intermediate- and solar-type stars. In: E. H. Levy and J. I. Lunine (eds), *Protostars and Planets III*. University of Arizona Press, Tucson, AZ, pp. 837–866.

Takato, N., S. J. Bus, H. Terada, T.-S. Pyo, and N. Kobayashi. 2004. Detection of a deep 3-μm absorption feature in the spectrum of Amalthea (JV). *Science*, **306**, 2224–2227.

Takeuchi, T., C. J. Clarke, and D. N. C. Lin. 2005. The differential lifetimes of protostellar gas and dust disks. *Astrophys. J.*, **627**, 286–292.

Wood, J. A. 2000. Pressure and temperature profiles in the solar nebula. *Space Sci. Rev.*, **92**, 87–93.

Yoder, C. F. 1979. How tidal heating in Io drives the Galilean orbital resonance locks. *Nature*, **279**, 767–770.

Yoder, C. F. and S. J. Peale. 1981. The tides of Io. *Icarus*, **47**, 1–35.

Zolensky, M. E., K. Nakamura, M. Gounelle, T. Mikouchi, T. Kasama, O. Tachikawa, and E. Tonoi. 2002. Mineralogy of Tagish Lake: An ungrouped type 2 carbonaceous chondrite. *Meteor. Planet. Sci.*, **37**, 737–761.

Zolotov, M. Yu. and B. Fegley. 2000. Eruption conditions of Pele volcano on Io inferred from chemistry of its volcanic plume. *Geophys. Res. Lett.*, **27**, 2789–2792.

5

The interior of Io

William B. Moore, Gerald Schubert, John D. Anderson, and John R. Spencer

Io is the Galilean satellite nearest to Jupiter and it is therefore subject to the most intense tidal forces. These forces deform Io in a way that is determined by the properties of Io's interior, thus, we can use measurements of the deformation of Io to obtain information on Io's internal structure. Io's rotational and tidal deformation was measured by imaging (Thomas *et al.*, 1998) and by Earth-based Doppler tracking of the *Galileo* spacecraft during several fly-bys of the satellite between 1999 and 2002 and during insertion of the spacecraft into Jupiter orbit in 1995 (Anderson *et al.*, 1996, 2001; Schubert *et al.*, 2004). Even prior to the *Galileo* spacecraft's observations of Io's tidal deformation, the moon's mass and radius and therefore density were known from *Pioneer* and *Voyager* spacecraft observations. The *Galileo* spacecraft data improved the accuracy of measurements of Io's mass and radius and determined Io's quadrupole gravitational coefficients.

Table 5.1 summarizes Io's basic physical properties. Io is about the size of the Earth's Moon, but it is considerably more dense (the lunar density is 3,341 $\mathrm{kg\,m^{-3}}$), indicating that there is more iron in Io than in the Moon. In fact, on the basis of density alone, it can be inferred that Io has an iron core of considerable size. Moreover, if the density is supplemented by shape information (the 3 ellipsoidal radii of the tidally and rotationally distorted Io) available from *Voyager* limb measurements, and it is assumed that Io is in hydrostatic equilibrium, the size of Io's iron core can be well constrained (Segatz *et al.*, 1988). So, even before the *Galileo* mission, we had a good idea about the basic structure of Io's interior. The *Galileo* measurements of the tidally and rotationally distorted Ionian gravitational field have verified the equilibrium shape of Io and have provided better constraints on interior models of the satellite. Below, we will show that Io is a two-layer body consisting of a metallic core and a silicate mantle. Io's intensive volcanic activity and crater-free surface also suggests it likely that the satellite has differentiated a global crustal layer below which lies a partially molten asthenosphere.

Table 5.1. Basic physical properties of Io (Schubert *et al.*, 2004).

Property	Value
Rotation rate, ω	4.1106×10^{-5} rad s^{-1}
Rotation period, $2\pi/\omega$	1.769 d
Orbital period	1.769 d
Radius, R	1,821.6 km
Mass, M	8.9319×10^{22} kg
Mean density	3,527.5 kg m^{-3}
Surface gravity, g	1.796 m s^{-2}
J_2	$1{,}859.5 \times 10^{-6}\, GM/R$
C_{22}	$558.8 \times 10^{-6}\, GM/R$
k_2	1.3043
q_r	1713.7×10^{-6}
$C/(MR^2)$	0.378

5.1 TIDAL AND ROTATIONAL DEFORMATION

Io is in synchronous rotation, meaning that its orbital period and rotational period are equal so that Io keeps one face to Jupiter at all times. Since Io is rotating, it experiences a centrifugal force that acts to flatten its shape. By keeping the same face to Jupiter, Io also experiences a steady tidal force that acts to elongate it along the line from Io to Jupiter. These forces are both nearly constant, since Io's rotation rate changes very slowly and its orientation toward Jupiter remains nearly fixed. Io has therefore had time to relax into an equilibrium shape which, to first order, is a triaxial ellipsoid, with the long axis pointing toward Jupiter and the short axis aligned with the rotation pole. In this section we show how the response of Io to tidal and rotational forces may be used to understand Io's interior.

The steady forcing potentials due to rotation and tides Φ_{2r} and Φ_{2t} are given by (Kaula, 1964):

$$\Phi_{2r} = \frac{\omega^2 r^2}{3}\left(P_{20}(\cos\theta) - 1\right) \tag{5.1}$$

$$\Phi_{2t} = -\frac{GM_J}{a}\left(\frac{r}{a}\right)P_{20}(\cos\alpha) \tag{5.2}$$

where ω is the rotational angular frequency, r is the radial distance from the center of the satellite, M_J is the mass of the primary (Jupiter), a is the semimajor axis of the satellite's orbit, θ is the colatitude measured from the north pole, and α is the angle from the line connecting the centers of the satellite and primary. The second term in brackets in (5.1) is spherically symmetric and does not contribute to the aspherical shape of Io, therefore we ignore it. The form of the tidal potential arises from a Taylor expansion of the gravitational potential of Jupiter in powers of r/a about the center of mass of Io, retaining only the r^2 term. The time-dependent parts of the tidal potential

depend on the eccentricity and lead to dynamic tides which drive the volcanic activity of Io as described below.

For a synchronously rotating satellite, Kepler's third law ($\omega^2 = GM_J/a^3$) and the trigonometric relationship $\cos\alpha = \sin\theta\cos\phi$ lead to the following time-independent potential Φ_2 at the surface of the satellite ($r = R$):

$$\Phi_2 = \Phi_{2t} + \Phi_{2r} = \omega^2 R^2 \left(-\frac{5}{6} P_{20}(\cos\theta) + \frac{1}{4} P_{22}(\cos\theta)\cos 2\phi \right) \tag{5.3}$$

where ϕ is the longitude about the rotation axis measured eastward from the sub-Jovian point.

The deformation of Io in response to the second degree potential given in (5.3) may be calculated by assuming a hydrostatic (or fluid) response. The billions of years over which these potentials have acted and the strong heating of Io evident in its volcanic activity should ensure that any stresses have been relaxed away by viscous deformation. The surface and internal density interfaces and iso-surfaces are therefore also equipotential surfaces, as required for hydrostatic balance.

The aspherical mass distribution arising from the deformation results in an additional deformation potential Φ_{2d}. The observed potential Φ is therefore the sum of the driving potential Φ_2 and the deformation potential Φ_{2d}. Since the deformation potential is linearly related to the driving potential, the observed potential may be generally expressed as:

$$\Phi = \frac{GM}{R}\left[-J_2 P_{20}(\cos\theta) + C_{22} P_{22}(\cos\theta)\cos 2\phi\right] \tag{5.4}$$

where J_2 and C_{22} are dimensionless potential coefficients. The linear relationship allows us to normalize the deformation potential by the driving potential, yielding the second-degree potential Love number k_2:

$$k_2 = \frac{\Phi_{2d}}{\Phi_2} = \frac{\Phi - \Phi_2}{\Phi_2} \tag{5.5}$$

It should be noted that the Love number will be a strong function of the forcing frequency for a viscoelastic body. The discussion here relates to the nearly zero-frequency (static) rotational and tidal potentials (5.3) and not to the semi-diurnal tides that are the result of Io's eccentricity and that give rise to its internal heating.

The value of k_2 for Io can be found by taking measurements of the gravitational field of Io to yield an estimate of Φ_{2d}, as suggested by Hubbard and Anderson (1978). Alternatively, the shape of Io can be measured from images of the limb to estimate the surface deformation directly. Both of these approaches have been applied to the data from the *Galileo* mission (Thomas *et al.*, 1998; Anderson *et al.*, 2001) and are reviewed in the next two sections.

5.2 IO'S GRAVITATIONAL FIELD

The gravitational field of Io was measured by Anderson *et al.* (2001) using Doppler tracking of the *Galileo* spacecraft as it flew by the satellite on four separate orbits. A

gravity field complete to degree and order three was solved for, but only the degree two components are significant. A combined solution for the degree-two components of Io's gravitational field was obtained yielding the dimensionless gravity field coefficients $J_2 = 1,846 \pm 4 \times 10^{-6}$ and $C_{22} = 554 \pm 1 \times 10^{-6}$. No significant S_{22} component (which would indicate a mis-alignment of the tidal bulge away from the line toward Jupiter) was found, nor were the asymmetric coefficients (e.g., C_{21}) different from zero. Thus, Io is deformed into a triaxial ellipsoid oriented toward Jupiter, as expected.

In order to improve the reliability of the solution, an a priori constraint that the observed coefficients J_2 and C_{22} would be in the 10/3 ratio as predicted by equations (5.3) and (5.4) was introduced. A solution without this constraint found similar values but suffered from large formal errors. Although in the literature this ratio is often used to show that a body is in hydrostatic equilibrium, the 10/3 ratio only demonstrates a linear response to the potential Φ_2. Departures from this ratio require mass anomalies with non-hydrostatic support, but the 10/3 value only indicates the absence of such mass anomalies, not the absence of, say, elastic stresses.

From the observed coefficients, we can construct an estimate of k_2. The C_{22} component is purely tidal, as can be seen from (5.1), making it simpler to write the ratio between the deformation potential (the observed C_{22} times GM/R) and the driving potential from (5.3) yielding:

$$k_2 = 4q_r C_{22} = 1.292 \pm 0.003 \tag{5.6}$$

where $q_r = \omega^2 R^3/GM$ is the ratio of the centrifugal and gravitational potentials at the equator. This value is significantly different from 1.5, the value for a homogeneous, fluid body, indicating a concentration of mass toward the center of Io that reduces the hydrostatic tidal response.

5.3 THE SHAPE OF IO

The aspherical deformation of Io may also be observed directly by analyzing images of the limb and fitting an ellipsoid. On a pixel by pixel basis, Thomas *et al.* (1998) solved for the position of the limb in 18 images obtained by the *Galileo* spacecraft, at resolutions from 5–20 km per pixel. The limb position is fit to within about 0.1 pixels.

The best-fit solutions for an arbitrary ellipsoid agreed well with solutions which were a priori constrained to have equilibrium ratios of the axes $(b-c)/(a-c) = 0.2459$ (including higher order corrections to the first-order value of 0.25), indicating that Io's aspherical shape is an equilibrium response to the potential given in (5.3). The principal axes of the best-fit ellipsoid are $a = 1,829.7 \pm 0.6$, $b = 1,819.2 \pm 0.5$, and $c = 1,815.8 \pm 0.4$ km.

Assuming that Io has an equilibrium shape, we can use the dimensions of the ellipsoid to derive an estimate of the surface deformation Love number h_2, defined as:

$$h_2 = \frac{u_r g}{\Phi_2} \tag{5.7}$$

where u_r is the amplitude of the degree-two radial deformation of the surface of the body, and g is the acceleration of gravity at the surface. We can estimate h_2 using the observed value of $(a-b) = 10.5 \pm 0.8\,\text{km}$ using the relationship (Dermott and Thomas, 1988):

$$h_2 = \frac{2}{3}\frac{(a-b)}{Rq} = 2.242 \pm 0.167 \tag{5.8}$$

For a hydrostatic body, $h_2 = k_2 + 1$, therefore the deformation observed by image analysis is consistent with that observed by Doppler tracking, though the gravitational measurements are considerably more precise.

5.4 IO'S INTERNAL DENSITY STRUCTURE

Having obtained estimates of k_2 and h_2, and confirmation that Io has an equilibrium shape, models of Io's interior density structure may be constructed to satisfy the Love numbers (which are not independent) and the total mass. With only two integral constraints, unique solutions are not possible, but families of likely solutions may be derived.

The mean density of Io is $3{,}528\,\text{kg}\,\text{m}^{-3}$, and silicate volcanism (as well as abundant sulfur) is observed at the surface (McEwen *et al.*, 1998). It is reasonable, then, to explore models of Io's interior consisting of an outer silicate layer and, possibly, a deep metallic core consisting of iron with some amount of sulfur. Nickel, which commonly occurs with iron, is a minor component of the core and is close enough in density to iron to make it indistinguishable for our purposes.

The maximum tidal deformation of a body is achieved for a homogeneous density fluid, where k_2 and h_2 reach maxima of 3/2 and 5/2 respectively. Io's observed k_2 Love number of 1.292 could be explained either by a density profile that increases toward the center, or by elastic stresses. Before pursuing differentiated models, we provide some results that arise from considering Io to be homogeneous in density but elastic. This will allow us to understand the limits the hydrostatic models place on the interior density structure. A homogeneous Io could exhibit a k_2 less than 3/2 only through elastic strength which resists the tidal and rotational forces throughout the billions of years over which these have been acting. As pointed out above, it is unlikely that such stresses have not relaxed over that time, but we pursue this model to see what limits can be placed on the mechanical behavior and internal density structure of Io.

The classical solution for a homogeneous elastic body was given by Love (1944) as:

$$k_2 = \frac{3}{2}\left(1 + \frac{19\mu}{2\rho g R}\right)^{-1} \tag{5.9}$$

where μ is the shear modulus of the material making up Io. We can use this relationship to derive an upper bound on the shear modulus $\mu < 2 \times 10^8\,\text{Pa}$. This is considerably lower than values typical for solids ($10^{10} - 10^{11}\,\text{Pa}$), indicating that Io's

interior cannot be entirely solid. If Io is not homogeneous, but instead has a dense core, this upper limit is reduced further.

Love numbers for differentiated bodies may be calculated using a method originally developed by Alterman *et al.* (1959) in which the deformations are decomposed into spherical harmonics and the resulting 6th-order system of differential equations describing the deformation is solved in a number of uniform property layers (Segatz *et al.*, 1998). For a simple, two-layer body, however, the Darwin–Radau relationship provides an approximate (though highly accurate for the densities involved in planetary materials) relationship between the hydrostatic Love numbers and the density distribution.

$$h_2 = k_2 + 1 = \frac{5}{1 + \left(\frac{5}{2} - \frac{15}{4}\gamma\right)^2} \tag{5.10}$$

where γ is the moment of inertia factor:

$$\gamma = \frac{C}{MR^2} = \frac{2}{5}\left[\frac{\rho_m}{\bar{\rho}} + \left(1 - \frac{\rho_m}{\bar{\rho}}\right)\left(\frac{r_c}{R}\right)^2\right] \tag{5.11}$$

where C is the maximum moment of inertia, ρ_m and $\bar{\rho}$ are the mantle and mean densities, respectively, and r_c is the core radius.

Figure 5.1 shows the core density (upper curves) and shell (mantle) density (lower curves) for the families of two-layer hydrostatic models that satisfy the observed k_2 and total mass for Io. The measurement uncertainty on k_2 is roughly the width of the solid lines. Also shown (dotted) are the densities of pure metallic iron, 8,000 kg m^{-3}, and iron–iron sulfide eutectic, 5,150 kg m^{-3} (Usselman, 1975) at pressures of $\sim$ 8 GPa, typical of Io's core.

The hydrostatic curves show that models with shell densities in the range of silicate rocks and core densities in the range for iron–iron sulfide mixtures have core radii between 0.37 and 0.52 of Io's radius. These models have silicate mantles with densities similar to the Earth's uppermost mantle or the bulk Moon (3,250–3,300 kg m^{-3}). Lower mantle densities require cores that are not metallic, but are mixtures of rock and metal.

We have shown above that the observations are consistent with an equilibrium shape for Io, but that does not exclude the possibility of elastic stress in, for example, a cold lithosphere. In order to alter the equilibrium shape of Io, this lithosphere would have to be frozen in when Io had a different shape, and it would have to maintain the stresses over billions of years. Since Io was most likely closer to Jupiter in the past, the frozen-in shape would actually be more distorted (less spherical) than the current forcing would dictate. Thus, the inferred structure would be less differentiated than the actual structure, causing the curves in Figure 5.1 to move away from the uniform density line. Although we consider it quite unlikely that Io's lithosphere is able to maintain such stresses over billions of years while magma courses through it to feed surface volcanism, elastic stresses would make our estimates of core size lower bounds.

In principle, elastic support could be constrained independently by the measured h_2, since it is only for hydrostatic models that h_2 is required to be $k_2 + 1$, but the

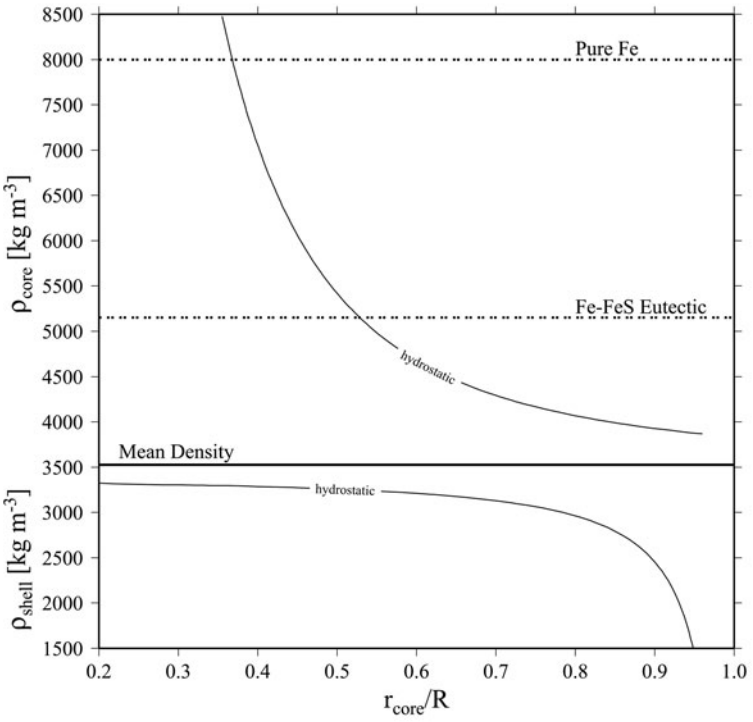

Figure 5.1. Two-layer models of Io consistent with the observed k_2 and mean density. The mean density is shown as a thick solid line dividing the core density curve (above) from the shell density curves (below). Also shown are the densities of pure Fe and the Fe–FeS eutectic.

measurement uncertainty on h_2 from the limb-fitting is too large to be helpful in this regard. A reduction in uncertainty by a factor of 2 in the h_2 measurement would allow this constraint to be used, at least for certain classes of models, to constrain the product of the lithospheric thickness and shear modulus.

Io's extensive volcanic activity suggests that the silicate mantle may be differentiated through the formation of a low-density crust (Keszthelyi and McEwen, 1997). We explore this possibility using three-layer models for the density structure (Anderson *et al.*, 2001). In order to reduce the degree of indeterminacy in the models, we restrict the core density to the end-member values for iron–iron sulfide mixtures. The results are not strongly sensitive to the assumed density of the crust for reasonable values between 2,500 and 3,000 kg m^{-3}, so we use an intermediate value appropriate to basalt of 2,750 kg m^{-3}. Figure 5.2 shows the resulting hydrostatic models that satisfy the observed k_2 and mean density as a function of crustal thickness.

The three-layer models show that a thick crust requires a dense mantle, which is not consistent with basaltic fractionation which removes iron from the mantle and leaves it less dense. If we restrict the mantle to densities near that of Earth's upper mantle (3,300 kg m^{-3}), then the crust must be less than about 40 km thick,

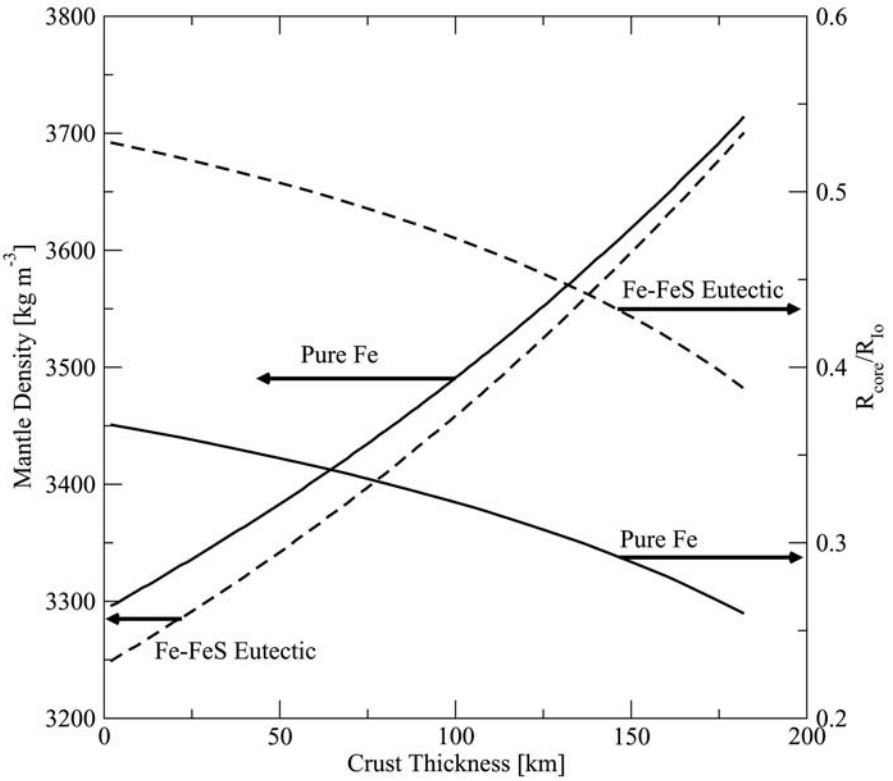

Figure 5.2. Mantle density (left axis) and fractional core radius (right axis) as a function of crustal thickness for the family of hydrostatic models satisfying the observed k_2 and mean density. The crustal density is 2,750 kg m^{-3}, and the range of core densities is most likely encompassed by the curves for pure Fe (solid) and the Fe–FeS eutectic (dashed).

independent of the density of the core. The radius of the core is mostly dependent on its density, ranging from about $0.35R_{Io}$ for a pure Fe composition to about $0.5R_{Io}$ for the Fe–FeS eutectic composition, for the same mantle density (3,300 kg m^{-3}).

Io may additionally have a partially molten asthenosphere, with a density intermediate between the differentiated crust and the unmelted mantle. With the constraints available, we cannot distinguish crust from asthenosphere and mantle. The smaller the density contrast between layers, the weaker the constraints on the layer thicknesses become. Such models are not inconsistent with the data, but the inherent indeterminacy makes them of little use.

5.5 THE COMPOSITION OF IO

Having determined the density structure of Io, we can now consider the chemical composition of Io and compare it to other Solar System bodies. The core of Io is 1/10

to 1/5 the total mass, depending on its composition, and the amount of iron in the core is 10–14% of the total. The Earth's core is nearly 1/4 its mass, the Moon's is less than 1/40 its mass, and the core of Mars is about 1/5 its mass. Mantle densities are restricted in a narrow range by the interior models (Figure 5.1), but mantle composition cannot be uniquely determined given the unknown temperature. Using the current equation of state data and assuming a pure olivine mantle, Sohl *et al.* (2002) derive mantle compositions between 76 and 85 wt% forsterite (Mg_2SiO_4) for super solidus mantles (temperatures between 1 and 1.2 times the solidus). The bulk Fe/Si ratios range from 1.3 to 1.5 for these models. Using a similar set of density models, Kuskov and Kronrod (2001) find that the L- and LL-chondrite meteorites are the best match for the composition of Io and derive a bulk Fe/Si ratio of 1.04 to 1.14. This value is very different from CI chondrites (1.71) (Kerridge and Matthews, 1988), the Moon (0.22-0.37) (Warren, 2005), or Mars (1.75–1.8) (Sohl *et al.*, 2005).

There is no real constraint on the composition of Io's core. Sulfur may be present at levels up to the eutectic (37 wt% FeS). Since the eutectic mixture would be the first to separate out, the core likely began eutectic but became more iron rich, as further heating would allow metallic iron to segregate. The amount of available metal depends critically on the oxidation state of Io's mantle and thus on that of the Jovian sub-nebula at Io's position. Hence, an independent measurement of the size of Io's core would provide a constraint on the redox conditions in the Jovian sub-nebula.

Io's composition seems to be consistent with the inference of orthopyroxene in surface magmas (Geissler *et al.*, 1999), since the L- and LL-chondrite compositions are pyroxene rich (Kuskov and Kronrod, 2001), although this was not accounted for in Sohl *et al.* (2002). The amount of iron in Io's mantle appears to be less than that in Mars, but considerably more than in the Moon or Earth. Io, then, appears to have condensed in an environment less oxidized than Mars, perhaps as a consequence of its formation in the Jovian sub-nebula.

5.6 IO'S SURFACE HEAT FLOW

An additional observation that can be brought to bear on the state of Io's interior is the heat flow at the surface. Unlike most bodies in the Solar System, which would require *in situ* methods to determine the heat flow, Io's surface heat flow can be estimated from remote observations of its thermal emission. Many discrete volcanic hot spots apparently account for most of the heat flow and their radiation is easily measured, but low-temperature emission from cooling lava flows may also be significant (Stevenson and McNamara, 1988; Veeder *et al.*, 1994), and is more difficult to separate from passive solar heating.

Disk-integrated, ground-based observations of Io's thermal emission provide uniform longitudinal coverage and a long time base, allowing study of the spatial

(longitudinal) and temporal variability of the heat flow. Veeder *et al.* (1994) constrained models of the passive component by wavelength-dependent changes in Io's thermal emission during Jupiter eclipses, by photometric observations of the bolometric albedo (Simonelli and Veverka, 1988) and *Voyager* infrared observations of Io's nightside temperature (Pearl and Sinton, 1982; McEwen *et al.*, 1996). They concluded that Io's average heat flow is more than $2.5\,W\,m^{-2}$ (10^{14} W global total), with only modest temporal or spatial variability. They considered their estimate to be a lower limit because the ground-based data are not very sensitive to radiation from high-latitude anomalies, and because they did not include the possible contribution from heat conducted through Io's lithosphere.

Voyager infrared imaging spectrograph (IRIS) observations of Io (Pearl and Sinton, 1982; McEwen *et al.*, 1996) in the far infrared (5–50 μm), provide an independent measure of heat flow. The typical spatial resolution of these observations is a few hundred kilometers, which is sufficient to resolve individual hot spots. Relatively high spectral resolution allows some separation of passive and endogenic radiation within each field of view by fitting multiple black bodies to each spectrum and assuming that the lowest temperature contribution is passive. However, the data do not provide globally homogeneous coverage. Extrapolating from the Jupiter-facing hemisphere, where coverage is best, and assuming that Loki, which radiates more heat than any other Io hot spot (about 25% of the total), is unique, McEwen *et al.* (1996) estimated a minimum global heat flow of $1.85\,W\,m^{-2}$, with likely additional contributions from conducted heat and widespread low-temperature hot spots.

Endogenic emission is more readily separated from passive emission at night, when the passive component is minimized. *Voyager* IRIS obtained sporadic night-time coverage of Io, but the first hemispheric maps of broadband night-time emission came from *Galileo* photopolarimeter and radiometer (PPR) observations (Spencer *et al.*, 2000; Rathbun *et al.*, 2004). Low-latitude night-time temperatures away from the obvious hot spots are near 95 K, and drop more slowly than expected at high latitudes (e.g., 85 K at 70°S, 258°W). Making the assumption that at low latitudes the background temperature is entirely due to passive emission, and that all emission at higher temperatures is endogenic, Rathbun *et al.* (2004) estimated global heat flow to be $2\,W\,m^{-2}$, assuming that Loki is unique. The lack of fall-off in temperature with latitude would then imply excess endogenic emission at high latitudes. Rathbun *et al.* (2004) also determined that at low latitudes the diurnal surface temperatures away from the obvious hot spots was consistent with expected passive temperatures, given the bolometric albedo determined by Simonelli *et al.* (2001). Non-hot-spot endogenic emission, from conducted heat or widespread old cooling lava flows (Matson *et al.*, 2001) is therefore probably less than $1\,W\,m^{-2}$. From a global inventory of Io's thermal radiation from a variety of sources, McEwen *et al.* (2004) obtained a global heat flow estimate of $2.1 \pm 0.7\,W\,m^{-2}$. The possibility of excess endogenic heat at high latitudes inferred from the warm night-time polar temperatures was incorporated into an updated version of their 1994 thermal model by Veeder *et al.* (2004) resulting in an estimated global heat flow of $3 \pm 1\,W\,m^{-2}$. In summary, Io's total heat flow is still not precisely known, but all techniques give values in the range from 1.5–4 $W\,m^{-2}$ ($0.6–1.6\times10^{14}$ W total).

5.7 THERMAL AND RHEOLOGICAL STRUCTURE

The tremendous heat flow measured at the surface of Io is the result of silicate volcanism, with typical inferred eruption temperatures of 1,200–1,400 K, and extreme temperatures over 1,800 K (McEwen *et al.*, 1998). It is likely that the sulfur-based volcanism observed by *Voyager* is also driven by silicate magma. Io is the most volcanically active body in the Solar System. The surface is so active that not a single impact crater has been identified in the images of the satellite. In this section we explore the implications of such activity for the thermal and rheological structure of the interior.

Despite the intensity of the volcanic activity on Io and the inferred high temperatures of its interior, Io supports some of the highest and steepest topography of any planetary body. Mountains up to 17 km high dot the surface (Jaeger *et al.*, 2003) and oddly, these are not volcanoes. Instead, volcanic centers are generally depressions, while the mountains appear to be fault-bounded tectonic uplifts. The presence of such large topography seems incompatible with a lithosphere that must allow the transport of $\sim 10^{14}$ W of heat.

A solution to this problem was found by O'Reilly and Davies (1981), who proposed a heat-pipe mechanism for heat transport through Io's lithosphere accomplished by melt transport through fissures. The most important implication of this model is that, as successive eruptions spread across the surface and cool, they bury the flows of previous eruptions, resulting in an advective transport of cold material from the surface downward.

In order to match the observed heat flow, Io must be resurfaced globally by silicate magma to a depth of 1–2 cm every year. This is then the rate at which material is advected downward within the lithosphere. The equation for the temperature T in the lithosphere is then:

$$\frac{k}{\rho c_P}\frac{d^2T}{dz^2} = v\frac{dT}{dz} - \frac{H}{\rho c_P} \tag{5.12}$$

where k is the thermal conductivity, ρ is the density, c_P is the specific heat, z is the depth from the surface, v is the downward velocity (resurfacing rate), and H is the volumetric heat production. The temperature must match the surface temperature T_s at the surface and the melting temperature T_m at the base of the lithosphere. The solution in the case of no heat production is:

$$T(z) = T_s + \frac{(T_m - T_s)\left(\exp^{\lambda\xi} - 1\right)}{\exp^{\lambda} - 1} \tag{5.13}$$

where $\xi = z/D$ is the depth normalized by the thickness of the lithosphere D, and the dimensionless parameter $\lambda = Dv\rho c_P/k$ is the advective velocity normalized by the conductive velocity scale. This can be related to the heat flux carried by melting F as follows:

$$\lambda = \frac{Dc_P F}{k\left[L_f + c_P(T_m - T_s)\right]} \tag{5.14}$$

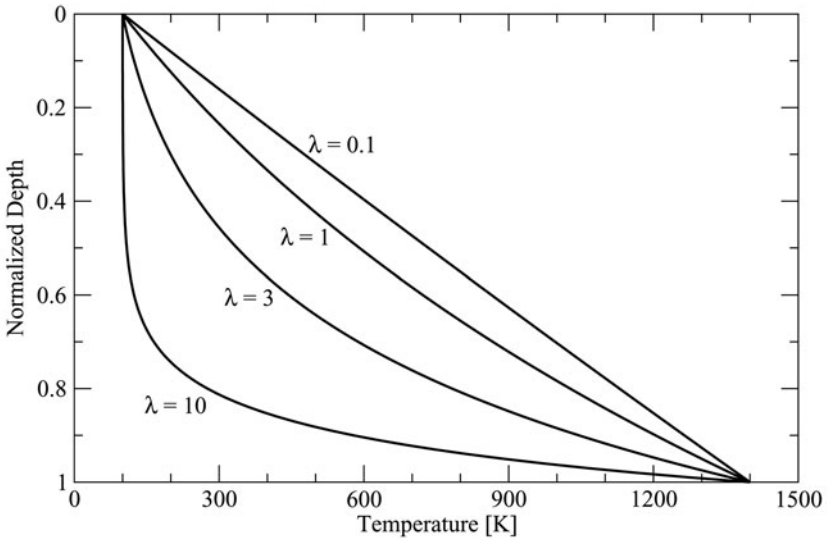

Figure 5.3. Temperature as a function of normalized depth for different values of λ, the normalized advective velocity defined in the text.

where L_f is the latent heat of fusion of the silicate rocks. For a heat flux of 2.5 W m^{-2} and a 30 km thick lithosphere, λ is about 10. Solutions for different values of λ are shown in Figure 5.3. For λ of 3, more than 80% of the thickness of the lithosphere is below 900 K, and for λ of 10, more than 95% of the lithosphere is cold enough to sustain elastic stresses for very long periods of time. This is how Io's lithosphere can support huge mountains while at the same time allowing a heat flux of 2.5 W m^{-2} to pass through.

The very steep gradient at the base of the lithosphere and the continuous flux of material through it means that any chemical layering in the lithosphere (i.e., crust) must be very closely linked to the rheological structure. That is, the crust and lithosphere are essentially the same. Schenk *et al.* (2001) pointed out that the lithosphere must be at least as thick as the tallest mountains ($\sim$15 km) if the mountains form as thrust blocks. In order to form the mountains by compressive stresses due to the global resurfacing, a thickness of at least 12 km is required (Jaeger *et al.*, 2003). As an upper limit, the tidal deformation will be restricted by a thick, strong lithosphere, so we can determine the maximum thickness elastic lithosphere (shear modulus 10^{11} Pa) that will allow Io to dissipate the observed heat flow. This limit turns out to not be very useful, since a 500-km elastic lithosphere is required to reduce the maximum dissipation below 10^{14} W.

What sort of melt fractions does the heat-pipe mechanism imply for the asthenosphere? It is straightforward to calculate the melt segregation velocity due to Darcy flow driven by the buoyancy of the melt (e.g., Scott and Stevenson, 1986):

$$\phi v = \frac{k_\phi g \Delta\rho}{\eta_m} \tag{5.15}$$

where ϕ is the melt volume fraction (porosity), g is the gravitational acceleration, $\Delta\rho$ is the difference between the solid and melt densities ($\sim$500 kg m^{-3}), η_m is the melt viscosity ($\sim$1,000 Pa s), and k_ϕ is the permeability, which is related to the porosity by a function of the form:

$$k_\phi = \frac{b^2\phi^n}{\tau} \tag{5.16}$$

where b is a typical grain size ($\sim$1 cm), and n and τ are constants which are functions of the geometry of the melt. The dependence of k_ϕ on grain size is overly simplified in this model, since real systems may have broad grain size distributions. Using the 1 cm yr^{-1} resurfacing velocity (which is actually the melt flux ϕv) and inserting experimentally determined values for the constants n (3) and τ (200) (Wark and Watson, 1998; Liang *et al.*, 2001) results in an estimate for ϕ between 10 and 20% (Moore, 2001). Melt fractions exceeding this will transport too much heat (the heat transported goes as k_ϕ), thus cooling the asthenosphere and bringing the melt fraction back to the equilibrium value.

Based on petrological models (using L- and LL-chondrite compositions, above), it has been pointed out by Keszthelyi *et al.* (1999, 2004) that the highest temperatures (up to 1,870 K) observed from surface eruptions on Io (McEwen *et al.*, 1998) require very high melt fractions (above 50%) in Io's interior. The apparent low viscosity of Ionian magmas also suggests ultramafic compositions and high melt fractions. Generalizing this to a global "mushy magma ocean" Keszthelyi *et al.* (2004) arrive at a model for Io's interior that is partially molten throughout, decreasing from 60% melt at the base of the lithosphere to 10–20% at the base of the mantle. Though attractive for its explanation of the very highest magma temperatures observed, it has not been shown how such a melt distribution can be maintained against melt segregation and the resulting heat loss (as described above), or how such a rheological structure can allow sufficient tidal heat generation (Moore, 2001). The temperature of most eruptions observed on Io (1,200–1,400 K) seem to be consistent with the melt fractions (10–20%) required for thermal equilibrium (Moore, 2001), so perhaps there are local processes that account for the high-temperature outliers.

A rough estimate for the thickness of the asthenosphere may be obtained by extrapolating along the adiabat from the temperature at the top of the melt zone to the solidus:

$$d = \frac{\Delta T_m}{(dT/dz)_m - (dT/dz)_{ad}} \tag{5.17}$$

where $\Delta T_m = \phi L_f / c_P$ is the temperature excess required to reach a melt fraction ϕ, and the denominator is the difference between the slopes of the solidus ($\sim$ 0.8 K km^{-1}) and the adiabat ($\sim$ 0.1 K km^{-1}). Using the melt fractions estimated above, the asthenosphere is 60–120 km thick.

The physical state of Io's core cannot be determined from the *Galileo* spacecraft's observations of Io's permanent tidal deformation. The density difference between solid and liquid core material is too small to be resolvable from these data. If Io had a magnetic field, it would be possible to conclude that at least part of the core would have to be liquid. However, multiple fly-bys of Io by the *Galileo* spacecraft have shown

that Io does not possess an internal magnetic field (Kivelson *et al.*, 2004). All that can be concluded from the absence of a magnetic field is that there is insufficient convective activity in Io's core to support a dynamo. The core could be completely solid or liquid; it could even be partially solidified, although the lack of dynamo action would be more difficult to understand if there were a growing solid inner core in Io. Because Io's mantle is so intensely heated, it seems most likely that Io has no magnetic field because it has a completely liquid core that is kept from cooling and convecting by the surrounding hot mantle (Weinbruch and Spohn, 1995).

The state of the core is also not determined by the amount of tidal dissipation in Io, which is determined almost entirely by the viscosity of the mantle. Early work using parameterized (Q-model) dissipation (Peale *et al.*, 1979; Cassen *et al.*, 1982) suggested that a liquid core was required in order to allow the mantle to dissipate sufficient heat, but this is not supported by the results of more detailed calculations using the solutions to the equations of motion for viscoelastic bodies (Segatz *et al.*, 1988; Moore, 2003). The difference in dissipation between fluid cores and elastic cores in such models is less than a factor of 3.

5.8 THERMAL AND ORBITAL EVOLUTION

Io is unique in the Solar System in that its primary source of internal heat is not radioactive decay but tidal dissipation (Peale *et al.*, 1979). The tidal heat source is not only capable of much greater heating rates, it evolves with the orbit of Io, since it depends on both the distance of Io from Jupiter (the semi-major axis) and the eccentricity of Io's orbit. Tidal heating is also very sensitive to the rheology of Io's interior. The heat source is therefore coupled to both the orbit and the interior temperature. This results in a very different thermal evolution for Io than for other bodies of similar size (e.g., the Moon).

The tidal heating of Io's interior is a result of the resonant orbital interactions between Io, Europa, and Ganymede, which have orbital periods that are in the ratio $\tau_I{:}\tau_E{:}\tau_G = 1{:}2{:}4$. The orbits of all three satellites have evolved together into what is called the Laplace resonance, where the conjunctions of each satellite with its nearest outward neighbor occur when the inner satellite is at perijove (nearest to Jupiter) and the outer satellite at apojove (furthest from Jupiter), thus maximizing their separation. These repetitive alignments cause the orbits to remain elliptical, even though dissipation of tidal energy in the satellites should tend to circularize their orbits (while dissipation in Jupiter tends to make them more eccentric).

In addition to the effects of dissipation on eccentricity, tides raised on the satellite tend to reduce the semi-major axis of the orbit (i.e., the satellite tends to spiral inward). Thus, Io's orbital evolution is tightly coupled to the thermal evolution of its interior. Conversely, tides raised on Jupiter by the satellite cause the satellite to spiral outward (like the Moon). Thus, Io's actual rate of orbital migration represents a balance between dissipation in Io and dissipation in Jupiter. Indeed, this orbital migration is thought to be the process by which the resonant configuration is assembled (Yoder, 1979).

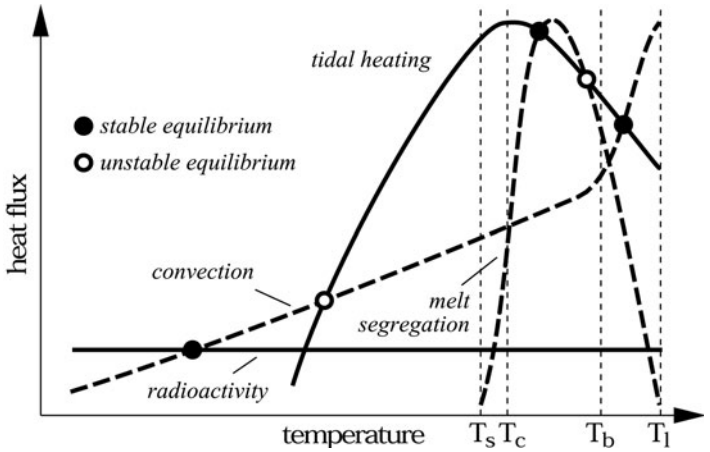

Figure 5.4. Depiction of the possible thermal equilibria (circles) in a tidally heated body. Heat sources (radioactivity and tidal heating) are shown as solid lines, and heat transport mechanisms (convection and melt segregation) are shown as dashed lines. Also marked schematically are the solidus T_s, critical T_c, breakdown T_b, and liquidus T_l temperatures.

The coupled thermal–orbital evolution of Io (and Europa and Ganymede) is a complex dynamical system with a wide possible range of behaviors. The interior temperature is set by the balance between tidal heating and heat transport (convective or magmatic). Orbital evolution is driven by dissipation in Io. Fischer and Spohn (1990) studied the coupled system including a simplified orbital evolution (linearized about the Laplace resonance) and convective heat transport, and recognized that there are multiple equilibria for the thermal state of Io, as illustrated in Figure 5.4, depicting the possible thermal equilibria in a tidally heated body. Radioactivity (solid line) produces the same heating regardless of temperature, while tidal heat production (solid curve) depends strongly on temperature, increasing with temperature until the Maxwell time (viscosity over shear modulus) of the material approaches the tidal forcing period. At a critical temperature (T_c) slightly above the solidus the shear modulus begins to decrease rapidly (Berckhemer *et al.*, 1982), resulting in a drop in tidal heating. At the breakdown temperature T_b, the solid matrix loses coherence, and the material becomes dominated by the mechanical properties of the liquid and the tidal heating is greatly reduced. Convective heat transport (dashed curve) increases with temperature, as the viscosity decreases, becoming extremely efficient as the liquidus temperature T_l is approached. Melt segregation (as described above) can only occur between the solidus and liquidus, and is not efficient above the breakdown temperature (since there is no longer any solid matrix for the melt to segregate from). Depending on the details of the heat production and transport processes, not all of these equilibria may be realized, so we use a qualitative diagram to illustrate the possible range of behaviors.

Fischer and Spohn (1990) identified the highest and lowest temperature equilibria (the points where the solid tidal heat and radioactivity curves intersect the dashed

convection curve) and noted that at times of low eccentricity, the high-temperature equilibrium may cease to exist. This is because low eccentricity shifts the tidal heat production curve downward, and it may fail to intersect the convective heat transport curve at all. Such episodes are followed by rapid cooling, as Io evolves toward the more common radioactivity driven convective equilibrium. Conversely, extremely high eccentricity could cause the low-temperature equilibrium to vanish, resulting in runaway heating toward the high-temperature equilibrium. Moore (2003) investigated the tidal–convective equilibrium (for the current eccentricity, independent of the orbital evolution) and concluded that the high-temperature equilibrium, while present, cannot explain the observed heat flow, thus a different heat transport process (melt segregation) was necessary.

Melt segregation can introduce additional equilibria as shown in Figure 5.4. These equilibria are necessarily between the solidus and liquidus temperatures (T_s and T_l). The simplified calculation given in Section 5.7 required melt fractions of 10–20% to achieve equilibrium. This equilibrium is stable, but may disappear at times of low eccentricity. Since this equilibrium is reached at temperatures lower than the convective equilibrium (this is a consequence of the high viscosity of rocks, even when partially molten), it is likely that Io never reaches the high-temperature convective equilibrium. Io's volcanic activity and high heat flow strongly suggest that Io is in (or near) an equilibrium state with melt segregation balancing tidal heat production.

It is not known whether our roughly three decades of heat flow observations are representative of the long-term average, but if 10^{14} W is the rate of energy dissipation in Io, then if we know the rate of dissipation in Jupiter, we can predict the rate at which Io's orbit is evolving. Unfortunately, the mechanisms by which tidal motions are dissipated in a deep atmosphere such as Jupiter's are not understood at present. We are therefore left with trying to measure the orbital evolution to estimate dissipation in Jupiter.

Recent attempts to measure the rate of Io's orbit migration using astrometric measurements of satellite mutual events (eclipses) disagree on both the rate and the direction of the orbital migration. The process used to infer the migration rate of Io from the mutual event timing is apparently quite model dependent, since Lieske (1987) derives a rate of change of the mean motion of Io $\dot{n}/n$ of $-0.74 \pm 0.87 \times 10^{-11}\,\mathrm{yr}^{-1}$, while a more recent measurement using a different orbital theory by Aksnes and Franklin (2001) yields a rate of $+36 \pm 10 \times 10^{-11}\,\mathrm{yr}^{-1}$.

We can put certain bounds on the total outward migration of Io's orbit (assuming Europa and Ganymede have moved in concert) by assuming Io formed as close to Jupiter as possible (2.4 R_J) and evolved to its current orbital distance over the age of the Solar System. This upper bound on the migration rate, however, is still much too low to account for Io's current dissipation rate, which depends on the maintenance of a high eccentricity (and thus high dissipation in Jupiter) (Yoder and Peale, 1981). We are therefore forced to conclude that Io's orbital evolution has not been steady over the age of the Solar System, or that the current heat flow does not represent a long-term average of the tidal dissipation.

Either case is possible, since we do not know if the Laplace resonance is primordial or if it was assembled more recently by orbital migration. Furthermore, Io's

surface heat flow represents dissipation integrated over some unknown transport time. However, if most of the heat is carried by melt segregation, as seems to be the case (above and Moore, 2003) the transport time is short (tens of years), and the heat flow does reflect recent tidal dissipation. A longer transport time regulated by convective motions would allow for the possibility of oscillatory states in which the heat flow and dissipation are out of phase (Fischer and Spohn, 1990; Hussmann and Spohn, 2004).

5.9 SUMMARY

The *Galileo* mission to Jupiter has greatly advanced our understanding of Io. It is now clear that Io is a differentiated body consisting of a metallic core and a silicate mantle. The radius of the core is between 0.37 and 0.52 times Io's radius, depending on the unknown composition. The composition of the mantle is also not known precisely, but the best analogy to Io's composition are the L- and LL-chondrite meteorites. The bulk Fe–Si ratio is well below CI chondrites and Mars, but higher than the Moon. The physical state of the core is unknown, but it is likely liquid (due to the intensely heated mantle above). Though a differentiated crust of some sort is inevitable, we cannot constrain its thickness or composition.

The strong lithosphere required to support the observed mountains is a consequence of the large flux of molten rock to the surface, which rapidly buries older, cold flows. This melt segregation is responsible for nearly all of Io's very high surface heat flux, and most likely drives the sulfur volcanism that makes Io's surface so distinctive. Melt fractions in the mantle required to balance the observed heat flow are 10–20%, which is consistent with the bulk of the temperature estimates for surface flows, though there may be localized regions at higher temperature with higher melt fractions.

Since Io's heat flow is dominated by the relatively rapid process of melt segregation, the available heat flow data are most likely representative of the average heat production by tidal dissipation in Io's interior. Though measurements of the orbital evolution of Io are at present inconclusive, future measurements (e.g., from an orbiter) should establish its rate of migration and constrain the dissipation in Jupiter.

5.10 REFERENCES

Aksnes, K. and F. A. Franklin. 2001. Secular acceleration of Io derived from mutual satellite events. *Astronomical Journal*, **122**(5), 2734–2739.

Alterman, Z., H. Jarosch, and C. L. Pekeris. 1959. Oscillations of the Earth. *Proc. R. Soc. London Ser. A.*, **252**, 80–95.

Anderson, J. D., W. L. Sjogren, and G. Schubert. 1996. Galileo gravity results and the internal structure of Io. *Science*, **272**, 709–712.

Anderson, J. D., R. A. Jacobson, E. L. Lau, W. B. Moore, and G. Schubert. 2001. Io's gravity field and interior structure. *J. Geophys. Res.*, **106**, 32963–32969.

Berckhemer, H., W. Kampfmann, E. Aulbach, and H. Schmeling. 1982. Shear modulus and Q of forsterite and dunite near partial melting from forced-oscillation experiments. *Phys. Earth Planet. Int.*, **29**, 30–41.

Cassen, P. M., S. J. Peale, and R. T. Reynolds. 1982. Structure and evolution of the Galilean satellites. In: D. Morrison and M. S. Matthews (eds), *Satellites of Jupiter*. University of Arizona Press, Tucson, AZ, pp. 93–128.

Dermott, S. F. and P. C. Thomas. 1988. The shape and internal structure of Mimas. *Icarus*, **73**, 25–65.

Fischer, H. J. and T. Spohn. 1990. Thermal–orbital histories of viscoelastic models of Io (J1). *Icarus*, **83**, 39–65.

Geissler, P. E., A. S. McEwen, L. Keszthelyi, R. Lopes-Gautier, J. Granahan, and D. P. Simonelli. 1999. Global color variations on Io. *Icarus*, **140**(2), 265–282.

Hubbard, W. B. and J. D. Anderson. 1978. Possible flyby measurements of Galilean satellite interior structure. *Icarus*, **33**, 336–341.

Hussmann, H. and T. Spohn. 2004. Thermal–orbital evolution of Io and Europa. *Icarus*, **171**(2), 391–410.

Jaeger, W. L., E. P. Turtle, L. P. Keszthelyi, J. Radebaugh, and A. S. McEwen. 2003. Orogenic tectonism on Io. *Journal of Geophys. Res.*, **108**(E8), doi:10.1029/2002JE001946.

Kaula, W. M. 1964. Tidal dissipation by solid friction and the resulting orbital evolution. *Rev. Geophys.*, **2**, 661–685.

Kerridge, J. F. and M. S. Matthews. 1988. *Meteorites and the Early Solar System*. University of Arizona Press, Tucson, AZ.

Keszthelyi, L. and A. McEwen. 1997. Magmatic differentiation of Io. *Icarus*, **130**, 437–448.

Keszthelyi, L., A. S. McEwen, and G. J. Taylor. 1999. Revisiting the hypothesis of a mushy global magma ocean in Io. *Icarus*, **141**, 415–419.

Keszthelyi, L., W. L. Jaeger, E. P. Turtle, M. Milazzo, and J. Radebaugh. 2004. A post-Galileo view of Io's interior. *Icarus*, **169**(1), 271–286.

Kivelson, M. G., F. Bagenal, W. S. Kurth, F. M. Neubauer, C. Paranicas, and J. Saur. 2004. Magnetospheric interactions with satellites. In: F. Bagenal, T. E. Dowling, and W. B. McKinnon (eds), *Jupiter: The Planet, Satellites and Magnetosphere*. Cambridge University Press, Cambridge, UK, pp. 513–536.

Kuskov, O. L. and V. A. Kronrod. 2001. Core sizes and internal structure of the Earth's and Jupiter's satellites. *Icarus*, **151**, 204–227.

Liang, Y., J. D. Price, D. A. Wark, and E. B. Watson. 2001. Nonlinear pressure diffusion in a porous medium: Approximate solutions with applications to permeability measurements using transient pulse decay method. *Journal of Geophys. Res.*, **106**, 529–535.

Lieske, J. H. 1987. Galilean satellite evolution: Observational evidence for secular changes in mean motions. *Astron. Astrophys.*, **176**, 146–158.

Love, A. E. H. 1944. *A Treatise on the Mathematical Theory of Elasticity*. Dover, New York.

Matson, D. L., T. V. Johnson, G. J. Veeder, D. L. Blaney, and A. G. Davies. 2001. Upper bound on Io's heat flow. *Journal of Geophys. Res.*, **106**(E12), 33021–33024.

McEwen, A. S., Keszthelyi, L. P., Spencer, J. R., Schubert, G., Matson, D. L., Lopes-Gautier, R., Klaasen, K. P., Johnson, T. V., Head, J. W., Geissler, P. *et al.* 1998. High-temperature silicate volcanism on Jupiter's moon Io. *Science*, **281**(5373), 87–90.

McEwen, A. S., N. R. Isbell, K. E. Edwards, and J. C. Pearl. 1996. Temperatures on Io: Implications to geophysics, volcanology, and volatile transport. *Lun. Planet. Inst. Conf. Abs.*, **27**, 843.

McEwen, A. S., L. P. Keszthelyi, R. Lopes, P. M. Schenk, and J. R. Spencer. 2004. The lithosphere and surface of Io. In: F. Bagenal, T. E. Dowling, and W. B. McKinnon

(eds), *Jupiter: The Planet, Satellites and Magnetosphere*. Cambridge University Press, Cambridge, UK, pp. 307–328.

Moore, W. B. 2001. The thermal state of Io. *Icarus*, **154**, 548–550.

Moore, W. B. 2003. Tidal heating and convection in Io. *Journal of Geophys. Res.*, **108**, 5096, doi:10.1029/2002JE001943.

O'Reilly, T. C. and G. F. Davies. 1981. Magma transport of heat on Io: A mechanism allowing a thick lithosphere. *Geophys. Res. Lett.*, **8**, 313–316.

Peale, S. J., P. Cassen, and R. T. Reynolds. 1979. Melting of Io by tidal dissipation. *Science*, **203**, 892–894.

Pearl, J. C. and W. M. Sinton. 1982. Hot spots of Io. In: D. Morrison and M. S. Matthews (eds), *Satellites of Jupiter*. University of Arizona Press, Tucson, AZ, pp. 724–755.

Rathbun, J. A., J. R. Spencer, L. K. Tamppari, T. Z. Martin, L. Barnard, and L. D. Travis. 2004. Mapping of Io's thermal radiation by the Galileo photopolarimeter–radiometer (PPR) instrument. *Icarus*, **169**(1), 127–139.

Schenk, P., H. Hargitai, R. Wilson, A. McEwen, and P. Thomas. 2001. The mountains of Io: Global and geological perspectives from Voyager and Galileo. *Journal of Geophys. Res.*, [in press].

Schubert, G., J. D. Anderson, T. Spohn, and W. B. McKinnon. 2004. Interior composition, structure and dynamics of the Galilean satellites. In: F. Bagenal, T. E. Dowling, and W. B. McKinnon (eds), *Jupiter: The Planet, Satellites and Magnetosphere*. Cambridge University Press, Cambridge, UK, pp. 281–306.

Scott, D. R. and D. J. Stevenson. 1986. Magma ascent by porous flow. *Journal of Geophys. Res.*, **91**, 9283–9296.

Segatz, M., T. Spohn, M. N. Ross, and G. Schubert. 1988. Tidal dissipation, surface heat flow, and figure of viscoelastic models of Io. *Icarus*, **75**, 187–206.

Simonelli, D. P. and J. Veverka. 1988. Bolometric albedos and diurnal temperatures of the brightest regions on Io. *Icarus*, **74**(2), 240–261.

Simonelli, D. P., C. Dodd, and J. Veverka. 2001. Regolith variations on Io: Implications for bolometric albedos. *Journal of Geophys. Res.*, **106**(E12), 33241–33252.

Sohl, F., T. Spohn, D. Breuer, and K. Nagel. 2002. Implications from Galileo observations on the interior structure and chemistry of the Galilean satellites. *Icarus*, **157**(1), 104–119.

Sohl, F., G. Schubert, and T. Spohn. 2005. Geophysical constraints on the composition and structure of the Martian interior. *Journal of Geophys. Res.*, [in press].

Spencer, J., J. Rathbun, L. Travis, L. Tamppari, L. Barnard, T. Martin, and A. McEwen. 2000. Io's thermal emission from the Galileo photopolarimeter–radiometer. *Science*, **288**(5469), 1198–1201.

Stevenson, D. J. and S. C. McNamara. 1988. Background heatflow on hotspot planets – Io and Venus. *Geophys. Res. Lett.*, **15**(13), 1455–1458.

Thomas, P., *et al.* 1998. The shape of Io from Galileo limb measurements. *Icarus*, **135**(1), 175–180.

Usselman, T. M. 1975. Experimental approach to the state of the core. *American Journal of Science*, **275**, 291–303.

Veeder, G. J., D. L. Matson, T. V. Johnson, D. L. Blaney, and J. D. Gougen. 1994. Io's heat flow from infrared radiometry: 1983–1993. *J. Geophys. Res.*, **99**, 17095–17162.

Veeder, G. J., D. L. Matson, T. V. Johnson, A. G. Davies, and D. L. Blaney. 2004. The polar contribution to the heat flow of Io. *Icarus*, **169**(1), 264–270.

Wark, D. A. and E. B. Watson. 1998. Grain-scale permeabilities of texturally equilibrated, monomineralic rocks. *Earth Planet. Sci. Lett.*, **164**, 591–605.

Warren, P. H., "New" lunar meteorites: Implications for composition of the global lunar surface, lunar crust, and the bulk Moon. *Meteoritics & Planet. Sci.*, **40**(3), 477–506.
Wienbruch, U. and T. Spohn. 1995. A self-sustained magnetic field on Io? *Planetary and Space Science*, **43**, 1045–1057.
Yoder, C. F. 1979. How tidal heating in Io drives the Galilean orbital resonance locks. *Nature*, **279**, 767–770.
Yoder, C. F. and S. J. Peale. 1981. The tides of Io. *Icarus*, **47**, 1–35.

6

Ionian mountains and tectonics: Insights into what lies beneath Io's lofty peaks

Elizabeth P. Turtle, Windy L. Jaeger, and Paul M. Schenk

6.1 INTRODUCTION

A world of extremes, Io, in addition to displaying extensive volcanism, supports some of the highest mountains in the Solar System. Yet, in an apparent paradox, very few of the mountains actually resemble volcanoes; the majority of the towering peaks appear to be tectonic structures: uplifted and sometimes tilted blocks, which are bounded by steep scarps and, in many cases, fractured (Figure 6.1). However, there are no obvious tectonic patterns revealed in the global mountain distribution beyond a bimodal variation of number density with longitude (Figure 6.2; Schenk *et al.*, 2001; Kirchoff and McKinnon, 2005) and local associations with paterae, and Io's ubiquitous volcano–tectonic depressions (e.g., Masursky *et al.*, 1979; Whitford-Stark, 1982; Carr *et al.*, 1998; McEwen *et al.*, 2000; Radebaugh *et al.*, 2001; Jaeger *et al.*, 2003; see examples in Figure 6.1). Current evidence indicates that ultimately the mountains do owe their existence to the incredible rate of volcanic resurfacing: the resulting subsidence can induce more than sufficient compressive stresses in the lithosphere, driving mountains up by extensive thrust faulting (Schenk and Bulmer, 1998; Jaeger *et al.*, 2003).

The existence of well over one hundred of these structures imposes constraints on the structure of Io's mechanical lithosphere and their characteristics provide insights into interior and crustal properties. The state of the mountains is intimately related to other geologic processes acting on Io (e.g., both extrusive and intrusive volcanism, Io's internal tidal dynamics, and surficial mass wasting). Therefore, the processes by which the mountains form and evolve have implications for many different aspects of Io. In this chapter we describe the current state of understanding, derived from *Voyager* and *Galileo* observations and analyses thereof, of Io's mountains, their formation and evolution, and the implications for Io's tectonics and lithosphere.

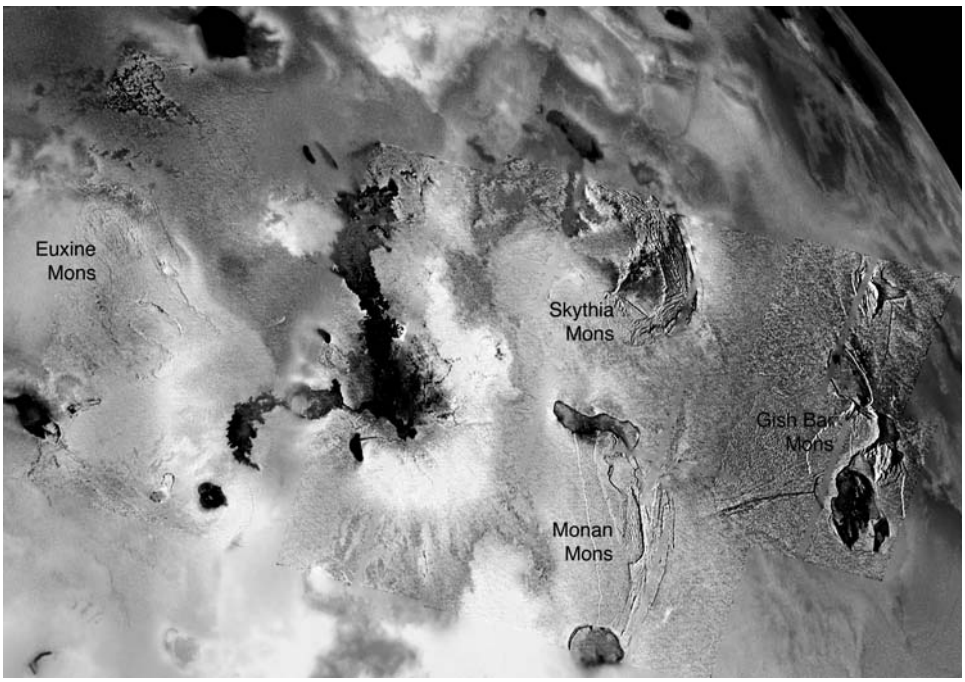

Figure 6.1. This moderate-resolution, ~500 m per pixel, regional mosaic combined with lower resolution, 1.3 km per pixel, color images acquired by *Galileo* includes several examples of Ionian mountains and volcanic centers. The mountains are isolated from each other, but a high fraction of those in this region are associated with paterae. The illumination, which is from the left, accentuates the topography and surface textures. This effect is strongest on the eastern side where the solar incidence angle is 21–28° and weakens toward the west where the Sun is higher, solar incidence angle ~37–45°: compare the visibility of ~10 km high Gish Bar Mons, between Gish Bar Patera to the south and Estan Patera to the north; ~6 km high Monan Mons, between Monan Patera to the north and Ah Peku Patera to the south; and ~7 km high Euxine Mons. (See also color section.)

6.2 OBSERVATIONS

6.2.1 Global distribution

Here we use the term "mountain" generally to refer to landforms that rise significantly (>~1 km) above the surrounding terrain, regardless of their specific morphologic classification (mesas, plateaus, peaks, ridges, etc.). As a whole these structures are typically on the order of 100 km across and rise to heights of several kilometers above the surrounding plains (e.g., Schaber, 1980; Carr *et al.*, 1998), with a mean height of ~6 km and a maximum (to date) of 17.5 ± 1.5 km, at Boösaule Montes (Schenk *et al.*, 2001). Carr *et al.* (1998) documented ~100 Ionian mountains and plateaus in images from the *Voyager* and early *Galileo* missions. Since then Schenk *et al.* (2001) and

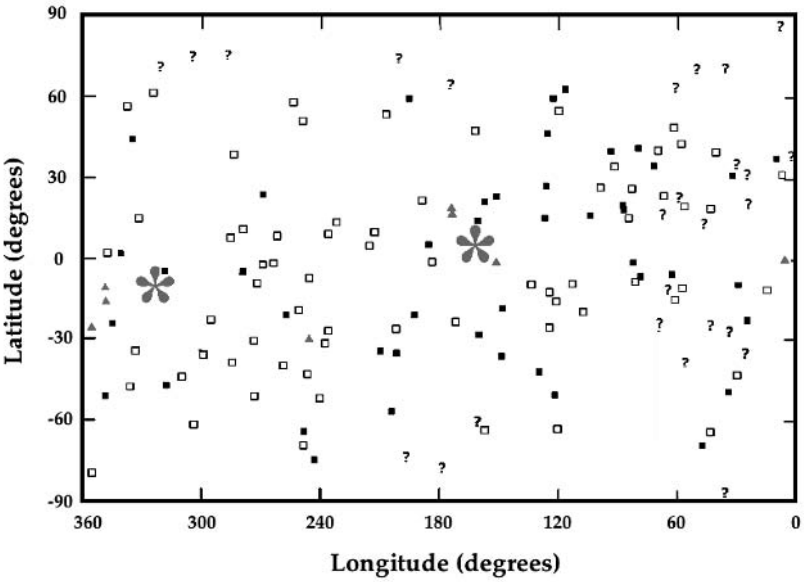

Figure 6.2. A plot of the locations of Ionian mountains (small symbols) reported by Carr *et al.* (1998), Schenk *et al.* (2001), and Jaeger *et al.* (2003; also Jaeger, 2005), as verified by Jaeger (2005) and updated here to include the locations of prominent shield volcanoes identified in Schenk *et al.* (2004) (cf. Appendix 2). The symbol ▲ is used for volcanic constructs, ■ for tectonic mountains in contact with at least one patera, □ for tectonic mountains that do not contact any paterae, and ? for mountains whose relationship to paterae could not be determined. The two regions identified by Schenk *et al.* (2001) as having higher concentrations of volcanic centers (and lower concentrations of mountains) are indicated by large asterisks.

Jaeger *et al.* (2003; also Jaeger, 2005) have further refined databases of the characteristics of Io's topographic structures, bringing the total number of mountains reported to 151; however, not all of the features identified in the early study were confirmed by the later investigations. The number of positively identified Ionian mountains is converging on ~135, with some uncertainty remaining for features with borderline heights (~1 km) and/or ambiguous morphologies (Appendix 2), or for which the viewing conditions were unfavorable. (NB. One significant complicating factor is that the ability to detect even several-km-high mountains in images depends strongly upon the solar incidence angle. Io's surface is highly variegated and regions are frequently blanketed by material erupted from plumes, so although mountainous regions can have distinctive textures and sometimes colors, even the most rugged terrains are not necessarily apparent as such when viewed at high Sun angles (i.e., in the absence of topographic shading).)

The mountains are typically isolated from each other. There are no patterns in their distribution that suggest organized global-scale tectonic processes such as terrestrial plate tectonics. Carr *et al.* (1998) noted no obvious correlations between Io's mountains and its numerous hot spots and plumes; however, they did note an

apparent association between mountains and paterae that had also been observed by Masursky *et al.* (1979). More recent studies based on the complete *Galileo* data set have demonstrated that the global distribution of mountains exhibits two moderate enhancements in number density centered around 25°N, 65°W and 20°S, 265°W (Figure 6.2; e.g., Schenk *et al.*, 2001; Kirchoff *et al.*, 2003; Kirchoff and McKinnon, 2005). Intriguingly these regions are essentially anticorrelated with two peaks identified in the distributions of features identified as (or in some cases inferred based on albedo and/or color to be) volcanic centers of all types, at longitudes of 165°W and 325°W (Schenk *et al.*, 2001) and of paterae at longitudes of 150°W and 330°W (Radebaugh *et al.*, 2001).

The apparent global anticorrelation between mountains and volcanic features makes all the more curious the observations that at the local scale a significant fraction of mountains seems to be closely associated with paterae (e.g., Masursky *et al.*, 1979; Schaber, 1980; Whitford-Stark, 1982; McEwen *et al.*, 2000). Indeed, McEwen *et al.* (2000) examined images taken by the *Galileo* spacecraft during its first three close Io fly-bys, finding that, of the 13 mountains imaged at resolutions higher than 0.5 km per pixel, 6 are incised by paterae. These mountains are located within a region of relatively high mountain density and low volcanic center density (Schenk *et al.*, 2001; Kirchoff and McKinnon, 2005). Including all of the *Galileo* observations, Jaeger (2005) showed that, of the 97 mountains identified as tectonic, 40 (41%) are in *direct* contact with paterae, calculating the probability of this correlation occurring by chance to be less than ~1%. Based on the refined mountain statistics presented here (Appendix 2), of 104 mountains likely to be tectonic in origin, 39 (38%) contact paterae. For comparison, of the 417 paterae imaged at pixel scales less than 3.2 km that were documented by Radebaugh *et al.* (2001), only 13% are in contact with mountains. More recent harmonic analysis by Kirchoff *et al.* (2003; see also Kirchoff and McKinnon, 2005), confirms these results: for small order and degree (comparable with global-scale wavelengths) there is an anti-correlation of mountains and volcanic centers, but at higher order and degree correlations are observed.

6.2.2 Morphology

Io's mountains (again, using the term to encompass elevated landforms in general) exhibit significant morphologic variety (e.g., Figures 6.1 and 6.3–6.6). Only a few seem to be volcanic constructs (e.g., Carr *et al.*, 1998; McEwen *et al.*, 2000; Schenk *et al.*, 2001; Jaeger *et al.*, 2003): mountains rarely appear to have vents or calderas at, or flows emanating from, their summits and none correspond to identified hot spots or vent regions for active plumes. Instead, most appear to have tectonic origins, resembling uplifted or tilted blocks (e.g., Carr *et al.*, 1998, Schenk and Bulmer, 1998), and often exhibiting steep scarps and fractures (e.g., McEwen, 1985; McEwen *et al.*, 2000; Turtle *et al.*, 2001, 2004; Jaeger *et al.*, 2003). Of the 135 mountains documented in Appendix 2, six appear to be volcanoes. The rest appear likely to be tectonic in origin but have considerable morphologic diversity, which complicates interpretation. For example, Io has numerous low-lying (several hundred meters to ~1 kilometer) mesa-like topographic features with irregular margins. Several such features are included in

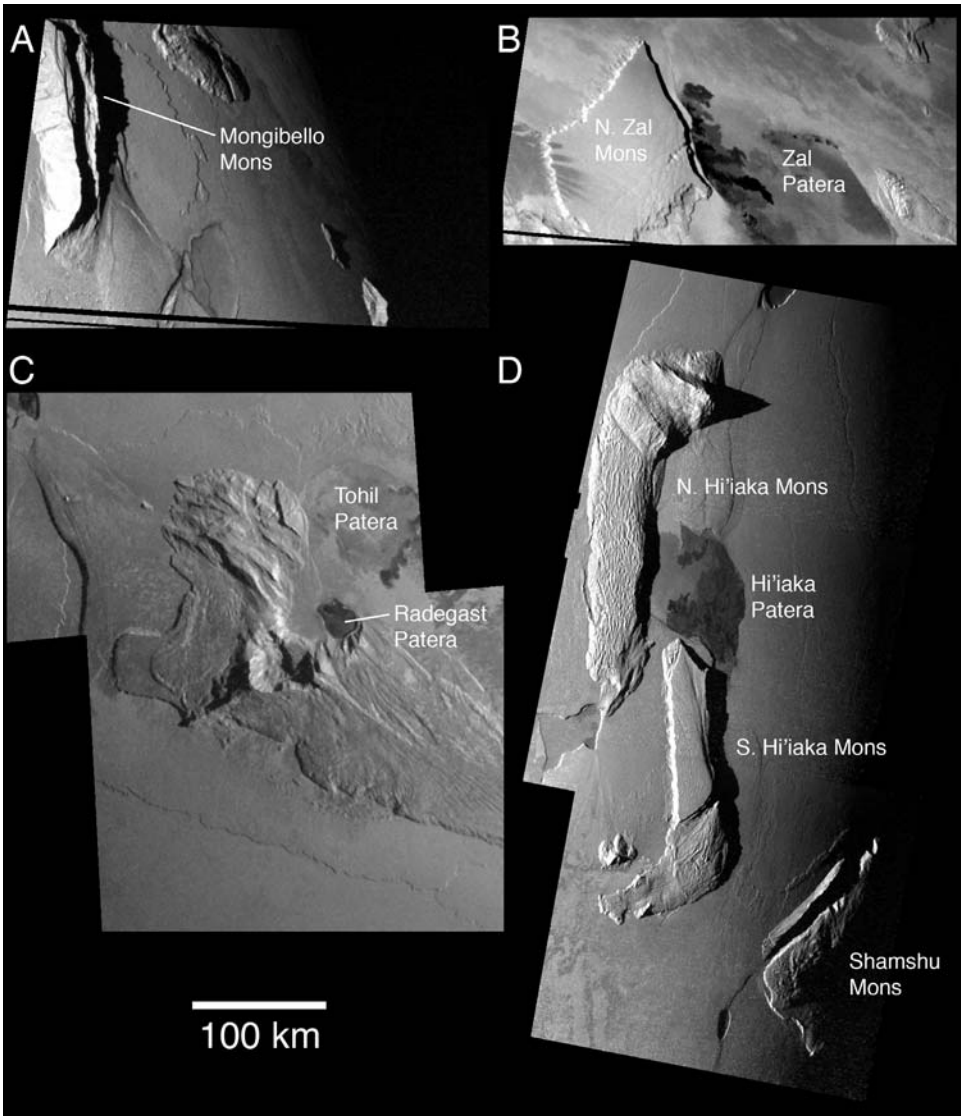

Figure 6.3. *Galileo* images of Ionian mountains: (A) Near-terminator view of Mongibello Mons (jagged double ridge at left) at 335 m per pixel, illuminated from the left. (B) Near-terminator view of North Zal Montes and Zal Patera at ~260 m per pixel, illuminated from the left. To the north-west the mountain is smooth with arcuate margins, whereas its south-eastern margin is slumping outward in long landslides. Lava flows emanate from a fracture that parallels the eastern margin of North Zal Montes. (C) Moderate-resolution, ~325 m per pixel, mosaic of Tohil Mons and neighboring Tohil and Radegast Paterae seen near the terminator, illumination is from the right (cf. Figure 6.4). (D) Near-terminator view of Hi'iaka and Shamshu Montes at ~360 m per pixel, illuminated from the left.

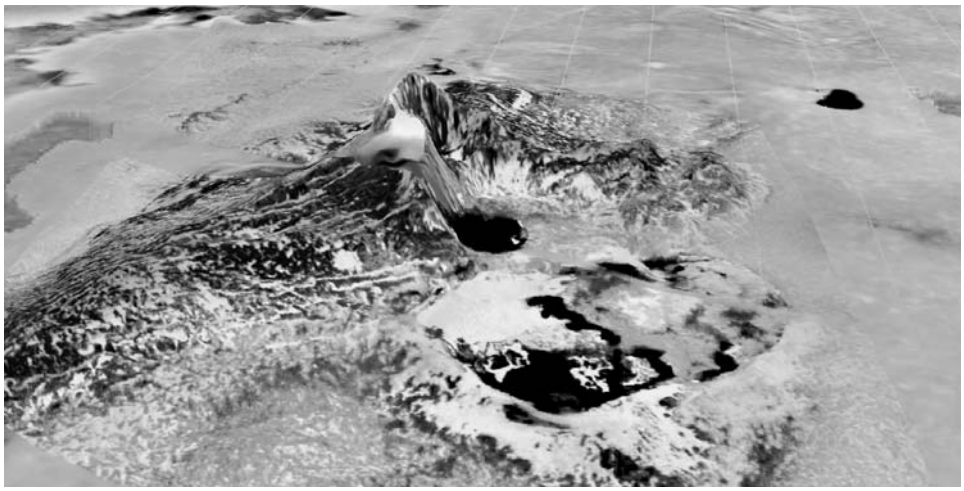

Figure 6.4. Perspective view of Tohil Mons looking south-west. Color-coding represents topography (red is high) (see color section). Topography is derived from stereo analysis by P. Schenk. Tohil Mons is comprised of several parts, including a broad lineated plateau to the east (left in this view) truncated by a small dark patera (center), and a circular, faulted plateau to the north-west (right). Each plateau is 3–5 km high, and between them lies a circular amphitheater with a crest rising 8 km above the surrounding plains. Vertical exaggeration is a factor of ~25.

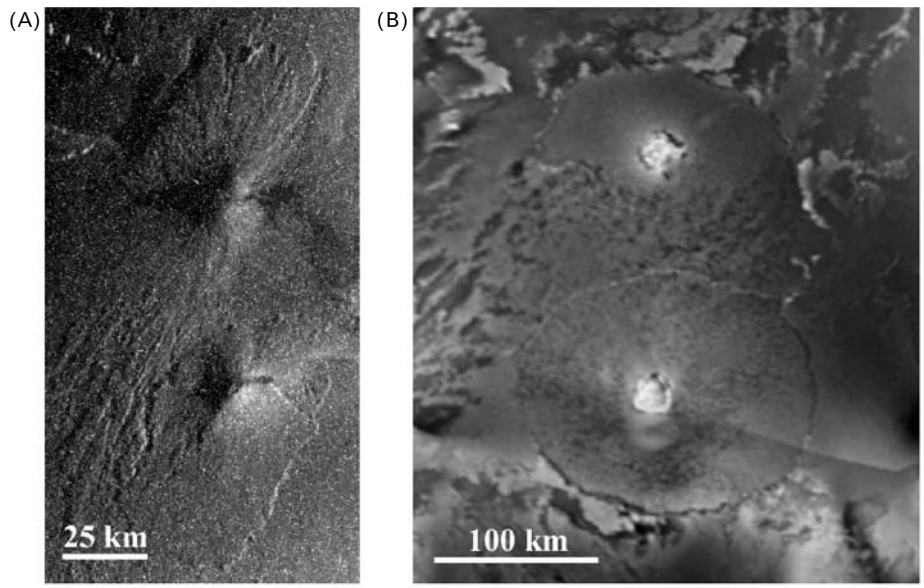

Figure 6.5. Examples of mountains classified as volcanic structures. (A) Two shield volcanoes located near the plume Zamama at 16.8°N, 173.7°W and 18.7°N, 174.4°W. (B) Apis Tholus (10.9°S, 348.7°W) and Inachus Tholus (15.8°S, 348.8°W), which are substantially larger than other Ionian volcanic constructs.

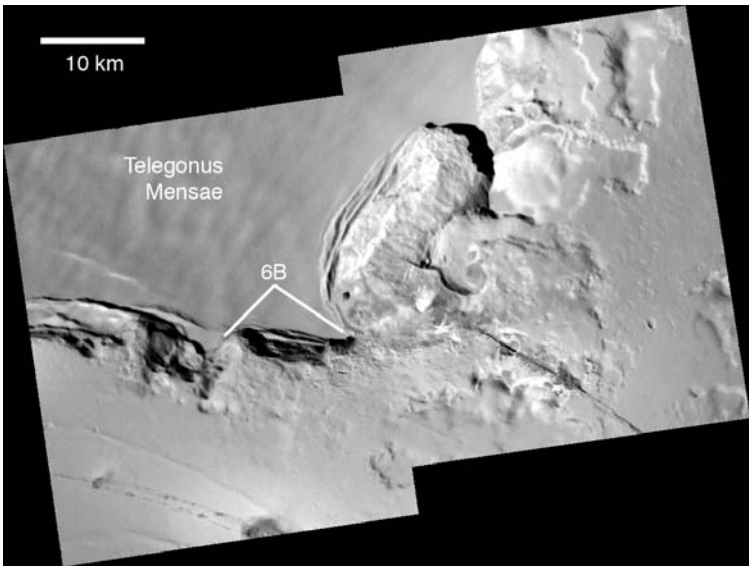

(A)

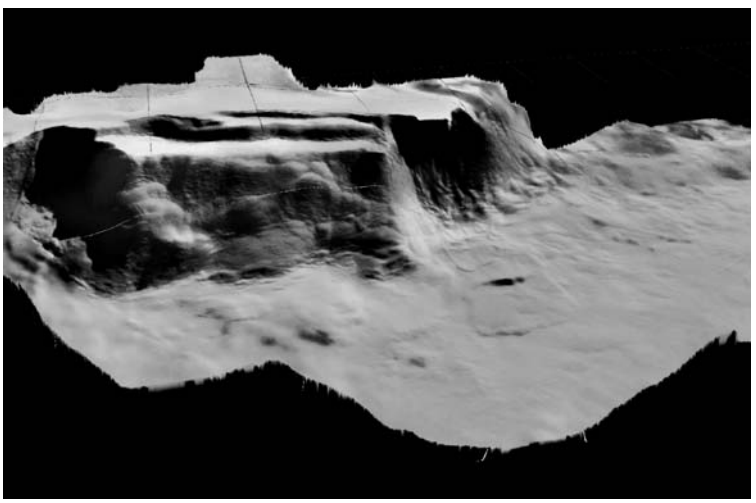

(B)

Figure 6.6. (A) High-resolution (42 m per pixel) mosaic of the south-eastern margin of Telegonus Mensae. The label 6B indicates the section of the scarp illustrated in (B). Illumination is from the upper right. (B) Perspective view of southern scarp of Telegonus Mensae looking north. Color-coding represents topography (red is high) (see color section); total relief is ~1.5 km. Topography is derived from stereo analysis by P. Schenk. A small (~4 km long, ~2 km wide), low (~100 m) landslide is evident at center right. Note the wrinkled appearance of the scarp and terrace face, suggesting down-slope creep of surface material. Vertical exaggeration is a factor of ~50.

Appendix 2 because their heights slightly exceed 1 km, but their origins remain uncertain; possibilities include eroded lava plains and degraded tectonic structures. Therefore, the number of tectonic mountains in Appendix 2 is conservatively estimated to be 104 by excluding all mountains that exhibit volcanic morphologies, those that were not imaged well enough to determine their gross morphology, and all structures not conclusively determined to be $\geq$2 km in height (to filter out the genetically ambiguous low-lying mesas). Their morphologies range from jagged peaks (e.g., Figures 6.3(C,D) and 6.4) and ridges (e.g., Figure 6.3(A)) several kilometers high, to lower, more rounded structures with gentler slopes (e.g., Monan Mons in Figure 6.1, see also color section), to low, flat-topped or tilted plateaus with steep margins (e.g., Figures 6.3(B) and 6.6). The margins of many structures show evidence of outward collapse through slumping and large landslides (e.g., Skythia and Gish Bar Montes in Figure 6.1) and a few have steeper, scalloped scarps (e.g., Figure 6.3(B); see also further examples of mountain morphologies in Schenk and Bulmer, 1998; Moore *et al.*, 2001; McEwen *et al.*, 2000; Turtle *et al.*, 2001, 2004). In some cases, morphologic differences, which are sometimes observed across a single structure, may simply illustrate variations in the deterioration of mountains by mass wasting or heterogeneities in the composition, volatile content, and material properties of the Ionian crust. For example, tall, rugged mountains might be more likely to form in silicate-rich regions and lower plateaus in regions with more sulfur-rich compounds. Moreover, these variations could be influenced by different mountain formation mechanisms and local lithospheric conditions, such as the thermal gradient.

Structural control

Several morphologic characteristics of Ionian mountains support the hypothesis that they are tectonic in origin. Many of the structures have strikingly straight, angular, or curvilinear margins (e.g., Hi'iaka Mons and the ridge and valley to the west of Shamshu Mons (Figure 6.3(D)) and North Zal Mons (Figure 6.3(B))). Other mountains have linear elements, or assemblages within them, for example the scarps that cut the center of Skythia Mons (Figure 6.1, see also color section), the ridges that make up Mongibello (Figure 6.3(A)) and Ionian Montes, and the ridge running south-west from the peak of Tohil Mons (Figures 6.3(C) and 6.4). However, in most cases, the orientations of the structural features of neighboring mountains do not appear to be related to each other. Another aspect of several mountains that is consistent with tectonic origins is their asymmetric profiles: for example, Euboea Mons (Schenk and Bulmer, 1998) and Gish Bar Mons (Turtle *et al.*, 2001) have relatively steep scarps on one side with gentler slopes on the other, suggestive of tilted crustal blocks. In fact, in each of these cases it appears that the surface layers along the shallower slopes have failed in massive landslides (Schenk and Bulmer, 1998; Turtle *et al.*, 2001).

The *Galileo* images also revealed a few examples of what appear to be linear surface fractures: a scarp that is several hundred kilometers long and up to 1.5 kilometers high runs south along the eastern edge of North Zal Mons (Figure 6.3(B)) and, intriguingly from a tectonic standpoint, the *western* edge of South Zal

Mons; smaller fractures are observed in the plains to the east of Telegonus Mensae and along the eastern margin of Skythia Mons; and a Y-shaped feature cuts the plains to the west of Gish Bar Patera (Figure 6.1; a higher resolution view is available in Turtle *et al.*, 2004, Figure 10a). The first two of these exhibit evidence for recent volcanic activity (Turtle *et al.*, 2001, 2004). However, there is little information about the topography of these features aside from the upper limit on the height of the one east of North Zal Mons (Turtle *et al.*, 2001), so whether they are strictly sites of extension or of incipient mountain building cannot be assessed. To be visible despite Io's high rate of resurfacing, these features would have to be relatively young; at the present estimated resurfacing rate, 0.1–1 cm yr^{-1} averaged globally (e.g., Johnson *et al.*, 1979; Blaney *et al.*, 1995; Phillips, 2000; McEwen *et al.*, 2004), it would only take 10^4–10^5 years to bury 100 m of topography, and the rate of degradation by mass wasting may be even higher.

Relationship to volcanism

Although rare, there are a few topographic structures that do appear to have volcanic origins (Figure 6.5). The most significant of these are the Tholi, Apis, and Inachus (Figure 6.5(B)), that were observed by *Voyager* (sadly a spacecraft anomaly during *Galileo*'s only close fly-by of the sub-Jovian hemisphere resulted in the loss of its only opportunity to observe these intriguing features (Turtle *et al.*, 2004)). These circular structures are ~1.5 km high with central caldera-like depressions 2–3 km deep (Schenk *et al.*, 2004). Most of Io's radial volcanic flow fields appear to be relatively low, broad shield volcanoes, including the two 2-km-high shield volcanoes just west of the Zamama flow field (Figure 6.5(A); Schenk *et al.*, 2004; Turtle *et al.*, 2004) and very shallow Emakong Patera (Williams *et al.*, 2001). *Galileo* observations of the site of the Zamama plume and flow field (Turtle *et al.*, 2004) revealed that the lava flows emanate from one of two conical volcanic constructs (as predicted by Keszthelyi *et al.*, 2001) that are up to 2 km high (based on shadow measurements and photoclinometry). Nearby Tsũi Goab Tholus (Turtle *et al.*, 2004, Figure 11; Williams *et al.*, 2004), appears to be a smaller shield volcano with two depressions near its summit, and another similar cone is located near Pele (Moore *et al.*, 1986); however, in general, such structures are rare on Io.

Some paterae appear to be incised into low plateaus or broad, shield-like features (e.g., Chaac, Thomagata, and Reshef Paterae). For example, 56 km by 26 km Thomagata Patera is 1.2–1.6 km deep (based on measurements of the shadows cast by the patera walls) and set into a raised plateau more than 100 km across, the western margin of which rises only ~200 m above the plain (Turtle *et al.*, 2004). It is not clear whether these structures were created by eruptions from the paterae, or if they were pre-existing topographic features that have been eaten away by the formation of the paterae.

Although few of the mountains are actual volcanic constructs, as previously mentioned, there is a statistically significant correlation between mountains and paterae: the margins of 41% of well documented mountains are in direct contact with at least one patera, 12% are in contact with two or more paterae (Jaeger *et al.*,

2003; Jaeger, 2005). One region with a concentration of such relationships is the area encompassing Euxine Mons and Gish Bar Mons (Figure 6.1). Euxine Mons itself, almost completely surrounds a circular depression, which may be a patera that has not erupted recently. Monan Mons directly abuts two paterae: to its north lies the oddly shaped Monan Patera, which Lopes-Gautier *et al.* (1999) identified as an active hot spot, and which exhibits deposits of the red material that is commonly associated with active volcanic venting (McEwen *et al.*, 1998a; Geissler *et al.*, 1999; Lopes-Gautier *et al.*, 1999; Phillips, 2000) at its margins; and to the south lies another patera, Ah Peku. Gish Bar Patera appears to eat into an apparent landslide deposit from Gish Bar Mons to the north, which is in turn, bordered to the north by a second patera, Estan Patera. Indeed the only large mountain in this region that is not associated with a patera is Skythia Mons, although it too is bordered by a fracture that may also exhibit some small reddish deposits, which would be consistent with current or very recent volcanic activity. The associations of mountains with paterae are more common than one would expect from unrelated, spatially random distributions of mountains and paterae; Jaeger (2005) derived that the probability of the observed correlation occurring by chance is less than $\sim$1%.

Surface modification and mass wasting

The modification and degradation of Ionian mountains also provide key insights into the types of surficial processes active on Io and their rates (e.g., Moore *et al.*, 2001), and the *Galileo* images have revealed a few places on the surface in great detail, $\sim$10 m per pixel. Though the mountains are thought to expose the oldest rock units on Io (e.g., Smith *et al.*, 1979; Schaber, 1980), no impact craters have been identified on them. Therefore, their crater retention ages must be younger than 10^6–10^7 years (Johnson *et al.*, 1979; Zahnle *et al.*, 2003; McEwen *et al.*, 2004), which is not terribly surprising given that modification of their surfaces appears to be dominated by mass-wasting processes and deposition of material from volcanic plumes. To some extent the variations in mountain morphology may illustrate an aging sequence for Ionian mountains, from steep, angular peaks (e.g., Gish Bar and Hi'iaka Montes (Figures 6.1 and 6.3(D)), to gentler, more rounded slopes (e.g., Monan and western Shamshu Montes (Figures 6.1 and 6.3(D)). However, significant variations in morphology within individual structures or complexes (e.g., Tvashtar (Turtle *et al.*, 2001; Turtle *et al.*, 2002, Figure 7) and Telegonus (Figure 6.6)), indicate that the differences cannot be due solely to age; there must also be heterogeneities in the compositional, rheological, structural, and thermal properties of the crust at scales of 10s–100s of kilometers.

Slumping and landsliding dominate at both large and small scales (e.g., Figure 6.6) and can occur in close proximity to each other, demonstrating spatial variation in material properties, including porosity and the presence of liquid filling the pore spaces, over distances of several kilometers. Many topographic structures have hummocky surface textures which appear to be due to massive outward slumping (e.g., the southern margin of the eastern patera of Tvashtar Catena (Turtle *et al.*, 2002, their fig. 7) and the eastern and south-western margins of Skythia Mons (Figure 6.1)).

In a number of places, the headscarps of discrete landslides can be seen (e.g., Skythia Mons, N. Zal Montes, and Telegonus Mensae (Figures 6.1, 6.3(B), and 6.6(A), respectively). Although suspected to be a site of possible sapping due to its morphology as seen at lower resolution and an association of very bright material, presumably SO_2, Telegonus was revealed by *Galileo* images to be the site of gravity driven mass wasting in the form of slumps, downslope creep, and landslides (Figure 6.6(B)). Amphitheaters on the south-eastern margin and straight scarps along the $\sim$1.5 km high (from measurements of stereo observations, Figure 6.6(B)) southern margin exhibit morphologies typical of slumping: flat-topped blocks with hummocky textures along their bases. Interestingly, there are slope-parallel lobes (up to $\sim$1 km long) on the face of this block that suggest some manner of downslope creep; the average slope of the scarp can be constrained by the illumination geometry to be less than 26°. Near the scarp's eastern edge a succession of at least three landslides can be seen, the most extensive of which is 3.8 km long, 2.1 km wide, and less than 100 m thick at its distal end (Figure 6.6(B)).

Some mountains are covered with ridges that parallel the mountains' margins (e.g., Monan Mons and northern Hi'iaka Montes (Figures 6.1 and 6.3(D)). Superficially similar features are observed in regions without obvious topography (Bart *et al.*, 2004), but where slopes are clear the ridges may be caused by folding of a thin, detached surface layer sliding downslope under the influence of gravity (Heath, 1985; Moore *et al.*, 2001). By approximating this as a single elastic layer under compression Turtle *et al.* (2001) estimated its thickness to be $\sim 70\,\text{m} \leq h \leq \sim 550\,\text{m}$ from the wavelength of the folds and approximations for other surface parameters. The amplitudes and wavelengths of ridges on individual mountains appear to be generally uniform even though there are some differences in ridge morphology from mountain to mountain. If the ridges are caused by slip along a weak stratigraphic boundary, the uniformity would suggest that there is little variation in the slope of the detachment surface and that the mountains were uplifted and tilted as fairly coherent blocks despite the pervasively fractured nature of the Ionian lithosphere. In the case of North Hi'iaka Mons, stereo data presented by Schenk *et al.* (2001) show a gently and relatively uniformly sloped plateau.

6.2.3 Stratigraphy

Surprisingly there is little direct evidence for layering within Io's crust, although circumstantial evidence abounds. The simple fact that the crust forms by continual burial of materials ranging from silicate lava flows to volatile plume deposits, requires that it consist of interbedded materials of varying properties, and, as discussed previously, extensive layers of sulfur-rich material, presumably pyroclastic in origin, may provide the zones of weakness implied by massive slope failures as Schenk and Bulmer (1998) suggested occurred at Euboea Montes. There are also hints of layers observed in some high-resolution observations (e.g., Tohil and Ot Montes (the latter is shown in Turtle *et al.*, 2002, Figure 2)). However, there is no unambiguous evidence for layering in the very-high-resolution (9.6 m per pixel) views of the southern scarp of Telegonus Mensae (Turtle *et al.*, 2004, Figure 5b). Layers a

few tens of meters thick would be resolved directly and thinner, ledge-forming layers should also be evident; however, mass-wasting processes appear to dominate the scarp's morphology, masking any small-scale, internal structure. In a few places (e.g., Shamshu and Tohil Montes), very bright areas are visible on scarps, which may indicate that SO_2 is being exposed by erosion or seeping out of the scarps in these locations.

There is some morphologic evidence (e.g., surrounding Tvashtar Catena (Turtle *et al.*, 2002, their fig. 7) and near Telegonus Mensae (Figure 6.6(A))) for erosion by sapping as McCauley *et al.* (1979) hypothesized would result from liquefied SO_2 seeping out at the bases of steep scarps, although sublimation degradation or disaggregation by chemical decomposition may be more realistic thermodynamically if sapping is occurring away from geothermal anomalies (Moore *et al.*, 2001). Below these arcuate scarps the terrain often consists of a series of thin, layered deposits and occasional kilometer-scale blocks and hummocks, which may be landslide debris or remnants of coherent, volatile-poor material left behind when the less consolidated material was eroded. Given that Io's plateaus commonly stand at least several hundred meters above the surrounding plains, the relative paucity of such material (at least inasmuch as can be constrained at the image resolutions currently available) would indicate that the SO_2 is able to carry away fine-grained sulfur and silicate particles quite efficiently as it vaporizes and expands into the Ionian atmosphere (Moore *et al.*, 2001).

6.3 INTERPRETATIONS AND IMPLICATIONS

6.3.1 Mountain formation mechanism(s)

An elegant solution to the apparent irony of the mountains on such an incredibly volcanically active planet not being volcanoes themselves was proposed by Schenk and Bulmer (1998). Io's global average volcanic resurfacing rate over the past few decades is estimated to be $\sim 1\,\mathrm{cm\,yr^{-1}}$ (Johnson *et al.*, 1979; Blaney *et al.*, 1995; Phillips, 2000; McEwen *et al.*, 2004) if due primarily to lava flows, although uncompressed plume deposits could yield much higher resurfacing rates (Phillips, 2000). Furthermore, over the short time period of the *Voyager–Galileo* era, the resurfacing rate has been observed to vary widely over the surface of the planet (Phillips, 2000; Geissler *et al.*, 2004), although it may tend to average out globally over geologic timescales (e.g., Carr *et al.*, 1998). At a rate of $1\,\mathrm{cm\,yr^{-1}}$ it would only take 10^6 years for the current surface to become buried to a depth of 10 km. So the rapid resurfacing rate drives comparably rapid subsidence.

Considering the crust as a series of spherical, progressively older shells, as each shell is buried deeper and deeper its radius, and consequently its surface area, decreases, generating horizontal compressive stresses throughout the lithosphere. Within several kilometers of the surface, these stresses exceed the compressive strength of rock and they are a likely driving mechanism for uplifting Io's mountains by thrust faulting. Moreover, the magnitude and continual generation

of these stresses suggests that Io's lithosphere should be pervasively fractured. This manner of mountain building is consistent with the correlation observed between mountains and paterae on the local scale: depending on the local geology, in some cases orogenic thrust faults may serve to alleviate compressive crustal stresses sufficiently that the faults can act as conduits along which magma can ascend to the surface (Turtle *et al.*, 2001; Jaeger *et al.*, 2003). Another consequence of the rapid subsidence rate is that lithospheric temperatures remain quite cold to great depths (O'Reilly and Davies, 1981), only undergoing significant heating within a narrow zone near the base of the lithosphere; therefore, assuming efficient remixing of heated crustal material with the mantle, the crust and the mechanical lithosphere would be essentially identical.

A hypothesis for the observed global-scale anticorrelation of mountains and volcanic centers is that a sustained reduction in Io's volcanic activity on a local, regional, or global scale would allow more extensive conductive lithospheric heating, and that the resulting thermal expansion would induce compressive stresses at the base of the lithosphere (McKinnon *et al.*, 2001). In this scenario, fluctuations in the thermally induced stresses due to variations in resurfacing rates could lead to alternating episodes of compressive and tensile faulting in the upper part of the lithosphere. McKinnon *et al.* (2001) hypothesized that, as a consequence of repeated normal and reverse faulting, Io's surface might be analogous to the chaos terrain of Europa with coherent crustal blocks (i.e., mountains) floating within a matrix of highly disrupted material. This scenario would be consistent with other interpretations of some mountains having undergone extensional faulting as McEwen (1985) and Heath (1985) suggested for Danube Planum, although other proposed mountain formation mechanisms do not preclude post-orogenic extensional stresses.

Jaeger *et al.* (2003) compared the stresses from mechanical and thermal sources (i.e., subsidence and conductive heating, respectively) and found that, ignoring the localized effects of intrusions and assuming a uniform resurfacing rate of $1\,\mathrm{cm\,yr^{-1}}$, the peak stress generated by thermal expansion can exceed that caused by subsidence for lithospheres thinner than about 40 km. However, the integrated effect of thermal expansion on lithospheric compression is not as great as that of subsidence: the subsidence induced stress is large for much of the lithosphere (Figure 6.7), while, for current estimates of the resurfacing rate (Johnson *et al.*, 1979; Carr, 1986; Blaney *et al.*, 1995; Phillips, 2000; McEwen *et al.*, 2004; Geissler *et al.*, 2004), only the lowermost lithosphere is significantly heated (O'Reilly and Davies, 1981). Thus, while the stresses induced by thermal expansion can locally exceed those produced by subsidence, they act on a much smaller fraction of the lithosphere.

The stresses of global subsidence and thermal expansion are sufficient to generate significant uplift on Io by compressional faulting. However, these stresses alone cannot explain the isolated nature of the distribution of Ionian mountains. Schenk and Bulmer (1998) suggested that failure could be triggered by crustal anisotropies or localized weakening or fracturing due to volcanic activity. Turtle *et al.* (2001) demonstrated using numerical simulations that, without such focusing mechanisms, global compressive stresses acting on an extensively faulted, uniform lithosphere would be likely to produce parallel mountain ranges rather than isolated massifs. Therefore,

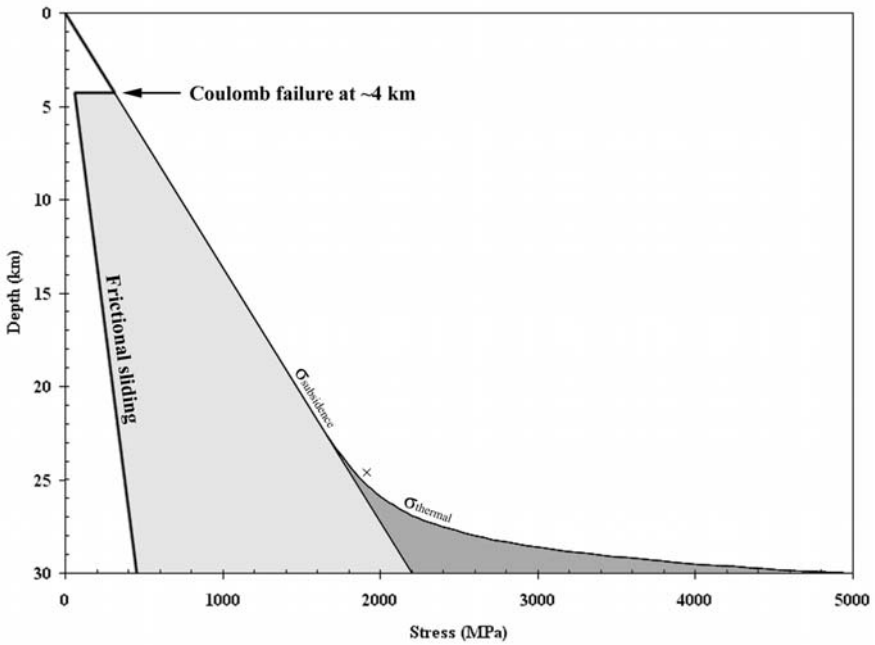

Figure 6.7. The compressive strength of the Ionian lithosphere and the magnitude of the compressive horizontal stress ($\sigma_{\text{subsidence}} + \sigma_{\text{thermal}}$) as a function of depth for a 30-km-thick lithosphere. The maximum compressive strength of Io's lithosphere at the surface is assumed to be 275 MPa (the maximum compressive strength of unconfined rock samples of gabbro and several other rock types (Ahrens, 1995)). Thrust faults are assumed to form at 30°, and the resurfacing rate is assumed to be $1\,\text{cm}\,\text{yr}^{-1}$. The resulting equation for Coulomb failure is $\tau = 79.4 + 0.58\sigma_n$, where τ is the critical shear stress (in MPa) and σ_n is the normal stress (in MPa). On Io, the compressive horizontal stress due to subsidence is sufficient to initiate faulting at a depth of ~4 km. Once faults exist, stress should be relieved by slip along these pre-existing planes of weakness. According to Byerlee's Law, frictional sliding is governed by the equation $\tau_f = 0.85\sigma_n$, where τ_f is the shear stress at which sliding begins. The solid black line illustrates the approximate stress state of the lithosphere and the shaded regions show the stress in excess of this that is available to drive mountain uplift. The light gray region shows the magnitude of the compressive stress due to subsidence and the dark gray region shows the contribution of thermal expansion.

there must be a mechanism or mechanisms that localize the lithospheric compressive stresses. Jaeger *et al.* (2003) investigated the role that the dynamics of Io's asthenosphere may play in focusing stresses. Models for Io's interior suggest an asthenospheric layer at least 50–200 km thick, which is strongly heated by tidal dissipation (e.g., Segatz *et al.*, 1988; Spohn, 1997; Keszthelyi *et al.*, 1999; Ross *et al.*, 1990; Radebaugh, 2005; Ojakangas and Stevenson, 1986; Greenberg, 1982; Schubert *et al.*, 2004). Modeling by Tackley *et al.* (2001) suggests that the interior of Io is likely to be vigorously convecting, an idea that is well supported by the large number of hot spots scattered about Io's surface. Wherever thermally buoyant asthenospheric

diapirs impinge on the base of the lithosphere, the overlying material is thinned and upwarped (e.g., Crough, 1979, 1983; Sleep, 1992), an idea applied to Io by McEwen (1995). Such lithospheric swells should focus horizontal compressive stresses into an inverted conic shape expanding from the base of the lithosphere over the diapir head and intersecting the surface at the perimeter of the swell (see Jaeger *et al.*, 2003, Figure 10). This stress pattern is corroborated by axially symmetric, 2-D, finite-element modeling that takes into account the surface curvature of Io (Turtle *et al.*, 2001). In the most simplistic case, failure along a sector of this cone will result in a thrust fault with an arcuate trace, a common feature of thrust faults and one that is observed at several mountains on Io (e.g., Monan Mons (Figure 6.1)). However, the length scale and characteristic spacing of mountains may not necessarily correspond to the diameter of a swell; a single swell could influence the formation of multiple mountains. Additionally, more complex stress patterns would arise where heterogeneities exist or wherever there is interference between stress fields induced by neighboring lithospheric swells. Multiple thrust-fault localization mechanisms are almost certainly at work: spatial variations in material properties and lithospheric structure, as well as spatial and temporal variations in the resurfacing rate and thermal conditions, will result in localizing stresses in the lithosphere, thereby facilitating the uplift of mountains as isolated structures rather than as ordered thrust belts.

The diapiric focusing mechanism would also be consistent with the observed correlation between mountain and patera formation: once the stress has been alleviated by mountain uplift, magma supplied by the thermal diapir could buoyantly rise toward the surface using the overlying fractures and faults as conduits for its ascent. Because the thrust fault is a compressive interface, magma may ascend more readily at tear faults along the margins of the thrust sheet. If thrust faulting over-shortens material in the upper lithosphere as McKinnon *et al.* (2001) suggest, extension may also occur at the trailing edge of a thrust sheet. Once thrust faulting effectively dissipates the local compressive stress, magma may use the thrust fault plane as a conduit as well.

Monan Mons displays a number of the features predicted by such a model. The diapir focusing mechanism predicts a circular concentration of compressive stress at the surface, which is likely to produce a thrust fault with an arcuate trace, although this fault profile alone is not diagnostic of the diapir model. Crescent shapes are common in thrust faults because they allow for maximum compression at the center of the thrust sheet and progressively less slip toward the margins. At Monan Mons the trace of the thrust fault is concave westward, which would indicate that the hanging wall moved east (Elliot, 1976; see also Jaeger, 2005, Figure 2.11). Faults or fracture zones that are not subject to a large compressive stress make more likely conduits for magma ascent. The trailing edge of a thrust sheet is one such region, and the shear zones that bound a thrust sheet are others. Therefore, paterae may preferentially form at these locations. Monan Patera is an elongate depression with active volcanism occurring around its margin as indicated by red deposits (cf., McEwen *et al.*, 1998a; Geissler *et al.*, 1999; Lopes-Gautier *et al.*, 1999; Phillips, 2000). Its longitudinal axis is roughly perpendicular to that of the adjacent mountain, consistent with what would be expected if Monan Patera were situated along a sinistral shear zone at the edge of a

thrust sheet (Figure 6.1; Jaeger, 2005, Figure 2.11). Moreover, there is also a patera at the dextral shear zone on the opposite side of the thrust sheet (i.e., at the opposite end of the mountain).

The morphology of the Hi'iaka Montes (~7.4°S, ~78.7°W; Figure 6.3(D)) suggests an intriguing hypothesis regarding their tectonic evolution. Both mountains consist of ~4 km high, north–south ridges that slope gently downward to the west (Schenk *et al.*, 2001), the shapes of which are strikingly complementary: the northern end of North Hi'iaka Mons consists of a ~11 km high peak where the mountain extends to the east, and the southern end of South Hi'iaka Mons appears to consist of a landslide deposit where it hooks to the west. The geometry of these mountains suggests that they may once have formed a single massif that subsequently sheared apart along a dextral (right-lateral) strike–slip fault (McEwen *et al.*, 2000). The planimetric shapes of the north and south margins of Hi'iaka Patera and the volcano–tectonic depression separating the two mountains, lend credence to this hypothesis. Apart from a landslide headscarp in the north, the two margins' planimetric shapes are identical over the entire ~50 km of their lengths. If the northern patera margin were translated ~70 km to the south it would match up with its southern counterpart. These observations hint at unique regional-scale shear deformation within the Hi'iaka Montes complex, although they are not conclusive (a further *Galileo* observation planned to observe Hi'iaka under different illumination conditions to help constrain this history was lost due to a spacecraft anomaly (Turtle *et al.*, 2004)).

6.3.2 Lithospheric thickness

Io's lithosphere has generally been assumed to need to be tens of kilometers thick in order to form and support mountains of the observed heights (e.g., Nash *et al.*, 1986; Carr *et al.*, 1998). The thrust faulting scenario for mountain building outlined above provides another constraint on the thickness of the lithosphere. As resurfacing buries a shell of material from Io's surface to the base of the lithosphere, its effective radius is reduced and it is heated. Jaeger *et al.* (2003) calculated the lithospheric volume change due to subsidence and thermal expansion as a function of lithospheric thickness by integrating the strain in a shell of material over depth. Conservation of volume dictates that any reduction in volume at depth be balanced by an uplift of the same volume at the surface. By comparing the total estimated volume of Io's mountains with the estimated lithospheric volume loss, Jaeger *et al.* (2003) placed a lower limit of 12 km on Io's lithospheric thickness (Figure 6.8), consistent with estimates based on intact mountain heights (Schenk *et al.*, 2001). This value is a lower limit because (1) additional material can be accommodated by means other than mountain uplift (e.g., compaction of pore space or broad, low uplifts) and (2) the base levels from which mountain heights were measured could have been too high (e.g., mass wasting deposits around mountains could have artificially elevated the levels from which the heights were measured). These calculations can also place a weak upper limit on lithospheric thickness. For example, if the lithosphere of Io were 50 km thick, as was used in one model by Keszthelyi and McEwen (1997), nearly

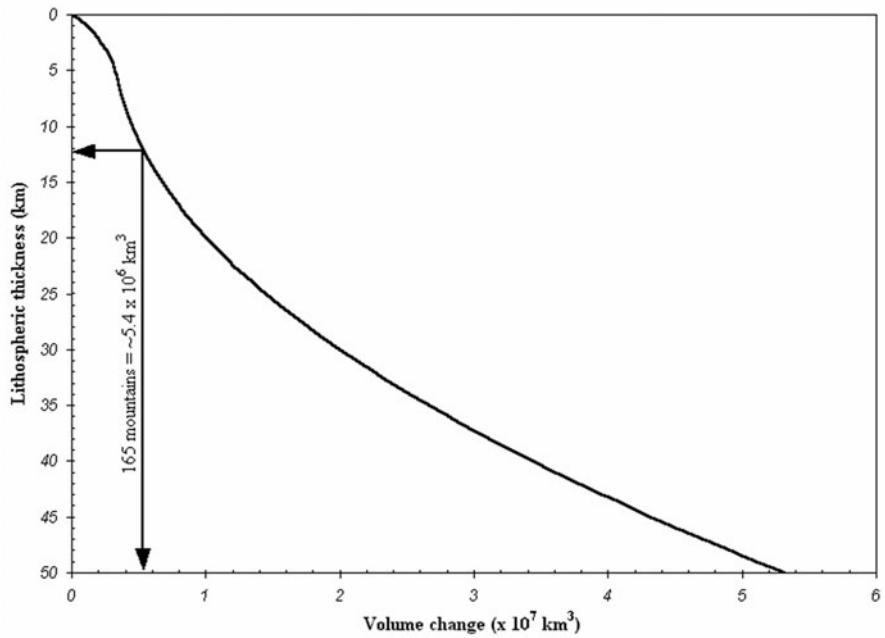

Figure 6.8. The estimated volume of uplifted material is the sum of the volumes of material displaced by subsidence stresses, thermal expansion, and the extent to which the compressibility of lithospheric rock can counteract those processes, plotted as a function of lithospheric thickness (after Jaeger, 2005, Figure 2.8). The upper limit of 165 Ionian mountains (extrapolated from the upper limit of the number of mountains observed, 145, to account for the lack of global coverage) would correspond to ~54 million km^3 of material which yields a lower limit of ~12 km for the lithospheric thickness; the observed number of 145 mountains corresponds to roughly 47 million km^3 and a slightly lower value for the lower limit on lithospheric thickness.

48 million km^3 of material, the equivalent of >1,450 average-sized mountains (Schenk *et al.*, 2001), would need to be accommodated in ways other than mountain uplift. Leone and Wilson (2001) estimated that Io's uppermost crust could have a porosity as high as ~30%; compaction of such pore space could accommodate a significant volume of material. Much volume could also be concealed in broad, regional uplifts with shallow, and therefore difficult to detect, topography. Gaskell *et al.* (1988) reported such basins and swells using *Voyager* data, but these were not matched by analyses of the *Galileo* data (Thomas *et al.*, 1998; Oberst and Schuster, 2004), which are not subject to the geometric distortions of *Voyager* imaging. So in each case any long-wavelength topography may represent residual error. Regional variations in elevation appear to be limited to no more that ±1 km from the mean triaxial ellipsoid (Thomas *et al.*, 1998; Oberst and Schuster, 2004). Given these uncertainties a lithospheric thickness of 50 km might be reasonable; however, extremely thick lithospheres (e.g., ≥100 km (Ross and Schubert, 1985; Anderson *et al.*, 2001)), become difficult to reconcile due to the excessive amount of uplifted material that would need to have gone undetected.

6.3.3 Crustal composition and stability

The great heights of the mountains suggest that the crust consists of a strong silicate component, although the low thermal gradient (O'Reilly and Davies, 1981) does to some extent mitigate the concern of Clow and Carr (1980) that a crust composed predominantly of sulfur-rich materials would be able to support only the lowest topographic features observed (~1 km). Nonetheless, based on the extent of silicate volcanism that has been observed (e.g., McEwen *et al.*, 1998b; Keszthelyi *et al.*, 2001; McEwen *et al.*, 2004; and references therein), Io's crust is expected to have a significant silicate component.

There is ample evidence for the existence of weaker, more volatile materials within the crust. For example, vast landslides appear to have occurred at Euboea and Gish Bar Mons (Schenk and Bulmer, 1998; McEwen *et al.*, 2000). There are also widespread eroding layered plains (e.g., Schaber, 1980) as well as several examples of higher scarps that appear to be retreating, but which have left surprisingly little debris. In cases where mountains abut paterae, there are only a few examples where debris from small landslides from the mountains can be seen on the floors of the paterae (e.g., Gish Bar, Shamshu, Radegast, and Hi'iaka Paterae). This observation indicates that volcanic resurfacing is proceeding more rapidly than the mass wasting of the mountains. It furthermore suggests that a large proportion of the material that collapses from mountains into paterae, which are hypothesized to be manifestations of lava lakes (Lopes *et al.*, 2004), is consumed, an idea which is easier to explain if a substantial fraction of the material is volatile. However, in some cases, especially those of catastrophic landslides, the massive deposits could make such drastic alterations to patera boundaries that we might not be able to identify them as such.

Volcanic resurfacing on Io adds new material to the top of the crust at a rapid rate and the fate of this material as it is buried deeper and deeper within the crust, and of that material that eventually reaches the base of the crust, is of fundamental importance to understanding Io. Assuming that the crust is not growing thicker, it must be recycled back into the mantle at a comparable rate. It is possible that this transition is entirely thermal: a shell of crustal material subsides and heats up, eventually to the point that the timescale for it to become entrained in convection is shorter than that of subsidence. Another possibility is that blocks of material at the base of the crust are plucked by drag forces induced by the convecting asthenosphere. A third possibility is that, as the intense compression associated with subsidence drives out volatiles and collapses pore spaces, the lower crust becomes denser than the underlying material and delaminates along pre-existing zones of structural weakness. Jaeger *et al.* (2004) examined this last possibility by starting with a variety of bulk silicate compositions for Io, evolving the crust and mantle iteratively via volcanic reprocessing until equilibrium was achieved, and then modeling the density structure of the crust. The evolution of Io's crust and mantle from the bulk silicate starting composition was determined using the MELTS program (Ghiorso and Sack, 1995; Asimow and Ghiorso, 1998) for a range of upper mantle temperatures. Jaeger *et al.* (2004) made several assumptions in modeling the crust's density profile: (1) they used the geothermal gradient of O'Reilly and Davies (1981); (2) they assumed a subsidence rate

of $1\,\mathrm{cm\,yr^{-1}}$ (and the analysis is quite sensitive to this parameter); (3) because subsidence generates large compressive stresses at a rapid rate, they assumed that the stress state is governed by Byerlee's/Amonton's law of frictional sliding; (4) their crust (as derived from bulk silicate) was generally of a mafic igneous composition, and they assumed that SO_2 fills the pore space in this rock but does not get interbedded with it to any significant depth; and (5) they assumed a porosity of 25% at the surface and an exponential decrease with depth (Leone and Wilson, 2001). They found that the crust of Io would be gravitationally unstable if upper mantle temperatures exceed ~1,600 K: density inversions between the lower crust and upper mantle were found to exist over a narrow range of upper mantle temperatures (~1,550–1,600 K). This density inversion is conducive to crustal recycling by delamination. These findings initially seemed at odds with observational constraints on internal temperatures (e.g., a lower limit on magma liquidus temperature of ≥1,870 K was derived from data from a 1997 eruption at Pillan (Davies *et al.*, 2001). As more is learned about Ionian magma temperatures and the complexities of the derivation thereof, the highest temperature estimates have been revised down somewhat such that the two approaches are now in good agreement (Radebaugh *et al.*, 2004; Milazzo *et al.*, 2005); however, such constraints are generally restricted to lower limits on liquidus temperatures.

6.4 CONCLUSIONS

A better understanding of the processes responsible for forming Io's mountains is emerging from the data from both the *Voyager* and *Galileo* missions, and continued analysis thereof. Io's rapid resurfacing results in a unique tectonic environment in which the tremendous compressional stresses, induced by the high subsidence rate, fracture the cold lithosphere and uplift mountains by thrust faulting. The lack of a global tectonic pattern can be explained by heterogeneities in the lithospheric composition, structure, and stress field, which serve to focus the stresses with random orientations, thereby localizing mountain building. Many if not all such lithospheric heterogeneities can also be attributed to variations in volcanic activity. For example, spatial and temporal changes in the style of volcanic activity (e.g. changes in the proportion of volatiles deposited), will significantly affect the strength of the lithosphere. A change in the rate of volcanic activity will be reflected in the subsidence rate and therefore the thermal profile of the lithosphere in that region, perhaps explaining the bimodal variation observed in the number of mountains with longitude. Activity within the asthenosphere, such as local upwellings, will affect the stress field in the overlying lithosphere, preferentially facilitating faulting in some regions. And, of course, thrust faulting itself will alleviate local compressional lithospheric stresses, thereby making it easier for magma to rise along the same faults and perhaps even reach the surface to form paterae at the mountains' feet (cf., Keszthelyi *et al.*, 2004). At first glance, it appears surprising that Io's mountains are not volcanoes; nonetheless, despite their tectonic nature, their origins are ultimately a consequence of Io's extreme level of volcanic activity.

6.5 REFERENCES

Ahrens, T. J. 1995. *Rock Physics and Phase Relations: A Handbook of Physical Constants*. American Geophysical Union, Washington D.C.

Anderson, J. D., R. A. Jacobson, E. L. Lau, W. B. Moore, and G. Schubert. 2001. Io's gravity field and interior structure. *J. Geophys. Res.*, **106**, 32963–32969.

Asimow, P. D. and M. S. Ghiorso. 1998. Algorithmic modifications extending MELTS to calculate subsolidus phase relations. *American Mineralogist.*, **83**, 1127–1132.

Bart, G. D., E. P. Turtle, W. L. Jaeger, L. P. Keszthelyi, and R. Greenberg. 2004. Ridges and tidal stress on Io. *Icarus*, **169**, 111–126.

Blaney, D. L., T. V. Johnson, D. L. Matson, and G. J. Veeder. 1995. Volcanic eruptions on Io: Heat flow, resurfacing, and lava composition. *Icarus*, **113**, 220–225.

Carr, M. H. 1986. Silicate volcanism on Io. *J. Geophys. Res.*, **91**, 3521–3532.

Carr, M. H., A. S. McEwen, K. A. Howard, F. C. Chuang, P. Thomas, P. Schuster, J. Oberst, G. Neukum, G. Schubert, and the Galileo Imaging Team. 1998. Mountains and calderas on Io: Possible implications for lithospheric structure and magma generation. *Icarus*, **135**, 146–165.

Clow, G. D. and M. H. Carr. 1980. Stability of sulfur slopes on Io. *Icarus*, **44**, 729–733.

Crough, S. T. 1979. Hotspot epeirogeny. *Tectonophysics*, **61**, 321–333.

Crough, S. T. 1983. Hotspot swells. *Ann. Rev. of Earth and Planet. Sci.*, **11**, 165–193.

Davies, A. G., L. P. Keszthelyi, D. A. Williams, C. B. Phillips, A. S. McEwen, R. M. C. Lopes, W. D. Smythe, L. W. Kamp, L. A. Soderblom, and R. W. Carlson. 2001. Thermal signature, eruption style, and eruption evolution at Pele and Pillan on Io. *J. Geophys. Res.*, **106**, 33079–33104.

Elliot, D. 1976. The energy balance and deformation mechanism of thrust sheets. *Phil. Trans. R. Soc. Lond. A.*, **283**, 289–312.

Gaskell, R. W., S. P. Synnott, A. S. McEwen, and G. G. Schaber. 1988. Large-scale topography of Io: Implications for internal structure and heat transfer. *Geophys. Res. Lett.*, **15**, 581–584.

Geissler, P. E., A. S. McEwen, L. Keszthelyi, R. Lopes-Gautier, J. Granahan, and D. P. Simonelli. 1999. Global color variations on Io. *Icarus*, **140**, 265–282.

Geissler, P., A. S. McEwen, C. B. Phillips, L. P. Keszthelyi, and J. Spencer. 2004. Surface changes on Io during the Galileo mission. *Icarus*, **169**, 29–64.

Ghiorso, M. S. and R. O. Sack. 1995. Chemical mass transfer in magmatic processes. IV: A revised and internally consistent thermodynamic model for the interpolation and extrapolation of liquid–solid equilibria in magmatic systems at elevated temperatures and pressure. *Contrib. Mineral Petrol.*, **119**, 197–212.

Greenberg, R. 1982. Orbital interactions of the Galilean satellites. In: D. Morrison (ed.), *Satellites of Jupiter*. University of Arizona Press, Tucson, AZ, pp. 65–92.

Heath, M. J. 1985. Io: Mountains and crustal extension. *Conference on Heat and Detachment in Crustal Extension on Continents and Planets*. Lunar and Planet. Inst., Houston, TX, Contrib. #575, pp. 50–54.

Jaeger, W. L. 2005. Select problems in planetary structural geology: Global-scale tectonics on Io, regional-scale kinematics on Venus, and local-scale field analysis on Earth application to Mars. Ph.D. thesis, University of Arizona, AZ.

Jaeger, W. L., E. P. Turtle, L. P. Keszthelyi, and A. S. McEwen. 2002. The effect of thrust fault geometries on the surface deformation of Io: Implications for mountains and paterae. *Lunar Planet. Sci. Conf.*, **XXXIII**, Abstract #1741.

Jaeger, W. L., E. P. Turtle, L. P. Keszthelyi, J. Radebaugh, A. S. McEwen, and R. T. Pappalardo. 2003. Orogenic tectonism on Io. *J. Geophys. Res.*, **108**, doi:10.1029/2002JE001946.

Jaeger, W. L., L. P. Keszthelyi, and E. P. Turtle. 2004. Lithospheric recyclying on Io: The role of delamination. *Lunar Planet. Sci. Conf.*, **XXXV**, Abstract #2048.

Johnson, T. V., A. F. Cook II, C. Sagan, and L. A. Soderblom. 1979. Volcanic resurfacing rates and implications for volatiles on Io. *Nature*, **280**, 746–750.

Keszthelyi, L. and A. S. McEwen. 1997. Magmatic differentiation of Io. *Icarus*, **130**, 437–448.

Keszthelyi, L., A. S. McEwen, and G. J. Taylor. 1999. Revisiting the hypothesis of a mushy global magma ocean in Io. *Icarus*, **141**, 415–419.

Keszthelyi, L., A. S. McEwen, C. B. Phillips, M. Milazzo, P. Geissler, D. Williams, E. P. Turtle, J. Radebaugh, D. Simonelli, and the Galileo SSI Team. 2001. Imaging of volcanic activity on Jupiter's moon Io by Galileo during Galileo Europa Mission and Galileo Millennium Mission. *J. Geophys. Res.*, **106**, 33025–33052.

Keszthelyi, L. P., W. L. Jaeger, E. P. Turtle, M. Milazzo, and J. Radebaugh. 2004. A post-Galileo view of Io's interior. *Icarus*, **169**, 271–286.

Kirchoff, M. R. and W. B. McKinnon. 2005. Mountain building on Io: An unsteady relationship between volcanism and tectonism. *Lunar Planet. Sci. Conf.*, **XXXVI**, Abstract #2245.

Kirchoff, M. R., W. B. McKinnon, P. Schenk. 2003. Spherical harmonic analysis of mountain and volcanic center distribution on Io. *EOS Trans. AGU*, **84**, Fall Meet. Suppl., #P41A-0399.

Leone, G. and L. Wilson. 2001. Density structure of Io and the migration of magma through its lithosphere. *J. Geophys. Res.*, **106**, 32983–32995.

Lopes-Gautier, R., A. S. McEwen, W. B. Smythe, P. E. Geissler, L. Kamp, A. G. Davies, J. R. Spencer, L. Keszthelyi, R. Carlson, F. E. Leader, *et al.* 1999. Active volcanism on Io: Global distribution and variations in activity. *Icarus*, **140**, 243–264.

Lopes, R. M. C., L. W. Kamp, W. D. Smythe, P. Mouginis-Mark, J. Kargel, J. Radebaugh, E. P. Turtle, J. Perry, D. Williams, R. W. Carlson *et al.* 2004. Lava lakes on Io? Observations of Io's volcanic activity from Galileo NIMS during the 2001 flybys. *Icarus*, **169**, 140–174.

Masursky, H., G. G. Schaber, L. A. Soderblom, and R. G. Strom. 1979. Preliminary geological mapping of Io. *Nature*, **280**, 725–729.

McCauley, J. F., B. A. Smith, and L. A. Soderblom. 1979. Erosional scarps on Io. *Nature*, **280**, 736–738.

McEwen, A. S. 1985. Hot-spot tectonics on Io. *Conference on Heat and Detachment in Crustal Extension on Continents and Planets*. Lunar and Planet. Inst., Houston, TX, Contrib. #575, pp. 76–80.

McEwen, A. S., SO_2-rich equatorial basins and epeirogeny of Io. *Icarus*, **113**, 415–422.

McEwen, A. S., L. Keszthelyi, P. Geissler, D. P. Simonelli, M. H. Carr, T. V. Johnson, K. P. Klaasen, H. H. Breneman, T. J. Jones, J. M. Kaufman, *et al.* 1998a. Active volcanism on Io as seen by Galileo SSI. *Icarus*, **135**, 181–219.

McEwen, A. S., L. Keszthelyi, J. R. Spencer, G. Schubert, D. L. Matson, R. Lopes-Gautier, K. P. Klaasen, T. V. Johnson, H. W. Head, P. Geissler *et al.* 1998b. High-temperature silicate volcanism on Jupiter's moon Io. *Science*, **281**, 87–90.

McEwen, A. S., M. J. S. Belton, H. H. Breneman, S. A. Fagents, P. Geissler, R. Greeley, J. W. Head, G. Hoppa, W. L. Jaeger, T. V. Johnson *et al.* 2000. Galileo at Io: Results from high-resolution imaging. *Science*, **288**, 1193–1198.

McEwen, A. S., L. Keszthelyi, R. Lopes, P. Schenk, and J. Spencer. 2004. The lithosphere and surface of Io. In: F. Bagenal, W. McKinnon, and T. Dowling (eds), *Jupiter: Planet, Satellites and Magnetosphere*. Cambridge University Press, Cambridge, UK, pp. 307–328.

McKinnon, W. B., P. M. Schenk, and A. Dombard. 2001. Chaos on Io: A model for formation of mountain blocks by crustal heating, melting, and tilting. *Geology*, **29**, 103–106.

Milazzo, M. P., L. P. Keszthelyi, J. Radebaugh, A. G. Davies, E. P. Turtle, P. Geissler, K. P. Klaasen, and A. S. McEwen. 2005. Volcanic activity at Tvashtar Catena, Io. *Icarus*, **179**, 235–251.

Moore, J. M., A. S. McEwen, E. F. Albin, and R. Greeley. 1986. Topographic evidence for shield volcanism on Io. *Icarus*, **67**, 181–183.

Moore, J. M., R. J. Sullivan, F. C. Chuang, J. W. Head, A. S. McEwen, M. P. Milazzo, B. E. Nixon, R. T. Pappalardo, P. M. Schenk, and E. P. Turtle. 2001. Landform degradation and slope processes on Io: The Galileo view. *J. Geophys. Res.*, **106**, 33223–33240.

Nash, D. B., C. F. Yoder, M. H. Carr, J. Gradie, and D. M. Hunten. 1986. Io. In: J. A. Burns and M. S. Matthews (eds), *Satellites*. University of Arizona Press, Tucson, TX, pp. 629–688.

Oberst, J. and P. Schuster. 2004. Vertical control point network and global shape of Io. *J. Geophys. Res.*, **109**, doi:10.1029/2003J002159.

O'Reilly, T. C. and G. F. Davies. 1981. Magma transport of heat on Io: A mechanism allowing a thick lithosphere. *Geophys. Res. Lett.*, **8**, 313–316.

Ojakangas, G. W. and D. J. Stevenson. 1986. Episodic volcanism of tidally heated satellites with application to Io. *Icarus*, **66**, 341–358.

Phillips, C. B. 2000. Voyager and Galileo views of volcanic resurfacing on Io and the search for geologic activity on Europa. Ph.D. thesis, University of Arizona, Tucson, TX, 269pp.

Radebaugh, J. 2005. Formation and evolution of paterae on Jupiter's moon Io. Ph.D. thesis, University of Arizona, Tucson, TX.

Radebaugh, J., L. P. Keszthelyi, A. S. McEwen, E. P. Turtle, W. Jaeger, and M. Milazzo. 2001. Paterae on Io: A new type of volcanic caldera? *J. Geophys. Res.*, **106**, 33005–33020.

Radebaugh, J., A. S. McEwen, M. P. Milazzo, L. P. Keszthelyi, A. G. Davies, E. P. Turtle, and D. D. Dawson. 2003. Observations and temperatures of Io's Pele Patera from Cassini and Galileo spacecraft images. *Icarus*, **169**, 65–79.

Ross, M. N. and G. Schubert. 1985. Tidally forced viscous heating in a partially molten Io. *Icarus*, **64**, 391–400.

Ross, M. N., G. Schubert, T. Spohn, and R. W. Gaskell. 1990. Internal structure of Io and the global distribution of its topography. *Icarus*, **85**, 309–325.

Schaber, G. G. 1980. The surface of Io: Geologic units, morphology, and tectonics. *Icarus*, **43**, 302–333.

Schenk, P. M. and M. H. Bulmer. 1998. Origin of mountains on Io by thrust faulting and large-scale mass movements. *Science*, **279**, 1514–1517.

Schenk, P. M., H. Hargitai, R. Wilson, A. McEwen, and P. Thomas. 2001. The mountains of Io: Global and geological perspectives from Voyager and Galileo. *J. Geophys. Res.*, **106**, 33201–33222.

Schenk, P. M., R. Wilson, and A. Davies. 2004. Shield volcano topography and the rheology of lava flows on Io, 2004. *Icarus*, **169**, 98–110.

Schubert, G., J. D. Anderson, T. Spohn, and W. B. McKinnon. 2004. Interior composition, structure and dynamics of the Galilean satellites. In: F. Bagenal, W. McKinnon, and T. Dowling (eds), *Jupiter: Planet, Satellites and Magnetosphere*. Cambridge University Press, Cambridge, UK, pp. 281–306.

Segatz, M. T., T. Spohn, M. Ross, and G. Schubert. 1988. Tidal dissipation, surface heat flow, and figure of viscoelastic models of Io. *Icarus*, **75**, 187–206.

Sleep, N. H. 1992. Hotspot volcanism and mantle plumes. *Ann. Rev. of Earth and Planet. Sci.*, **20**, 19–43.

Smith, B. A., L. A. Soderblom, T. V. Johnson, A. P. Ingersoll, S. A. Collins, E. M. Shoemaker, G. E. Hunt, H. Masursky, M. H. Carr, M. E. Davies *et al.* 1979. The Jupiter system through the eyes of Voyager 1. *Science*, **204**, 951–972.

Spohn, T. 1997. Tides of Io. In: H. Wilhelm, W. Zurm, and H.-G. Wenzel (eds), *Tidal Phenomena*. Springer, Heidelberg, Germany, pp. 345–377.

Tackley, P. J., G. Schubert, G. A. Glatzmaier, P. Schenk, J. T. Ratcliff, and J.-P. Matas. 2001. Three-dimensional simulations of mantle convection in Io. *Icarus*, **149**, 79–93.

Thomas, P. C., M. E. Davies, T. R. Colvin, J. Oberst, P. Schuster, G. Neukum, M. H. Carr, A. McEwen, G. Schubert, and M. J. S. Belton. 1998. The shape of Io from Galileo limb measurements. *Icarus*, **135**, 175–180.

Turtle, E. P., W. L. Jaeger, L. P. Keszthelyi, A. S. McEwen, M. Milazzo, J. Moore, C. B. Phillips, J. Radebaugh, D. Simonelli, F. Chuang, *et al.* 2001. Mountains on Io: High-resolution Galileo observations, initial interpretations, and formation models. *J. Geophys. Res.*, **106**, 33175–33199.

Turtle E. P., W. L. Jaeger, L. P. Keszthelyi, A. S. McEwen, M. Milazzo, J. Moore, C. B. Phillips, J. Radebaugh, D. Simonelli, F. Chuang, *et al.* 2002. Correction to: Mountains on Io: High-resolution Galileo observations, initial interpretations, and formation models. *J. Geophys. Res.*, **107**, doi:10.1029/2002JE001928.

Turtle E. P., L. P. Keszthelyi, A. S. McEwen, J. Radebaugh, M. Milazzo, D. Simonelli, P. Geissler, D. A. Williams, J. Perry, W. L. Jaeger. 2004. The final Galileo SSI observations of Io: Orbits G28-I33. *Icarus*, **169**, 3–28.

Whitford-Stark, J. L. 1982. The Mountains of Io. *Lunar Planet. Sci. Conf.*, **XIII**, 859–860.

Williams, D. A., R. Greeley, R. M. C. Lopes, and A. G. Davies. 2001b. Evaluation of sulfur flow emplacement on Io from Galileo data and numerical modeling. *J. Geophys. Res.*, **106**, 33161–33174.

Williams, D. A., P. M. Schenk, J. M. Moore, L. P. Keszthelyi, E. P. Turtle, W. L. Jaeger, J. Radebaugh, M. P. Milazzo, R. M. C. Lopes, and R. Greeley. 2004. Mapping of the Culann-Tohil region of Io from Galileo imaging data. *Icarus*, **169**, 80–97.

Zahnle, K., P. Schenk, H. Levison, and L. Dones. 2003. Cratering rates in the outer Solar System. *Icarus*, **163**, 263–389.

7

Active volcanism: Effusive eruptions

David A. Williams and Robert R. Howell

7.1 INTRODUCTION

Io's most remarkable characteristic is its active volcanism. Volcanic eruptions on Io consist of effusions of lava as long lava flows, as lava lakes, and as fire fountains, as well as explosive plumes of gas and dust. In this chapter we review the major types of eruptions thought to occur on Io, with emphasis on their extrusive components, based on the major results from the *Galileo* mission. These include the possible discovery of very high temperature lavas which are consistent with pre-historic terrestrial ultramafic lavas, evidence for silicate lava lakes and compound flow fields, and sulfur and possibly sulfur dioxide flows. In this context we also discuss the nature of several important volcanic centers as shown from *Galileo* high-resolution observations.

7.2 CONTEXT: TERRESTRIAL EFFUSIVE VOLCANISM

Effusive volcanism, exemplified by lava flows and lava lakes, is ubiquitous on Earth, and evidence of effusive volcanism is found throughout the geologic record, dating as far back as the Archean (e.g., De Witt and Ashwal, 1997). As on other planets, the products and emplacement styles of lava flows on Earth are dependent upon the volume and flow rate of the lava, the eruption environment in which the flows are emplaced (subaerial, subaqueous, or subglacial), and the chemical composition (including gas and crystal contents) of the erupted lava (e.g., Zimbelman and Gregg, 2000). The majority of erupted lavas on Earth, as on other planets, is silicate, specifically *mafic* (magnesium- and iron-rich) in composition (e.g., BVSP, 1981). Typically, mafic lavas (i.e., basalts) tend to be relatively low in silica and alumina ($<55\%$ SiO_2, $<15\%$ Al_2O_3: see e.g., McBirney, 1993) and relatively high in magnesia and iron ($>5\%$ MgO, $>10\%$ FeO_{tot}). This results in relatively low-viscosity (50–300 Pa·s) fluid lava flows capable of long distance flow (tens to

hundreds of kilometers) given appropriate effusion rates and emplacement mechanisms (i.e., channels or tubes). Basalts, similar to those that erupt on Kilauea, Hawaii, and elsewhere in the Solar System, can have these characteristics for appropriate compositions, temperatures, and eruption rates. Another possible candidate material for Io's lavas are ultramafic lavas (e.g., komatiites), known to have erupted in the Precambrian, and thought to have had much higher magnesia contents (>18% MgO) and even lower viscosities (0.1–10 Pa·s: e.g., Huppert and Sparks, 1985), although the flow dimensions and emplacement styles of these lavas remain equivocal. More silica-rich, *felsic* lavas (andesites and rhyolites) are common on Earth, have higher dynamic viscosities (>500 Pa·s), and tend to produce relatively shorter, stubby, blocky flows and lava domes (e.g., Schmincke, 2004). Dacitic compositions have been identified recently by spectroscopy on Mars (Christensen *et al.*, 2005); however, andesitic and rhyolitic lavas have not been positively identified on any planet other than Earth, and will not be discussed further. In addition to these and other more rare silicate lavas, non-silicate lava flows have erupted on Earth, including carbonatites (carbonate-dominated lavas) and sulfur flows (important for Io). The nature of terrestrial sulfur flows will be discussed shortly.

In addition to lava composition (including volatile gas content (primarily H_2O, CO_2, SO_2, H_2S, and HCl) and the presence of various types of solids in the lava, which vary widely), the products and emplacement styles of terrestrial lavas are controlled by the environment in which they are emplaced. The term "environment" in this context includes not only the nature of the ground on which the lava flows (e.g., factors such as slope and confining topography, and composition, degree of consolidation, and volatile content of the substrate) but also the temperature and nature of the overlying material (air, water, or ice). Most studies of lava flows over the last two centuries have focused on understanding the emplacement dynamics of subaerial lava flows, using the active basaltic volcanoes of Mauna Loa and Kilauea (Hawaii) and Etna (Italy) as benchmarks (e.g., Rhodes and Lockwood, 1995; Heliker *et al.*, 2003; Bonaccorso *et al.*, 2004). More recently, the advent of research submersibles has allowed the study of submarine lava flows, and ongoing study of volcanoes in Iceland has led recently to focused research in volcano–ice interactions (e.g., Smellie and Chapman, 2002). Because our focus is in understanding effusive volcanism on Io from relatively low-resolution orbital spacecraft data (similar in context to aerial photographs and satellite imagery obtained of terrestrial flows), we will concentrate our discussion in this brief overview on the types and emplacement styles of subaerial terrestrial basalt lava flows.

In general, terrestrial basaltic flows are emplaced with two primary morphologies: pahoehoe and 'a'a (e.g., Wentworth and Macdonald, 1953; block flows are a less common third type not discussed here). Pahoehoe flows tend to have smooth, ropy surfaces, whereas 'a'a flows tend to have rough, fragmental surfaces (Hess and Poldervaart, 1967). Basaltic eruptions often start as pahoehoe and transition into 'a'a downstream. Pahoehoe flows are typically fed by lava tubes in compound flow fields, which grow by budding of individual lobes at the distal end of the tube, and by inflation as fresh lava accumulates under a thin insulating crust (Hon *et al.*, 1994). 'A'a flows are typically fed by open channel flow, often at higher effusion rates and over

steeper slopes than pahoehoe flows, and usually have higher gas contents than pahoehoe flows. These and other factors result in fragmentation of the lava into many small, clinkery pieces as cooling and crystallization proceeds (MacDonald, 1967). However, these descriptions are generalized, and it has proven difficult to disentangle all of the separate factors which control the emplacement of basaltic lava flows. In both cases cooling of the flows is dominated by radiative heat loss from their upper surfaces; a similar process occurs on Io, but is much greater due to the cold vacuum and thin transient atmosphere that is present there. When a basaltic magma chamber erupts its contents into an overlying confined depression, a lava lake can form. Such a feature is distinct from a ponded lava flow as long as the source of the lava in a lava lake can be continually replenished from the underlying chamber.

An important ongoing debate regards the emplacement style(s) of large-volume basaltic provinces, particularly continental flood basalts (CFBs). This is important for Io as large-volume flow fields akin to CFBs are clearly recognized in spacecraft images. CFBs, typified by the Columbia River Flood Basalt Province (e.g., Reidel and Hooper, 1989), are hundreds of kilometers long and contain tens to hundreds of individual flow units ~5–50 m thick. Originally, these flow fields were hypothesized to form by rapid emplacement of thick, turbulent, high effusion rate lava eruptions over shallow ($<1^\circ$) slopes (Shaw and Swanson, 1970). New studies suggest that at least some parts of several CFBs were slowly emplaced as initially thin, compound, inflationary pahoehoe flow fields (Self *et al.*, 1997). The potential role of rapid, perhaps turbulent, emplacement of lava flows has been of interest primarily in the study of Precambrian komatiite flows, as turbulent flow is a natural consequence of the inferred lava compositions and observed flow thicknesses of komatiites (Huppert and Sparks, 1985). However, recent work on terrestrial komatiites has found evidence for more Hawaiian-like compound emplacement at some localities (e.g., Cas and Beresford, 2001). Because no terrestrial ultramafic (komatiite) eruptions have ever been observed, their emplacement style(s) have been inferred from the chemical and physical properties of rock samples and study of the morphologies of metamorphosed and structurally disrupted Archean and Proterozoic outcrops (see e.g., Hill *et al.*, 1990, 2001). The role of emplacement styles of mafic and ultramafic lava flows in regards to Ionian eruptions will be discussed in later sections.

Effusive sulfur volcanism is rare on Earth, although yellow, fumerolic sulfur deposits are a common occurrence at many volcanoes (Banfield, 1954). Active sulfur lava flows have been observed at many volcanoes, including Siretoko-Iosan, Japan; Lastarria, Chile; Arenal and Poas, Costa Rica; and Vulcano, Italy, and sulfur flow deposits have been identified at many other volcanoes (see Kargel *et al.*, 1999 for a review). Terrestrial sulfur flows are thought to have formed from mobilization of remelted fumerolic sulfur deposits (Watanabe, 1940; Skinner, 1970), in which melting was induced by an adjacent heat source, either hot volcanic gases and/or hydrothermal waters (Watanabe, 1940; Oppenheimer, 1992) or intrusion of fresh silicate magma (Greeley *et al.*, 1984; Naranjo, 1985) on or near fumerolic sulfur deposits. Most sulfur flows are thought to be emplaced in a style similar to that of modern basaltic flows, as they have morphologies consisting of multi-lobed flows with surficial crusts, pahoehoe and 'a'a surface textures, and tubes and channels (Watanabe, 1940;

Greeley *et al.*, 1984; Naranjo, 1985). Harris *et al.* (2000) reported evidence for "self-combusting" sulfur flows at Vulcano, Italy, in which hot sulfur flows moving through topographic depressions thermally eroded solid sulfur in their substrates, leaving erosion trenches that were tens of centimeters wide and deep.

Unlike silicate lavas, sulfur lavas undergo dramatic color changes as they crystallize and interact with other materials. Understanding these color changes in sulfur is important in understanding volcanism on Io, as we see a wide range of colorful sulfur deposits in spacecraft images. On Earth, for example, the 1998 Vulcano self-combusting sulfur flows were yellow to moderate olive–brown ($<120^{\circ}$C) in color and contained higher temperature (120–160°C) interior zones of dark red sulfur. This differs from the active flows of the 1936 Siretoko-Iosan eruption that were described as "chocolate brown", and cooled to a yellow–green color (Watanabe, 1940). A solidified Mauna Loa sulfur flow was reported as yellow in color (Greeley *et al.*, 1984). Some of the color changes are due to the reorganization of sulfur molecules during cooling (Theilig, 1982), whereas other changes are due to small (<1 wt%) impurities (e.g., chalcophile elements, opaque crystals, carbonaceous or organic materials) in the lava (Kargel *et al.*, 1999). Even exposure to a vacuum induces color changes in sulfur, turning yellow, tan, and brown sulfur white within ~100 hours (Nash, 1987). Unmelted yellow sulfur powder brightens to a very light yellow/white–gray when exposed to radiation (see e.g., Steudel *et al.*, 1986; Nash, 1987). More work on terrestrial sulfur and sulfur flows is needed to better understand the role of sulfur color changes on Io's surface appearance.

7.3 PREVIOUS WORK: INSIGHTS FROM *VOYAGER* AND TELESCOPIC STUDIES

7.3.1 Introduction: initial indications and discovery of volcanism

Our understanding of the nature of effusive eruptions on Io has changed considerably over time as *Voyager*, *Galileo*, and ground-based observations have refined the estimates of the temperature ranges involved, as higher spatial resolution observations have revealed morphological detail, and as both higher spatial resolution and a longer time base have revealed more fully the range of eruption types which occur.

Although ground-based observations were obtained in the 1970s, which in retrospect detected thermal emission from volcanic eruptions, they were not clearly recognized as such until 1979 when the first theoretical predictions of volcanism were made (Peale *et al.*, 1979) and *Voyager I* observed obvious evidence of plumes, volcanic surface features, and infrared emission (Morabito *et al.*, 1979; Smith *et al.*, 1979; Hanel *et al.*, 1979). With that evidence it became clear that the high in-eclipse infrared brightness observed earlier by Hanson (1973) and also by Morrison and Cruikshank (1973), and attributed to unusual thermal inertia values, was due at least in part to thermal emission from volcanic hot spots. The same was true for the infrared outburst observed by Witteborn *et al.* (1979) on 20 February

1978. In that observation, excess 4.0–5.4 μm emission present for only one night had a spectrum roughly corresponding to a 600 K black body covering an area of 8,000 km^2. Witteborn *et al.* had in fact discussed the possibility of volcanic activity in their paper but dismissed it as unlikely and concentrated on other possible explanations.

7.3.2 Early results from the *Voyager* observations: the sulfur vs. silicate controversy

The visible images and infrared spectra obtained by the *Voyager* spacecraft revealed clear evidence of effusive volcanism (summarized in Schaber, 1982), such as flow-like features radiating from central vents or the margins of paterae (volcano–tectonic depressions similar to calderas), albedo patterns thought to indicate lava lakes within paterae, and indirect evidence that various plains units might have been created by numerous flows. However, it remained unclear how much of that activity was directly due to silicate volcanism and how much was due to sulfur. Sulfur had been detected in the Jovian magnetosphere (Kupo *et al.*, 1976) and sulfur dioxide frost and gas had been recognized in ground-based spectra (Smythe *et al.*, 1979; Nash and Nelson, 1979; Fanale *et al.*, 1979) and spacecraft observations of the Loki region (Pearl *et al.*, 1979). The unusual color patterns present in regions such as Ra Patera (Pieri *et al.*, 1984) were also thought to be indicative of sulfur (perhaps quenched) in various stages of cooling (Section 7.2). However, the lack of spectral features or flow morphologies that could unambiguously be attributed to elemental sulfur led to continuing controversy regarding the relative importance of sulfur vs. silicate volcanism (Sagan, 1979; Young, 1984). Those in favor of predominately silicate volcanism argued that volatile sulfur and sulfur compounds simply acted as "paint" on a primarily silicate surface.

One argument against the presence of sulfur came from the observed strength of the lithosphere, as indicated by the presence of steep topography such as high patera walls (Clow and Carr, 1980). If temperature increased with depth at a rate implied by: (1) the high heat flow measured by Morrison and Telesco (1980), Matson *et al.* (1981), and Sinton (1981), coupled with (2) the commonly assumed conductive transport of that heat, then at shallow depths any sulfur would soften and produce too weak a lithosphere. Many Io researchers failed to appreciate the early arguments of O'Reilly and Davies (1981) that the very high resurfacing rates associated with predominately advective transport of heat via magma could in fact suppress the geothermal gradient to a value far below what would be implied by conductive transport, thus resulting in a cold lithosphere, strong even in the presence of sulfur.

On the other hand, part of an initial bias toward sulfur volcanism also resulted from an unfortunate wavelength gap in the *Voyager* instrumentation which made high-temperature silicate activity less obvious. The *Voyager* vidicon-based imager had filters covering the 0.35-0.62 μm range while the IRIS spectrometer had little sensitivity shortward of 4 μm. As a result, the high spatial resolution visible camera could not detect thermal emission while the relatively low spatial resolution infrared spectrometer saw emission almost completely dominated by the cooler but areally much larger portions of the hot spots. The center-of-gap wavelength of ~2 μm corresponds to the peak of the Planck black-body emission from a 1,500-K surface and therefore

Voyager was relatively insensitive to such surfaces. Typical analysis of *Voyager* infrared observations (Pearl and Sinton, 1982) consisted of few-component blackbody models where the highest temperature components were less than or equal to ~650 K – a value still attributable to sulfur. The consensus view did not begin to shift to silicate-dominated volcanism until two events occurred. First, in an early prescient paper Carr (1986) recognized that silicate flows cooled so quickly that their surfaces would also be dominated by low temperatures. Those type models were further developed by Davies (1996) and Howell (1997). Second, ground-based monitoring programs (discussed below) eventually detected outbursts still young enough to be dominated by high-temperature material too hot to be consistent with sulfur (Johnson *et al.*, 1988, Blaney *et al.*, 1995, Blaney *et al.*, 1997; Stansberry *et al.*, 1997).

7.3.3 Initial insights from the ground-based monitoring program

Several intensive ground-based monitoring programs began immediately after the *Voyager* discovery of volcanism provided an explanation for the previously anomalous infrared measurements. Most notable were the Hawaii group of Bill Sinton and coworkers (e.g., Sinton, 1980; Sinton *et al.*, 1980; Sinton, 1981; Sinton *et al.*, 1983) and the Jet Propulsion Laboratory (JPL) group (e.g., Matson *et al.*, 1981; Johnson *et al.*, 1984; Veeder *et al.*, 1994). Those initial observations provided wider spectral and temporal coverage than the brief *Voyager I* and *Voyager II* fly-bys, but with no spatial resolution beyond what could be gleaned from variations in the hemisphere-wide integrated flux. Eclipse observations by the above groups and others such as Morrison and Telesco (1980) provided the most direct way to separate hot spot emission from reflected and reradiated sunlight thus giving global heat-flow estimates, but the measurements were applicable only to the Jupiter-facing hemisphere. Monitoring of photometric variations due to Io's rotation could be used to locate in longitude particularly bright hot spots, and longer term observations could establish their stability and eruption lifetimes. Initial results indicated heat flow values in the range of 1–2.5 $W\,m^{-2}$, higher than expected from the simplest steady-state tidal heating models (Yoder, 1979), thereby raising questions of whether non-equilibrium models or intermittent styles of activity were required. While infrared observations showed considerable variability, comparison of modern visible wavelength rotational light curves with those obtained decades earlier showed no detectable variation (Morrison *et al.*, 1979). This implied that despite the high ($\geq$1 $mm\,yr^{-1}$) resurfacing rates and the dramatic local albedo changes seen in the four short months between the *Voyager I* and *II* images, Io's surface somehow maintained persistent hemispheric albedo patterns.

7.3.4 Continuing analysis of *Voyager* observations

Continued analysis of *Voyager* data led to further insights regarding volcanic activity on Io. For example, McEwen and Soderblom (1983) recognized two types of volcanic plumes typified by the volcanoes Pele and Prometheus. The first was thought to be characterized by short eruption times of days to weeks, by plume heights of ~300 km,

by sulfur lava vent temperatures of ~650 K, and by dark plume deposits containing little SO_2. The second was thought to be characterized by lower temperature reservoirs with several year-long eruption times, plume heights from 60–100 km, and by ring deposits ~250 km in diameter, rich in SO_2. *Galileo* results (see Chapter 8) have confirmed the existence of distinctly different plume types, but we now know the connection to underlying lava activity is different than originally assumed.

A comparison of *Voyager* imaging and infrared data led to the discovery (McEwen *et al.*, 1985) of a well-defined correlation between volcanic hot spots and low-albedo features. Most of the low-albedo features occurred on the floors of volcanic paterae. The correlation was ascribed to the absence of bright materials, such as SO_2 frost, and the presence of a low-albedo substance. However, *Voyager* images did not provide enough spectral detail to uniquely determine the nature of the low-albedo material, and liquid sulfur, silicate–sulfur mixtures, and various other substances were all considered possible. The spectra did not appear consistent with pure silicates. The temperature distribution obtained, 200–400 K, was (once again partly due to wavelength gaps) consistent with liquid sulfur, but the presence of sulfur lava could not be determined conclusively.

7.3.5 Further development of ground-based observations: individual hot spots and silicate temperatures

During the 1980s various infrared techniques were developed providing sufficient spatial resolution to monitor thermal output from individual Ionian hot spots. These included speckle interferometry (Howell and McGinn, 1985; McLeod and McCarthy, 1991), polarimetry (Goguen and Sinton, 1985), Galilean satellite mutual occultation photometry (Goguen *et al.*, 1988; Medina *et al.*, 1989; Descamps *et al.*, 1992; Spencer *et al.*, 1994), Jupiter occultation photometry (Spencer *et al.*, 1990), and improvements in infrared cameras and telescope image quality such that hot spots could be directly resolved on the 1.2-arcsecond disk of Io (Spencer *et al.*, 1994). Continued monitoring also provided observations of unusual events, including an outburst in 1986 (Johnson *et al.*, 1988) which clearly had a temperature (~900 K) in the silicate range. Limited observations were also obtained with the NICMOS instrument on the Hubble Space Telescope (HST) (Goguen *et al.*, 1998). The observations showed continued although varying activity at major *Voyager*-era hot spots such as Loki and Pele, as well as surprisingly stable activity at newly discovered but fainter sources such as Kanehekili (Spencer *et al.*, 1990). The ground-based observation programs were intensified during the *Galileo* era (Howell *et al.*, 2001) to provide context for the more detailed but temporally isolated spacecraft observations. For example, they provided temporal constraints on the timing of the Tvashtar eruption seen by *Galileo*. They also enabled the recognition of patterns of activity such as the reoccurring brightenings seen at Loki.

Because Loki is the largest and often the brightest hot spot on Io it is also the best characterized, but the precise nature of the activity remains uncertain. Questions also exist concerning how representative this activity is of other smaller hot spots. The observations summarized in Rathbun *et al.* (2002) show that from 1988 through 2000

Loki brightened significantly every ~540 days, with the bright period lasting approximately ~230 days. As best as can be discerned from the limited *Galileo* observations, the brightenings correspond to a resurfacing wave that sweeps counterclockwise around the dark section of the patera. Rathbun *et al.*'s preferred interpretation is that the wave represents the foundering of the solid crust of a silicate lava lake (see Section 7.4.2), and the period represents the time required for new crust to thicken to the point where a density instability leads to overturn. Analysis and modeling of near-infrared mapping spectrometer (NIMS) data by Lopes *et al.* (2002) and Howell and Lopes (2004) is also consistent with the lava lake model. However, a comparison of Loki's activity with terrestrial lava lakes (Gregg and Lopes, 2004) reveals significant differences. Davies (2003) has produced thermal models of Loki, and believes the wave could also be consistent with spreading lava flows confined by patera walls. The situation became more complicated in 2000 when the semi-periodic behavior seemed to end and Loki entered an apparently more sustained but intermediate level of activity (Rathbun *et al.*, 2003).

7.4 NEW INSIGHTS: *GALILEO* AT IO (1996–2001)

The *Galileo* mission to Jupiter afforded researchers the opportunity to obtain a wide range of data on Io's volcanoes, primarily from the solid-state imager (SSI), NIMS, and the photopolarimeter and radiometer (PPR). Not only did these instruments image Io at a wide range of resolutions covering various parts of the visible, near-infrared, and thermal-infrared portions of the electromagnetic spectrum, but also they imaged various parts of Io repeatedly during the course of the nominal and two extended missions (1996–2001). Having both varying spatial and temporal resolutions was instrumental in identifying many aspects of the styles of volcanic eruptions on Io. In this section, we discuss the new insights into effusive volcanism on Io garnered through these various SSI, NIMS, and PPR observations. To aid in the discussion we created a chart (Figure 7.1) to correlate inferred compositions of effusive products to eruption styles identified from repeated imaging.

7.4.1 Composition of volcanic products

Insights into the chemical composition of volcanic products on Io was provided by analysis of SSI color data (Geissler *et al.*, 1999: 6 wavelengths: violet, green, red, 756 nm, 889 nm, 968 nm; see Klaasen *et al.*, 1984 for filter bandpasses) and NIMS spectroscopy (Carlson *et al.*, 1992; Smythe *et al.*, 1995: coverage of the 1–5.2-μm range with resolution of 0.025 μm), as well as data from HST (Spencer *et al.*, 2000a). Basically, Io can be subdivided into four main color units: yellow, gray–white, black, and red. The yellow unit covers about 40% of Io's surface (Geissler *et al.*, 1999) as large expanses of equatorial plains, with more localized greenish-yellow patches observed in some paterae. Geissler *et al.*'s (1999) comparison of *Galileo* SSI color data to the laboratory spectra of >650 rocks and minerals suggested

VOLCANISM ON IO				
	Inferred Lava Composition (based on SSI color and NIMS spectroscopy)			
Inferred Eruption Style (based on repeated SSI, NIMS, & PPR imaging)		Black (Silicate-dominated)	Yellow (Sulfur-dominated)	White (SO_2-dominated)
	Explosion-dominated (Short duration, energetic events, very high brightness temperatures)	Pillan, Thor, Tvashtar (Rapidly-emplaced, possibly turbulent, mafic to ultramafic flows)	Ra flow field ? (Large-volume, bright, flow-like deposits associated with dramatic event, 1994-95)	None detected
	Intra-Patera (Variable durations, activity confined in paterae, variable brightness temperatures)	Loki, Pele, Tupan patera floors (Lava lakes, mafic to ultramafic flows)	None detected	None detected
	Flow-dominated (Long duration, continuous output, high brightness temperatures)	Prometheus, Amirani (Slowly-emplaced, compound inflationary mafic flows)	None detected	None detected
	Unnamed (Short duration, weak event, low brightness temperatures)		Tsui Goab Fluctus (Small-volume, inflationary sulfur flow)	None detected
	Unidentified (Unknown eruption style)			Balder, Tohil (Glacial-like flow?)

Figure 7.1. Chart relating volcanism on Io to inferred composition of volcanic products and eruption styles, emphasizing emplacement of effusive materials.

that the yellow materials were most consistent with cyclo-octal sulfur (S_8) with or without a covering of SO_2 frosts deposited by plumes. Alternatively, Hapke (1989) hypothesized that the yellow color on Io could be produced by polysulfur oxide and S_2O without requiring large quantities of elemental sulfur. The rare greenish-yellow patches on some patera floors were suggested by Geissler *et al.* (1999) to be composed either of some type of sulfur compound contaminated by iron, or lava flows composed of silicates rich in olivine or pyroxene with or without sulfur-bearing contaminants. Geissler *et al.*'s interpretations of the "green spots" suggest intimate interaction between silicate lava and either sulfurous flows or plume deposits (see also McEwen *et al.*, 2000; Williams *et al.*, 2000a).

The gray–white color unit covers about 27% of Io's surface (Geissler *et al.*, 1999) as extensive equatorial plains and as diffuse rings around active vents, and has been thought to be dominated by solid sulfur dioxide. This unit was extensively studied by NIMS, which observed several different strength bands of SO_2 that could be analyzed to assess grain size and abundance (e.g., Douté *et al.*, 2001, 2002, 2004). The white unit was found to be mostly coarse- to moderate-grained SO_2 snow (Carlson *et al.*, 1997), likely resulting from plume fallout that has undergone recrystallization (Douté *et al.*,

2001, 2002). However, high spatial resolution NIMS data showed that color alone is not in itself a good indicator to map SO_2 distribution or granularity (pure SO_2 is transparent in visible light), suggesting that the SO_2 in the gray–white color unit is often mixed with other contaminants, especially where strong NIMS signatures of SO_2 coincide with non-gray–white materials (e.g., Lopes-Gautier *et al.*, 2000; Douté *et al.*, 2002, 2004).

The black color unit covers about 1.4% of the surface (Geissler *et al.*, 1999) and is mostly restricted to very dark patera floors, lava flow fields, or dark diffuse materials near or surrounding active vents, which correlate with active or recently active hot spots (Lopes-Gautier *et al.*, 1999, 2000; Lopes *et al.*, 2001). *Galileo* multicolor studies of the black materials (Geissler *et al.*, 1999) found that their visible/near-IR spectra were most consistent with Mg-rich orthopyroxene (enstatite or bronzitehypersthene), as indicated by their strong 0.9-μm absorption. The dark materials are hypothesized to be silicate lava flows (within flow fields), or lava lakes (within paterae), or pyroclastic deposits (within diffuse deposits near paterae), of mafic to ultramafic composition.

The red color unit is found either as local red patches and rings on or around some active vents (e.g., Pele), or as regional red–orange units in polar regions. The red has been interpreted to come from short-chain sulfur molecules (S_3, S_4) that result, in the case of the red patches and rings, from condensation and recrystallization of S_2-rich volcanic gases in the plumes of active vents (Spencer *et al.*, 2000a). These short-chain sulfur molecules are probably ephemeral in nature (reverting back to yellow, long-chain S_8 upon cooling), and thus require continual replenishment to be observed. The more maroon–red polar units result from breakdown of cyclo-octal sulfur (S_8) by charged particle irradiation (Johnson, 1997). Alternatively, recent studies of *Galileo* NIMS spectra of the red diffuse deposit south of Marduk combined with laboratory analyses suggest that at least some red deposits on Io result from solid sulfuryl chloride (Cl_2SO_2) or sulfur dichloride (Cl_2S) that condensed on SO_2 snow from Cl-bearing gases in active plumes (Schmitt and Rodriguez, 2003).

In summary, the various compositional analyses during the *Galileo* era, using SSI color data and NIMS spectroscopy, supplemented by HST and other data (e.g., Spencer *et al.*, 2000a), has led to the tentative identification of at least three distinct volcanic compositions on Io: silicate, sulfur, and sulfur dioxide, although gaseous SO_2 in volcanic plumes was identified during the *Voyager* fly-bys (Pearl *et al.*, 1979). As we shall see, these three materials occur in a variety of morphologies and are combined in various ways through Io's active volcanic processes.

7.4.2 Eruption styles

One of the primary advantages of repeated imaging of the anti-Jovian hemisphere during the *Galileo* mission was obtaining the potential to catch volcanoes in various parts of their eruption cycles, to identify both the *types* of eruptions occurring, and how those eruptions *evolved*. Through correlation of the SSI, NIMS, and PPR observations during each orbital fly-by with those of previous fly-bys, a set of three primary types of eruption styles were identified: flow-dominated volcanism

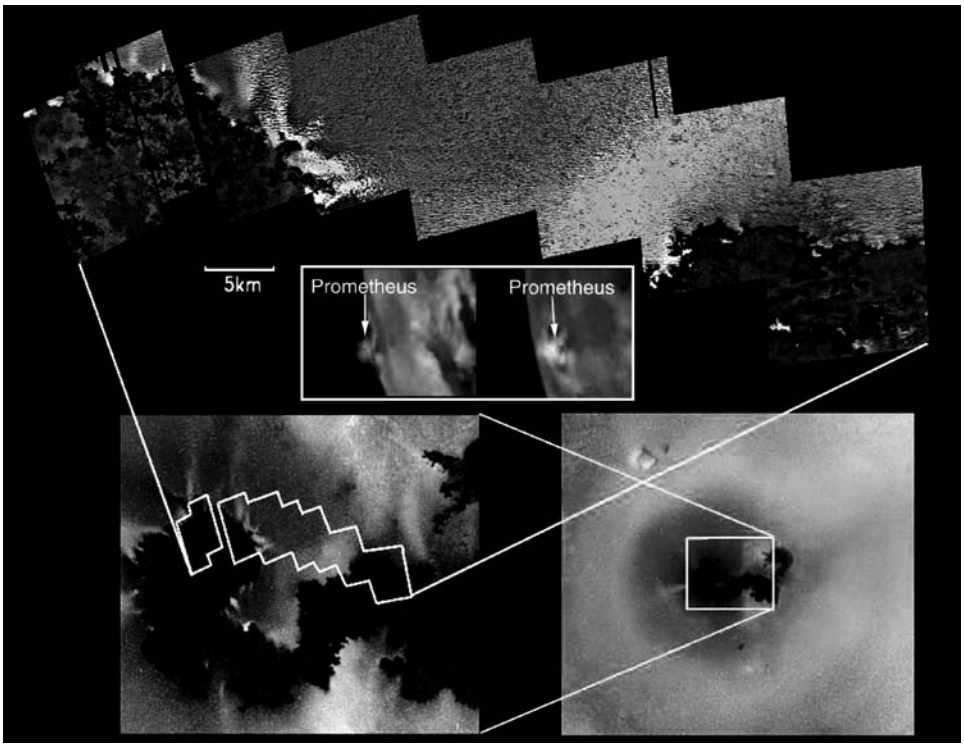

Figure 7.2. A montage of *Galileo* SSI images of the Prometheus volcano at several different resolutions, which identify various aspects of the flow-dominated eruption style. These eruptions produce compound silicate flow fields that are slowly emplaced over months to years, with measured temperatures consistent with terrestrial basaltic volcanism (Keszthelyi *et al*., 2001). Note the small dark patches in the flow field indicative of recent breakouts. Heat from advancing flows vaporize SO_2 snow producing jet-like flow front plumes (Kieffer *et al*., 2000; Milazzo *et al*., 2001). The central inset shows examples of the Prometheus plume. (See also color section.)

(formerly Promethean), explosion-dominated volcanism (formerly Pillanian), and intra-Patera volcanism (formerly Lokian). A previous designation system of these styles using the names of specific Ionian volcanoes was abandoned by mutual consent of Io researchers at the 2005 Io Workshop.

Flow-dominated (formerly Promethean) eruptions (Keszthelyi *et al*., 2001), typified by eruptions at the Ionian volcanoes Prometheus (Figure 7.2) and Amirani (Figure 7.3), originate from either paterae or fissures, and produce extensive compound lava flow fields through repeated small breakouts of lava, similar to the slowly emplaced (months to years), compound inflationary flow fields in Hawaii. NIMS temperature measurements at these sites are consistent with temperatures associated with terrestrial basaltic volcanism. These eruptions are long-lived, steady eruptions that can last years at a time, and often include small ($<$200 km high) explosive plumes of vaporized sulfurous country materials

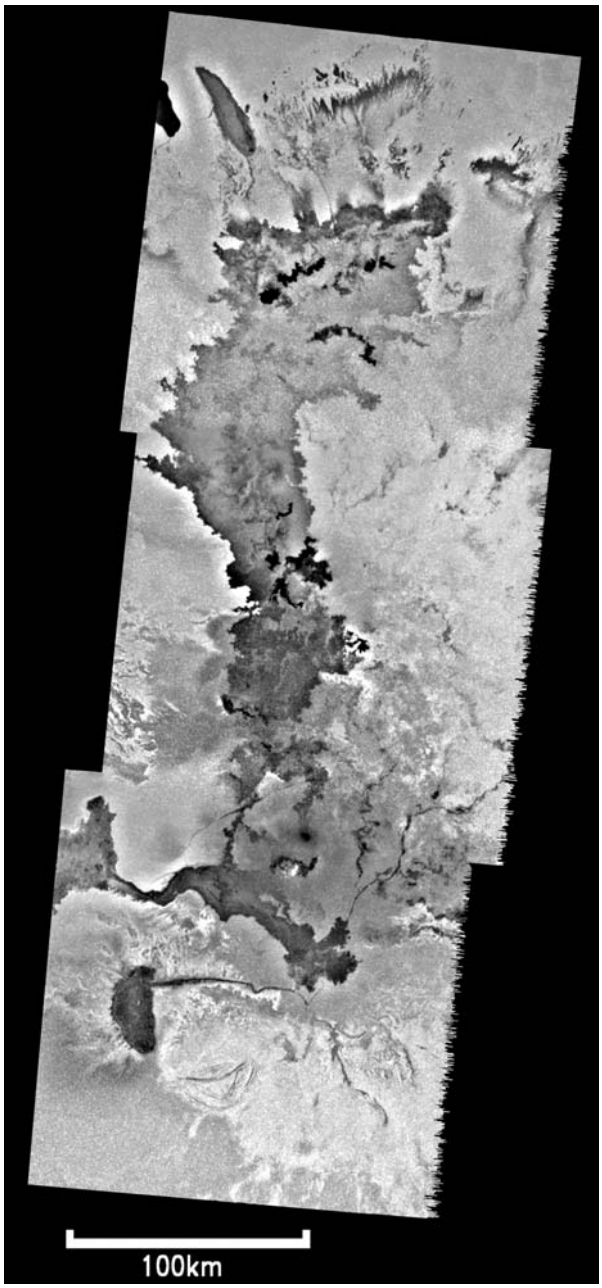

Figure 7.3. The Amirani flow field, as imaged by the *Galileo* SSI in February 2000. Amirani, like Prometheus, is an example of a flow-dominated eruption style, with dark lava flows slowly emplaced over many years (note the freshest, darkest flows near the top of the field). Presumably tube-fed lavas from southern Amirani are thought to feed the Maui flow field (off the image at bottom left) through a >300 km long active tube system, the longest known in the Solar System.

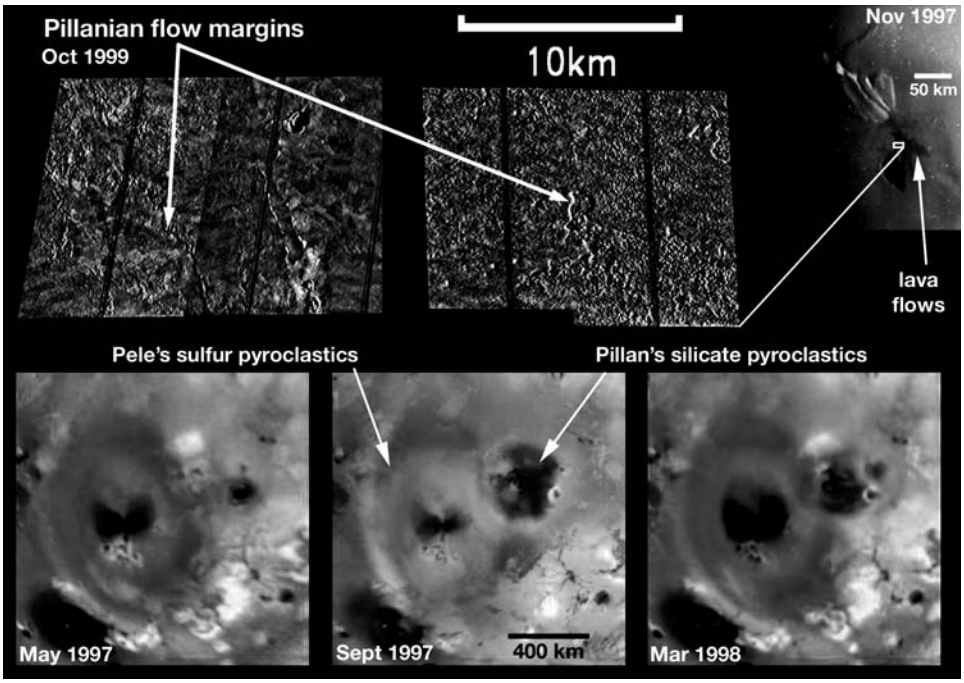

Figure 7.4. A montage of *Galileo* SSI images of the Pillan volcano at several different resolutions, which identify various aspects of an explosion-dominated (formerly Pillanian) eruption style. (*top*) The Pillan lava flow field, which emanated from fissures that fracture a mountain north of the caldera. (*bottom*) Changes to Pillan's surroundings (including Pele's red ring) due to activity at these volcanoes. These eruptions produce extensive flow fields that are rapidly emplaced over days to weeks, with measured temperatures consistent with terrestrial mafic to ultramafic volcanism (Keszthelyi *et al.*, 2001). (See also color section.)

that erupt from the edges of flow fronts (Kieffer *et al.*, 2000; Milazzo *et al.*, 2001), somewhat similar to the rootless conduits found in pahoehoe flow fields fed by lava tubes. The plumes associated with flow-dominated eruptions appear to be dominantly SO_2 gas formed as the hot lava vaporizes SO_2 snow on the plains, though ephemeral accumulations of diffuse red material (usually near the primary hot spot) may suggest the presence of S_2 gas in some areas. The vaporized SO_2 quickly refreezes and forms bright jets perpendicular to the flow front margins (Figure 7.2). The location of the plume source changes as the flow field slowly advances, which for the case of Prometheus covered a distance of 75–95 km between *Voyager* (1979) and initial *Galileo* observations (1996). Higher resolution *Galileo* SSI observations of equivalent resolution but separated by $\sim$3 months clearly show fresh breakouts of lava in the Prometheus and Amirani flow fields, similar in morphology to those seen in aerial photographs of the Pu'u' O'o'-Kupaianaha flow field, Kilauea Volcano, Hawaii (Keszthelyi *et al.*, 2001).

Explosion-dominated (formerly Pillanian) eruptions (Keszthelyi *et al.*, 2001), typified by some eruptions observed at the Pillan (Figure 7.4), Tvashtar

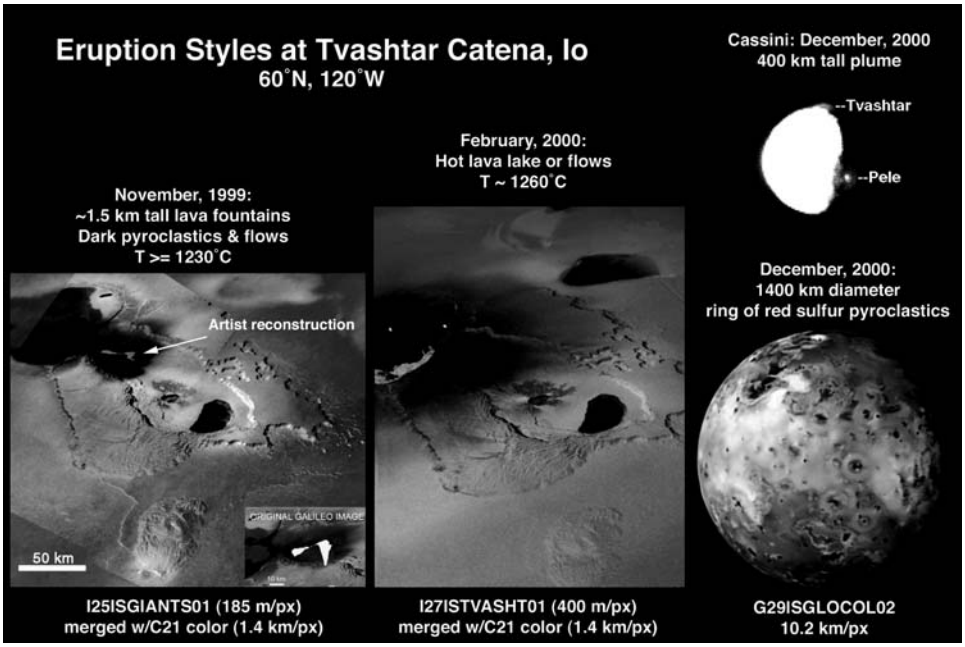

Figure 7.5. A montage of *Galileo* SSI and *Cassini* imaging science subsystem (ISS) images showing a range of eruption styles at Tvashtar. In November 1999 Tvashtar had a possibly flow-dominated eruption, producing a lava fountain and flow field. In February 2000 an intra-Patera eruption could have occurred, producing fresh material in a lava lake (or possibly just a confined lava flow). In December 2000, the *Cassini* spacecraft recorded an explosion-dominated eruption, from which *Galileo* imaged a large red ring deposit of sulfur. It remains unclear whether any new flows were emplaced (rapidly or otherwise) after the December 2000 event. (See also color section.)

(Figure 7.5), Surt, and Pele Volcanoes, also originate from either paterae or fissures. However, these eruptions differ from flow-dominated eruptions in that most of the energy of the eruption is directed into a short-lived, vigorous event that last days to weeks. These eruptions are discrete events compared with the more or less continuous flow-dominated eruptions like those at Prometheus. These eruptions produce both extensive pyroclastic deposits and dark lava flow fields. Temperatures associated with terrestrial mafic to ultramafic volcanism are correlated with these events. Explosion-dominated eruptions typically include large (>200 km high) explosive plumes, which occur due to the interaction of silicate magma with either juvenile or meteoric sulfurous volatiles. This most often results in large (~1,200 km diameter) red rings of short-chain sulfur around the source regions. However, the summer 1997 eruption at Pillan produced a ~400 km diameter dark diffuse deposit of silicate material, along with the highest temperatures recorded by the SSI and NIMS (~1,550°C: McEwen *et al.*, 1998b; ~1,600°C: Davies *et al.*, 2001). These temperatures, along with the identification of silicates in the black materials on Io (Geissler *et al.*, 1999),

suggested that either ultramafic or superheated basaltic volcanism was occurring on Io (McEwen *et al.*, 1998b; Kargel *et al.*, 2003). However, recent re-evaluation of the *Galileo* data and additional modeling of temperature fits to these data suggest that temperatures associated with these explosion-dominated eruptions may be more consistent with less ultramafic compositions ($T \sim 1{,}200$–$1{,}300^{\circ}$C), more like those theorized for lunar mare basalts or terrestrial komatiitic basalts (see also Williams *et al.*, 2000b).

In terms of effusive products, explosion-dominated eruptions often produce areally extensive flow fields, but over a shorter eruption duration than the flow-dominated eruptions. For example, an $\sim$3,100-km^2 flow field formed between 52–167 days during the summer 1997 eruption at Pillan (Williams *et al.*, 2001a). The calculated volumetric flow rate for these lavas is $\sim$1,740–7,450 m^3 s^{-1}, similar to the flow rates for the 1783 Laki eruption and theorized for the Rosa member of the Columbia River Flood Basalt (Thordarson and Self, 1993, 1998), but far above those for typical Hawaiian flows. The morphology of the Pillan lava flows, as imaged at $\sim$20–30 m per pixel by the *Galileo* SSI in October 1999, shows an exceptionally rough, disrupted and platy upper surface, that was suggested to result from rapidly emplaced flows (Williams *et al.*, 2001a). Whether highly ultramafic compositions or turbulent lava flow are components of the emplacement of these flow fields cannot be assessed at present. However, it is clear that flow fields associated with explosion-dominated eruptions tend to be more rapidly emplaced than those associated with flow-dominated eruptions. At this point it is important to note, however, that many Ionian volcanoes produce both flow-dominated and explosion-dominated eruptions. For example, the *Galileo* spacecraft detected components of both flow-dominated and explosion-dominated eruptions at the Tvashtar Volcano during close fly-bys between 1999–2001 (Keszthelyi *et al.*, 2001; Turtle *et al.*, 2004; Milazzo *et al.*, 2005).

Intra-Patera (formerly Lokian) eruptions (Lopes *et al.*, 2004) are confined within paterae, or volcano–tectonic depressions similar to terrestrial calderas found in great number across Io's surface, ranging in size from 2–202 km diameter. These eruptions occur with or without associated plumes, and often erupt as lava lakes, some of which undergo occasional overturning or resurfacing of their upper solid crusts. The volcanoes of Loki (Io's most powerful volcano: Figure 7.6), Pele, Emakong (Figure 7.7), and Tupan (Figure 7.8) are all thought to produce this eruption style, though Pele also produces explosion-dominated eruptions (Lopes *et al.*, 2001; Radebaugh *et al.*, 2001, 2004). Combined Earth-based telescopic and *Galileo* PPR monitoring over many years led to the detection of reoccurring, almost periodic brightenings at Loki that have been interpreted as repeated foundering and growth of the crust of a lava lake on the floor of the Loki caldera (Spencer *et al.*, 2000b; Rathbun *et al.*, 2002; see also Section 7.3.5). The margins of these paterae are usually bright in NIMS images, indicating hot edges that are consistent with terrestrial lava lakes. Most of Io's active volcanoes, as identified by NIMS hot spots, coincide with these paterae, suggesting that most lava resurfacing on Io is confined within paterae, and that the high resurfacing rates on Io as a whole are dominated by plume eruptions and their deposits (Lopes *et al.*, 2004).

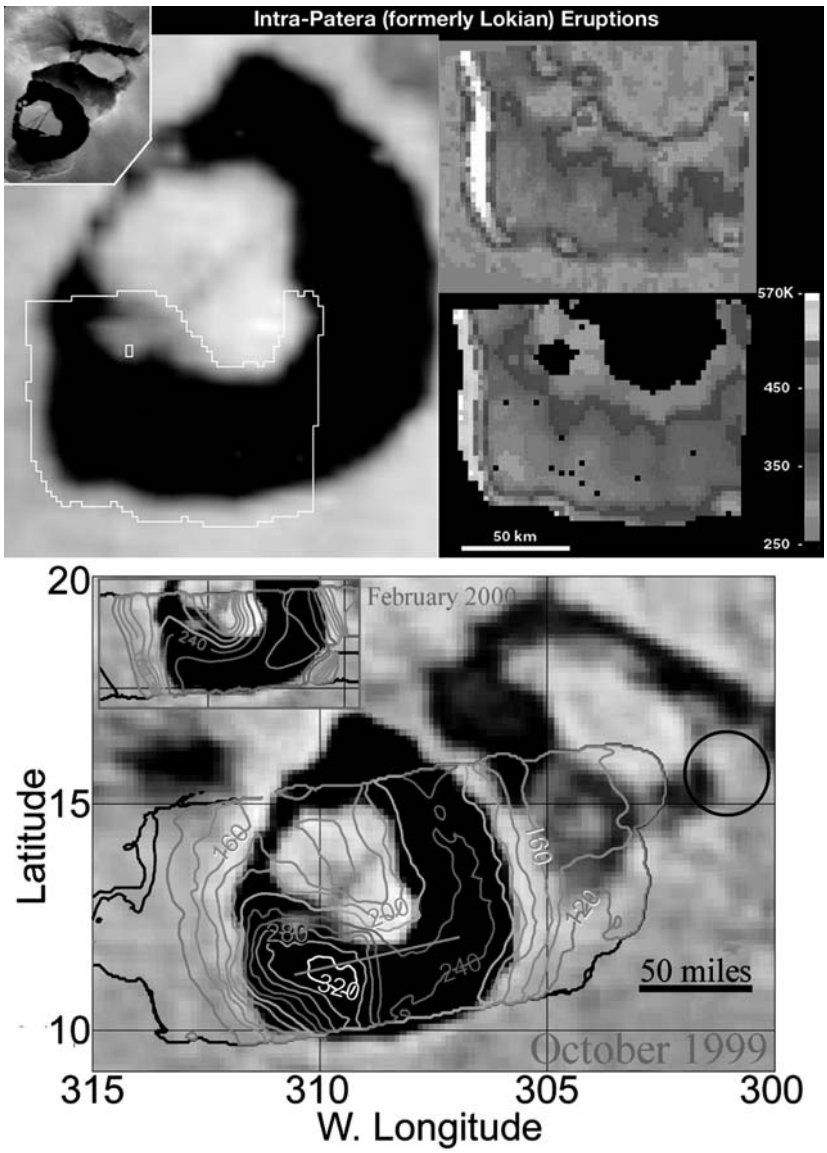

Figure 7.6. A montage of *Voyager* and *Galileo* SSI, NIMS, and PPR images of Loki volcano at several different resolutions and times, which identify various aspects of an intra-Patera (formerly Lokian) eruption style. These eruptions produce lava lakes that are overturned over months to years, with measured temperatures typically consistent with terrestrial basaltic volcanism (Lopes *et al.*, 2004). The color panel at upper right (see color section) is a NIMS map at 2.5 μm showing a hot edge (white: $T \sim 840$ K) at the western wall, whereas the image at lower right is a NIMS temperature map showing warmer and cooler parts of the patera floor. The bottom image shows PPR data over an image of Loki, showing the migration of the hottest part of the patera floor from west to east (from Spencer *et al.*, 2000b).

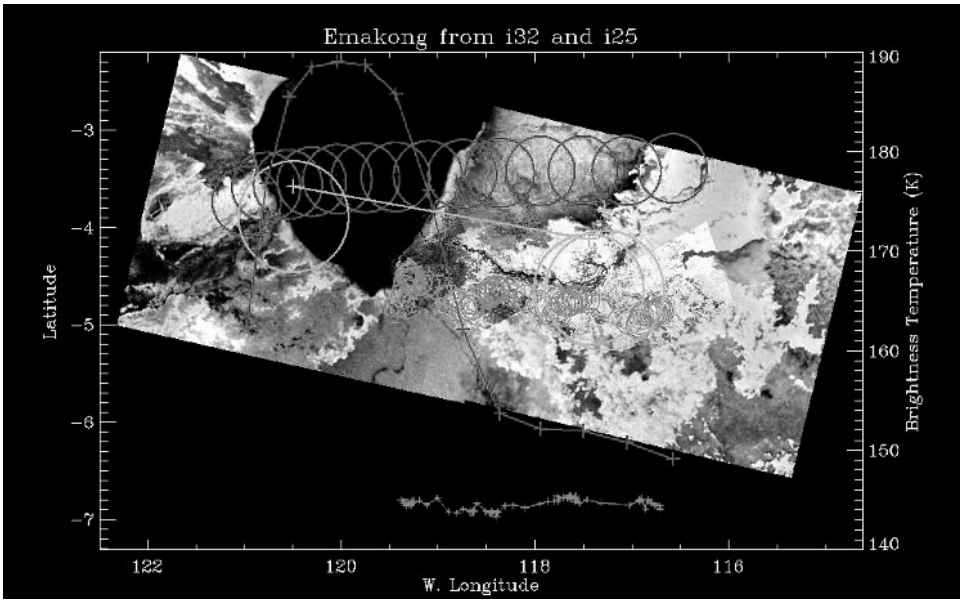

Figure 7.7. *Galileo* PPR data superposed upon SSI images of Emakong Patera. The PPR data demonstrates the very cold surface of the floor of Emakong Patera and its surrounding bright flows. NIMS data also showed that SO_2 frost is stable on parts of the patera floor, which suggests that Emakong may represent a cooled, inactive sulfur volcano (or alternatively, a very cooled silicate volcano with silicate flows heavily mantled by sulfurous deposits: Williams *et al.*, 2001b). (See also color section.)

Some paterae (e.g., Loki, Tupan) have bright "islands" in their interiors that are partially or completely surrounded by the inferred lava lakes. How these cold islands are maintained for years when hot lava sources are adjacent is a mystery. In the case of Tupan (Figure 7.8), heat from the lava lake appears to melt bright sulfur deposits along the margins of the lake, which accumulate as bright "puddles" on the dark surface. Diffuse red deposits, presumably short-chain sulfur crystallized from S_2 gas, cover the margins of the patera and large parts of the central island. NIMS temperature estimates for active paterae typically fall in the range consistent with terrestrial basaltic to ultramafic volcanism (Lopes *et al.*, 2001, 2004; Radebaugh *et al.*, 2004), although PPR observations show that the dark surface of Emakong Patera is very cold (Figure 7.7); NIMS also showed that SO_2 is stable on the dark surface in some areas, and might represent an inactive, solidified sulfur lava lake.

7.4.3 Styles of non-silicate flow emplacement

Most sulfur and SO_2 volcanism on Io is thought to be *secondary* (i.e., due to remelting and mobilization of crustal sulfurous materials by adjacent silicate heat sources), as originally suggested from *Voyager*-era studies by Greeley *et al.* (1984). Examples

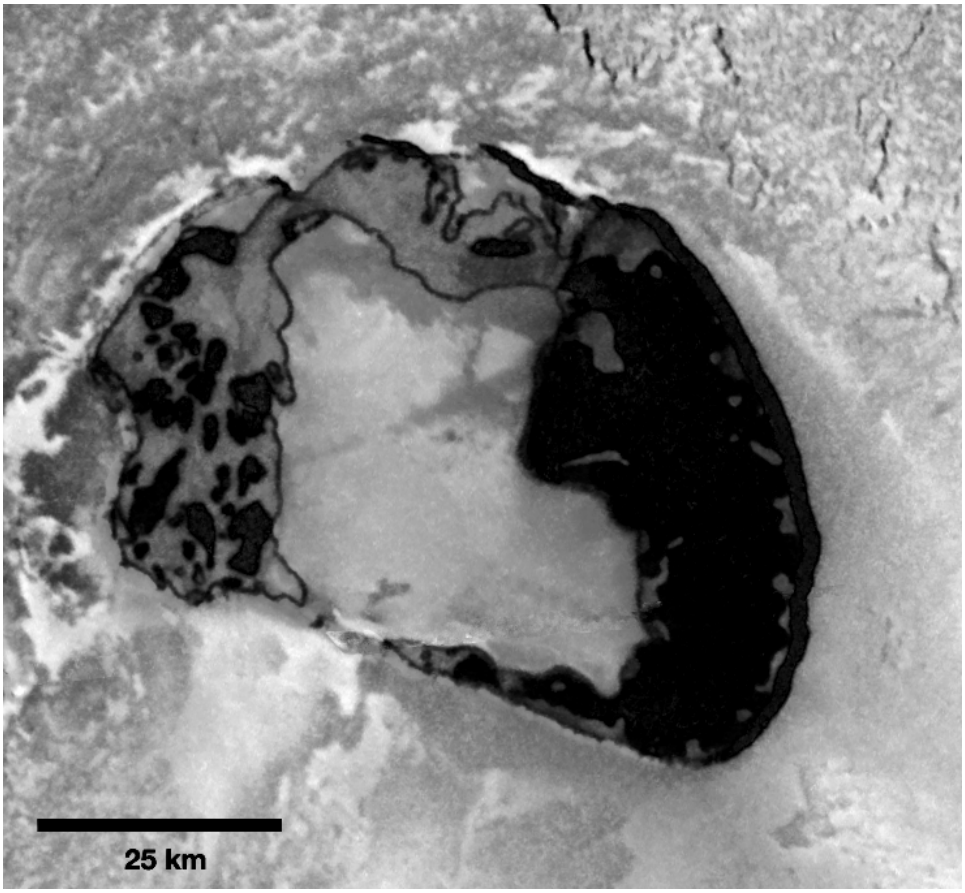

Figure 7.8. *Galileo* SSI image of Tupan Patera obtained in October 2001, another example of an intra-Patera eruption style. Heat from the lava lake appears to melt bright sulfur deposits along the margins of the lake, which accumulate as bright "puddles" on the dark surface of the lake. Diffuse red deposits, presumably short-chain sulfur crystallized from S_2 gas, cover the margins of the patera and large parts of the central island. This is the highest resolution color image of Io obtained during the *Galileo* mission (132 m per pixel). (See also color section.)

include bright lava flows surrounding smaller volume dark flows at Sobo Fluctus in the Chaac–Camaxtli region (Williams *et al*., 2002), and white (presumably SO_2-rich) flow front plumes jetting normal to the flow margins of the Prometheus flow field (Kieffer *et al*., 2000; Milazzo *et al*., 2001). During the *Galileo* era there was limited evidence for primary sulfur volcanism (i.e., not associated with nearby silicates). In 1994–1995, prior to *Galileo*'s arrival at Jupiter, there was a dramatic brightening detected by HST at the Ra Patera Volcano (Spencer *et al*., 1997), and subsequent imaging by SSI showed clear surface changes in the form of bright, flow-like deposits of large areal extent (McEwen *et al*., 1998a). *Voyager*-era studies of Ra Patera

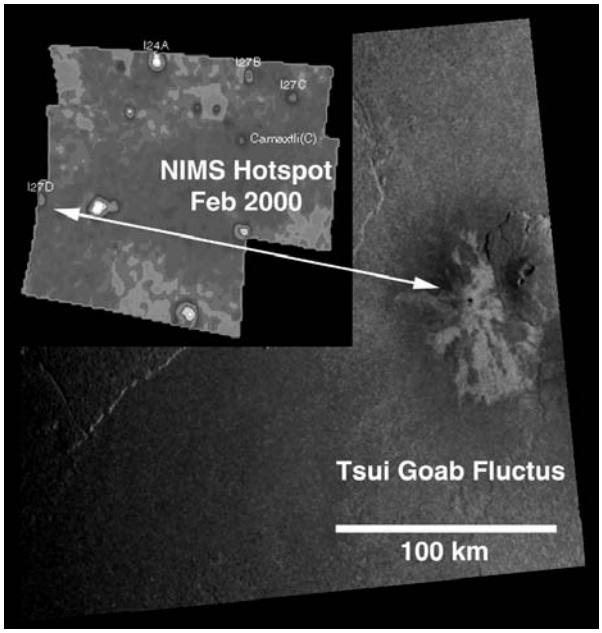

Figure 7.9. Low-resolution NIMS hot spot image (*inset*), with white arrows showing the correlation of the I27D hot spot of Lopes *et al.* (2001) with the bright flow field of Tsũi Goab Fluctus in the Culann-Tohil region as imaged by the SSI during October 2001. This is the only location of potentially active, primary sulfur effusive volcanism detected during the *Galileo* mission. (See also color section.)

suggested it was a likely site for sulfur volcanism (Pieri *et al.*, 1984), and if the correlation between bright yellow materials and sulfur holds true, then the 1994–1995 event at Ra may be an example of an explosion-dominated style eruption including sulfur flows. However, no repetition of such an event has since been detected, either by *Galileo*, HST, or Earth-based telescopes.

An ~290 km long, yellow and white–gray flow extends north-east from the dark caldera-like Emakong Patera, which Williams *et al.* (2001b) suggested might be part of a large primary or secondary sulfur flow field making up the Bosphorus Regio area of Io. Although the colors of the Emakong flows match those of sulfur that has undergone radiation exposure (e.g., Nash, 1987), and the flow is fed by a dark curvilinear channel (consistent with hot sulfur), no surface changes were detected at Emakong during the *Galileo* mission. The best evidence for active sulfur volcanism occurred during the February 2000 fly-by, when NIMS detected a weak hot spot at Tsũi Goab Fluctus (Figure 7.9), a bright flow field adjacent to an apparently inactive small shield volcano in the Culann–Tohil region (Williams *et al.*, 2004). The temperature measured by NIMS (~260±95°C) falls with the range of molten sulfur, and there is no indication of any adjacent silicate volcanic activity. However, there was no evidence of surface changes in Tsui Goab Fluctus after the February 2000 event (SSI

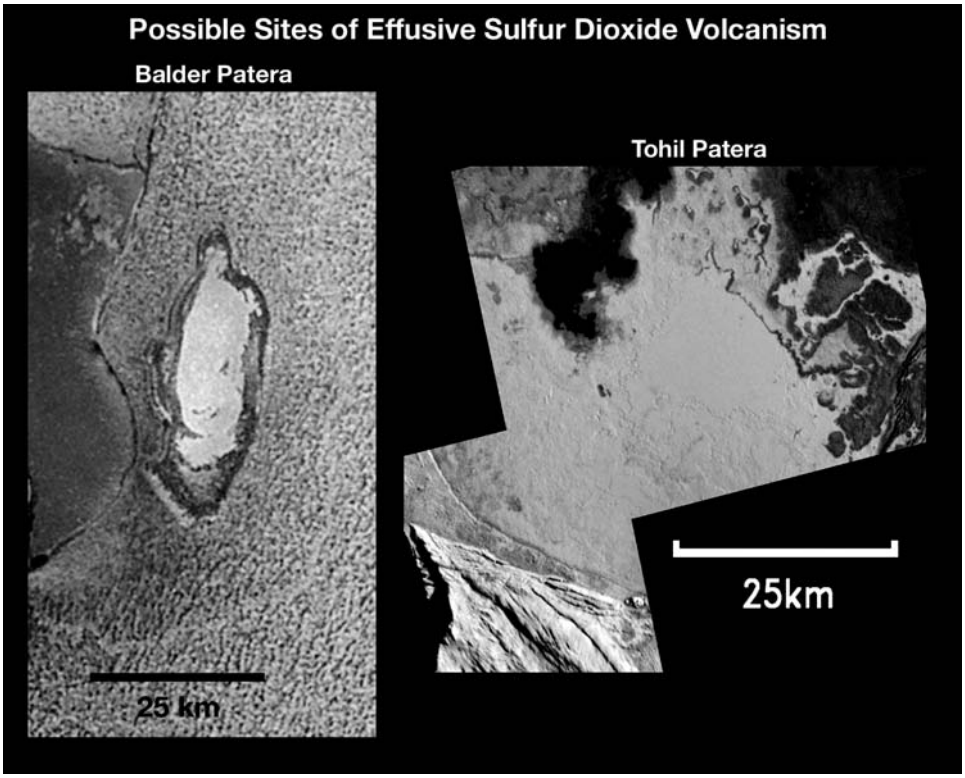

Figure 7.10. *Galileo* SSI images showing possible sites of effusive SO_2 volcanism on Io. (*left*) Balder Patera in the Chaac–Camaxtli region (Williams *et al*., 2002), site of a proposed glacial-like flow (Smythe *et al*., 2000). (*right*) Tohil Patera in the Culann-Tohil region (Williams *et al*., 2004), the south-west section of which has an enhanced SO_2 signature and flow-like margins in its interior. (See also color section.)

coverage was of low-resolution), so if fresh sulfur flows were emplaced, they did not cover any new terrain.

Evidence for effusive SO_2 volcanism is scant; most surface changes that show variations in SO_2 content resolvable by NIMS are in the form of regional variations in the plains (Douté *et al*., 2001, 2002, 2004), which are likely due to redistribution and/or recrystallization of explosively emplaced SO_2 snow produced by freezing of volcanic gases (Carlson *et al*., 1997). However, NIMS detected a strong signature of SO_2 confined to the floor of Balder Patera in the Chaac–Camaxtli region (Williams *et al*., 2002), which SSI shows to have a homogeneous white-colored patera floor (Figure 7.10). It is unclear why the floor should be so enriched in SO_2 relative to the surrounding plains. Smythe *et al*. (2000) proposed that an SO_2 glacial-like flow may have erupted and flooded the patera floor. Although the dynamics of such a flow have not yet been explored, mapping in the Culann-Tohil region has detected another

region of possible effusive SO_2 material. The south-east section of Tohil Patera contains a white material in which high-resolution SSI images show has apparent flow margins (Williams *et al.*, 2004); NIMS indicates that this region also has a signature of enhanced SO_2, although not as abundant as that at Balder Patera. Although these images are intriguing, additional assessment of the potential for SO_2 flows must await further study.

7.4.4 Volcano distribution

Volcanoes on Io (and for that matter, the mountains too) do not appear to follow a distinct global pattern, suggesting that any surface expression of internal dynamics (convection) is subtle. Active hot spots appear to be randomly distributed (Lopes-Gautier *et al.*, 1999). The distribution of mountains and paterae (including those which have not been observed to be active) is, however, not random, as both types of features are concentrated toward lower latitudes and follow a bimodal distribution with longitude (based on available imagery). The greatest frequency of mountains occurs in two large antipodal regions near the equator at about 65° and 265° (Schenk *et al.*, 2001). In contrast, the volcanic patera follow a similar distribution but 90° out of phase with that of the mountains (Radebaugh *et al.*, 2001). The bimodal distribution pattern for paterae and other volcanic centers matches the expected pattern of heat flow from asthenospheric tidal heating (Ross *et al.*, 1990) and the pattern of internal convection within the mantle predicted from simulations (Tackley *et al.,* 2001). Jaeger *et al.* (2003) found that 41% of tectonically derived mountains are associated with paterae, and suggested that orogenic faults on Io act as conduits for magma ascent, fueling patera formation near mountains (see Chapter 6).

7.5 SUMMARY AND OUTSTANDING QUESTIONS

With the end of the *Galileo* mission, future studies of Io will rely upon the increasingly sophisticated observations possible from newly developed techniques at large ground-based observatories. Advanced speckle techniques (Marchis *et al.*, 2000, 2001) and adaptive optics systems (Marchis *et al.*, 2002; de Pater, 2004) are now producing infrared images of Io comparable with those obtained by the *Galileo* NIMS instrument during the early (non-Io-targeted) fly-bys. These techniques are also now being combined with spectral observations beyond the instrument capabilities of *Galileo*. These types of observations will enable us to address several outstanding questions regarding the nature of activity on Io. For example, the existing eruption record suggests there may be a change in eruption style with latitude, with larger, more violent, but less frequent eruptions dominating at high latitudes. However, the current statistics are insufficient to firmly conclude this. Another outstanding question is the presence of ultramafic temperatures above the liquidus temperature of basalt. These were detected during, for example, the 1997 Pillan eruption (McEwen *et al.*, 1998b), but recent reanalyses of *Galileo* data cast the occurrence of ultramafic temperatures in doubt (A. G. Davies and L. P. Keszthelyi, pers. commun., 2006). High spatial

resolution observations at short enough wavelengths will be able to test for such temperatures during future eruptions. As techniques and telescope apertures increase (with corresponding increases in resolution) it will be possible to address additional questions.

In conclusion, observation of Io's volcanoes using data obtained by the *Galileo* spacecraft indicate that many, if not most, active volcanoes show evidence of producing both explosive and effusive deposits, and many volcanoes produce eruptions of more than one eruption style. For example, the Pele Volcano typically produces both intra-Patera and explosion-dominated events, whereas the Tvashtar Volcano was observed by *Galileo* to produce apparently all three types of eruption styles. Clearly, there is a complex and varying interaction between silicate magma with various volatile materials, including sulfur, SO_2, and perhaps Cl (Schmitt and Rodriguez, 2003). Heat from silicate magmas and lavas clearly mobilizes sulfur-rich surroundings, producing both extrusive and explosive sulfurous volcanic materials. The evidence for primary effusive sulfur and sulfur dioxide flows remains equivocal. What is clear from *Galileo* observations is that most resurfacing by lava flows is confined within paterae involving probable lava lakes. In addition, while various styles of lava flow emplacement involving silicate and sulfurous flows appear to occur on Io, the dominant mechanism for resurfacing the moon as a whole is by emplacement of explosive plume deposits driven by magma-volatile interactions. Yet many questions remain: What are the hottest temperatures of erupting silicate lavas on Io? Are these lavas ultramafic or superheated basalts? How extensive are primary sulfur flows? Are there actually extrusive SO_2 flows, and how are they emplaced? How do paterae form and maintain connections with their magma sources? Is there an "asthenosphere", and does it allow for a subsurface connection between primary volcanic centers? Answers to these and other questions about Io's volcanism must be addressed by ground-based observing campaigns while we await future missions to the Jovian system.

7.6 REFERENCES

Banfield, A. F. 1954. Volcanic deposits of elemental sulphur. *Can. Min. Metall. Bull.*, **47**, 769–775.

Basaltic Volcanism Study Project. 1981. *Basaltic Volcanism on the Terrestrial Planets*. Pergamon Press, New York, 1286pp.

Blaney, D. L., Johnson, T. V., Matson, D. L., and Veeder, G. J. 1995. Volcanic eruptions on Io: Heat flow, resurfacing, and lava composition. *Icarus*, **113**, 220–225.

Blaney, D. L., Veeder, G. J., Matson, D. L., Johnson, T. K., Goguen, J. D., and Spencer, J. R. 1997. Io's thermal anomalies: Clues to their origins from comparison of ground-based observations between 1 and 20 μm. *Geophys. Res. Lett.*, **24**, 2459–2462.

Bonaccorso, A., Calvari, S., Coltelli, M., Del Negro, C., and Falsaperla, S. 2004. *Mt. Etna: Volcano Laboratory* (Am. Geophys. Un. Monograph, 143). American Geophysical Union, Washington, D.C., 369pp.

Carlson, R. W., Weissman, P. R., Smythe, W. D., and Mahoney, J. C. 1992. Near-infrared mapping spectrometer experiment on Galileo. *Space Sci. Rev.*, **60**, 457–502.

Carlson, R. W., Smythe, W. D., Lopes-Gautier, R. M. C., Davies, A. G., Kamp, L. W., Mosher, J. A., Soderblom, L. A., Leader, F. E., Mehlman, R., Clark, R. N., *et al.* 1997. The distribution of sulfur dioxide and other infrared absorbers on the surface of Io. *Geophys. Res. Lett.*, **24**, 2479–2482.

Carr, M. H. 1986. Silicate volcanism on Io. *Journal Geophys. Res.*, **91**, 3521–3532.

Cas, R. A. F. and Beresford, S. W. 2001. Field characteristics and erosional processes associated with komatiitic lavas: Implications for flow behavior. *Can. Mineral.*, **39**, 505–524.

Christensen, P. R., and 11 coauthors. 2005. Evidence for magmatic evolution and diversity on Mars from infrared observations. *Nature*, **436**, doi:10.1038/nature03639.

Clow, G. D. and Carr, M. H. 1980. Stability of sulfur slopes on Io. *Icarus*, **44**, 268–279.

Davies, A. G. 1996. Io's volcanism: Thermo-physical models of silicate lava compared with observations of thermal emission. *Icarus*, **124**, 45–61.

Davies, A. G. 2003. Temperature, age and crust thickness distributions of Loki Patera on Io from Galileo NIMS data: Implications for resurfacing mechanism. *Geophys. Res. Lett.*, **30**, doi:10.1029/2003GL018371.

Davies, A. G., Keszthelyi, L. P., Williams, D. A., Phillips, C. B., McEwen, A. S., Lopes, R. M. C., Smythe, W. D., Kamp, L. W., Soderblom, L. A., and Carlson, R. W. 2001. Thermal signature, eruption style and eruption evolution at Pele and Pillan on Io. *Journal Geophys. Res.*, **106**, 33079–33104.

de Pater, I., Marchis, F., Macintosh, B. A., Roe, H. G., Le Mignant, D., Graham, J. R., and Davies, A. G. 2004. Keck AO observations of Io in and out of eclipse. *Icarus*, **169**, 250–263.

De Wit, M. J. and Ashwal, L. D. 1997. *Greenstone Belts*. Oxford University Press, New York, 809pp.

Descamps, P., Arlot, J. E., Thuillot, W., Colas, F., Vu, D. T., Bouchet, P., and Hainaut, O. 1992. Observations of the volcanoes of Io, Loki and Pele, made in 1991 at the ESO during an occultation by Europa. *Icarus*, **100**, 235–244.

Douté, S., Schmitt, B., Lopes-Gautier, R., Carlson, R., Soderblom, L., Shirley, J., and the Galileo NIMS Team. 2001. Mapping SO_2 frost on Io by the modeling of NIMS hyperspectral images. *Icarus*, **149**, 107–132.

Douté, S., Lopes, R., Kamp, L. W., Carlson, R., Schmitt, B., and the Galileo NIMS Team. 2002. Dynamics and evolution of SO_2 gas condensation around Prometheus-like volcanic plumes on Io as seen by the Near-Infrared Mapping Spectrometer. *Icarus*, **158**, 460–482.

Douté, S., Lopes, R., Kamp, L. W., Carlson, R., Schmitt, B., and the Galileo NIMS Team. 2004. Geology and activity around volcanoes on Io from the analysis of NIMS spectral images. *Icarus*, **169**, 175–196.

Fanale, F. P., Brown, R. H., Cruikshank, D. P., and Clark, R. N. 1979. Significance of absorption features in Io's IR reflectance spectrum. *Nature*, **280**, 761–763.

Geissler, P. E., McEwen, A. S., Keszthelyi, L., Lopes-Gautier, R., Granahan, J., and Simonelli, D. P. 1999. Global color variations on Io. *Icarus*, **140**, 265–282.

Goguen, J. D. and Sinton, W. M. 1985. Characterization of Io's volcanic activity by infrared polarimetry. *Science*, **230**, 65–69.

Goguen, J. D., Lubenow, A., and Storrs, A. 1998. HST NICMOS images of Io in Jupiter's shadow. *Bull. Am. Astro. Soc.*, **30**, 1120.

Goguen, J. D., Matson, D. L., Sinton, W. M., Howell, R. R., and Dyck, H. M. 1988. Io hot spots: Infrared photometry of satellite occultations. *Icarus*, **76**, 465–484.

Greeley, R., Theilig, E., and Christensen, P. 1984. The Mauna Loa sulfur flow as an analog to secondary sulfur flows (?) on Io. *Icarus*, **60**, 189–199.

Gregg, T. K. P. and Lopes, R. M. 2004. Lava lakes on Io: New perspectives from modeling. *Lunar & Planetary Science Conference*, **XXXV**, Abstract #1558.

Hanel, R., Conrath, B., Flaser, M., Kunde, V., Lowman, P., Maguire, W., Pearl, J., Pirraglia, J., Samuelson, R., Gautier, D., Gierasch, P. *et al.* 1979. Infrared observations of the Jovian system from Voyager 1. *Science*, **204**, 972–976.

Hansen, O. L. 1973. Ten-micron eclipse observations of Io, Europa, and Ganymede. *Icarus*, **18**, 237–246.

Hapke, B. 1989. The surface of Io: A new model. *Icarus*, **79**, 56–74.

Harris, A. J. L., Sherman, S. B., and Wright, R. 2000. Discovery of self-combusting volcanic sulfur flows. *Geology*, **28**, 415–418.

Heliker, C., Swanson, D. A., and Takahashi, T. J. 2003. *The Pu'u' O'o'-Kupaianaha Eruption of Kilauea Volcano, Hawai'i: The First 20 Years* (USGS Prof. Pap., **1676**). U.S. Geological Survey, Reston, Virginia, 206pp.

Hess, H. H. and Poldervaart, A. 1967. *Basalts: The Poldervaart Treatise on Rocks of Basaltic Composition*. Interscience Publishers, New York.

Hill, R. E. T., Barnes, S. J., Gole, M. J., and Dowling, S. E. 1990. *Physical Volcanology of Komatiites* (Geol. Soc. Austral. (W.A. Div.) Excursion Guide Book 1). Geological Society of Australia (Western Australia Division), Perth, 100pp.

Hill, R. E. T., Barnes, S. J., and Dowling, S. E. 2001. *Komatiites of the Norseman-Wiluna Greenstone Belt, Western Australia: A Field Guide* (Geol. Surv. West. Austral. Rec., **2001/10**). Geological Survey of Western Australia, Perth, 71pp.

Hon, K., Kauahikaua, J., Delinger, R., and Mackay, K. 1994. Emplacement and inflation of pahoehoe sheet flows: Observations and measurements of active lava flows on Kilauea Volcano, Hawaii. *Geol. Soc. Am. Bull.*, **106**, 351–370.

Howell, R. R. 1997. Thermal Emission from Lava Flows on Io. *Icarus*, **127**, 394–407.

Howell, R. R. and McGinn, M. T. 1985. Infrared speckle observations of Io: An eruption in the Loki region. *Science*, **230**, 63–65.

Howell, R. R., Spencer, J. R., Goguen, J. D., Marchis, F., Prangé, R., Fusco, T., Blaney, D. L., Veeder, G. J., Rathbun, J. A., Orton, G. S., Grocholski, A. J. *et al.* 2001. Ground-based observations of volcanism on Io in 1999 and early 2000. *J. Geophys. Res.*, **106**, 33129–33140.

Howell, R. R. and Lopes, R. M. 2004. Characterization of activity at Loki from Galileo and ground-based observations. *Lunar & Planetary Science Conference*, **XXXV**, Abstract #2071.

Huppert, H. E. and Sparks, R. S. J. 1985. Komatiites I: Eruption and flow. *J. Petrol.*, **26**, 694–725.

Jaeger, W. L., Turtle, E. P., Keszthelyi, L. P., Radebaugh, J., and McEwen, A. S. 2003. Orogenic tectonism on Io. *J. Geophys. Res.*, **108**, doi:10.1029/2002JE001946.

Johnson, R. E. 1997. Polar caps on Ganymede and Io revisited. *Icarus*, **128**, 469–471.

Johnson, T. V., Morrison, D., Matson, D. L., Veeder, G. J., Brown, R. H., and Nelson, R. M. 1984. Volcanic hotspots on Io: Stability and longitudinal distribution. *Science*, **226**, 134–137.

Johnson, T. V., Veeder, G. J., Matson, D. L., Brown, R. H., and Nelson, R. M. 1988. Io: Evidence for silicate volcanism in 1986. *Science*, **242**, 1280–1283.

Kargel, J. S., Delmelle, P., and Nash, D. B. 1999. Volcanogenic sulfur on Earth and Io: Composition and spectroscopy. *Icarus*, **142**, 249–280.

Kargel, J. S., and 23 coauthors. 2003. Extreme volcanism on Io: Latest insights at the end of Galileo era. *Eos*, **84**, 313, 318.

Keszthelyi, L., McEwen, A. S., Phillips, C. B., Milazzo, M., Geissler, P., Turtle, E. P., Radebaugh, J., Williams, D. A., Simonelli, D., Breneman, H. *et al.* 2001. Imaging of volcanic activity on Jupiter's moon Io by Galileo during GEM and GMM. *J. Geophys. Res.*, **106**, 33025–33052.

Kieffer, S. W., Lopes-Gautier, R., McEwen, A., Smythe, W., Keszthelyi, L., and Carlson, R. 2000. Prometheus: Io's wandering plume. *Science*, **288**, 1204–1208.

Klaasen, K. P., Clary, M. C., and Janesick, J. R. 1984. Charge-coupled device television camera for NASA's Galileo Mission to Jupiter. *Opt. Eng.*, **23**, 334–342.

Kupo, I., Mekler, Y., and Eviatar, A. 1976. Detection of ionized sulfur in the Jovian magnetosphere. *Astrophys. Journal Lett.*, **205**, L51–L53.

Lopes-Gautier, R., McEwen, A. S., Smythe, W. B., Geissler, P. E., Kamp, L., Davies, A. G., Spencer, J. R., Keszthelyi, L., Carlson, R., Leader, F. E., *et al.* 1999. Active Volcanism on Io: Global distribution and variations in activity. *Icarus*, **140**, 243–264.

Lopes-Gautier, R., Douté, S., Smythe, W. D., Kamp, L. W., Carlson, R. W., Davies, A. G., Leader, F. E., McEwen, A. S., Geissler, P. E., Kieffer, S. W., *et al.* 2000. A close-up look at Io in the infrared: Results from Galileo's Near-Infrared Mapping Spectrometer. *Science*, **288**, 1201–1204.

Lopes, R. M. C., Kamp, L. W., Douté, S., Smythe, W. D., Carlson, R. W., McEwen, A. S., Geissler, P. E., Kieffer, S. W., Leader, F. E., Davies, A. G., *et al.* 2001. Io in the near-infrared: NIMS results from the Galileo fly-bys in 1999 and 2000. *J. Geophys. Res.*, **106**, 33053–33078.

Lopes, R. M. C., Kamp, L. W., Davies, A. G., Smythe, W. D., Carlson, R. W., Douté, S., McEwen, A., Turtle, E. P., Leader, F., Mehlman, R., *et al.* 2002. Galileo's last fly-bys of Io: NIMS observations of Loki, Tupan, and Emakong calderas. *Lunar & Planetary Science Conference*, **XXXIII**, Abstract #1739.

Lopes, R. M. C., Kamp, L. W., Smythe, W. D., Mouginis-Mark, P., Kargel, J., Radebaugh, J., Turtle, E. P., Perry, J., Williams, D. A., Carlson, R.W., *et al.* 2004. Lava lakes on Io: Observations of Io's volcanic activity from Galileo NIMS during the 2001 fly-bys. *Icarus*, **169**, 140–174.

MacDonald, G. A. 1967. Forms and structures of extrusive basaltic rocks. In: Hess, H. H. and Poldervaart, A. (eds), *Basalts: The Poldervaart Treatise on Rocks of Basaltic Composition*. Interscience Publishers, New York, pp. 1–58.

McBirney, A. R. 1993. *Igneous Petrology*. Jones & Bartlett Publishers, London, 508pp.

McEwen, A. S. and Soderblom, L. A. 1983. Two classes of volcanic plumes on Io. *Icarus*, **55**, 191–217.

McEwen, A. S., Soderblom, L. A., Matson, D. L., and Johnson, T. V. 1985. Volcanic hot spots on Io: Correlation with low-albedo calderas. *J. Geophys. Res.*, **90**, 12345–12379.

McEwen, A. S., Keszthelyi, L., Geissler, P., Simonelli, D. P., Carr, M. H., Johnson, T. V., Klaasen, K. P., Breneman, H. H., Jones, T. J., Kaufman, J. M., *et al.* 1998a. Active volcanism on Io as seen by Galileo SSI. *Icarus*, **135**, 181–219.

McEwen, A. S., Keszthelyi, L., Spencer, J. R., Schubert, G., Matson, D. L., Lopes-Gautier, R., Klaasen, K. P., Johnson, T. V., Head, J. W., Geissler, P., *et al.* 1998b. High-temperature silicate volcanism on Jupiter's moon Io. *Science*, **281**, 87–90.

McEwen, A. S., Belton, M. J. S., Breneman, H. H., Fagents, S. A., Geissler, P., Greeley, R., Head, J. W., Hoppa, G., Jaeger, W. L., Johnson, T. V. *et al.* 2000. Galileo at Io: Results from high-resolution imaging. *Science*, **288**, 1193–1198.

McLeod, B. A., McCarthy, D. W., Jr., and Freeman, J. 1991. Global high-resolution imaging of hotspots on Io. *Astronom. Journal*, **102**, 1485–1489.

Marchis, F., Prangé, R., and Christou, J. 2000. Adaptive optics mapping of Io's volcanism in the thermal IR (3.8 μm). *Icarus*, **148**, 384–396.

Marchis, F., Prangé, R., and Fusco, T. 2001. A survey of Io's volcanism by adaptive optics observations in the 3.8-μm thermal band (1996–1999). *J. Geophys. Res.*, **106**, 33141–33160.

Marchis, F., de Pater, I., Davies, A. G., Roe, H. G., Fusco, T., Le Mignant, D., Descamps, P., Macintosh, B. A., and Prangé, R. 2002. High-resolution Keck adaptive optics imaging of violent volcanic activity on Io. *Icarus*, **160**, 124–131.

Matson, D. L., Ransford, G. A., and Johnson, T. V. 1981. Heat flow from Io JI. *J. Geophys. Res.*, **86**, 1664–1672.

Medina, F., Echevarria, J., Ledezma, E., and Martinez, F. 1989. Infrared observations of Io during the mutual events of 1985: Evidence of volcanic activity? *Astronomy and Astrophysics*, **220**, 313–317.

Milazzo, M. P., Keszthelyi, L. P., and McEwen, A. S. 2001. Observations and initial modeling of lava–SO_2 interactions at Prometheus, Io. *J. Geophys. Res.*, **106**, 33121–33128.

Milazzo, M. P., Keszthelyi, L. P., Radebaugh, J., Davies, A. G., Turtle, E. P., Geissler, P., Klaasen, K. P., Rathbun, J. A., and McEwen, A. S. 2005. Volcanic activity at Tvashtar Catena, Io. *Icarus*, **179**, 235–251.

Morabito, L. A., Synnott, S. P., Kupferman, P. N., and Collins, S. A. 1979. Discovery of currently active extraterrestrial volcanism. *Science*, **204**, 972.

Morrison, D. and Cruikshank, D. P. 1973. Thermal properties of the Galilean satellites. *Icarus*, **18**, 224–236.

Morrison, D. and Telesco, C. M. 1980. Io: Observational constraints on internal energy and thermophysics of the surface. *Icarus*, **44**, 226–233.

Morrison, D., Pieri, D., Johnson, T. V., and Veverka, J. 1979. Photometric evidence on long-term stability of albedo and colour markings on Io. *Nature*, **280**, 753–755.

Naranjo, J. A. 1985. Sulphur flows at Lastarria volcano in the North Chilean Andes. *Nature*, **313**, 778–780.

Nash, D. B. 1987. Sulfur in vacuum: Sublimation effects on frozen melts, and applications to Io's surface and torus. *Icarus*, **72**, 1–34.

Nash, D. B. and Nelson, R. M. 1979. Spectral evidence for sublimates and adsorbates on Io. *Nature*, **280**, 763–766.

Oppenheimer, C. 1992. Sulphur eruptions at Volcán Poás, Costa Rica. *J. Volcanol. Geotherm. Res.*, **49**, 1–21.

O'Reilly, T. C. and Davies, G. F. 1981. Magma transport of heat on Io: A mechanism allowing a thick lithosphere. *Geophys. Res. Let.*, **8**, 313–316.

Peale, S. J., Cassen, P., and Reynolds, R. T. 1979. Melting of Io by tidal dissipation. *Science*, **203**, 892–894.

Pearl, J. C. and Sinton, W. M. 1982. Hot spots of Io. In: D. Morrison and M. S. Matthews (eds), *Satellites of Jupiter*. University of Arizona Press, Tucson, AZ, pp. 724–755.

Pearl, J., Hanel, R., Kunde, V., Maguire, W., Fox, K., Gupta, S., Ponnamperuma, C., and Raulin, F. 1979. Identification of gaseous SO_2 and new upper limits for other gases on Io. *Nature*, **280**, 755–758.

Pieri, D., Baloga, S. M., Nelson, R. M., and Sagan, C. 1984. Sulfur flows of Ra Patera, Io. *Icarus*, **60**, 685–700.

Radebaugh, J., Keszthelyi, L. P., McEwen, A. S., Turtle, E. P., Jaeger, W., and Milazzo, M. 2001. Paterae on Io: A new type of volcanic caldera? *J. Geophys. Res.*, **106**, 33005–33020.

Radebaugh, J., McEwen, A. S., Milazzo, M. P., Keszthelyi, L. P., Davies, A. G., Turtle, E. P., and Dawson, D. D. 2004. Observations and temperatures of Io's Pele Patera from Cassini and Galileo spacecraft images. *Icarus*, **169**, 65–79.

Rathbun, J. A., Spencer, J. R., Davies, A. G., Howell, R. R., and Wilson, L. 2002. Loki, Io: A periodic volcano. *Geophys. Res. Lett.*, **29**(10), 10.1029/2002GL014747.

Rathbun, J. A., Johnson, S. T., and Spencer, J. R. 2003. Loki, Io: An update from ground-based data. *Lunar & Planetary Science Conference*, **XXXIV**, Abstract #1375.

Reidel, S. P. and Hooper, P. R. 1989. *Volcanism and Tectonism in the Columbia River Flood Basalt Province* (Geol. Soc. Am. Sp. Pap., **239**). Geological Society of America, Boulder, 386pp.

Rhodes, J. M. and Lockwood, J. P. 1995. *Mauna Loa Revealed: Structure, Composition, History, and Hazards* (Am. Geophys. Un. Monograph, **92**). American Geophysical Union, Washington, D.C., 348pp.

Ross, M. N., Schubert, G., Spohn, T., and Gaskell, R. W. 1990. Internal structure of Io and the global distribution of its topography. *Icarus*, **85**, 309–325.

Sagan, C. 1979. Sulphur flows on Io. *Nature*, **280**, 750–753.

Schaber, G. G. 1982. The geology of Io. In: Morrison, D. and Matthews, M. S. (eds), *Satellites of Jupiter*. University of Arizona Press, Tucson, TX, pp. 556–597.

Schenk, P. M., Hargitai, H., Wilson, R., McEwen, A., and Thomas, P. 2001. The mountains of Io: Global and geological perspectives from Voyager and Galileo. *J. Geophys. Res.*, **106**, 33201–33222.

Schmitt, B. and Rodriguez, S. 2003. Possible identification of local deposits of Cl_2SO_2 on Io from NIMS/Galileo spectra. *J. Geophys. Res.*, **108**(E9), 5104, doi:10.1029/2002JE001988.

Schmincke, H.-U. 2004. *Volcanism*. Springer, Berlin, 324pp.

Self, S., Thordarson, T., and Keszthelyi, L. 1997. Emplacement of continental flood basalt lava flows. In: J. J. Mahoney and M. F. Coffin (eds), *Large Igneous Provinces: Continental, Oceanic, and Planetary Flood Volcanism* (Am. Geophys. Un. Monograph, **100**). American Geophysical Union, Washington, D.C., pp. 381–410.

Shaw, H. R. and Swanson, D. A. 1970. Eruption and flow rates of flood basalts. In: Gilmour, E. H. and Stradling, D. (eds), *Proceedings of the 2nd Columbia River Basalt Symposium*. East Washington State Press, Cheney, pp. 271–299.

Sinton, W. M. 1980. Io's 5 micron variability. *Astrophys. Journal Lett.*, **235**, L49–L51.

Sinton, W. M. 1981. The thermal emission spectrum of Io and a determination of the heat flux from its hot spots. *J. Geophys. Res.*, **86**, 3122–3128.

Sinton, W. M., Tokunaga, A. T., Becklin, E. E., Gatley, I., Lee, T. J., and Lonsdale, C. J. 1980. Io: Ground-based observations of hot spots. *Science*, **210**, 1015–1017.

Sinton, W. M., Lindwall, D., Cheigh, F., and Tittemore, W. C. 1983. Io: The near-infrared monitoring program, 1979–1981. *Icarus*, **54**, 133–157.

Skinner, B. J. 1970. A sulfur lava flow on Mauna Loa. *Pac. Sci.*, **24**, 144–145.

Smellie, J. L. and Chapman, M. G. 2002. *Volcano–Ice Interaction on Earth and Mars* (Geol. Soc. Sp. Pub., **202**). The Geological Society, London, 431pp.

Smith, B. A., Soderblom, L. A., Johnson, T. V., Ingersoll, A. P., Collins, S. A., Shoemaker, E. M., Hunt, G. E., Masursky, H., Carr, M. H., Davies, M. E. *et al.* 1979. The Jupiter system through the eyes of Voyager 1. *Science*, **204**, 951–957.

Smythe, W. D., Nelson, R. M., and Nash, D. B. 1979. Spectral evidence for SO_2 frost or adsorbate on Io's surface. *Nature*, **280**, 766.

Smythe, W. D., Lopes-Gautier, R., Ocampo, A., Hui, J., Segura, M., Soderblom, L. A., Matson, D. L., Kieffer, H. H., McCord, T. B., Fanale, F. P., *et al.* 1995. Galilean

satellite observation plans for the near-infrared mapping spectrometer experiment on the Galileo spacecraft. *J. Geophys. Res.*, **100**, 18957–18972.

Smythe, W. D., Lopes-Gautier, R., Douté, S., Kieffer, S. W., Carlson, R. W., Kamp, L., and Leader, F. E. 2000. Evidence for massive sulfur dioxide deposit on Io. *Bull. Am. Astron. Soc.*, **32**(3), 1047.

Spencer, J. R., Shure, M. A., Ressler, M. E., Sinton, W. M., and Goguen, J. D. 1990. Discovery of hotspots on Io using disk-resolved infrared imaging. *Nature*, **348**, 618–621.

Spencer, J. R., Clark, B. E., Toomey, D., Woodney, L. M., and Sinton, W. M. 1994. Io hot spots in 1991: Results from Europa occultation photometry and infrared imaging. *Icarus*, **107**, 195–208.

Spencer, J. R., McEwen, A. S., McGrath, M. A., Sartoretti, P., Nash, D. B., Noll, K. S., and Gilmore, D. 1997. Volcanic resurfacing of Io: Post-repair HST imaging. *Icarus*, **127**, 221–237.

Spencer, J. R., Jessup, K. L., McGrath, M. A., Ballester, G. E., and Yelle, R. 2000a. Discovery of gaseous S_2 in Io's Pele plume. *Science*, **288**, 1208–1210.

Spencer, J. R., Rathbun, J. A., Travis, L. D., Tamppari, L. K., Barnard, L., Martin, T. Z., and McEwen, A. S. 2000b. Io's thermal emission from the Galileo Photopolarimeter–Radiometer. *Science*, **288**, 1198–1201.

Stansberry, J. A., Spencer, J. R., Howell, R. R., Dumas, C., and Vakil, D. 1997. Violent silicate volcanism on Io in 1996. *Geophys. Res. Lett.*, **24**, 2455–2458.

Steudel, R., Holdt, G., and Young, A. T. 1986. On the colors of Jupiter's satellite Io: Irradiation of solid sulfur at 77 K. *J. Geophys. Res.*, **91**, 4971–4977.

Tackley, P. J., Schubert, G., Glatzmaier, G. A., Schenk, P., Ratcliff, J. T., and Matas, J.-P. 2001. Three dimensional simulations of mantle convection in Io. *Icarus*, **149**, 79–91.

Theilig, E. 1982. A primer on sulfur for the planetary geologist (NASA Contractor Report 3594). NASA, Reston, VA, 34pp.

Thordarson, T. and Self, S. 1993. The Laki (Skaftár Fires) and Grímsvötn eruptions in 1783–1785. *Bull. Volcanol.*, **55**, 233–263.

Thordarson, T. and Self, S. 1998. The Roza Member, Columbia River Basalt Group: A gigantic pahoehoe lava flow field formed by endogeneous processes? *J. Geophys. Res.*, **103**, 27411–27445.

Turtle, E. P., Keszthelyi, L. P., McEwen, A. S., Radebaugh, J., Milazzo, M., Simonelli, D. P., Geissler, P., Williams, D. A., Perry, J., Jaeger, W. L. *et al.* 2004. The final Galileo SSI observations of Io: Orbits G28-I33. *Icarus*, **169**, 3–28.

Veeder, G. J., Matson, D. L., Johnson, T. V., Blaney, D. L., and Goguen, J. D. 1994. Io's heat flow from infrared radiometry: 1983–1993. *J. Geophys. Res.*, **99**, 17095–17162.

Watanabe, T. 1940. Eruptions of molten sulphur from the Siretoko-Isan Volcano, Hokkaid, Japan. *Jpn. J. Geol. Geog.*, **17**, 289–310.

Wentworth, C. K. and Macdonald, G. A. 1953. Structures and forms of basaltic rocks in Hawaii. *U.S. Geol. Surv. Bull.*, **994**, 1–98.

Williams, D. A., Wilson, A. H., and Greeley, R. 2000a. A komatiite analog to potential ultramafic materials on Io. *J. Geophys. Res.*, **105**, 1671–1684.

Williams, D. A., Fagents, S. A., and Greeley, R. 2000b. A reassessment of the emplacement and erosional potential of turbulent, low-viscosity lavas on the Moon. *J. Geophys. Res.*, **105**, 20189–20205.

Williams, D. A., Davies, A. G., Keszthelyi, L. P., and Greeley, R. 2001a. The summer 1997 eruption at Pillan Patera on Io: Implications for ultrabasic lava flow emplacement. *J. Geophy. Res.*, **106**, 33105–33119.

Williams, D. A., Greeley, R., Lopes-Gautier, R. M. C., and Douté, S. 2001b. Evaluation of sulfur flow emplacement on Io from Galileo data and numerical modeling. *J. Geophys. Res.*, **106**, 33161–33174.

Williams, D. A., Radebaugh, J., Keszthelyi, L. P., McEwen, A. S., Lopes, R. M. C., Douté, S. and Greeley, R. 2002. Geologic mapping of the Chaac-Camaxtli region of Io from Galileo imaging data. *J. Geophys. Res.*, **107**, 5068, doi:10.1029/2001JE001821.

Williams, D. A., Schenk, P. M., Moore, J. M., Keszthelyi, L. P., Turtle, E. P., Jaeger, W. L., Radebaugh, J., Milazzo, M. P., Lopes, R. M. C., and Greeley, R. 2004. Mapping of the Culann-Tohil region of Io from Galileo imaging data. *Icarus*, **169**, 80–97.

Witteborn, F. E., Bregman, J. D., and Pollack, J. B. 1979. Io: An intense brightening near 5 micrometers. *Science*, **203**, 643–646.

Yoder, C. F. 1979. How tidal heating in Io drives the Galilean orbital resonance locks. *Nature*, **279**, 767–770.

Young, A. T. 1984. No sulfur flows on Io. *Icarus*, **58**, 197–226.

Zimbelman, J. R. and Gregg, T. K. P. 2000. *Environmental Effects on Volcanic Eruptions: From Deep Oceans to Deep Space*. Kluwer Academic/Plenum Publishers, New York, 260pp.

8

Plumes and their deposits

Paul E. Geissler and David B. Goldstein

8.1 INTRODUCTION

The *Voyager 1* spacecraft's discovery in 1979 of enormous plumes of dust and gas reaching hundreds of kilometers above Io's surface provided the first spectacular evidence of active volcanism beyond Earth. Four months later, the fly-by of *Voyager 2* revealed changes in the distribution and vigor of the plumes that hinted at the variability of explosive eruptions on Io. Decades of observations by ground-based and Earth-orbiting telescopes and the recent targeted campaigns by the *Galileo* and *Cassini* missions have since revealed much about the nature of Io's volcanic plumes. At the same time, theoretical advances have deepened our understanding of the dynamics and chemistry of these intriguing phenomena.

Over 400 volcanic paterae dot the surface of Io (Radebaugh *et al*., 2001), and more than 150 active hot spots have been detected through their thermal emission (Lopes *et al*., 2004). Only a handful of these volcanoes have so far been seen to produce explosive eruptions (defined here as emplacing pyroclastic deposits). Plumes of gas and dust have been observed from 16 different volcanic centers on Io (Table 8.1). Several other sites of recent plume activity can be inferred from surface changes and frost deposits. The temporal behavior of the plumes ranges from episodic big bangs to quasi-continuous fountains; several of the plumes have apparently been sustained for decades. Observations of the plumes and their deposits indicate two distinct classes of plumes on Io: giant plumes that vent sulfur-rich gases from the interior of the moon and spray-paint the surface with enormous red rings, and more numerous smaller plumes that are produced when hot flows of silicate lava impinge on volatile surface ices of SO_2.

Io's plumes are generated when volatile vapors are violently expelled from volcanoes, at speeds reaching up to $1\,\mathrm{km\,s^{-1}}$. Many of the dynamical features displayed by Io's plumes are expected from the flow of gas out of a nozzle and into a near-vacuum. Close to the vent, the gas behaves as a continuum and the

Table 8.1. Plumes observed on Io. Latitudes and longitudes are those of the center of the surface changes produced by the plumes. Heights of dust columns are listed for *Galileo* era plumes seen near the limb, corrected for geometric foreshortening.

Name	Lat.	Lon.	Orb.	Image	Filter	GMT (M/D/Y H:M)	Res. (km/pixel)	Meas. height (km)	Meas. error (km)	Corr. height (km)	Corr error (km)	Position/ notes
Kanehekili	−19	34	G8	s0394435001	VIOLET	5/6/1997 22:52	13.0	70.2	13	75	14	limb
	−16	36	E11	s0420900323	VIOLET	11/8/1997 18:45	19.5	100.7	20	101	20	limb
Masubi	−44	54	C21	s0506406118	VIOLET	7/2/1999 4:04	2.6	82.2	20	87	21	limb
	−44	54	C21	s0506406153	VIOLET	7/2/1999 4:05	3.3	91.0	10	96	11	limb
	−44	54	C21	s0506406800	GREEN	7/2/1999 4:11	1.6	74.9	10	80	11	limb
	−44	54	C21	s0506584123	VIOLET	7/3/1999 10:04	16.7	93.9	20	99	21	limb
	−44	54	C22	s0512352501	VIOLET	8/12/1999 22:09	10.8	63.1	20	64	20	limb
	−44	54	C22	s0512375600	VIOLET	8/13/1999 2:02	12.8	64.0	20	92	29	limb
	−44	54	I31	s0615693301	VIOLET	8/7/2001 12:58	19.6	61.4	20	91	30	limb
	−44	54	I31	s0615816301	VIOLET	8/8/2001 9:42	19.9					terminator
Amirani	21	112	C22	s0512420523	VIOLET	8/13/1999 9:37	15.9	36.6	15	66	27	limb
	21	112	C22	s0512436201	GREEN	8/13/1999 12:15	16.4	72.9	15	75	15	limb
	21	112	C22	s0512436223	VIOLET	8/13/1999 12:15	16.4	73.6	15	76	15	limb
	21	112	C22	s0512447700	GREEN	8/13/1999 14:11	16.5	36.4	20	86	47	limb
	21	112	C22	s0512447723	VIOLET	8/13/1999 14:12	16.5	36.8	20	87	47	limb
	23	115	E4	s0374850023	VIOLET	12/20/1996 10:27	18.3	40.4	20	72	36	limb
	24	116	G8	s0394478123	VIOLET	5/7/1997 6:09	9.8	52.8	15	60	17	limb
Maui	19	122								57–148		VGR obs.
Tvashtar	63	122	G29									Cassini obs.
Thor	39	131	I31	s0615325146	VIOLET	8/4/2001 22:56	18.3	103.3	18	107	19	limb
Prometheus	−1	155	G2	s0359402500	VIOLET	9/2/1996 23:15	30.8					terminator
	−1	155	G2	s0359653300	VIOLET	9/4/1996 17:31	21.9					terminator
	−1	155	G2	s0359722942	VIOLET	9/5/1996 5:15	18.7	56.5	20	86	30	limb
	−1	155	G2	s0359729642	VIOLET	9/5/1996 6:23	19.0	76.1	20	76	20	limb
	−1	155	G2	s0359736542	VIOLET	9/5/1996 7:33	19.3	38.9	20	67	35	limb
	−1	155	C3	s0368558239	CLEAR	11/6/1996 6:10	3.5					disk
	−1	155	E4	s0374575922	VIOLET	12/19/1996 12:15	11.7					disk
	−1	155	E6	s0383600826	VIOLET	2/19/1997 21:07	10.9					terminator
	−1	155	G8	s0394435001	VIOLET	5/6/1997 22:52	13.0					terminator
	−1	155	G8	s0394505123	VIOLET	5/7/1997 10:41	10.0	89.9	10	90	10	limb
	−1	155	C9	s0401785407	VIOLET	6/27/1997 13:33	8.3	66.4	16	71	17	limb

	−1	155	C9	s0401863204	VIOLET	6/28/1997 2:40	6.2	295.7	60	74	15	disk
	−1	155	C9	s0401876300	VIOLET	6/28/1997 4:52	12.7					terminator
	−1	155	E11	s0420730085	VIOLET	11/7/1997 14:05	9.3	68.2	10	79	12	limb
	−1	155	E11	s0420789285	VIOLET	11/8/1997 0:03	8.0					terminator
	−1	155	C21	s0506492200	VIOLET	7/2/1999 18:34	10.0					terminator
	−1	155	C22	s0512466924	VIOLET	8/13/1999 17:26	16.3	48.9	20	72	29	limb
Culann	−20	161	G1	s0350029700	CLEAR	6/30/1996 3:46	10.5					eclipse
	−20	161	G2	s0359729642	VIOLET	9/5/1996 6:23	19.0					limb, marginal detection
	−20	161	G8	s0394394200	CLEAR	5/6/1997 16:00	18.6					eclipse
	−20	161	E15	s0449843800	CLEAR	5/31/1998 0:17	14.0					eclipse
	−20	161	E15	s0449847913	CLEAR	5/31/1998 0:58	13.4					eclipse
Zamama	18	171	G1	s0349673978	VIOLET	6/26/1996 15:49	13.9	75.3	15	79	16	limb
	18	172	G8	s0394519124	VIOLET	5/7/1997 13:03	10.5	61.0	20	62	20	limb
	19	175	E11	s0420730085	VIOLET	11/7/1997 14:05	9.3	29.6	10	80	27	limb
	19	175	E11	s0420743485	VIOLET	11/7/1997 16:20	9.0	66.1	20	67	20	limb
	19	175	E11	s0420789285	VIOLET	11/8/1997 0:03	8.0					disk
	18	176	E14	s0440873652	VIOLET	3/29/1998 0:37	3.0					disk
	18	176	I24	s0520873452	VIOLET	10/11/1999 18:05	6.7					terminator
Volund	22	177								96–98		VGR obs.
Marduk	−23	211	G8	s0394552545	VIOLET	5/7/1997 18:41	11.4	51.0	20	52	20	limb
	−23	211	E11	s0420773085	VIOLET	11/7/1997 21:19	8.2	76.0	8	76	8	limb
	−25	212	C21	s0506405768	VIOLET	7/2/1999 4:01	2.9	32.9	10	92	28	limb
Pillan	−11	242	C9	s0401863204	VIOLET	6/28/1997 2:40	6.2	99.3	20	109	22	limb
	−12	243	E11	s0420789285	VIOLET	11/8/1997 0:03	8.0	105.4	25	118	28	limb
Pele	−18	255	E4	s0374850023	VIOLET	12/20/1996 10:27	18.3	180.9	20	426	47	limb
Loki	17	301								16–35		VGR obs.
	19	305								166–382		VGR obs.
Ra	−10	323	G1	s0350024288	VIOLET	6/29/1996 2:50	9.9	91.8	10	104	11	limb
Acala	10	335	G7	s0389608268	CLEAR	4/3/1997 1:29	33.3					eclipse
	10	335	G8	s0394394200	CLEAR	5/6/1997 16:00	18.6					eclipse
	10	335	C9	s0401957745	CLEAR	6/28/1997	14.6					eclipse
	10	335	C10	s0413546765	CLEAR	9/18/1997 3:34	13.3					eclipse
	10	335	C10	s0413799045	CLEAR	9/19/1997 22:40	11.4					eclipse
	10	335	E11	s0420858600	CLEAR	11/8/1997 11:44	13.7					eclipse
	12	331	E15	s0449843800	CLEAR	5/31/1998 0:17	14.0					eclipse
	12	331	E15	s0449847913	CLEAR	5/31/1998 0:58	13.4					eclipse

flow is dominated by momentum. The gas quickly accelerates and cools, both due to expansion and to thermal radiation. At the top of the plume, momentum is overcome by gravity and the gas collapses back toward the surface. Depending on plume density, the high-altitude flow may produce a canopy shaped shock as it encounters downfalling gas and decelerates below the speed of sound. The falling gas, approaching the top of the day-time atmosphere, may experience a second shock as it deposits a ring of condensed material about the source region. Moderately energetic flows can bounce when they re-impact, scouring the surface and producing successive concentric rings. Very small particles of solid or liquid phases will flow with the gas, but larger dust particles will decouple from the flow and follow ballistic trajectories.

In addition to presenting a fascinating display of gas dynamics, Io's plumes are important because of their effects on the surface and atmosphere of the satellite. Io's surface is continually coated with the fallout from plumes in a constantly changing variety of colors. Plumes contribute to the rapid resurfacing responsible for the burial of impact craters on the satellite's young surface. Explosive eruptions demonstrate the diverse styles of volcanic activity and provide direct indications of the composition of Io's interior. The plumes also add substantially to the structure of the tenuous atmosphere, affecting the composition and flux of materials escaping from Io and feeding the neutral clouds and plasma torus. Ejection of dust from Io's largest plumes creates the dust streams that emanate from Io and pervade the Jovian system and interplanetary space far from Jupiter.

This chapter will review what has so far been learned about Io's volcanic plumes from Earth-based observations, theoretical and numerical studies, and the recent results of *Galileo* and *Cassini*, and will highlight some of the outstanding unanswered questions. Io's plumes were vigorously studied soon after their discovery, and many important papers were published prior to the arrival of *Galileo* with results that remain useful today. Cook *et al*. (1979) first considered both ballistic and hydrodynamic models as limiting cases of plume flow, and concluded that the plume characteristics were best explained by dense flows that produced canopy shocks. Strom and Schneider (1982) presented detailed observational descriptions of the plumes that were imaged by *Voyagers 1* and *2*. Kieffer (1982) provided a thorough theoretical treatment of the thermodynamics of plumes and their possible sources. Johnson and Soderblom (1982) pointed out the possible roles of plumes in global resurfacing and heat flow. McEwen and Soderblom (1983) first recognized the distinction between the two classes of plumes on Io that is a central theme of this chapter.

Compared with the sources and sinks of plume materials, the appearance and behavior of Io's plumes are fairly well known from direct observation. Much of the uncertainty concerning these phenomena comes from considering the volcanic sources of plumes and the ultimate fate of plume materials long after they are shot from the surface. The nature of the vents and the volcanic plumbing that produces plumes is touched upon in Chapter 7. The influence of plumes on the structure and composition of the atmosphere is covered in Chapter 10. The escape of materials from Io and the effects of volcanism on the neutral clouds, plasma torus, and Jovian magnetosphere are described in Chapter 11.

8.2 OBSERVATIONS OF PLUMES

The plumes of Io have been studied with a variety of observational approaches. During day-time, plumes can best be seen when illuminated at high phase angles, via sunlight reflected by fine particles of solid or liquid that are entrained with or condensed from the vapor. Plumes have also been imaged in transmitted light, silhouetted against the disk of Jupiter (Spencer *et al.*, 1997) or casting shadows on the surface of Io. Plume gases have been observed through auroral emissions at near-infrared (de Pater *et al.*, 2002), visible (Geissler *et al.*, 1999, 2004a), and ultraviolet (Roesler *et al.*, 1999; Retherford *et al.*, 2000) wavelengths and inferred from analyses of thermal emission at millimeter wavelengths (Lellouch *et al.*, 1992, 1996). These diverse data sets yield various perspectives of plumes that are the pieces of a puzzle that must be put together by theory.

8.2.1 Dust

The most detailed information on plume morphologies comes from close-up images of eruptions that were taken in sunlight and show the distribution of dust-sized particles which may include entrained silicates, snow, and supercooled droplets. Consistent with the evidence presented by plume deposits and surface changes, images of these dust columns suggest two distinct types of volcanic plumes on Io.

Most dust plumes tend to be small and optically dense, typically reaching heights of less than 100 km. The archetype of this class of smaller plumes is Prometheus (Figure 8.1), which has been seen actively fountaining SO_2-rich gas and dust at every favorable observing opportunity since the *Voyager* fly-bys. The location of Prometheus's source has migrated more than 80 km over the 20 year interval between *Voyager* and *Galileo*, tracking the foot of a lava flow that has been issuing from a small patera to the east (McEwen *et al.*, 1998). The presently active plume is centered over an expanse of recently emplaced silicate lava. It is suggested that the plume arises when hot silicate lavas bury the icy, SO_2-rich substrate (Kieffer *et al.*, 2000). Smaller jets at the active margin of the flow can also be seen in *Galileo* images (Milazzo *et al.*, 2001). Several similarly sized plumes are associated with lava flows elsewhere on the satellite. The morphology of these smaller plumes ranges from fountain- to umbrella-shaped, with an optically thick core near the source region. An image of the shadow of Prometheus, taken during *Galileo*'s orbit 9, shows a dense vertical column of dust topped by a mushroom-shaped canopy. A central spike in the column may be populated by fine particulates (Zhang *et al.*, 2004). Wispy filaments have been spotted in the dust streams from Prometheus, suggestive of plume electrification (Peratt and Dessler, 1988).

The second class of plumes, exemplified by Pele (Figure 8.2), is rarer and more energetic than the first. These giant plumes are faint and difficult to see in reflected light, but typically form shield-shaped dust streams that reach heights up to 400 km. Pele was nearly invisible to *Galileo*'s imaging system but could be clearly seen spanning an expanse more than 1,000 km across in ultraviolet images taken by *Cassini*'s camera (Porco *et al.*, 2003). Pele's source appears to be an actively

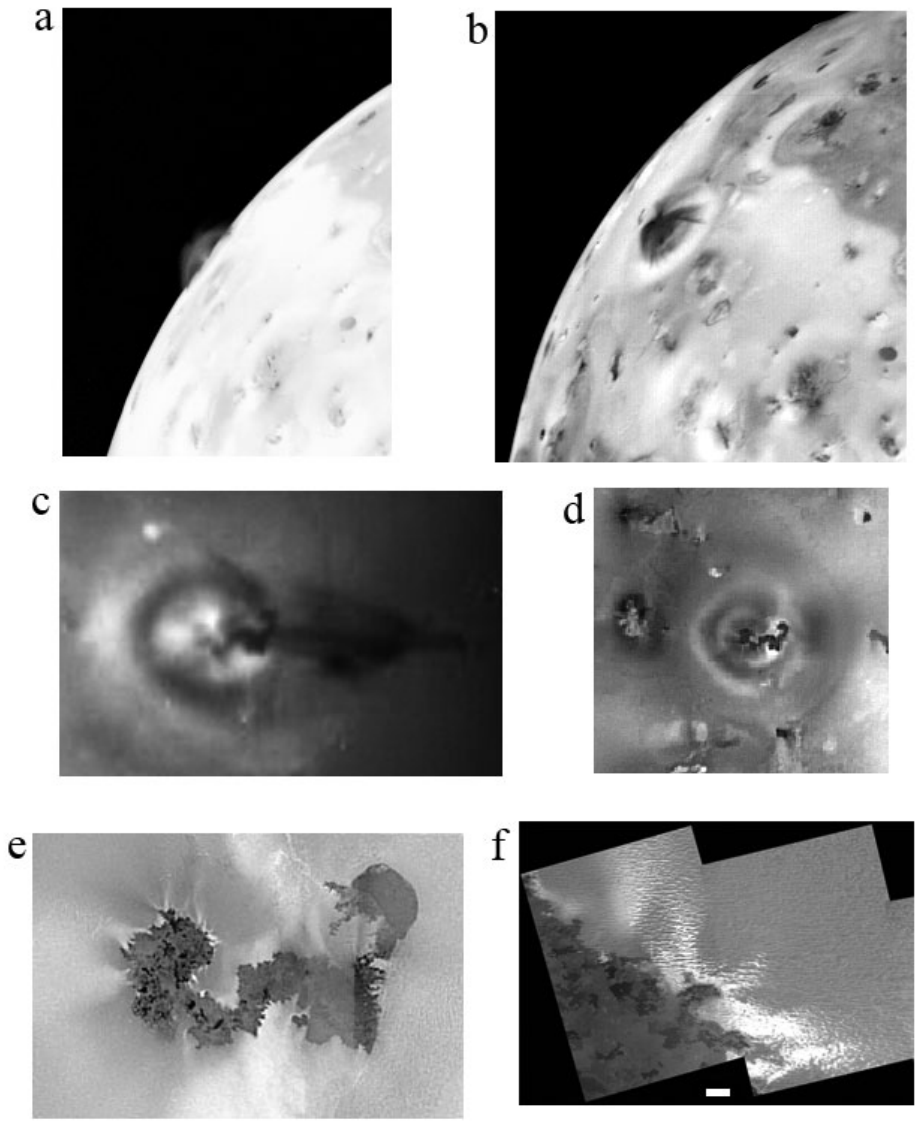

Figure 8.1. Prometheus, the archetype of small plumes. (a) *Voyager 1* image profiling Prometheus's umbrella-shaped dust plume along Io's limb (NASA press release image PIA00374). (b) Oblique *Voyager 1* image showing filaments in the dust plume (NASA press release image PIA00373). (c) *Galileo* image of the shadow cast by the plume (NASA press release image PIA00703). (d) *Galileo* violet-filter image of Prometheus's concentric rings, taken on orbit 14 (NASA press release image PIA01604). (e) *Galileo* image of the source of the plume, a lava flow that extends ~100 km westwards from Prometheus Patera (NASA press release image PIA2565). (f) Close-up view of the margin of the lava flow, showing fresh deposits of bright SO_2 frost where the dark silicate lava has encroached on the icy surface. Scale bar is 1 km long (NASA press release image PIA02568).

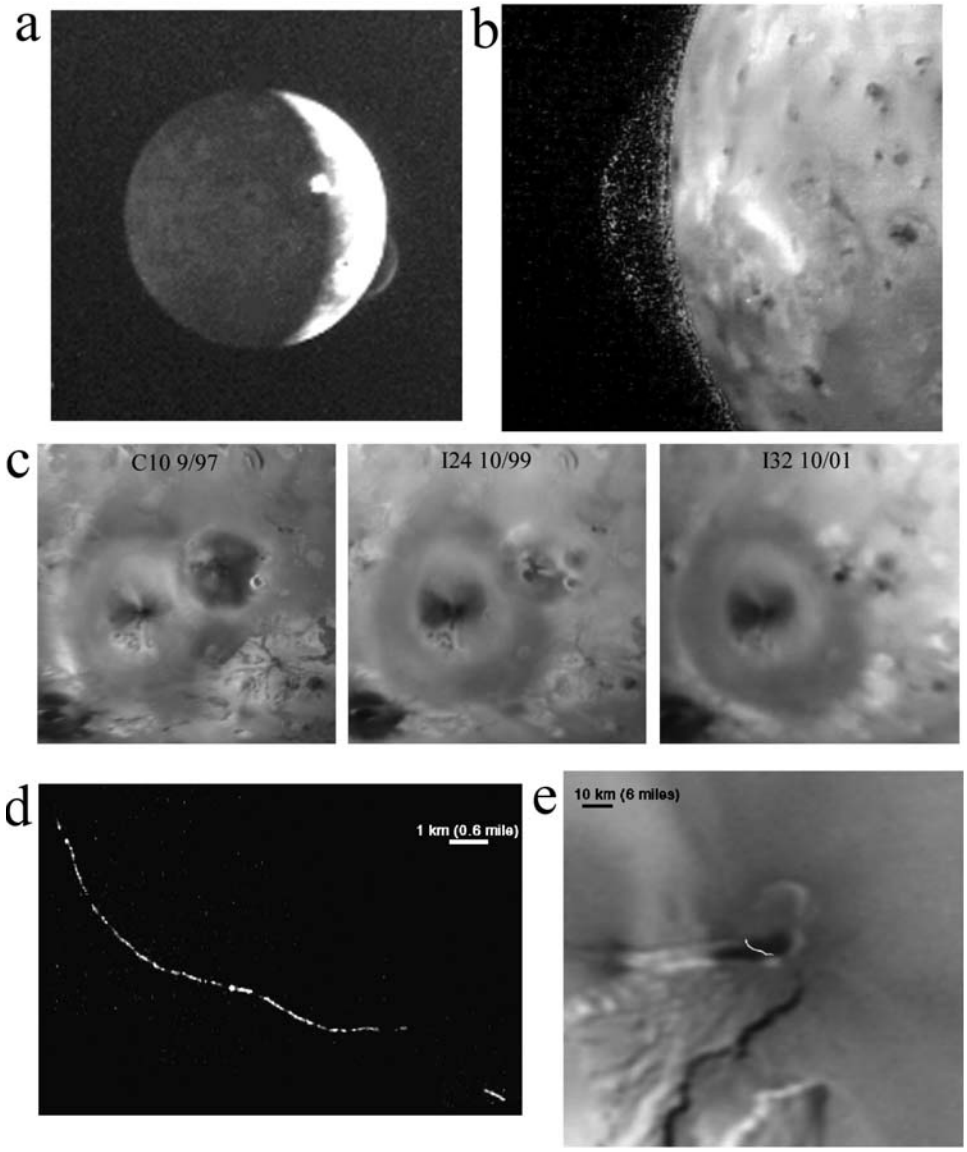

Figure 8.2. Pele, the archetype of giant plumes. (a) Discovery image: this low-resolution *Voyager 1* optical navigation image provided the first spectacular evidence of active extra-terrestrial volcanism. Pele is on the sunlit limb, Loki is on the terminator (NASA press release image PIA00379). (b) *Voyager 1* ultraviolet image of the dust plume (NASA press release image PIA01530). (c) *Galileo* images showing changes in Pele's plume deposit over a 4-year period. (d) Hot lava at the source of the plume glows in the darkness of Io's night (NASA press release image PIA02511). (e) The night-time image placed in the context of a *Voyager 1* image, showing that the glows occur along the edge of the patera, similar to terrestrial lava lakes (NASA press release image PIA02511).

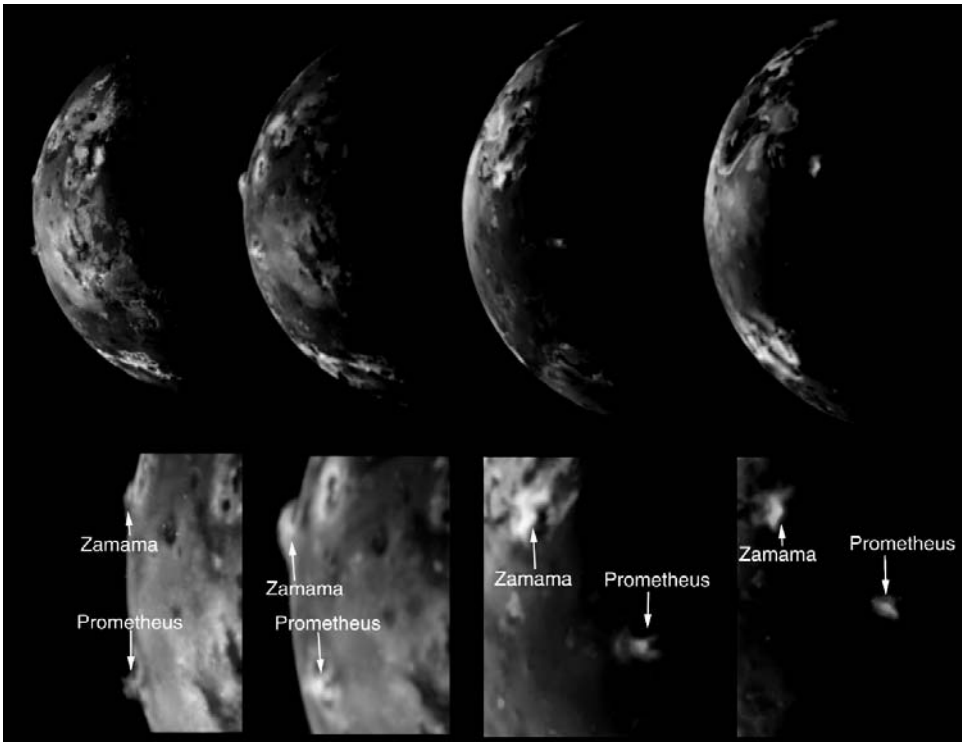

Figure 8.3. Zamama and Prometheus (see also color section). This sequence of four images watches as two small plumes rotate onto the disk of Io. The blue colors of the plumes are caused by the light-scattering properties of the dust particles (NASA press release image PIA01652).

overturning lava lake that continually exposes hot lava and exhales sulfur-rich gases from Io's interior.

Dust plumes can be seen in daylight to have bluish colors that contrast with the yellow and orange hues of Io's surface (Figure 8.3). The blue colors are caused by the wavelength-dependent light-scattering behavior of small dust particles. The color, brightness and opacity of dust plumes yield information on the dust grain size distributions and the dust deposition rates of the eruptions. However, the dust particle sizes and dust plume masses derived from photometric analyses vary greatly, depending on the assumptions made.

Collins (1981) applied a Rayleigh scattering law to *Voyager 1* color observations of Loki's plume, effectively assuming that the particles were much smaller than the wavelength of visible light. He found that particles on the order of 1–10 nm in radius comprised most of the mass of the plume. A second population of particles with distinctly redder colors was found in the core of the plume and interpreted to be made up of particles larger than 1,000 nm. From the brightness of the plume, the total mass of particles was inferred to be between 10^8 and 10^{11} kg, with the larger values corresponding to smaller (1-nm) particles. Assuming a dynamical lifetime (flight

time) of order 10^3 seconds, these masses imply dust production rates of 10^5–$10^8\,\mathrm{kg\,s^{-1}}$.

On the other hand, Spencer *et al.* (1997) fit a Mie scattering law to color observations of Pele's plume taken by the Hubble Space Telescope (HST). Mie theory assumes that the particles are comparable in size to the light wavelength. Pele's scattering properties were fit by particles 50–80 nm in radius with a total dust mass of only 10^6 kg. Applying the same theory to the data of Collins (1981), the authors found that Loki's plume could also be accounted for by larger particles of 50 nm radius with a smaller plume mass of 10^6 kg, implying dust eruption rates of order $10^3\,\mathrm{kg\,s^{-1}}$. Spencer *et al.* regarded their estimate as an upper limit, since the attenuation by Pele's plume could equally well be accounted for by SO_2 gas absorption in a vapor plume with a mass of 10^8 kg. Indeed, later HST observations (Spencer *et al.*, 2000) showed that much of the plume's opacity could be ascribed to gaseous S_2, further reducing the possible attenuation due to dust particles. The HST observations also suggested that Pele's plume is highly variable, appearing and disappearing on timescales of just 21 hours (Spencer *et al.*, 1997).

Geissler and McMillan (2006) fit Mie scattering models to *Galileo* visible color observations of the optically thick dust columns from Prometheus-type plumes. The results agree with those of Spencer *et al.* (1997), suggesting that the conspicuous dust plumes are made up of coarse-grained "ash" particles with radii on the order of 100 nm, and total masses on the order of 10^6 kg per plume. However, long-exposure images of Thor in sunlight show a faint outer envelope in addition to the optically thick core, similar to the structure of Loki. The outer envelope is apparently populated by particles small enough to be carried along with the gas flow, perhaps formed by condensation of sulfurous "snowflakes" as suggested by the plasma instrumentation aboard *Galileo* as it flew through Thor's plume (Frank and Paterson, 2002). The total mass of these fine, nearly invisible particles may be much greater than that of the coarser ash, and could account for significant resurfacing.

8.2.2 Gas

Plumes are also prominent at night and during eclipses, when they display an ethereal glow produced by the stimulation of the gases by charged particles, similar to terrestrial aurorae (Figure 8.4). The plumes can be seen at visible wavelengths as distinct knots or bubbles within an assortment of auroral glows that are present even when no plumes are active, including limb glows and equatorial emissions that periodically shift locations with the changing orientation of Jupiter's magnetic field. Only plumes near the electrical poles of Io (the sub-Jovian and anti-Jovian points) are in a position to be stimulated by the currents connecting Io to Jupiter. Exceptionally large plumes in other locations, such as the eruption of Tvashtar in late 2000, can sometimes be seen in emission because of the high density of emitting molecules.

The eclipse images show that the gas issuing from small Prometheus-type plumes extends much farther from Io's surface than the dust component, reaching heights and breadths up to 5 times as large as dust columns seen in daylight. The gases vented by

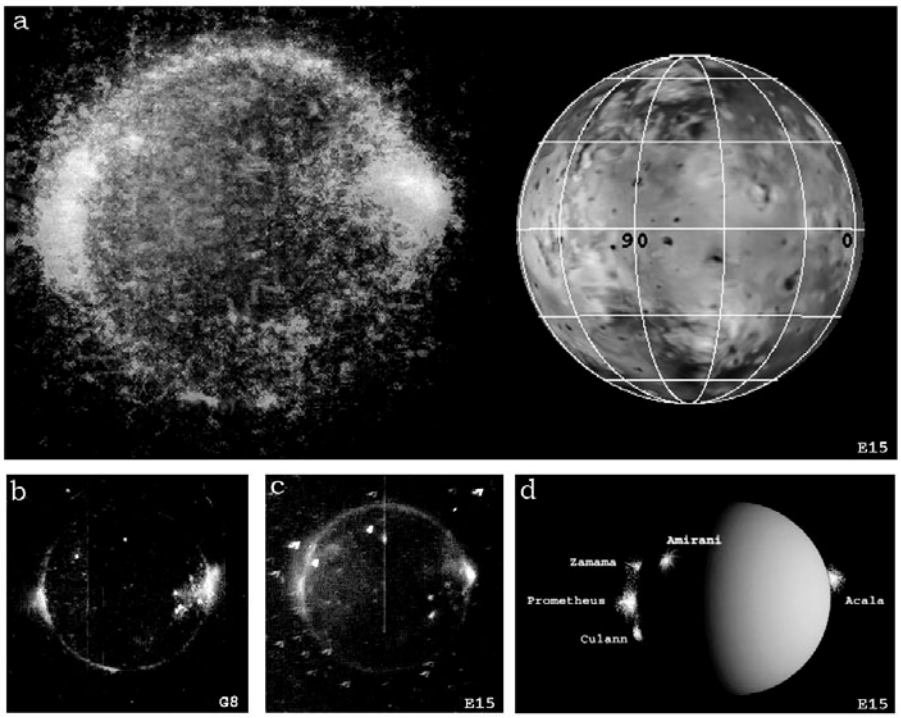

Figure 8.4. *Galileo* images of plumes in eclipse. (a) Visible-color image of atmospheric emissions during an eclipse in orbit 15 (*left*) compared with the sunlit appearance of the same hemisphere (*right*) (see also color section). The visible emissions are stimulated by charged particles, similar to terrestrial aurorae. The blue–white glows are produced by SO_2, and are concentrated at the locations of active plumes. The red and green glows are produced by atomic oxygen and atomic sodium, respectively (NASA press release image PIA01637). (b) Clear-filter image of the glows seen 1 year earlier, during the eclipse of orbit 8. The bright points on the disk show lava glowing by thermal emission. (c) Clear-filter image of glows seen during the eclipse of orbit 15. (d) Schematic diagram showing the locations of active plumes at the time of orbit 15 observations.

adjacent plumes often combine to form a megaplume above the most active regions. Some plumes such as Acala and Culann could be seen in emission during eclipse but were invisible in daylight, confirming a prediction (Johnson *et al*., 1995) of the existence of stealth plumes that are largely free of dust.

The spectra of these auroral emissions yield information on the makeup and abundance of the gases, as well as the intensity of the electrical currents that excite the emissions (Geissler *et al*., 1999, 2001a, 2004a). Molecular species such as SO_2 produce strong ultraviolet and visible continuum emissions that impart a bluish hue to the visible aurorae. The diffuse glows associated with the plumes in Figure 8.4 appear to be due to molecular SO_2 emission. Atomic species, including O, Na, and K, produce line emissions at longer visible and near-infrared wavelengths that are diagnostic of

their composition; however, present observations lack the spectral and spatial resolution needed to determine whether the abundance of atomic species in plumes differs from that of the background atmosphere.

Plume gases have also been identified spectroscopically at ultraviolet, infrared, and millimeter wavelengths. The observed gas compositions suggest two distinct classes of plumes. Sulfur-rich gases, including S_2, S, and SO, have been detected in Pele's plume along with larger abundances of SO_2 (e.g., McGrath *et al.*, 2000; Spencer *et al.*, 2000; Jessup *et al.*, 2004b). In contrast, only SO_2 was detected in spatially resolved ultraviolet observations of the Prometheus plume (Jessup *et al.*, 2004a), and the upper limit placed on the abundance of S_2 indicates a distinctly different composition for Prometheus than for Pele. However, temporal variations in the abundance of S_2 in Pele's plume were also noted (Jessup *et al.*, 2004b), including periods when it remained undetected. Recent microwave observations (Lellouch *et al.*, 2003) detected gaseous sodium chloride inferred to have been vented from volcanoes, providing a source for the Na and Cl detected in the atmosphere, neutral clouds, and plasma torus.

The observations of Jessup *et al.* (2004a) allowed them to estimate the excess column density of SO_2 gas at Prometheus at $5 \times 10^{16}\,\mathrm{cm}^{-2}$ and use this to derive a volcanic venting rate of $10^4\,\mathrm{kg\,s}^{-1}$. Slightly larger gas column densities were derived for Pele from earlier ultraviolet observations (Spencer *et al.*, 2000), but the larger volume of Pele requires an order of magnitude more massive plume.

8.3 OBSERVATIONS OF PLUME DEPOSITS

The deposits laid down by the plumes have also been studied with a variety of techniques. High-resolution images show the shapes, extents, and colors of the deposits, and the obvious changes in the appearance of the surface allow us to monitor plume activity over intervals between spacecraft visits. The thin SO_2 frosts deposited by many plumes are conspicuous at high phase angles, providing a means to identify sites of recent plume eruptions based on the optical scattering behavior of the surface (Geissler *et al.*, 2001b). Plume deposits can be clearly seen as fine grained frosts in the *Galileo* near-infrared mapping spectrometer (NIMS) measurements of the abundance and grain size of SO_2 as determined by infrared spectroscopy (Douté *et al.*, 2002).

Plume deposits can be annular, concentric, or irregular in plan. The sizes, shapes, and colors of the deposits divide into two categories, consistent with the two classes of plumes first suggested by *Voyager* observations of plume deposits (McEwen and Soderblom, 1983). Giant plumes produce enormous red rings up to 600 km in radius that are poor in SO_2 and may be dominantly made up of condensed sulfur. The smaller plumes produce SO_2-rich deposits that are typically less than 200 km in radius and are white or yellow in color unless contaminated with silicates. The two types of plume deposits are illustrated in Figure 8.5, which shows the superposition of the small plume deposit from Pillan on the giant red ring of Pele.

Pele's plume deposit consists of two parts: a black butterfly shaped pattern of ejecta near the patera surrounded by an enormous oval ring of red material. The dark

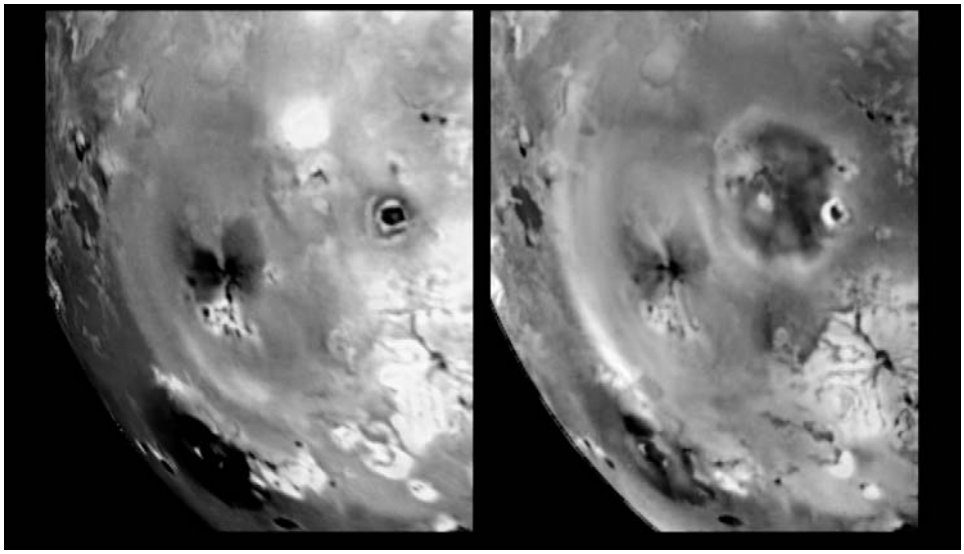

Figure 8.5. Two types of plume deposits. This pair of *Galileo* images shows the giant red ring of Pele, before (*left*) and after (*right*) the eruption of Pillan. Pele's annulus is elongated in the north–south direction, and reaches 720 km southwards from the source patera. Pillan's deposit is typical of small, SO_2-rich plumes that deposit ejecta up to 200 km from the eruption, except that it is colored by dark silicates (NASA press release image PIA00744). (See also color section.)

deposits changed very little during the period of *Galileo* observations, whereas the red ring was constantly in flux (Figure 8.1). These observations suggest two distinct populations of particles within Pele's plume. The composition of the dark inner deposits is not known, but it is reasonable to suspect that they may be made up of silicates entrained with the gas flow. Similar black deposits were emplaced by the nearby eruptions of Babbar and Pillan, and the near-infrared spectrum of these deposits shows an absorption feature at a wavelength of 0.9 μm, indicative of silicates (Geissler *et al.*, 2000). The red ring is elongated in the north–south direction, reaching a maximum radius of about 650 km. Several workers have suggested that Pele's red deposits are made up of short-chain sulfur allotropes such as S_3 and S_4 that are condensed from the gas phase (Moses and Nash, 1991; McEwen *et al.*, 1998; Spencer *et al.*, 2000; Moses *et al.*, 2002a). Faint bright deposits interior to the red ring appeared and disappeared during the *Galileo* observations, presumably caused by SO_2 entrained with or condensed by the plume.

Prometheus's deposit is a set of concentric rings superimposed on the older deposits laid down during the *Voyager* fly-bys (Figure 8.1). Color images taken during *Galileo*'s 8th and 14th orbits show four distinct rings, with radii of 72 km (bright yellow), 95 km (dark), 125 km (white), and 200 km (faint yellow, visible at high phase angles and prominent in NIMS SO_2 maps such as those in Douté *et al.*, 2002). In addition, the ghost of a ring fragment to the east is centered on the *Voyager* era plume

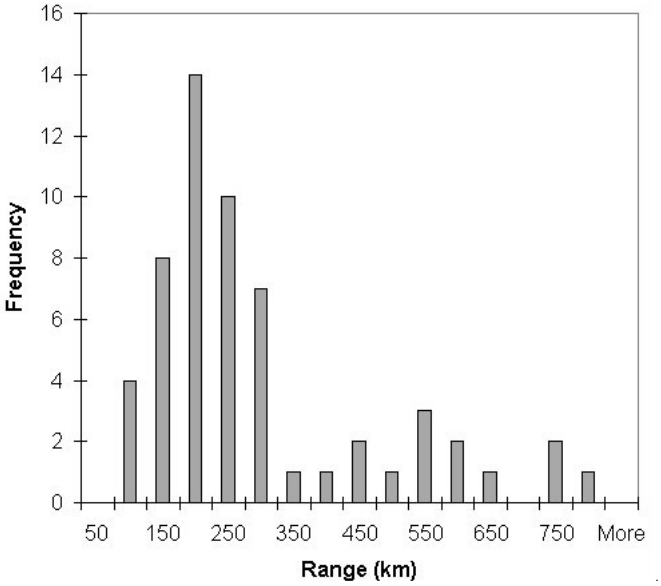

Figure 8.6. Maximum ranges of new plume deposits. This chart shows the frequency of plume-related surface changes observed on Io during the 5-year period of *Galileo* monitoring as a function of the maximum range of the deposits from their sources. The bimodal distribution results from the two distinct classes of plumes: the more numerous, smaller plumes produced deposits that reached no more than 300 km from their sources, whereas the giant plumes produced red rings with a broad range of radii averaging 600 km (from Geissler *et al.*, 2004b).

location. Concentric structures are common among rings and ring fragments from several other small plumes such as Culann, Zamama, and Marduk. An asymmetric red deposit stains the surface near Prometheus Patera, presumed to be the source of the silicate lava.

Many smaller explosive eruptions produce irregular deposits. Kanehekili's repeated eruptions seldom formed discernable rings. Irregular deposits alternated with circular structures at Amirani, Culann, Zamama, and Marduk. All of the red deposits flagging these eruptive centers are irregular; only giant plumes produce red rings.

Galileo's monitoring of Io over a 5-year period showed that surface changes took place repeatedly near the sites of many smaller plumes, indicating the sustained flow of lava from these volcanic centers. Pele's giant deposits also altered repeatedly throughout the mission, and ephemeral giant red rings appeared in several unexpected locations, including Tvashtar, Dazhbog, Surt and un-named volcanic centers south of Karei (12°S, 13°W) and near the north pole (80°N, 100°W). Some eruptive centers gave notice of impending explosions through changes in the brightness or color of patera surfaces prior to erupting. On the other hand, examples of episodic eruptions were seen from both classes of plumes that gave little warning beforehand and quickly returned to sleep afterward.

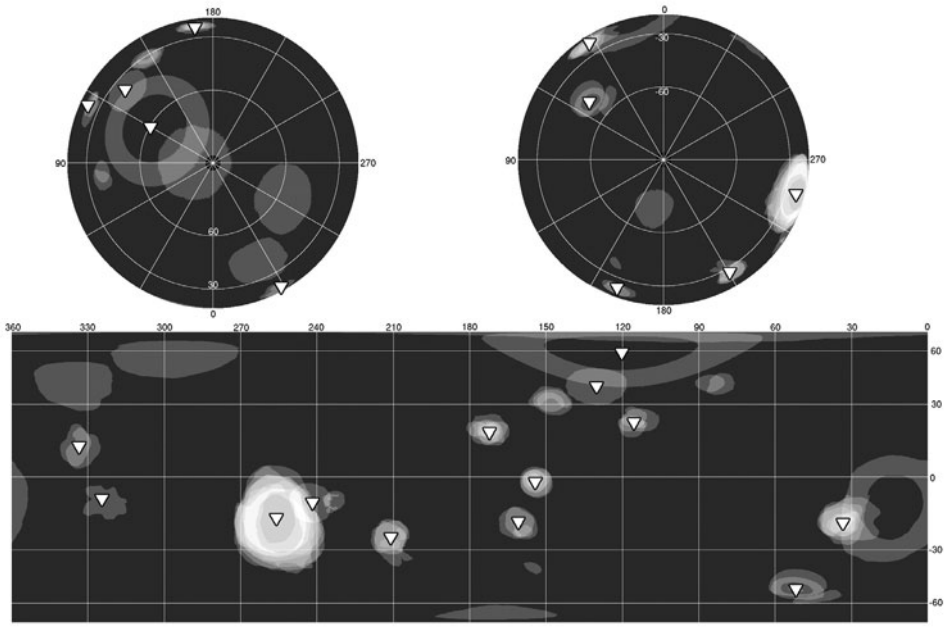

Figure 8.7. Plume deposits and plume sightings map. A map of the locations of large-scale surface changes (circular and irregular gray regions) and the sightings of plumes (triangles) during the *Galileo* era shows that every active plume produced visible changes in the appearance of the surrounding surface. In addition, several surface changes of similar character took place elsewhere on Io but the plumes that produced them were missed by *Galileo* (from Geissler *et al.*, 2004b).

The division between the two classes of plumes is clearly demonstrated by the bimodal distribution of maximum ranges of new plume deposits observed during the 5-year period of *Galileo* monitoring (Figure 8.6). All of the surface changes produced by the smaller, SO_2-rich plumes fell within 300 km of their sources, with most reaching only 200 km. All of the larger surface changes resulted from the emplacement of new red rings from giant plumes, with a broad range of sizes averaging 600 km in radius. A map of the locations of large-scale surface changes and the sightings of plumes on Io during the *Galileo* era (Figure 8.7) shows that every active plume produced visible changes in the appearance of the surrounding surface. In addition, several surface changes of similar character took place but the plumes that produced them were missed by *Galileo*.

8.4 PLUME SOURCES

The most thorough theoretical discussion of possible source reservoirs and vent geometries was presented by Kieffer (1982). She considered both SO_2 and S as potential driving fluids, and examined a variety of plausible initial conditions

ranging from low entropy (boiling liquids) to high entropy (vapors). She showed that flows emerging from depth through vertical conduits would be overpressurized relative to the ambient atmospheric pressure, but that expansion in a surface crater could reduce the pressure over relatively short distances ($\sim$1 km) to ambient. These would be pressure-balanced plumes, and would be likely to have a regular structure like the umbrella-shaped plumes. In contrast, flows erupting directly from conduits without such craters would be overpressurized relative to the ambient atmosphere, fluid velocities across the exit plane could vary wildly, and plume geometries would be expected to be irregular.

The plume sources so far observed on Io include lava lakes, lava flows, and fissures. No vents have been seen even in the highest resolution images, and craters that are several km across and more than 1 km deep can probably be ruled out by the observations. We suppose that the plumes are all overpressurized, and the difference between giant plumes and smaller plumes must result from the properties of the flow rather than the shapes of the vents.

Giant plumes appear to be produced by primary volcanic gases from paterae and lava lakes. Pele is a persistently bright hot spot at visible wavelengths, displaying temperatures (>1,500 K; Radebaugh *et al.*, 2004) consistent with freshly exposed mafic to ultramafic silicates (see Chapters 7 and 9). Close-up images of Pele at night (Figure 8.1) showed glowing lava near the margins of the patera, similar to actively overturning lava lakes on Earth. Fire-fountaining was seen at Tvashtar, driven by gases exsolved from the silicates. The fountaining lava reached more than a kilometer above the patera surface and was imaged by *Galileo* during orbit 25, just as Tvashtar began spouting its giant red ring. The red rings deposited by giant plumes are interpreted to be the condensation products of sulfur-rich gases that are absent from the smaller, SO_2-rich plumes. The dark diffuse deposits near the eruptive centers of giant plumes may be made up of silicate ash that was entrained with the flow, consistent with silicate sources. Given the high temperatures of the silicate magmas, the likely volatiles (S, SO_2) driving the giant plumes are certainly in the high entropy vapor state.

The smaller plumes all seem to be associated with lava flows. High-resolution images show the distinctive morphology of tube-fed flows of pahoehoe-type lava at Prometheus, Culann, Amirani, and elsewhere. Another crucial clue is the mobility of the plume sources. Loki developed a plume at a new location between the visits of *Voyager 1* and *Voyager 2*. Prometheus's source wandered more than 80 km westwards over the 20-year interval before the arrival of *Galileo*. Masubi's ring moved dramatically during the *Galileo* mission, and the centers of the disturbances at Amirani, Zamama, and Culann also shifted from one eruption to the next. In spite of these changes in location, the size and shape of Prometheus's plume appear remarkably constant over time. To account for this constancy, Kieffer *et al.* (2000) suggest that such plumes arise from shallow, choked conduits in the silicate lavas that allow subsurface slurries of molten SO_2 to vaporize and escape. They explain the steadiness of the eruption by noting that the mass eruption rate depends on the product of the subsurface fluid flow density times its velocity. In intermediate entropy fluids made up of mixtures of SO_2 liquid and vapor, the sonic velocity of the flow increases as the

density decreases, keeping the mass flux constant. Bright streaks of recondensed SO_2 can also be produced by small plumes at the margins of silicate lava flows (Milazzo *et al.*, 2001; Figure 8.1). Color images show venting of SO_2 from active jets near the flow front of Prometheus, as hot lava encroached on the frigid surface. The red deposits near Prometheus Patera and other eruptive centers are localized near the sources of the silicate lavas, consistent with the interpretation that the red materials are condensed from sulfur-rich gases directly exhaled by the silicates.

8.5 PLUME CHEMISTRY

The gases vented from the silicate magma provide important indications of the composition of Io's interior, along with the spectra of the lavas themselves. These gases originate in thermal equilibrium with the silicates but are subsequently altered by photolysis, condensation, chemical reaction, radiolysis, and recrystallization in equilibrium with the frigid surface ices or warm lavas upon which they fall.

Theoretical calculations (Zolotov and Fegley, 1999, 2000) of major volcanic gas chemistry, constrained by the observed abundances of S_2, SO, and SO_2 in Pele's plume (Spencer *et al.*, 2000; McGrath *et al.*, 2000), have been used to determine the oxygen fugacity of Pele's silicate lava. The implied high oxygen fugacity indicates that Io is differentiated and the mantle is free of metallic iron. These equilibrium calculations also yield estimates of the temperature of the magma (1,440 K) and the vent pressure (10^{-5}bar) of the plume.

Lesser abundances of the elements Na, K, and Cl are expected from alkaline ultrabasic magmas (Fegley and Zolotov, 2000). The composition of the vent gases depends critically on the (Na + K)/Cl ratio, which is still poorly known. High ratios should produce chlorides plus metals (Na and K), whereas chlorides plus chlorine are predicted for values of the ratio less than unity. Salts, sulfides, and sulfates are the expected condensation products in either case, and sputtering of these surface deposits probably contributes to the alkali metals and chlorine in the neutral clouds and plasma torus. Postberg *et al.* (2006) made the surprising finding that the dust escaping Io detected up to 1 AU from Jupiter by the Cosmic Dust Analyzer of *Cassini* was mostly made up of NaCl rather than sulfur compunds. Either NaCl dominates the dust composition because it is more refractory than sulfur species, or the dust that escapes is mostly NaCl because it is more easily ionized than sulfur species.

Compounds such as S_2 and S_2O require active volcanic sources because they are rapidly destroyed by sunlight after injection into Io's atmosphere, producing S, SO, O, and O_2 instead (Moses *et al.*, 2002a). Likewise, oxides of the alkali metals are quickly depleted by photolysis in favor of K, Na, Cl, KCl, and NaCl (Moses *et al.*, 2002b).

Substances vented by the plumes continue to alter even after condensation and deposition on the surface. The bright red hues of the giant plume deposits fade to pale yellows as short-chain sulfur allotropes such as S_3 and S_4 equilibrate to the more stable cyclo-octal form of sulfur (S_8). This fading takes place rapidly along the equator (on a timescale of months; Geissler *et al.*, 2004) but is inhibited at the reddish poles, either

because of lower temperatures or an increased flux of charged particles at high latitudes (Johnson, 1997). Along the equator, the fine grained frosts of SO_2 laid down by the smaller plumes are converted over time to coarse grained ices with markedly different light scattering properties (Geissler *et al.*, 2001b), presumably by annealing and recrystalization.

8.6 PLUME DYNAMICS AND MODELING

8.6.1 When plumes form

What features characterize a plume that make it distinct from other gas releases such as evaporation from a small region? It seems likely that there is a range of plume sizes and that some small ones or those lacking visible particulates (''stealth'' plumes of Johnson *et al.*, (1995)) or obvious rings have simply not yet been observed. Perhaps three parameters, source density, temperature, and size, are sufficient to determine whether a gas source is a real ''plume''. Zhang (2004) examined circular disk sources of sublimating gas and found that when no surrounding sublimating atmosphere is present (at night), a ratio of thermal-based scale height to vent size, $S = RT/gr$, determines whether a source has enough thermal clout to develop a canopy shock. Here, R is the SO_2 gas constant, T the source surface temperature, g the surface gravity, and r the source disk radius. If $S > 1$, the source gas rises and expands and cools before forming a distinct canopy shock. Otherwise, the gas simply expands away from the source without shocking. If a gas source is too weak compared with a surrounding sublimation atmosphere, the atmosphere will confine it. Zhang (2004) suggests that for a distinct plume to rise above and blanket the atmosphere (rather than the other way around) the plume shock height should be greater than the scale height of the atmosphere. Also, the plume vent pressure should exceed the surrounding atmosphere surface pressure.

8.6.2 Types of plume models

Plume dynamics modeling can be broadly classified by the dimensionality of the flow and the manner of fluid representation. The simplest models would represent the plume as hemispherical or cylindrical uniform regions of effluent having no other spatial structure. Models in 1-D have been developed to explore the photochemistry of such plumes (Moses *et al.*, 2002a) but strong assumptions must be made about expansion and diffusion processes in the flow (e.g., eddy diffusion, thermal diffusion, no shocks). A 2-D flow representation is generally needed to accommodate the most important competing effects of gas-dynamic expansion and gravity. Moreno *et al.* (1991) simulated an axisymmetric plume and examined its interaction with a sublimation atmosphere. The most extensive axisymmetric simulations have been those of Austin and Goldstein (1995, 1998) and Zhang *et al.* (2003a,b,c; 2004) in which a range of detailed physical phenomena were explored. A fully 3-D representation is needed to understand non-simple sources, plume–plume interactions (e.g.,

Figure 8.5), and plume interactions with the flowing sublimation atmosphere or plume interactions with the Jovian plasma torus. No fully 3-D gas dynamic simulations have been presented.

Various models from Stochastic–Ballistic (SB) in the free-molecular regime, to rarefied gas dynamics in the transitional regime, to computational fluid dynamics (CFD) in the continuum regime, have been developed. The SB model, that simply tracks a spray of non-interacting particles, can satisfactorily reproduce aspects of the plume shape and ring deposition of some plumes by careful manipulation of the initial conditions. However, the thermal motion of individual particles and their collisions are not taken into account in an SB model so that the resulting flow field does not reflect features such as shocks or the acceleration and cooling of the gas through expansions which should occur at certain locations. Emitted radiation thus cannot be well modeled and motions of the gas molecules and entrained solid or liquid particles are independent of each other. The SB model may be suitable for understanding the small inclined sprays produced along the margins of intrusive lava flows (Milazzo *et al.*, 2001) because the length scales are small and gravity does not force the flow to fall back on itself. Larger volcanic plumes, however, exhibit a wide range of physical phenomena that can only be accommodated if the gas flow is at least partially collisional. Continuum CFD models capture more of the physics of the flow: they can be used all the way from the below-ground source of the effluent out into the expanding plume core flow. Yet beyond the several-kilometer-high core flow region, the gas may still continue to expand. In the intermediate region between the near-vent core flow and a much higher canopy shock (and, of course, from near the exobase on out to infinity) the Navier–Stokes equations of fluid mechanics do not apply and a rarefied gas model must be used. In such low-density flow regions, the continuum assumption breaks down because the mean free path of molecules becomes comparable to the length scale of flow (or radiating) features. However, the continuum approach may produce qualitatively reasonable solutions and may be the only current practical means of modeling some physics such as turbulence.

The difficulties posed by the SB and CFD flow models are overcome by the direct simulation Monte Carlo (DSMC) approach (Bird, 1994) which has been applied to volcanic plume modeling and sublimation driven flows by the UT Austin group. In the DSMC approach, fluid molecules and entrained particulates are individually represented as they translate and undergo collisions with each other and with boundaries. In DSMC a tremendous amount of physical detail can be included and the flow can be accurately modeled from deep within the continuum regions to the vacuum of space. DSMC is only limited by the prohibitive computational cost of modeling dense flows in which applicable Knudsen numbers are less than 0 (10^{-4} to 10^{-5}); for such flows a hybrid CFD/DSMC solution is needed.

8.6.3 Model boundary conditions

Regardless of the modeling approach chosen, the choice of reasonable boundary conditions is crucial. Among the most important of those boundary conditions are the source gas pressure, velocity, temperature, constituents, solid and liquid fraction,

particle size distribution, and level of non-equilibrium. Kieffer *et al.* (2000) have suggested that the tendency of the gases to be choked in nozzle-like conduits is a reasonable constraint. Yet the nature of the solid and liquid particles coming out of the ground is poorly constrained as is the level of non-equilibrium. Here, non-equilibrium refers not only to local thermo-chemical non-equilibrium, but also to the level of velocity and thermal slip between the co-moving gas and particles, the radiative non-equilibrium between the gas, the particles, and the surrounding vent or ground surface (Zhang *et al.*, 2003c and Zhang, 2004), and the thermodynamic non-equilibrium among different molecular energy modes within the gas (rotational, vibrational, translational). Most modelers to date have assumed complete equilibrium single or two-phase flow from a circular or point-like vent. The next most important boundary condition is the nature of the gas–surface interaction surrounding the source. (Solid or liquid particles that fall to the ground most likely stick.) Ingersoll (1989) assumed a sticking coefficient α. Zhang *et al.* assume $\alpha = 1$ (all stick) for incoming "condensible" molecules like SO_2 onto SO_2 ice but also assume a flux of molecules out of the surface to match the temperature-dependent equilibrium vapor pressure. Sticking coefficients are a crude way to model a little-known process in that they sweep many dependencies under the rug. But for microscopically rough and cold engineering surfaces in non-clean environments, it is often found that $\alpha = 1$ is a good approximation.

8.6.4 Stochastic/ballistic results

Some of the earliest theoretical results were those of Cook *et al.* (1979) using a shock front model and a SB model. Strom *et al.* (1981) and later Strom and Schneider (1982), examined these models further and introduced a few corrections. In the SB model, the representative gas particles introduced at a disk-like or point-like source are assigned initial velocities and are subsequently tracked until they strike the surface. Such an approach can reproduce certain observed features such as a domed canopy plume shape, circular ring deposits, and some of the brightness structure of the smaller Prometheus-type plumes. Lellouch in his 1996 review paper used a ballistic model to simulate volcanic plumes and interpreted the millimeter wave data to obtain a column density near the plume center of $\sim 10^{18}\,\mathrm{cm}^{-2}$ and the average column density over the plume of $\sim 10^{16}\,\mathrm{cm}^{-2}$, which agree better with that derived by Strobel and Wolven (2001), Feldman *et al.* (2000), and McGrath *et al.* (2000). Glaze and Baloga (2000) used the SB approach to try to solve the inverse problem of, given the apparent areal distribution of fallout in the main Prometheus ring, what combination of particle energies and flow angles near the vent are required? They suggest that the flow truncated beyond 75° from the vertical and a 0.08 standard deviation of particle speeds can reasonably reproduce the ring shape and size. However, it appears that the parameters they choose to match do not tightly constrain the needed source parameters and that the lack of consideration of collisional gas dynamics may bias the resulting conclusions about the source conditions. Douté *et al.* (2002) use the Glaze and Baloga model to study the evolution of surface patterns as the source region of the Prometheus plume moved. Long-term effects of sublimation and the re-exposure of underlying materials complicate the picture. Modestly good fits to the east/west areal

frost distributions are found if the movement of the source is uniform over time but the north/south distributions are not well reproduced. The SB model cannot account for the secondary humps in frost distribution outside of the main ring; those humps are likely a collisional gas effect. The SB model is almost certainly suitable for studying the motions of the larger (>1 mm) pyroclastic particles as they disengage from the gas flow just above the source, but is probably less suitable for studying gas flow.

8.6.5 Analytic results

Kieffer's (1982) model accounted for compressible, multi-phase flow and argued that a roughly conical crater could develop due to the erosion by high-speed exiting flow. The flow would reach such speed by gas-dynamic acceleration past a sonic throat (a local geometrical constriction) near the end of a possibly long conduit. Kieffer *et al.* (2000) suggest that the fact that the source of the remarkably unchanged Prometheus plume has wandered many kilometers between *Voyager* and *Galileo* monitoring indicates that the vent is a rootless conduit through the lava flow rather than dispersed lateral jets at changing places along the margin; lava overflows pre-existing snowfields, superheating the vaporizing products and producing the surprisingly constant shaped plume via choked two-phase flow.

8.6.6 Computational fluid dynamics results

Moreno *et al.* (1991) developed 2-D axisymmetric numerical models based on the conservation equations of inviscid, compressible gas dynamics to simulate both sublimation and volcanic atmospheres. They were the first to simulate the re-entry shocks but, due to a lack of spatial resolution and a narrowly focused jet-like input, did not find a canopy shock. Moreno *et al.* were able to model deposition rings, compute regions where snow condensation may occur in a plume, relate plume dynamic time- and length scales to loss mechanisms of atmospheric species to the plasma torus, and explore the relative contributions of the volcanic and sublimation atmospheres on the day and night sides of Io. Though they obtain flows having features modestly consistent with observations and more recent DSMC simulations, they have extended an inviscid flow model well beyond its range of applicability.

8.6.7 Direct simulation Monte Carlo results

Perhaps the most complete and detailed models of the plumes are provided by the DSMC simulations of Zhang *et al.* (2003a,b,c; 2004) based on the earlier DSMC simulations of Austin and Goldstein (1995, 1998). The Zhang papers include hot band transition in the rotational radiation model, discrete line emission from the three SO_2 vibration modes, a spherical planet with variable gravity, fully or partially coupled gas/dust flows, and multiple gas species. They find that the general umbrella-shaped plumes can best be created with nearly uniform vertical flow out of a circular source suggestive of a hot lava lake or a modestly deep conduit in which turbulent flow has made the velocity/density profile fairly uniform. A surrounding re-entry shock occurs

as the high Mach number expanding gas falls back on top of the ambient atmosphere. For this re-entry shock to occur, the stagnation pressure of the falling gas must be equaled or exceeded by the vapor pressure of the ambient atmosphere. The re-entry shock is oblique and as the gas subsequently expands, rises, and falls again it may undergo repeated bounces or re-entry shocks. Surprisingly, the flow through the re-entry shock can lead to either frost deposition or removal in different areas depending on the surface temperature; the post-shock gas may push away the upper reaches of the sublimation atmosphere thus reducing the surface pressure and creating radially outward winds that promote greater sublimation than condensation. Diurnally averaged frost deposition profiles, however, produce a net ring about where condensation occurs over the cold night-time surface.

By modeling small non-condensible particles in the flow, Zhang *et al.* (2004) are able to match several key observable features including limb photographs, photographs of the shadow cast by Prometheus, and ring structure. Figure 8.8 (from Zhang *et al.*, 2004) shows an attempt to match the *Voyager* limb image of Prometheus with entrained 1-nm particles. The gas column density shows a clear region of strong expansion and a canopy shock at about 50 km altitude. The surface temperature T_s on the left- and right-hand sides of Figures 8.8(b) and 8.8(c) are different and were chosen so that the dust column density images best match the *Voyager* data. This required a slightly greater T_s on the left (108 K) than on the right (106 K) to promote a slightly greater gas-dynamic bounce on the left. Particles tend to produce rings having sharp boundaries with a notable spike in deposition near the inner or outer ring edges, depending on the plume size. While particles larger than about 10 nm tend to deposit as the gas turns through the first re-entry shock, smaller particles turn with the gas and are deposited in an outer more broad ring. Other possible effluents move with the dominant SO_2 flow implying the following. (1) Even large fractions of S_2 (up to 40%) in the plume have a negligible influence on the plume structure because the gas cooling near the vent is dominated by expansion and vibrational line emission (radiation losses) from SO_2. (2) The primary deposition ring surrounding the vent is where virtually all vent material falls out (at $T_s < \sim 111$ K). There may be subsequent deposition rings but they consist mostly of material scoured off the surface below the primary re-entry shock. Since S_2 has a negligible vapor pressure at reasonable surface temperatures, it is not scoured and no subsequent S_2 rings are expected. Hence, Pele-type plumes have a single red ring. (3) Trace gas species entrained in the main SO_2 flow, such as sodium, are blocked by the SO_2 canopy shock from reaching appreciably above that shock. Hence, steady plumes even of Pele's scale do not appear capable of ejecting molecules or dust grains directly into escape trajectories without the intervention of some other source of energy (e.g., plasma heating of the plume canopies).

8.7 INTERACTIONS WITH THE ENVIRONMENT

The most obvious environmental effect of plumes is the rapid repainting of the surface with their colorful deposits. The eruption of Pillan blackened an area of $\sim$200,000 km^2

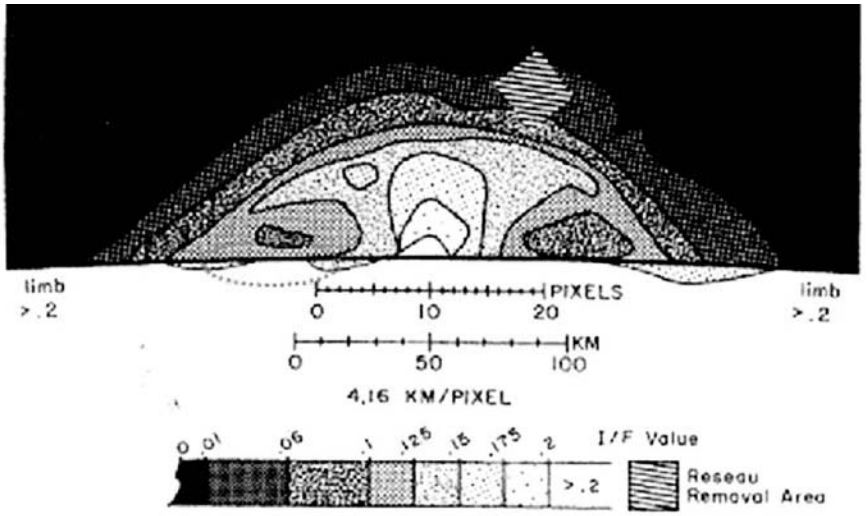

(a)

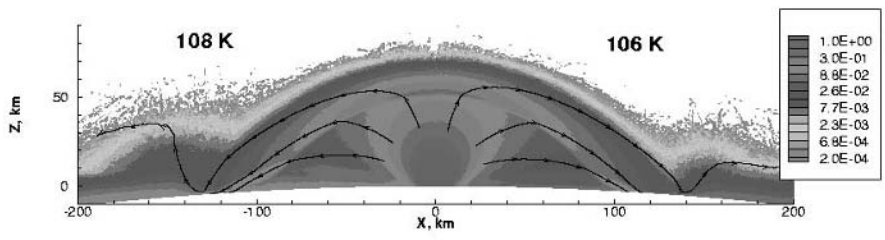

(b)

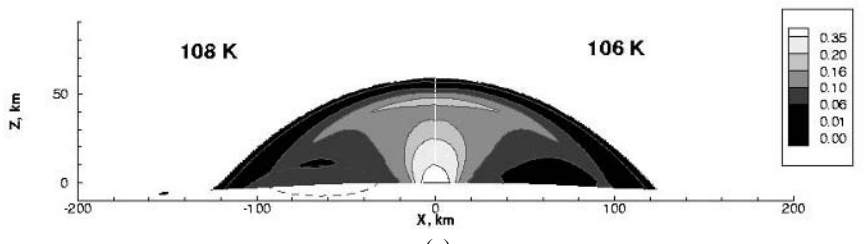

(c)

Figure 8.8. (a) *Voyager* image of the brightness of the Prometheus plume (from Strom and Schneider, 1982). Note the general sickle shape of the contours and the presence of a small signal near the surface on the left. (b) DSMC simulated number density contours (normalized by $5 \times 10^{16}\,\mathrm{m}^{-3}$) of gas with a surface temperature of 108 K on the left and 106 K on the right. Select gas flow streamlines are also shown. (c) Normalized column density contours of 1-nm particles entrained in the gas flow. Notice the low altitude "dust cloud" circled on the left reflecting a settling time through the local atmosphere under the canopy of ~1,200 s. No cloud is seen on the right reflecting a settling time of only a couple of hundred seconds there. (See also color section.)

on a timescale of weeks, obscuring a large portion of Pele's red ring. Three years later, most of Pillan's pyroclastic deposits had vanished beneath a renewed red ring from Pele and bright frost from nearby Kaminari. Do the plume deposits simply coat the surrounding surfaces, or do they bury them? Estimates of the deposition rates of plume sediments vary greatly, ranging from 10^3 kg s^{-1} for Pele (Spencer *et al.*, 1997) to 10^7 kg s^{-1} for both Pele and Pillan (Cataldo *et al.*, 2002). A globally averaged resurfacing rate of $\sim$1 mm yr^{-1} is required in order to account for the erasure of impact craters on Io (Spencer and Schneider, 1996), equivalent to the emplacement of 1,000 m^3 s^{-1}. Plume deposit thicknesses of order 5 mm yr^{-1} are needed to account for this resurfacing, given that roughly one-fifth of Io's surface was coated by plume fallout during the *Galileo* mission. Only massive plumes, with dust production rates of order 10^5 kg s^{-1}, could produce such deposition. Much of the resurfacing could instead be accomplished by the eruption of silicate lava flows: Amirani alone is estimated to have erupted 50–500 m^3 s^{-1} of new lava flows between subsequent *Galileo* observations, assuming that the flows were 1–10 m thick (Keszthelyi *et al.*, 2001). However, silicate lava flows cover only a small fraction of the surface, and the most powerful volcanic upheavals are confined to lava lakes like Loki. In contrast, plume deposits mantle areas that are hundreds to thousands of times greater than the lava flows and patera that produced them. This redistribution of material may account for the apparent absence of flooded and partially destroyed impact craters on Io.

There is no doubt about the significance of the contribution of volcanic plumes to Io's atmosphere. *Voyager 1* first identified SO_2 in Loki's plume that was attributed to volcanic outgassing (Pearl *et al.*, 1979). The earliest Earth-based detections of atmospheric SO_2 and SO showed spectral broadening and Doppler shifting that was ascribed to volcanic plumes (Lellouch *et al.*, 1990, 1992, 1996). As pointed out in Chapter 10, gases such as NaCl and S_2 that have negligible vapor pressure at Io's surface temperature require volcanic sources. The patchy nature of the tenuous atmosphere can best be explained by a combination of sublimation and volcanic venting (Ingersoll, 1989; Lellouch 1996; see also Chapter 10).

Once lofted into the atmosphere, the gas and dust ejected from plumes can be ionized by sunlight and impacting charged particles, swept away by the Jovian magnetic field, and spread throughout the Jovian system. Variations in the composition and mass of the neutral clouds and plasma torus are believed to be caused by volcanic eruptions on Io (Brown and Bouchez, 1997). Moses *et al.* (2002a) suggest that measurements of the S : O ratio in the plasma torus may be an effective means of remotely monitoring giant plume eruptions on Io. Correlations between the flux of $\sim$10-nm dust particles recorded by the *Galileo* Dust Detector and the record of giant plume eruptions on Io during the 5-year tenure of the spacecraft indicate that ejection of dust from the most energetic plumes is chiefly responsible for the dust streams emanating from Io into interplanetary space (Krüger *et al.*, 2003).

The electrical currents that connect Io to Jupiter directly impinge on the plumes near the sub-Jupiter and anti-Jupiter points. Io is an effective electrical generator, powered by the magnetic field of Jupiter as it sweeps past the conducting satellite (Chapter 11). Part of Io's conductivity is through its ionosphere, but the conduction of

current into the interior of Io through plumes is an intriguing possibility (Gold, 1979). Spokes and filaments have been seen in Prometheus that appear similar to plasma-arc discharges observed in the laboratory (Peratt and Dessler, 1988), although they could instead result from multiple sources along the lava flow. Powerful currents could produce interesting disequilibrium chemical reactions within the plumes and possibly heat the surface of the satellite near the plume sources. These effects would be local, however, as the power generated globally by electrical induction is two orders of magnitude less than that derived from tidal heating.

8.8 CONCLUSIONS AND OUTSTANDING QUESTIONS

Recent observations and theoretical advances have filled many of the gaps in our knowledge of Io's plumes, but have also presented new puzzles. The process of assimilating the recent results and integrating the insights from different disciplines has not yet been completed, and we expect the list below will be expanded in the near future.

8.8.1 Conclusions

Several important lessons have been learned since the *Voyager* fly-bys and the subsequent analyses of those observations. The most obvious of these are summarized here.

- Extensive *Galileo* observations of dust plumes, gas plumes, and plume deposits confirm the post-*Voyager* suggestion (McEwen and Soderblom, 1983) that there are two distinct classes of plumes on Io. All of the plumes seen during the 5 years of *Galileo* observations can be described as either giant plumes, with characteristics similar to Pele, or smaller plumes that share the properties of Prometheus. Fundamentally, these two classes of plumes erupt from reservoirs at two distinct temperatures. Equating (to first order) the thermal energy of the plume gases to their kinetic energy and to the work done in transporting them across Io's surface, we have (Glaze and Baloga, 2000):

$$3/2\,kT = 1/2\,mv^2 = 1/2\,mgr$$

  where r is the radius of a typical plume deposit, k is Boltzmann's constant, and the mass m is the same for both SO_2 and S_2. The observed factor of $\sim$3 difference in ring radii for the two classes of plumes ($\sim$600 km for the giant plumes vs. $\sim$200 km for Prometheus-types) implies a corresponding factor of $\sim$3 difference in source gas temperature, assuming all other factors are equal.

- Both the gas and dust plumes were separately seen by *Galileo*, during eclipse and during day-time, respectively. In addition, *Galileo* eclipse observations confirmed the existence of high-entropy stealth plumes rich in gas but largely free of dust, as predicted by Johnson *et al.* (1995). More work remains to be done on these observations, particularly in cases where gas and dust plumes from the same locations were seen simultaneously or near-contemporaneously, but initial indications are that Prometheus-type gas plumes are larger than their dusty counterparts by a factor of 2–5. This mismatch in size suggests that the dust decouples from the gas flow in smaller plumes, and places a lower limit on the dust particle sizes, since dust smaller than ~10 nm is obliged to follow the gas for reasonably dense flows (Zhang *et al.*, 2004).
- The compositions of volcanic gases emitted from both Pele and Prometheus have been directly determined from HST ultraviolet observations. Sulfur-rich gases were detected in Pele's plume but not in that of Prometheus. This is consistent with the widely held interpretation (e.g., Spencer *et al.*, 2000; Moses *et al.*, 2002a) that Pele's brilliant red ring and other similar deposits elsewhere on Io are made up of short-chain sulfur allotropes such as S_3 and S_4 that are condensed from the gas phase. The composition of volcanic gases from Pele has also been used to infer the equilibrium chemistry of Io's interior.
- We have also determined that purely ballistic or hydrodynamic models are insufficient to describe the complexity of Io's plumes. Direct numerical simulations have revealed additional structures and phenomena that could not be recognized in earlier theoretical treatments, such as the patterns and strength of thermal emission, the distribution of particulates in the canopies, and the relationship between the background atmosphere, the surface temperature, and the deposition rings of condensates and particulates.

8.8.2 Outstanding questions

A number of new and old problems point out the weaknesses in our understanding of plume phenomena, and suggest directions for further research:

- Why are there two classes of plumes? The observed magma temperature of Pele (~1,500 K) and the temperature inferred from equilibrium chemical considerations (1,440 K) are equal to within the measurement uncertainty. The temperature of magma arising from deep sources is presumably controlled by tidal heating within Io and the mechanics of convection and eruption. By the arguments given above, the Prometheus-type plumes vent gases at ~1/3 of that temperature (i.e., 500 K or less), indicating a different energy source and/or driving fluid. Perhaps by coincidence, the critical temperatures of sulfur and of sulfur dioxide (above which they cannot be condensed) differ by a factor of 3.05. Sulfur's critical temperature is 1,313 K (Kieffer, 1982), little less than the probable temperature of silicate magmas erupting from Io's interior. We speculate that the maximum range of Prometheus-type plumes may be reached when encroaching silicate lava heats SO_2 to the critical temperature

(430 K for SO_2, Kieffer, 1982), at which point it can no longer be contained in the liquid phase.

- Where are the vents? The nature of plume vents or other source edifices is still unknown and poorly constrained by observations. While we have reasonably good simulations of rarified gas flow, the links to the subsurface source regions are presently lacking. Zhang *et al.* (2004) avoid this problem by postulating a virtual vent that is a circular source some distance above the surface with a fixed radius (order of kilometers), across which the initial conditions of the gas flow are assumed. Below this plane, the geometry of the source vent (be it the end of a long fissure or bubbles bursting in a lava lake) is undetermined.
- Does it snow on Io? The genesis of the dust in Io's plumes remains a mystery. There exists the possibility of snowfall on Io – condensation of S_x or SO_2 snowflakes or rain drops from the vapor phase as the plumes expand and cool – but the relative roles of condensation vs. lofting of existing dust particles are still unknown. It is theoretically possible, and appears observationally likely, that both entrainment and condensation take place in many of Io's plumes. At present, the particle sizes and implied mass eruption rates remain model dependent. The wider spectral range and better spectral resolution of the *Galileo* and *Cassini* imaging observations (in comparison with *Voyager* data) can be used to improve our knowledge of the dust particle size distributions and deposition rates.
- How do plume materials escape from Io? A reliable result of the numerical simulations is that steady, sufficiently dense plumes are effectively contained by their canopy shocks, preventing even very volatile species from directly escaping Io. On the other hand, volcanic influences on the population of ions in the plasma torus and on the flux of dust in the Jovian magnetosphere have been well established by the observations. One solution to this apparent contradiction could be unsteadiness in the vigor or supply of gas to the plumes. Pulses or other temporal variations in plume output invalidate the steady-state conditions assumed in the dynamical simulations and may provide the means for materials to penetrate the canopy shock and escape. Alternatively, addition of energy from solar or plasma heating may eject materials from the top of plumes, either directly (by imparting kinetic energy) or indirectly (by ionization, allowing external electrodynamic forces to sweep away gas and dust). Sputtering by charged particles may be the major means of atmospheric escape (Chapter 11).
- Other theoretical concerns. The implications of plume unsteadiness have yet to be investigated: if a plume pulses or suddenly shuts off, how long does it take before the effects are felt on the other side of Io? How long until the Jovian magnetosphere feels the change? Such knowledge is needed if we are to monitor plume activity on Io from, for example, changes in the S : O ratio of the plasma torus. In addition, the extent of the interaction between the plumes and the sublimation atmosphere remains an open issue. Properly addressing such questions presents a challenge for the future that will likely require a full 3-D, planet-wide simulation that includes both the dynamic atmosphere and the violent volcanic plumes of Io.

8.9 REFERENCES

Austin, J. V. and Goldstein, D. B. 1995. Direct numerical simulation of low density atmospheric flow on Io. In: M. Capitelli (ed.), *Molecular Physics and Hypersonic Flows*. Kluwer Academic Publishers, Dordrecht, The Netherlands, pp. 749–758.

Austin, J. V. and Goldstein, D. B. 1998. Simulation of Supersonic Rarefied Atmospheric Flows on Io. In: *Rarefied Gas Dynamics: Proceedings of the 21st International Symposium on Rarefied Gas Dynamics* (vol. 2). Cepadues-Editions, Toulouse, France, pp. 681–688.

Bird, G. A. 1994. *Molecular Gas Dynamics and the Direct Simulation of Gas Flows*. Oxford University Press, Oxford, UK.

Brown, M. E. and Bouchez, A. 1997. The Response of Jupiter's Magnetosphere to an outburst on Io. *Science*, **278**, 268–271.

Cataldo, E., Wilson, L., Lane, S., and Gilbert, J. 2002. A model for large-scale volcanic plumes on Io: Implications for eruption rates and interactions between magmas and near-surface volatiles. *Journal of Geophysical Research*, **107**(E11), 5109, doi:10.1029/2001JE001513.

Collins, S. A. 1981. Spatial color variations in the volcanic plume at Loki, on Io. *Journal of Geophysical Research*, **86**, 8621–8626.

Cook, A. F., Shoemaker, E. M., and Smith, B. A. 1979. Dynamics of volcanic plumes on Io. *Nature*, **280**, 743–746.

de Pater, I., Roe, H., Graham, J. R., Strobel, D. F., and Bernath, P. 2002. NOTE: Detection of the Forbidden SO a^{1}Delta$\rightarrow$X^{2}Sigma- Rovibronic Transition on Io at 1.7 mm. *Icarus*, **156**, 296–301.

Douté, S., Lopes, R., Kamp, L. W., Carlson, R., Schmitt, B., and The Galileo NIMS Team. 2002. Dynamics and evolution of SO_2 gas condensation around Prometheus-like volcanic plumes on Io as seen by the near infrared mapping spectrometer. *Icarus*, **158**, 460–482.

Fegley, B. and Zolotov, M. Y., 2000. Chemistry of sodium, potassium, and chlorine in volcanic gases on Io. *Icarus*, **148**, 193–210.

Feldman, P. D., Strobel, D. F., Moos, H. W., Retherford, K. D., Wolven, B. C., McGrath, M. A., Roesler, F. L., Woodward, R. C., Oliversen, R. J., and Ballester, G. E. 2000. Lyman-Alpha Imaging of the SO_2 distribution on Io. *Geophysical Research Letters*, **27**, 1787.

Frank, L. A. and Paterson, W. R. 2002. Plasmas observed with the Galileo spacecraft during its flyby over Io's northern polar region. *Journal of Geophysical Research (Space Physics)*, **107**, 31–1.

Geissler, P. E. and McMillan, M. 2006. Galileo observations of volcanic plumes on Io. *Icarus*, in review.

Geissler, P. E., McEwen, A. S., Ip, W., Belton, M. J. S., Johnson, T. V., Smyth, W. H., and Ingersoll, A. P. 1999. Galileo imaging of atmospheric emissions from Io. *Science*, **285**, 870–874.

Geissler, P. E., McEwen, A. S., Phillips, C., Keszthelyi, L., Turtle, E., Lopes-Gautier, M. M. R., Simonelli, D. P., Williams, D. A., and Galileo Imaging Team. 2000. New Results on Io's Color and Composition. *Lunar and Planetary Institute Conference*, Abstracts 31.

Geissler, P. E., Smyth, W. H., McEwen, A. S., Ip, W., Belton, M. J. S., Johnson, T. V., Ingersoll, A. P., Rages, K., Hubbard, W., and Dessler, A. J. 2001a. Morphology and time variability of Io's visible aurora. *Journal of Geophysical Research*, **106**, 26137–26146.

Geissler, P., McEwen, A., Phillips, C., Simonelli, D., Lopes, R. M. C., and Douté, S. 2001b. Galileo imaging of SO_2 frosts on Io. *Journal of Geophysical Research*, **106**, 33253–33266.

Geissler, P., McEwen, A., Porco, C., Strobel, D., Saur, J., Ajello, J., and West, R. 2004a. Cassini observations of Io's visible aurorae. *Icarus*, **172**, 127–140.

Geissler, P., McEwen, A., Phillips, C., Keszthelyi, L., and Spencer, J. 2004b. Surface changes on Io during the Galileo mission. *Icarus*, **169**, 29–64.

Glaze, L. and Baloga, S. 2000. Stochastic–ballistic eruption plumes on Io. *Journal of Geophysical Research*, **105**, 17579–17588.

Gold, T. 1979. Electrical origin of the outbursts on Io. *Science*, **206**, 1071–1073.

Ingersoll, A. P. 1989. Io meteorology: How atmospheric pressure is controlled locally by volcanos and surface frosts. *Icarus*, **81**, 298–313.

Jessup, K. L., Spencer, J. R., Ballester, G. E., Howell, R. R., Roesler, F., Vigel, M., and Yelle, R. 2004a. The atmospheric signature of Io's Prometheus plume and anti-Jovian hemisphere: Evidence for a sublimation atmosphere. *Icarus*, **169**, 197–215.

Jessup, K. L., Spencer, J., and Yelle, R. 2004b. Variability and Composition of Io's Pele Plume. AAS/Division for Planetary Sciences Meeting Abstracts 36.

Johnson, R. E. 1997. NOTE: Polar "Caps" on Ganymede and Io revisited. *Icarus*, **128**, 469–471.

Johnson, T. V. and Soderblom, L. A. 1982. Volcanic eruptions on Io: Implications for surface evolution and mass loss. In: D. Morrison (ed.), *Satellites of Jupiter*. University of Arizona Press, Tuscon, AZ, pp. 634–646.

Johnson, T. V., Matson, D. L., Blaney, D. L., Veeder, G. J., and Davies, A. 1995. Stealth plumes on Io. *Geophysical Research Letters*, **22**, 3293–3296.

Keszthelyi, L., McEwen, A. S., Phillips, C. B., Milazzo, M., Geissler, P., Turtle, E. P., Radebaugh, J., Williams, D. A., Simonelli, D. P., Breneman, H. H. *et al*., 2001. Imaging of volcanic activity on Jupiter's moon Io by Galileo during the Galileo Europa Mission and the Galileo Millennium Mission. *Journal of Geophysical Research*, **106**, 33025–33052.

Kieffer, S. W. 1982. Dynamics and thermodynamics of volcanic eruptions: Implications for the plumes of Io. In: D. Morrison (ed), *Satellites of Jupiter*. University of Arizona Press, Tuscon, AZ, pp. 647–723.

Kieffer, S. W., Lopes-Gautier, R., McEwen, A., Smythe, W., Keszthelyi, L., and Carlson, R. 2000. Prometheus: Io's wandering plume. *Science*, **288**, 1204–1208.

Krüger, H., Geissler, P., Horányi, M., Graps, A. L., Kempf, S., Srama, R., Moragas-Klostermeyer, G., Moissl, R., Johnson, T. V., and Grün, E. 2003. Jovian dust streams: A monitor of Io's volcanic plume activity. *Geophysical Research Letters*, **30**(21), SSC 3-1, doi:10.1029/2003GL017827.

Lellouch, E. 1996. Io's atmosphere: Not yet understood. *Icarus*, **124**, 1–21.

Lellouch, E., Encrenaz, T., Belton, M., de Pater, I., and Gulkis, S. 1990. Io's atmosphere from microwave detection of SO_2. *Nature*, **346**, 639–641.

Lellouch, E., Belton, M., de Pater, I., Paubert, G., Gulkis, S., and Encrenaz, T. 1992. The structure, stability, and global distribution of Io's atmosphere. *Icarus*, **98**, 271–295.

Lellouch, E., Belton, M., Ballester, G. P., and de Pater, I. 1994. Millimeter-wave observations of Io's atmosphere: New data and new models. *Bull. Am. Astron. Soc*., **26**, 1136.

Lellouch, E., Strobel, D. F., Belton, M. J. S., Summers, M. E., Paubert, G., and Moreno, R. 1996. Detection of Sulfur Monoxide in Io's Atmosphere. *Astrophysical Journal*, **459**, L107.

Lellouch, E., Paubert, G., Moses, J. I., Schneider, N. M., and Strobel, D. F. 2003. Volcanically emitted sodium chloride as a source for Io's neutral clouds and plasma torus. *Nature*, **421**, 45–47.

Lopes, R. M. C., Kamp, L. W., Smythe, W. D., Mouginis-Mark, P., Kargel, J., Radebaugh, J., Turtle, E. P., Perry, J., Williams, D. A., Carlson, R. W. *et al.* 2004. Lava lakes on Io: Observations of Io's volcanic activity from Galileo NIMS during the 2001 fly-bys. *Icarus*, **169**, 140–174.

McEwen, A. S. and Soderblom, L. 1983. Two classes of volcanic plumes on Io. *Icarus*, **58**, 197–226.

McEwen, A. S., Keszthelyi, L., Geissler, P., Simonelli, D. P., Carr, M. H., Johnson, T. V., Klaasen, K. P., Breneman, H. H., Jones, T. J., Kaufman, J. M. *et al.* 1998. Active Volcanism on Io as Seen by Galileo SSI. *Icarus*, **135**, 181–219.

McGrath, M. A., Belton, M. J. S., Spencer, J. R., and Sartoretti, P. 2000. Spatially resolved spectroscopy of Io's Pele plume and SO_2 atmosphere. *Icarus*, **146**, 476–493.

Milazzo, M. P., Keszthelyi, L. P., and McEwen, A. S. 2001. Observations and initial modeling of lava–SO_2 interactions at Prometheus, Io. *Journal of Geophysical Research*, **106**, 33121–33128.

Moreno, M. A., Schubert, G., Baumgardner, J., Kivelson, M. G., and Paige, D. A. 1991. Io's volcanic and sublimation atmospheres. *Icarus*, **93**, 63–81.

Moses, J. I. and Nash, D. B. 1991. Phase transformations and the spectral reflectance of solid sulfur: Can metastable sulfur allotropes exist on Io? *Icarus*, **89**, 277–304.

Moses, J. I., Zolotov, M. Y., and Fegley, B. 2002a. Photochemistry of a volcanically driven atmosphere on Io: Sulfur and oxygen species from a Pele-type eruption. *Icarus*, **156**, 76–106.

Moses, J. I., Zolotov, M. Y., and Fegley, B. 2002b. Alkali and chlorine photochemistry in a volcanically driven atmosphere on Io. *Icarus*, **156**, 107–135.

Pearl, J., Hanel, R., Kunde, V., Maguire, W., Fox, K., Gupta, S., Ponnamperuma, C., and Raulin, F. 1979. Identification of gaseous SO_2 and new upper limits for other gases on Io. *Nature*, **280**, 755–758.

Peratt, A. L. and Dessler, A. J. 1988. Filamentation of volcanic plumes on the Jovian satellite Io. *Astrophysics and Space Science*, **144**, 451–461.

Porco, C. C., West, R. A., McEwen, A., Del Genio, A. D., Ingersoll, A. P., Thomas, P., Squyres, S., Dones, L., Murray, C. D., Johnson, T. V. *et al.* 2003. Cassini imaging of Jupiter's atmosphere, satellites, and rings. *Science*, **299**, 1541–1547.

Postberg, F., Kempf, S., Sramaa, R., Green, S., Hillier, J., McBride, N., and Grün, E. 2006. Composition of jovian dust stream particles. *Icarus*, in press.

Radebaugh, J., Keszthelyi, L. P., McEwen, A. S., Turtle, E. P., Jaeger, W., and Milazzo, M. 2001. Paterae on Io: A new type of volcanic caldera? *Journal of Geophysical Research*, **106**, 33005–33020.

Radebaugh, J., McEwen, A. S., Milazzo, M. P., Keszthelyi, L. P., Davies, A. G., Turtle, E. P., and Dawson, D. D. 2004. Observations and temperatures of Io's Pele Patera from Cassini and Galileo spacecraft images. *Icarus*, **169**, 65–79.

Retherford, K. D., Moos, H. W., Strobel, D. F., Wolven, B. C., and Roesler, F. L. 2000. Io's equatorial spots: Morphology of neutral UV emissions. *Journal of Geophysical Research*, **105**, 27157–27166.

Roesler, F. L., Moos, H. W., Oliversen, R. J., Woodward, R. C., Retherford, K. D., Scherb, F., McGrath, M. A., Smyth, W. H., Feldman, P. D., and Strobel, D. F. 1999. Far-ultraviolet imaging spectroscopy of Io's atmosphere with HST/STIS. *Science*, **283**, 353.

Spencer, J. R. and Schneider, N. M. 1996. Io on the eve of the Galileo Mission. *Annual Review of Earth and Planetary Sciences*, **24**, 125–190.

Spencer, J. R., Jessup, K. L., McGrath, M. A., Ballester, G. E., and Yelle, R. 2000. Discovery of Gaseous S_2 in Io's Pele Plume. *Science*, **288**, 1208–1210.

Spencer, J. R., Sartoretti, P., Ballester, G. E., McEwen, A. S., Clarke, J. T., and McGrath, M. A. 1997. Pele plume (Io): Observations with the Hubble Space Telescope. *Geophysical Research Letters*, **24**, 2471–2474.

Strobel, D. F. and Wolven, B. C. 2001. The atmosphere of Io: Abundances and sources of sulfur dioxide and atomic hydrogen. *Astrophys. Space Sci.*, **277**, 271–287.

Strom, R. G., Schneider, N. M., Terrile, R. J., Cook, A. F., and Hansen, C. 1981. Volcanic eruptions on Io. *Journal of Geophysical Research*, **86**, 8593–8620.

Strom, R. G. and Schneider, N. M. 1982. Volcanic eruption plumes on Io. In: D. Morrison (ed.), *Satellites of Jupiter*. University of Arizona Press, Tuscon, AZ, pp. 598–633.

Zhang, J. 2004. Simulation of gas dynamics, radiation and particulates in volcanic plumes on Io. University of Texas at Austin PhD Dissertation, May, 2004.

Zhang, J., Goldstein, D. B., Varghese, P. L., Gimelshein, N. E., Gimelshein, S. F., and Levin, D. A. 2003a. Simulation of gas dynamics and radiation in volcanic plumes on Io. *Icarus*, **163**, 182–197.

Zhang, J., Goldstein, D. B., Varghese, P. L., Gimelshein, N. E., Gimelshein, S. F., Levin, D. A., and Trafton, L. M. 2003b. DSMC modeling of gas dynamics, radiation and particulates in Ionian volcanic jets. In: A. Ketsdever and E. P. Muntz (eds), *Proceedings of 23rd International Symposium on Rarefied Gas Dynamics* (vol. 663). AIP, New York, pp. 704–711.

Zhang, J., Miki, K., Goldstein, D. B., Varghese, P. L., and Trafton, L. M. 2003c. Modeling of radiation above Io's surface from Pele-type volcanic plumes and underground from the conduit wall. *Lunar and Planet. Sci.*, **XXXIV**, Abstract #2123.

Zhang, J., Goldstein, D. B., Varghese, P. L., Trafton, L. M., Miki, K., and Moore, C. 2004. Numerical modeling of ionian volcanic plumes with entrained particulates. *Icarus*, **172**, 479–502.

Zolotov, M. Y. and Fegley, B. 1999. Oxidation state of volcanic gases and the interior of Io. *Icarus*, **141**, 40–52.

Zolotov, M. Y. and Fegley, B. 2000. Eruption conditions of Pele volcano on Io inferred from chemistry of its volcanic plume. *Geophysical Research Letters*, **27**, 2789–2792.

9

Io's surface composition

Robert W. Carlson, Jeff S. Kargel, Sylvain Douté, Laurence A. Soderblom, and J. Brad Dalton

9.1 INTRODUCTION

The Jovian system presents a panorama of extremes, containing the largest planet in the Solar System surrounded by an equally large and energetic magnetosphere. Orbiting within this magnetosphere is a quartet of planet-sized bodies, the Galilean satellites. The outer three are (water) ice covered bodies. The innermost satellite, Io, differs from the others by being covered by a different kind of ice, frozen sulfur dioxide, and exhibiting the youngest surface in the Solar System, constantly being resurfaced as the most volcanically active body in the Solar System. Incessant tidal kneading heats Io's crust and mantle. This heat escapes through lava flows and eruptions, producing towering volcanic plumes and a dynamic atmosphere. Some plume material escapes to the magnetosphere, forming neutral and ionized belts of gas and plasma around Jupiter and painting neighboring satellites with implanted atoms and ions.

The constantly changing surface is colored from a palette of reds, yellows, greens, grays, white, and black. Fire and ice cover the surface as sulfur, sulfur dioxide, silicates, and unidentified materials derived from plumes, lava lakes, lava flows, fire fountains, and possibly sulfur and sulfur dioxide flows. The surface composition provides clues to the processes that form the surface but also hides information about composition at depth, tantalizing us with puzzling, unidentified colors and spectral features. The observed composition is the result of numerous processes, ranging from initial formation and differentiation, continual cycling of the interior, volcanic activity, plume deposition and redistribution through sublimation, and eventual burial or escape as dust and molecules. In this chapter we summarize what is known and not known about Io's surface composition and some relationships to

volcanic and atmospheric processes. Recent reviews and summaries are given by Geissler (2003), McEwen *et al.* (2004), and Lopes and Williams (2005).

9.1.1 Properties and environment of Io

With a density of 3.53 g cm^{-3}, Io is the highest density object in the outer Solar System and must be composed mainly of silicates, with little H_2O content, if any. Formation models of the Galilean satellites relate the radial decrease in satellite densities (higher ice content with increasing distance from Jupiter) to the radial decrease in Jovian nebula temperatures and ice condensation regions during satellite formation (Lunine *et al.*, 2004; Schubert *et al.*, 2004; see also Chapter 4). However, current models cannot state how much water was incorporated in the newly formed Io. A Jovian nebula snow line beyond Io is consistent with observations but it seems feasible that some water as hydrated silicates was incorporated during formation (Pollack and Fanale, 1982). Almost all such water, if any was accreted, was subsequently lost, because we do not see much water on the surface today. The sulfurous surface indicates that Io formed inside an equivalent condensation front for S-bearing compounds, but the sulfur must have been initially introduced as comparatively refractory metal sulfides, rather than sulfur oxides, because the latter are even more volatile that H_2O.

Galileo radio science results indicate an Fe or Fe–FeS metallic core and at least the outer part should be molten, but there is no internally generated magnetic field (Schubert *et al.*, 2004; see also Chapter 5). The density model suggests a silicate mantle surrounding the core. A recent model finds that the core is completely molten as are portions of the silicate mantle (Keszthelyi *et al.*, 2004). Observed levels of volcanic activity and the corresponding volume of lava relative to the size of Io suggests that each part of Io has been subject to numerous (hundreds) of episodes of melting (Keszthelyi and McEwen, 1997; Keszthelyi *et al.*, 2004), so what we see today is substantially a product of repeated partial melting and crystallization and volatile loss as well as partial recondensation of volatiles on a volcanic surface. This history suggests that there is much uncertainty attached to any estimations of the conditions during the nebula origins of Io or of its initial composition. There have been ample opportunities to generate in Io the most intense igneous and volatile fractionations of any object in the Solar System (Kargel *et al.*, 2003).

Io resides in the heart of Jupiter's powerful magnetosphere and has long been known to interact with it, being bombarded by energetic magnetospheric particles, producing neutral and plasma belts (torii) around Jupiter, and modulating Jupiter's decametric radio emission (see Chapter 11). Io is bombarded by electrons and ions, with the electron component being the most intense. However, the region of electron irradiation is probably limited to the trailing side due to rapid depletion electrons in the flux tubes (Paranicas *et al.*, 2003). The proton flux is more uniform but may be only $\sim$1% of the electron flux (Paranicas *et al.*, 2003). Io also electrically couples to the Jovian upper atmosphere along magnetic flux lines and may be a source of sulfur ions in Jupiter's atmosphere at the foot of the flux tube. Ion and electron sputtering is a major source of atoms, molecules, ions, and dust grains to the magnetosphere. The magnetosphere modifies the surface by radiolysis and implantation, but volcanic and

sublimational resurfacing is rapid so the resulting concentration of radiolytic products may be unimportant. Exceptions may occur on the trailing side, where the flux of energetic electrons is large, or in polar regions, where sublimational resurfacing is slow.

9.1.2 A brief history of Io composition determinations

Io's unusual orange color was recognized by Hertzsprung in 1911 (Kuiper, 1951) and for many years was the reddest object known in the outer Solar System. The darker, redder poles were observed by Minton in 1973 and Murray in 1975 and suggested by Morrison and Burns (1976) to be due to charged-particle irradiation effects since *Pioneer* measurements showed a strong coupling between the magnetosphere and Io (see review by Morrison and Burns,1976; see also Chapter 2). The surface composition was unknown, but absence of an ammonia and methane atmosphere, as possessed by Jupiter, was established by Kuiper (1951). The absence of water ice was first noted by Kuiper in a 1957 abstract, and verified using infrared filter photometry, prism spectrometers, and Fourier transform spectrometers (see review by Johnson and Pilcher, 1977). Much of the early work on Io's surface and atmospheric composition was influenced by the report of post-eclipse brightening (Binder and Cruikshank, 1964), an elusive and yet unverified phenomenon.

Noting that formation models suggested incorporation of hydrated silicates, Fanale and coworkers postulated an evaporate salt surface for Io, where salt-rich water driven from the hot interior evaporates from the surface, leaving bright salt pans (Fanale *et al.*, 1977). Alternatively, Io's low ultraviolet reflectivity prompted Wamsteker *et al.* (1973) to propose sulfur as a constituent based on laboratory measurements although Johnson and McCord had proposed polysulfides in 1971 (Johnson and McCord, 1971). Nelson and Hapke (1978) discussed sulfur allotropes and suggested their presence, possibly produced in volcanic fumeroles, to explain Io's color. Reviews of sulfur on Io and properties of sulfur were given by Sill and Clark (1982) and Nash *et al.* (1986) but significant advances have been made in understanding sulfur subsequent to these reviews. The salt hypothesis was bolstered by the discovery of Io's Na cloud by R. A. Brown in 1974, followed by Trafton's discovery of K in the neutral torus. The notion of sulfur on the surface was boosted by Kupo *et al.*'s (1976) detection of S^+ in the plasma torus (see review by Thomas *et al.*, 2004b).

On the eve of *Voyager*'s first fly-by of the Jupiter system, unidentified bands were found in Io's infrared spectrum (Cruikshank *et al.*, 1978; Pollack *et al.*, 1978; Fink *et al.*, 1978), intense, transient infrared brightening was observed from Io (Witteborn *et al.*, 1979), and tidal heating was predicted that could lead to widespread and recurrent volcanism (Peale *et al.*, 1979). *Voyager* indeed found volcanism (Morabito *et al.*, 1979) and gaseous sulfur dioxide over an active vent (Pearl *et al.*, 1979), leading to the rapid identification of condensed SO_2 as the IR surficial absorber (Hapke, 1979; Fanale *et al.*, 1979; Smythe *et al.*, 1979).

The relatively low temperatures measured by *Voyager*'s IRIS instrument and similarities between Io's colorful, variegated surface and the many colors of sulfur

allotropes suggested the existence of sulfur flows (Sagan, 1979; Pieri *et al.*, 1984) and sulfur volcanism. However, the ductile behavior of sulfur at depths of just a few hundred meters is inconsistent with the kilometer-scale mountains and cliffs on Io (Carr *et al.*, 1979; Clow and Carr, 1980). Ground-based measurements of Io's volcanoes indicated temperatures of ~900 K and, since this temperature is much greater than the 500-K boiling point of sulfur, silicate volcanism was suggested (Johnson *et al.*, 1988). Subsequent measurements showed even higher temperatures, consistent with high-temperature silicate volcanism (see review by McEwen *et al.*, 2000).

During the 16 years between the *Voyager* fly-bys and *Galileo*'s arrival at Jupiter, numerous spectral measurements were obtained from ground-based telescopes, International Ultraviolet Explorer (IUE), International Space Observatory (ISO), and the Hubble Space Telescope (HST). Hot spot monitoring was carried out by Sinton *et al.* (1983). The longitudinal distribution of surficial SO_2 was measured by IUE (Nelson *et al.*, 1980; Nelson *et al.*, 1987) and ground-based infrared spectroscopy (Howell *et al.*, 1984) while SO_2 maps were derived from *Voyager* and HST images. Additional features were found in ground-based infrared spectra, prompting extensive laboratory work and numerous suggestions for spectral identifications (discussed later). High-resolution spectra of Io were obtained by Schmidt *et al.*'s ISO observations (see Schmitt and Rodriguez, 2000). Eleven years after *Voyager*'s discovery of SO_2 in the atmosphere, Lellouch *et al.* (1990) obtained microwave measurements of atmospheric SO_2, followed by Ballester *et al.*'s (1994) ultraviolet measurement of atmospheric SO_2 from HST. Atmospheric SO was later observed by Lellouch *et al.* (1996) and NaCl was observed in volcanic plumes, finally resolving the puzzle of Io's sodium source (Lellouch *et al.*, 2003). Plume modeling by Zolotov, Fegley, and co-workers provided insight into surface composition and volcanic plumes. A pre-*Galileo* summary of Io spectroscopy and surface composition is found in Nash and Betts (1998) and a pre-*Galileo* review of Io was presented by Spencer and Schneider (1996).

Formation of the *International Jupiter Watch* in 1990 (Russell *et al.*, 1990), with monitoring of Io through its *Io Watch* component, provided temporal coverage of time-variable phenomena in the Jovian system to complement the forthcoming *Galileo* measurements. These important ground-based and Earth-orbiting measurements continued throughout *Galileo*'s observational phase and still continue today.

Galileo arrived at Jupiter in December 1995 and carried infrared and ultraviolet spectrometers for compositional mapping (near-infrared mapping spectrometer (NIMS) and ultraviolet spectrometer (UVS)), a photopolarimeter and radiometer instrument (PPR) for thermal measurements, and a camera with narrow and wide-band filters (solid-state imaging system (SSI)). Additionally, various fields and particle instruments that provided *in situ* compositional data in the vicinity of Io as well as magnetic field and plasma wave measurements. The *Galileo* mission and its experiment complement are described in a volume of *Space Science Reviews* (Russell, 1992; see also Chapter 3). Remote-sensing observations during the Io fly-by at Jupiter orbit insertion were precluded due to problems with the spacecraft's tape recorder and no close encounters with Io occurred during the prime mission, limiting the spatial resolution of Io observations during that period. Following the prime mission,

two extended missions did provide numerous close fly-bys of Io. Unfortunately, spectral scanning in the NIMS instrument became inoperative due to radiation damage prior to the first of the close Io fly-bys, so contiguous spectra of Io at high spatial resolution were never obtained by NIMS. This limitation severely degraded the NIMS search for silicate minerals, but thermal and compositional mappings (SO_2) were performed with the remaining fixed-wavelength channels. Despite the low data rate from loss of the high-gain antenna, the *Galileo* data set has high science content and more discoveries are expected from continued analysis of these and Earth-based observations.

9.2 SPECTROSCOPIC DETERMINATIONS OF IO'S COMPOSITION

9.2.1 Overview

Compositional information is derived from numerous sources, including surface reflection and thermal spectroscopy, emission spectroscopy from the atmosphere and torus, x-ray spectroscopy, and *in situ* plasma and plasma wave measurements. Reflectance spectroscopy is the most widely exploited technique, performed from ground-based and Earth-orbiting telescopes and from the *Galileo* spacecraft in Jupiter orbit. As a summary and introduction to the discussion that follows, reflectance spectra of Io, adopted and extended from the compilation by Spencer *et al.* (2004), are shown in Figure 9.1 with diagnostic spectral features delineated in Table 9.1 and discussed below.

The ultraviolet region shows absorption features from atmospheric and surficial SO_2 in the 200–240-nm region and a longer wavelength band from condensed SO_2 centered at 280 nm. There could be some absorption from S_8 and polymeric sulfur S_∞ as well. The edge at 330 nm is indicative of SO_2. For the visible region, the edge extending from 400–500 nm is characteristic of sulfur although disulfur monoxide and polysulfur oxide (PSO) have also been attributed to this absorption. An absorption feature at 560 nm is attributed to tetrasulfur S_4. Io's dark caldera material exhibits an absorption feature at 890 nm that has been attributed to iron-containing silicates. The broad rise between $\sim$1 μm and $\sim$2 μm in the infrared is unexplained; candidate absorbers are Fe-containing silicates or salts, sulfides, impure sulfur, or sulfur polymers. From 1.98 μm to 5.2 μm, most of the features are due to sulfur dioxide including isotopic bands. The feature at 3.15 μm is apparently not due to SO_2; H_2O has been suggested as the absorber and oxyhydroxides are possible. An absorption band at 3.94 μm, superimposed on an SO_2 absorption plateau, has been suggested to be due to H_2S or, more recently, Cl_2SO_2 and $ClSO_2$. Thermal emission spectra (Figure 9.4) show evidence for S_8, SO_2, possibly SO_3, and perhaps others. Spectra of Io's plumes (not shown) indicate sulfur (S_2) and sodium chloride. Emission spectra of the Io torus (not shown) indicate that Na, K, and Cl atoms are being ejected from the surface or plumes, along with sulfur and oxygen. The above constituents and other plausible candidates that have been suggested are discussed below.

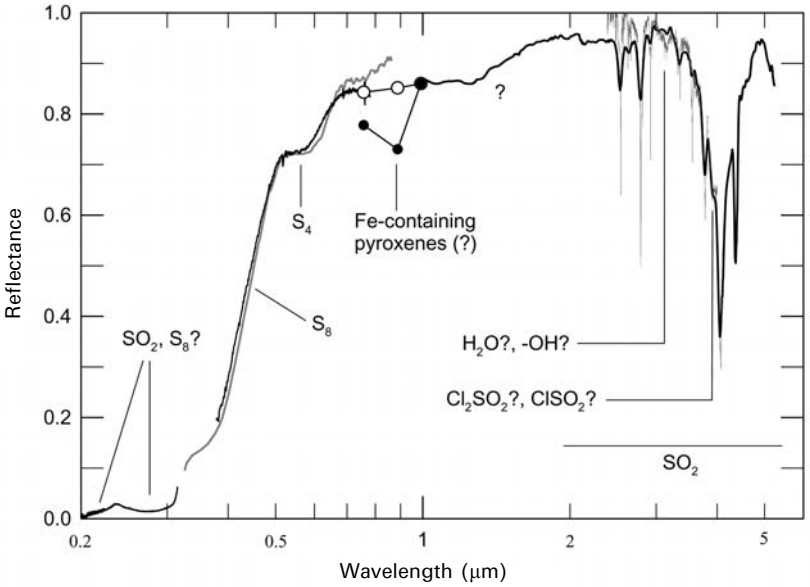

Figure 9.1. Solar reflectance spectra of Io. The ultraviolet HST measurements in the 200- to 310-nm region are from Jessup *et al.* (2002); ground-based measurements from 330–860-nm data (blue line; see also color section) and from 380–780 nm (black line) are from Nelson and Hapke (1978) and Spencer *et al.* (1995), respectively. Scaled *Galileo* SSI multicolor spectrophotometry of white areas (open circles) and dark areas (filled circles) are from Geissler *et al.* (1999). Modest resolution near-infrared measurements by *Galileo* NIMS (black line) are from Carlson *et al.* (1997) while the higher resolution ISO spectrum (red line) is from Schmitt and Rodriguez (2003). Many of these spectra are summarized in the compilation by Spencer *et al.* (2004).

9.2.2 Sulfur

Properties of sulfur

There has been considerable progress in elucidating the properties of sulfur in the past two decades, summarized recently in several articles in two volumes (Steudel, 2003a, b). Since sulfur is an important component of Io's surface, we summarize its properties using the above-mentioned reviews, along with the review by Sill and Clark (1982) and original research papers.

Physical properties. Sulfur can exist in many different sizes of molecular clusters S_n, generally as chains (catena-S) or rings (cyclo-S). Small sulfur molecules, where $n = 2$, 3, or 4, form chains whereas molecules with $n = 6$ to at least 20 form rings. The $n = 5$ molecule can produce either chains or rings, but the lowest energy state is the ring form. A number of isomers are possible for each n. The ring structures are more stable than chains, and molecules with an even number of sulfur atoms are more stable than those with odd numbers of molecules.

Table 9.1. Io's spectral features with known or suggested identifications of surface species and related atoms and molecules.

Type of spectrum	Wavelength, wavenumber, or spectral region	Identifications and suggestions	Notes
Solar reflectance	200–300 nm	SO_2, possible S_8, S_∞	Primarily SO_2
Solar reflectance	350–500 nm	Absorption edge; S_8, S_∞, possible polysulfur oxides (PSO)	$S_8(\beta)$ likely
Solar reflectance	~560 nm	S_4, but Na_2S, S_2O, Cl_2S, and color-centers also suggested	S_4 most likely
Solar reflectance	~900 nm	Fe-containing orthopyroxene (enstatite)	No olivine
Solar reflectance	1–1.6 μm	Fe-containing salts, feldspars, FeS_2, polymeric S (S dangling bonds) sulfur with impurities	Ubiquitous feature, enhanced in southern polar region, depleted in Pele plume deposit
Solar reflectance	1.98–5 μm	SO_2	Ubiquitous frost
Solar reflectance	3–5 μm	H_2SO_3 suggested for some SO_2 bands	Production rate extremely small compared with resurfacing rate
Solar reflectance	3.15 μm	H_2O in SO_2, mineralic OH, HCl	Enhanced concentration in bright equatorial SO_2 snowfields
Solar reflectance	3 μm	H_2O?	Localized feature
Solar reflectance	3.92 μm	H_2S (?), Cl_2SO_2 (?)	H_2S unstable on Io
Mid-infrared thermal emission (*Voyager*)	400–600 cm^{-1}	S_8, SO_2, SO_3, S_2O rings	Detailed analysis unpublished. See Figure 9.4.
Plume spectra	Ultraviolet, visible, microwave	S_2, SO, NaCl, KCl (possible)	Powerful method for Io composition studies
Exosphere and torii emission spectra	Various	Neutral Na, K, Cl, S, SO and ions of O, S, Cl	Upper limits for other species given by Na *et al.* (1998)
Plasma wave features	Ion cyclotron	SO2, SO, H2S, Cl, S ions	H_2S signal sporadic, noisy

In the vapor phase, between 473 K and 1,273 K, molecules with 2–10 atoms are formed and some of these molecules exist as two different isomers (S_4 in particular). At low temperatures, the cyclic S_8, S_7, and S_6 forms dominate, but at higher temperatures S_3 and then S_2 are the most abundant. S_4 is most abundant at 900 K (Steudel *et al.*, 2003).

Liquid sulfur at low temperature contains rings with 6 to at least 35 atoms and probably even larger rings and polymers, denoted S_∞. Above 523 K the small chains S_2, S_3, S_4, and S_5 are also present.

In the solid state many of these allotropes form one or more stable crystals. For example, the most stable form of sulfur is S_8, the cyclo-octal form sometimes called λ-S, which can crystallize into orthorhombic and two different monoclinic forms, denoted $S_8(\alpha)$, $S_8(\beta)$, and $S_8(\lambda)$, respectively. High molecular weight sulfur molecules, polymeric sulfur, denoted S_μ or S_∞, form long chains and probably contain large ringed molecules as well. The α-form of S_8 is the only thermodynamically stable form below 367 K and assemblages of the more unstable molecules eventually revert to $S_8(\alpha)$ at annealing rates that are not well established. $S_8(\beta)$ can be long-lived below 198 K. The polymeric form S_∞ and $S_8(\beta)$ have been studied by Moses and Nash (1991), who showed that these forms can exist as long-lived metastable species on Io.

Solid sulfur phases are bound by Van der Waals forces so the crystals are friable and have low melting points. The melting points for $S_8(\alpha)$ and $S_8(\beta)$ are about 388 K and 393 K, respectively (Eckert and Steudal, 2003).

Spectroscopic properties. The S_2 molecule absorbs in the Schumann–Runge band $B^3\Sigma_g^- \leftarrow X^3\Sigma_u^-$ from the ultraviolet to 500 nm or greater, with the band origin occurring at 316 nm, and appears pale violet in the vapor state (Meyer *et al.*, 1972; Eckert and Steudal, 2003). S_3 has an absorption band with diffuse structure centered at 400 nm and extending to ~500 nm. S_4 exhibits two continua, a band centered at about 530 nm and absorbing between ~460–590 nm that is attributed to the C_{2v} isomer and a weaker band of the C_{2h} form at 625 nm (Meyer *et al.*, 1972; Eckert and Steudal, 2003). It is the 530-nm S_4 (C_{2v}) system that causes sulfur vapor to appear red (Meyer *et al.*, 1972). The molar extinction coefficient for S_3 is ~ 10× that of S_4. Weak bands around 750 nm are observed in the vapor but their origin is unknown (Meyer *et al.*, 1972). S_8 vapor shows a strong absorption band at ~280 nm, a minimum or inflection point at 245 nm, and a stronger band extending down to 210 nm and below (Bass, 1963).

The red absorbing tetrasulfur S_4 can be formed during co-deposition of S_2+Kr when $S_2 : Kr > 1 : 200$, forming a red film. Films of S_2 in Kr produced with lesser amounts of S_2 yield S_4 when irradiated with visible light (Meyer and Stroyer-Hansen, 1972). Annealing of S_2 in a Kr matrix also produces the 530-nm feature of S_4 (Meyer *et al.*, 1972).

Liquid S_8 at its melting point (393 K) is yellow due to the strong ultraviolet absorption and vibrational broadening that extends the wing of the absorption band into the blue end of the visible spectrum. As the temperature rises, the absorption shifts to longer wavelengths and other catena-S and chained-S contribute to the absorption. Between 573–973 K, the 400-nm absorption band of S_3 becomes

apparent, and this band and the 530-nm band of S_4 (C_{2v}) are found between 773–1,173 K. The deep red and red–brown color of liquid sulfur above 673 K has been attributed to a mix of greenish-yellow S_3, the purple–red S_4, and short-chains that can absorb at longer wavelengths. For temperatures >673 K, the increased density of chain radicals produces an absorption band at ~950 nm due to excitation of the chain ends – dangling bonds (Hosokawa *et al.*, 1994; Eckert and Steudal, 2003). The absorption can extend to 1.3 μm and beyond.

Condensed sulfur vapor and quenched sulfur melts frozen at low temperatures exhibiting various colors ranging from black, green, or red that arise from small molecules and radicals trapped in the solid (Eckert and Steudal, 2003). Vapor condensed at 77 K is yellow for furnace temperatures of 415–475 K, green for temperatures of 475–550 K, olive green at 550–800 K, and purple for 800–1,200 K. The purple color changed to olive green when the sample's temperature was elevated from 77 K to 195 K. All films except the purple ones were stable at 195 K (Meyer *et al.*, 1971; Eckert and Steudal, 2003; Radford and Rice, 1960; Chatelain and Buttet, 1965). Quenched red sulfur is metastable at 77 K and converts to yellow polymeric sulfur at 194 K (Meyer *et al.*, 1971).

In the solid phase, cyclic and polymeric sulfur compounds absorb strongly in the ultraviolet with a wing extending into the visible due to thermal excitation of ground-state vibrational levels and, for S_8, phonon-assisted indirect transitions (Eckert and Steudal, 2003). This absorption causes these molecules to appear yellow at room temperature and, if not exposed to ultraviolet radiation (see below), they become white (for S_8, S_{12}, S_{20}) or light yellow (S_6, S_7, S_{10}) at Io-like temperatures (Eckert and Steudal, 2003). Absorption spectra of S_8 and polymeric S show an absorption maximum at ~275–280 nm, an absorption minimum at 250 nm, and strong absorption at shorter wavelengths, similar to the absorption properties of S_8 vapor (Nelson and Hapke, 1978; Sill and Clark, 1982). Sulfur is so absorbing below 400 nm that the reflection properties of most allotropes resemble metals, yielding a flat reflectance spectrum from Fresnel reflection. The 350–500-nm absorption profiles of $S_8(\beta)$ and S_∞ differ somewhat from the S_8 profile (Moses and Nash, 1991). Impurities in sulfur can also alter the absorption and spectral properties (see below).

Raman and infrared spectra are reviewed by Eckert and Steudal (2003) for many allotropes. The infrared-active lines of $S_8(\alpha)$ include the bending transitions at 190–200 cm^{-1} and 240 cm^{-1} and stretching transitions in the 465–480 cm^{-1} region. The infrared spectrum of $S_8(\beta)$ is not available. Polymeric sulfur S_∞ exhibits a strong band at 460 cm^{-1} and a weaker one at 423 cm^{-1}.

Photolytic and radiolytic properties. Under ultraviolet photolysis, white S_8 at 77 K turns yellow (Steudel *et al.*, 1986; Hapke and Graham, 1989), possibly due to generation of S_3. Other allotropes become intense yellow (S_7, S_{10}), grayish-yellow (S_{12}, S_{20}, S_∞), or brownish-yellow (S_6). S_8 stays yellow while the allotropes revert to normal yellow upon heating to room temperature. The timescale at Io's illumination level is a few hours to establish color, and up to a few weeks to achieve equilibrium (Steudel *et al.*, 1986). Photolysis of S_8 in solutions produces bands at 325, 420, 530, and 600 nm (Casal and Scaino, 1985; Nishijima *et al.*, 1976). These are likely from S_3

(400-nm band) and S_4 (530- and 600-nm bands), suggesting that S_8 photolyzes to $S_3 + S_5$ and $S_4 + S_4$. The band at 325 nm may arise from the S_5 molecule but its absorption spectrum is unknown (Eckert and Steudal, 2003).

Energetic electrons and ions bombarding Io's surface will initiate chemical reactions and produce new molecules. These radiolytic reactions are approximately independent of the specific type of ionizing radiation (e.g., electrons, ions, γ-rays, x-rays). Proton irradiation of S_8 at 20 K produces multicolored samples that become black–brown–dark brown at 144 K (Moore, 1984). Under γ-ray irradiation S_8 turns deep red or red–brown and this color remains stable only at low temperature, rapidly reverting to yellow upon warming to room temperature (Radford and Rice, 1960). Nelson *et al.* (1990) performed x-ray irradiations of S_8 and found absorption bands at 420 and 520 nm, consistent with the formation of S_3 and S_4. The 420-nm S_3 feature disappears upon warming to 180 K, but the 520-nm feature remains, reduced somewhat in strength. S_3 produced in an electric discharge disappears when warmed to 130 K while S_4 disappears between 130 and 180 K, producing S_8 (Hopkins *et al.*, 1973). Photolytically produced S_4 has a lifetime of $\sim$60 hours at 171 K (Meyer and Stroyer-Hansen, 1972). Sputtering of S_8 yields mainly S_2 but atomic sulfur and all molecules up to S_8 are present at the $\sim$10% level (Boring *et al.*, 1985; Chrisey *et al.*, 1988).

Impurities in sulfur. As with ice, quartz, and many other minerals, optical transmission into, and scattering from, the interiors of sulfur crystals enables disseminated absorbers (impurities) to modify the effective reflectance spectra of dirty sulfur. This effect has been noted for natural sulfur samples (Kargel *et al.*, 1999) and is further indicated in Figure 9.2 for the case of laboratory controlled disseminations of pyrite (FeS_2) in sulfur (Kargel *et al.*, 2000; MacIntyre *et al.*, 2000). The pyrite imposes differing spectroscopic effects depending on both its grain size and its abundance, and also on the grain size of the sulfur.

Trace amounts of other types of impurities can have even more drastic effects on the spectral properties of sulfur if the impurity either ruptures the polymeric bonds in sulfur or tangles them. In general, elements close to sulfur in the periodic table of the elements have an affinity for sulfur, but unlike chalcophile transition metals (such as Fe, Ni, Cu, and Mn), these elements also have significant solubilities in molten sulfur. The strong chalcophile affinities of many elements has been noted in analyses of natural sulfur samples (Kargel *et al.*, 1999). When these molten mixtures crystallize, the impurities commonly attach to the ends of polymer chains or intrude within them, thus modifying the polymeric state and other physical properties of the sulfur. Since polymer chain length can be large, even small amounts of these impurities can have a large effect on polymerization and spectral reflectivity. This is shown in the case of tellurium in sulfur in Figure 9.3 (Kargel *et al.*, 2000; MacIntyre *et al.*, 2000).

Sulfur on Io

Wamsteker *et al.*'s (1973) suggestion for sulfur on Io was based on the similarity of the 350–500-nm absorption edge, prominent in Io's spectrum, to laboratory reflectance spectra measured by Sill (1973). Sulfur was also thought to be consistent with the

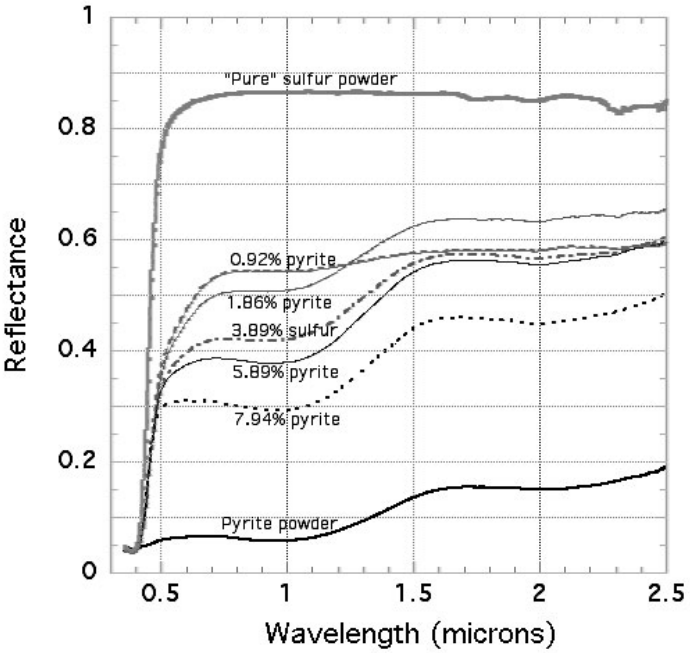

Figure 9.2. Spectra of sulfur with pyrite at various concentrations.

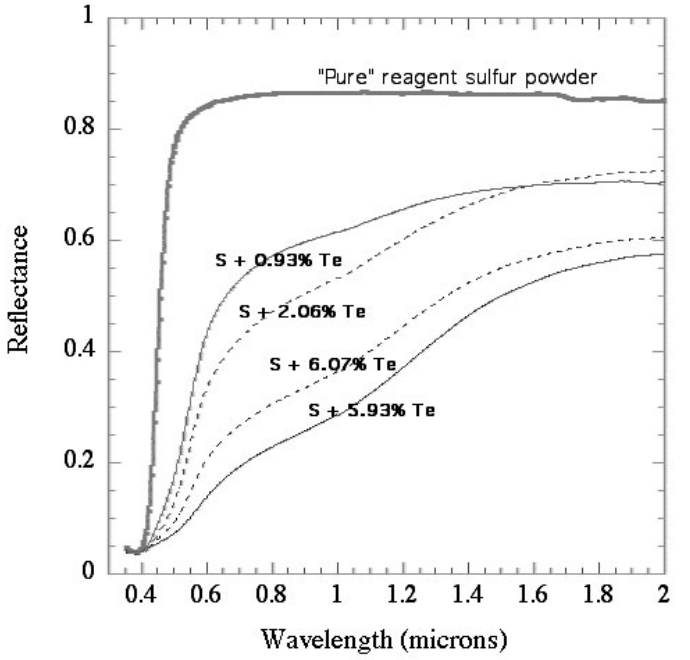

Figure 9.3. Spectra of sulfur with tellurium at various concentrations.

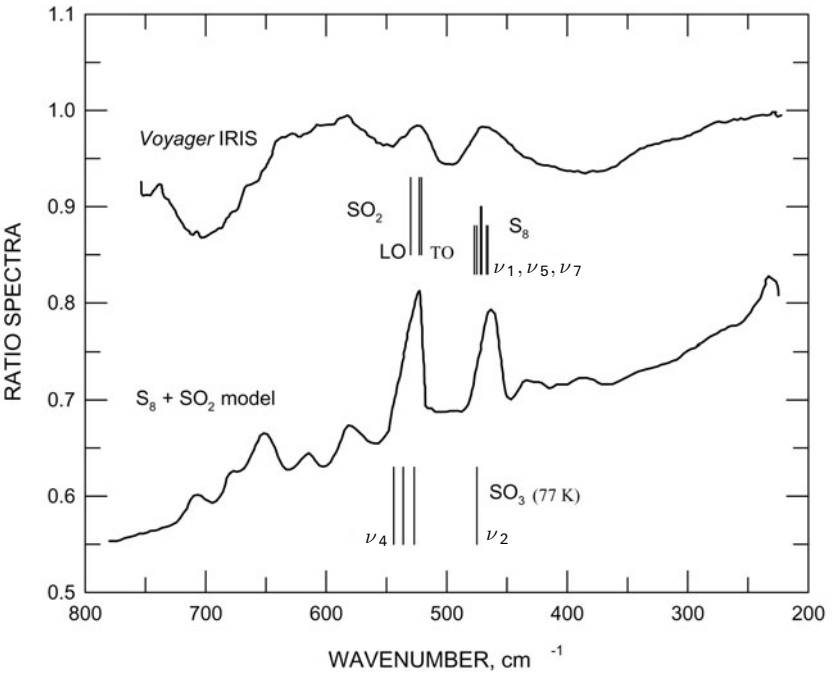

Figure 9.4. *Voyager* thermal emission spectrum of Io and model. The thermal emission spectrum is an average of 78 spectra, divided by an estimated thermal (black body) background. The model is for an unspecified $S_8 + SO_2$ mixture. The positions of fundamental S_8 and SO_2 absorptions are indicated as well as those for the strongest SO_3 bands. The data and model are from Hanel *et al.* (2003).

putative post-eclipse brightening arising from temperature drops during eclipse that shift the sulfur absorption edge to shorter wavelengths, causing the net albedo to be larger when the satellite emerges from eclipse. However, this color effect was not found in *Galileo* images of Io (Simonelli *et al.*, 1994), perhaps due to the presence of non-$S_8(\alpha)$ allotropes that show less color change with temperature (Moses and Nash, 1991). Furthermore, Steudal *et al.* have shown that exposing S_8 for a few days at Io's ultraviolet irradiation level produces a yellow-colored form of sulfur whose color is then insensitive to temperature changes (Steudel *et al.*, 1986). Nelson and Hapke's (1978) ground-based spectrophotometry showed the 400–500-nm edge, an absorption band at 560 nm, and an absorption edge at 330 nm. The latter was attributed to mixtures of sulfur allotropes, but SO_2 absorption provides a better explanation (Nelson *et al.*, 1987; Nelson *et al.*, 1980). Io's 560-nm feature, previously suggested to be from ferric iron (Nash and Fanale, 1977) or color centers in evaporite salts (Fanale *et al.*, 1974, 1977) was identified for the first time with S_4 by Nelson and Hapke (1978).

Additional evidence for elemental sulfur on Io was found in *Voyager* IRIS thermal emission spectra (Figure 9.4; Pearl, 1988; Hanel *et al.*, 2003). Two

features were observed, a band at 525 cm^{-1}, attributed to SO_2, and a band at 470 cm^{-1}, tentatively assigned as the ν_5 band of S_8 (Pearl, 1988) although infrared-active bands of ν_7 and ν_1 transitions can also contribute to the 470-cm^{-1} complex (Eckert and Steudal, 2003). The model fit of Figure 9.2 assumed a temperature decrease with depth of 25 K cm 1^{-1}. No abundances were given (although S_8 is apparently more abundant than SO_2, see Moses and Nash, 1991) and no definitive analysis has been published so this identification remains tentative.

The first spectroscopically definitive measurements of elemental sulfur at Io were the observations of atomic and molecular sulfur (S_2) in the Pele plume by McGrath *et al.* (2000) and Spencer *et al.* (2000).

The existence of sulfur on Io has been proven but the abundance remains in question. Early objections to the presence of massive amounts of sulfur by Young (1984) were based on the white appearance of $S_8(\alpha)$ at Io's temperature, contrary to Io's orange–yellow appearance. This argument was countered by Moses and Nash (1991) who showed that other allotropes ($S_8(\beta)$ and S_∞) that match Io's reflectance spectrum (and color) can be long-lived under Io conditions. Additionally, the rapid ultraviolet yellowing of sulfur at Io-like temperatures found by Steudal *et al.* (1986) negates Young's color argument. Young further suggested that the chromophores S_3 and S_4 would be unstable on Io. Based on the above discussions of S_3 and S_4 this is certainly true for S_3 and there are no spectral features from Io that suggests its presence there. The S_4 (C_{2v}) molecule that likely provides at least some of Io's red tint may have a lifetime of months at Io or more (see below).

A second objection to ubiquitous sulfur on Io was formulated by Hapke (1989) and is based on discrepancies between Io's spectra and spectra of S_8 in the 330–420-nm region. Io spectra show less of an abrupt transition at 400 nm than those of S_8 and many other allotropes. Hapke's alternative model used S_2O and polysulfur oxides (PSO) to explain the shape in this wavelength region and these compounds, with SO_2, produced good fits. Moses and Nash (1991) found that spectral matches – with metastable but long-lived sulfur allotropes – were as good or better than those using S_2O and PSO. Therefore, sulfur, even in large amounts, is not precluded and may be preferred as a dominant surface material on Io.

High spectral resolution (1.8-nm) measurements of Io's leading and trailing hemispheres from HST by Spencer *et al.* (1995) were compared with models containing SO_2+ sulfur (from Moses and Nash, 1991) and $PSO + SO_2 + S_2$ (from Hapke, 1989). Excellent fits were found for each set of candidate species although the 560-nm band is somewhat discrepant. Nash (1993) suggested that $Na_2S + S_2O$ provided a better fit in this wavelength region. S_2O samples show an absorption band at 560 nm but this is probably due to S_4 in the laboratory samples (Hapke, 1989). Inclusion of S_4 absorption in the models considered by Spencer *et al.* may improve the fits without resorting to sodium sulfide or disulfur monoxide.

Io's 560-nm feature was first observed by Johnson and McCord (1970) and is a persistent feature. If it is attributed to S_4, and if S_4 is unstable on Io, the global occurrence and persistence of the feature suggests continuing production of S_4. Sources may include ultraviolet photolysis or radiolysis by energetic electrons and ions from Jupiter's magnetosphere, as well as continual replacement by plume S_4 and

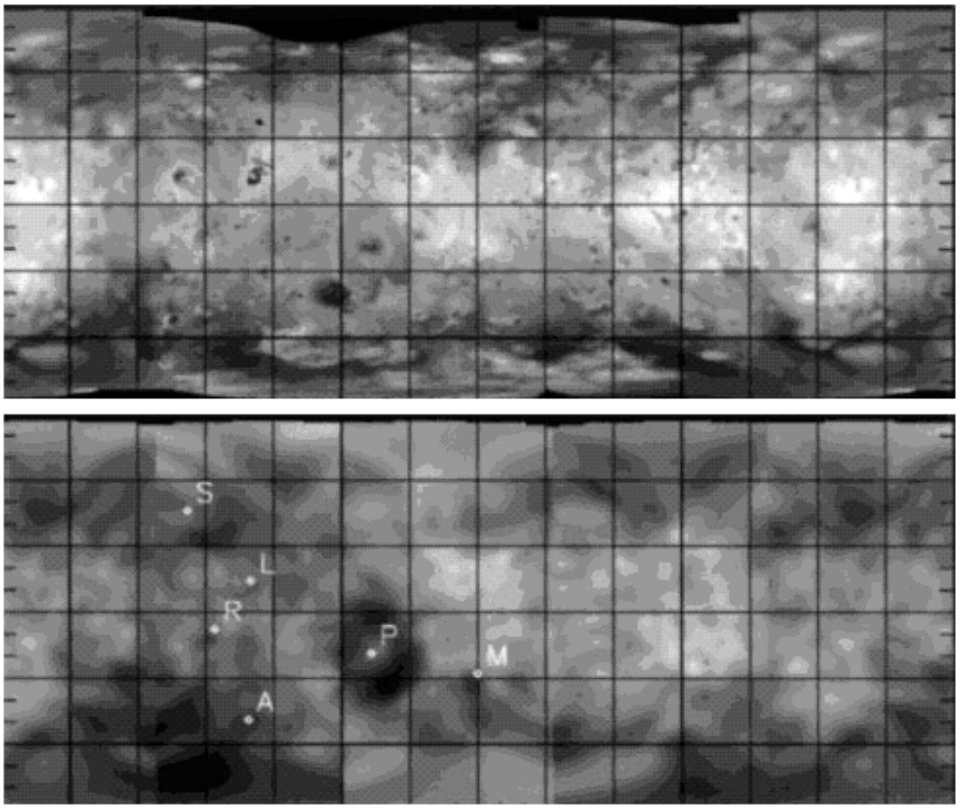

Figure 9.5. Map of Io's S_4 feature. Absorption by tetrasulfur, shown in the bottom panel as black, is evident in Pele's (P) deposition ring and polar regions. A reference map is at the top (from Spencer *et al.*, 1997).

S_2 (direct deposition of S_2 and annealing of S_2 deposits form S_4) and perhaps S_2O (partial thermal decomposition of S_2O form S_3 and S_4 (Hapke, 1989; Hapke and Graham, 1989)).

Evidence for plume sources of S_4 or S_4 precursors is given in HST images indicative of the absorption strength in the 560-nm band (Spencer *et al.*, 1997). These images show strong red absorption in the Pele deposition ring and the polar regions (Figure 9.5). Gaseous species present in Pele-like plumes include SO_2, S_2, SO, and S (Zolotov and Fegley, 2000). The computed molar concentration of disulfur monoxide is about 1/1,000 that of SO_2 and S_2. S_3 and S_4 are even less abundant than S_2O. Thus, Spencer *et al.* (2000) and Zolotov and Fegley (2000) concluded that photolyzed S_2 deposited by the plume could produce S_3 and S_4 in the ring and that this source was more likely that one involving S_2O. Many red regions on Io have faded to the background yellow over time. The lifetime of S_4, if that is the chromophore, is difficult to estimate for Pele due to its continual activity, but a red, Pele-sized ring south of Karei disappeared 2 months after its initial observation (Geissler *et al.*, 2004).

The Pele plume's O/S ratio in 1999 was about 1.5 (Zolotov and Fegley, 2000) but the gas signature of the Pele plume is variable with time. Additional plumes containing S_2 have been inferred (Jessup *et al.*, 2005). Using Douté *et al.*'s (2001) SO_2 map and assuming that the non-SO_2 material is S_8, then elemental sulfur is slightly more abundant by area than SO_2 in the equatorial region (area ratio $\sim 0.6 : 0.4$) and the average equatorial oxygen to sulfur ratio is $O/S \sim 0.5$. However, the temporally variable fractionation and an unknown gas-to-particulate ratio preclude any quantitative comparison between the relative abundance of SO_2 and S_8 in plumes and deposits on the surface.

The red color of the poles resembles red sulfur glass and it was suggested that this form, possibly produced by radiolysis, would be more stable at the colder poles than in lower latitudes (Spencer *et al.*, 1997). Wong and Johnson (1996b) suggested that SO_2 condensing at the poles would be quickly radiolyzed and continually produce a dark sulfurous residue. The poles are covered by SO_2, yet are dark in the visible, so the SO_2 frost layer must be quite thin and radiolysis must be more rapid than the condensation rate ($\sim 10^{12}$ SO_2 molecules cm^{-2} s^{-1}). Wong and Johnson find that each molecule has received ~ 10 eV which is sufficient to decompose SO_2 and produce dark refractory material.

A possible sulfur feature is found in the broad absorption extending from 1 μm (or less) to about 1.6 μm (Figure 9.1). It was first noted by Pollack *et al.* (1978) and confirmed by *Galileo* measurements (Carlson *et al.*, 1997). The absorption appears to be pervasive on Io although it is absent in Pele's deposition ring and diminished in some dark regions including the green deposits within the Chaac caldera (Lopes *et al.*, 2001). The absorption is strongest in the southern polar region. This absorption has been attributed to long-chain sulfur polymers by Carlson (2002), based on spectral similarities to radiation products formed in proton irradiation of sulfates (Nash and Fanale, 1977). This long-wavelength absorption feature may be due to sulfur dangling bonds (Eckert and Steudal, 2003; Hosokawa *et al.*, 1994). Other suggested identifications, discussed later, include iron-containing salts or feldspars (Pollack *et al.*, 1978) and iron sulfide (FeS_2, "fools gold", Kargel *et al.*, 1999).

Though not diagnostic of specific substances, the wavelength and slope shift of the visible absorption edge of Io can be attributed to the general types of impurities common in terrestrial volcanogenic sulfur (Kargel *et al.*, 1999; Kargel *et al.*, 2000; MacIntyre *et al.*, 2000); these spectroscopic effects are somewhat like some of those induced by radiolysis and can similarly produce various colored forms of sulfur. An example is the reddening modification due to dissolution of Te in sulfur (Figures 9.2 and 9.3); similar effects have been shown for Se-doped sulfur (Kargel *et al.*, 2000; MacIntyre *et al.*, 2000). This similarity can be understood because both mechanisms involve breaking of sulfur polymer bonds. Since we know that radiolysis occurs, and chemical impurities are inevitable, probably both mechanisms contribute to the color palette of Io. Other elements, such as phosphorus, cause tangling of sulfur polymer bonds, thereby inducing a different set of physical effects on sulfur; in large amounts, phosphorus forms a series of brightly colored yellow and red phosphorus sulfides. All of these elements affect the viscosity of molten sulfur and its freezing behavior, and so they have additional spectroscopic effects related to crystallization vs. quenching and annealing.

9.2.3 Sulfur dioxide

Properties of sulfur dioxide

Physical properties. SO_2 is a colorless gas at room temperature, for low-pressure liquefying at ~263 K and freezing at ~200 K. Over the temperature range from 90 K and 120 K which represents approximate extremes for non-volcanic areas on Io, the SO_2 vapor pressure varies by five orders of magnitude, from 10^{-4} nbar to 10 nbar. Consequently, there is a diurnal sublimation and condensation cycle, transporting and redistributing SO_2 across the surface. SO_2 is amorphous when condensed at temperatures <70 K, but crystallizes for temperatures >70 K (Schmitt *et al*., 1994). Condensed SO_2 forms many different textures (Nash and Betts, 1995). The condensation, evaporation, and metamorphism of pure SO_2 and mixed ices at temperatures relevant to Io have been discussed by Sandford and Allamandola (1993).

Spectral properties. The fundamental absorption bands of SO_2 occur at 19 μm (520 cm^{-1}), 9 μm (1,140 cm^{-1}), and 7.1–7.7 μm (1,300–1,345 cm^{-1}) for the ν_2, ν_1, and ν_3 vibrations, respectively (see Schmitt *et al*., 1994; Khanna *et al*., 1995; Nash and Betts, 1995, for near- and mid-infrared spectroscopic studies). In crystalline materials these vibrations are modified by crystal field effects and also form combination bands with other molecular (internal) modes and lattice phonons (external modes) (Khanna *et al*., 1995; Quirico *et al*., 1996). Numerous combination bands produce a rich infrared absorption spectrum in the 1.9–5-μm region; Figure 9.6 shows theoretical reflectance spectra for various grain sizes based on the optical constants measured by Schmitt *et al*. (1994). Infrared reflectance spectra of SO_2 frosts have been measured by Hapke (1979), Smythe *et al*. (1979), Fanale *et al*. (1979), and at higher resolution by Nash and Betts (1995). Far-ultraviolet to near-infrared spectra of frosts were obtained by Hapke *et al*. (1981) and Wagner *et al*. (1987). Visible and near-ultraviolet reflectance spectra were measured by Nash *et al*. (1980). A very sharp edge at 330 nm is found with a reflectance minimum at ~280 nm and a weaker absorption at 350 nm. Hapke *et al*.'s spectra show these bands and other reflectance minima at 225 nm and 184 nm (Wagner *et al*., 1987). The *Solar System Ices* book (Schmitt *et al*., 1998a) contains useful reviews of SO_2 properties by both Schmitt *et al*. and Nash and Betts.

Radiolytic properties. Proton bombardment of SO_2 ice produces SO_3 (monomeric and polymeric), sulfur, and sulfate (Moore, 1984). Irradiation of liquid SO_2 with γ-rays (which produce ~500 keV Compton electrons) yields SO_3, S, and O_2, the latter probably produced in $O + SO_3$ reactions (Rothschild, 1964). Similar reactions may occur in the solid phase. SO_2 subjected to electrical discharge produces SO_3, S_2O, S_3, S_4, O_3, and polysulfur oxides (Hopkins *et al*., 1973).

Spectroscopy and spectral mapping of Io's SO_2

SO_2 was first identified in Io's atmosphere from absorption in the ν_3 band (Pearl *et al*., 1979). This identification prompted laboratory experiments that quickly explained Io's 4- μm absorption feature (Cruikshank *et al*., 1978; Pollack *et al*., 1978; Fink *et al*.,

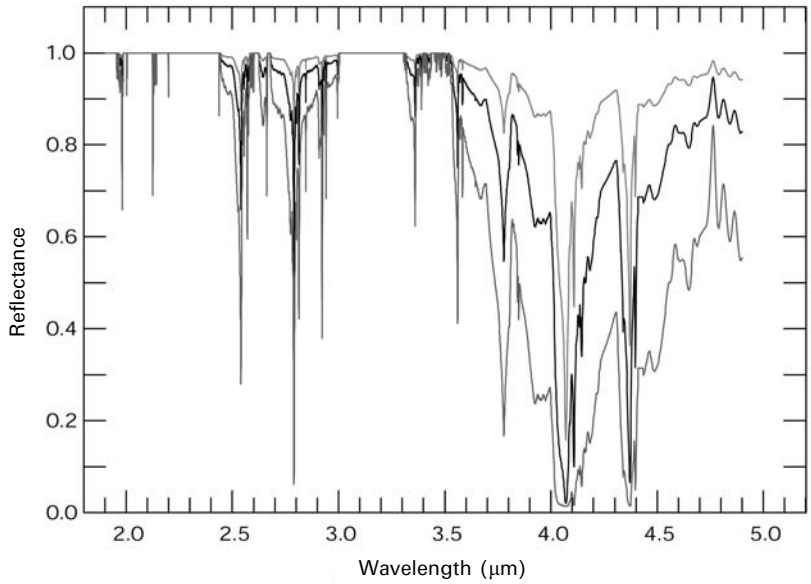

Figure 9.6. Theoretical reflectance spectra for SO_2 frost. The diffuse reflectance spectra of optically thick frosts of 10, 100, and 1,000 μm grains are shown as blue, black, and red lines, respectively (see color section). The optical constants of Schmitt *et al.* (1994, 1998b) were used.

1978) as condensed SO_2 (Hapke, 1979; Fanale *et al.*, 1979; Smythe *et al.*, 1979). Since then, Io's surficial, atmospheric, and extra-atmospheric SO_2 has been mapped and monitored by various techniques.

The surface component is measured at ultraviolet and infrared wavelengths. The sharp ultraviolet edge at 330 nm observed in Nelson and Hapke's (1978) ground-based measurements (Figure 9.1) was originally attributed to sulfur but later found to be consistent with laboratory spectra of SO_2 (Nash *et al.*, 1980). This edge was also found in IUE spectra and these spectra were used to map the longitudinal distribution of SO_2 (Nelson *et al.*, 1980; Nelson *et al.*, 1987), finding that the SO_2 abundance was stable over 8 years. Maximum SO_2 abundance was found in Io's leading hemisphere, particularly in the longitude range of 90–240 W. The SO_2 abundance was minimum in the 300–30 W region.

The 200–310-nm spectrum of Io has recently been obtained from HST and shows both atmospheric and surficial SO_2 (Jessup *et al.*, 2002). There may still be some minor puzzles about Io's UV spectrum. The 225-nm SO_2 absorption found in Hapke *et al.*'s spectrum is not apparent in the HST measurements, and the 350-nm feature appears to be absent. It may be that strong sulfur absorption hides the latter feature. Although sulfur absorption could also influence the 200- to 300-nm spectrum, SO_2's extreme volatility probably produces a thin, ultraviolet-opaque frosting over any exposed, cold sulfur.

Ground-based infrared measurements by Howell *et al.* (1984) showed that SO_2 occurred as a frost, rather than an adsorbate, and was present in most units on Io's surface, in contrast to earlier ultraviolet analyses that indicated SO_2 covering $<20\%$ of the average projected surface area (Nash *et al.*, 1980). Howell *et al.* pointed out that the ultraviolet and infrared results were consistent if analyzed using intimate mixing rather than areal mixing as used in the earlier ultraviolet study.

Other spectral measurements of Io's SO_2 were performed by Cruikshank (see Salama *et al.*, 1994), Howell *et al.* (1989), Trafton *et al.* (1991), Larson *et al.* (1992), Lester *et al.* (1992), Salama *et al.* (1994), Sandford *et al.* (1994), and Schmitt *et al.* (1994). Many of the features observed in the spectra were misidentified (see later discussions) due to the lack of laboratory SO_2 spectra, a situation rectified by the laboratory work of Schmitt *et al.* (1994) and Nash and Betts (1995). Of particular note are two weak SO_2 lines observed from Io (at 1.982 and 2.125 μm) that required centimeter path lengths to observe in the laboratory. Sandford and Allamandola (1993) inferred that some of Io's SO_2 is present as a glassy, transparent, and relatively thick ice and not as a frost, consistent with rapid annealing of surface deposits. Multiple refractive scatterings through large grains is also a possibility. Using NIMS data and recently developed analysis algorithms, Soderblom *et al.* (in preparation) have mapped the strength of these weak bands (and others), showing that they appear over most of Io but are strongest in the equatorial regions (Figure 9.7).

A high-resolution spectrum of Io's leading hemisphere has been obtained from the ISO and presented by Schmitt and Rodriguez (2003). Analysis of this spectrum is currently underway.

SO_2 spatial distribution and processes

The *Galileo* NIMS experiment obtained low spatial resolution (120–350 km per pixel) spectral maps on global scales. SO_2 is found everywhere, except in hot volcanic areas (Carlson *et al.*, 1997; Douté *et al.*, 2001). The fractional coverage and mean grain size of SO_2 frost, assumed to be linearly mixed with a spectrally neutral component (e.g., sulfur), has been mapped by Douté *et al.* (2001) using numerous NIMS data sets. These two properties provide clues about the physical state of solid SO_2 which depends on the relative rates of SO_2 condensation, metamorphism, and sublimation (Douté *et al.*, 2001, 2002, 2004). The fractional coverage and mean grain size are combined into a spectral unit map (Douté *et al.*, 2001; Figure 9.8) and can be discussed in terms of four units: I, rich in SO_2 with fine-grained frost; II, rich in SO_2 with coarse-grained frost; III, depleted in SO_2, fine-grained frost; and IV, depleted in SO_2, coarse-grained frost.

A layer of relatively fresh SO_2 frost (Unit I) covers 50–70% of large areas mostly located at medium and high latitudes (30°–60°) and generally devoid of permanent hot spots. At the margins of these areas, the SO_2 coverage remains high but the mean grain size increases substantially, suggesting metamorphism. These SO_2-rich regions show a correlation with active plumes, the plumes generally being on the same meridian but at a lower latitude. One exception is Prometheus, the closest field of abundant SO_2 being to the east, in Bosphorus Regio (100°–150° of longitude).

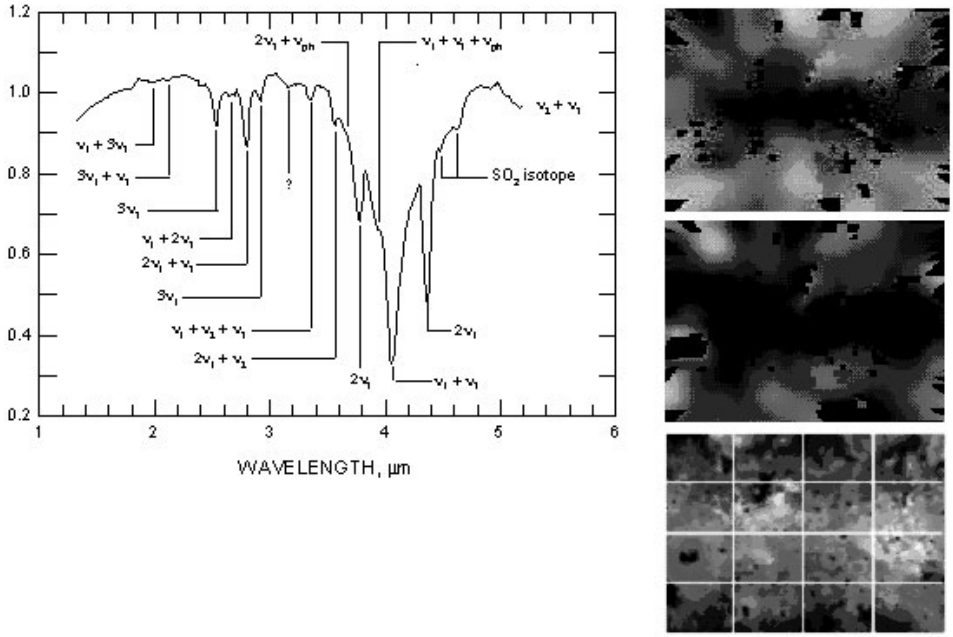

Figure 9.7. Spectrum of Io and equivalent-width maps. Maps of the absorption strength (equivalent width) of the 1.98-μm SO_2 band (*top*) and the 3.15-μm band (*middle*) are shown at the right, with black signifying more absorption. Note the strong equatorial enhancement of the unknown 3.15-μm absorber (possibly H_2O) and its correlation with both the weak, long-path-length SO_2 feature and the bright deposits in the Io reference map (*bottom*). (See also color section.)

Nonetheless all these regions likely represent condensation areas of SO_2 gas migrating from the plumes. The plumes consist of gas and particles that rise to altitudes of tens to hundreds of kilometers before collapsing back and striking the surface at supersonic speeds, generating shock waves and high pressures (Zhang *et al.*, 2003). The pressure increase causes partial dynamic condensation of SO_2, often forming rings of fallout material. The remaining gas contributes to a net longitudinal flux of volcanic SO_2 that flows toward medium and high latitudes (Douté *et al.*, 2001, 2002; Moreno *et al.*, 1991; Wong and Johnson, 1996a, 1996b). The gas condenses where the average temperatures are sufficiently low (~110 K).

For a given condensation field associated with a plume, the degree of metamorphism will depend on the condensation rate compared with the metamorphism timescale. The green (Unit I) regions associated with Pele–Pillan, Marduk, Amirani–Maui, and Prometheus may exhibit the most recent activity and the highest SO_2 emission rate. Culann, Volund, and Zamama appear to be less active.

The regions depleted in SO_2 (SO_2 surface coverage <35%, Units III and IV) represent approximately 60% of the total surface area observed by NIMS. The Jupiter-facing quadrant of the trailing hemisphere contains many of these

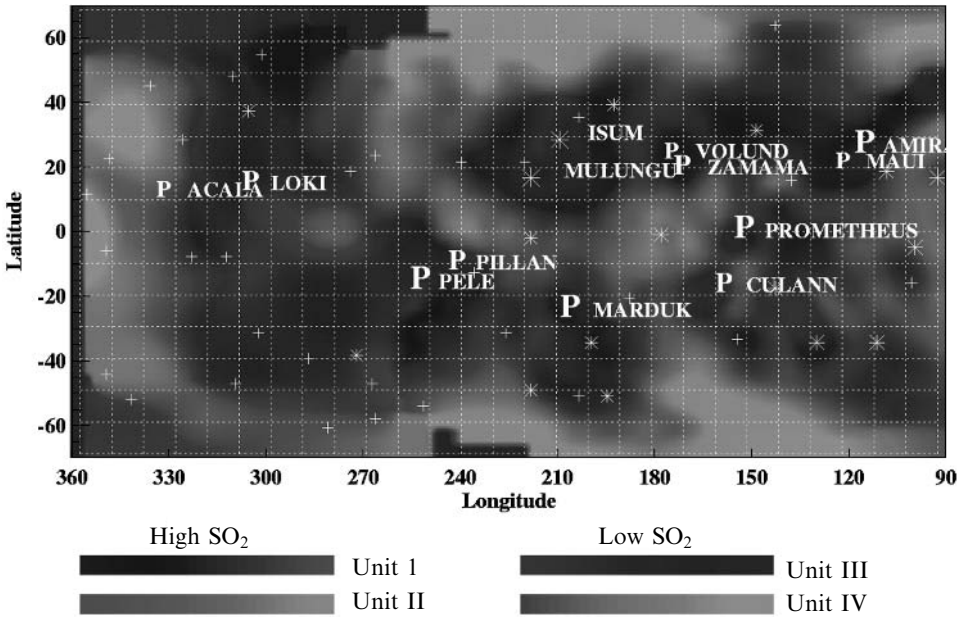

Figure 9.8. Sulfur dioxide spectral unit map. The plumes (P) are sources of fine-grained SO_2 frost (Unit I, green; see color section) deposits, generally poleward of the low-latitude plumes. Hot spot locations are denoted with stars and crosses, with stars being long-lived hot spots and crosses denoting sporadic thermal features. Metamorphosed SO_2 snowfields (Unit II) are shown as light green and yellow. SO_2-poor areas (Units III, IV) occur in the 270 to $>360^{\circ}$W longitude region.

SO_2-poor regions, a finding consistent with Nelson *et al.*'s (1980, 1987) measurements of the longitudinal distribution of SO_2, noted previously. The SO_2-frost depleted regions contain many hot spots and plumes. Recent deposition of hot pyroclastic flow materials from nearby volcanic centers and/or mean temperatures above the stability point of SO_2 in the range $\approx$110–200 K (Douté *et al.*, 2002) may prevent the formation of significant frost deposits. Isum and Mulungu are hot spots centered within an extended area displaying remarkably low SO_2 frost coverage. These hot spots lack plumes to provide SO_2 and the regions may also possess higher mean temperatures than elsewhere, resulting in low SO_2 coverage. Marduk and Zamama, in contrast, are located in regions showing high SO_2 abundance. This suggests that the condensation/sublimation ratio is above the average of these thermally active regions. A higher SO_2 production rate and/or lower regional temperatures could provide an explanation.

Optically thick but patchy frost deposits lie near the equator of the anti-Jovian hemisphere and are characterized by medium frost coverage (35–50%) and by coarse grains (300–500 μm), as indicated in the 1.98-μm map discussed above (Figure 9.7). The condensation of volcanic SO_2 can occur during night-time, but under sunlight equatorial frost sublimates. The sublimational atmosphere creates a high-pressure zone that prevents gaseous SO_2 from spreading from the plumes to the equator. Io's

equatorial temperatures are often close to the SO_2 instability point, favoring metamorphism of the frost and perhaps distillation of SO_2 by repeated sublimation and condensation. Some equatorial regions (e.g., Bosphorus Regio) display an SO_2 areal abundance that exceeds the usual background level of 45% (Douté *et al.*, 2002). This enhanced concentration may be due to either an intense incoming flux of gas coming from a neighboring plume (dynamic condensation) or a negative thermal anomaly ($\sim$110 K) causing cold trapping.

Mechanisms controlling the emission of SO_2 and other compounds from different types of volcanoes, and how these products evolve, can be derived from regional-scale observations at high spatial resolution (Douté *et al.*, 2002; Douté and Schmitt, 2003; Lopes-Gautier *et al.*, 2000; Lopes *et al.*, 2004; Williams *et al.*, 2002). Persistent hot spots such as Prometheus, Culann, Surya, and Tupan are thought to emit a great variety of gases, some of which will condense at Io's surface near their source regions. Associated fields of freshly condensed SO_2 are easily observed, and deposits of more refractory compounds with higher (e.g., S_8) or lower (e.g., NaCl) molecular weight may also be present (although their exact nature is unknown). Three different mechanisms of emission are proposed for the volatile compounds, and supported by the distribution maps. These are (a) the interaction between flowing lava and pre-existing volatile deposits on the surface, (b) the direct degassing from the lava, and (c) the eruption of a liquid aquifer from underground.

The geometric elongation of Prometheus's SO_2 deposition ring coupled with higher SO_2 concentration values within its eastern part is the best illustration of mechanism (a). Temporal development of a 95 km long lava field displaced the sublimation front, and thus also the plume and its associated circular ring of deposition.

Amirani also emits a large amount of SO_2 gas, perhaps by a similar interaction of fresh lava with the volatiles of the underlying plains. Nevertheless, SO_2 frost is not the major component of the bright white ring surrounding Amirani and seen in visible images. The eruption style is presumably different with the white compounds being degassed from the lava at a single vent (mechanism (b)) and SO_2 being principally sublimated along the numerous active boundaries of the Amirani flow (mechanism (a)). Mechanism (b) may operate for some Pillanian eruptions like the Thor eruption that occurred during the summer of 2001 (Lopes *et al.*, 2004) and that created a 800 km diameter white ring of fallout partly composed of solid SO_2.

Mechanism (c) may have been operative inside a small caldera to the east of Chaac and on the north-western flank of the volcanic edifice Emakong. These areas exhibit an extremely deep SO_2 absorption that is indicative of abundant, pure, and perhaps icy SO_2 deposits. The SO_2 is topographically confined by the caldera walls, suggesting sapping or an eruption of an SO_2 liquid aquifer (Smythe *et al.*, 2000, Lopes *et al.*, 2001).

9.2.4 Other sulfoxides

Sulfur monoxide

We mention SO for completeness since it is an atmospheric constituent but is not observed as a surface component. Lellouch *et al.* (1996) found SO in the atmosphere at

a level of a few % of SO_2 and SO^+ was found in Io's ionosphere (Russell and Kivelson, 2001). SO can be produced photochemically in the atmosphere and is an important component in plumes, second only to SO_2 (Zolotov and Fegley, 1998, 2000). Indeed, SO infrared electronic-band emission has been observed during eclipse and attributed to thermally excited SO in plumes (de Pater *et al.*, 2002) see also (McGrath *et al.*, 2004).

The vapor pressure and condensation properties are not established; we assume that SO molecules can condense or be trapped on Io's surface. Sulfur monoxide is a reactive, unstable compound, decomposing to form SO_2 and S_2O (Baklouti *et al.*, 2004). The fundamental vibrational transition in the condensed phase at 31 K is at 1,137 cm^{-1} (Hopkins and Brown, 1975) so the overtone band will occur at ~4.4 μm but the exact position is not established. Strong overlapping sulfur dioxide absorption features occur in this region in Io's spectra; consequently, searches for the presence of SO will be hindered by imprecise knowledge of the SO band position.

Sulfur trioxide

Sulfur trioxide and sulfur are the primary products of SO_2 radiolysis (Moore, 1984; Rothschild, 1964). SO_3 molecules that accumulate are themselves destroyed by radiolysis, producing SO_2 and the secondary product O_2 that can escape the surface. With time, an initial SO_2 surface would be transformed to elemental sulfur and atmospheric oxygen if there are no other processes affecting the sample. This mechanism, if operative over a long period of time, potentially could explain the elemental sulfur-rich surface of Io as an additional process or an alternative to the internally driven process described by Lewis (1982), which could yield elemental sulfur by incongruent melting of metal sulfides. During this slow degradation process, a radiolytic equilibrium will be attained, with a constant $SO_3 : SO_2$ abundance ratio. Radiolysis by electrons at Io will produce $\sim 3 \times 10^{12}$ SO_3 molecules s^{-1} cm^{-2} and an $SO_3 : SO_2$ ratio of 0.1 (or greater) may be expected, based on results by Moore. However, two processes will reduce the $SO_3 : SO_2$ ratio. The first is resurfacing and was considered earlier by Moore for proton excitation, predicting an $SO_3 : SO_2$ ratio of 10^{-4}. This ratio will be different for electron irradiation. A resurfacing rate of 1 mm yr^{-1} provides $\sim 6 \times 10^{13}$ molecules s^{-1} cm^{-2}, a factor of 20 greater than the SO_3 production rate by electron irradiation on Io, implying an $SO_3 : SO_2$ ratio of 0.05. The second limiting effect is sublimation and condensation, occurring at a rate of $\sim 0.4 \times 10^{14}$ SO_2 molecules s^{-1} cm^{-2}, a factor of 13–130 times greater than the SO_3 production rate. Any SO_2 lost by radiolysis is quickly replenished, gradually burying the SO_3. We therefore do not expect SO_3 to be present as a major species but it may be present at the few % level.

Khanna *et al.* (1995) studied the spectra of SO_3 at temperatures relevant to Io and found absorption features at 465 and 524 cm^{-1} that they suggested may be present in Io's thermal emission spectrum (see spectral locations, Figure 9.4). The two corresponding bands in the *Voyager* IRIS spectrum were attributed to S_8 and SO_2 by Pearl (1988) and Hanel *et al.* (2003) but the natural strength of the sulfur band is 100 times weaker than that of the SO_2 band. Therefore, if the abundances of sulfur and

SO_2 were comparable on Io's surface then some other absorber produces the 465 cm^{-1} emissivity feature. Khanna *et al.* suggest that SO_3 contributes to both features.

Laboratory spectra also show an SO_3 absorption band complex with prominent features at 4.04 and 4.09 μm (Khanna *et al.*, 1995). These bands straddle the 4.07 μm SO_2 feature but NIMS Io spectra do not show any characteristics attributable to SO_3 absorption (Schmitt and Rodriguez, 2003). Quantitative upper limits have not been established. The most likely locations for SO_3 to be present are the trailing hemisphere and polar regions.

Disulfur monoxide and polysulfur oxides

Disulfur monoxide (S_2O, arranged as bent SSO) is an unstable molecule at Io temperatures, decomposing to form SO_2 and S_3 (Steudel and Steudel, 2004). S_3 and S_2O can then react to form S_5O and bimolecular decomposition of the latter produces SO_2, S_3, and S_4. This decomposition of S_2O occurs at 100 K or below (Blukis and Myers, 1965; Hapke and Graham, 1989) and explains the red color of S_2O when deposited at cryogenic temperatures (Steudel and Steudel, 2004). Pure or nearly pure S_2O concentrations can undergo radical-chain polymerization forming polysulfur oxides (PSO) – chains of sulfur atoms with occasional oxygen atoms attached to the side.

The fundamental SO stretch band of pure condensed S_2O occurs at 1,165 cm^{-1}, the SO bend at 388 cm^{-1}, and the SS stretch at 679 cm^{-1} (Blukis and Myers, 1965). The SO stretch bands for S_5O and PSO are at 1,119 and 1,123 cm^{-1}, respectively (Steudel, 2003c). The formation and mid- to near-infrared spectra of S_2O and PSO are currently being studied in B. Schmitt's laboratory (Baklouti *et al.*, 2004). Photolysis of S_2O produces a cyclic isomer (Lo *et al.*, 2002).

The original motivation for Hapke's (1989) suggestion for S_2O and PSO on Io was to explain Io's near-ultraviolet reflectance spectrum that he showed was discrepant with $S_8(\alpha)$ reflectance. It was later shown that reflectance by other sulfur allotropes was consistent with Io's spectrum (see above), so there is presently no need to invoke S_2O or PSO on Io. Additionally, S_2O is a minor constituent in the plumes (<1% molar, Zolotov and Fegley, 2000) and will be reduced even further by thermal decomposition reactions as discussed above, producing plume S_5O that will be deposited on the surface and then photolyzed to SO_2 and elemental sulfur (Steudel and Steudel, 2004). Conversely, plume sulfur monoxide (see above) may react to form S_2O, so the monomers and PSO may be present as minor species with their signatures evident as overtones at ~2,330 cm^{-1} (4.29 μm) and 2,246 cm^{-1} (4.45 μm) respectively. These predicted positions straddle the strong $2\nu_1$ band of SO_2 and although no features attributable to S_2O or PSO are evident, uncertainty in the positions and strengths preclude establishing upper limits. The cyclic form of S_2O may be present on Io based on features at 800 and 580 cm^{-1} in the *Voyager* thermal emission spectrum that may match transitions of cyclic S_2O (Lo *et al.*, 2002).

Sulfates, sulfites, sulfuric acid, and sulfurous acid

The most oxidized form of sulfur is sulfate, SO_4^{2-}. This chemical class is a common and stable end-product of sulfur oxidation. Sulfite, SO_3^{2-}, is a less oxidized group.

Numerous sulfate and sulfite salts have been studied and suggested as candidates for Io's surface (Nash and Fanale, 1977) and could be observable through combination bands in the 4–5-μm region (Nyquist *et al.*, 1997). There are no obvious unidentified features in NIMS Io spectra in this region (a band at 4.62 μm thought possibly due to a sulfate is here attributed to SO_2). Alkali sulfates are minor species in Io plumes but can form localized deposits (see the Na_2S discussion below). Upper limits for sodium sulfate and sulfite on Io have been established at 25% and 40%, respectively, by Howell *et al.* (1989). The NIMS data can provide more stringent upper limits for these and other salts but this work has not yet been performed.

Sulfuric acid, H_2SO_4, a familiar substance in the laboratory and in industry, is common in acid fumaroles and hot springs on Earth and is likely also on Europa and on Mars, where ice and water vapor indicate a fairly high activity of H_2O. Sulfuric acid is not stable where water activity is nil, and this would appear to describe Io.

In contrast to many acids (e.g., sulfuric, carbonic, and hydrochloric) the undissociated sulfurous acid molecule H_2SO_3 has never been observed in the laboratory or nature. Voegele *et al.* (2004) have calculated the thermodynamic stability of this molecule at low temperatures, finding that it is long-lived at 100 K and suggested that proton irradiation of Io's SO_2 surface would produce H_2SO_3. However, using the proton flux of $6.5 \times 10^4\ s^{-1}\ cm^{-2}$ from Paranicas *et al.* (2003), the production rate of H_2SO_3 molecules would be at most $3.25 \times 10^4\ s^{-1}\ cm^{-2}$. This rate is only one billionth of the mean resurfacing rate (see the SO_3 section), so it is highly unlikely that sulfurous acid is present in measurable quantities.

9.2.5 Sulfides

Hydrogen sulfide, H_2S, has been often suggested as a surface component on Io based on features at 3.9 μm in spectra of Io (Nash and Nelson, 1979; Nash and Howell, 1989; Salama *et al.*, 1990). However, SO_2 exhibits a shoulder at this wavelength and *Galileo* NIMS spectra are consistent with SO_2 absorption alone over most of Io. A few isolated regions show enhanced absorption at 3.92 μm that is inconsistent with SO_2. Schmitt and Rodriguez (2003) performed laboratory studies of H_2S and compared their results with NIMS spectra. Dilute H_2S mixed in SO_2 does not fit the NIMS spectra as the H_2S band is at ~3.85 μm; an upper limit of 10^{-4} is given for the dilute H_2S mixing ratio (Schmitt and Rodriguez, 2003). Grains of H_2S ice do absorb at 3.92 μm but H_2S ice is very unstable at Io temperatures, with a vapor pressure 10^4 times that of SO_2 at 110 K. Since H_2S is not observed in the atmosphere (McGrath *et al.*, 2004) it seems unlikely that H_2S ice is abundant on the surface. We note however that during the I27 orbital pass of Io by *Galileo*, Russell and Kivelson (2001) found a broad ion cyclotron signature in the vicinity of H_2S^+, Cl^+, and S^+ ions. These signals were absent on other orbits and if the I27 signals are indeed due to H_2S, sulfur, and chlorine ions, then the enhancement may be caused by time variability of Io's exosphere that may in turn be related to transient volcanic emissions.

H_2S_2 has been considered by Schmitt and Rodriguez (2003) who point out that the abundance of this species in Io plumes should be lower than the HS abundance and should vary as the H/S ratio. Though the position of the SH stretching mode of H_2S_2

diluted in SO_2 is not known it may occur at 3.92 μm. For H_2S_2 to be abundant enough to produce the observed 3.92 band (see the Cl_2SO_2 discussion), it would require higher H/S ratios than are consistent with global limits and would result in the production of H_2S and H_2O at levels that are not observed.

Sodium sulfide, Na_2S, has also been a popular candidate for Io's surface as this molecule contains sodium, known to be in the Io torus, as well as sulfur. It was originally proposed by Nash and Nelson (1979) who found a 4-μm feature in spectra of Na_2S that might have explained Io's feature, but the laboratory 4-μm feature was later found to be due to carbonate contamination (Nash, 1988). In the visible region, Na_2S exhibits an absorption feature at ~560 nm (see S_2 above) and mixtures of the sulfide with sulfur and SO_2 produce good fits to Io's spectrum (Nash, 1993). He suggested sulfide volcanism and that Na_2S deposits could cover 15–20% of Io's surface. Na_2S is only a minor component in Io plumes (Fegley and Zolotov, 2000; Moses *et al.*, 2002; Schaefer and Fegley, 2005), even for those with low Cl : Na ratios, and an average molar abundance is estimated at $<10^{-4}$. However, as with Na_2SO_4 and alkali halides, Na_2S condenses at high temperature and can form localized red deposits around vents and can coat pyroclastic silicate particles (Fegley and Zolotov, 2000). The infrared spectrum of Na_2S appears bland (Nash, 1988) so no identifications or limits are available.

Since Io may have a core containing iron sulfide, it is reasonable to consider the presence of iron sulfides such as FeS_2 (pyrite and marcasite) and FeS (pyrohotite, actually $Fe_{1-x}S$, due to an iron-deficient lattice) (Lewis, 1982). Spectra of these materials, especially pyrite, show considerable variations, but there is generally a broad absorption band extending from the visible to ~1.5 μm with a minimum at ~0.9 μm. Kargel *et al.* (1999) have suggested FeS_2 as a candidate for Io based on the 1-μm band and the colors that FeS_2 imparts to sulfur, being gray–black and green and similar to some colors on Io (see Figure 9.2), and based on the common dispersion of significant pyrite (commonly the major impurity) in terrestrial volcanogenic sulfur. The distribution of the 1-μm absorber on Io may provide clues to whether it is iron sulfide or not. Although the absorber appears to be present over most of Io, and enhanced in the southern polar region, it is deficient in the Pele deposition ring (Carlson *et al.*, 1997). Thus, volcanic plumes appear not to be sources of iron sulfide if this one example is representative. The identity of the 1-μm absorber and the role of iron sulfides is not resolved. Granahan (2004) claimed detection of iron sulfide based on a 3-μm feature. However, the reference sulfide laboratory spectra contained the ubiquitous H_2O 3-μm band (Salisbury *et al.*, 1991) and therefore were not representative of anhydrous iron sulfides.

9.2.6 Metals, salts, and halogen compounds

The discovery of Na and K in the Io neutral torus fostered many laboratory, theoretical, and observational studies of potential Ionian alkali salts and sulfides. A corresponding molecular ion (NaX^+) has been postulated to provide energetic Na atoms in the neutral torus by dissociative recombination (see summary in Thomas *et al.*, 2004a) but the major anion was unknown until Kuppers and Schneider (2000)

discovered Cl^+ in the Io torus, suggesting NaCl as a major salt on Io. Thermochemical models of Ionian plumes with alkali and halogen atoms predicted that NaCl would be the major salt component (Fegley and Zolotov, 2000; Moses *et al.*, 2002; Schaefer and Fegley, 2005).

Sodium chloride and possibly potassium chloride in Io's atmosphere was discovered by Lellouch *et al.* (2003), finally resolving the 28 year old puzzle of the source of Na in the Io torus (Hunten, 2003). Lellouch *et al.* simultaneously measured two NaCl lines and several SO_2 lines so an abundance ratio can be derived although the resulting value is model dependent. Their preferred model is a patchy distribution arising from volcanic sources, with plume SO_2 bouncing once before depositing on the surface while the less volatile NaCl molecules deposit immediately when striking the surface (no bounces). In this model the $NaCl/SO_2$ molar ratio is 0.3–1.3%. The observed $NaCl/SO_2$ ratio is less than the 4% ratio predicted by Fegley and Zolotov (2000) but is consistent with CI chondritic compositions. Volcanic NaCl can deposit on the surface and can be photodissociated, producing atmospheric Na and Cl atoms (Feaga *et al.*, 2004). The NaCl source rate found by Lellouch *et al.* is sufficient to supply the torus. An NaCl surface abundance in the per cent range or less, relative to SO_2, is therefore expected. Surficial NaCl will be hard to observe because rotational transitions are hindered in the condensed state and the fundamental stretch band occurs at 20 μm. NaCl spectra are featureless from the infrared to the ultraviolet. Color centers produced by irradiation have been discussed but are too broad to be diagnostic (see references and discussion in Moses *et al.*, 2002). Since NaCl is not by itself volatile at Io's surface temperatures, there may be a tendency for it to become covered by more volatile materials and thus to get buried.

Another chlorine compound, Cl_2SO_2 (sulfuryl chloride) has been investigated by Schmitt and Rodriguez (2003) who studied the infrared spectrum and vapor pressure of this molecule. They found absorption bands in the NIMS range at 3.92, 3.57, and 4.24 μm. A feature at 3.92 μm is present in localized regions near Marduk that they suggest is possibly due to Cl_2SO_2 produced by reactions of plume-derived atomic chlorine with surface SO_2. Such reactions are observed when Cl_2 is photolyzed in frozen Cl_2–SO_2 mixtures in rare gas matrices and proceeds through the intermediate $ClSO_2$ molecule (see discussion and references in Schmitt and Rodriguez (2003) and Moses *et al.* (2002)). Condensed Cl_2SO_2 has a lower vapor pressure than SO_2 so it is thermodynamically stable on the surface. The unshielded photochemical lifetime is about 3 years and can be greatly increased if minor amounts of sulfur are mixed in. Schmitt and Rodriguez (2003) suggest that a chlorine-rich volcanic eruption at Marduk produced atomic chlorine that then reacted with the surface to produce an ephemeral layer of Cl_2SO_2-rich SO_2. A 1 mm thick layer containing 1% Cl_2SO_2 provides sufficient absorption at 3.92 μm to match the Marduk spectra while the 3.57 and 4.24-μm features are muted, consistent with the observations.

Since chlorine atoms are globally present in Io's atmosphere, $ClSO_2$ and Cl_2SO_2 are continuously being produced (and photochemically destroyed), giving a equilibrium concentration that is less than that observed at Marduk. It is possible that diluted Cl_2SO_2 may explain the emission feature observed by *Voyager* around 587 cm^{-1} (Schmitt and Rodriguez, 2000).

Cl_2S (sulfur dichloride) is predicted to be present in volcanic plumes and is the dominant sulfur–chlorine molecule produced photochemically (Moses *et al.*, 2002). It is dark red in the liquid phase, prompting Schmitt and Rodriguez (2003) to suggest that this molecule may provide the red coloration near Marduk, where the above-mentioned Cl_2SO_2 may have been observed, and possibly elsewhere.

Hydrochloric acid, HCl, may be produced in Io's volcanoes and is the second most abundant hydrogen-bearing volcanic effluent at low H/S atomic ratios, SH being slightly more abundant (Fegley and Zolotov, 2000). The fundamental vibrational mode for the free HCl molecule occurs at about 3.3 μm. The position for trace amounts of HCl in SO_2 ice is not known but may be shifted sufficiently to be a candidate for Io's 3.15-μm absorber.

9.2.7 Water and hydroxides

Water

Early spectroscopic investigations of water on Io were compromised by lack of long path length SO_2 spectra and the inability to simulate Io's rich spectrum in thin film mixture studies. However, despite some earlier mis-steps, all of these studies included a common band that remains unidentified and may be indicative of water or hydroxyl on Io. This suggestive band occurs at 3.15 μm and was first reported by Salama *et al.* (1990) who also reported a companion band at 2.97 μm. They performed laboratory measurements of $H_2O : H_2S : SO_2$ thin films and found features at approximately 2.97 and 3.15 μm. These they attributed to the symmetric and anti-symmetric OH stretch transitions (ν_1 and ν_3) of water dimers and higher multimers complexed with sulfur dioxide $(H_2O)_n \cdot SO_2$. (The bands of monomer complexes occur at shorter wavelengths and are obscured by stronger SO_2 bands in Io's spectrum.) Although the ν_1 transition is much weaker than the ν_3 transition in the free molecule, in H_2O–SO_2 complexes the strengths of the two bands are comparable (Schriver *et al.*, 1988). The 3.15-μm band was also present in Io spectra reported by Sandford *et al.* (1994) but the 2.97-μm feature was absent. The presence of the 3.15-μm band and the absence of the 2.97-μm band was confirmed by both *Galileo* NIMS and ISO measurements (Carlson *et al.*, 1997; Schmitt and Rodriguez, 2003). The near-equality of the ν_1 and ν_3 water complex transitions in laboratory spectra (Schriver *et al.*, 1988) indicates that two bands should be present, and if the measurements of Salama *et al.* (1990) are correct, then a 2.97-μm ν_3 band should be present and of equal or somewhat greater strength than the 3.15-μm band. This is not observed in the *Galileo* or ISO data, contraindicating H_2O on Io. Further laboratory work is required before H_2O can be definitely ruled out. In particular, experiments with small amounts of H_2O in pure SO_2 should be performed as Salama *et al.*'s experiments had H_2S at concentrations 10–30× that of H_2O so $(H_2O \cdot H_2S) \cdot SO_2$ complexes may have formed instead of $(H_2O)_n \cdot SO_2$.

Additional but weak evidence for water is given in localized multi-channel spectra obtained by NIMS after the scanning motion of the grating ceased operation in I24 (Douté *et al.*, 2004). These coarse-resolution data (12 points) exhibit a broad, shallow band at 3 μm that may be indicative of water or a hydrate in localized bright deposits

north-west of Gish Bar Patera. This same band was found by Granahan (2004) in Io's mountainous areas.

Hydroxides

The 3.15-μm feature could arise from the OH stretching transition in a hydroxide. Salama *et al.* (1994) considered NaOH but found a wavelength mismatch. Oxy-hydroxides such as AlOOH (diaspore and boehmite) and FeOOH (goethite) show OH transitions in this wavelength region but none of these provide an exact match. (Riskin, 1974).

9.2.8 Silicates

Formation models of the Galilean satellites predict silicates as a major component, but firm evidence for their presence on the surface is lacking. Silicates may be difficult to detect due to the pervasive SO_2 frosting that covers much of the surface through sublimation and condensation. It is likely that only the warm volcanic regions show exposed silicates; this conjecture is consistent with the low or non-existent concentration of Si in Io's extended atmosphere (Na *et al.*, 1998). A limit of 1.4% of Si relative to Na was found whereas chondritic abundances show Si abundance 22 times greater than that for sodium.

The lack of evidence for silicates is also partly due to the loss, early in the *Galileo* mission, of the NIMS detector that sampled the 1–1.3-μm region that is diagnostic of silicate Fe^{2+} absorption features. This reduced capability was exacerbated by the loss of grating scan motion just as the high spatial resolution portion of the mission began.

While early determinations of the temperatures of Io's volcanoes suggested sulfur volcanism, Carr *et al.* (1979) and Clow and Carr (1980) argued that silicates must be present in the near surface, providing the strength needed to support Io's mountains. Volcanic temperatures of ~900 K observed by Johnson *et al.* (1988) ruled out sulfur volcanism and provided strong evidence for silicate volcanism. *Galileo* measurements indicated even higher lava temperatures, >1,700 K (McEwen *et al.*, 1998), higher than the melting points of common basalts. Such high temperatures require superheating, ceramic volcanism (Kargel *et al.*, 2003), or high melting point silicates (see Chapter 7).

There is suggestive evidence for the presence of Mg-rich, high melting point silicates, in particular for ultramafic rocks called komatiites, magnesium-rich volcanic rocks from the Earth's earliest volcanoes. The SSI camera had filters with average effective wavelengths of 418, 560, 664, 731, 757, 888, and 990 nm for Io (Klaasen *et al.*, 1997). For some of Io's dark calderas a reflectance minimum was found in the 888-nm filter and is suggestive of the presence of a silicate (McEwen *et al.*, 1998; Geissler *et al.*, 1999). Although absorption at this wavelength is often associated with a ferric iron absorption in, for example, hematite, for a few silicate minerals, the usual 1-μm ferrous iron feature of silicates appears at 0.9 μm (see the USGS and ASTER spectral libraries, *http://speclab.cr.usgs.gov* and *http://speclab.jpl.nasa.gov/*, respectively). These minerals are the orthopyroxenes enstatite and hypersthene. Magnesium-rich enstatite is a mineral that has been found in one example of

komatiite – the Commondale greenstone belt of South Africa – although komatiites generally contain the minerals olivine (as does Commondale greenstone) and clinopyroxene. Large amounts of olivine are inconsistent with the SSI data (Geissler *et al.*, 1999) or Pollack *et al.*'s (1978) ground-based spectra. For comparison, some ultramafic rock spectra are presented by Hunt *et al.* (1974).

If high-temperature silicate volcanism has been a frequent or continuous and widespread phenomenon on Io, the possibility exists that volatilization and recondensation of Mg, Fe, Si, and O has caused a significant fractionation of these elements with respect to Ca and Al, with a consequent shift of some silicate magmatic systems outside the region of familiar peridotite-based igneous processes (Kargel *et al.*, 2003). This process can potentially explain an Io that has super-high-temperature silicate magmatism without involvement of iron silicates, since iron-bearing components may have segregated into the core and/or to the base of the mantle under this extreme igneous processing regime. The ceramic volcanism concept involves a reduced importance of Fe–oxide-bearing eutectic igneous phase relations (which characterize normal peridotite- and basalt-based systems) due to the intervention of vapor distillation in the differentiation process. The crust, in this scenario, would be highly enriched in refractory Ca–Al-rich and Fe-poor silicates. Hence, spectroscopists may be looking for the wrong silicate minerals, and the right ones may be hard to detect without having much of an iron component.

The likely presence of highly magnesian orthopyroxene in crustal lava has implications for interior models. In one scenario the mantle and crust, depleted of iron during formation of an iron-rich core, remains undifferentiated by high amounts of partial melting and recycling of the lithosphere back into the mantle (McEwen *et al.*, 1998; Keszthelyi *et al.*, 2004). Alternatively, Io could be strongly differentiated (Keszthelyi and McEwen, 1997), with a low-density felsic crust rich in alkalis and aluminum, a Mg-rich upper mantle (the lava source), and an Fe, Ca-rich lower mantle. Pollack *et al.* (1978) suggested that the 1-μm absorber could indicate the presence of feldspars on Io's surface, consistent with a differentiated crust. However, Keszthelyi *et al.* (2004) argue that orthopyroxene-rich lavas can be present on Io if the crust is continuously mixed back into the mantle.

9.3 SUMMARY

Except for hot volcanic regions, Io's surface is being constantly covered by sulfur dioxide from volcanic plumes. Daily sublimation and condensation of SO_2 frosts the surface, hiding trace plume species. In addition to plume sources, solidified liquid SO_2 flows are also thought to be present on the surface.

The plumes bring other species to the surface. Sulfur is thought to be mainly introduced to the surface as a plume effluent such as S_2, which is converted within the plumes or on the surface to S_4, and then combines to form S_8, sulfur polymers, or both. Minor plume species are NaCl and probably KCl, and atomic chlorine that may produce $ClSO_2$ and related compounds.

If water is present on Io it is rare. A weak, unidentified band at 3.15 μm may indicate the presence of H_2O at the ppm level, but laboratory work needs to establish the spectral position of dilute concentrations of water in SO_2 and sulfur at temperatures relevant to Io. The broad unidentified absorption in the 1-μm region needs to be investigated in order to narrow the range of plausible candidates.

Pyroxene silicates may be present in hot volcanic caldera but the evidence is not conclusive. High spatial resolution adaptive optics near-infrared spectroscopy of volcanic caldera may show the ferrous iron bands of silicates in the 1-μm region. Mid-infrared spectroscopy of volcanic thermal emission may show emissivity features of the emitting surface.

Calculations of the thermo-chemistry of Io's volcanic plumes are important for interpreting observations and predicting species that may be on the surface. Plume spectroscopy is a promising tool to search for new species and improve understanding of this enigmatic satellite.

9.4 REFERENCES

Baklouti, D., B. Schmitt, and O. Brissaud. 2004. Infrared study of lower sulfur oxides on Io's surface. *Bull. Amer. Astron. Soc.*, **36**, 16.07.

Ballester, G. E., M. A. McGrath, D. F. Strobel, X. Zhu, P. D. Feldman, and H. W. Moos. 1994. Detection of the SO_2 atmosphere on Io with the Hubble Space Telescope. *Icarus*, **111**, 2–17.

Bass, A. M. 1963. The optical absorption of sulfur. *J. Chem. Phys.*, **21**, 80–82.

Binder, A. B. and D. P. Cruikshank. 1964. Evidence for an atmosphere on Io. *Icarus*, **3**, 299–305.

Blukis, U. and R. J. Myers. 1965. Disulfur monoxide. III: Its infrared spectrum and thermodynamic functions. *J. Phys. Chem.*, **69**, 1154–1156.

Boring, J. W., Z. Nansheng, D. B. Chrisey, D. J. O'Shaugnessy, J. A. Phipps, and R. E. Johnson. 1985. The production and sputtering of S_2 by keV ion bombardment. In: C. I. Lagerkvist, B. A. Lindblad, H. Lundstedt, and H. Rickman (eds), *Asteroids, Comets, Meteors II*. Uppsala Universitet Press, Uppsala, Sweden, pp. 229–234.

Carlson, R. W. 2002. The diverse surface compositions of the Galilean satellites. In: *Solar System Remote Sensing* (LPI Contribution No. 1129). Lunar and Planetary Institute, Houston, p. 9.

Carlson, R. W., W. D. Smythe, R. M. C. Lopes-Gautier, A. G. Davies, L. W. Kamp, J. A. Mosher, L. A. Soderblom, F. E. Leader, R. Mehlman, R. N. Clark *et al.* 1997. The distribution of sulfur dioxide and other infrared absorbers on the surface of Io. *Geophys. Res. Lett.*, **24**, 2479–2482.

Carr, M. H., H. Masursky, R. G. Strom, and R. J. Terrile. 1979. Volcanic features of Io. *Nature*, **280**, 729–733.

Casal, H. L. and J. C. Scaino. 1985. Transient intermediates in the photochemistry of elemental sulphur in solution. *C. Photochem.*, **30**, 253–257.

Chatelain, Y. A. and J. Buttet. 1965. Electron paramagnetic studies of unstable sulfur forms. In: B. Meyer (ed.), *Elemental Sulfur*. Interscience, New York, pp. 208–215.

Chrisey, D. B., R. E. Johnson, J. W. Boring, and J. A. Phipps. 1988. Ejection of sodium from sodium sulfide by the sputtering of the surface of Io. *Icarus*, **75**, 233–244.

Clow, G. D. and M. H. Carr. 1980. Stability of sulfur slopes on Io. *Icarus*, **44**, 269–279.

Cruikshank, D. P., T. J. Jones, and C. B. Pilcher. 1978. Absorption-bands in spectrum of Io. *Astrophys. J.*, **225**, L89–L92.

de Pater, I., H. G. Roe, J. R. Graham, D. F. Strobel, and P. Bernath. 2002. Detection of the forbidden SO $a^1\Delta$-$X^3\Sigma^-$ rovibronic transition on Io at 1.7 mm. *Icarus*, **156**, 296–301.

Douté, S. and B. Schmitt, 2003. Io's thermal stage and the spatial distribution of solid SO_2 abundance. *Icarus* (submitted).

Douté, S., B. Schmitt, R. Lopes-Gautier, R. Carlson, L. Soderblom, and J. Shirley. 2001. Mapping SO_2 frost on Io by the modeling of NIMS hyperspectral images. *Icarus*, **149**, 107–132.

Douté, S., R. M. C. Lopes, L. W. Kamp, R. W. Carlson, and B. Schmitt. 2002. Dynamics and evolution of SO_2 gas condensation around Prometheus-like volcanic plumes on Io as seen by the near-infrared mapping spectrometer. *Icarus*, **158**, 460–482.

Douté, S., R. Lopes, L. W. Kamp, R. Carlson, and B. Schmitt. 2004. Geology and activity around volcanoes on Io from the analysis of NIMS spectral images. *Icarus*, **169**, 175–196.

Eckert, B. and R. Steudal, 2003. Molecular spectra of sulfur molecules and solid sulfur allotropes. *Top. Curr. Chem.*, **231**, 31–98.

Fanale, F. P., T. V. Johnson, and D. L. Matson. 1974. Io: Surface evaporite deposit. *Science*, **186**, 922–925.

Fanale, F. P., T. V. Johnson, and D. L. Matson. 1977. Io's surface and the histories of the Galilean satellites. In: J. A. Burns (ed.), *Planetary Satellites*. University of Arizona Press, Tucson, AZ, pp. 379–405.

Fanale, F. P., R. H. Brown, D. P. Cruikshank, and R. N. Clark. 1979. Significance of absorption features in Io's IR absorption spectrum. *Nature*, **280**, 761–763.

Feaga, L. M., M. A. McGrath, P. D. Feldman, and D. F. Strobel. 2004. Detection of atomic chlorine in Io's atmosphere with the Hubble Space Telescope GHRS. *Astrophys. J.*, **610**, 1191–1198.

Fegley, B. and M. Y. Zolotov. 2000. Chemistry of sodium, potassium, and chlorine in volcanic gases on Io. *Icarus*, **148**, 193–210.

Fink, U., H. P. Larson, L. A. Lebofsky, M. Feierberg, and H. Smith. 1978. The 2–4 μm spectrum of Io. *Bull. Amer. Astron. Soc.*, **10**, 580 (abstract).

Geissler, P. E. 2003. Volcanic activity on Io during the Galileo era. *Annu. Rev. Earth Planet. Sci.*, **31**, 175–211.

Geissler, P. E., A. S. McEwen, L. Keszthelyi, R. Lopes-Gautier, J. Granahan, and D. P. Simonelli. 1999. Global color variations on Io. *Icarus*, **140**, 265–282.

Geissler, P. E., A. McEwen, C. Phillips, L. Keszthelyi, and J. Spencer. 2004. Surface changes on Io during the Galileo mission. *Icarus*, **169**, 29–64.

Granahan, J. C. 2004. The detection of iron sulfide on Io. *Lunar and Planetary Science*, **XXXV**. Lunar and Planetary Institute, Houston, p. 1872.

Hanel, R. A., B. J. Conrath, D. E. Jennings, and R. E. Samuelson. 2003. *Exploration of the Solar System by Infrared Remote Sensing*. Cambridge University Press, Cambridge, UK.

Hapke, B. 1979. Io's surface and environs: A magmatic–volatile model. *Geophys. Res. Lett.*, **6**, 799–802.

Hapke, B. 1989. The surface of Io: A new model. *Icarus*, **79**, 56–74.

Hapke, B. and F. Graham. 1989. Spectral properties of condensed phases of disulfur monoxide, polysulfur oxide, and irradiated sulfur. *Icarus*, **79**, 47–55.

Hapke, B., E. Wells, J. Wagner, and W. Partlow. 1981. Far-UV, visible, and near-IR reflectance spectra of frosts of H_2O, CO_2, NH_3 and SO_2. *Icarus*, **47**, 361–367.

Hopkins, A. G. and C. W. Brown. 1975. Infrared spectrum of sulfur monoxide. *J. Chem. Phys.*, **62**, 2511–2512.

Hopkins, A. G., S.-Y. Tang, and C. W. Brown. 1973. Infrared and Raman spectra of the low-temperature products from discharged sulfur dioxide. *J. Amer. Chem. Soc.*, **95**, 3486–3490.

Hosokawa, S., T. Matsuoka, and K. Tamura. 1994. Optical absorption spectra of liquid sulphur over a wide absorption range. *J. Phys. Condens. Matter*, **6**, 5273–5282.

Howell, R. R., D. P. Cruikshank, and F. P. Fanale. 1984. Sulfur dioxide on Io: Spatial distribution and physical state. *Icarus*, **57**, 83–92.

Howell, R. R., D. B. Nash, T. R. Geballe, and D. P. Cruikshank. 1989. High-resolution infrared spectroscopy of Io and possible surface materials. *Icarus*, **78**, 27–37.

Hunt, G. R., J. W. Salisbury, and C. J. Lenhoff.1974. Visible and near infrared spectra of minerals and rocks. IX: Basic and ultrabasic igneous rocks. *Modern Geology*, **5**, 15–22.

Hunten, D. M., 2003. Sodium at Io. *Nature*, **421**, 30–31.

Jessup, K. L., J. Spencer, G. E. Ballester, R. Yelle, F. Roessler, and R. R. Howell. 2002. Spatially resolved UV spectra of Io's Prometheus plume and anti-Jovian hemisphere. *Bull. Amer. Astron. Soc.*, **34**, 40.02.

Jessup, K. L., J. R. Spencer, and R. Yelle. 2005. Sulfur volcanism on Io. *Bull. Amer. Astron. Soc.*, **37**, 765 (abstract).

Johnson, T. V. and T. McCord. 1970. Galilean satellites: The spectral reflectivity 0.30–1.10 microns. *Icarus*, **13**, 37–42.

Johnson, T. V. and T. B. McCord. 1971. Spectral geometric albedo of the Galilean satellites, 0.3 to 2.5 microns. *Astrophys. J.*, **169**, 589–594.

Johnson, T. V. and C. B. Pilcher. 1977. Satellite spectrophotometry and surface compositions. In: J. A. Burns (ed.), *Planetary Satellites*. University of Arizona Press, Tucson, AZ, pp. 232–268.

Johnson, T. V., G. J. Veeder, D. L. Matson, R. H. Brown, R. M. Nelson, and D. Morrison. 1988. Io: Evidence for silicate volcanism in 1986. *Science*, **242**, 1280–1283.

Kargel, J. S., P. Delmelle, and D. B. Nash. 1999. Volcanogenic sulfur on Earth and Io: Composition and spectroscopy. *Icarus*, **140**, 249–280.

Kargel, J. S., T. MacIntyre, J. B. Dalton, and R. N. Clark. 2000. Io's sulfur: Surface distribution and chemical nature of impurities. *Bull. Amer. Astron. Soc.*, **32**, 29.08 (abstract).

Kargel, J., R. Carlson, A. Davies, B. Fegley Jr., A. Gillespie, R. Greeley, R. R. Howell, K. L. Jessup, L. Kamp, L. Keszthelyi *et al.*, 2003. Extreme volcanism on Io: Latest insights at the end of Galileo Era. *EOS Trans. Amer. Geophys. U.*, **84**, 313, 318.

Keszthelyi, L. and A. McEwen. 1997. Magmatic differentiation on Io. *Icarus*, **130**, 437–448.

Keszthelyi, L., W. L. Jaeger, E. P. Turtle, M. Milazzo, and J. Radebaugh. 2004. A post-Galileo view of Io's interior. *Icarus*, **169**, 271–286.

Khanna, R. K., J. C. Pearl, and R. Dahmani. 1995. Infrared-spectra and structure of solid-phases of sulfur-trioxide: Possible identification of solid SO_3 on Io surface. *Icarus*, **115**, 250–257.

Klaasen, K. P., M. J. S. Belton, H. H. Breneman, A. S. McEwen, M. E. Davies, R. J. Sullivan, C. R. Chapman, G. Neukum, and C. M. Heffernan. 1997. Inflight performance characteristics, calibration, and utilization of the Galileo solid-state imaging camera. *Opt. Eng.*, **36**, 3001–3027.

Kuiper, G. P. 1951. Planetary atmospheres and their origin. In: G. P. Kuiper (ed.), *The Atmospheres of the Earth and Planets*. University of Chicago Press, Chicago, pp. 306–405.

Kuppers, M. and N. M. Schneider. 2000. Discovery of chlorine in the Io torus. *Geophys. Res. Lett.*, **27**, 513–516.

Larson, H. P., R. Timmerman, and U. Fink. 1992. High-resolution observations of the 2.125-μm feature in Io's spectrum during 1975 and 1976. *Icarus*, **95**, 325–328.

Lellouch, E., M. J. S. Belton, I. de Pater, S. Gulkis, and T. Encrenaz. 1990. Io's atmosphere from microwave detection of SO_2. *Nature*, **346**, 639–641.

Lellouch, E., D. F. Strobel, M. J. S. Belton, M. E. Summers, G. Paubert, and R. Moreno. 1996. Detection of sulfur monoxide in Io's atmosphere. *Astrophys. J.*, **459**, L107–L110.

Lellouch, E., G. Paubert, J. I. Moses, N. M. Schneider, and D. F. Strobel, 2003. Volcanically emitted sodium chloride as a source for Io's neutral clouds and plasma torus. *Nature*, **421**, 45–47.

Lester, D. F., L. M. Trafton, T. F. Ramseyer, and N. I. Gaffney. 1992. Discovery of a second narrow absorption feature in the near-infrared spectrum of Io. *Icarus*, **98**, 134–140.

Lewis, J. S. 1982. Io: Geochemistry of sulfur. *Icarus*, **50**, 103–114.

Lo, W.-J., Y.-J. Wu, and Y.-P. Lee. 2002. Isomers of S_2O: Infrared absorption spectra of cyclic S_2O in solid Ar. *J. Chem. Phys.*, **117**, 6655–6661.

Lopes, R. M. C. and D. A. Williams. 2005. Io after Galileo. *Rep. Prog. Phys.*, **68**, 303–340.

Lopes, R. M. C., L. W. Kamp, S. Douté, W. D. Smythe, R. W. Carlson, A. S. McEwen, P. E. Geissler, S. W. Kieffer, F. E. Leader, A. G. Davies, *et al.*, 2001. Io in the near infrared: Near-Infrared Mapping Spectrometer (NIMS) results from the Galileo flybys in 1999 and 2000. *J. Geophys. Res.*, **106**, 33053–33078.

Lopes, R. M. C., L. W. Kamp, W. D. Smythe, P. Mouginis-Mark, J. Kargel, J. Radebaugh, E. P. Turtle, J. Perry, D. A. Williams, R. W. Carlson *et al.* 2004. Lava lakes on Io: Observations of Io's volcanic activity from Galileo NIMS during the 2001 fly-bys. *Icarus*, **169**, 140–174.

Lopes-Gautier, R., S. Douté, W. D. Smythe, L. W. Kamp, R. W. Carlson, A. G. Davies, F. E. Leader, A. S. McEwen, P. E. Geissler, S. W. Kieffer *et al.* 2000. A close-up look at Io from Galileo's near-infrared mapping spectrometer. *Science*, **288**, 1201–1204.

Lunine, J. I., A. Coradini, D. Gautier, T. C. Owen, and G. Wuchterl. 2004. The origin of Jupiter. In: F. Bagenal, T. E. Dowling, and W. McKinnon (eds), *Jupiter: The Planet, Satellites, and Magnetosphere* (Cambridge Planetary Science series). Cambridge University Press, Cambridge, UK, pp. 19–34.

MacIntyre, T., J. S. Kargel, B. Dalton, and R. Clark. 2000. Reflection spectra of impure sulfur: Io and new lab results. *Bull. Amer. Astron. Soc.*, **32**, 30.06, 1049 (abstract).

McEwen, A. S., L. Keszthelyi, J. R. Spencer, G. Schubert, D. L. Matson, R. Lopes-Gautier, K. P. Klaasen, T. V. Johnson, J. W. Head, P. Geissler *et al.* 1998. High-temperature silicate volcanism on Jupiter's moon Io. *Science*, **281**, 87–90.

McEwen, A. S., R. Lopes-Gautier, L. Keszthelyi, and S. W. Kieffer. 2000. Extreme volcanism on Jupiter's moon Io. In: J. Zimbelman and T. Gregg (eds), *Environmental Effects on Volcanic Eruptions: From Deep Oceans to Deep Space*. Kluwer Academic Press/Plenum Publishers, New York, pp. 179–205.

McEwen, A. S., L. P. Keszthelyi, R. Lopes, P. M. Schenk, and J. R. Spencer. 2004. The lithosphere and surface of Io. In: F. Bagenal, T. E. Dowling, and W. B. McKinnon (eds), *Jupiter: The Planet, Satellites, and Magnetosphere* (Cambridge Planetary Science series). Cambridge University Press, Cambridge, UK, pp. 307–328.

McGrath, M. A., M. J. S. Belton, J. R. Spencer, and P. Sartoretti. 2000. Spatially resolved spectroscopy of Io's Pele plume and SO_2 atmosphere. *Icarus*, **146**, 476–493.

McGrath, M. A., E. Lellouch, D. F. Strobel, P. D. Feldman, and R. E. Johnson. 2004. Satellite atmospheres. In: F. Bagenal, T. E. Dowling, and W. B. McKinnon (eds), *Jupiter*. Cambridge University Press, Cambridge, UK, pp. 457–483.

Meyer, B. and T. Stroyer-Hansen. 1972. Infrared spectrum of S_4. *J. Phys. Chem.*, **76**, 3968–3969.

Meyer, B., T. V. Oommen, and D. Jensen. 1971. The color of liquid sulfur. *J. Phys. Chem.*, **75**, 912–917.

Meyer, B., T. Stroyer-Hansen, and T. V. Oommen. 1972. The visible spectrum of S_3 and S_4. *J. Molec. Spectrosc.*, **42**, 335–343.

Moore, M. H. 1984. Studies of proton-irradiated SO_2 at low-temperatures: Implications for Io. *Icarus*, **59**, 114–128.

Morabito, L. A., S. P. Synnott, P. N. Kupferman, and S. A. Collins. 1979. Discovery of currently active extraterrestrial volcanism. *Science*, **204**, 972.

Moreno, M. A., G. Schubert, J. Baumgardner, M. G. Kivelson, and D. A. Paige. 1991. Io's volcanic and sublimation atmospheres. *Icarus*, **93**, 63–81.

Morrison, D. and J. A. Burns. 1976. The Jovian satellites. In: T. Gehrels (ed.), *Jupiter*. University of Arizona Press, Tucson, AZ, pp. 991–1034.

Moses, J. I. and D. B. Nash. 1991. Phase transformations and the spectral reflectance of solid sulfur: Can metastable sulfur allotropes exist on Io? *Icarus*, **89**, 277–304.

Moses, J. I., M. Y. Zolotov, and B. Fegley. 2002. Alkali and chlorine photochemistry in a volcanically driven atmosphere on Io. *Icarus*, **156**, 107–135.

Na, C. Y., L. M. Trafton, E. S. Barker, and S. A. Stern. 1998. A search for new species in Io's extended atmosphere. *Icarus*, **131**, 449–452.

Nash, D. B. 1988. Infrared reflectance spectra of Na_2S with contaminant Na_2CO_3: Effects of adsorbed H_2O and CO_2 and relation to studies of Io. *Icarus*, **74**, 365–368.

Nash, D. B. 1993. A case for Na_2S on Io's surface: Sulfide volcanism? *Io: An International Conference, San Juan Capistrano*.

Nash, D. B. and B. H. Betts. 1995. Laboratory infrared spectra (2.3–23 μm) of SO_2 phases: Applications to Io surface analysis. *Icarus*, **117**, 402–419.

Nash, D. B. and B. H. Betts. 1998. Ices on Io: Composition and texture. In: B. Schmitt, C. de Bergh, and M. Festou (eds), *Solar System Ices. Astrophysics and Space Science Library*. Kluwer, Dordrecht, The Netherlands, pp. 607–638.

Nash, D. B. and F. P. Fanale. 1977. Io's surface composition based on reflectance spectra of sulfur/salt mixtures and proton irradiation experiments. *Icarus*, **31**, 40–80.

Nash, D. B. and R. R. Howell. 1989. Hydrogen sulfide on Io: Evidence from telescopic and laboratory infrared spectra. *Science*, **244**, 454–456.

Nash, D. B. and R. M. Nelson. 1979. Spectral evidence for sublimates and adsorbates on Io. *Nature*, **280**, 763–766.

Nash, D. B., F. P. Fanale, and R. M. Nelson. 1980. SO_2 frost: UV–visible reflectivity and Io surface coverage. *Geophys. Res. Lett.*, **7**, 665–668.

Nash, D. B., M. H. Carr, J. Gradie, D. M. Hunten, and C. F. Yoder. 1986. Io. In: J. A. Burns and M. S. Matthews (eds), *Satellites*. University of Arizona Press, Tucson, AZ, pp. 629–688.

Nelson, R. M. and B. W. Hapke. 1978. Spectral reflectivities of the Galilean satellites and Titan, 0.32 to 0.86 micrometers. *Icarus*, **36**, 304–329.

Nelson, R. M., A. L. Lane, D. L. Matson, F. P. Fanale, D. B. Nash, and T. V. Johnson. 1980. Longitudinal distribution of sulfur dioxide frost. *Science*, **210**, 784–786.

Nelson, R. M., A. L. Lane, D. L. Matson, G. J. Veeder, B. J. Buratti, and E. F. Tedesco. 1987. Spectral geometric albedos of the Galilean satellites from 0.24 to 0.34 micrometers: Observations with the International Ultraviolet Explorer. *Icarus*, **72**, 358–380.

Nelson, R. M., W. D. Smythe, B. W. Hapke, and A. J. Cohen. 1990. On the effect of x-rays on the color of elemental sulfur: Implications for Jupiter's satellite Io. *Icarus*, **85**, 326–334.

Nishijima, C., N. Kanamuru, and K. Titmura. 1976. Primary photochemical processes of sulfur in solution. *Bull. Chem. Soc. Japan*, **49**, 1151–1152.

Nyquist, R. A., C. L. Putzig, and M. A. Leugers. 1997. *Infrared and Raman Spectral Atlas of Inorganic Compounds and Organic Salts*. Academic Press, San Diego.

Paranicas, C., B. H. Mauk, R. W. McEntire, and T. P. Armstrong. 2003. The radiation environment near Io. *Geophys. Res. Lett.*, **30**, 1919 SSC 1911–1914.

Peale, S. J., P. Cassen, and R. T. Reynolds. 1979. Melting of Io by tidal dissipation. *Science*, **203**, 892–894.

Pearl, J. 1988. A review of Voyager IRIS results on Io. *Eos, Trans. Amer. Geophys. Union*, **69**, 394 (abstract).

Pearl, J., R. Hanel, V. Kunde, W. Maguire, K. Fox, S. Gupta, C. Ponnamperuma, and F. Raulin. 1979. Identification of gaseous SO_2 and new upper limits for other gases on Io. *Nature*, **280**, 755–758.

Pieri, D. C., S. M. Baloga, R. M. Nelson, and C. Sagan. 1984. Sulfur flows on Ra Patera, Io. *Icarus*, **60**, 685–700.

Pollack, J. B. and F. P. Fanale. 1982. Origin and evolution of the Jovian satellite system. In: D. Morrison (ed.), *Satellites of Jupiter. Space Science Series*. University of Arizona Press, Tucson, AZ, pp. 872–910.

Pollack, J. B., F. C. Witteborn, E. F. Erickson, D. W. Strecker, B. J. Baldwin, and T. E. Bunch. 1978. Near-infrared spectra of the Galilean satellites: Observations and compositional implications. *Icarus*, **36**, 271–303.

Quirico, E., B. Schmitt, R. Bini, and P. R. Salvi. 1996. Spectroscopy of some ices of astrophysical interest: SO_2, N_2, and $N_2 : CH_4$ mixtures. *Planet. Space Sci.*, **44**, 973–986.

Radford, H. E. and F. O. Rice. 1960. Green and purple sulfur: Electron spin resonance studies. *J. Chem. Phys.*, **33**, 774–776.

Riskin, Y. I. 1974. The vibrations of protons in minerals: Hydroxyl, water, and ammonium. In: C. V. Farmer (ed.), *The Infrared Spectra of Minerals*. Mineralogical Society, London, pp. 137–181.

Rothschild, W. G. 1964. γ-Ray decomposition of pure liquid sulfur dioxide. *J. Am. Chem. Soc.*, **86**, 1307–1309.

Russell, C. T. (ed.). 1992. *The Galileo Mission* (Space Sci. Rev., Vol. 60). Kluwer, Dordrecht, The Netherlands.

Russell, C. T. and M. G. Kivelson. 2001. Evidence for sulfur dioxide, sulfur monoxide, and hydrogen sulfide in the Io exosphere. *J. Geophys. Res.*, **106**, 33267–33272.

Russell, C. T., J. J. Caldwell, I. de Pater, J. Goguen, M. Klein, B. L. Lutz, N. M. Schneider, W. M. Sinton, and R. A. West. 1990. International Jupiter Watch: A program to study the time variablilty of the Jovian system. *Adv. Space Res.*, **10**, 239–242.

Sagan, C. 1979. Sulfur flows on Io. *Nature*, **280**, 750–753.

Salama, F., L. J. Allamandola, F. C. Witteborn, D. P. Cruikshank, S. A. Sandford, and J. D. Bregman. 1990. The 2.5–5.0-μm spectra of Io: Evidence for H_2S and H_2O frozen in SO_2. *Icarus*, **83**, 66–82.

Salama, F., L. J. Allamandola, S. A. Sandford, J. D. Bregman, F. C. Witteborn, and D. P. Cruikshank. 1994. Is H_2O present on Io? The detection of a new strong band near $3590\,cm^{-1}$ (2.79 μm). *Icarus*, **107**, 413–417.

Salisbury, J. W., L. S. Walter, N. Vergo, and D. M. D'Aria. 1991. *Infrared (2.1–25 μm) Spectra of Minerals* (Johns Hopkins Studies in Earth and Space Science). The Johns Hopkins University Press, Baltimore.

Sandford, S. A. and L. J. Allamandola. 1993. The condensation and vaporization behaviour of ices containing SO_2, H_2S, and CO_2: Implications for Io. *Icarus*, **106**, 478–488.

Sandford, S. A., T. R. Geballe, F. Salama, and D. Goorvitch. 1994. New narrow infrared absorption features in the spectrum of Io between 3600 and 3100 cm^{-1} (2.8–3.2 μm). *Icarus*, **110**, 292–302.

Schaefer, L. and B. Fegley. 2005. Alkali and halogen chemistry in volcanic gases on Io. *Icarus*, **173**, 454–468.

Schmitt, B. and S. Rodriguez. 2000. Tentative identification of a chlorine molecule at Io's surface. *Bull. Amer. Astron. Soc.*, **32**, 29.10.

Schmitt, B. and S. Rodriguez. 2003. Possible identification of local deposits of Cl_2SO_2 on Io from NIMS/Galileo spectra. *J. Geophys. Res.*, **108**, 5104.

Schmitt, B., C. de Bergh, E. Lellouch, J.-P. Maillard, A. Barbe, and S. Douté. 1994. Identification of three absorption bands in the 2-μm spectrum of Io. *Icarus*, **111**, 79–105.

Schmitt, B., C. de Bergh, and M. Festou (eds). 1998a. *Solar System Ices. Astrophysics and Space Science Library*. Kluwer, Dordrecht, The Netherlands.

Schmitt, B., E. Quirica, F. Trotta, and W. M. Grundy. 1998b. Optical properties of ices from the UV to infrared. In: B. Schmitt, C. DeBergh, and M. Festou (eds), *Solar System Ices. Astrophysics and Space Science Library*. Kluwer, Dordrecht, The Netherlands, pp. 199–240.

Schriver, A., L. Schriver, and J. P. Perchard. 1988. Infrared matrix isolation studies of complexes between water and sulfur dioxide: Identification and structure of the 1:1, 1:2, and 2:1 species. *J. Molec. Spect.*, **127**, 125–142.

Schubert, G., J. D. Anderson, T. Spohn, and W. B. McKinnon. 2004. Interior composition, structure, and dynamics of the Galilean satellites. In: F. Bagenal, T. E. Dowling, and W. McKinnon (eds), *Jupiter: The Atmosphere, Satellites, and Magnetosphere*. Cambridge Univ. Press, Cambridge, UK, pp. 281–306.

Sill, G. T. 1973. Reflectance spectra of solids of planetary interest. *Comm. Lunar Planet. Lab.*, **10**, 1–7.

Sill, G. T. and R. N. Clark. 1982. Composition of the surfaces of the Galilean satellites. In: D. Morrison (ed.), *Satellites of Jupiter*. University of Arizona Press, Tucson, AZ, pp. 174–212.

Simonelli, D. P., J. Boucher, P. Helfenstein, J. Veverka, and M. O'Shaughnessy. 1994. Search for temperature-related albedo changes in nightside and posteclipse images. *Icarus*, **107**, 375–387.

Sinton, W. M., D. Lindwall, F. Cheigh, and W. C. Tittemore. 1983. Io: The Near-infrared Monitoring Program, 1979–1981. *Icarus*, **54**, 133–157.

Smythe, W. D., R. M. Nelson, and D. B. Nash. 1979. Spectral evidence for SO_2 frost or adsorbate on Io's surface. *Nature*, **280**, 766.

Smythe, W. D., R. Lopes-Gautier, S. Douté, S. W. Kieffer, R. W. Carlson, L. Kamp, and F. Leader. 2000. Evidence for massive sulfur dioxide deposit on Io. *Bull. Amer. Astron. Soc.*, **32**, 1047–1048.

Spencer, J. R. and N. M. Schneider. 1996. Io on the Eve of the Galileo Mission. *Annu. Rev. Earth Planet. Sci.*, **24**, 125–190.

Spencer, J. R., W. M. Calvin, and M. J. Person. 1995. Charge-coupled-device spectra of the galilean satellites: Molecular-oxygen on Ganymede. *J. Geophys. Res.*, **100**, 19049–19056.

Spencer, J. R., A. S. McEwen, M. A. McGrath, P. Sartoretti, D. B. Nash, K. S. Noll, and D. Gilmore. 1997. Volcanic resurfacing of Io: Post-repair HST imaging. *Icarus*, **127**, 221–237.

Spencer, J. R., K. L. Jessup, M. A. McGrath, G. E. Ballester, and R. Yelle. 2000. Discovery of gaseous S_2 in Io's Pele plume. *Science*, **288**, 1208–1210.

Spencer, J. R., R. W. Carlson, T. L. Becker, and J. S. Blue. 2004. Maps and spectra of Jupiter and the Galilean satellites. In: F. Bagenal, T. E. Dowling, and W. B. McKinnon (eds), *Jupiter: The Planet, Satellites, and Magnetosphere*. Cambridge University Press, Cambridge, UK, pp. 689–698.

Steudel, R. (ed.). 2003a. *Elemental Sulfur and Sulfur-Rich Compounds. I: Top. Curr. Chem.*, **230**. Springer, Berlin.

Steudel, R. (ed.). 2003b. *Elemental Sulfur and Sulfur-Rich Compounds. II: Top. Curr. Chem.*, **231**. Springer, Berlin.

Steudel, R. 2003c. Sulfur-rich oxides S_nO and S_nO_2 ($n > 1$). *Top. Curr. Chem.*, **231**, 203–230.

Steudel, R. and Y. Steudel. 2004. The thermal decomposition of S_2O forming SO_2, S_3, S_4, and S_5O: An ab initio MO study. *Eur. J. Inorg. Chem.*, **2004**, 3513–3521.

Steudel, R., G. Holdt, and A. T. Young. 1986. On the colors of Jupiter's satellite Io: Irradiation of solid sulfur at 77 K. *J. Geophys. Res.*, **91**, 4971–4977.

Steudel, R., Y. Steudel, and M. W. Wong. 2003. Speciation and thermodynamics of sulfur vapor. *Top. Curr. Chem.*, **230**, 117–134.

Thomas, N., F. Bagenal, T. W. Hill, and J. K. Wilson. 2004a. The Io neutral clouds and plasma torus. In: F. Bagenal, T. E. Dowling, and W. McKinnon (eds), *Jupiter*. Cambridge University Press, Cambridge, UK, pp. 561–592.

Thomas, N., F. Bagenal, T. W. Hill, and J. K. Wilson. 2004b. The Io neutral clouds and plasma torus. In: F. Bagenal, T. E. Dowling, and W. McKinnon (eds), *Jupiter: The Planet, Satellites, and Magnetosphere*. Cambridge University Press, Cambridge, UK, pp. 561–591.

Trafton, L., D. F. Lester, T. F. Ramseyer, F. Salama, S. A. Sandford, and L. J. Allamandola. 1991. A new class of absorption features in Io's near-infrared spectrum. *Icarus*, **89**, 264–276.

Voegele, A. F., T. Loerting, C. S. Tautermann, A. Hallbrucker, E. Mayer, and K. R. Liedl. 2004. Sulfurous acid (H_2SO_3) on Io? *Icarus*, **169**, 242–249.

Wagner, J., B. Hapke, and E. Wells. 1987. Atlas of reflectance spectra of terrestrial, lunar, and meteoritic powders and frosts from 92 to 1800 nm. *Icarus*, **69**, 14–28.

Wamsteker, W., R. L. Kroes, and J. A. Fountain. 1973. On the surface composition of Io. *Icarus*, **23**, 417–424.

Williams, D. A., J. Radebaugh, L. P. Keszthelyi, A. S. McEwen, R. M. C. Lopes, S. Douté, and R. Greeley. 2002. Geologic mapping of the Chaac–Camaxtli region of Io from Galileo imaging data. *J. Geophys. Res.*, **107**, doi:10.1029/2001JE001821.

Witteborn, F. C., J. C. Bregman, and J. P. Pollack. 1979. Io: An intense brightening near 5 micrometers. *Science*, **203**, 643–646.

Wong, M. C. and R. E. Johnson. 1996a. A three-dimensional azimuthally symmetric model atmosphere for Io. 1: Photochemistry and the accumulation of a nightside atmosphere. *J. Geophys. Res.*, **101**, 23243–23254.

Wong, M. C. and R. E. Johnson. 1996b. A three-dimensional azimuthally symmetric model atmosphere for Io. 2: Plasma effect on the surface. *J. Geophys. Res.*, **101**, 23255–23259.

Young, A. T., 1984. No sulfur flows on Io. *Icarus*, **58**, 197–226.

Zhang, J., D. B. Goldstein, P. L. Varghese, N. E. Gimelshein, S. F. Gimelshein, and D. A. Levin. 2003. Simulation of gas dynamics and radiation in volcanic plumes on Io. *Icarus*, **163**, 182–197.

Zolotov, M. Y. and B. Fegley. 1998. Volcanic production of sulfur monoxide (SO) on Io. *Icarus*, **132**, 431–434.

Zolotov, M. Y. and B. Fegley. 2000. Eruption condition of Pele volcano on Io inferred from chemistry of its volcanic plume. *Geophys, Res. Lett.*, **27**, 2789–2792.

10

Io's atmosphere

Emmanuel Lellouch, Melissa A. McGrath, and Kandis Lea Jessup

10.1 INTRODUCTION, EARLY STUDIES, AND MAIN ISSUES

Our knowledge of Io's atmosphere has undergone a major revision in the last fifteen years. By 1990, observational information was restricted to several clear but indirect pieces of evidence, a single direct infrared detection by *Voyager* in 1979, and a number of upper limits from ultraviolet spectroscopy. Even loosely constrained, Io's atmosphere was quickly recognized as bearing unique features among planetary atmospheres, the most prominent being its apparent spatial and temporal variability, and possible direct relationship to Ionian volcanism. This lack of data did not hinder, in the 1980–1990 decade, theoretical studies on the horizontal, vertical, and chemical structure of Io's atmosphere. Since 1990, the direct detection of Io's atmosphere from Earth or Earth orbit in different wavelength ranges, along with recent results on Io volcanism and surface composition from *Galileo*, has given a much firmer basis to our perception of Io's atmosphere, justifying, in turn, the development of more elaborate chemical, thermal, dynamical, and volcanic models. In this chapter, we focus on these recent observational and theoretical developments. Earlier studies, which were extensively covered in previous reviews by Johnson and Matson (1989), Trafton *et al.* (1995), Lellouch (1996), and Spencer and Schneider (1996) are only briefly covered here. The reader is also referred to the comprehensive review of McGrath *et al.* (2004) for additional details and figures.

The first definite evidence for an atmosphere around Io was obtained in 1973 with the *Pioneer 10* detection of relatively dense ionospheric layers above Io's surface near the terminator (Kliore *et al.*, 1974, 1975). Very different ionospheric profiles (termed "dayside" and "nightside", although both actually occurred very close to the terminator) were detected at entry and exit and preliminary estimates of the neutral atmosphere required to explain these data yielded surface pressures of 10^{-8}–10^{-9} bars. Shortly after, optical observations detected atomic sodium around Io (Brown, 1974), and it was quickly established that the observed sodium formed a neutral cloud

of atoms in orbit around Jupiter that had escaped non-thermally from Io, implying a source of Na in Io's atmosphere or at the surface. Further evidence for atmospheric escape was obtained from the optical detection of a potassium cloud (Trafton, 1975) and of ionized sulfur in the magnetosphere (Kupo *et al.*, 1976). In 1979, *Voyager* observations confirmed the importance of sulfur and oxygen ions in Jupiter's magnetosphere (e.g., Broadfoot *et al.*, 1979; Bridge *et al.*, 1979).

The "watershed event" for Io's atmosphere occured the same year with a triple discovery: the presence of active volcanism on Io's surface (Morabito *et al.*, 1979), the attribution of a 4.1 μm feature in Io's infrared spectrum to solid SO_2 (Fanale *et al.*, 1979; Smythe *et al.*, 1979), and the detection of gaseous SO_2 at 7.3 μm over the volcanic center Loki Patera by *Voyager*/infrared imaging spectrograph (IRIS) (Pearl *et al.*, 1979). The IRIS spectrum was interpreted as indicating a 10^{-7} bar local atmosphere at 130 K (column density $= 5\times10^{18}\,cm^{-2}$), although a subsequent reinterpretation (Lellouch *et al.*, 1992) has shown it to be consistent with lower pressures (5–40 nanobar, i.e., $(2.5–20)\times10^{17}\,cm^{-2}$) and higher temperatures (up to 400 K). Note that Loki was the only region with enough 7 μm continuum radiation to illuminate any SO_2 gas, so that the *Voyager* observation, in itself, did not rule out a global atmosphere. After this single observation, Io's atmosphere eluded further detection for another 11 years, but several attempts in the ultraviolet were useful at placing upper limits on the global SO_2 amount. The most significant result was obtained by Ballester *et al.* (1990) from the International Ultraviolet Explorer (IUE), who placed an upper limit of $2\times10^{17}\,cm^{-2}$, for a homogeneous SO_2 atmosphere, implying, by comparison with the *Voyager* result, a strong horizontal non-uniformness.

The early and *Voyager* discoveries represented an enormous step forward, but immediately raised the *essential* question that is still probably focusing most research efforts on Io's atmosphere. Was SO_2 gas detected around Loki because Loki emitted a SO_2-rich volcanic plume, or rather because the SO_2 frost in that region was able to sustain a significant atmosphere? Indeed, given the SO_2 sublimation vapor pressure curve, a 0.1 μbar atmosphere is in equilibrium with SO_2 frost at 130 K, a reasonable temperature for Io's surface. Extending this issue to Io's atmosphere as a whole, the basic questions were: Is Io's atmosphere primarily supported by sublimation equilibrium, or dynamically maintained by volcanic output? How far does a plume atmosphere propagate horizontally? Is the atmosphere, away from volcanic centers, collisionally thin or thick to the penetration of thermal ions from the plasma torus? Can the atmosphere also be sputter-generated? Did the *Pioneer 10* observations suggest a global atmosphere but with substantial lateral variations?

These limited observations set the stage for the development of models. Models either addressed the atmospheric vertical thermal and compositional structure, with the prime goal of reproducing the *Pioneer 10* ionosphere with surface conditions indicated by *Voyager*, or were concerned with the horizontal distribution of surface pressure and associated dynamics. It was not until the mid-1990s that the two approaches attempted to merge (see below). Models of the first type included notably the extensive work of Kumar (e.g., 1980, 1985) who established the thermal budget of an SO_2 atmosphere and the basics for its photochemistry. As

detailed below, energy sources for Io's atmosphere include solar ultraviolet heating, plasma ion heating (e.g., Johnson, 1989) and Joule heating (ignored in the early models, and accounted for the first time by Strobel *et al*., 1994). Aeronomical models at that time generally suggested very warm atmospheres (e.g., 500 K at 20 km altitude, 2,000 K at 80 km). However, these models mistreated or ignored non-local thermodynamic equilibrium (LTE) SO_2 infrared cooling, and omitted rotational cooling. Photochemical models of a pure SO_2 or of an SO_2–Na atmosphere, including ionospheric chemistry, were developed (e.g., Kumar, 1985; Summers, 1985). Though these models had only moderate success in reproducing the *Pioneer 10* ionospheric density profiles, they did indicate that Io's atmosphere must also contain significant amounts of SO, O_2, and atomic S and O. Given the estimated supply rates to the torus, about 1×10^{28} and 4×10^{27} s^{-1} for O and S respectively, it was realized that Io's atmosphere has a short lifetime – of the order of 10 days – and must be replenished continuously to offset its escape loss.

Early models describing the horizontal distribution of the SO_2 atmosphere fell into three categories: "buffered", "dynamical", and "sputtered". In buffered models, the distribution of gas reflects strict local vapor pressure equilibrium with the surface ice. Most of the models assumed uniform frost coverage, but varied in the estimate of the frost temperature controlling the atmospheric pressure. Variants included the "equilibrium model", the "regional cold-trapping model" (both described by Fanale *et al*., 1982), and the "subsurface cold-trapping model" of Matson and Nash (1983). Due to the very steep SO_2 vapor pressure curve with temperature, the associated pressures differed by orders of magnitude, and the models predicted enormous pressure variations with solar zenith angle (SZA). Dynamical models (Ingersoll *et al*., 1985; Ingersoll, 1989; Moreno *et al*., 1991) addressed the issue of pressure redistribution from supersonic winds, creating regions of net sublimation in an equatorial band and regions of net condensation at mid-latitudes (30°–70°). These models were extended to the case of non-uniform frost and of volcanic atmospheres. Ingersoll (1989) developed the concept of "averaging length" (i.e., the characteristic dimension (of order 50–100 km) over which each frost patch controls its own pressure), and established the equivalence between volcanic venting and sublimation in maintaining the surface pressure. For both sources, the key factor controlling the areal extent of the atmosphere remains the frost temperature distribution, so these studies left open the possibilities of patchy and extended atmospheres on Io. Because sublimating SO_2 frosts are losing mass, the ultimate source of Io's atmosphere is volcanic output. Nonetheless, the distinction between buffered and volcanic atmospheres is significant as the associated vertical structures (hydrostatic and plume-like, respectively) are very different, with dynamical, thermal, and compositional implications. In addition, a sublimation atmosphere probably collapses at night and in eclipse, while a volcanic atmosphere does not. Sputtering models (see review in Cheng and Johnson, 1989) demonstrated that the impact of energetic magnetospheric particles onto the surface can generate a giant rarefied atmosphere. Such an atmosphere, or "corona", is self-limited to $\sim10^{16}$ cm^{-2} since sufficient gas build-up halts further ion penetration, but the mechanism may still be the dominant source of atmosphere in some specific locations (e.g., high-latitude, nightside). The case of

sputtering of a pre-existing, collisionally thick atmosphere was also studied (McGrath and Johnson, 1987).

10.2 RECENT OBSERVATIONAL PROGRESS

10.2.1 The SO_2 atmosphere

Millimeter observations

Since the first detection of SO_2 gas in emission in a rotational line at 222 GHz in January 1990 (Lellouch *et al.*, 1990), millimeter-wave heterodyne spectroscopy has provided a new technique to probe Io's atmosphere. Such observations were acquired mostly with the IRAM 30-m telescope, and yielded useful data in 1991, 1993, 1994, 1995, 1999, and 2002. These observations do not resolve Io's disk, are concentrated around maximum eastern elongation (orbital longitude $L = 90^\circ$) or western elongation ($L = 270^\circ$), and have low temporal (i.e., longitudinal) resolution. They thus primarily sample the dayside leading and trailing sides (as opposed to the sub-Jovian and anti-Jovian hemispheres).

A dozen SO_2 lines have been detected over the years. They span a factor of $\sim$20 in line intensity, but with one exception all have relatively low energy levels (8–165 cm^{-1}). They result from LTE thermal emission of the atmosphere (Lellouch *et al.*, 1992). All detected SO_2 lines appear in emission (Figure 10.1). Line contrasts reach 20–40 K in brightness temperature, implying that the mean dayside SO_2 gas temperature is higher than the mean surface brightness temperature, by at least 20–40 K, and maybe by much more, if the dayside atmosphere covers only a fraction of Io's surface and/or if the lines are not optically thick.

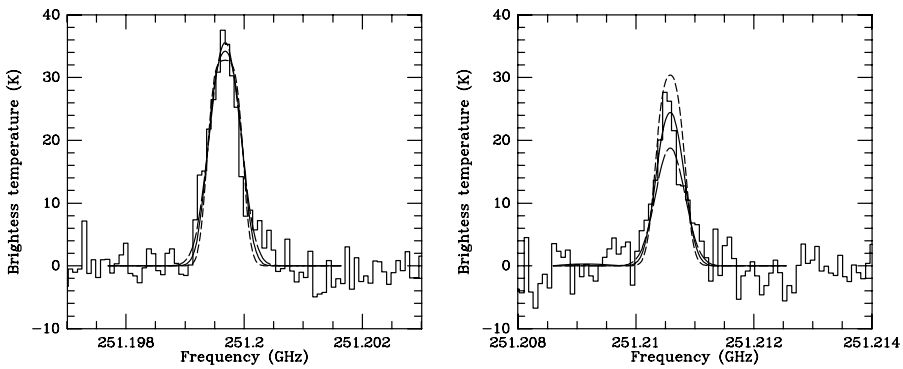

Figure 10.1. Illustration of temperature determination from SO_2 millimeter observations. The 251.2 GHz SO_2 doublet, observed on 26 November 1999 on Io's trailing side, is here compared with three hydrostatic models. Solid line: atmospheric temperature $T_{atm} = 400$ K, surface pressure $p = 2.7$ nbar (i.e., 1.4×10^{17} cm^{-2}), projected atmospheric coverage $f_p = 14\%$. Short-dashed line: $T_{atm} = 250$ K, $p = 1.7$ nbar, $f_p = 20\%$. Long-dashed line: $T_{atm} = 600$ K, $p = 2.5$ nbar, $f_p = 26\%$. For each temperature, the surface pressure is determined by fitting the line width. The relative line contrast is best fit for $T_{atm} = 400$ K (from Lellouch *et al.*, 2000).

The observed lines, fully resolved, are generally symmetric about their central frequency, although the most recent observations may suggest more complex lineshapes. The line width of the strongest lines (full width at half-maximum, FWHM) is ~ 600 kHz at 220 GHz and scales as the line frequency, indicating Doppler broadening – collisional broadening would anyway imply an implausible 10^{-4} bar surface pressure. The line FWHM/frequency ratio, $\sim 2.7 \times 10^{-6}$, gives a temperature of 910 K for thermal broadening, or a velocity of $0.8\,\mathrm{km\,s^{-1}}$ for bulk velocity broadening.

The first interpretation of these data (Lellouch *et al.*, 1990, 1992) assumed Io's SO_2 atmosphere to be in hydrostatic equilibrium. In this case, $T_{\mathrm{atm}} = 910$ K is an upper limit to the mean atmospheric temperature. Since the bulk of Io's atmosphere is likely to be at a much colder temperature (see radiative models below), the line widths were interpreted as being affected by saturation effects. In this framework, the analysis of a single strong line indicates that the atmosphere is comfortably collisionally thick (5×10^{16} to $5 \times 10^{17}\,\mathrm{cm^{-2}}$ column density) but covers a restricted fraction of Io's disk. A more precise characterization, however, requires multi-line observations, whereby the relative contrast of several lines of different strengths constrain their saturation degree and helps disentangle the opacity/temperature/column density/coverage variables. The "atmospheric coverage" observable is f_p, the fraction of the projected surface (disk) covered by the atmosphere. Converting f_p to actual *hemispheric coverage* f_h, requires knowing how the gas is distributed. A common assumption is that the atmosphere is restricted to a circular region around disk center (i.e., close to the subsolar point, in which case $f_h = 1 - (1 - f_p)^{1/2}$.

The need for "multi-line" observations motivated most of the SO_2 millimeter-wave observations over 1991–1999. In retrospect, they did not give a completely consistent picture of Io's atmosphere, especially regarding the mean atmospheric temperature and the fractional coverage of the atmosphere. The early observations (1991–1994) indicated a very hot ($T_{\mathrm{atm}} = 500$–600 K), dense (surface pressure $\sim$3–15 nbar), and very localized ($f_p = 5$–$8\%, f_h = 2.5$–4%) atmosphere on the trailing side, and a somewhat cooler (250–400 K) and more extended ($f_p = 12$–16%, $f_h = 6$–9%) atmosphere on the leading (Lellouch *et al.*, 1992; Lellouch, 1996). In all these observations, the hemispheric-average column density was in the range $(1$–$2) \times 10^{16}\,\mathrm{cm^{-2}}$, with a tendency for higher values on the trailing than on the leading. Subsequent observations (1999) confirmed this general picture, but provided somewhat different temperature and atmospheric coverage numbers, namely $T_{\mathrm{atm}} = 400$ K and $f_h = 8\%$ on the trailing side vs. $T_{\mathrm{atm}} = 200$ K and $f_h = 24\%$ on the leading (Lellouch *et al.*, 2000). In contrast, the January 2002 observations (leading + trailing), which included a high-energy ($404\,\mathrm{cm^{-1}}$) line, indicated a rotational temperature of only 180 ± 60 K (Lellouch *et al.*, 2003). Thus, the gas temperature estimated from these multi-line observations has decreased over the years, and it is unclear if this is due to actual variability or to signal-to-noise limitations in the early data sets.

Although the SO_2 millimeter emissions are permanently detectable, temporal and orbital variability can be directly seen on the data themselves. A clear example was observed in June 1995, with an unusually sharp 143-GHz line compared with other years (Lellouch, 1996). The most likely interpretation is an increase of the atmospheric

areal extent, along with a decrease of either the surface pressure or gas temperature. In fact, this observation, unlike all other millimeter observations, is consistent with a global atmosphere. Strong lines observed in 1999 were about 50% stronger than in 1990–1994 (McGrath *et al.*, 2004, Figure 1), interpreted as a generally higher surface coverage. The unprecedented S/N levels of the 1999 observations allowed the exploration of orbital variations of line characteristics beyond the leading/trailing contrast. The main findings are: (i) a suggested increase in the integrated line strengths over L = 40–135 and a decrease over L = 240–340; (ii) a more definite variation of line frequency with orbital position, with a global blueshift by $\sim$100 m s^{-1} on the leading side and a similar redshift on the trailing side. The interpretation remains uncertain, although it might be related either to volcanic plume emission geometry (see below) or to angular momentum transfer from the plasma flow hitting Io's trailing side at $\sim$57 km s^{-1} (see discussion in McGrath *et al.*, 2004).

The high temperatures on at least the trailing side inferred from the early millimeter observations are at odds with radiative–conductive models (Strobel *et al.*, 1994) which predict that the atmosphere never warms above 200 K in the first scale height. This may suggest that the hydrostatic interpretation of the millimeter data is incorrect. Ballester *et al.* (1994) first proposed that the millimeter line widths primarily reflect velocity dispersion within gaseous plumes rather than a combination of temperature and saturation effects. Lellouch (1996) presented simplified models based on this idea. The introduction of a new parameter, namely the plume ejection velocity, controlling the line widths, relaxes the constraints on the gas temperature. The hemispheric-average column densities of (0.6–2.5)$\times 10^{16}$ cm^{-2} obtained in these models are comparable with those in the hydrostatic models, but the data can now be fit even with low temperatures, and therefore the atmosphere is no longer necessarily "hot and localized" – a typical surface coverage is then $f_h \sim 30\%$ for an assumed $T_{\rm atm} = 200$ K. However, because the plumes are small (e.g., r = 135 km for an ejection velocity of $\sim$0.5 km s^{-1} as indicated by the data), they must be very numerous (50–300) to cover a significant fraction of one hemisphere. This large number may be somewhat decreased if allowance is made for a non–zero horizontal flow which increases the plume size. This number can be reduced further if a mixture of small and Pele-class plumes is assumed. With the $\sim$150 active volcanic centers observed by *Galileo* (Lopes-Gautier *et al.*, 1999; Lopes *et al.*, 2004), 50 active plumes may not be unreasonable, especially if many of them are the invisible "stealth" plumes (i.e., those with a low condensate content) postulated by Johnson *et al.* (1995). The possible existence of almost purely gaseous plumes has been demonstrated by Kieffer (1982) in the case of a high-entropy erupting fluid from a reservoir of superheated SO_2 vapor in contact with a deep, hot, and dense silicate melt (1,400 K, 40 bar). While already complex to implement, the plume models presented by Lellouch (1996) certainly represent a rough and simplistic description of the complex physics of volcanic plumes (see Section 3.3, and Chapter 8).

Ultraviolet observations

SO_2 gas absorbs strongly in the ultraviolet region. Since 1992, this has been exploited in numerous successful ultraviolet observations, starting with the first ultraviolet

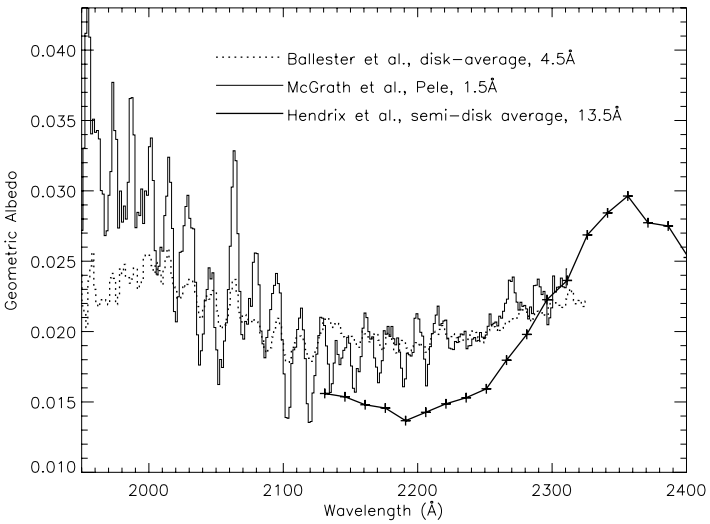

Figure 10.2. Comparison of three mid-ultraviolet spectra of Io, illustrating the importance of spectral resolution in detecting SO_2 in Io's atmosphere (from McGrath *et al.*, 2004). For each observation, the spectral resolution, in Angstroms, is indicated.

images of Io (Paresce *et al.*, 1992) and the first spectroscopic detection of SO_2 in the ultraviolet (Ballester *et al.*, 1994). Spectroscopic observations divide between disk-averaged (Ballester *et al.*, 1994; Trafton *et al.*, 1996; Jessup *et al.*, 2005) and disk-resolved (Hendrix *et al.*, 1999; McGrath *et al.*, 2000; Spencer *et al.*, 2000; Jessup *et al.*, 2004a) measurements. Unlike the millimeter-wave spectrum, the ultraviolet spectrum is primarily sensitive to the column-integrated abundance of the absorbing gases, but not directly for their temperature, except for a general decrease in the band contrast with increasing temperature and subtle variations in the band peak position and skewness (see e.g., Wu *et al.*, 2000). Analysis is subject to two complications. The first one comes from the fact that, as pointed out by Belton (1982), the SO_2 ultraviolet spectrum has a very complex structure of many densely packed lines that has not been resolved in laboratory measurements, so that line-by-line position and intensity information is not available. In this situation, applying Beer's law at a spectral resolution comparable with that of the measurements can lead to significant underestimates of absorber abundance. Band models are much preferred, and several modelers have followed the treatment by Ballester *et al.* (1994). The other complication is due to the poorly known contribution of Io's surface to the overall geometric albedo. Indeed, SO_2 frost, present on Io's surface, has broadly similar spectral properties as SO_2 gas; while SO_2 frost is known to be dark in the ultraviolet, it is impossible to reliably predict the absolute surface reflectance and its spectral dependence. As a consequence, only observations with a spectral resolution enabling us to distinguish characteristic gas spectral features unambiguously constrain gas abundances (Figure 10.2).

This situation has led, in particular, to competing interpretations for the imaging data. For example, the early ultraviolet images of Sartoretti *et al.* (1994, 1996) can be

modeled either purely in terms of variations of surface properties, or by assuming that the darkest regions seen in the images represent SO_2 gas. The latter explanation was preferred by Sartoretti *et al.* (1996), who concluded to the presence of SO_2 patches (one of which is Pele) with typical column densities of $\sim 1 \times 10^{18}\,cm^{-2}$, covering 11–15% of the projected surface. Because these early ultraviolet images were insensitive to SO_2 column densities below $\sim 8 \times 10^{16}\,cm^{-2}$, the presence of a lower density component could not be ascertained.

Disk-averaged spectroscopic observations were initially obtained in 1992 with the Hubble Space Telescope (HST) Faint Object Spectrograph (FOS) and Goddard High-Resolution Spectrograph (GHRS) instruments (Ballester *et al.*, 1994; Trafton *et al.*, 1996), covering altogether the 1,975–2,350 Å range. Additional data with HST/FOS were acquired in 1994 and 1996 (Jessup *et al.*, 2005). Not surprisingly in view of the lack of spatial resolution, the data can generally be fit by a variety of models, ranging from hemispherically uniform to localized (either in latitude bands or in spatially confined patches) atmospheres. Typically, uniform models indicated SO_2 column densities of $(5–10) \times 10^{15}\,cm^{-2}$. Patchy atmospheres were found to satisfy the data, provided that the local column densities remained below $(1–3) \times 10^{17}\,cm^{-2}$ and the hemispheric coverage (f_h) exceeded 8–23% (Ballester *et al.*, 1994; Trafton *et al.*, 1996). Cold temperatures ($T_{atm} = 110–250$ K) are preferred. Jessup *et al.* (2005) found that a two-component model, consisting of a low-density ($10^{15}–10^{16}\,cm^{-2}$) component covering 50–100% of the observed hemisphere and a high-density ($10^{17}–10^{18}\,cm^{-2}$) component, restricted to 2–10% of the surface, provided an optimum match to the 1994–1996 FOS data. The 1994 and 1996 FOS data show somewhat deeper absorptions on the leading side than on the trailing side. From optimized fits, Jessup *et al.* (2005) interpret these variations as being due to a larger SO_2 column density on the leading side in 1996 ($(3–4) \times 10^{16}\,cm^{-2}$ vs. $(1–3) \times 10^{16}\,cm^{-2}$ on the trailing for an atmosphere covering a $\pm 30^\circ$ equatorial band), and a possibly higher gas temperature on the trailing side in 1994. The first of these conclusions is moderately inconsistent with the finding by Trafton *et al.* (1996) of a 30% denser atmosphere on the trailing side than on the leading in 1992. Nonetheless, a global analysis of the FOS and GHRS data, assuming an atmosphere distributed uniformly across the disk, indicates that the disk-average column densities did not vary temporally by more than a factor of 2 between 1992 and 1996.

Another important feature of the ultraviolet spectrum of Io, first noted from HST/FOS data at 2,250–3,300 Å, is the absence of fine structure due to SO_2 bands in the near-ultraviolet ($\lambda > 2{,}500$ Å). Clarke *et al.* (1994) interpreted this as ruling out a global atmosphere denser than $4 \times 10^{16}\,cm^{-2}$. However, they indicated that a very dense, localized component (e.g., $2 \times 10^{19}\,cm^{-2}$ over a 10% area), was not inconsistent with the data. At such very high column densities, the 2,800–3,100 Å range is saturated to 100% absorption, even in the continuum between lines, consequently showing no spectral contrast. Hendrix *et al.* (1999), using the *Galileo* ultraviolet spectrometer, obtained a spectrum of similar spectral resolution and coverage (though extending down to 2,100 Å) as that of Clarke *et al.* (1994). Though their spectrum did not resolve the individual SO_2 multiplets (Figure 10.2) and was limited to a single large aperture, covering the 120°W–150°W longitudes and encompassing all latitudes, these data

provided the first disk-resolved observations of Io's atmosphere. In addition to the features described by Clarke *et al.* (1994), a clear decrease of the albedo shortward of 2,360 Å was observed. Hendrix *et al.* (1999) attributed this behavior to SO_2 gas absorption, and inferred very large ($1\times10^{19}\,cm^{-2}$) column densities over 25% of the aperture. They also found that 35% of the observed surface is covered by a $4\times10^{17}\,cm^{-2}$ component, the remaining 40% being gas-free.

In spite of their inherent ambiguity, these various observations lended credit to the idea of spatial variations in Io's surface pressure. These variations were finally demonstrated by the spatially resolved HST/FOS 1996 observations of McGrath *et al.* (2000). The targets were chosen to sample different physical conditions that are likely to exist on Io's surface: (1) the Pele Volcano (18°S, 257°W); (2) Ra (7°S, 318°W), a potentially active region bright in the visible and dark in the ultraviolet, indicating abundant SO_2 frost; and (3) a reference region at 45°S and 300°W, designated as "T3", dark in visible and bright in ultraviolet (i.e., presumably frost-poor). All three targets were within 10° of the subsolar longitude at the time of observation. The spectral resolution (1.5 Å), spatial resolution (0.26″), and S/N were unprecedented in these observations (Figure 10.2). Best fit SO_2 column densities and temperatures were found to be $3.25\times10^{16}\,cm^{-2}$, $1.5\times10^{16}\,cm^{-2}$, and $7\times10^{15}\,cm^{-2}$, and 280, 150, 200 K, for Pele, Ra, and T3 respectively. The interpretation of the differences in SO_2 column density, however, remains uncertain because the degree of volcanic activity, especially at Ra, during the observations was unknown. It is, in particular, hard to know whether the difference between Pele and Ra is due to a difference in activity, or to a longitudinal variation of the low-latitude sublimated SO_2 column density (Spencer *et al.*, 2005). In any case, the observation of SO_2 at T3 – a region in which no active plume has ever been observed – was strong evidence for a relatively widespread atmosphere, and the factor-of-two (only) lower column density measured at T3 compared with Ra indicated a drop in SO_2 pressure with latitude being much more gradual than predicted by the early sublimation models (McGrath *et al.*, 2000).

From imaging of the Pele plume against dark sky and silhouetted against Jupiter during Io transit, performed only 7 days after the McGrath *et al.* (2000) observations, Spencer *et al.* (1997) determined its height and 2,720 Å opacity. The plume was not detected at 3,400 and 4,100 Å. This wavelength-dependent optical depth was interpreted as due to absorption by either small dust particles or SO_2 gas with $3.7\times10^{17}\,cm^{-2}$ column density. However, as discussed below, HST/STIS (Space Telescope Imaging Spectrogaph) observations of the Pele plume in 1999 indicated much lower (factor-of-10) SO_2 column densities in the plume (Spencer *et al.*, 2000) and a series of strong absorption lines due to gaseous S_2 at 2,400–3,100 Å. In retrospect, this indicates that the source of opacity in the Pele images was primarily absorption by S_2, with negligible dust extinction and only a minor contribution due to gas SO_2. This also probably applies to the 2,600 and 2,850 Å images presented by Sartoretti *et al.* (1994, 1996).

Building upon the results of McGrath *et al.* (2000), a more complete investigation of the longitudinal and latitudinal distribution of Io's SO_2 atmosphere was achieved by Jessup *et al.* (2004a). They used HST/STIS with a 0.1″-wide slit, centered over the Prometheus plume and oriented at ~45°, to sample regions, with and without

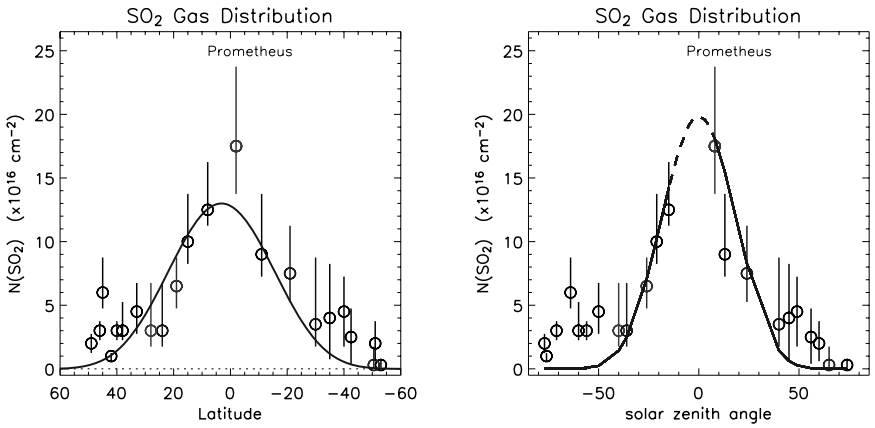

Figure 10.3. SO_2 gas distribution as a function of latitude and solar zenith angle, determined from HST/STIS observations (Jessup *et al.*, 2004). Results are compared with predictions from two versions of a simple sublimation model (see text for details).

active volcanic hot spots, on the anti-Jovian hemisphere, extending $\pm 50^\circ$ latitude. The inferred SO_2 column densities peaked at 1.25×10^{17} cm^{-2} near the equator (i.e., eight times the value determined by McGrath *et al.*, 2000, for Ra), with an additional 5×10^{16} cm^{-2} enhancement over Prometheus, which corresponds to a volcanic output of $\sim 10^4$ kg s^{-1} (and not 10^5 kg s^{-1} as stated in Jessup *et al.*). Although the slit encompassed several volcanic hot spots or plume sites (e.g., Volund, Zamama, Tupan, Malik), no local SO_2 enhancement was detected besides the one at Prometheus. The SO_2 column densities fall off smoothly as a function of latitude or SZA (Figure 10.3). Although the slit orientation and the absence of diurnal monitoring in this single observation prevented disentangling longitudinal (i.e., geographical), diurnal, and latitudinal variations, it appears that below $\pm 30^\circ$ latitude, the data can well be matched by a simple sublimation model with a subsolar/equatorial frost temperature of 117.3 ± 0.6 K and frost temperatures either: (i) in instantaneous equilibrium (SZA control); or (ii) in equilibrium with diurnally averaged sunlight (latitudinal control). In contrast, the decrease in SO_2 away from Prometheus is slower than expected from a single isolated volcanic source (Zhang *et al.*, 2003). At mid-latitudes (30–50°), the decrease in the SO_2 column density with latitude is much shallower than predicted by the two versions of the simple sublimation model, confirming the McGrath *et al.* (2000) result based on the comparison between Ra and T3. This behavior could result from a latitudinal decrease of the frost albedo, an increase of pressure due to hydrodynamic flow (as discussed hereafter in Section 10.3.5), or the presence of active volcanic venting at these latitudes. Nonetheless, the Jessup *et al.* (2004a) results were generally interpreted as supportive of the sublimation atmosphere concept, and, when compared with the McGrath *et al.* (2000) results, provided the first clear evidence for dramatic longitudinal variations. Finally, these observations revealed the first detection of near ultraviolet (2,800 Å) continuum emission, which appears to be correlated with the inferred SO_2 columns.

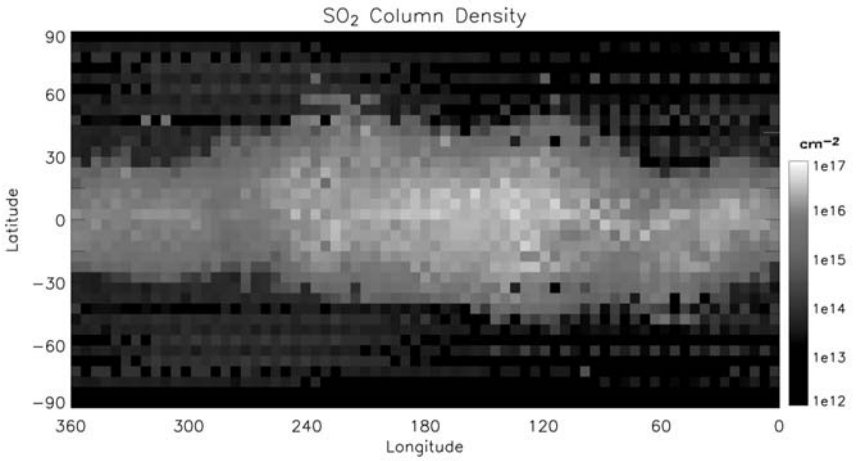

Figure 10.4. 2-D SO_2 gas distribution, as inferred from Lyα images (from Feaga *et al.*, 2004a). (See also color section.)

The most global view of Io's SO_2 atmosphere at spatial scales >200 km is provided by the analysis of HI Lyα images acquired by HST/STIS over 1997–2001. These images, first obtained by Roesler *et al.* (1999), show that the Lyα reflectance pattern consists of two mid-to-high latitude (>45°) bright patches at the 2 kR level, while the equatorial latitudes are dark, with ~0.7 kR at disk center. Though Roesler *et al.* (1999) envisaged several explanations for the observed structure, the explanation of absorption of surface-reflected solar Lyα by low-latitude atmospheric SO_2 was shown to be the most likely by Feldman *et al.* (2000) and Strobel and Wolven (2001), as SO_2 is a strong continuum absorber at Lyα (cross section $\sigma = 3.9\times10^{-17}$ cm^2). This interpretation is consistent with the absence of bright polar regions during eclipse (McGrath *et al.*, 2004). Using various assumptions on the surface reflectivity at Lyα, Feldman *et al.* (2000) found equatorial SO_2 column densities in the range $(0.5\text{–}4)\times10^{16}$ cm^{-2}. Strobel and Wolven (2001) analyzed one of these images by constructing spatial models of the Lyα emission, based on longitudinally homogeneous model atmospheres with column densities decreasing sharply from $(1\text{–}1.7)\times10^{16}$ cm^{-2} to $\sim3\times10^{14}$ cm^{-2} poleward of 50° latitude. These models capture the essential observational features and suggest that Io's atmosphere is restricted to a ±30–40° band in which lateral inhomogeneities (at the resolution of the data) are modest. Strobel and Wolven (2001) interpreted this in the context of numerous (10–200) plume atmospheres, with a total emission rate of $\sim5\times10^{30}$ s^{-1}. A more comprehensive study of the Lyα images was performed by Feaga *et al.* (2004). They found that the data show a fairly stable latitude/longitude pattern (Figure 10.4), in which the region of strong Lyα attenuation extends to higher latitudes (~±40°) on the anti-Jovian hemisphere than on the sub-Jovian side (~±25°). Modeling of these data indicated maximum column densities $\sim1\times10^{16}$ cm^{-2} on the sub-Jovian hemisphere and ~4 times higher on the anti-Jovian. There is overall little, if any, evidence for temporal – as opposed to

longitudinal – variability in the Lyα data, though the low SO_2 column density at 45°S ($\sim 3\times10^{14}$ (i.e., a factor of 25 smaller than the McGrath *et al.* (2000) measurement at T3) may indicate time variations. Note finally that the Lyα images show limb-to-limb atmospheric absorption, and therefore no evidence for a diurnal variation of the SO_2 column densities.

Infrared observations

Ground-based, disk-averaged, mid-infrared observations of Io, performed over 2001–2005 at NASA/IRTF (Infrared Telescope Facility), led to the detection of ~15 lines belonging to the ν_2 band of SO_2 at 519–531 cm^{-1}, achieving the first infrared detection of SO_2 in Io's atmosphere since the *Voyager* discovery (Spencer *et al.*, 2005). With possible marginal exceptions, lines were always observed in absorption. Dramatic variations in line depth as a function of orbital longitude were observed, with the strongest feature at 530.412 cm^{-1} varying from 7% absorption at L = 180 to 1% at L = 315, at an observed resolution of 57,000. Unlike in the millimeter observations, thermal emission in the mid-infrared occurs in a strongly non-LTE regime, with important radiative exchanges with the surface and deep space. This complicates the analysis considerably, since the associated source function, as characterized by the vibrational temperature as a function of altitude, depends on the combination of atmospheric kinetic temperature (unknown but assumed to be horizontally and vertically constant), atmospheric density, and surface temperature distribution. As a consequence, the line depths do not uniquely determine the atmospheric conditions. Nonetheless, the maximum line depths indicate that the mean gas temperature is surprisingly low (below ~150 K), and the most plausible interpretation of the data is that the equatorial column density varies from $\sim 1.5\times10^{17}\,cm^{-2}$ at L = 180 to $\sim 1.5\times10^{16}\,cm^{-2}$ near L = 300, generally consistent with ultraviolet spectroscopy and imaging. Comparison of data taken in 2001, 2002, 2004, and 2005 indicate that, with the possible exception of longitudes near 180 between 2001 and 2002, the SO_2 column densities are very stable with time, and in particular did not decrease between 2001 and 2005. Since this period corresponded to a recession of Io from the Sun, presumably accompanied by a cooling of its surface frosts, the constancy of the SO_2 columns possibly argues for a dominantly volcanic support of the atmosphere.

10.2.2 Minor molecular species

Beyond SO_2, a number of other molecular compounds have been successfully searched for in Io's atmosphere. A special effort was made on SO, which was predicted to be a significant species by all photochemical and thermo-chemical models (e.g., Kumar, 1982, 1985; Wong and Johnson, 1996; Summers and Strobel, 1996; Zolotov and Fegley, 1998a). The first detection of SO was achieved from millimeter observations (Lellouch *et al.*, 1996), and four separate SO lines have now been detected, with a contrast typically half that of the strong SO_2 lines. In the framework of hydrostatic models, the observations cannot distinguish between a

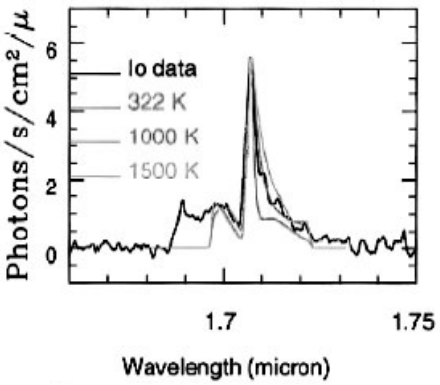

Figure 10.5. The detection of infrared emission from SO in eclipse. The band structure indicates a rotational temperature of ~1,000 K (from De Pater *et al.*, 2002). (See also color section.)

hemispheric SO atmosphere – in this situation, a barely collisionally thick SO atmosphere with a $(2–6)\times10^{14}\,cm^{-2}$ column density is indicated – and an SO component co-located with SO_2 on a restricted fraction of Io's surface with a 4–10% SO/SO_2 mixing ratio. In the case of volcanic models, the SO/SO_2 mixing ratio within the erupting plumes is also in the range 3–10%.

In the ultraviolet, the disk-resolved observations of McGrath *et al.* (2000) are consistent with the presence of SO at a relative mixing ratio of about 10% of SO_2, consistent with the millimeter-wave detection (and with possible spatial variations), although the unambiguous identification of SO bands in the ultraviolet albedo is very difficult because the SO cross sections are very similar to SO_2.

A third observation of SO was achieved from infrared spectroscopy of Io during eclipse with Keck II, leading to the detection of the forbidden electronic $a^1\Delta \longrightarrow X^3\Sigma^-$ transition of SO at 1.71 μm (De Pater *et al.* 2002, their fig. 5). The detection was later confirmed by Goguen and Blaney (2001). These emissions are thought to originate from volcanic vents, Loki and Janus/Kanehekili for the two observations, respectively. The Keck II observations indicate an emission rate of $\sim2\times10^{27}$ photons per second. De Pater *et al.* (2002) discussed many possible mechanisms for this emission and concluded that it was caused by direct ejection of SO molecules in the excited $a^1\Delta$ state from the vent at a ~1,500 K quenching temperature. Other processes such as solar or electron excitation of SO, electron impact dissociation of SO_2, or ionospheric recombination of SO_2^+, all of which can produce excited SO, seem to fail by at least 1–2 orders of magnitude. The shape of the band indicates a ~1,000 K rotational temperature. Because rotational levels are easily thermalized, this temperature may represent the actual kinetic temperature of the emitting gas as it is vented.

From imaging and spectroscopy of the Pele plume on Io's limb and against Jupiter, Spencer *et al.* (2000) discovered molecular S_2 through 15–20 bands belonging to the $B^3\Sigma_u^- – X^3\Sigma_g^-$ system at 2,500–3,000 Å, in addition to a detection of SO_2 gas at shorter wavelengths. Their tangential SO_2 column density of $\sim7\times10^{16}\,cm^{-2}$, when converted to a vertical column (~ factor of 2 decrease) is in remarkably good agreement with the $\sim3.25\times10^{16}\,cm^{-2}$ column density found by

McGrath *et al.* (2000). The S_2 to SO_2 mixing ratio in the plume is 0.08–0.3. This spectacular discovery, though not unexpected (since sulfur vapor has been proposed for a long time to be the driver of the Pele plume (McEwen and Soderblom, 1983)), appears extremely valuable to infer chemical conditions in the volcanic source region. Comparing with the thermo-chemical equilibrium calculations of Zolotov and Fegley (1999), the observed S_2/SO_2 ratio implies equilibration with silicate magmas near the quartz–magnetite–fayalite buffer for a 1,400 K temperature or near the wurstite–magnetite buffer at 1,800 K. The S_2 detection may be the key in explaining the red deposits near Pele and other active regions, as S_2 is unstable against photolysis, producing reddish S_3 and S_4 molecules by polymerization. Additional observations of plume transits on the Io limb in 2003–2004 (Jessup *et al.*, 2004b) indicated a temporal variability of the S_2 abundance in the Pele plume, including periods where the gas was only marginally detected, a positive detection of S_2 near Io's equator, and its prominent absence in Prometheus, in agreement with the McEwen and Soderblom (1983) classification.

The most recently detected molecular species in Io's atmosphere is gaseous NaCl, achieved in January 2002 (Lellouch *et al.*, 2003) from rotational line emission, via the detection of emission lines at 234.252 and 143.237 GHz. The disk-averaged column density is in the range $(0.8–20)\times10^{13}$ cm^{-2}, with a preferred value of 4×10^{13} cm^{-2} (i.e., about 0.4% of SO_2). Because of its vanishingly low vapor pressure at Io's temperature, the most likely source of NaCl is direct volcanic output, though sputtering of salt-bearing atmospheric aerosols is not excluded. Volcanic plume models indicate total volcanic emission rates of $(2–8)\times10^{28}$ NaCl molecules per second (i.e., typically 0.3–1.3% of the SO_2 rates). Though the observational data cannot directly prove it, NaCl is probably restricted to less extended regions than SO_2 because of increased photolytic and condensation losses. The detection of NaCl is important because it provides a source for the sodium clouds surrounding Io (see below).

Eight other compounds (CO, H_2S, OCS, S_2O, ClO, CS, NaOH, KCl) were searched for unsuccessfully at millimeter wavelengths. The most significant of the associated upper limits is probably a stringent 10^{-10} bar upper limit on a global H_2S atmosphere (Lellouch *et al.*, 1992). An upper limit of 2×10^{14} cm^{-2} for the abundance of CS_2 was set by McGrath *et al.* (2000) from ultraviolet observations.

10.2.3 Atomic species

Five atomic species have been identified in Io's atmosphere or more extended neutral clouds. Observations of the strong resonance transitions of Na (and to a lesser extent of K) provide the basis of most of our knowledge of Io's neutral cloud dynamics and interaction with the plasma torus. Since these observations principally probe escaped sodium rather than the bound atmosphere near the surface, they do not, however, provide direct information on the sources of alkalis, the most likely of which are: (i) plasma sputtering of the surface where sodium may occur in different forms (see discussion in McGrath *et al.*, 2004); and (ii) direct volcanic supply. Mutual eclipses between Io and other Galilean satellites (Schneider *et al.*, 1991; Burger *et al.*, 2001) have allowed observations of Io's corona down to $\sim1.4\,R_{Io}$ and radial profiles of the

Na column density to be derived. The Na corona appears denser on the sub-Jupiter compared with the anti-Jupiter side, with an average radial profile $\mathcal{N}_{Na}(b) = 2.2 \times 10^{12}\, b^{-2.34}$ for $b > 1.5\,R_{Io}$ (Burger *et al.*, 2001). Extrapolation of the profile down to the surface agrees reasonably well with an estimate ($\mathcal{N} \sim 4 \times 10^{12}\,cm^{-2}$) based on the detection of Na emission in Jupiter eclipse, probably excited by torus electrons (Bouchez *et al.*, 2000). Based on *Galileo* images, Burger *et al.* (1999) identified a fast sodium jet with a source region much smaller than Io, perhaps confined to volcanically active regions. Potassium measurements have been made down to $\sim 10\,R_{Io}$, giving column densities at that distance of $\sim (0.4\text{–}1.5) \times 10^{9}\,cm^{-2}$, and the Na/K ratio was derived and shown to be constant from 10–20 R_{Io} at a value of 10 ± 3 (Brown, 2001).

O, S, Na, K, and Cl emissions, produced by collisional excitation of neutrals in the atmosphere and corona by torus electrons, have also been detected. Though richly documented (e.g., Oliversen *et al.*, 2001), these atomic emissions are not straightforward to interpret in terms of atmospheric properties for a variety of reasons, particularly because the observed brightnesses are diagnostic of both the neutral densities and plasma conditions, and because the predominant excitation mechanism (direct excitation of atomic species or molecular dissociative excitation) is uncertain. Assumptions and simplifications have to be made, and forward modeling, as opposed to inversion, is generally the most successful approach. Nonetheless, these observations have provided valuable constraints on the nature of the atmosphere and its composition. Regarding sodium, an exciting recent development (Mendillo *et al.*, 2004; Wilson *et al.*, 2002) exploits observations of the extended Na nebula to show that the shape and brightness of this cloud is determined by the mechanism and rate of Na escape, and is correlated with the infrared activity level of Io (known to be indicative of volcanic activity, particularly lava flows). Wilson *et al.* (2002) argue that this provides evidence that escape of material from Io's atmosphere occurs predominantly from collisionally thick regions rather than from the exosphere.

Atomic sulfur and oxygen have been observed extensively both in the plasma torus since 1981 (Brown, 1981; Durrance *et al.*, 1983; see Chapter 11), and near Io since 1986 (Ballester *et al.*, 1987). A common, albeit rough, approach to interpretation of the near-Io observations has been to assume electron excitation of the atomic species, and constant electron density (n_e) and temperature (T_e) along the line-of-sight. From disk-average *IUE* spectra, and assuming canonical torus values of $T_e = 5\,eV$ and $n_e = 2{,}000\,cm^{-3}$, Ballester (1989) inferred minimum oxygen column densities of $\mathcal{N}_O > (4\text{–}7) \times 10^{13}\,cm^{-2}$. Limits on the sulfur column density of $2.2 \times 10^{12} cm^{-2} < \mathcal{N}_S < 7 \times 10^{15}\,cm^{-2}$ were also derived. In the spatially resolved spectroscopic observations of McGrath *et al.* (2000) described earlier, emission from the SI] 1900,1914 Å doublet was detected over Pele and T3, and the sulfur column density above Pele was estimated to be $\mathcal{N}_S \sim 1 \times 10^{14}\,cm^{-2}$. From HST/STIS data resolving the 1,479 Å multiplet, Feaga *et al.* (2002) obtained an improved determination of the S tangential column density, independent of electron density and temperature, and found it to be $3.6 \times 10^{12} cm^{-2} < \mathcal{N}_S < 1.7 \times 10^{14}\,cm^{-2}$ (as revised by McGrath *et al.* (2004); the vertical column density is a factor of ~7 lower). Spatial profiles of SI] and OI] emissions with a

resolution of $\sim$0.05 R_{Io} out to distances of $\sim$10 R_{Io} were determined by Wolven *et al.* (2001). Though these intensities vary considerably with System III longitude, probably in response to varying local electron density, the ratio of the sulfur to oxygen emission is fairly constant in time and with distance from Io.

Monochromatic (HST) and eclipse broadband (*Galileo*/SSI and *Cassini*/ISS) images have revealed a complex morphology of the atomic emissions, characterized by five notable features: equatorial "spots", volcanic plume glows, a limb-brightened ring of emission just off the disk, diffuse atmospheric emissions (also referred to as "glow"), and emission from Io's extended corona. The spots (often referred to as the "Io aurora") are brightest along the equator and near the sub-Jupiter and anti-Jupiter points. They are observed to rock about the equator in concert with the changing orientation of the background Jovian magnetic field, constraining the electrodynamic interaction between plasma and satellite (Saur *et al.*, 2000; Saur and Strobel, 2004; see below). The limb-brightened rings of sulfur and oxygen emission imply that both species form global components of the atmosphere.

In the *Galileo*/SSI images of Io taken during 14 eclipses over 1996–1998 (Geissler *et al.*, 1999; see Chapter 8) equatorial spots are seen in all filters, but most prominently in the violet, while the diffuse glow is detected in the green filter. The identity of the emitters cannot be unambiguously determined, however, several candidates were proposed by Geissler *et al.*, including [OI] 6,300 and 6,363 Å, Hα 6,563 Å, and SII 6,720, 6,730 Å in the red filter; [OI] 5,577 Å and NaI 5,889, 5,896 Å in the green filter; and molecular emission from SO_2 in the violet filter. The likely role of oxygen in the SSI red filter, of sodium in the green, and of SO_2 (or SO) continuum emission in the violet was confirmed by the high spectral resolution observations of Bouchez *et al.* (2000), who detected auroral emission from [OI] 6,300, 6,363, 5,577 Å and Na 5,889, 5,896 Å, but no emission in the SSI violet region. This is also consistent with the detection of the equatorial glows in near-ultraviolet *Cassini*/ISS images (Geissler *et al.*, 2004), whose narrow filters compared with *Galileo* reduced the ambiguity in emitter identification, and which, in addition, confirmed a much larger vertical extent of the O emissions (up to 900 km) compared with the SO_2, confined near the surface. Additional emissions, in the 730–800-nm and 390–500-nm ranges, were attributed to atomic potassium and molecular disulfur (S_2), respectively.

The evolution of the atomic emissions shortly before, after, and during eclipses potentially provides a powerful diagnostic of the sources, nature, and stability of Io's atmosphere. Disk-averaged observations of Io passing into Jupiter shadow (Clarke *et al.*, 1994) showed that the far-ultraviolet sulfur and oxygen emissions decreased by a factor of $\sim$ 3 within 20 min of Io entering eclipse. In contrast, Geissler *et al.* (1999) report an increase of the plume glows in a comparison of images obtained 11 min after the start of an eclipse and 41 min later. A dramatic, factor-of-2, increase in the S and O emission brightnesses was observed from HST/STIS in February 2000 by Wolven *et al.* (2001) when Io emerged into sunlight after eclipse, and interpreted as the recovery of a sublimation-supported SO_2 atmosphere. Retherford (2002) quantified these changes for the spots, the limb glow, and the extended corona, and estimated that the collapse timescales for the molecular atmosphere, atomic atmosphere, and corona after ingress are $\sim$5 min, $\leq$30 min (conservatively), and $\sim$280 min (i.e., longer than the

duration of an eclipse) respectively, consistent with the STIS eclipse observations. Geissler *et al.* (2004) showed evidence for a longer timescale for ingress dimming compared with egress brightening, from which they concluded that partial atmospheric collapse occurs, although the persistence of the equatorial aurora throughout eclipse indicates the existence of a volcanically supported component. Saur and Strobel (2004) developed an electrodynamic interaction model to interpret these results. Though seemingly intuitive, the decrease of the far-ultraviolet emissions upon eclipse entry is in fact not straightforward because far-ultraviolet intensities do not vary monotonically with the SO_2 column densities, as too dense an atmosphere will limit the atmospheric penetration of the electrons. A maximum of the far-ultraviolet emission typically occurs for column densities of $\sim 2\times10^{14}\,\mathrm{cm}^{-2}$. Saur and Strobel (2004) modeled the evolution of radiation in eclipse and found that the non-condensible atmospheric component must remain below $\sim(3–5)\times10^{14}\,\mathrm{cm}^{-2}$; otherwise, the emissions would *brighten* during eclipse. They further show that the existence of equatorial spots thoughout eclipse , as observed by Geissler *et al.* (2004), provides a *lower limit* to this component of $\sim(3–5)\times10^{14}\,\mathrm{cm}^{-2}$. While the coincidence with the upper limit may be somewhat accidental, the combination of the two provides a tight constraint on the volcanic component. Saur and Strobel (2004) conclude that sublimation dominates over volcanic emission by at least an order of magnitude in maintaining the SO_2 atmosphere. Finally, the post-eclipse growth of the Na fluorescent emission was recently studied by Morgan *et al.* (2004). They found that, as time passes after eclipse, sodium, initially confined to large distances from Io, progressively increases in the vicinity of Io. This was interpreted as due either to re-exposure of surface sodium to sputtering due to sublimation of SO_2 condensed during eclipse, or to a temperature dependence of the sputtering process.

The detections of Cl ions in the plasma torus (Kueppers and Schneider, 2000; Feldman *et al.*, 2001) and of NaCl in the atmosphere have motivated searches for atomic chlorine in Io's bound atmosphere. Using spatially resolved HST/STIS spectral images, Retherford (2002) identified Cl emission at two wavelengths in the equatorial spots, at a relative abundance ratio of Cl/O $\sim$0.07–1%. Feaga and McGrath (2004) used archival disk-averaged HST/GHRS data acquired over 1994–1996 to detect two Cl multiplets, and inferred self-consistent relative ratios of chlorine, sulfur and oxygen, namely $\mathrm{Cl/O} = 0.017\pm0.008$, $\mathrm{Cl/S} = 0.1\pm0.05$, and $\mathrm{S/O} = 0.18\pm0.08$. They also find evidence for large temporal variations of the chlorine emission, which supports a volcanic origin for NaCl.

10.2.4 Ionosphere

As mentioned above, the interpretation of the initial detection of Io's ionosphere by *Pioneer 10* met only limited success. Since then, results from a series of six *Galileo* radio occultation measurements in 1997 (Hinson *et al.*, 1998) have greatly clarified the situation. A first important point is that the viewing geometry in radio-occultations always puts both the entrance and exit measurements within a few degress of the terminator. As a result, both measurements primarily sample the sunlit atmosphere, as even when they occur above the night-time terminator, only the lower few kilometers

of the atmosphere are in darkness. Thus, the *Galileo* occultations in fact sampled a wide variety of geometries of the sunlit hemisphere relative to the plasma ram direction, yielding information on the distribution and motion of the plasma near Io. The plasma distribution shows two components. The first is present within a few hundred kilometers of Io's surface throughout the upstream and downstream hemispheres and resembles a bound ionosphere. Vertical electron density profiles for this component were derived at 10 locations near Io's terminator. The peak density exceeded $5 \times 10^4 \text{cm}^{-3}$ at 9 out of 10 locations, with a maximum of $2.8 \times 10^5 \text{ cm}^{-3}$. The peak density varied systematically with Io longitude, with maxima near the centers of the sub- and anti-Jovian hemispheres (i.e., in correspondence with the auroral glows seen in eclipse), and minima near the centers of the downstream and upstream hemispheres. This pattern may be related to the Alfvénic current system induced by Io's motion through the magnetospheric plasma. The vertical extent of the bound ionosphere increases from ~200 km near the center of the upstream hemisphere to ~400 km near the boundary between leading and trailing hemispheres.

The second component is highly asymmetric, consisting of a wake that appears only on the downstream side and extends to distances as large as $10\ R_{Io}$. Plasma near Io's equatorial plane was measured to move from Io in the downstream direction, with velocity increasing from 30 to 57 km s^{-1} from 3 to 7 Io radii. The latter velocity corresponds to corotation, suggesting that bulk plasma motion was being observed. From the entire data set, it appears that the major factor determining the morphology of the ionosphere is the plasma ram direction. The *Galileo* measurements generally confirm the original *Pioneer 10* results, providing strong evidence that the ionosphere is stable. They also demonstrate that the *Pioneer 10* entrance profile was dominated by wake electrons, which in retrospect explains the inability of the 1-D photochemical models to match this profile.

10.3 RECENT MODELING DEVELOPMENTS

As outlined in the introduction, studies of Io's atmosphere were largely dominated by modeling in the 1980–1990 decade. Because of the complexity of the Io surface/atmosphere/ionosphere/plasma torus system, most modeling work has focused on single aspects of the problem, such as the atmospheric vertical structure, its photochemistry, its horizontal distribution, or its interaction with the plasma torus. The wealth of new data acquired in the last 15 years prompted a reassessment of most of these "single aspect" models. Additionally, they justified the development of more elaborate, multi-dimensional, "unified" models. We now review these recent modeling efforts.

10.3.1 Modern buffered models

The early ultraviolet observations of Ballester *et al.* (1990, 1994) motivated Kerton *et al.* (1996) to reconsider the sublimation equilibrium models of Fanale *et al.* (1982) which gave SO_2 abundances larger than the observed SO_2 abundances or upper limits.

The Kerton *et al*. models rectified some of the oversimplifications in the treatment of surface radiative equilibrium by including a variety of physical processes previously ignored: latent heat of SO_2 frost sublimation, thermal conduction, diurnal rotation, internal heat flow, and deposition of solar energy below the surface (''solid-state greenhouse effect''). Results of these improved models, expected to give a more accurate representation of Io's surface temperatures and hence equilibrium pressures, differ from the early picture in several ways. First, the surface temperature and pressure gradients toward the periphery of Io's disk are much more gradual than in the standard equilibrium models. Second, the surface temperature distribution is no longer symmetric about the subsolar point, since accounting for heat conduction shifts the maximum temperature slightly from the subsolar point toward the dusk terminator. These improvements result in reduced column abundances, more consistent with the Ballester *et al*. (1994) results. Note however that some model parameters, such as the frost albedo, the thermal conductivity, and the efficiency of subsurface greenhouse, are uncertain, so a range of SO_2 distributions remains possible. In the most extreme cases (the high-conductivity C/R/L model, their Figure 6, and the subsurface greenhouse model, their Figure 8), the SO_2 pressure near the poles is many orders of magnitude lower than near the terminators, which is qualitatively consistent with interpretations of the Lyα images (Feldman *et al*., 2000; Strobel and Wolven, 2001; Feaga *et al*., 2004).

10.3.2 Volcanic gas composition models

The continuous improvement of our knowledge of the atmospheric composition, and in particular, the gaseous plume composition information now available for Pele, prompted the development of thermo-chemical models of Ionian volcanic gas chemistry (Zolotov and Fegley, 1998a, 1998b, 1999, 2000; Fegley and Zolotov, 2000; Schaefer and Fegley, 2005). By analogy with volcanic eruptions on Earth where gases erupted at temperatures ≥ 900 K are hot enough for thermo-chemical equilibrium, the basic idea of these models is that eruption temperatures on Io – measured to range up to 1,700 K – are high enough that volcanic gases chemically equilibrate in the vent vicinity during eruptions. In contrast, volcanic gases are assumed to be quenched in the cooling expanding plumes. Inputs to the models are the eruption temperature, total pressure, and bulk elemental composition of the volcanic gases. This kind of model allows one to calculate an atmospheric composition as a function of the eruption conditions, or, vice versa, to use a measured (global or local) composition to infer physical and chemical conditions in the erupting magma (in particular the oxidation state) as well as information on the vent pressure. The major results of these models are summarized below.

Zolotov and Fegley (1998a) show that SO is a natural product of thermodynamical equilibrium in erupted materials, and that the observed SO/SO_2 mixing ratio (3–10%) can be fit for suitable combinations of gas pressure, temperature, and $O/S < 2$ ratio at the vent. Zolotov and Fegley (1998b) further predict S_2O to be an important volcanic species, reaching 1–6% of SO_2 in the vicinity of SO_2–S_2 vents erupting from magmas of 1–100 bar total pressure. Regarding sodium and alkalis, NaCl is the

expected dominant Na- and Cl-bearing volcanic gas for high-temperature (>1,400 K) eruptions (Fegley and Zolotov, 2000). Its abundance is expected to reflect the elemental Cl/S in the erupting magmas and is nominally predicted to be 4%. The lower abundance measured by Lellouch *et al.* (2003), 0.3–1.3% in the "volcanic models", appears in fact more consistent with a chondritic composition (having $Cl/S = 0.01$), a surprising result given that higher Na/S and Cl/S are expected in Io's lithosphere due to igneous differentiation. Alternate explanations for the low apparent $NaCl/SO_2$ ratio are discussed by Lellouch *et al.* (2003). Fegley and Zolotov further predict a suite of Cl- and K-bearing molecular species, including notably KCl, $(NaCl)_2$, SCl_2, and S_2Cl. The list of potential molecules was recently extended to other alkali and halogen species, including Rb, Cs, F, Br, and I compounds (Schaefer and Fegley, 2005). Finally, Zolotov and Fegley (2000) used the observed SO_2–SO–S_2–S Pele plume composition (Spencer *et al.*, 2000; McGrath *et al.*, 2000) to present a detailed chemical model for the plume. Though, given Pele's known variability, it is risky to fold data taken 3 years apart into a single plume model, this approach suggests an $\sim 10^{-5}$-bar pressure in the vicinity of the vent, and implies that the Pele plume gas last equilibrated at magmatic temperature and was not significantly altered in the eruption. The composition of the Pele plume does indicate that Io is differentiated, and that metallic iron and free carbon are not abundant in bulk silicates on Io.

10.3.3 Radiative models

Radiative models are concerned with calculations of the atmospheric vertical (temperature and density) profile from an analysis of the heat budget. Most of these models were developed in 1-D and for the case of a pure SO_2, hydrostatic, atmosphere. Strobel *et al.* (1994) developed the first comprehensive model of Io's vertical thermal structure, extending and improving upon the models by Kumar (1985) and Lellouch *et al.* (1992). They solved the time-dependent, 1-D heat balance equation with heat transport by diffusive and radiative processes. Heating sources include solar heating in the ultraviolet and near-infrared bands of SO_2, as well as plasma and Joule heating. Radiative losses are due to non-LTE cooling by SO_2 rotational and vibrational lines, for which a new and elaborate treatment was developed. Two cases were considered in the Strobel *et al.* models, a high-density atmosphere representative of the (smaller fractional coverage, larger column abundance) regime typified by the early interpretation of the millimeter observations, and a low-density atmosphere intended to represent the (larger fractional coverage, lower column abundance) regime typified by the early disk-averaged ultraviolet observations (Figure 10.6). Their model predicts the existence of a mesopause in Io's atmosphere when the surface pressure exceeds $\sim$10 nbar, as already noted by Lellouch *et al.* (1992). With a lower scale height temperature consistently below 200 K, none of the model atmospheres generated with solar heating only were hot enough to satisfy the hydrostatic interpretation of the millimeter data, nor the bulk atmospheric temperature of 200–400 K derived from the ultraviolet data. Plasma heating, associated with impacting thermal ions from the Io plasma torus as they sweep by Io's exosphere/upper atmosphere (Johnson, 1989), and Joule heating, driven by the penetration of Jupiter's

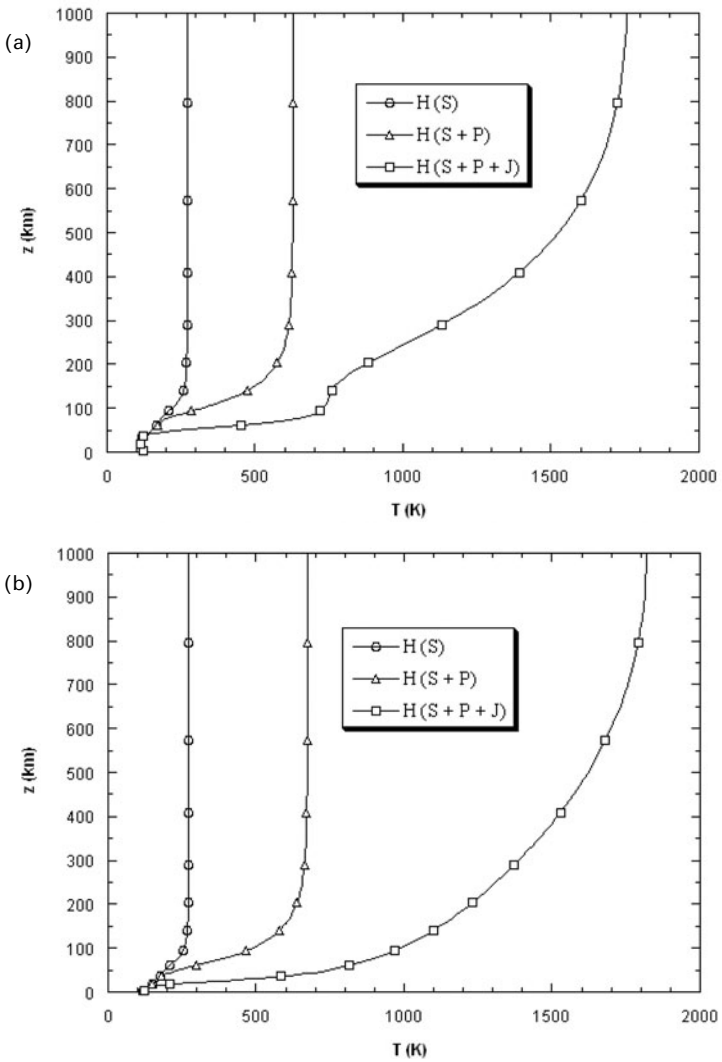

Figure 10.6. Effects of solar (S), solar + plasma (S + P), and solar + plasma + Joule (S + P + J) heating on the vertical thermal structure of Io's atmosphere. (a) Surface pressure = 130 nbar. Note the presence of a mesosphere. (b) Surface pressure = 3.5 nbar (from Strobel *et al*., 1994).

corotational electric field into Io's conducting ionosphere, can raise the atmospheric temperature considerably (up to 1,800 K). However, unless it penetrates significantly below the exobase, plasma heating primarily elevates the exospheric temperature. Joule heating can in principle produce an atmosphere with a bulk temperature greater than 200 K, but only for surface pressures in the range 0.1–1 nbar, so that none of the models appears warm enough to satisfy the hydrostatic interpretation of the early millimeter observations. Strobel *et al.* (1994) also established that radiative time

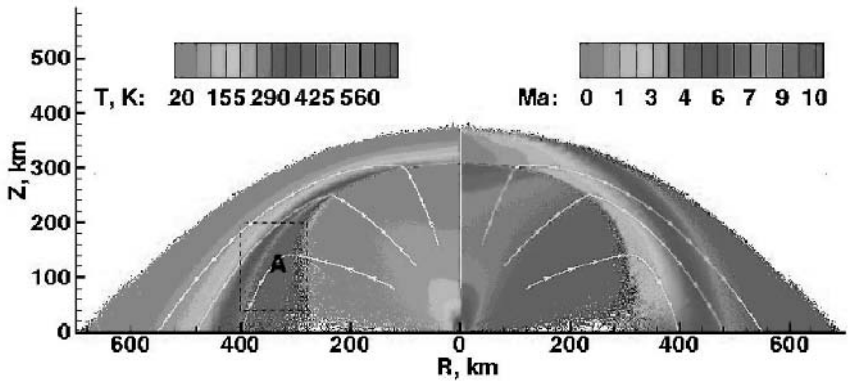

Figure 10.7. Model of an isolated Pele-type volcanic plume. Contours of the temperature and Mach number are shown (from Zhang *et al*., 2003). (See also color section.)

constants are short (~20 min in the mesosphere and ~1 hr in the thermosphere), competitive with dynamical timescales.

Recently, thermal calculations have been extended to plume atmospheres (see extended discussion in Chapter 8). These complex models (Zhang *et al*., 2003) consist of Monte Carlo simulations of gas dynamics and describe phenomena such as plume expansion and re-entry shock, including the effect of radiative cooling. They consider the case of nightside isolated plumes, and the case of dayside plumes erupting in a background atmosphere. Figure 10.7 shows model results for gas temperature and Mach number for the case of an isolated Pele-type plume. Such models show interesting features, such as multiple bounce shock structure around Prometheus-like plumes (not shown in the example of Figure 10.7), or the depletion of frost on the dayside from plume erosion. Venting rates needed to sustain the observed column densities are estimated. In a more recent study, Zhang *et al*. (2004) modeled the entrainment of particulates in the gas flow, and were generally successful at reproducing the plume structures, shadows, brightness distribution, and deposition patterns observed in the *Voyager* and *Galileo* images. Based on the lateral extent of some plumes, and the absence of observable dust clouds (which constrains dust settling times), they inferred constraints on the density of the background sublimation atmosphere, for which they found an equilibrium temperature in the range 110–118 K. In most of the Zhang *et al*. (2003, 2004) models, number densities in the vent vicinity reach 5×10^{11} cm^{-3}, for a column density of $\sim 10^{18}$ cm^{-2} within ~20 km of the vent. Column densities averaged over the plumes are in reasonable agreement with the volcanic atmosphere interpretation of the millimeter and Lyα data (Lellouch, 1996; Strobel and Wolven, 2001).

10.3.4 Photochemical models

Photochemical models of Io's atmosphere, also mostly developed in the context of 1-D hydrostatic atmospheres, aim at predicting an equilibrium atmospheric composi-

tion. Making use of the thermal structure of Strobel *et al.* (1994), Summers and Strobel (1996) focused renewed effort on the photochemical modeling in order to gauge the sensitivity of the chemical structure to vertical transport rates, and to evaluate the possibility that O_2 and/or SO may be significant dayside or nightside constituents. Unlike the earlier photochemical models, they tested both low and high values of the eddy mixing rate. Their results confirmed the prediction (Kumar, 1985) that SO is an important atmospheric constituent. Comparing the SO/SO_2 mixing ratio derived from the millimeter observations with the Summers and Strobel (1996) model, in which SO is assumed to be lost at maximum diffusive rates to the surface and the exobase, indicates an effective vertical eddy diffusion coefficient K in the range 3×10^6 to $3\times10^7\,cm^{-2}\,s^{-1}$. This is much less than estimated by Summers and Strobel from a dimensional analysis of Ingersoll's (1989) model of regional frost patch control, which gives $K\sim10^9\,cm^{-2}\,s^{-1}$. Another way of looking at the problem is to note that, with typical SO_2 column densities of $(1–4)\times10^{33}$ molecules on a hemisphere, and a SO_2 photolytic rate of $\sim8\times10^{-6}\,s^{-1}$, the SO hemispheric production rate is $(0.8–3.2)\times10^{28}\,s^{-1}$, which must be balanced by transport. For a hydrostatic atmosphere, considering vertical eddy, vertical molecular, and horizontal transport, a characteristic transport time of 10^4 s can be assumed. This leads to a hemispheric average of $(4–16)\times10^{14}\,cm^{-2}$ SO molecules, in agreement with observations. In contrast, for photolysis in a plume atmosphere, the flight time is only 500–1,000 s, and the mechanism seems to fail by a factor of 5–10. Thus, if Io's atmosphere is in dynamical equilibrium with volcanic sources rather than hydrostatic, the origin of SO may be thermo-chemical rather than photochemical.

While the Summers and Strobel (1996) calculations included several minor molecular Na species, none of the cases considered could simultaneously produce the large atomic and molecular Na escape rates of Wilson and Schneider (1994) and Smyth and Combi (1988) and provide a good match to the *Pioneer 10* ionospheric profile. Finally, although the production of a tenuous molecular oxygen atmosphere from SO_2 photolysis was confirmed, Summers and Strobel found that the fast reaction between S and O_2 severely limits the O_2 column density to much lower levels (10^{-4} times) than calculated by Kumar and Hunten (1982).

Moses *et al.* (2002a,b) have revisited the 1-D aeronomic models in order to address how active volcanism might affect the standard picture of photochemistry on Io. Although still based on a static atmospheric structure, these models study the photochemistry of an atmosphere compositionally enriched by volcanic emissions, as described for the Pele-type eruptions by the thermo-chemical equilibrium calculations discussed above. The models address the effects of photolysis, chemical kinetics, condensation, and vertical eddy and molecular diffusion on the subsequent evolution of the volcanic gas. The first paper focuses on sulfur and oxygen species. As might be expected, if S_2 is a common volcanic gas, the sulfur species (S, S_2, S_3, S_4, SO, and S_2O) are enhanced relative to the oxygen species (O and O_2), as compared with frost sublimation (i.e., initially SO_2-only) models. Possible variations in the SO/SO_2 ratio, tentatively reported by McGrath *et al.* (2000), may reflect the spatial and temporal variability of volcanic SO. Many of the volcanic species (S_2, S_3, S_4, and S_2O) are short-lived (from minutes to a few hours at the most), due to

condensation or photolytic loss, so these species are expected to be rapidly removed from the atmosphere once volcanic plumes are shut off. Their second paper extends the study to alkali and chlorine species, for which it is predicted that NaCl, Na, Cl, KCl, and K are the dominant species generated from Pele-type eruptions, for a wide range of conditions. Again, these species all have short atmospheric lifetimes, so their presence implies continuous volcanic output. The Moses *et al.* (2002b) study further shows that even if molecular NaCl dominates in the lower atmosphere, atomic Na and Cl are respectively the major Na- and Cl-bearing species at the exobase. The upward flux of NaCl at the top of the atmosphere is only ~0.1% of the upward (volcanic) flux at the bottom; the corresponding atomic Na and Cl flux at the top are ~10–20 times larger. Combined with the NaCl volcanic emission rates measured by Lellouch *et al.* (2003), this indicates escape fluxes of 2×10^{25} to 2×10^{26} Na and Cl atoms per second. This range is consistent with estimates of the supply rate of low-speed sodium in the neutral clouds, and with the production rate of the molecular ions (NaX^+) invoked to explain the high-velocity Na* features. As the Cl/S and Na/S ratio in the torus are comparable (~2%), Lellouch *et al.* (2003) conclude that: (i) NaCl is the common parent of sodium and chlorine in Io's environment, mostly through escape of photolytically produced Na and Cl; and that (ii) unless plume dynamics preferentially enhance the escape of molecular NaCl, the production of fast sodium is not dominated by direct ionization of NaCl, but rather by reactions of atomic Na with other torus molecular ions.

10.3.5 "Unified" models

Although models have yet to capture the full complexity of Io's atmosphere, first steps have now been taken to combine descriptions of the vertical structure, horizontal transport, and photochemistry. In a series of papers (Wong and Johnson, 1995, 1996; Wong and Smyth, 2000; Smyth and Wong, 2004), Wong and co-workers attempted to predict, in the framework of a sublimation driven hydrostatic SO_2 atmosphere axisymmetric about the subsolar point, the 2-D atmospheric structure, including composition, as a function of altitude and SZA. Unlike the plume atmosphere models mentioned above, which use a direct simulation Monte Carlo (DSMC) method, the Wong and co-workers' simulations use a continuum fluid model. The first paper focused on the effect of plasma heating on the sublimation-driven flow of an SO_2 atmosphere. It was found that plasma heating is most important near the exobase, raising the exobase altitude and the fraction of the surface over which the atmosphere is collisionally thick, with implications for the supply to the torus. Joule heating, radiative cooling, vertical transport, and photochemistry, were all included in the model of Wong and Johnson (1996), which was mainly concerned with SZA variations, and in particular the possibility that non-condensible species (O_2 and possibly SO) could accumulate, dominate the atmospheric dynamics, and build up on the nightside. They found, in particular, that the build-up of a nightside atmosphere does not suppress the dayside-to-nightside atmospheric flow but reduces it, and raises the overall atmospheric pressure. Wong and Smyth (2000) extended these calculations to high- and low-density SO_2 atmospheres at both

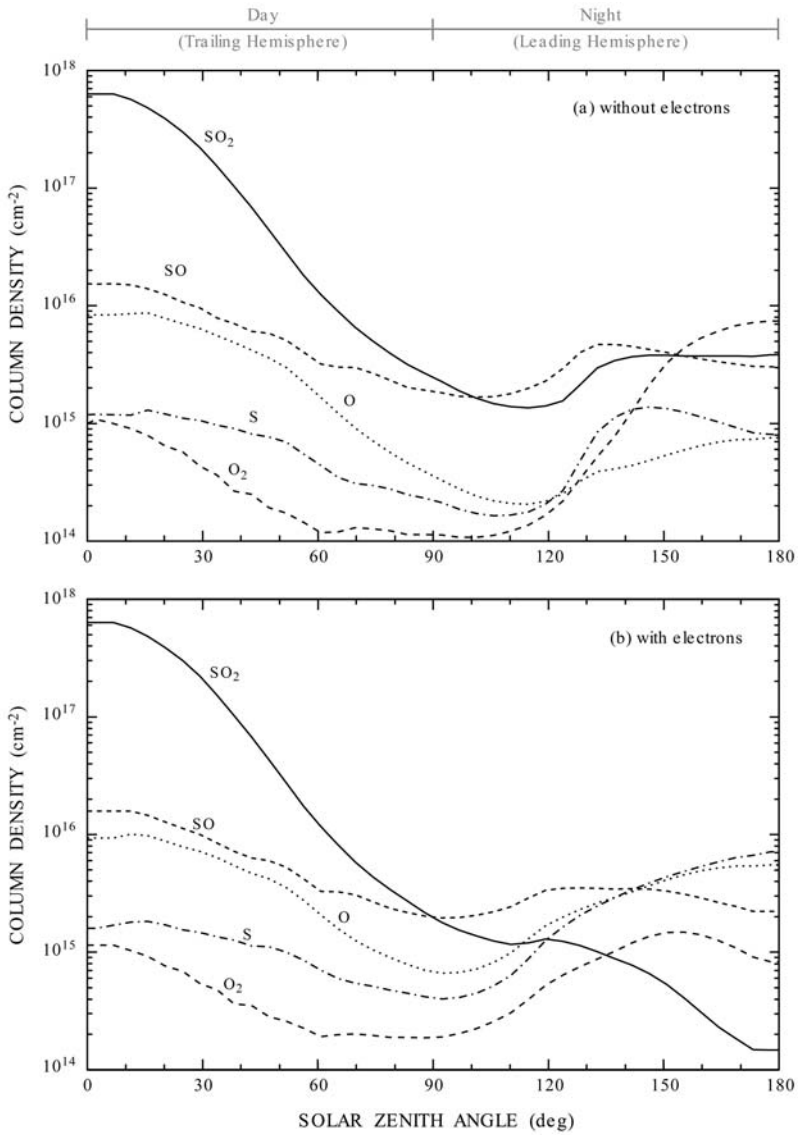

Figure 10.8. Impact of electron chemistry on neutral column densities in Io's atmosphere. Calculations apply to a sublimation atmosphere with a subsolar surface temperature of 120 K at western elongation (from Smyth and Wong, 2004).

western and eastern elongation, using an updated version of the multispecies hydrodynamic code, including an updated treatment of plasma heating, as well as simple Na chemistry. Assuming that O_2 and SO are both non-condensible, they find that gas-phase reactions between them can produce a substantial amount of SO_2 in the nightside atmosphere. These calculations also illustrate a huge variability of the

exobase altitude and temperature as a function of SZA. Different SZA-dependences of the pressure and composition occur at eastern and western elongation, as a consequence of the plasma energy being added to the dayside (western) or nightside (eastern) hemisphere. The calculations achieve a 3–7% SO/SO_2 mixing ratio on the dayside, consistent with observations. They also predict substantial amounts of O_2 and SO on the nightside, typically $10^{15}\,cm^{-2}$ or more. This is at odds with the results of Summers and Strobel (1996) and results from the assumption that SO is non-condensible. Most recently, Smyth and Wong (2004) modeled the impact of electron chemistry on the atmospheric composition and structure. Being confined to an interaction layer at column densities of several $10^{15}\,cm^{-2}$, electron chemistry is important primarily only on the nightside. There, compared with the model of Wong and Smyth (2000), SO_2 is drastically reduced, SO and O_2 are significantly reduced, and S and O are dramatically enhanced to become the dominant species (Figure 10.8).

10.4 SYNTHESIS AND PROSPECTS

10.4.1 The emerging picture

Data obtained since 1990 reach a number of reassuringly consistent conclusions, the most prominent of which being that Io's SO_2 atmosphere is tenuous but well collisionally thick, permanently detectable on both its leading and trailing dayside hemispheres, and relatively stable, with only limited variability observed to date. This readily excludes the purely subsurface cold trap and purely sputtered models. Furthermore, the ensemble of data gives direct evidence for a generally widespread atmosphere, but with significant horizontal variations in pressure. These variations consist of: (i) modest (at the resolution of the measurements (i.e., $\sim$200 km at best)) local density enhancements over active plumes at low- to mid-latitudes; (ii) longitudinal variations of the SO_2 column density in the equatorial region, with a maximum on the anti-Jupiter hemisphere, perhaps by a factor as much as 10; and (iii) a general decrease of the gas pressure with increasing latitude, rather smooth in tropical regions, but probably sharp at latitudes above $\pm 45^\circ$. These features are consistent with most of the ultraviolet and infrared measurements, which converge to indicate mean column densities of $\sim(1\text{–}5)\times 10^{16}$, covering typically 50–70% of Io's dayside atmosphere, mostly but not exclusively at low latitudes.

Although the distribution of Io's atmosphere is too complex to be accurately characterized by a single phrase such as "patchy" or "extended", this emerging picture generally favors the (larger surface coverage, smaller column abundance) regime as opposed to the (smaller surface coverage, higher column abundance) regime. This contradicts the initial interpretation of the millimeter-wave observations, which depicted Io's atmosphere as confined to a very small ($<$10%) fraction of the surface. Better agreement is achieved with the "volcanic model" interpretation of these data, in which the extremely patchy character of the atmosphere can be relaxed. This latter interpretation is thus preferable, although it requires the difficult-to-assess scenario in which the atmosphere results from direct output from tens to hundreds of

volcanic centers. Taking published numbers at face value, a severe discrepancy remains with the *Galileo*/ultraviolet spectrometer (UVS) data which invoked very high column densities. Reconciliation may be possible if the broadband structure seen in the UVS data is due to surface materials rather than SO_2 gas, and/or if very dense patches are smaller than the ~200-km resolution of the Lyα images (see McGrath *et al.*, 2004). Except for the initial *Voyager*/IRIS measurement, and for which the SO_2 abundance has been revised downwards, there is in fact little compelling observational evidence for very large localized enhancements. This, however, may be the result of insufficient spatial resolution, as both the "averaging length" estimate of Ingersoll (1989) and the detailed calculations of Zhang *et al.* (2003) suggest that an order-of-magnitude decrease of the column density occurs within a few tens of kilometers of plume centers.

10.4.2 The volcanic vs. sublimation nature of Io's atmosphere

Trying to settle the "essential" question that arose after the initial discovery of SO_2 in Io's atmosphere remains risky, and Io's atmosphere seems to express a dual nature. We first stress that while active volcanism has long been recognized to be the ultimate source of Io's atmosphere (e.g., Ingersoll, 1989), the question of whether its immediate source is sublimation or volcanic venting is significant, in terms of vertical structure, thermal structure, lifetime, response to insolation variations, and composition, as amply illustrated by the recent models.

The bulk features of Io's atmosphere, as summarized above, are in fact consistent both with sublimation equilibrium and with a volcanic maintenance of the atmosphere. A typical column density of 3×10^{16} cm^{-2} (i.e., a mean pressure of 0.6 nbar), is consistent with a sublimation temperature of 112 K or, equivalently (rescaling from Ingersoll, 1989) a total volcanic source of ~30 ton s^{-1}. As pointed out by Spencer *et al.* (2005), the longitudinal distribution of SO_2, peaked on the anti-Jovian hemisphere, is consistent with the *Galileo*-derived maps of the SO_2 frost distribution (Douté *et al.*, 2001), which indicate that SO_2 frost is nearly ubiquitous on Io, but most abundant on the anti-Jovian hemisphere. However, the same is true for active volcanic plumes (Lopes-Gautier *et al.*, 1999), and in general regions of high frost content correlate well with plume longitudes. Unlike most active plumes, confined to tropical regions, SO_2 frost is present up to high latitudes. However, the lack of SO_2 gas poleward of ~45° does not argue for volcanic support, as it might just result from the surface temperature being too cold there.

Several observational results favor a predominantly sublimation-driven atmosphere. These include the relatively modest increase of the SO_2 pressure over active plumes (e.g., 40% only at Prometheus in the Jessup *et al.*, 2004a observations) and the fact that SO_2 gas has been detected at places where no active plume has even been observed (e.g., T3 in McGrath *et al.*, 2000). This may indicate an atmosphere globally sustained by sublimation, with only local enhancements due to volcanic output. The evolution of the far-ultraviolet/visible atomic features and the Na fluorescent emission during eclipse is generally consistent with sublimation/condensation processes. The interpretation by Saur and Strobel (2004) of this behavior assigns a minor role

($\leq$10%) to volcanic emissions in the direct maintenance of the SO_2 atmosphere as a whole.

Conversely, numerous observations favor the volcanic atmosphere concept. This includes: (i) the detection of SO_2 in the Pele plume at the terminator (i.e., in a place where the surface temperature is too cold for important sublimation to take place); (ii) the presence of species that have a negligible (NaCl, S_2) or uncertain (SO) vapor pressure; and (iii) the interpretation of the SO infrared observations in terms of hot excited SO directly emitted by Loki. These three results demonstrate that active plumes can directly inject measurable amounts of gases, although they do not explicitly address the question of the *spatial* extent of plume atmospheres and of the atmospheric control away from the visible plumes. To these relatively direct proofs, must be added a few circumstantial evidences. First, the fact that the "volcanic atmosphere" interpretation of the millimeter observations is to be preferred. In this respect, it must be noted that such "plume-like" models have not been applied to the analysis of other data. A second aspect is the apparent lack of diurnal variation in the Lyα images. This is a natural consequence of the volcanic model, although it can conceivably be accomodated by the sublimation model if the frost has a high thermal inertia. In the same spirit, the general lack of correlation between the infrared-derived column densities and heliocentric distance, except perhaps on the anti-Jupiter hemisphere, also tends to favor a direct volcanic support of the atmosphere. Albeit limited and insufficiently documented, the existence of temporal variability in the millimeter and some ultraviolet data sets may also be viewed in support of a volcanic atmosphere, since, with typical sublimating rates of 1 mm yr^{-1} and an SO_2 ice layer at least several centimeters thick (Schmitt *et al.*, 1994), a sublimation atmosphere is expected to be stable against short-term fluctuations. The correlation between the appearance and brightness of the extended sodium nebula with the IR activity level also points to a volcanic control of the atmosphere, although a mechanism by which lava flow would affect the atmosphere remains to be devised (Mendillo *et al.*, 2004). In addition to observations, the success of Zhang *et al.* (2003, 2004) in reproducing the mean gas density over the plumes as well as the general plume appearance, gives strong credit to the volcanic atmosphere concept.

10.4.3 Remaining uncertainties and future measurements

Future progress in our knowledge of Io's atmosphere will require further observations, some of which can be already identified. Local time vs. geographical effects must be disentangled in longitudinal variations, possibly by tracking a given region when it rotates from dawn to dusk. Abundance profiles must be determined systematically as a function of distance from volcanic centers, and individual volcanoes must be resolved.

The least well-constrained parameter in Io's atmosphere is the characteristic gas temperature T_{atm}. The Keck II observation of SO indicates that at least a fraction of the volcanic gas is hot (1,000 K) – implying that the thermodynamics of eruptive plumes are more complex than a mere adiabatic expansion. In the millimeter, the

hydrostatic interpretation of data from successive years has given contradictory results for T_{atm} (from 600–180 K), and the preferred volcanic interpretation does not constrain the gas temperature. In the ultraviolet, while many authors have simply assumed values for T_{atm}, the temperatures inferred by Ballester *et al.* (1994), McGrath *et al.* (2000), Spencer *et al.* (2000), and Jessup *et al.* (2004a, 2005) range from 110–500 K, with a general preference for 200–300 K. Though this problem is formidably difficult, especially for a volcanic atmosphere which is expected to exhibit huge lateral temperature variations, the determination of the characteristic temperature of the atmosphere and its variation with height should now be a priority. Local wind measurements would be of extremely high value in providing clues on local and global atmospheric dynamics. Current millimeter-data provide disk-averaged wind measurements, but their interpretation is uncertain (see McGrath *et al.*, 2004). Finally, observing the nightside molecular atmosphere would also provide very strong constraints on the atmospheric nature. Some of the above measurements can already be (or will soon be) performed from Earth or Earth-orbit, but several will require the operation of an Io orbiter.

From the theoretical/modeling point of view, efforts to link the different aspects addressed by current models should be undertaken. For example, while the ''unified'' models of Wong and co-workers address the coupling between vertical structure, planetary scale horizontal transport, and photochemistry, they do not include any description of volcanic plumes, and the validity of their continuum fluid model is uncertain in low-pressure regions. Conversely, while the Zhang *et al.* (2003, 2004) models may provide the most realistic description of the local structure of plume atmospheres, they do not provide a description of Io's atmosphere as a whole, and additionally do not include any chemistry. Thermo-chemistry in volcanic gases is best depicted in the models by Zolotov and Fegley, but these models merely assume equilibrium near the vent source and instantaneous quenching well above the vent, without detailed consideration of interactions between the near-magma gas and the more extended volcanic atmosphere. The task of bringing these various pieces together promises to be formidable, but the success of the different models in their respective applicability fields seems to warrant the effort.

Io's atmosphere, its apparent dual nature, and its interactions with the surface and the plasma environment, are clearly unique in the Solar System. Enormous progress in its knowledge has been achieved since our virtual state of ignorance at the end of the 1980s. Important questions do remain, but at least they seem to be now well posed, and a roadmap to solve them may be drawn.

10.5 REFERENCES

Ballester, G. E. 1989. Ultraviolet observations of the atmosphere of Io and the plasma torus. PhD thesis, Johns Hopkins University, Baltimore, MD.

Ballester, G. E., Moos, H. W., Feldman, P. D., Strobel, D. F., Summers, M. E., Bertaux, J.-L., Skinner, T. E., Festou, M. C., and Lieske, J. H. 1987. Detection of neutral oxygen and sulfur emissions near Io using IUE. *Astrophys. J.*, **319**, L33–L38.

Ballester, G. E., Strobel, D. F., Moos, H. W., and Feldman, P. D. 1990. The atmospheric abundance of SO_2 on Io. *Icarus*, **88**, 1–23.

Ballester, G. E., McGrath, M. A., Strobel, D. F., Zhu, X., Feldman, P. D., and Moos, H. W. 1994. Detection of the SO_2 atmosphere of Io with the Hubble Space Telescope. *Icarus*, **111**, 2–17.

Belton, M. J. S. 1982. An interpretation of the near-ultraviolet absorption spectrum of SO_2. Implications for Venus, Io and laboratory measurements. *Icarus*, **52**, 49–165.

Bouchez, A. H., Brown, M. E., and Schneider, N. M. 2000. Eclipse Spectroscopy of Io's Atmosphere. *Icarus*, **48**, 316–319.

Bridge, H. S., Belcher, J. W., Lazarus, A. J., Sullivan, J. D., Bagenal, F., McNutt, R. L., Jr., Ogilvie, K. W., Scudder, J. D., Sittler, E. D., and Vasyliunas, V. M. 1979. Plasma observations near Jupiter: Initial results from Voyager 1. *Science*, **204**, 972–976.

Broadfoot, A. L., Belton, M. J., Takacs, P. Z., Sandel, B. R., Shemansky, D. E., Holberg, J. B., Ajello, J. M., Moos, H. W., Atreya, S. K., Donahue, T. M. *et al.* 1979. Extreme ultraviolet observations from Voyager 1 encounter with Jupiter. *Science*, **204**, 979–982.

Brown, R. A. 1974). Optical line emission from Io. In: A. Woszczyk and C. Iwaniszewska (eds), *Exploration of the Planetary System*. D. Reidel Publ. Corp., Dordrecht, The Netherlands, pp. 527–531.

Brown, M. E. 2001. Potassium in Europa's atmosphere. *Icarus*, **151**, 190–195.

Brown, R. A. 1981. The Jupiter hot plasma torus: Observed electron temperature and energy flows. *Astrophys. J.*, **244**, 1072–1080.

Burger, M. H., Schneider, N. M., and Wilson, J. K. 1999. Galileo's close-up view of the Io sodium jet. *Geophys. Res. Lett.*, **26**, 3333–3336.

Burger, M. H., Schneider, N. M., de Pater, I., Brown, M. E., Bouchez, A. H., Trafton, L. M., Sheffer, Y., Barker, E. S., and Mallama, A. 2001) Mutual event observations of Io's sodium corona. *Astrophys. J.*, **563**, 1063–1074.

Cheng, A. F. and Johnson, R. E. 1989. Effects of magnetospheric interactions on origin and evolution of atmospheres. In: S. K. Atreya, J. B. Pollack, and M. S. Matthews (eds), *Origin and Evolution of Planetary and Satellites Atmospheres*. University of Arizona Press, Tucson, AZ, pp. 683–722.

Clarke, J. T., Ajello, J., Luhmann, J., Schneider, N., and Kanik, I. 1994. Hubble Space Telescope ultraviolet spectral observations of Io passing into eclipse. *J. Geophys. Res.*, **99**, 8387–8402.

De Pater, I., Roe, H. G., Graham, J. R., Strobel, D. F., and Bernath, P. 2002. Detection of the forbidden SO $a^1\Delta \rightarrow X^3\Sigma^-$ rovibronic transition on Io at 1.7 μm. *Icarus*, **156**, 196–301.

Douté, S., Schmitt, B., Lopes-Gautier, N., Carlson, R., Soderblom, L., Shirley, J., and the Galileo NIMS Team. 2001. Mapping SO_2 frost on Io by the modeling of NIMS hyperspectral images. *Icarus*, **149**, 107–132.

Durrance, S. T., Feldman, P. D., and Weaver, H. A. 1983. Rocket detection of ultraviolet emission from neutral oxygen and sulfur in the Io torus. *Astrophys. J.*, **267**, L125–L129.

Fanale, F. P., Brown, R. H., Cruikshank, D. P., and Clark, R. N. 1979. Significance of absorption features in Io's IR reflectance spectrum. *Nature*, **280**, 760–761.

Fanale, F. P., Banerdt, W., Elson, L., Johnson, T. V., and Zurek, R. 1982. Io's surface: Its phase composition and influence on Io's atmosphere and Jupiter's magnetosphere. In: D. Morrison (ed.), *Satellites of Jupiter*. University of Arizona Press, Tucson, AZ, pp. 756–781.

Feaga, L. M., McGrath, M. A., and Feldman, P. 2002. The abundance of atomic sulfur in the atmosphere of Io. *Astrophys. J.*, **570**, 439–446.

Feaga, L. M., McGrath, M. A., Feldman, P. D., and Strobel, D. F. 2004. Dependence of Io's SO_2 atmospheric column density on surface features. *Bull. Amer. Astron. Soc.*, **36**, 16.06.

Feaga, L. M. and McGrath, M. A. 2004. Detection of atomic chlorine in Io's atmosphere with the Hubble Space Telescope GHRS. *Astrophys. J.*, **610**, 1191–1198.

Fegley, B. and Zolotov, M. Y. 2000. Chemistry of sodium, potassium, and chlorine volcanic gases on Io. *Icarus*, **148**, 193–210.

Feldman, P. D., Strobel, D. F., Moos, H. W., Retherford, K. D., Wolven, B. C., McGrath, M. A., Roesler, F. L., Woodward, R. C., Oliversen, R. J., and Ballester, G. E. 2000. Lyman-α imaging of the SO_2 distribution on Io. *Geophys. Res. Lett.*, **27**, 1787–1790.

Feldman, P. D., Ake, T. B., Berman, A. F., Moos, H. W., Sahnow, D. J., Strobel, D. F., Weaver, H. A., and Young, P. R. 2001. Detection of chlorine ions in the *Far Ultraviolet Spectroscopic Explorer* spectrum of the Io plasma torus. *Astrophys. J.*, **554**, L123–L126.

Geissler, P. E., McEwen, A., Ip, W., Belton, M. J. S., Johnson, T. V., Smyth, W. H., and Ingersoll, A. P. 1999. Galileo imaging of atmospheric emissions from Io. *Science*, **285**, 870–874.

Geissler, P., McEwen, A., Porco, C., Strobel, D., Saur, J., Ajello, J., and West, R. 2004. Cassini observations of Io's visible aurorae. *Icarus*, **172**, 127–140.

Goguen, J. and Blaney, D. L. 2001. Io's 1–2.5μm spectrum in eclipse with SpeX at IRTF. *Bull. Amer. Astron. Soc.*, **33**, 24.02.

Hendrix, A. R., Barth, C. A., and Hord, C. W. 1999. Io's patchy SO_2 atmosphere as measured by the Galileo ultraviolet spectrometer. *J. Geophys. Res.*, **104**, 11817–11826.

Hinson, D. P., Kliore, A. J., Flasar, F. M., Twickern, J. D., Schinder, P. J., and Herrera, R. G. 1998. Galileo radio occultation measurements of Io's ionosphere and plasma wake. *J. Geophys. Res.*, **103**, 29343–29357.

Ingersoll, A. P. 1989. Io meteorology: How atmospheric pressure is controlled locally by volcanos and surface frosts. *Icarus*, **81**, 298–313.

Ingersoll, A. P., Summers, M. E., and Schlipf, S. G. 1985. Supersonic meteorology of Io: Sublimation driven flow of SO_2. *Icarus*, **64**, 375–390.

Jessup, K. L., Spencer, J. R., Ballester, G. E., Howell, R. R., Roesler, F., Vigel, M., and Yelle, R. 2004a. The atmospheric signature of Io's Prometheus plume and anti-Jovian hemisphere: Evidence for a sublimation atmosphere. *Icarus*, **169**, 197–215.

Jessup, K. L., Spencer, J., and Yelle, R. 2004b. Variability and Composition of Io's Pele Plume. *Bull. Amer. Astron. Soc.*, **36**, 09.02.

Jessup, K. L., Ballester, G., Zhu, X., and Combi M. 2005. Io's changing atmosphere: Temporal variability in the SO_2 and SO column densities on Io at eastern and western elongation. *Icarus* (submitted).

Johnson, R. E. 1989. Plasma heating of an SO_2 atmosphere on Io. *GRL.*, **16**, 1117–1120.

Johnson, T. V. and Matson, D. L. 1989. Io's tenuous atmosphere. In: S. K. Atreya, J. B. Pollack, and M. S. Matthews (eds), *Origin and Evolution of Planetary and Satellites Atmospheres*. University of Arizona Press, Tucson, AZ, pp. 661–682.

Johnson, T. V., Matson, D. L., Blaney, D. L., Veeder, G. J., and Davies, A. G. 1995. Stealth plumes on Io. *Geophys. Res. Lett.*, **22**, 3293–3296.

Kerton, C. R., Fanale, F. P., and Salvail, J. R. 1996. The state of SO_2 on Io's surface. *J. Geophys. Res.*, **101**, 7555–7563.

Kieffer, S. W. 1982. Dynamics and thermodynamics of volcanic eruption: Implications for the plumes on Io. In: D. Morrison (ed.), *Satellites of Jupiter*. University of Arizona Press, Tucson, AZ, pp. 647–723.

Kliore, A. J., Cain, D. L., Fjeldbo, G., Siedel, B. L., Sykes, M., and Rasool, S. I. 1974. Preliminary results on the atmospheres of Io and Jupiter from Pioneer 10 S-band occultation experiment. *Science*, **183**, 323–324.

Kliore, A. J., Fjeldbo, G., Siedel, B. L., Sweetnam, D. N., Sesplaukis, T. T., and Woiceshyn, P. M. 1975. Atmosphere of Io from Pioneer 10 occultation measurements. *Icarus*, **24**, 407–419.

Kueppers, M. and Schneider, N. M. 2000. Discovery of chlorine in the Io torus. *Geophys. Res. Lett.*, **27**, 513–516.

Kumar, S. 1980. A model for the atmosphere and ionosphere of Io. *Geophys. Res. Lett.*, **7**, 9–12.

Kumar, S. 1982. Photochemistry of SO_2 in the atmosphere of Io and implications on atmospheric escape. *J. Geophys. Res.*, **87**, 1677–1693.

Kumar, S. 1985. The SO_2 atmosphere and ionosphere of Io: Ion chemistry, atmospheric escape, and models corresponding to the Pioneer 10 radio occultation measurements. *Icarus*, **61**, 101–123.

Kumar, S. and Hunten, D. M. 1982. The atmospheres of Io and other satellites. In: D. Morrison (ed.), *Satellites of Jupiter*. University of Arizona Press, Tucson, AZ, pp. 782–806.

Kupo, I., Mekler, Y., and Eviatar, A. 1976. Detection of ionized sulfur in the Jovian magnetosphere. *Astrophys. J.*, **205**, L51–L53.

Lellouch, E. 1996. Urey prize lecture. Io's atmosphere: Not yet understood. *Icarus*, **124**, 1–21.

Lellouch, E., Belton, M., De Pater, I., Gulkis, S., and Encrenaz, T. 1990. Io's atmosphere from microwave detection of SO_2. *Nature*, **346**, 639–641.

Lellouch, E., Belton, M., de Pater, I., Paubert, G., Gulkis, S., and Encrenaz, T. 1992. The structure, stability, and global distribution of Io's atmosphere. *Icarus*, **98**, 271–295.

Lellouch, E., Strobel, D. F., Belton, M. J. S., Summers, M. E., Paubert G., and Moreno, R. 1996. Detection of sulfur monoxide in Io's atmosphere. *Astrophys. J.*, **459**, L107–L110.

Lellouch, E., Paubert, G., Strobel, D. F., and Belton, M. 2000. Millimeter-wave observations of Io's atmosphere: The IRAM 1999 campaign. *Bull. Amer. Astron. Soc.*, **32**, 3511.

Lellouch, E., Paubert, G., Moses, J. I., Schneider, N. M., and Strobel, D. F. 2003. Volcanically-emitted sodium chloride as a source for Io's neutral clouds and plasma torus. *Nature*, **421**, 45–47.

Lopes, R. M. C., Kamp, L. W., Smythe, W. D., Mouginis-Mark, P., Kargel, J., Radebaugh, J., Turtle, E. P., Perry, J., Williams, D. A., Carlson, R. W., and Douté, S. 2004. Lava lakes on Io: observations of Io's volcanic activity from Galileo NIMS during the 2001 fly-bys. *Icarus*, **169**, 140–174.

Lopes-Gautier, R., McEwen, A. S., Smythe, W. B., Geissler, P. E., Kamp, L., Davies, A. G., Spencer, J. R., Keszthelyi, L., Carlson, R., Leader, F. E., *et al.* 1999. Active volcanism on Io: Global distribution and variations in activity. *Icarus*, **140**, 243–264.

Matson, D. L. and Nash, D. 1983. Io's atmosphere: pressure control by regolith cold trapping and surface venting. *J. Geophys. Res.*, **88**, 4771–4783.

McEwen, A. S. and Soderblom, L. A. 1983. Two classes of volcanic plumes on Io. *Icarus*, **55**, 191–217.

McGrath, M. and Johnson, R. E. 1987. Magnetospheric plasma sputtering of Io's atmosphere. *Icarus*, **69**, 519–531.

McGrath, M. A., Belton, M. J. S., Spencer, J. R., and Sartoretti, P. 2000. Spatially resolved spectroscopy of Io's Pele plume and SO_2 atmosphere. *Icarus*, **146**, 476–493.

McGrath, M. A., Lellouch, E., Strobel, D. F., Feldman, P. D., and Johnson, R. E. 2004. Satellites atmospheres. In: F. Bagenal, T. Dowling, and W. McKinnon (eds), *Jupiter. The Planet, Satellites, and Magnetosphere*. Cambridge University Press, UK, pp. 457–483.

Mendillo, M., Wilson, J., Spencer, J., and Stansberry, J. 2004. Io's volcanic control of Jupiter's extended neutral clouds. *Icarus*, **170**, 430–442.

Morabito, L. A., Synnott, S. P., Kupferman, P. N., and Collins, S. A. 1979. Discovery of currently active extraterrestrial volcanism. *Science*, **204**, 972.

Moreno, M. A., Schubert, G., Baumgardner, J., Kivelson, M. G., and Paige, D. A. 1991) Io's volcanic and sublimation atmospheres. *Icarus*, **93**, 63–81.

Morgan, T. H., Potter, A. E., Corliss, J. B., Killen, R.-M., Scherb, F., and Woodward, R. C. 2004. Post-eclipse growth of Io's sodium emissions. *Bull. Amer. Astron. Soc.*, **36**, 1099.

Moses, J. I., Zolotov, M. Y., and Fegley, B. 2002a. Photochemistry of a volcanically driven atmosphere on Io: Sulfur and oxygen species from a Pele-type eruption. *Icarus*, **156**, 76–106.

Moses, J. I., Zolotov, M. Y., and Fegley, B. 2002b. Alkali and chlorine photochemistry in a volcanically driven atmosphere on Io. *Icarus*, **156**, 107–135.

Oliversen, R. J., Scherb, F., Smyth, W. H., Freed, M. E., Woodward Jr., R. C., Marconi, M. L., Retherford, K. D., Lupie, O. L., and Morgenthaler, J. P. 2001. Sunlit Io Atmospheric [OI] 6300 Å emission and the plasma torus. *J. Geophys. Res.*, **106**, 6183–26194.

Paresce, F., Sartoretti, P., Albrecht, R., Barbieri, C., Blades, J. C., Boksenberg, A., Crane, P., Deharveng, J. M., Disney, M. J., Jakobsen, P., *et al.* 1992. Near-ultraviolet imaging of Jupiter's satellite Io with the Hubble Space Telescope. *Astron. Astrophys.*, **262**, 617–620.

Pearl, J. C, Hanel, R., Kunde, V., Maguire, W., Fox, K., Gupta, S., Ponnamperuma, C. and Raulin, F. 1979. Identification of gaseous SO_2 and new upper limits for other gases on Io. *Nature*, **288**, 757–758.

Retherford, K. D. 2002. Io's aurora: HST/STIS observations. PhD thesis, Johns Hopkins University, Baltimore, MD.

Roesler, F. L., Moos, H. W., Oliversen, R. J., Woodward, R. C., Jr., Retherford, K. D., Scherb, F., McGrath, M. A., Smyth, W. H., Feldman, P. D. and Strobel, D. F. 1999. Far-ultraviolet imaging spectroscopy of Io's atmosphere with HST/STIS. *Science*, **283**, 353–356.

Sartoretti, P., Belton, M. J. S., and McGrath, M. A. 1996. SO_2 distributions on Io. *Icarus*, **122**, 273–287.

Sartoretti, P., McGrath, M. A., and Paresce, F. 1994. Disk-resolved imaging of Io with the Hubble Space Telescope. *Icarus*, **108**, 272–284.

Saur, J. and Strobel, D. F. 2004. Relative contributions of sublimation and volcanoes to Io's atmosphere inferred from its plasma interaction during solar eclipse. *Icarus*, **171**, 411–420.

Saur, J., Neubauer, F. M., Strobel, D. F., and Summers, M. E. 2000. Io's ultraviolet aurora: Remote sensing of Io's Interaction. *Geophys. Res. Lett.*, **27**, 2893–2896.

Schaefer, L. and Fegley, B., Jr. 2005. Alkali and halogen chemistry in volcanic gases on Io. *Icarus*, **173**, 454–468.

Schmitt, B., de Bergh, C., Lellouch, E., Maillard, J.-P., Barbe, A., and Douté, S. 1994. Identification of three absorption bands in the 2-μm spectrum of Io. *Icarus*, **111**, 79–105.

Schneider, N. M., Hunten, D. M., Wells, W. K., Schultz, A. B., and Fink, U. 1991. The structure of Io's corona. *Astrophys. J.*, **368**, 298–315.

Smyth, W. H. and Combi, M. R. 1988. A general model for Io's neutral gas clouds I and II. *Astrophys. J.*, **328**, 397–411.

Smyth, W. H. and Wong, M. C. 2004. Impact of electron chemistry on the structure and chemistry of Io's atmosphere. *Icarus*, **171**, 171–182.

Smythe, W. D., Nelson, R. M., and Nash, D. B. 1979. Spectral evidence for SO_2 frost or absorbate on Io's surface. *Nature*, **280**, 766–767.

Spencer, J. R. and Schneider, N. M. 1996. Io on the eve of the Galileo mission. *Ann. Rev. Astron. Astrophys.*, **24**, 125–190.

Spencer, J. R., Sartoretti, P., Ballester, G. E., McEwen, A. S., Clarke, J. T. and McGrath, M. A. 1997. Pele plume (Io): Observations with the Hubble Space Telescope. *Geophys. Res. Lett.*, **24**, 2471–2474.

Spencer, J. R., Lellouch, E., Richter, M. J., López-Valverde, M.-A., Jessup, K. L., Greathouse, T., and Flaud, J.-M. 2005. Mid-infrared detection of large longitudinal asymmetries in Io's SO_2 atmosphere. *Icarus* (in press).

Spencer, J. R., Jessup, K. L., McGrath, M. A., Ballester, G. E., and Yelle, R. 2000. Discovery of gaseous S_2 in Io's Pele plume. *Science*, **288**, 1208–1210.

Strobel, D. F. and Wolven, B. C. 2001. The atmosphere of Io: abundances and sources of sulfur dioxide and atomic hydrogen. *Astrophys. Space Sci.*, **277**, 271–287.

Strobel, D. F., Zhu, X., and Summers, M. E. 1994. On the vertical structure of Io's atmosphere. *Icarus*, **111**, 18–30.

Summers, M. E. 1985. Theoretical studies of Io's atmosphere. Ph.D. thesis, California Institute of Technology, Pasadena.

Summers, M. E. and Strobel, D. F. 1996. Photochemistry and vertical transport in Io's atmosphere and ionosphere. *Icarus*, **120**, 290–316.

Trafton, L. M. 1975. Detection of a potassium cloud near Io. *Nature*, **258**, 690–692.

Trafton, L. M., Matson, D. L., and Stansberry, J. A. 1995. Surface/atmosphere interaction and volatile transport (Triton, Pluto and Io). Submitted to *Solar System Ices*, eds. B. Schmitt, C. de Bergh, and M. Festou, Kluwer Academic, Dordrecht, The Netherlands.

Trafton, L. M., Caldwell, J. J., Barnet, C., and Cunningham, C. C. 1996. The gaseous sulfur dioxide abundance over Io's leading and trailing hemispheres: HST spectra of Io's C^1B_2–X^1A_1 band of SO_2 near 2,100 Å. *Astrophys. J.*, **456**, 384–392.

Wilson, J. K. and Schneider, N. M. 1994. Io's fast sodium: Implications for molecular and atomic escape. *Icarus*, **111**, 31–44.

Wolven, B. C., Moos, H. W., Retherford, K. D., and Feldman, P. D. 2001. Emission Profiles of neutral oxygen and sulfur in Io's exospheric corona. *J. Geophys. Res.*, **106**, 26155–16182.

Wong, M. C. and Johnson, R. E. 1995. The effect of plasma heating on sublimation-driven flow in Io's atmosphere. *Icarus*, **155**, 109–118.

Wong, M. C. and Johnson, R. E. 1996. A three-dimensional azimuthally symmetric model atmosphere for Io. 1: Photochemistry and the accumulation of a nightside atmosphere. *J. Geophys. Res.*, **101**, 23243–23254.

Wong, M. C. and Smyth, W. H. 2000. Model calculations for Io's atmosphere at eastern and western elongations. *Icarus*, **146**, 60–74.

Wu, R. C. Y., Yang, B. W., Chen, F. Z., Judge, J., Caldwell, J., and Trafton, L. M. 2000. Measurements of high-, room-, and low-temperature photoabsorption cross sections of SO_2 in the 2080- to 2950-A region, with applications to Io. *Icarus*, **145**, 289–296.

Zhang, J., Goldstein, D. B., Varghese, P. L., Gimelshein, N. E., Gimelshein, S. F., and Levin, D. A. 2003. Simulation of gas dynamics and radiation in volcanic plumes of Io. *Icarus*, **163**, 182–187.

Zhang, J., Goldstein, D. B., Varghese, P. L., Trafton, L., Moore, C., and Miki, K. 2004. Numerical modeling of ionian volcanic plumes with entrained particulates. *Icarus*, **172**, 479–502.

Zolotov, M. Yu. and Fegley, B. Jr. 1998a. Volcanic production of sulfur monoxide (SO) on Io. *Icarus*, **132**, 431–434.

Zolotov, M. Yu. and Fegley, B. Jr. 1998b. Volcanic origin of disulfur monoxide (S_2O) on Io. *Icarus*, **133**, 293–297.

Zolotov, M. Yu. and Fegley, B. Jr. 1999. Oxidation state of volcanic gases and the interior of Io. *Icarus*, **141**, 40–52.

Zolotov, M. Yu. and Fegley, B. Jr. 2000. Eruption conditions of Pele volcano on Io inferred from chemistry of its volcanic plume. *Geophys. Res. Lett.*, **27**, 2789–2792.

11

Io's neutral clouds, plasma torus, and magnetospheric interaction

Nicholas M. Schneider and Fran Bagenal

11.1 INTRODUCTION

The Jovian system would be dramatically different if Io were not volcanically active. The orbital resonances that power tidal heating not only alter Io beyond recognition, but also extend Io's influences throughout the Jovian magnetosphere, to other satellites, and even into its quadrant of the Solar System (Figure 11.1). In this chapter we will begin with a discussion about the material escaping from Io, and the vast neutral clouds it creates. We continue with the ionized ring of plasma called the Io torus that is created from Iogenic material. We then cover the way in which the plasma in turn affects Io and the other satellites, and conclude with the broader effects on the magnetosphere at large, the aurora at Jupiter, and the escape of material into interplanetary space.

The discovery of Io's broad influences on the Jovian system far predated the discovery of volcanism. Bigg (1964) discovered Io's controlling influence over Jupiter's decametric radio emissions. Brown (1974) observed sodium emission from Io, which Trafton (1974) soon demonstrated to come from extended neutral clouds and not Io itself. Soon thereafter, Kupo and Mekler (1976) detected emissions from sulfur ions, which Brown (1976) recognized as coming from a dense plasma analogous to an astrophysical nebula. With the prediction of volcanism by Peale *et al.* (1979) just before its discovery by *Voyager 1* (Morabito *et al.*, 1979), a consistent picture of Io's role began to emerge. *Voyager 1*'s discovery of Jupiter's aurora and extreme ultraviolet emission from the torus (Broadfoot *et al.*, 1979), along with its *in situ* measurements of the magnetosphere (reviewed in Dessler, 1983) extended our awareness of Io's effect on the larger system.

The ensuing 25 years of observation by interplanetary missions, Earth-orbiting observatories, and ground-based telescopes has deepened our understanding of Io's

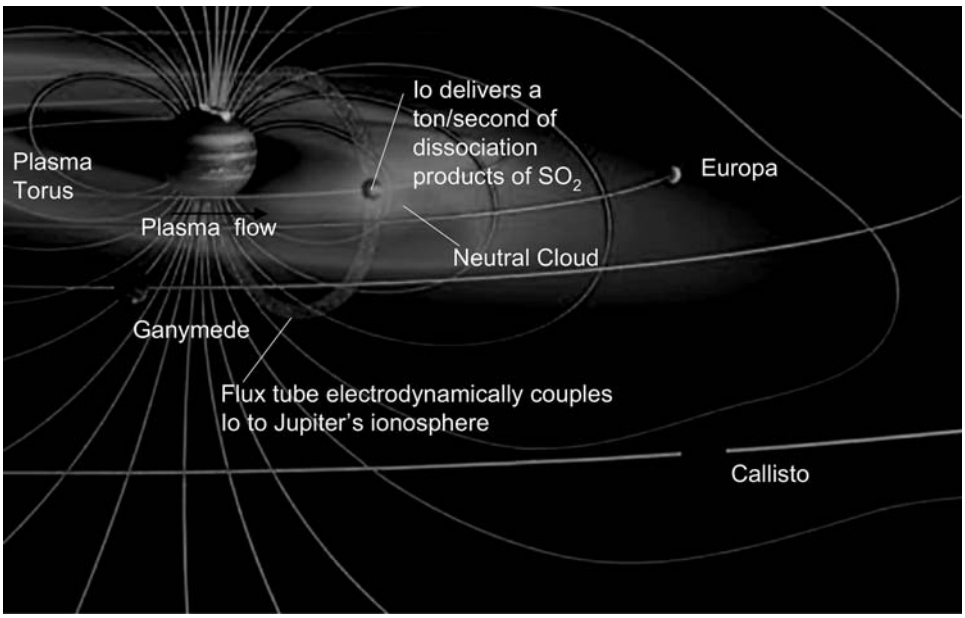

Figure 11.1. The main components of the Jupiter–Io system and their primary interactions. (See also color section.)

influences. Highlights include *Galileo*'s many close fly-bys of Io, with detailed fields-and-particle measurements of Io's interaction with the magnetosphere, and *Cassini*'s months-long ultraviolet observation of the torus (Steffl *et al.*, 2004a,b, 2006). Progress from Earth-based studies include the sensitive Hubble Space Telescope (HST) ultraviolet observations of Io's atmospheric emissions, and ground-based observations of new atomic and molecular species in Io's atmosphere and the plasma torus.

This chapter reviews the phenomena above with emphasis on their big picture connections to Io's volcanism. There are several excellent reviews on this same subject with greater technical detail. These topics are covered in several chapters of the book *Jupiter* (Bagenal *et al.*, 2004): Thomas *et al.* reviews the clouds and torus, Saur *et al.* and Kivelson *et al.* review magnetospheric interactions with Io and other satellites, and four additional chapters review the broader magnetospheric context. Our state of understanding before *Galileo* is summarized in Spencer and Schneider (1996).

11.2 NEUTRAL CLOUDS

Io's effect on the Jovian magnetosphere can be largely attributed to the fact that it has an unexpectedly large atmosphere for a small moon. Io's low gravity allows the atmosphere to escape by a variety of processes, and volcanic outgassing resupplies

Table 11.1. Material escaping from Io.

Material	Primary evidence	Proportion	
S, O	Atomic emissions in corona, neutral cloud Ionic emissions from torus Particle detection in torus	>90%	By element
Na, K	Atomic emissions from neutral clouds	1–few%	
Cl	Ionic emissions from torus	1–few%	
Molecules	Ion cyclotron waves near Io SO_2^+ or S_2^+ particle detections in cold torus NaX^+ in sodium stream	The proportion of mass escaping Io in molecular vs. atomic form is unknown	
Dust	Io-correlated dust streams composed primarily of NaCl	The proportion of mass lost in the form of dust is <0.1%	

it on a timescale of hours to days. The properties of the atmosphere, and the key processes responsible for maintaining it, are described in Chapter 10.

Io loses approximately 1 ton per second to the neutral clouds and magnetosphere, primarily atoms and molecules of sulfur and oxygen (Table 11.1). Over the age of the solar system, this accumulates to a net decrease in radius of about 2 km. While this loss is significant, Io is not in danger of running out of SO_2 in the lifetime of the solar system. It is plausible, however, that other volatile species such as H_2O were originally present on Io but then were completely lost earlier in its history through processes now depleting Io of SO_2 (Spencer and Schneider, 1996).

Escaping material is composed of the elements of volcanic volatiles SO_2, S_2, NaCl, KCl, and other plausible combinations. The dust detected far from Io has recently been shown to be primarily salt – NaCl (Postberg *et al.*, 2006), but supplied at too low a rate to account for all the sodium and chlorine in the system. It is noteworthy that although silicate volcanism occurs on Io's surface, no refractory elements such as Si, Fe, Mg, or Al have been detected in the neutral clouds or torus. Upper limits on these species place them below 1% in overall composition and well below their cosmic abundances relative to other observed species (Na *et al.*, 1998). This supports the prevailing theory that escape from Io occurs through the intermediary of the atmosphere, with little or no direct ejection from the surface. Note that direct ejection by the volcanoes is also considered negligible, as vent velocities even up to $1\,km\,s^{-1}$ are small compared with Io's escape velocity of $2.6\,km\,s^{-1}$.

Escape from Io occurs in a complex region where magnetospheric plasma flows through Io's upper atmosphere (Figure 11.2). The plasma in the torus approximately corotates with Jupiter, meaning that it travels at about $74\,km\,s^{-1}$ at Io's orbit, overtaking Io which orbits at $17\,km\,s^{-1}$. Torus plasma is partially diverted around Io by a conducting ionosphere, but ions and electrons flow through Io's exosphere at speeds of $57\pm30\,km\,s^{-1}$ (discussed further in Section 11.4) and undergo a variety of collisional interactions. In the interaction region, plasma physics, atmospheric

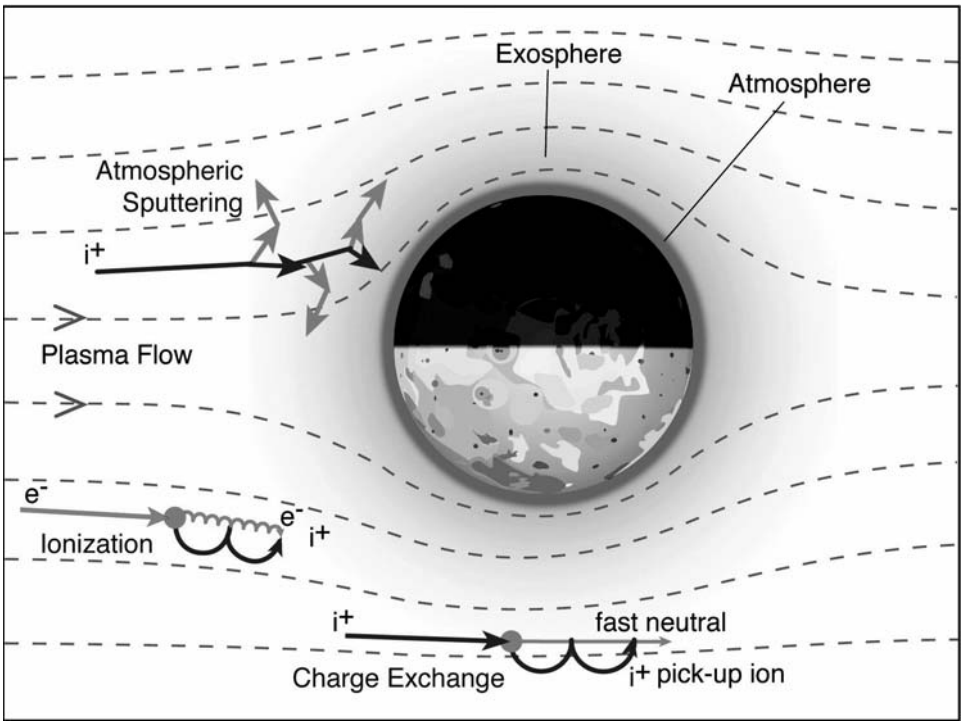

Figure 11.2. Important plasma/atmosphere interactions near Io. For simplicity the diagram shows the gyromotion for pick-up ions and electrons, but not for incident ions or electrons. The scale of the gyromotions has been greatly exaggerated: the gyroradius of a pick-up oxygen ion is 5 km, much less than Io's radius, and that of an electron is about 40,000 times smaller than the ion's. (See also color section.)

physics, ionospheric physics, atomic physics, and molecular physics all play controlling roles, which may explain why no comprehensive model of this region yet exists.

The variety of ion/electron/atom interactions each has key effects for the magnetosphere. Most importantly, torus ions collide with neutral atoms in the atmosphere, which in turn collide with other atoms in the process known as sputtering. Typically, one torus ion can transfer enough momentum for several atmospheric atoms or molecules to be ejected into Io's corona or possibly to escape from Io altogether. This is the primary pathway for material to be supplied to the neutral clouds and ultimately to the plasma torus. A second key reaction is electron impact ionization, in which a torus electron ionizes an atmospheric atom, which is then accelerated up to the speed of the plasma and leaves Io. Torus ions can also charge exchange with atmospheric neutrals, which results in a fresh ion and a high-speed neutral. Elastic collisions between ions and atoms can also eject material at speeds between those resulting from sputtering and charge exchange. Finally, electron-impact dissociation breaks down molecules into their component atoms. Approximate lifetimes for

Table 11.2. Characteristic timescales for escaping materials. These approximate timescales apply in the torus, outside of the interaction region ($n = 2{,}000$ electrons cm^{-3}, $T_e = 5\,eV$).

Process	Example	Lifetime
Electron impact ionization	$O + e^- \rightarrow O^+$	~ 100 hr[†]
	$S + e^- \rightarrow S^+$	$\sim$ 10 hr
	$Na + e^- \rightarrow Na^+$	$\sim$ 4 hr
Charge exchange	$O + O^+ \rightarrow O^+ + O^*$	$\sim$ 50 hr
Electron impact dissociation	$SO_2 + e^- \rightarrow SO + O$	$\sim$ 4 hr
Transport time to Hill sphere ($6\,R_{Io}$)	$3\,km\,s^{-1}$ (average)	$\sim$ 1 hr
Transport time across cloud ($6\,R_J$)	$3\,km\,s^{-1}$ (initial)	$\sim$ 20 hr

[†] Hot electrons may shorten the ionization lifetime for O (and other ions with high ionization potential) by a factor of 10.

examples of these processes are listed in Table 11.2. The tabulated numbers apply to average conditions in the torus, as conditions in the interaction regions are not well known. The tabulated values are therefore of greatest use for relative comparisons to other numbers in the table, as opposed to their numerical values.

Material escaping from Io forms distinct features depending primarily on the speed and direction characteristics of the ejection process (Figure 11.3). Sputtering, for example, produces a broad angular distribution of particles in a velocity distribution weighted toward low velocities. Most sputtering products have much less than Io's $2.6\,km\,s^{-1}$ escape velocity, and therefore travel along ballistic trajectories which will return them to Io (barring other reactions). These particles populate the corona or exosphere, which extends from Io's exobase to the boundary of the Hill sphere at about $6\,R_{Io}$ where Jupiter's gravity begins to dominate.

The sputtering velocity distribution has a tail extending above the escape velocity, and these atoms will form neutral clouds extending many R_J away from Io. The morphology of the clouds is controlled by celestial mechanics (dominated by Jupiter's gravity) and by loss processes from interactions with the plasma torus. An initially spherical cloud of atoms escaping radially from Io takes on a very different shape as Jupiter's gravity takes over. Atoms ejected backward at a few $km\,s^{-1}$ relative to Io's orbital motion of $17\,km\,s^{-1}$ have a speed below that needed for circular motion around Jupiter. These atoms will fall inward toward Jupiter, converting potential to kinetic energy and end up getting ahead of Io in its orbit. Similarly, particles whose launch velocities are aligned in the direction of Io's orbital motion have higher than circular velocities, and will travel on ellipses that take them farther from Jupiter, where they slow down and fall behind Io. The net result purely from celestial mechanics is a neutral cloud with one part extending ahead and inside Io's orbit, and another extending outside and behind. In about 20 hr, atoms launched from Io at only a few $km\,s^{-1}$ can reach distances of $6\,R_J$ ahead of, or behind, Io.

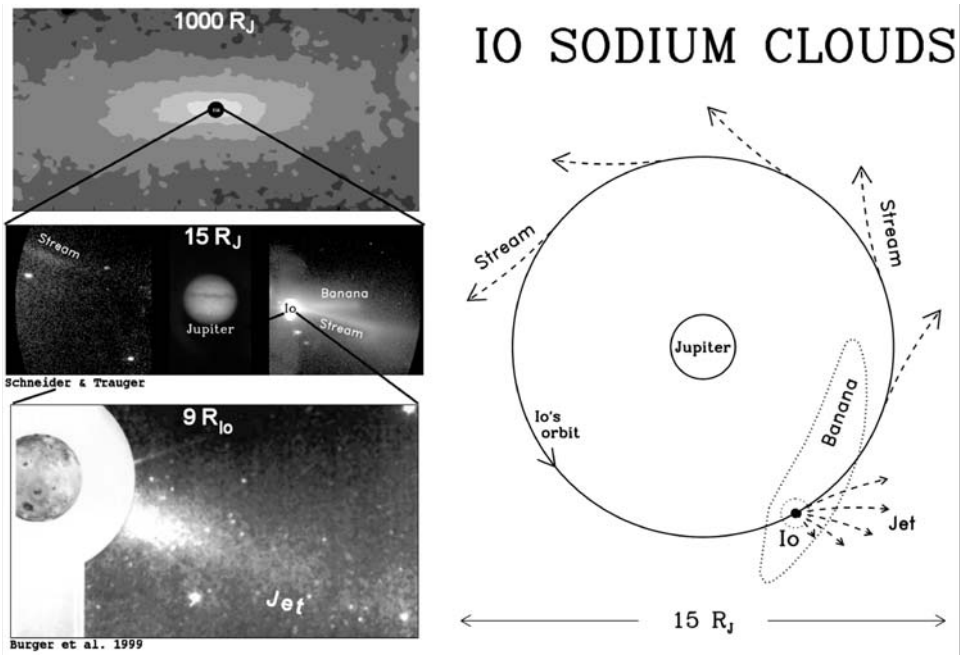

Figure 11.3. (*left*) Io's sodium cloud on three spatial scales, as imaged by ground-based observations of sodium D-line emission. (*right*) The features observed on the left are explained by the three atmospheric escape processes shown schematically. The "banana" cloud and stream are explained further in the text. (Courtesy Jody Wilson.)

The basic cloud shape resulting from celestial mechanics is further sculpted by loss processes arising from the plasma environment (Figure 11.3). Note that the leading cloud lies inside Io's orbit where the plasma is cool, so atomic lifetimes are significantly longer than those listed in Table 11.2. The "trailing cloud" is subjected to plasma warm enough to ionize much of the cloud, though the ionization rate depends on the species involved. Electrons with average energies $\sim$5 eV include enough in a high-energy tail to strip electrons from atoms with ionization potentials of 4–20 eV. (A small population of even hotter electrons may play an even more important role in ionization.) At one extreme, the 4-hr sodium lifetime against ionization is short compared with a typical transport time of 20 hr, so the trailing cloud is virtually non-existent. The decimation of the trailing cloud is so complete that at one point it was concluded that no atoms were ejected in that direction (i.e., from Io's leading hemisphere). Now, the accepted explanation for the sodium "banana" cloud that leads Io in its orbit is the rapid ionization of sodium atoms in the trailing cloud.

Other ejection processes create the distinct features in Io's neutral clouds shown in Figure 11.3. In a charge exchange reaction between torus ions and atoms in the neutral cloud, the ion takes an electron from the atom, becoming neutral and therefore decoupled from the magnetic field. The fast neutral escapes the Jovian system, since it retains its velocity as an ion: the $\sim$70 km s^{-1} bulk velocity of the plasma

plus a smaller random component from its thermal energy. (The escape velocity from Jupiter at the distance of Io's orbit is only $24\,\mathrm{km\,s^{-1}}$.) A second process known as molecular ion dissociation also creates a fast neutral spray. In one known example, sodium-bearing molecular ions (NaX^+, possibly $NaCl^+$) are picked up in the torus and carried downstream. Since dissociation of molecular ions is as fast as dissociation of neutral molecules, the ion is broken apart, creating a fast sodium atom some of the time. The trail of fresh molecular ions downstream from Io leads to a "stream" of fast neutrals that almost encircles Jupiter. Over many Io orbits and Jupiter rotations, fast neutrals create a tutu-shaped spray of sodium atoms with escape velocity from Jupiter. These populate the vast region sometimes called the Mendillosphere (Figure 11.3, top) after its discoverer (Mendillo *et al.*, 1990).

Clouds of sulfur and oxygen are much denser than the sodium cloud, but are governed by similar dynamics. Differences in reaction rates lead to dramatic differences in their spatial distributions. For example, the longer ionization lifetime for O and S (see Table 11.2) means that the outer trailing cloud may be comparable in density and extent to the inner leading cloud, an important fact when locating the source of fresh plasma. The molecular ion stream may be unique to sodium-bearing ions since their low ionization potential favors their creation in Io's ionosphere, meaning that "streams" of fast oxygen or sulfur are not expected. But the shorter lifetime of O^+ against charge exchange leads to a larger proportion of fast neutral oxygen atoms created through this process, and a correspondingly smaller proportion of oxygen relative to sulfur in the torus than the 2 : 1 ratio expected from the break-up of SO_2.

Our understanding of the sodium clouds is much better than that of oxygen and sulfur clouds, even though sodium is only a trace species. This puzzle can be traced to sodium's atomic structure, which allows sodium to scatter sunlight efficiently at visible wavelengths. Oxygen and sulfur atoms scatter sunlight at only ultraviolet wavelengths, where the Sun produces little light and where observations can only be made from space. These species therefore radiate by electron impact excitation which produces much fainter emissions.

11.3 THE PLASMA TORUS

The loss of neutral cloud atoms through ionization is the primary source of material for the plasma torus. Thus, the torus is a self-sustaining plasma, since it is the impact of torus ions on Io's surface or atmosphere that causes the sputtering that supplies the clouds in the first place. The stability of this feedback loop may depend on the nature of the plasma/atmosphere interaction described in the next section. Figure 11.4 shows the basic structure of the torus and its relationship to the neutral clouds.

Electron impact ionization of a slowly moving atom creates a fresh ion with a high velocity relative to the corotating plasma. Each pickup ion is therefore "picked up" by the fields that cause corotation, and spirals around its field line with a velocity equal to its initial motion "backward" relative to the plasma. Each fresh ion starts with a gyration velocity equal to the plasma flow speed in its rest frame, so has a gyroenergy

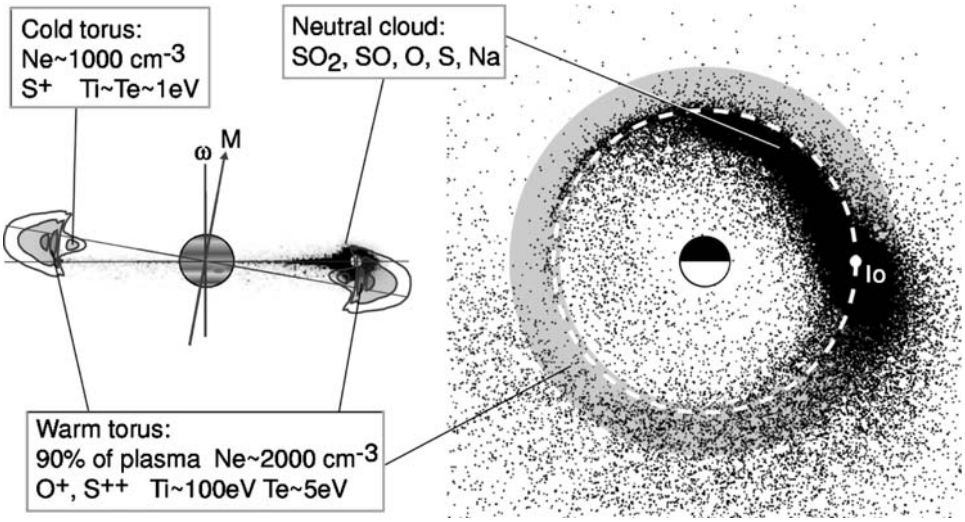

Figure 11.4. Schematic of the Io plasma torus and neutral clouds as seen from the side (*left*) and from above (*right*). Note that the plasma torus is tipped 7° relative to Jupiter's equator in a coordinate system that corotates with Jupiter, while the neutral clouds lie in the equatorial plane and move with Io along its orbit. In the side view, the torus is shown in cross section since the structure is basically the same throughout. The neutral cloud, however, is shown as a projection since its structure depends on Io's position.

dependent on its mass: 270 eV for O^+ and 540 eV for S^+ at Io's orbital distance. The energy of these fresh ions ultimately comes from Jupiter's rotation. The 57 km s^{-1} gyromotion of fresh pickup ions lies in the plane perpendicular to the local magnetic field. (If the gyroenergy were distributed into an isotropic Maxwellian distribution, the O^+ and S^+ ions would have temperatures of 2/3 their initial pickup energy (i.e., 170 eV and 340 eV, respectively).) Fresh oxygen pickup ions gyrate around magnetic field lines about twice per second with a 5-km gyroradius, as electrodynamical coupling to Jupiter's ionosphere causes the torus plasma to corotate with the planet (Figure 11.5).

The continuous ionization of the vast neutral clouds creates a ring of plasma encircling Jupiter near Io's orbit and moving around Jupiter at roughly the corotation speed. Some ions are created in Io's immediate vicinity, and others are picked up from the vast neutrals clouds many Io radii (or even Jupiter radii) away. Ions appear to reside in the torus for the order of 100 rotations, meaning that each rotation of the torus through the neutral clouds adds only ~1% new plasma. Coincidentally, the approximate ratio of neutral lifetime (<20 hr) and plasma transport timescale (~40 days) is also about 1%.

The study of the torus requires understanding of both microscopic and macroscopic behavior, much as geology combines understanding both rheology and landforms. First we will discuss the small-scale behavior of the plasma, and then return to the large-scale view.

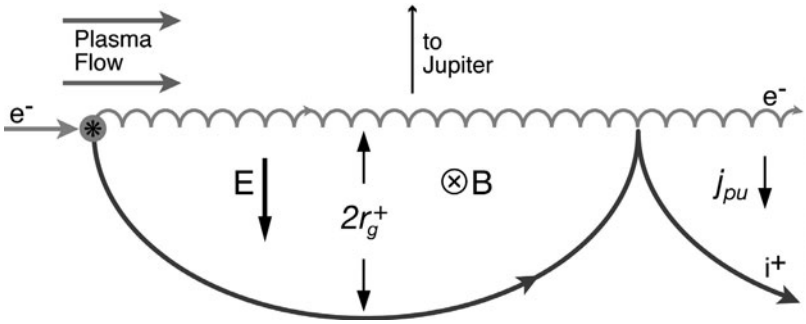

Figure 11.5. The pickup process. Pickup ions and electrons travel on cycloids in the frame comoving with Io, resulting from the addition of 57 km s^{-1} bulk velocity and 57 km s^{-1} gyrovelocity. The ion and electron cycloids are offset in opposite directions because of their opposite charges. Note that the electron cycloid is greatly enlarged for visibility.

One valuable microscopic view studies a representative torus "cubic centimeter" in isolation, supplied with neutral atoms. Detailed models (described as "Neutral Cloud Theory") consider reactions between ions and electrons, including those responsible for ionization and ion chemistry, for energy flows between species, and for radiation at all wavelengths. Models also assume plasma leaves the torus volume by outward radial transport, with characteristic lifetimes of tens of days. The goal is to explain the basic observed conditions of the torus, with a density of about 2,000 electrons cm^{-3}, an ion temperature of ~100 eV, an electron temperature of ~5 eV, and a composition dominated by O^+, S^{++}, S^+, O^{++}, and S^{+++} ions.

The first component of such models is mass balance. Only about one-third of the neutrals escaping from Io add net mass to the torus through electron impact ionization. Two-thirds of the neutrals undergo charge-exchange collisions in which the neutral becomes a fresh ion, and the incident torus ion becomes an escaping fast neutral. Thus, charge exchange can add energy to the torus without adding mass. The relative importance of ionization and charge exchange may fluctuate. Models of periods of high neutral source (e.g., at the time of the *Voyager 2* fly-by) are consistent with the transport rate increasing with source strength and charge exchange becoming less important.

The second component of such models is energy balance, which is more complicated (Figure 11.6). Early attempts of modeling the torus plasma assumed the creation and acceleration of fresh ions to be the sole source of energy in the torus. The fresh ions lose thermal energy to the ambient ions though Coulomb collisions, and the ambient ions similarly lose energy to ambient electrons. Ultimately, the torus electrons lose energy by moving electrons bound to ions into excited states, leading to the prodigious extreme ultraviolet (EUV), ultraviolet, and visible emissions from the torus. Thus, energy cascades from the warmest to coolest populations (see Figure 11.6).

Radiation is a rapid drain on the energy of torus electrons: each emitted EUV photon saps 10–20 eV from an electron, and the total energy contained in the ~5 eV

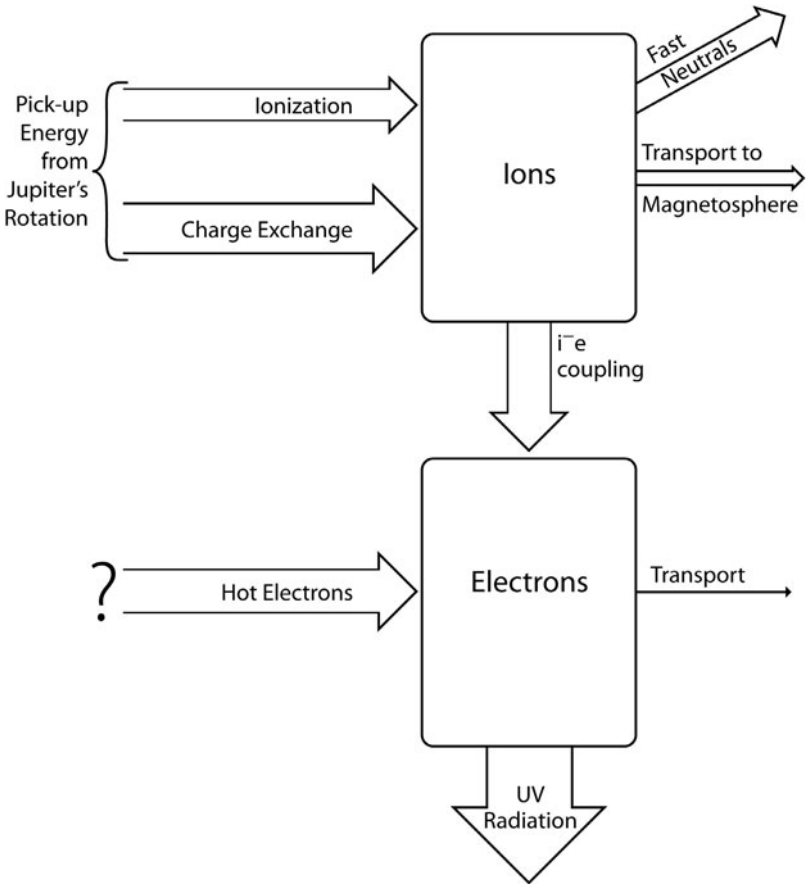

Figure 11.6. Typical energy flows in the Io plasma torus. The width of the arrows show the approximate fraction of energy on a particular path. Note that most or all of the energy ultimately is tapped from Jupiter's rotation, and most leaves through ultraviolet radiation caused by electron impact excitation of the ions.

thermal component of the electron distribution could only power the emissions for ~9 hours if the electrons were not rapidly re-energized. Similarly, each ionization takes at least 10 eV (and up to 35 eV for higher ionization states) from an electron, highlighting the importance of electrons at super-thermal energies.

Detailed modeling has shown that the supply of energy from fresh ions alone is not enough to maintain electrons hot enough to both power the observed radiation and maintain the ionization state. Simply increasing the ionization rate cannot solve this "energy crisis", since this also increases the energy drain to radiation and ionization. Thus, it is actually an "energy per ion" crisis, with too little energy being brought in by pickup to fuel each ion over its lifetime in the torus. Extra energy sources are required, with super-thermal electrons as the leading candidate, since they enhance ionization (particularly to higher ionization states) and increase the

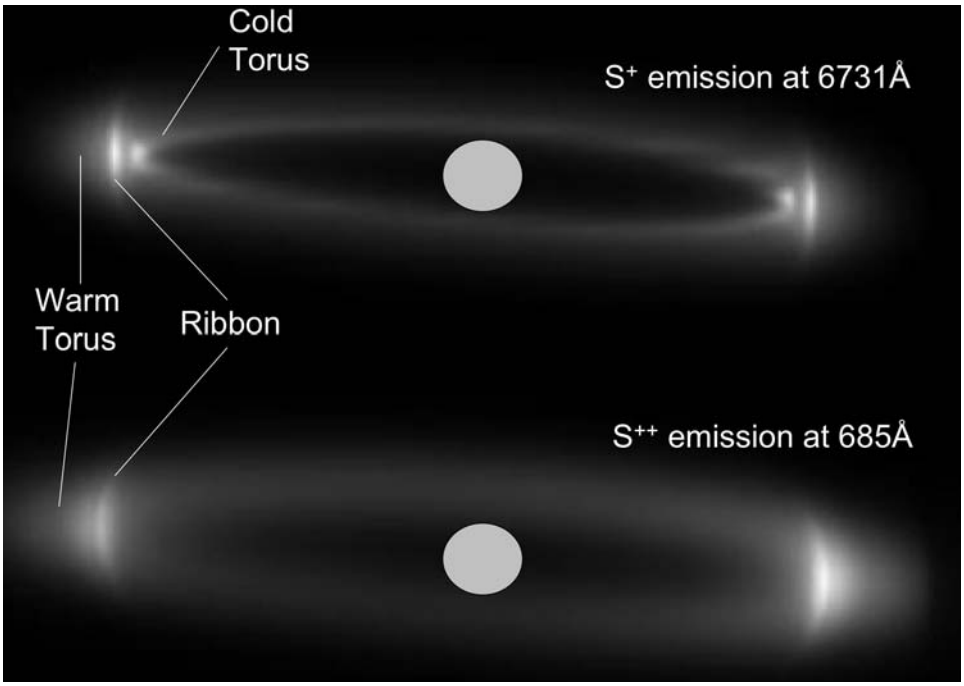

Figure 11.7. Regions of the plasma torus. This computed image shows optical S^+ emission (*top*) and EUV S^{++} emission (*bottom*). Note that S^+ dominates the cold torus and S^{++} dominates the warm torus. The ribbon is a tall, narrow ring which appears bright at the edges of the torus because of projection effects. The ribbon is typically the most prominent of the three regions for S^+, while in S^{++} emission the ribbon is a slight brightening at the inner edge of the warm torus. The structure of the torus can exhibit strong longitudinal variations, and the relative brightnesses of different regions can vary with time.

EUV output. Populations of only a few per cent of electrons that are $\sim 10\times$ hotter than the ambient electrons can close the gaps (in both ionization state and EUV emission rate) between models and observations. The specific source of energetic electrons is not yet identified, though there are several plausible theories. The remaining flow of energy comes from pickup ions, through ion–electron coupling to ultraviolet radiation. The contribution of hot electrons seems to vary substantially from $\sim 11\%$ during times of high source/transport rate (*Voyager 2*) to $\sim 60\%$ at times of low source/transport rate (*Cassini* fly-by, January 2001). Ultimately, very little of the energy created in the torus is transported into the magnetosphere beyond the torus, since much of the energy is lost by radiation and the escape of fast neutrals through charge exchange.

A macroscopic view of the torus provides a wealth of information that complements the energy insights derived from the preceding microscopic view. The structure of the torus reveals the magnetic and electric fields that shape it, and the transport of mass and energy through the system.

The basic shape of a tilted ring of plasma results from Jupiter's tilted magnetic field and its rapid 10-hr rotation (Figure 11.7). Torus plasma in Jupiter's magnetic field is confined toward the equator not by magnetic mirroring but by centrifugal forces. Jupiter's rapid rotation means that a corotating ion at Io's orbit experiences about 1 g of force outward from the rotation axis. Individual ions spiral around field lines several times per second while oscillating up and down along field lines every few hours, all while corotating with the planet. Ions in a Maxwellian velocity distribution will distribute themselves along the magnetic field line in a Gaussian centered around the point farthest from Jupiter's rotation axis. The locus of all such positions around Jupiter is called the centrifugal equator. In an approximately dipolar magnetic field tipped like Jupiter's, $\sim 10^\circ$ from the rotation axis, the centrifugal equator has 2/3 of the tilt, or $\sim 7^\circ$ from Jupiter's rotational equator. As the tilted torus corotates with Jupiter, the torus viewed from Earth appears to wobble $\pm 7^\circ$. Non-dipolar components to the field can measurably warp the centrifugal equator.

The preceding particle perspective of the plasma is complemented by a fluid perspective. Even though the particles interact on timescales of hours to days, it is sufficient to view the plasma distribution along the field as a balance between the internal pressure of the plasma and the centrifugal force, much as an atmosphere lies in a balance between pressure and gravity. The fluid approach allows addition of further complexity associated with multiple species of differing mass and/or charge, thermal anisotropy, and the small electric field arising from any charge separation between ions and electrons.

The torus vertical structure reveals ion temperatures. The north–south ("vertical" $= z$-axis) variation in plasma density n about the centrifugal equator is a Gaussian function ($n = n_o \exp(-(z/H)^2)$) where the scale height H is primarily governed by the ion temperature T_i and the mass of the ions. For H in units of Jovian radii, R_J, we have $H \sim 0.64\,(T_i/A_i)^{1/2}$ where T_i is in eV and A_i is average ion mass in atomic mass units.

The torus radial structure reveals plasma transport processes. Though the strong magnetic field of Jupiter confines the torus plasma and inhibits radial spreading, the sulfur- and oxygen-dominated plasma filling Jupiter's magnetosphere must have come from Io. Therefore, transport across field lines must occur. Though the processes are not well understood, radial transport can be thought of as a diffusive process that is strongly influenced by centrifugal forces. Thus, outward flow is energetically favored, and inward transport is considerably slower (Thomas *et al.*, 2004).

We can now understand the three main regions of the Io torus. The outer ($\sim$6–7 R_J) region has hot ($\sim$100 eV), relatively fresh plasma that moves outward on timescales of tens of days. The narrow ($\sim$5.6–6 R_J) ribbon is a stagnated region of modest neutral sources and slow transport rates, so the plasma has time to radiate away thermal energy and cool to ion temperatures of $\sim$20 eV. The inner cold torus lacks a significant source of new ions, and transport is so slow that the plasma has time to cool to <1 eV.

The picture so far of a tilted ring locked to Jupiter's magnetic field and corotating with the planet is an excellent first approximation to the torus. The addition of several small but significant effects completes the picture. First, though the tilted ring is locked

to the magnetic field, the plasma that makes up the ring is slowly slipping backward relative to the reference frame corotating with Jupiter. This sub-corotation is caused by imperfect coupling between the torus plasma and Jupiter's ionosphere (described in Section 11.5) and can result in plasma slipping 1–5% behind rigid corotation.

Second, plasma flow down Jupiter's magnetotail appears to impose an electric field across the torus, though the exact mechanism is not clear. As plasma travels around Jupiter, the electric field causes it to move a few per cent closer to Jupiter on the dusk side, and farther on the dawn side. This small shift causes non-linear compression and heating on the dusk side, making it up to twice as bright as the dawn side at EUV wavelengths.

Finally, longitudinal asymmetries in the torus create differences in brightness and/or composition from one side of the torus to the other. As Jupiter rotates, an observer monitoring either side of the torus will record periodic variations (see review by Thomas, 1993). Substantial progress in understanding these periodicities was made possible by months of torus monitoring by the *Cassini* UltraViolet Imaging Spectrometer (UVIS) during its Jupiter fly-by. Underlying asymmetries in electron temperature appear to cause asymmetries in ionization state and brightness. It has been suggested that there are two populations of hot electrons whose densities are modulated with magnetic longitude. One population corotates with the planet and the other sub-corotates. The torus exhibits significant asymmetries when the two modulations are in phase (Figure 11.8, top), and becomes longitudinally uniform when they are out of phase. The source mechanism of the hot electrons is unknown.

In addition to the "geometric" variabilities described above, the torus and neutral clouds undergo large temporal variability on timescales of months. On the face of it, such variation is not surprising, given the tremendous variability in volcanic activity and the volcanic origin of magnetospheric materials. But a deeper look shows the connection is not so obvious: volcanoes do not directly eject material into the clouds and torus, and Io's atmosphere is likely to play a buffering role on escape processes. The challenge in answering this central question has been collecting sufficient data on multiple phenomena thought to be causally connected.

To date no studies have unambiguously tied torus variation to volcanic activity, but several studies have connected a few links in the chain. Brown and Bouchez (1997), in a 6-month simultaneous study of the sodium cloud and sulfur torus, found that a rise in neutral sodium was followed several weeks later by an increase in sulfur ions. In a separate multi-year study, Mendillo *et al.* (2004) found a positive correlation between volcanic infrared brightness and the brightness of the distant sodium cloud (Figure 11.9). While these connections are promising, it bears noting that they both depend on sodium as a proxy for all neutrals – which is especially doubtful for the fast sodium supplying the distant sodium cloud. At present it is not feasible to monitor other neutral species as easily as sodium despite their expected higher densities.

The *Cassini* fly-by of Jupiter provided an excellent opportunity for observing many related phenomena in the torus. Figure 11.8 (top) shows the 30% decline in power of EUV emissions (normalized by $1/\text{distance}^2$) observed as the spacecraft approached Jupiter. Properties of the plasma, derived by modeling the EUV

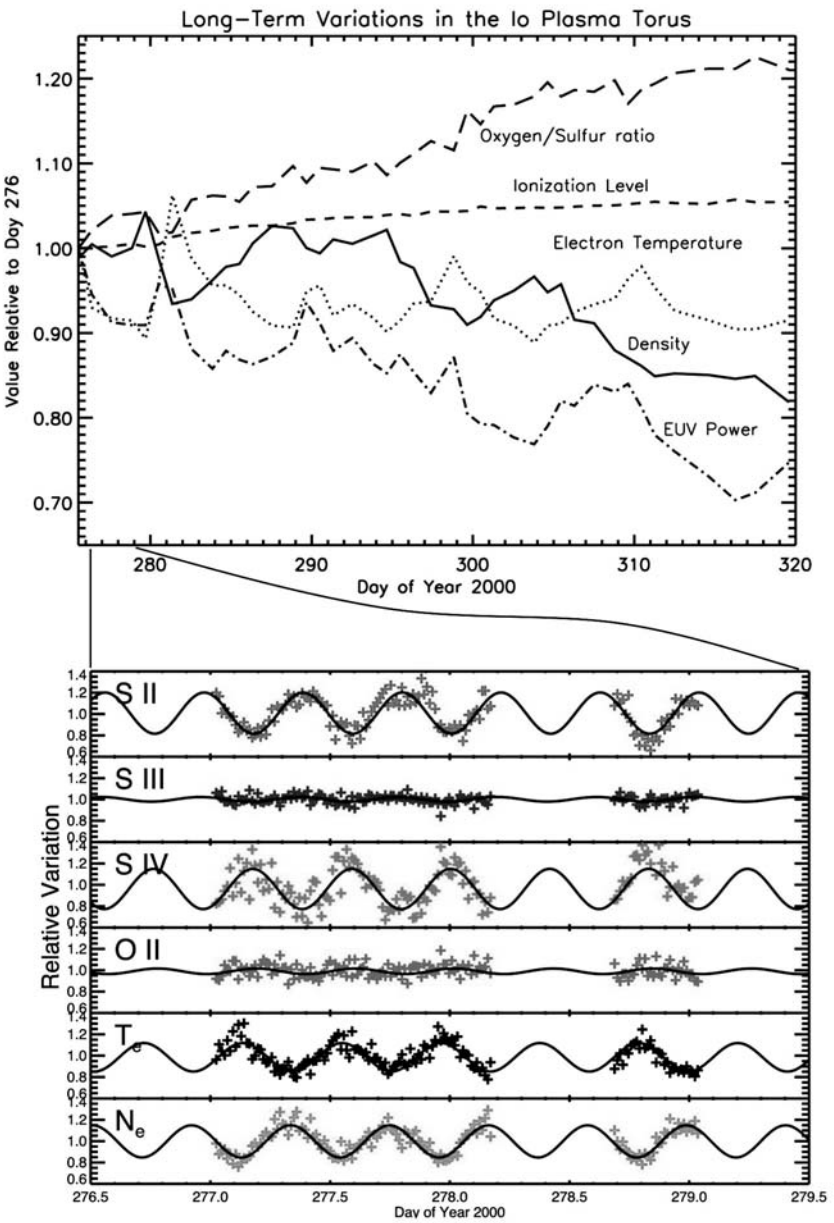

Figure 11.8. *Cassini* UVIS results for the short-term (*bottom*) and long-term (*top*) variation of the torus. Note that over periods of days, regular brightness variations are indications of structures in the torus moving in and out of the field of view. Over periods of weeks to months, variability is probably due to changing volcanic activity on Io. The inset shows a period of high periodic variation which waned in the following weeks but later reappeared at the same phase. The changing amplitude leads to the interpretation of two variations at slightly different periods which add when in phase but cancel when out of phase.

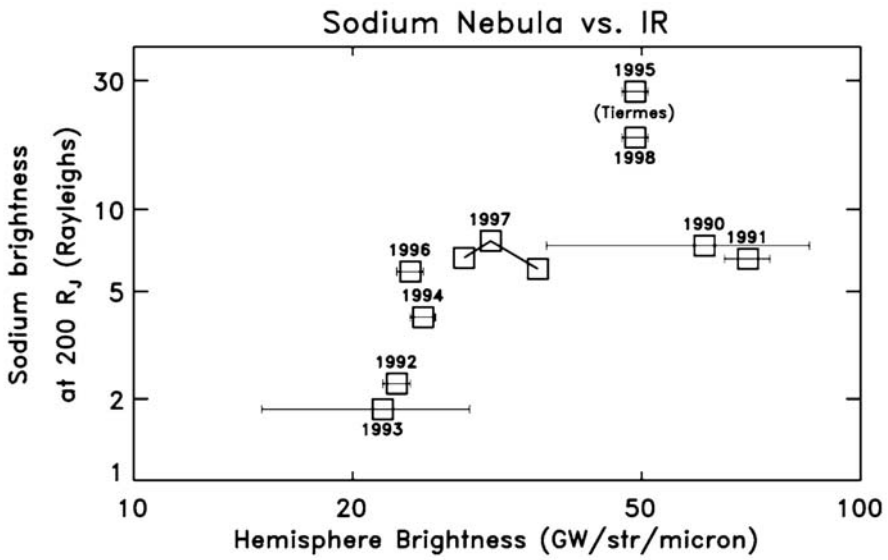

Figure 11.9. Tentative correlation between infrared emission from Io volcanoes (horizontal axis) and the distant sodium D-line emission (vertical axis). No specific mechanism connecting the two observables has been proposed (from Mendillo *et al.*, 2004).

spectra, showed corresponding long-term variations. These long-term variations are consistent with a ~3-fold increase in production of neutral atoms by Io over a ~1-month timescale occurring a month or so before UVIS started making observations of the torus (Delamere *et al.*, 2003). Such an increase in production of neutrals may have accompanied the ~1,000-fold increase in Iogenic dust coincident with *Galileo* observations of extensive surface changes and infrared emissions at the location of the Tvashtar Volcano (summarized in Krueger *et al.*, 2003). Variations in density and temperature of the warm torus (by factors of ~2) observed between *Voyagers 1* and *2*, multiple *Galileo* fly-bys, and *Cassini*, as well as comparable variations in ground-based observations of S^+ emissions, hint that torus conditions vary with Io's volcanic activity, though the specific process remains undetermined.

11.4 LOCAL INTERACTION WITH IO'S ATMOSPHERE AND NEUTRAL CLOUDS

The interaction of magnetospheric plasma with Io's atmosphere involves a complicated combination of electrodynamics, plasma physics, atmospheric processes, and atomic reactions. One of the first things to notice about the plasma flow around Io is that it is unlike the simple case of a rock submerged in a stream, where the fluid flows around and over the obstacle. Figure 11.10 shows that the strong magnetic field of Jupiter affects the interaction so that the flow around Io instead resembles fluid flow around a cylinder. (Note that a strong intrinsic magnetic field at Io has been ruled out

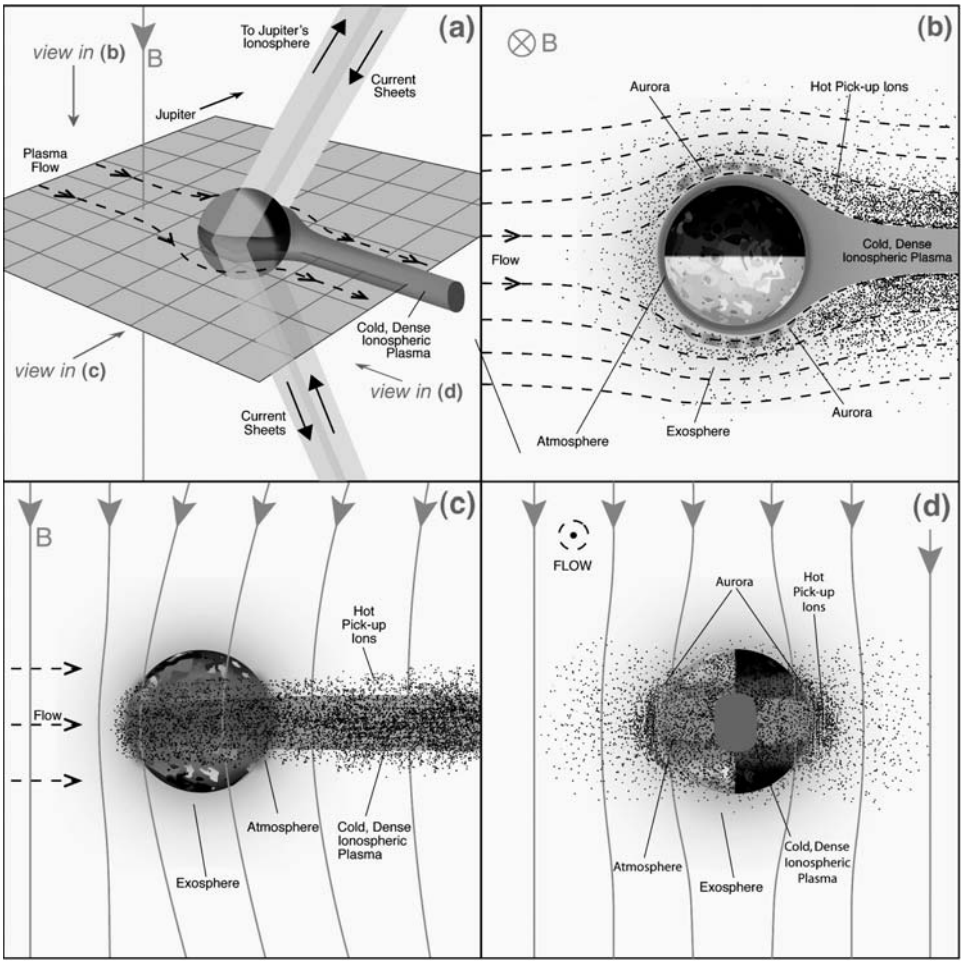

Figure 11.10. Four views of the interaction between Io and the plasma torus. (a) A 3-D view showing the current sheets that couple Io and the surrounding plasma to Jupiter's ionosphere. (b) A cross section of the interaction looking down on the north pole of Io, in the plane of Io's equator, when Io is located between the Sun and Jupiter (orbital phase 180°, local noon in magnetospheric coordinates). (c) A projected view of the Io interaction from the Sun toward Jupiter. (d) A projected view of the interaction from downstream in the flowing plasma (ahead of Io in its orbit). (See also color section.)

by *Galileo* fly-bys over the poles.) This simplified sketch of the interaction is based on telescopic observations of atmospheric properties and auroral emissions, multiple fly-bys by the *Galileo* spacecraft, and various different approaches to modeling pieces of the interaction puzzle.

Io's motion through the plasma creates a tremendous electrical current. A common physics lab experiment involves dragging a wire through a magnetic field

and measuring the current that is induced along the wire. Basically, Io acts like a length of wire moving relative to the corotating plasma, which is threaded by Jupiter's magnetic field. The flanks of Io facing toward and away from Jupiter act as the ends of the wire. While Io's surface or interior may be modestly conducting, the current is more likely carried in other conducting materials surrounding Io, such as its ionosphere and the plasma produced by ionization of its neutral corona. Currents in a plasma do not easily flow across the magnetic field but do flow readily along the field, so the currents induced across Io are closed by currents that flow along field lines between Io and Jupiter's polar ionosphere in both hemispheres. Observations by the *Voyager 1* and *Galileo* spacecraft indicate that the net current in each circuit is about 3 million Amps.

This simple current system deflects most of the corotating plasma as it approaches Io. Most of the plasma flows around the moon with only $\sim$10% impinging on Io's deep atmosphere. The energy of the impact helps to heat and expand the atmosphere below, contributing to escape of neutrals. On the inner and outer flanks of Io, the plasma speeds up to get around the obstacle, though deeper in the atmosphere the flow may be slowed. The flanks are the main regions where the flowing plasma collides with the neutral atmosphere and corona: inelastic collisions heat the neutrals, electrons excite or ionize the neutrals, and ions and neutrals exchange electrons. Collisions between the plasma and neutrals allow the plasma to conduct some of the current across Io – a conduction current.

A little farther from Io, electron impact ionization of the neutral corona produces pickup ions which gyrate around the local magnetic field with a speed equal to the relative motion between the original neutral and the local plasma flow (see Figure 11.5). Ions have gyroradii of many kilometers, while the tiny mass of the fresh electrons results in very small gyromotion in the opposite direction. The difference in gyroradii of the fresh electrons and heavy pickup ions results in a small charge separation that creates a current in the radial direction – a pickup current. The relative contributions from the conduction current through Io's ionosphere vs. the pickup current generated by ion pickup remains an issue of debate that awaits more sophisticated models (e.g., see review by Saur *et al.*, 2004).

The acceleration of freshly ionized material ("mass loading") exerts a drag on the surrounding plasma flow that consequently slows down. Field aligned currents couple the mass-loaded plasma to the giant flywheel Jupiter, the ultimate source of both pickup ("thermal") energy and kinetic energy of bulk corotational motion for the magnetospheric plasma. While the Jupiter flywheel is essentially an infinite source of momentum, the coupling mechanism is of limited efficiency. Three limitations potentially contribute to the poor coupling: insufficient transfer (via eddy diffusion) of momentum from Jupiter's lower atmosphere to the neutral atmosphere at ionospheric levels; insufficient collisional coupling between the neutral atoms and ions in the ionosphere (equivalent to low electrical conductivity); or a lack of electrons between the torus and ionosphere to carry the coupling currents. The relative importance of each of these three cases is an issue of current debate and research. In all scenarios the resulting sub-corotation varies primarily with the amount of mass loading in a given radial range.

One of major questions in Jupiter's magnetosphere is whether most mass loading happens in the near-Io interaction, or in the broad neutral clouds far from Io. There is no doubt that substantial pickup occurs near Io, based simply on the exposure of the upper atmosphere to pickup by the magnetosphere. Pickup near Io is also supported by evidence of fresh pickup ions of molecules (SO_2^+, SO^+, S_2^+, H_2S^+) near Io with dissociation lifetimes of just a few hours. But a closer look shows that the bulk of the Iogenic source comes from ionization of atomic sulfur and oxygen farther from Io. *Galileo* measurements of the plasma fluxes downstream of Io suggest that the plasma source from ionization of material in the immediate vicinity (within $\sim 5\,R_{Io}$) of Io is less than $300\,kg\,s^{-1}$ which is $\sim$15% of the canonical net ton-per-second Iogenic source (Bagenal, 1997; Saur *et al.*, 2003). The remainder must come from ionization of the extended clouds. It is not clear whether this was a typical situation nor well-established how much the net source and relative contributions of local and distant processes vary with Io's volcanic activity.

While most of the impacting plasma is diverted to Io's flanks, some is locked to field lines that are carried through Io itself. This $\sim$10% of upstream plasma is rapidly decelerated and moves slowly ($\sim$3–7 $km\,s^{-1}$) over the poles. Most of the particles are absorbed by the moon or its tenuous polar atmosphere so that the almost stagnant polar flux tubes are evacuated of plasma. Downstream of Io, the *Galileo* instruments detected a small trickle of the cold, dense ionospheric plasma that is stripped away. This cold, dense "tail" had a dramatic signature (>10 times the background density) but the nearly stagnant flow ($\sim 1\,km\,s^{-1}$) meant that the net flux of this cold, ionospheric material is at most a few per cent of the Iogenic source and is presumably quickly assimilated into the surrounding torus plasma.

11.5 COUPLING TO JUPITER'S POLAR IONOSPHERE

The presence of a volcanically active moon in the magnetosphere has significant effects on Jupiter itself. Io's electrodynamic coupling to Jupiter's polar ionosphere has been clear since the 1964 discovery that Io triggers Jovian radio emission. Studies over the past 40 years have revealed many clues but important specifics of this coupling process remain a puzzle. Figure 11.11 presents a simplified cartoon of the current picture.

Jupiter's radio emissions provide a strong but enigmatic set of clues to the interaction with the ionosphere. When Io lies at certain locations in its orbit relative to Earth, and Jupiter's magnetic field is near specific orientations relative to Io, decametric radio emissions are beamed toward Earth. These geometrical constraints led radio astronomers to conclude that the radio emission seems to be narrowly beamed along hollow cones (60–90° cone half-angle, with only $\sim$1.5° thickness), generated by electrons gyrating about the local magnetic field. It remains unclear what process actually generates the radio emission or why the radio emission is so tightly restricted along the edges of cones.

A second influence on Jupiter is evident in infrared and ultraviolet emissions from Jupiter's auroral zones (Clarke *et al.*, 2004). The precipitation of Iogenic particles into Jupiter's polar atmosphere causes observable emissions and significant chemical

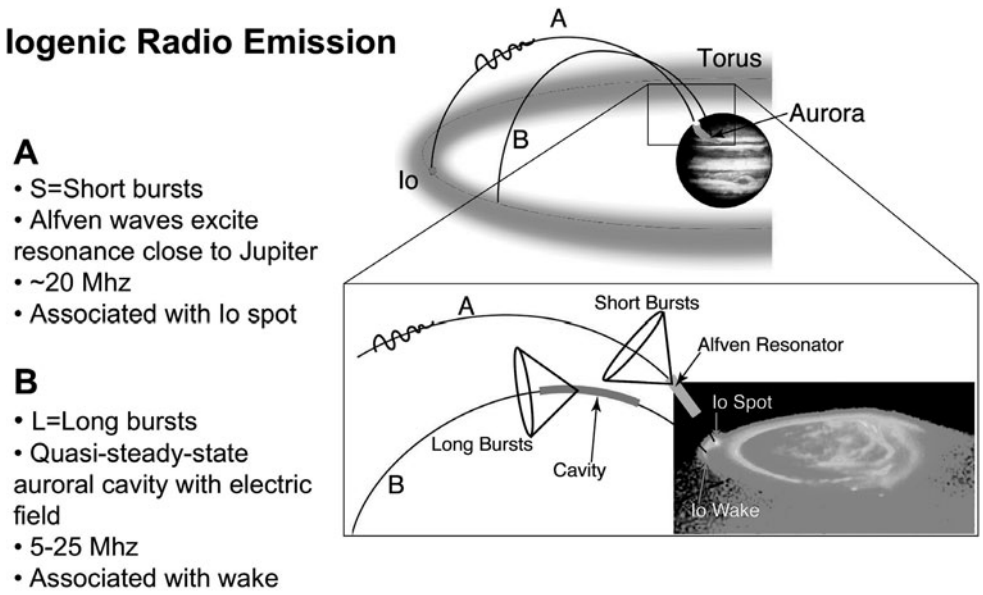

Figure 11.11. Geometry and mechanisms for Io-generated radio emissions from Jupiter's ionosphere. (See also color section.)

change, creating aerosols that darken the poles. While virtually all Jupiter's main aurorae are ultimately attributable material from Io spreading out through the magnetosphere, a particularly direct influence can be seen in the form of bright spots at the footprints of the flux tube that connects Io to Jupiter's ionosphere. Hubble ultraviolet images also revealed an extensive ultraviolet "wake" that started at Io's footprint and stretched half way around Jupiter. These auroral emissions indicate that substantial fluxes of electrons from Io are bombarding Jupiter's atmosphere. The question is how does Io generate these electron beams? An emerging picture begins to explain the basic features of both the radio and auroral emissions. The immense current flowing through Io's ionosphere couples to Jupiter's ionosphere via a direct, quasi-steady current loop just like a loop of wire. The current flowing along field lines deposits the energy that causes the ultraviolet and infrared emissions. Magnetic disturbances (Alfvén waves) caused by Io propagate along the same field lines and cause the radio emissions. Alfvén waves may excite a resonance close to the ionosphere of Jupiter, that may be responsible for short bursts of radio emission (S-bursts, lasting a few minutes) that seem to be emitted in the vicinity of the foot of the flux tube coupled to Io. Downstream of Io (leading Io in its orbit), longer bursts of radio emission (L-bursts, lasting $\sim$2 hr) may be caused by Alfvénic disturbances that bounce between the ionosphere and the torus, or may be associated with currents that accelerate the newly picked up plasma toward corotation.

The major difficulty in describing the coupling between the Io interaction region and auroral phenomena is understanding how currents can flow in the low-density

region between the plasma torus and Jupiter's ionosphere. Experience on Earth suggests that regions of strong electric field (sometimes called auroral cavities) develop which accelerate ions and electrons. It may be in such an auroral cavity region that the radio emissions are generated. Regions of electric field parallel to the magnetic field also allow the magnetospheric flux tubes to slip relative to the ionosphere. Our understanding of these high-latitude processes will remain entirely speculative until the *Juno* mission flies over the poles of Jupiter and measures the particles and fields in the auroral regions.

Iogenic plasma has broad influences in the magnetosphere as a whole. The outward diffusion of torus material creates a relatively dense and energetic plasma environment for the other Galilean satellites. Europa and Ganymede have measurable oxygen atmospheres created and lit up by the impact of Iogenic plasma, and Europa's trailing hemisphere is stained by the implantation of sulfur ions from Io.

In an even larger picture, Io's influence extends past Jupiter and into interplanetary space. Io's steady-state ton-per-second loss to the magnetosphere implies the same loss from the magnetosphere. Very little mass is lost to Jupiter itself, so most leaves the system entirely, either as fast neutrals (Figure 11.3) or plasma flowing out of Jupiter's magnetotail. The glow of fast neutrals can be seen to distances of one AU from Jupiter, and *Voyager* observations showed that Jupiter's magnetotail extends past Saturn.

In closing, Io's volcanic activity has profound and unexpected influences on its atmosphere, Jupiter's magnetosphere, the other Jovian satellites, and Jupiter itself. If the present loss rate of volcanic gases has persisted for the age of the Solar System, it means Io has shrunk at least 2 km, with the material escaping the Jupiter system entirely and ultimately being carried by the solar wind to the heliopause.

11.6 OUTSTANDING ISSUES

Despite the strong evidence for the basic picture presented here, many fundamental questions remain unanswered in the study of the neutral clouds, the torus, and magnetospheric interactions:

- How does the Iogenic source of plasma vary with volcanic activity on Io?
- What causes the variability – and stability – of the torus and neutral clouds?
- Is the "salt dust" emitted from Io of volcanic origin? How does it escape from Io?
- What creates the hot electrons apparently required to explain the state of the torus? Why is part of the hot electron population localized and sub-corotating?
- Where do currents actually flow near Io – ionosphere (conduction) or pickup?
- How much of the supply to the torus is picked up close to Io vs. far away?
- What is the feedback of the plasma interaction on Io's atmosphere?
- What is the nature of the coupling between Jupiter's ionosphere, Io, and the torus?
- How are radio emissions generated?

11.7 REFERENCES

Bagenal, F., T. Dowling, and W. McKinnon (eds). 2004. *Jupiter: The Planet, Satellites, Magnetosphere*. Cambridge University Press, Cambridge, UK.

Bagenal, F. 1997. Ionization source near Io from Galileo wake data. *Geophys. Res. Lett.*, **24**, 2111–2114.

Bigg, E. K. 1964. Influence of the satellite Io on Jupiter's decametric emission. *Nature*, **203**, 1008–1010.

Broadfoot, A. L., M. J. S. Belton, P. Z. Takacs, B. R. Sandel, D. E. Shemansky, J. B. Holberg, J. M. Ajello, S. K. Atreya, T. M. Donahue, H. W. Moos, *et al*. 1979. Extreme ultraviolet observations from Voyager 1 encounter with Jupiter. *Science*, **204**, 979–982.

Brown, M. E. and Bouchez, A. H. 1997. The response of Jupiter's magnetosphere to an outburst on Io. *Science*, **278**, 268–271.

Brown, R. A. 1974. Optical line emission from Io. In: R. A. Brown (ed.), *Exploration of the Planetary System*. Reidel, Dordrecht, The Netherlands, pp. 527–531.

Brown, R. A. 1976. A model of Jupiter's sulfur nebula. *Ap. J.*, **206**, L179–L183.

Clarke, J. T., D. Grodent, S. W. H. Cowley, E. J. Bunce, P. Zarka, J. E. P. Connerney, T. Satoh. 2004. Jupiter's aurora. In: F. Bagenal, T. E. Dowling, and W. B. McKinnon (eds), *Jupiter: The Planet, Satellites and Magnetosphere*. Cambridge University Press, Cambridge, UK, pp. 537–560.

Delamere, P. A. and F. Bagenal. 2003. Modeling variability of plasma conditions in the Io torus. *J. Geophys. Res.*, **108**, SMP 5–1.

Dessler, A. J. (ed.). 1983. *Physics of the Jovian Magnetosphere*. Cambridge University Press, Cambridge, UK.

Kivelson, M. G., F. Bagenal, W. S. Kurth, F. M. Neubauer, C. Paranicas, and J. Saur. 2004. Magnetospheric interactions with satellites. In: F. Bagenal, T. E. Dowling, and W. B. McKinnon (eds.), *Jupiter: The Planet, Satellites and Magnetosphere*. Cambridge University Press, Cambridge, UK, pp. 513–536.

Krüger, H., M. Horányi, and E. Grün. 2003. Jovian dust streams: Probes of the Io plasma torus. *Geophys. Res. Lett.*, **30**, 1.

Kupo, I., Y. Mekler, and A. Eviatar. 1976. Detection of ionized sulphur in the Jovian magnetosphere. *Astrophys. J.*, **205**, L51–L54.

Mendillo, M., J. Baumgardner, B. Flynn, and J. W. Hughes. 1990. The extended sodium nebula of Jupiter. *Nature*, **348**, 312–314.

Mendillo, M., J. Wilson, J. Spencer, and J. Stansberry. 2004. Io's volcanic control of Jupiter's extended neutral clouds. *Icarus*, **170**, 430–442.

Morabito, L. A., S. P. Synott, P. N. Kupferman, S. A. Collins. 1979. Discovery of currently active extraterrestrial volcanism. *Science*, **204**, 972.

Na, C. Y., L. M. Trafton, E. S. Barker, and A. S. Stern. 1998. A search for new species in Io's extended atmosphere. *Icarus*, **131**, 449–453.

Peale, S. J., P. Cassen, R. T. Reynolds. 1979. Melting of Io by tidal dissipation. *Science*, **203**, 892–894.

Postberg, F., S. Kempf, R. Srama, S. F. Green, J. K. Hillier, N. McBride, and E. Grün. 2006. Composition of jovian dust stream particles. *Icarus*, **183**, 122–134.

Saur, J., F. M. Neubauer, J. E. P. Connerney, P. Zarka, and M. G. Kivelson. 2004. Plasma interaction of Io with its plasma torus. In: F. Bagenal, T. E. Dowling, and W. B. McKinnon (eds), *Jupiter: The planet, Satellites and Magnetosphere*. Cambridge University Press, Cambridge, UK, pp. 537–560.

Saur, J., D. F. Strobel, F. M. Neubauer, and M. E. Summers. 2003. The ion mass loading rate at Io. *Icarus*, **163**, 456–468.

Spencer, J. R. and N. M. Schneider. 1996. Io on the eve of the Galileo Mission. *Annual Review of Earth and Planetary Sciences*, **24**, 125–190.

Steffl, A. J., A. Stewart, F. Ian, and F. Bagenal. 2004a. Cassini UVIS observations of the Io plasma torus. I: Initial results. *Icarus*, **172**, 78–90.

Steffl, A. J., F. Bagenal, A. Stewart, and F. Ian. 2004b. Cassini UVIS observations of the Io plasma torus. II: Radial variations. *Icarus*, **172**, 91–103.

Steffl, A. J., P. A. Delamere, and F. Bagenal. 2006. Cassini UVIS observations of the Io plasma torus. III: Observations of temporal and azimuthal variability. *Icarus*, **180**, 124–140.

Thomas, N., 1993. The variability of the Io plasma torus. *J. Geophys. Res.*, **98**, 18737–18750.

Thomas, N., F. Bagenal, T. W. Hill, and J. K. Wilson. 2004. The Io neutral clouds and plasma torus. In: F. Bagenal, T. E. Dowling, and W. B. McKinnon (eds), *Jupiter: The Planet, Satellites and Magnetosphere*. Cambridge University Press, Cambridge, UK, pp. 561–591.

Trafton L., T. Parkinson, and W. Macy, 1974. The spatial extent of sodium emission around Io. *Ap. J.*, **190**, L85.

12

Outstanding questions and future explorations

Franck Marchis, John R. Spencer, and Rosaly M. C. Lopes

12.1 INTRODUCTION

Although our knowledge of Io had been significantly advanced by several missions (*Pioneer 10* in December 1973, *Pioneer 11* one year later, and especially the *Voyager* twin probes in 1979), the arrival of the *Galileo* spacecraft in 1995 brought unprecedented opportunities to observe Io. *Galileo* orbited the Jovian system for 8 years, obtaining numerous observations of Io in several wavelength ranges (Chapter 3). The study of these data, complemented by recent data from ground-based telescopes and the Hubble Space Telescope (HST), has revolutionized our understanding of the nature of this most exotic moon. The previous chapters have summarized the state of our knowledge of Io, from the interior to the torus, and made clear that many key questions remain unanswered. After the demise of *Galileo*, these questions must be addressed by continuing work on already acquired data, by new ground-based and space telescope observations and, in the future, by new missions to the Jupiter system with dedicated observations of Io. Table 12.1 reviews the capabilities of several facilities (spacecrafts and telescopes) which were used or are in development to study this captivating satellite of Jupiter.

Io is a key target for future exploration. It is a fascinating world in its own right and, as the most dynamic body in the Solar System, this satellite occupies a unique place in planetary science. It is the only place beyond Earth where we can watch active volcanism happen on a large scale. The interconnections between orbit dynamics, interior, tectonics, volcanism, surface chemistry, and atmosphere, and the associated magnetospheric phenomena, can significantly help our understanding of the evolution of planets and satellites. Io is the best target for the study of tidal heating, a process of fundamental importance to the evolution of planetary satellite systems, and one that may greatly expand the habitability zone for extra-terrestrial life. Io's tidal heating is intimately connected to Europa's, which is thought to maintain an ocean of liquid water underneath an icy crust (e.g., Greeley *et al.*, 2004).

Table 12.1. Overview of facilities (spacecraft and telescopes) used or proposed to study Io.

Mission or telescope	Year of fly-by operation (performed or scheduled)	Instruments	Spatial resolution on Io	Main scientific results
Pioneer 10	December 1973	Radio, UV, IR photometers + visible imaging	No images recorded due to radiation	
Pioneer 11	December 1974	Radio, UV, IR photometers + visible imaging	1 visible image (resolution of 376 km) seen from North Pole	Characterization of the surface
Voyager 1	March 1979	IR spectrometer, visible camera (IRIS)	1 km in visible	Discovery of volcanic activity, 9 active centers, surface morphology, plumes
Voyager 2	July 1979	IR spectrometer, visible camera (IRIS)	10 km in visible	Study of 8 eruptions, surface morphology, plumes
Galileo spacecraft	December 1995–September 2003	SSI, NIMS, UVS, PPR, fields and particles (Chapter 3)	7 fly-bys, best visible resolution ~6 m, best IR (NIMS) ~1 km	~160 hot spots detected, plumes, close-up of eruptions, fields and particles data
Cassini spacecraft	January 2001	CIRS, ISS, UVIS, VIMS	60 km in visible	Two giant plumes, aurora, Pele activity
Hubble Space Telescope	Since 1990	UV–visible–NIR camera/spectrometers	~200 km in optical	Plume compositions, surface change
ESO-3.6 m + ADONIS	1996–2001	NIR + Thermal IR camera	~250 km in NIR	Hot spot activity
Keck-10 m + AO	Since 2000	NIR + thermal IR camera + spectro	~100 km in NIR	Hot spot activity and temperature, SO distribution
Gemini + GPI	2010	NIR + thermal IR camera + spectro	65 km in R-band (visible)	Hot spot activity and temperature, surface changes
TMT-30 m	April 2014	Undefined but visible + NIR camera + spectro	40 km in NIR 10 km in visible	Hot spot activity and temperature, surface changes
OWL-100 m	Complete in 2020	Undefined but visible + NIR camera + spectro	10 km in NIR	Hot spot activity and temperature, surface changes and morphology
New Horizon fly-by	February–March 2007	UV, visible, NIR camera + spectro	20 km	High-temperature volcanism, plumes, interaction with magnetosphere, SO emission

Io can help us better understand the early Earth, as Io provides a living example of how a planet responds to high heat flow analogous to the Earth's heat flow at the time life began. Io's prodigious volcanic activity, and possible ultramafic composition of the lavas, give us the opportunity to understand the Earth's early geologic activity. Io also provides an ideal testbed for understanding fundamental atmospheric, planetary escape, and magnetospheric processes.

12.2 OUTSTANDING ISSUES

12.2.1 Interior structure and relationship to the heat flow

What is the composition of the core?

A precise tracking of the *Galileo* spacecraft during its five fly-bys of Io satellite has provided new constraints on its interior. It is now clear that Io is a differentiated body consisting of a metallic core and a silicate mantle (Chapter 5). Gravity measurements, which were successfully collected during four fly-bys (Anderson *et al*., 2001) indicate that Io has a large core (between 0.37 and 0.52 times Io's radius, see Chapter 5), probably made of iron or iron sulfide as predicted by cosmochemical considerations (Consolmagno, 1981). In Chapter 5, the authors discuss the absence of a magnetic field signature, which was not detected even during the late *Galileo* fly-bys a few hundred kilometers above the north and south poles (Kivelson *et al*., 2001; Kivelson *et al*., 2004). This implies that little convection is taking place in the core of the satellite. The composition and origin of the core of Io remains uncertain. Better constraints on core composition will be difficult without *in situ* seismic data, but modeling of the chemistry of Io's volcanic gases can perhaps provide some constraints (Zolotov and Fegley, 2000).

What is Io's total heat flow?

An accurate measurement of the heat flow and its variability with time provides important constraints for the interior of Io. Io's rampant volcanism results from the dissipation of energy produced by tidal and orbital interactions with Jupiter, Europa, and to a lesser extent, Ganymede (Peale *et al*., 1979; Hussmann and Spohn, 2004; see also Chapter 5). Several measurements of Io's heat flow using several techniques and instruments have been published (Matson *et al*., 1981; Veeder *et al*., 1994) yielding a minimum average heat flow of $2.5\,\mathrm{W\,m^{-2}}$. Veeder *et al*. (2004) developed a new model ($3\pm1\,\mathrm{W\,m^{-2}}$) including the surprisingly warm polar regions observed with *Galileo*/photopolarimeter and radiometer (PPR) (Spencer *et al*., 2000), and attributed these to an excess of endogenic heat due to a different style of volcanism at high latitudes (Rathbun *et al*., 2004). However, uncertainties remain and most heat flow estimates are model dependent. To better understand the mechanism of tidal dissipation, the evolution of Io into the Laplace resonance, and its relation with Europa tidal heating, accurate measurements of Io's heat flow and its temporal variation is needed. Though this task can be addressed through improved models and intensive ground-based

observations, these should preferably be combined with spacecraft observations to broaden the wavelength and phase angle coverage.

What is the thickness of the lithosphere?

The thickness of the lithosphere is model dependent and several estimates, ranging from a few km to 100 km, have been proposed (Schubert *et al.*, 2004). However, a lithosphere thickness less than 30 km is inconsistent with the ~10 km heights of mountains on Io (Carr *et al.*, 1998). These mountains are evenly distributed on the surface of Io and most of those imaged by *Galileo* and *Voyager* show tectonic origin (Jaeger *et al.*, 2003). A minimum thickness of 12 km is necessary to form them by compressive stress at the base of the lithosphere, a scenario proposed by Schenk and Bulmer (1998). For a thick lithosphere (>30 km), magma advection is probably the main mechanism for transport of heat across the lithosphere instead of heat conduction. If conduction is negligible, an important consequence is that the remotely measured volcanic heat flows reported previously should therefore correspond to the total heat loss.

The origin of the mountains is still unclear (Chapter 6). Schenk *et al.* (2001) pointed out that if they are considered to be upthrust blocks, the lithosphere should be at least as thick as the tallest mountains (Boösaule Montes has a height of 17.5±3 km). In fact, the lithosphere may not be homogeneous, being thicker, for instance, where the mountains are located. High spatial resolution observations of the morphology of mountains through new spacecraft missions could provide direct information on their formation mechanism and further constraints on the lithospheric thickness.

12.2.2 Nature of the active volcanic centers

How does volcanism operate in extreme environments?

The modeling of eruptions through measurement of their thermal output as a function of wavelength, position, and time (e.g., Davies *et al.*, 2001; Williams *et al.*, 2001; Rathbun *et al.*, 2002) provides constraints on the eruptive centers (such as volumetric eruption rate, composition of the lava, type of volcanism). Similar studies are currently performed to study terrestrial volcanoes from Earth orbit (e.g., Harris *et al.*, 1999). For Earth, the analysis is complicated by the presence of a significant atmosphere and also because of the interaction with volatile elements (i.e., water) present on our planet. For Io the low spatial resolution of most available observations introduces uncertainties in the application of models.

The key to the study of the physical processes controlling volcanism is to separate the influences of magma composition and volatiles, tectono-physical processes (e.g., tidally-induced superheating, mantle plume ascent), and local conditions (e.g., gravity). Because of its low gravity, lack of plate tectonics, high magma temperatures, very low atmospheric pressure, and constant activity, Io provides an end-member example where we can test physical models of silicate volcanism. Observations at greater spatial and temporal resolution would be of great value in testing these models and further constraining eruption parameters.

What is the compositional range of Io's magmas?

Very high magma temperatures measured by *Galileo* at Pillan (Chapter 7) suggest ultramafic compositions, at least for one hot spot. This raises the question of how relatively primitive ultramafic volcanism (typically associated with the ancient Archean (3.8–2.5 Ga) on Earth) could persist on such a dynamically active body as Io where extreme differentiation should be expected (Keszthelyi and McEwen, 1997). Either the current style of volcanic activity is a geologically recent phenomenon (i.e., Io has only recently attained its resonant orbit with resulting tidal heating), or remixing of crustal material back into the mantle has prevented differentiation (see Keszthelyi *et al*. (2004) for one theory). Continued measurements of Io's volcanic thermal emission are needed to determine whether other hot spots exhibit similarly high temperatures that could imply that ultramafic volcanism is widespread. Several similar eruptions characterized by a very high temperature of magma and a brief short life (called Pillanian eruptions, see Chapter 7) have been observed with various techniques, such as Tvashtar with *Galileo* (e.g., Williams *et al*., 2001; Milazzo *et al*., 2005), and Surt with adaptive optics (AO) from the ground (Marchis *et al*., 2002). These eruptions correspond to the outbursts seen by photometric measurements from the ground (Stansberry *et al*., 1997; Howell *et al*., 2001). Because they are extremely bright and energetic, with relatively large areas of hot materials exposed, these eruptions give us the best opportunity to extract magma temperatures through spectroscopic measurements, before a significant amount of cooling has taken place. Such measurements are needed to constrain the composition of the magma that will provide a vital window into Io's interior composition and structure, and to provide an estimate of the highest lava temperatures. These measurements will be a high priority for future spacecraft exploration, though this question can also be addressed from the ground given enough telescope time to allow detection of the brightest and hottest eruptions, which are quite rare.

How do Io's very large volcanoes work?

The most widespread volcanic landforms on Io are paterae, in which eruptions are mostly confined within a caldera-like depression (Radebaugh *et al*., 2001; Lopes *et al*., 2004). A study by Jaeger *et al*. (2003) showed that 41% of the mountains on Io have one or more paterae adjacent to them, indicating a genetic link between mountains and paterae. Since *Voyager*, over 160 active volcanic centers have been observed (Lopes *et al*., 2004). Their distribution suggests the absence of large-scale plate tectonics on Io. At least 45 of these hot spots were seen active more than 4 times. Many highly persistent hot spots are found inside paterae, notably Loki and Pele. How do these eruptions behave? Are they lava lakes, perhaps constantly overturning (e.g., Rathbun *et al*., 2002), or are they temporary lava lakes, formed by a process akin to mid-ocean spreading centers on Earth (Gregg and Lopes, 2004)? How is the magma supplied to replenish these eruptions, which last for years or even decades? The presence of multi-kilometer-high eruption plumes that produce various colored pyroclastic deposits on the surface suggests complex interactions between magma and multiple volatile reservoirs, including sulfur, sulfur dioxide, and possibly halides and

others. Are magma–volatile interactions restricted to the shallow crust, or is there deeper assimilation and injection of volatiles by ascending magmas? Close-up spacecraft observations at ultraviolet, visible, and infrared wavelengths, with much better temporal and spatial coverage than *Galileo*, provide the best way to answer these questions, but continued ground-based monitoring of thermal emissions may also provide valuable insights.

Does sulfur volcanism exist on Io?

Sulfur is widespread on Io's surface, and sulfur flows may have been emplaced at various hot spots such as Ra Patera and Emakong (Chapter 7). Sulfur volcanism may play a secondary but important role in Io's resurfacing, but so far we have no proof that sulfur-dominated volcanic flows exist. This question can probably only be answered by high-resolution spacecraft observations capable of measuring the peak temperatures of active flows, or resolving the likely distinctive morphology of sulfur flows, as it is difficult to distinguish sulfur flows from sulfur-coated silicate flows using reflectance spectroscopy.

12.2.3 Io's young surface

Composition of surface

The composition of Io's surface is still not well understood. SO_2 frost is ubiquitous, covering most of the surface, and identifying other compounds has been difficult given the spatial resolution of the available observations (Chapter 9). The relationship between surface colors and composition is not straightforward, although the distribution of color units was well characterized by *Galileo*'s observations (Geissler *et al*., 1999; see also Chapter 9). Composition of the lavas on Io has only been determined indirectly through temperature and the relative roles of basaltic vs. ultramafic compositions have not been established (Chapter 7). Unfortunately, the near-infrared mapping spectrometer (NIMS) grating stopped moving when the instrument started observing Io at high spatial resolution (Chapter 3), therefore, the opportunity to spectrally characterize different geologic units at high spatial and spectral resolution was lost. New spectroscopic observations from spacecraft are needed to determine the composition of lavas and the detailed distribution of SO_2 and other compounds around Io's hot spots.

Resurfacing rate

Io's prodigious volcanic rate means that, even on timescales of months, surface changes can be identified. The lack of impact craters on the surface has long been attributed to the rapid resurfacing rate, however, the nature of the process is still unknown: does the resurfacing happen mostly because of volcanic products such as lava flows or, as suggested by Geissler *et al*. (2004), are plume deposits largely responsible? The fact that most activity on Io seems to be confined inside paterae, possibly as lava lakes (Lopes *et al*., 2004), and that relatively few large lava flows are

seen on the surface has challenged the early assumption that lavas were responsible for the burial of craters. Temporal observations of Io's activity (plume vs. flows and lava lakes) would better constrain the dominant resurfacing process.

12.2.4 Atmosphere and interaction with Jovian magnetosphere

Plumes: nature and formation

Io's volcanic plumes (Chapter 8) were not well studied by *Galileo*, because the low data rate prevented good spatial and temporal coverage, and only one plume source, Prometheus, was imaged at high enough spatial resolution in daylight to provide detailed insights into the plume generation mechanism. The Prometheus data suggest that the smaller "Prometheus-type" plumes are generated not by direct volcanic venting but by hot lavas volatilizing the SO_2-rich substrate (Kieffer *et al.*, 2000; Milazzo *et al.*, 2001). We do not know if all small plumes are generated this way, and we do not understand how this mechanism generates stable, long-lived, often symmetrical plumes. Additional high-resolution imaging of plume sources from future missions is needed to fully understand them, but in the meantime progress can be made in understanding existing data by the further development of numerical models of plume behavior. More detailed analysis of the composition of Prometheus-type plumes, by spectroscopy from future Earth-orbiting telescopes or missions to the Jupiter system are needed to further constrain the composition of the surface volatiles. The composition of the larger, more variable "Pele-type" plumes, which appear to result from direct volcanic venting, provides information on the chemistry of the magmas with which they have equilibrated in the vent, so these plumes will also be important targets for future compositional studies.

Characterization of the atmosphere

Io's tenuous atmosphere, dominated by sulfur and oxygen compounds, was discovered by *Pioneer 10* spacecraft (Kliore *et al.*, 1974). Since then it has been intensively studied in various wavelength ranges from millimeter to ultraviolet. However, a full atmospheric model, taking into account the full complexity of this atmosphere (including the effect of plasma heating and other factors) is not yet available (Chapter 10) and the atmosphere is still not well understood. We do not yet know whether the atmosphere is primarily supported by sublimation of Sun-warmed surface volatiles, or by volcanic venting, so we do not know whether the atmosphere collapses at night. More data on the variation in atmospheric density with surface location, time of day, and heliocentric distance is needed to answer this basic question. Non-volatile species such as the recently discovered NaCl, which cannot be supported by sublimation, should be tracers of direct volcanic input, allowing us to distinguish volcanic and sublimation sources if we could map atmospheric composition at high spatial resolution. In addition, the atmospheric temperature and its vertical variability is still poorly constrained, complicating reconciliation of the disparate source of data on the atmosphere from ultraviolet, infrared, and millimeter wavelengths.

Plasma transport and formation of the torus

The *Galileo* and *Cassini* fly-bys have provided much new information on the interaction between Io and the Jovian magnetosphere, particularly regarding the flux tube that allows the transfer of charged particles between the two bodies. But we still do not understand how variations in Io's volcanoes control the supply of plasma to the torus, mechanisms of dust formation, or many other details of the flow of matter and energy between Io, Jupiter, and the magnetospheric plasma (see Chapter 11 for more details).

12.3 GROUND-BASED TELESCOPES AND NEAR-EARTH TELESCOPES

Until the arrival of a new mission in the Jovian system with dedicated Io observations, the future exploration of Io and study of its volcanism lies for the next several years largely in the hands of ground-based observers.

12.3.1 The promise of ground-based telescope contributions

With the development of space-borne observatories, the ground-based observations of the Solar System objects have been relegated to a secondary place in the last two decades. Despite the large apertures of the recently developed telescopes, the effect of atmospheric turbulences is still preponderant. The angular resolution on the images is limited to *seeing* (i.e., $\sim 0.7''$ in visible light from a very good site such as on the top of Mauna Kea in Hawaii) quite close to the angular diameter of Io ($\sim 1.2''$) at its opposition. In the near-infrared Io can be routinely resolved by direct imaging with useful spatial resolution approaching $0.3''$ (Spencer *et al.*, 1990). To break this "seeing barrier" and access the diffraction-limited resolutions of current telescopes ($0.040''$ in the near-infrared on a 10-m telescope), several techniques, which take advantage of the development of several technologies, have been developed. The concept of adaptive optics (AO) was proposed by Babcock (1953), but it was necessary to wait until the end of the 1980s before the first prototypes (Starfire and Come-on) were developed independently by several groups based in the U.S.A. and France. The AO systems provide in real time an image with an angular resolution close to the diffraction limit of the telescope. Because of technological limitations, linked to the way the wave front is analyzed, most of the AO systems procure a correction that is partial and slightly variable in time in the near-infrared (1–5 μm). These systems were made available to the astronomical community on 4-m class telescopes less than 10 years ago. Marchis *et al.* (2000, 2001) have used the ADONIS AO system on the 3.6-m ESO (European Southern Observatory) telescope to monitor Io volcanic activity over a period of 4 years at a wavelength of 3.8 μm. The spatial resolution obtained in these observations was $0.15''$, or ~ 500 km on Io. At these long wavelengths, only the brightest hot spots could be seen against the sunlit disk of Io (~ 4 per hemisphere) and the measurement of their individual flux was complicated by the limited angular resolution. With the advent of the 8-m class telescopes, the detectability of hot spots on Io increased drastically. Approximately 5–8 active sources were detected on one

3-μm image using the AO system available on the Keck 10-m telescope which provides an angular resolution of $0.05''$ at 2.2 μm (i.e., 130 km on Io at its opposition). Because the hot spots can be also seen at longer wavelengths (5 μm), their temperature (between 500 and 1,000 K) and emission area can be also estimated (Marchis *et al.*, 2005). Additionally to these faint active centers, Marchis *et al.* (2002, 2005) reports the detection of several active centers at a shorter wavelength range (<2.5 μm) which have higher temperatures ($T > 1{,}300$ K) and are more energetic. Because these hot spots are detected in a large wavelength range (down to 1 μm on several occasions), it has been possible to constrain the type of activity using a basaltic lava cooling model (Davies, 1996). Surt-2001, the largest eruption ever witnessed in the Solar System, was luckily detected by Marchis' group at its beginning in February 2001 with the Keck AO system. The intensity profile indicates the presence of a vigorous, high-temperature volcanic eruption ($T >$1,400 K), consistent with either a basaltic or ultramafic eruption. The type of eruption that produces this thermal signature (Pillanian) is thought to have incandescent fire fountains of molten lava which can be several kilometers high, propelled at great speed out of the ground by expanding gases, accompanied by extensive lava flows on the surface. The integrated thermal output of this eruption was close to the total estimated output of Io ($\sim 10^{14}$ W, Veeder *et al.*, 1994).

Several AO systems are or will be soon available on 8-m-class telescopes (MMT, GranteCan, LBT) and the AO techniques have become more reliable and accessible to a wider community. The extended temporal baseline of ground-based observations is highly complementary to the intensive but short-baseline coverage provided by spacecraft. Current AO systems provide data with the same or better spatial resolution as most of the global *Galileo*/NIMS observations taken during the *Galileo* tour (i.e. ~200–300 km) (Lopes-Gautier *et al.*, 1999; Douté *et al.*, 2001). A new generation of integral field spectrographs is now commissioned on several 8-m-class telescopes, such as SPIFFI for the VLT 8-m telescope and OSIRIS for the Keck 10-m telescope. By obtaining 2-D spatial coverage and spectral coverage simultaneously, they will give the opportunity to record in half an hour a spectral cube of Io's surface with a much better spectral resolution (R = 1,000–10,000) than *Galileo*/NIMS (R ~ 300) between 0.9 and 2.5 μm, helping to characterize the composition of the surface and the active volcanic centers. Moreover, after a radiation-induced anomaly stopped the movement of the grating, NIMS spectral sampling decreased to 12 wavelengths in the 1.0–4.7-μm range (Chapter 3). Despite this limited spectral coverage, Douté *et al.* (2004) obtained high spatial resolution maps of SO_2 abundance on Io's surface and proposed different mechanisms of formation for these areas linked with thermodynamic and volcanic processes. The spatial resolution of the data provided by the ground-based spectro-imager instruments will not be as high as the best regional maps from the *Galileo*/NIMS instrument (~150 km per pixel compared with 7–25 km per pixel) but they will help to better characterize changes in the composition of the surface due to volcanism (plume deposits, lava flow fields), as well as characterizing the temperature of the bright hot spots.

The next generation of AO systems is currently under development. These new "extreme AO" systems, built mostly to image planets around nearby stars, will

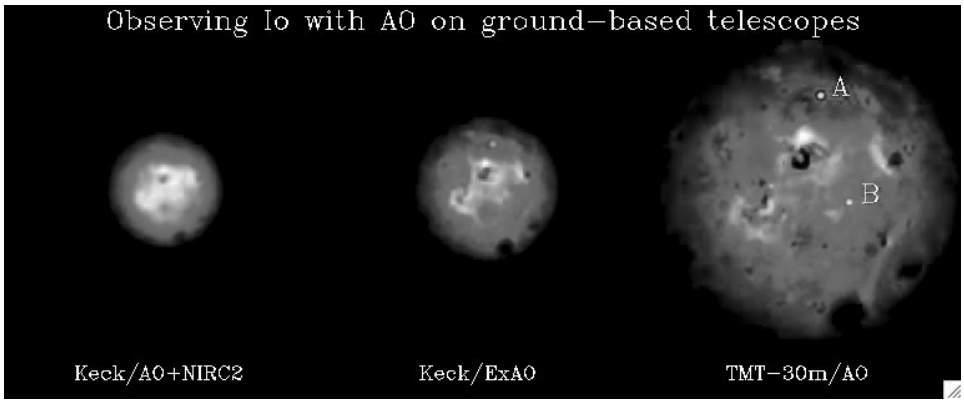

Figure 12.1. Observations of Io in H-band (1.6 μm) with several AO systems. Three AO system performances were simulated. The spatial resolution with the Keck AO is estimated to be 160 km on the center of the disk. An extreme AO system (ExAO) would provide a full correction of the wavefront for such a bright target, providing a sharper image, with a spatial resolution of 120 km on Io. Because of its larger aperture, the spatial resolution of 45 km, attainable on Io with the Thirty Meter Telescope (TMT), would be competitive with most of the global observations recorded by the *Galileo* spacecraft. On rare occasions the thermal output of hot spots is large enough at H-band to be detected in sunlit observations such as these. Thanks to the stability provided by ExAO, hot spot A is detected with this system. Hot spot B, with an intensity 12 times lower than the Keck AO limit of detection is clearly visible in the TMT simulation. More of these high-temperature eruptive centers could be studied with those new instruments helping to better constrain the composition of the magma. No *a posteriori* data processing to enhance the sharpness of the images (such as deconvolution) was applied to these simulations. (See also color section.)

surpass the performance of existing AO systems by two orders of magnitude in contrast – see, for instance, the Gemini Planet Imager instrument for the Gemini telescope (Macintosh *et al.*, 2004). To achieve such nearly perfect and stable correction, the reference targets must be brighter than 8th magnitude in I-band. Extreme AO systems would therefore also have the capabilities to image Io with a quasi-perfect angular resolution (very close to the diffraction limit of the telescope) between 0.6 and 5 μm, corresponding to 45 and 340 km on Io's surface at its opposition. Figure 12.1 illustrates the gain in angular resolution, comparing an extreme AO image taken in H-band (1.6 μm) of Io mounted on the Keck 10-m telescope and the same Jupiter-facing hemisphere observed with the current AO system. In H-band, even after the image was degraded to the resolution provided by the AO system, most of the features detectable are albedo marking such as the dark paterae (Loki patera is discernable at the center of Io) and bright regions covered by SO_2 frost. On rare occasions, when the temperature and surface covered by an active eruption is large enough (typically $T > 1{,}000\,\mathrm{K}$ for $S > 2\,\mathrm{km}^2$), its thermal output is sufficiently contrasted to be detected on the sunlit background. On the initial simulated image, we artificially added an eruption north of Loki (in Amaterasu Patera) with intensity four times lower

than the limit of detection of Keck AO. Because of the better stability of the extreme AO system, this hot spot is detected on the image provided. Therefore, the study of Io's volcanism (monitoring in particular) will benefit from this planet finder instrument. Infrared or laser-guide-star AO systems have the potential to allow diffraction-limited imaging of volcanic thermal emission in Jupiter eclipse, where high-temperature volcanism can be studied without competition from sunlight. The further promise of obtaining high angular resolution images shortward of 1 μm will be crucial to measuring high magma temperatures, and for imaging Io's plumes. Even at 10 μm, a useful spatial resolution of 600 km is possible on 10-m-class telescopes, allowing the major thermal sources to be detected and their contribution to the total output of Io better estimated.

The instruments mounted on a ground-based telescope are not restrained in size and weight as are those on board space vehicles. They can also be easily updated taking advantage of the most recent technology. For instance, high-resolution spectrographs ($R = 50{,}000$) in the mid-infrared (5–25 μm), such as TEXES (the Texas Echelon Cross Echelle Spectrograph; Lacy *et al.*, 2003), can be used to detect molecules in Io's atmosphere (Spencer *et al.*, 2005), and on large telescopes should allow mapping of the spatial distribution of the atmosphere.

Further advances in ground-based astronomy will come with the likely development in the next two decades of giant segmented mirror telescopes (GSMT). Several competitive projects are under study, such as the Thirty Meter Telescope (TMT) which should be built in partnership between the U.S.A. and Canadian institutes (Figure 12.2), the Euro50 (50 m) telescope, a project established between scientists in Finland, Ireland, Spain, Sweden, and the U.K., and finally the OverWhelmingly Large (OWL 100-m) telescope under study by the European Southern Observatory (ESO). The designs, under study, face several major challenges, such as the design of their enclosure, their weight, and their cost. These future telescopes will be equipped with AO systems (Russell *et al.*, 2004) to allow diffraction-limit performances (i.e., they will provide images with an angular resolution up to the milli-arcsec in the optical). On Figure 12.1, a simulated observation with the TMT 30-m of Io's Jupiter-facing hemisphere in H-band is given for comparison. The gain in angular resolution is sufficient to detect small albedo features at a spatial resolution of 30 km at 1 μm. Another hot spot whose intensity on the initial image was chosen to be 12 times lower than the detection limit of the Keck AO is clearly visible between Loki and Pele (labeled B).

12.3.2 Airborne telescopes

The SOFIA airborne observatory (Erickson, 2005) has the potential to make valuable contributions to the study of Io's atmosphere. Among the instruments being developed for SOFIA is EXES, a high-resolution, mid-infrared spectrograph that will be able to detect atmospheric absorptions from SO_2 and other species at wavelengths, such as the 7-μm region, where observations from the ground are difficult due to atmospheric H_2O absorption.

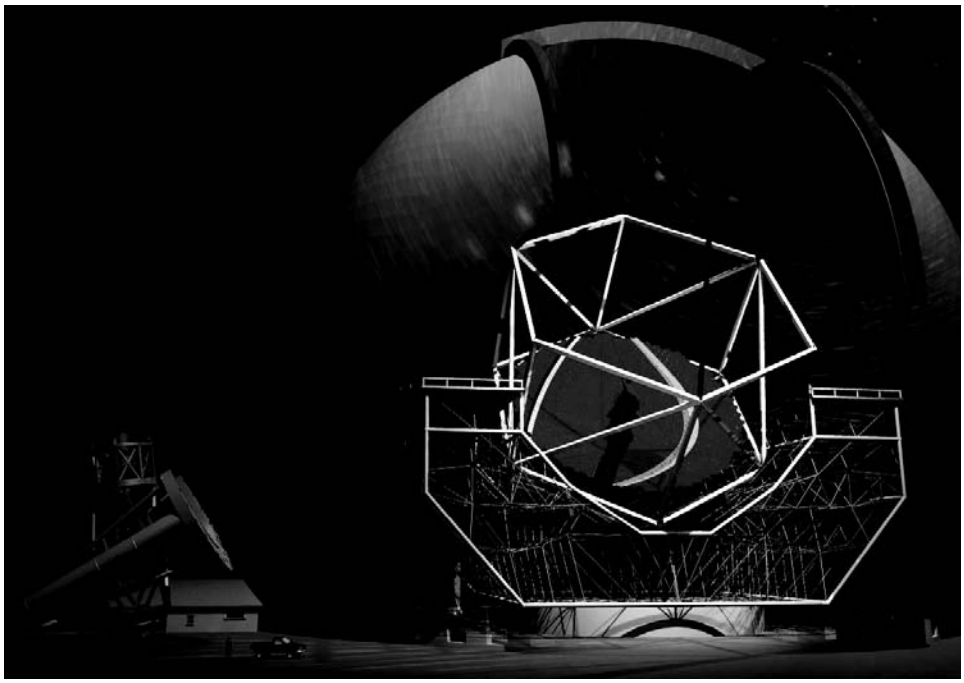

Figure 12.2. Artist's renderings of the TMT and comparison with the Palomar 5-m Hale telescope. This telescope, developed in partnership between the U.S.A. and Canadian institutes should be available in 2014. Because of the large size of its aperture, combined with the capabilities of AO systems, it will provide an unprecedented spatial resolution of Io, better than most of the *Galileo* spacecraft infrared observations (courtesy California Institute of Technology). (See also color section.)

12.3.3 Ultraviolet-dedicated telescopes

The ultraviolet region is largely inaccessible to ground-based observers and has been exploited very recently, mostly with the HST. For instance, the first spectroscopic detection of SO_2 gas (Ballester *et al.*, 1994) in this wavelength range led to numerous works attempting to estimate the distribution of this gas in the thin atmosphere of Io (Jessup *et al.*, 2004 and Chapter 10) and its link with volcanic activity, such as the density of dust particles and gas in the Pele plume. The ultraviolet light is an interesting wavelength range to study the interactions between the surface of Io, its atmosphere, and plasma surrounding the satellite. For instance, far-ultraviolet images of Jupiter from HST reveal polar auroral emissions (Rego *et al.*, 2001), and discrete emission from Io's magnetic footprint (Clarke *et al.*, 2004). Ultraviolet emission of atoms can also be used to detect the neutral cloud made of materials leaving Io (Chapter 11) through several processes. O and S emissions were detected in International Ultraviolet Explorer (IUE) spectra in the corona (at a distance $<500\ R_J$)

and extended clouds, which populates after ionization of the plasma torus. This atmosphere–clouds–plasma–magnetosphere interaction is central to the understanding of the system, but it is as difficult to model as it is to observe (Spencer and Schneider, 1996).

The ultraviolet spectrum shortward of 3,000 Å contains valuable information about Io's atmosphere and its interaction with the Jovian magnetosphere, but can only be observed from space. Io has been explored in this region by a succession of Earth-orbiting spacecraft, particularly the HST, though its ability to study Io in the ultraviolet has been severely hampered by the summer 2004 failure of the Space Telescope imaging spectrograph (STIS), which provided high spatial resolution information (about 20 pixels across Io's disk) on both absorptions by the molecular atmosphere and emission from atomic species. A replacement ultraviolet spectrograph, Cosmic Origins Spectrograph (COS), may be installed on HST if a servicing mission is eventually flown, but its low spatial resolution will limit its capabilities for studying Io. Much more could be done to understand Io's atmosphere and torus interactions with future diffraction-limited ultraviolet telescopes of even modest aperture (1-m aperture could still provide 20 pixels across Io at 2,500 Å), if placed above the Earth's atmosphere and equipped with high-efficiency ultraviolet instrumentation.

12.3.4 James Webb Space Telescope

The James Webb Space Telescope (JWST) is a large infrared-optimized telescope scheduled for launch in August 2013 (Sabelhaus *et al.*, 2005). The telescope will be equipped with a 6.5 m diameter primary mirror providing, therefore, images with an angular resolution no better than the current 10-m class, ground-based telescopes equipped with AO systems. The instrumentation of this ambitious project is limited to the infrared range, since most of the driving scientific themes (the study of galaxies with redshift $z > 1$, imaging of circumstellar disks, ...) mostly rely on this wavelength domain. However, JWST's high sensitivity is not an advantage for such a bright target as Io, and it will not carry instrumentation suitable for study of the atmosphere, for instance, so its usefulness for Io studies is probably limited.

12.4 FUTURE SPACE MISSIONS

Visits of space vehicles into the Jovian system are unfortunately rare. The *Pioneer 10* and *11* mission vehicles were the first spacecraft to ever visit Jupiter in December 1973 and December 1974, but it was only when the spacecraft *Voyager 1* in March 1979 crossed into the Jovian moon system that the volcanic activity of Io was finally revealed (Morabito *et al.*, 1979; see also Chapter 2), opening up a completely new world for planetary scientists. The *Galileo* mission to Jupiter (Chapter 3) was conceived to follow on the study of the Jovian system. The spacecraft arrived in December 1995 and was placed into elongated orbits around Jupiter, which were designed for close-up fly-bys of the Galilean moons. Although several problems

happened during the handful of fly-bys dedicated to Io, the instruments on board the spacecraft obtained unprecedented observations of Io that brought key discoveries, outlined in earlier chapters. The arrival of the *Cassini* mission in December 2000 while *Galileo* was orbiting in the inner part of the Jovian system gave a unique opportunity for multi-spacecraft observations of the Jovian system. However, *Galileo* was fundamentally limited in its ability to characterize Io's dynamic volcanism by its low data rate (i.e., many major eruptions that occurred during the mission were seen only as isolated snapshots). With the demise of the *Galileo* spacecraft in 2003, further observations of Io are restricted to telescopic observations from Earth, apart from observations that will be made from the *New Horizons* spacecraft in early 2007, during its Jupiter fly-by. Even with the fast progress made in the capabilities of ground-based instruments, long-term advances in understanding Io will require additional close-up studies by spacecraft.

12.4.1 *New Horizons* fly-by

The Pluto-bound *New Horizons* spacecraft (e.g., Stern and Spencer, 2003) will fly past Jupiter on 28 February 2007, and will obtain valuable observations of Io (Figure 12.3). Its closest approach distance of 2.2 million kilometers is over four times closer than that of *Cassini*, and its ultraviolet and near-infrared instrumentation surpasses that of both *Galileo* and *Cassini* in several respects. *New Horizons* will obtain global panchromatic imaging of Io with resolution of 20 km or better, to study surface changes since *Galileo*, though color imaging will be restricted to Jupiter-shine imaging of the Jupiter-facing hemisphere due to saturation on the dayside. Volcanic plumes will be inventoried over several orbits, providing time variability information and perhaps revealing correlations with dust streams that may be detected by the *New Horizons* dust instrument. There will also be global 0.8–2.5 μm imaging of nightside volcanic thermal emission with a spatial resolution of better than 200 km, allowing a detailed study of high-temperature volcanic thermal emission. Numerous disk integrated 500–1,800 Å spectra will document the atomic emissions from Io's atmosphere as a function of orbital and magnetospheric longitude, as well as torus emissions. Observations of several Io eclipses will document the response of the ultraviolet atmospheric emissions to eclipse, and will provide unprecedented spatial resolution on the 1.7-μm SO emissions detected in ground-based observations (de Pater *et al.*, 2002).

12.4.2 Future planned missions

Only one Jupiter mission is currently under development – the Juno Jupiter orbiter which is designed for detailed studies of Jupiter's interior, aurorae, and inner magnetosphere. Juno's studies of the Jovian plasma may illuminate some aspects of Io's interaction with the magnetosphere, but Juno will not carry instrumentation for useful observations of Io itself. Various incarnations of a Europa orbiter mission have been studied over the past decade, and such a mission is likely to carry remote-sensing instrumentation that will also provide valuable information on Io, even though

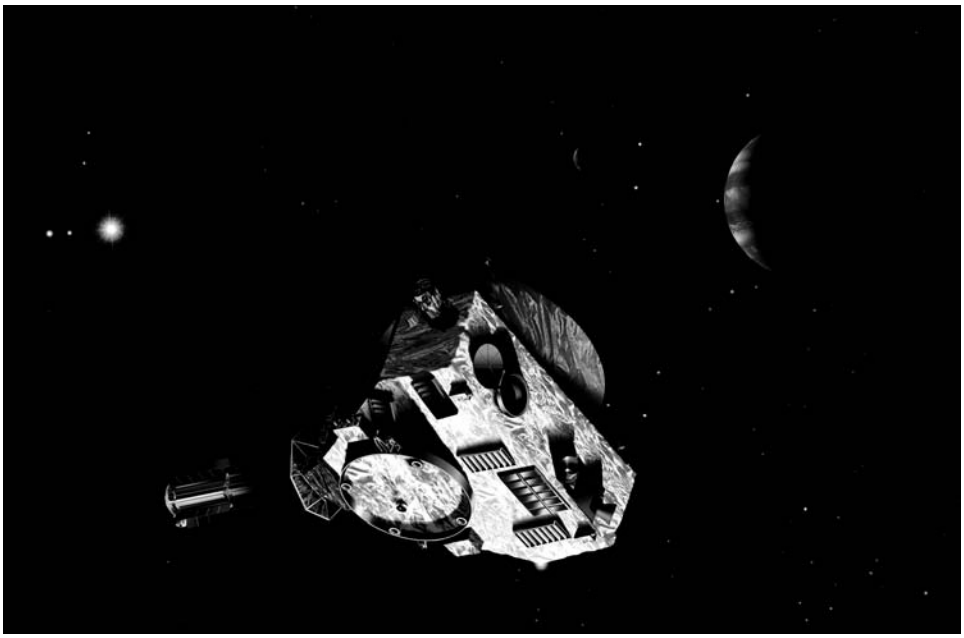

Figure 12.3. Artistic vision of the Pluto-bound *New Horizons* spacecraft flying past the Jovian system at the end of February 2007. Multi-wavelength observations (from ultraviolet to near-infrared) of Io's surface, plumes, and atmosphere will be recorded. (See also color section.)

radiation concerns would probably preclude close approaches to Io. However, until a Europa mission is funded and its payload is chosen, its potential contribution to Io science remains unknown.

12.4.3 A dedicated Io mission?

In 2001, at the request of the U.S. Office of Management and Budget, the National Academy of Sciences commissioned the National Research Council to do a study to assess the highest priority objectives in Solar System exploration for the next decade, 2003–2013. This study published in 2002 and commonly referred to as the Planetary Decadal Survey (Space Studies Board, 2003), solicited input from throughout the planetary science community and the general public. A series of white papers were submitted to the Survey Panel on many of the objects in the Solar System and why they were good candidates for future exploration (Sykes, 2002). One such paper was submitted on the future of Io exploration (Spencer *et al.*, 2002). Though an Io-dedicated spacecraft mission did not make the cut in terms of highest priority missions in the next decade (partly due to engineering and technology development issues), a future Io-dedicated mission was encouraged for the following decade (2013–2023) after certain technologies (e.g., radiation-hardened circuitry, advanced propulsion and communications) are developed for other missions. As we outlined in the Io

white paper (Spencer *et al.*, 2002), we envision a Jovicentric orbiter with an eccentric orbit with a perijove near Io and an orbital period of ~1 month. Based on our experience with *Galileo*, such an orbiter could survive the heavy radiation environment near Io for 4 years or more with ~50 monthly close Io fly-bys. This would enable repeated fly-bys of specific hemispheres or regions of Io with similar lighting geometries to emphasize study of time-variable phenomena, which is necessary for studies of active volcanism. Data downlink and distant observations would occur during more distant parts of the orbit. Useful instruments to be carried on such an orbiter include: ultraviolet spectrometer for atmospheric studies, high-resolution visible camera (1–10 m per pixel local imaging, 100 m per pixel global imaging), 1–5 -μm spectrometer with 1-km resolution, 10 and 20-mm imager with 10-km resolution, laser altimeter, mass spectrometer, and fields and particles instruments (Spencer *et al.*, 2002). Furthermore, the spacecraft would ideally carry several (~3) penetrators with 20-hr or better lifetimes to perform *in situ* studies of Io's surface. These penetrators would carry seismometers to reveal Io's internal structure, mass spectrometers to determine atmospheric composition during descent, and a surface composition instrument package. More limited missions along these lines have been previously proposed to NASA's Discovery Program (i.e., small, focused planetary missions) in the late-1990s/early-2000s (e.g., Smythe *et al.*, 1998; Esper *et al.*, 2003)

12.5 REFERENCES

Anderson, J. D., Jacobson, R. A., Lau, E. L., Moore, W. B., and Schubert, G. 2001. Io's gravity field and interior structure. *Journal of Geophysical Research*, **106**(E12), 32963–32970.

Babcock, H. W. 1953. The possibility of compensating seeing. *PASP* **65**, 229–236.

Ballester, G. E., McGrath, M. A., Strobel, D. F., Zhu, X., Feldman, P. D., and Moos, H. W. 1994. Detection of the SO_2 atmosphere on Io with the Hubble Space Telescope. *Icarus*, **111**(1), 2–17.

Carr, M. H., McEwen, A. S, Howard, K. A., Chuang, F. C., Thomas, P., Schuster, P., Oberst, J., Neukum, G., and Schubert, G. 1998. Mountains and caldera on Io: Possible implication for lithosphere structure and magma generation. *Icarus*, **135**, 146–165.

Clarke, J. T., Grodent, D., Cowley, S. W. H., Bunce, E. J., Zarka, P., Connerney, J. E. P., and Satoh, T. 2004. Jupiter's aurora. In: F. Bagenal, T. E. Dowling, and W. B. McKinnon (eds), *Jupiter: The Planet, Satellites and Magnetosphere* (Cambridge Planetary Science, Vol. 1). Cambridge University Press, Cambridge, UK, pp. 639–670.

Consolmagno, G. J. 1981. Io: Thermal models and chemical evolution. *Icarus*, **47**, 36–45.

Davies, A. G. 1996. Io's volcanism: Thermo-physical models of silicate lava compared with observations of thermal emission. *Icarus*, **124**(1), 45–61; *Journal of Geophysical Research*, **106**(E12), 33079–33104.

Davies, A. G., Kesthelyi, L. P., Williams, D. A., Phillips, C. B., McEwen, A. S., Lopes, R. M. C., Smythe, W. D., Kamp, L. W., Soderblom, L. A., and Carlson, R.W. 2001. Thermal signature, eruption style, and eruption evolution at Pele and Pillan on Io. *Journal of Geophysical Research*, **106**(E12), 33079–33104.

de Pater, I., Roe, H., Graham, J., Strobel, D. F., and Bernath, P. 2002. Detection of the forbidden SO rovibronic transition on Io at 1.7 mm. *Icarus*, **156**(1), 296–301.

Douté, S., Schmitt, B., Lopes-Gautier, R., Carlson, R., Soderblom, L., and Shirley, J. 2001. Mapping SO_2 Frost on Io by modeling of NIMS hyperspectral images. *Icarus*, **149**(1), 107–132.

Douté, S., Lopes, R., Kamp, L. W., Carlson, R., and Schmitt, B. 2004. Geology and activity around volcanoes on Io from the analysis of NIMS spectral images. *Icarus*, **169**(1), 175–196.

Jaeger, W. L., Turtle, E. P., Keszthelyi, L. P., Radebaugh, J., McEwen, A. S., Papallardo, R. T. 2003. Orogenic tectonism on Io. *Journal of Geophysical Research*, **108**(E8), 509, doi:10.1029/2002JE001946.

Jessup, K. L., Spencer, J. R., Ballester, G. E., Howell, R. R., Roesler, F., Vigel, M., and Yelle, R. 2004. The atmospheric signature of Io's Prometheus plume and anti-Jovian hemisphere: Evidence for a sublimation atmosphere. *Icarus*, **169**(1), 197–215.

Erickson, E. F. 2005. The SOFIA program. In: A. Wilson (ed.), *Proceeding of the dusty and molecular universe: A prelude to Herschell and ALMA*. ESA SP-557, The Netherlands, pp. 69–74.

Esper, J., Panetta, P., Coronado, P., Concha, M., Martinez, T., Scott, S., and Soldner, J., 2003. VOLCAN: A mission to explore Jupiter's volcanic moon Io. *Acta Astronautica*, **52**(2–6), 245–251.

Greeley, R., Chyba, C. F., Head, J. W., McCord, T. B., McKinnon, W. B., Pappalardo, R. T., Figueredo, P. H. *et al.* 2004. Geology of Europa. In: F. Bagenal, T. E. Dowling, and W. B. McKinnon (eds), *Jupiter: The Planet, Satellites and Magnetosphere* (Cambridge Planetary Science, Vol. 1). Cambridge University Press, Cambridge, UK, pp. 329–362.

Gregg, T. K. P. and Lopes, R. M. 2004. Lava lakes on Io: New perspectives from modeling. *Lunar and Planetary Science Conference, XXXV*, *Houston, TX, March 2004*.

Geissler, P. E., McEwen, A. S., Keszthelyi, L., Lopes-Gautier, R., Granahan, J., Simonelli, D. P. 1999. Global color variations on Io. *Icarus*, **140**(2), 265–282.

Geissler, P. E., McEwen, A., Phillips, C., Keszthelyi, L., and Spencer, J. 2004. Surface changes on Io during the Galileo mission. *Icarus*, **169**(1), 29–64.

Harris, A. J. L., Wright, R., and Flynn, L. P. 1999. Remote monitoring of Mount Erebus Volcano, Antarctica, using polar orbiters: Progress and prospects. *Int. J. Remote Sensing*, **20**(15, 16), 3051–3071.

Howell, R. R., Spencer, J. R., Goguen, J. D., Marchis, F., Prangé, R., Fusco, T., Blaney, D. L., Veeder, G. J., Rathbun, J. A., Orton, G. S., *et al.* 2001. Ground-based observations of volcanism on Io in 1999 and early 2000. *Journal of Geophysical Research*, **106**(E12), 33129–33140.

Hussmann, H. and Spohn, T. 2004. Thermal-orbital evolution of Io and Europa. *Icarus*, **171**(2), 391–410.

Keszthelyi, L. and McEwen, A. 1997. Magmatic differentiation of Io. *Icarus*, **130**(2), 437–448.

Keszthelyi, L., Jaeger, W. L., Turtle, E. P., Milazzo, M., and Radebaugh, J. (2004) A post-Galileo view of Io's interior. *Icarus*, **169**(1), 271–286.

Kieffer, S. W., Lopes-Gautier, R., McEwen, A. S., Keszthelyi, L., and Carlson, R. 2000. Prometheus, the wanderer. *Science*, **288**, 1204–1208.

Kivelson, M. G., Khurana, K. K., Russell, C. T., Joy, S. P., Volwerk, M., Walker, R. J., Zimmer, C., and Linker, J. A. 2001. Magnetized or unmagnetized: Ambiguity persists following Galileo's encounters with Io in 1999 and 2000. *Journal of Geophysical Research*, **106**(A11), 26121–26136.

Kivelson, M. G., Bagenal, F., Kurth, W. S., Neubauer, F. M., Paranicas, C., Saur, J. 2004. Magnetospheric interactions with satellites. In: F. Bagenal, T. E. Dowling, and W. B. McKinnon (eds), *Jupiter: The Planet, Satellites and Magnetosphere* (Cambridge Planetary Science, Vol. 1). Cambridge University Press, Cambridge, UK, pp. 513–536.

Kliore, A., Cain, D. L., Fjeldbo, G., Seidel, B. L., and Rasool, S. I. 1974. Preliminary results on the atmospheres of Io and Jupiter from the Pioneer 10 S-band occultation experiment. *Science*, **183**(4122), 323–324.

Lacy, J. H., Richter, M. J., Greathouse, T. K., Jaffe, D. T., Zhu, Q., and Knez, C. 2003. TEXES: Sensitive and versatile spectrograph for mid-infrared astronomy. Instrument design and performance for optical/infrared ground-based telescopes (I. Masaroni and A. D. Moorwood, eds). *Proceeding of the SPIE*, **4841**, 1572–1580.

Lopes, R. M. C., Kamp, L. W., Smythe, W. D., Mouginis-Mark, P., Kargel, J., Radebaugh, J., Turtle, E. P., Perry, J., Williams, D. A., Carlson, R. W. *et al.* 2004. Lava lakes on Io: Obervations of Io's volcanic activity from Galileo NIMS during the 2001 fly-bys. *Icarus*, **169**(1), 140–174.

Lopes-Gautier, R., McEwen, A. S., Smythe, W. B., Geissler, P. E., Kamp, L., Davies, A. G., Spencer, J. R., Keszthelyi, L., Carlson, R., Leader, F. E., *et al.* 1999. Active volcanism on Io: Global distribution and variation in activity. *Icarus*, **140**(2), 243–264.

Macintosh, B. A., Bauman, B., Wilhelmsen, E. J., Graham, J. R., Lockwood, C., Poyneer, L., Dillon, D., Gavel, D. T., Green, J. J., Lloyd, J. P. *et al.* 2004. Extreme adaptive optics planet imager: Overview and status, advancements in adaptive optics (D. Bonnacini, B. R. Ellerbroek, and R. Ragazzoni, eds). *Proceeding of the SPIE*, **590**, 359–369.

Marchis, F., Prangé, R., and Christou, J. 2000. Adaptive optics mapping of Io's volcanism in the thermal IR (3.8 μm). *Icarus*, **148**(2), 384–396.

Marchis, F., Prangé, R., and Fusco, T. 2001. A survey of Io's volcanism by adaptive Optics Observations in the 3.8 μm thermal band (1996–1999). *Journal of Geophysical Research*, **106**(E12), 33141–33160.

Marchis , F., de Pater, I., Davies, A. G., Roe, H. G., Fusco, T., Le Mignant, D., Descamps, P., Macintosh, B. A., and Prangé, R. 2002. High-resolution Keck adaptive optics imaging of violent volcanic activity on Io. *Icarus*, **160**(1), 124–131.

Marchis, F., Le Mignant, D., Chaffee, F. H., Davies, A. G., Kwok, S. H., Prangé, R., de Pater, I., Amico, P., Campbell, R., Fusco, T., *et al.* 2005. Keck AO survey of Io global volcanic activity between 2 and 5 mm. *Icarus*, **176**(1), 96–122.

Matson, D. L., Ransford, G. A., and Johnson, T. V. 1981. Heat flow from Io. *Journal of Geophysical Research*, **86**, 1664–1672.

Milazzo, M. P., Kezthelyi, L. P., and McEwen, A. S. 2001. Observations and initial modeling of lava: SO_2 interactions at Prometheus, Io. *Journal of Geophysical Research*, **106**, 33121–33128.

Milazzo, M. P., Keszthelyi, L. P., Radebaugh, J., Davies, A. G., Turtle, E. P., Geissler, P., Klaasen, K. P., Rathbun, J. A., and McEwen, A. S. 2005. Volcanic activity at Tvashtar Catena, Io. *Icarus*, **179**(1), 235–251.

Morabito, L. A., Synnott, S. P., Kupferman, P. N., and Collins, S. A. 1979. Discovery of currently active extraterrestrial volcanism. *Science*, **204**, 972.

Peale, S. J.. Cassen, P., and Reynolds, R. T. 1979. Melting of Io by tidal dissipation. *Science*, **203**, 892–894.

Radebaugh, J., Kesthelyi, L. P., McEwen, A. S., Turtle, E. P., Jaeger, W., Milazzo, M. 2001. Paterae on Io: A new type of volcanic caldera? *Journal of Geophysical Research*, **106**(E12), 33005–33020.

Rathbun, J. A., Spencer, J. R., Davies, A. G., Howell, R. R., and Wilson, L. 2002. Loki, Io: A periodic volcano. *Geophysical Research Letters*, **29**(10), 1443–1447.

Rathbun, J. A., Spencer, J. R., Tamppari, L. K., Martin, T. Z., Barnard, L., and Travis, L. D. 2004. Mapping of Io's thermal radiation by the Galileo photopolarimeter–radiometer (PPR) instrument. *Icarus*, **169**(1), 127–139.

Rego, D., Clark, J. T., Ben Jaffel, L., Ballester, G. E., Prangé, R., and McConnell, J. 2001. The analysis of the H Lyman alpha Emission line profile from Jupiter's aurora. *Icarus*, **150**(2), 234–243.

Russell, A. P., Monnet, G., Quirrenbach, A., Bacon, R., Redfern, M., Andersen, T., Ardeberg, A., Atad-Ettedgui, E., and Hawarden, T. G. 2004. Instruments for a European Extremely Large Telescope: The challenges of designing instruments for 30- to 100-m telescopes. Ground-based instrumentation for astronomy (A. F. Moorwood and I. Masanori, eds). *Proceeding of the SPIE*, **5492**, 1796–1809.

Sabelhaus, P. A., Campbell, D., Clampin, M., Decker, J., Greenhouse, M., Johns, A., Mensel, M., Smith, R., and Sullivan, P. 2005. An overview of the James Webb Space Telescope (JWST) project. UC/Optical/IR Space Telescopes (H. A. MacEwen (ed)). *Proceeding of the SPIE*, **5899**, 241–254.

Schenk, P. M. and Bulmer, M. H. 1998. Origin of mountains on Io by thrust faulting and large-scale mass movements. *Science*, **279**(5356), 1514.

Schenk, P., Hargitai, H., Wilson, R., McEwen, A., and Thomas, P. 2001. The mountains of Io: Global and geological perspectives from Voyager and Galileo. *Journal of Geophysical Research*, **106**(E12), 33201–33222.

Schubert, G., Anderson, J. D., Spohn, T., and McKinnon, W. B. 2004. Interior composition, structure and dynamics of the Galilean satellites. In: F. Bagenal, T. E. Dowling, and W. B. McKinnon (eds), *Jupiter: The Planet, Satellites and Magnetosphere* (Cambridge Planetary Science, Vol. 1). Cambridge University Press, Cambridge, UK, pp. 281–306.

Smythe, W. D., Lopes-Gautier, R., Blaney, D., Davies, A., Delamere, A., Fanale, F., Greeley, R., Johnson, R., Lane, A., Lellouch, E., *et al.* 1998. Getting back to Io. *Third International Conference on Low-Cost Planetary Missions, April 27–May 8, Cal. Institute of Technology*.

Spencer, J. R., Shure, M. A., Ressler, M. E., Sinton, W. M., and Goguen, J. D. 1990. Discovery of hotspots on Io using disk-resolved infrared imaging. *Nature*, **348**, 618–621.

Spencer, J. R. and Schneider, N. M. (1996) Io on the eve of the Galileo Mission. *Annual Review of Earth and Planetary Sciences*, **24**, 125–190.

Spencer, J. R., Rathbun, J. A., Travis, L. D., Tamppari, L. K., Barnard, L., Martin, T. Z., and McEwen, A. S. 2000. Io's thermal emission from the Galileo photopolarimeter–radiometer. *Science*, **288**, 1198–1201.

Spencer, J. R., Bagenal, F., Davies, A. G., de Pater, I., Herbert, F., Howell, R. R., Keszthelyi, L. P., Lopes, R. M. C., McGrath, M. A., Milazzo, M. P. *et al.* 2002. The future of Io exploration. *ASP Conference Proceedings, 272* (M. V. Sykes, ed.). Astronomical Society of the Pacific, San Francisco, pp. 201–216.

Spencer, J. R., Lellouch, E., Richter, M. J., Lopez-Valverde, M. A., Lea Jessup, K., Greathouse, T. K., and Flaud, J.-M. 2005. Mid-infrared detection of large longitudinal asymmetries in Io's SO_2 atmosphere. *Icarus*, **176**(2), 283–304.

Stansberry, J. A., Spencer, J. R., Howell, R. R., Dumas, C., and Vakil, D. 1997. Violent silicate volcanism on Io in 1996. *Geophysical Research Letters*, **24**, 2455.

Stern, A. and Spencer, J. 2003. New Horizons: The first reconnaissance mission to bodies in the Kuiper Belt. *Earth, Moon, and Planets*, **92**(1), 477–482.

Sykes, M.V. 2002. The future of Solar System exploration (2003–2013): Community contributions to the NRC Solar System Exploration Decadal Survey. *ASP Conference Proceedings, 272* (M. V. Sykes, ed.). Astronomical Society of the Pacific, San Francisco.

Veeder, G. J., Matson, D. L., Johnson, T. V., Blaney, D. L., and Goguen, J. D. 1994. Io's heat flow from infrared radiometry: 1983–1993. *Journal of Geophysical Research*. **99**(E8), 17095–17162.

Veeder, G. J., Matson, D. L, Johnson, T. V., Davies, A. G., and Blaney, D. L. 2004. The polar contribution to the heat flow of Io. *Icarus*, **169**(1), 264–270.

Williams, D. A., Davies, A. G, Kesthelyi, L. P., and Greeley, R. 2001. The summer 1997 eruption at Pillan Patera on Io: Implications for ultrabasic lava flow emplacement. *Journal of Geophysical Research*, **106**(E12), 33105–33120.

Zolotov, M. Y. and Fegley, B. 2000. Eruption conditions of Pele volcano on Io inferred from chemistry of its volcanic plume. *Geophysical Research Letters*, **27**(17), 2789–2792.

Appendix 1: Io's hot spots

Rosaly M. C. Lopes, Jani Radebaugh, Melissa Meiner, Jason Perry, and Franck Marchis

Detections of plumes and hot spots by *Galileo*, *Voyager*, HST, and ground-based observations.

Notes and sources

- (N) NICMOS hot spots detected by Goguen *et al*. (1998).
- (D) Hot spots detected by C. Dumas *et al*. in 1997 and/or 1998 (pers. commun.).
- Keck are hot spots detected by de Pater *et al*. (2004) and Marchis *et al*. (2001) from the Keck telescope using Adaptive Optics.
- (V, G, C) indicate *Voyager*, *Galileo*, or *Cassini* detection. Other ground-based hot spots detected by Spencer *et al*. (1997a).
- *Galileo* PPR detections from Spencer *et al*. (2000) and Rathbun *et al*. (2004).
- *Galileo* SSI detections of hot spots, plumes, and surface changes from McEwen *et al*. (1998, 2000), Geissler *et al*. (1999, 2004), Kezthelyi *et al*. (2001), and Turtle *et al*. (2004).
- *Galileo* NIMS detections prior to orbit C30 from Lopes-Gautier *et al*. (1997, 1999, 2000), Lopes *et al*. (2001, 2004), and Williams *et al*. (2004).
- Locations of surface features are approximate center of caldera or feature.

References

de Pater, I., F. Marchis, B. A. Macintosh, H. G. Rose, D. Le Mignant, J. R. Graham, and A. G. Davies. 2004. Keck AO observations of Io in and out of eclipse. *Icarus*, **169**, 250–263.

Goguen, J., A. Lubenow, and A. Storrs. 1998. HST NICMOS images of Io in Jupiter's shadow. *Bull. Am. Astron. Assoc.*, **30**, 1120.

Geissler, P. E., A. S. McEwen, L. Keszthelyi, R. Lopes-Gautier, J. Granahan, and D. P. Simonelli. 1999. Global color variations on Io. *Icarus*, **140**(2), 265–281.

Geissler, P. E., A. McEwen, C. Phillips, L. Keszthelyi, and J. Spencer. 2004. Surface changes on Io during the Galileo mission. *Icarus*, **169**(1), 29–64.

Keszthelyi, L., A. S. McEwen, C. B. Phillips, M. Milazzo, P. Geissler, E. P. Turtle, J. Radebaugh, D. A. Williams, D. P. Simonelli, H. H. Breneman *et al.* 2001. Imaging of volcanic activity on Jupiter's moon Io by Galileo during GEM and GMM. *J. Geophys. Res.*, **106**, 33025–33052.

Lopes-Gautier, R., A. G. Davies, R. Carlson, W. Smythe, L. Kamp, L. Soderblom, F. E. Leader, R. Mehlman, and the Galileo NIMS Team. 1997. Hot spots on Io: Initial results from Galileo's Near Infrared Mapping Spectrometer. *Geophys. Res. Lett.*, **24**(20), 2439–2442.

Lopes-Gautier, R., A. S. McEwen, W. Smythe, P. Geissler, L. Kamp, A. G. Davies, J. R. Spencer, R. Carlson, F. E. Leader, R. Mehlman, L. Soderblom, and the Galileo NIMS and SSI Teams. 1999. Hot Spots on Io: Global distribution and variations in activity. *Icarus*, **140**(2), 243–264.

Lopes-Gautier, R., S. Douté, W. D. Smythe, L. W. Kamp, R. W. Carlson, A. G. Davies, F. E. Leader, A. S. McEwen, P. E. Geissler, S. W. Kieffer *et al.* 2000. A close-up look at Io in the infrared: Results from Galileo's Near-Infrared Mapping Spectrometer. *Science*, **288**, 1201–1204.

Lopes, R., L. W. Kamp, S. Douté, W. D. Smythe, R. W. Carlson, A. S. McEwen, P. E. Geissler, S. W. Kieffer, F. E. Leader, E. Barbinis *et al.* 2001. Io in the near-infrared: NIMS results from the Galileo fly-bys in 1999 and 2000. *J. Geophys. Res.*, **106**(E12), 33053–33078.

Lopes, R., L.W. Kamp, W.D. Smythe, P. Mouginis-Mark, J. Kargel, J. Radebaugh, E. P. Turtle, J. Perry, D.A. Williams, R.W. Carlson, *et al.* 2004. Lava lakes on Io. Observations of Io's volcanic activity from Galileo during the 2001 fly-bys. *Icarus*, **169**(1), 140–174.

Marchis, F., R. Prangé, and T. Fusco. 2001. A survey of Io's volcanism by adaptive optics observations in the 3.8-micron thermal band (1996–1999). *J. Geophys. Res.*, **106**(E12), 33141–33160.

McEwen, A. S., L. Keszthelyi, P. Geissler, D. P. Simonelli, M. H. Carr, T. V. Johnson, K. P. Klaasen, H. H. Breneman, T. J. Jones, and J. M. Kaufman. 1998. Active volcanism on Io as seen by Galileo SSI. *Icarus*, **135**, 181–219.

McEwen, A. S., M. J. S. Belton, H. H. Breneman, S. A. Fagents, P. Geissler, R. Greeley, J. W. Head, W. L. Jaeger, T. V. Johnson, L. Keszthelyi *et al.* 2000. High-resolution views of Jupiter's moon Io. *Science*, **281**, 1193–1198.

Rathbun, J. A., J. R. Spencer, L. K. Tamppari, T. Z. Martin, L. Barnard, and L. D. Travis. 2004. Mapping of Io's thermal radiation by the Galileo photopolarimeter–radiometer (PPR) instrument. *Icarus*, **169**, 127–139.

Spencer, J. R., J. A. Rathbun, L. D. Travis, L. K. Tamppari, L. Barnard, and T. Z. Martin. 2000. Io's thermal emission from the Galileo photopolarimeter–radiometer. *Science*, **288**, 1198–1201.

Turtle, E. P., L. P. Keszthelyi, A. S. McEwen, J. Radebaugh, M. Milazzo, D. P. Simonelli, P. Geissler, D. A. Williams, J. Perry, W. L. Jaeger, K. P. Klaasen, H. H. Breneman, T. Denk, C. B. Phillips, and the Galileo SSI Team. (2004). The final Galileo SSI observations of Io: orbits G28–I33. *Icarus*, **169**, 3–28.

Williams, D. A., E. P. Turtle, L. P. Kezthelyi, W. L. Jaeger, J. Radebaugh, M. P. Milazzo, A. S. McEwen, J. M. Moore, R. M. C. Lopes, and R. Greeley (2004). Geologic mapping of the Culann-Tohil region of Io from Galileo imaging data. *Icarus*, **169**(1), 80–97.

Table A.1. Active volcanic centers on Io.

Volcanic center	Location of candidate surface feature, if known	Detected by *Galileo* SSI?	Detected by *Galileo* NIMS?	Detected by *Galileo* PPR?	Detected by *Voyager* IRIS?	Detected from ground or HST NICMOS?	Plume detected? (*Galileo* = G *Voyager* = V *Cassini* = C)	Surface change detected?	Notes
Ruwa Patera	0.5N, 2.7W	Yes	No	No	No	9812A?	No	No	Faint hot spot detected by SSI in several orbits
Nusku Patera	64.4S, 4.9W	No	No	No	Yes?	Keck (12/2001)	No	No	Detected from Keck (de Pater *et al.*, 2004)
Mbali Patera	31.4S, 6.8W	No	No	No	Yes		No	No	Red deposits
Unnamed (Keck "N")		No	No	No	No	1±1S, 9±1W	No	No	de Pater *et al.* (2004). Possibly part of Karei Complex
Unnamed (Keck "S")	11S, 11W	Yes (11S, 11W)	No	No	No	15±1S, 10±1W	No	No	Detected by SSI in C21 and from Keck (12/2001, de Pater *et al.*, 2004)
Unnamed	2.8S, 13.3W	Yes	No	No	No		No	No	Detected by SSI in several orbits
Unnamed (Keck "U")		No	No	No	No	31±1N, 14±1W	No	No	Detected from Keck (12/2001; de Pater *et al.*, 2004)
Unnamed	11.5S, 14W	Yes	No	No	No	9606C? 9906A?	No	No	Detected by SSI in several orbits
Karei Patera	2N, 16W	Yes	No	No	No	9608A? 9812A?	No	No	Detected by SSI in G8
Unnamed	6S, 19W	Yes	No	No	No		No	No	Detected by SSI in several orbits
Unnamed	1N, 21W	Yes	No	No	No		No	No	Detected by SSI in several orbits
Unnamed	1S, 23W	Yes	No	No	No		No	No	Detected by SSI in several orbits
Unnamed	5N, 23W	Yes	No	No	No		No	No	Detected by SSI in G8
Uta Patera	35.3S, 24.5W	No	No	No	Yes?	9606C? NICMOS 15?, Keck (12/2001)	No	No	Very low albedo Repeated ground-based detections (07/1998 and 12/2001 from Keck, also detected by C. Dumas)
Unnamed	9S, 27W	Maybe	7±3S, 34±3W	No	No		No	No	Faint hot spot in SSI G8, C10, and E15. Detected by NIMS in C30
Unnamed	16.5S, 27.9W	Yes	No	No	No	9606C?	No	No	Detected by SSI in several orbits
Unnamed (N. Polar)	69N, 30W	No	No	No	No	9610A?	No	Yes	N. Polar changes seen by SSI, unclear if location consistent with ground-detected hot spot. Error on ground-observed hot spot ~15 degrees
Kanehekili N and S	16S, 38W	14.5S, 33.4W 17.2S, 35.5W	12±10S, 34±4W	No	No	Numerous ground-based detections N5, Keck (12/2001)	G	Yes	Detected numerous times from the ground and by NIMS. Two active areas (N and S) detected by SSI.

Unnamed (Keck "W")		No	No	No	No	46±1N, 41±3W	No	No	Detected from Keck (12/2001, de Pater *et al.*, 2004)
Janus Patera	3S, 42.5W	Yes	2±3S, 39±3W	No	No	9606A?, N2, D, Keck (12/2001)	No	No	Detected several times from the ground (including by Keck on 12/2001). Detected by NIMS and SSI in several orbits. NIMS C30 data suggests two hot spots, second at 7±3S, 34±3W
Unnamed (Keck "V")		No	No	No	No	34±1N, 51±4W	No	No	Detected from Keck (12/2001, de Pater et al., 2004)
Unnamed	11N, 59W	Yes	No	No	No	990930B?	No	No	Detected by SSI in one orbit (C10)
Masubi	48S, 60W	Yes	45±2S, 56±2W	No	No	9808A?, Keck (12/2001)	V, G	Yes	New plume deposits, hot spot detected by SSI and NIMS in E11, I31. Hot spot detected by J. Spencer on 98/08/29 (faded by 98/08/31). Detected from Keck on 12/2001
Unnamed	60±15N, 60±15W	No	No	No	No	002A, NICMOS 14?	No	No	Detected by J. Spencer and R. Howell at 60±15N, 60±15W
Shamshu	9.8S, 63.6W	No	10±4S, 67±4W	No	No		No	No	
Unnamed (NIMS C30A, "Tejeto")	48.9S, 69.4W	No	49±1S, 68±1W	No	No	9808A? 9509A?	No	No	Possible site of outburst detected on 99/08/02 by R. Howell. Detected by NIMS in orbit C30, I31, I32
Zal Patera	40.5N, 74.9W	Yes	37±3N, 78±3W	No	No		No	Yes	Bright red deposits. Detected by SSI and NIMS in several orbits, including NIMS in I31 and I32
Tawhaki	3.1N, 75.1W	Yes	3±3N, 76±3W	No	No	9908A?	No	No	Detected during several orbits by SSI and NIMS, including by NIMS in I31. Possible site of outburst detected on 99/08/02 by R. Howell. Hot spot detected by NIMS before outburst (C21)
Unnamed		No	37±3S, 79±3W	No	No	Yes?	No	No	Detected by NIMS in E11 and I31
Hi′iaka Patera	3.1S, 79.8W	No	1±4S, 76±4W	No	No	Yes	No	Yes	Detected multiple times from the ground and by NIMS. Plume deposits detected by SSI in 1996/1997

(*continued*)

Table A.1. Active volcanic centers on Io (*cont.*).

Volcanic center	Location of candidate surface feature, if known	Detected by *Galileo* SSI?	Detected by *Galileo* NIMS?	Detected by *Galileo* PPR?	Detected by *Voyager* IRIS?	Detected from ground or HST NICMOS?	Plume detected? (*Galileo* = G *Voyager* = V *Cassini* = C)	Surface change detected?	Notes
Estan Patera (NIMS I31F and I31M)	24.6N, 86.2W	No	21± 2N, 87±2W and 20±1N, 81±1W	No	No		No	No	Detected by NIMS in I31, I32
Unnamed (NIMS 132J)	18.6S, 87.5W	No	19±1S, 87±1W	No	No		No	No	Detected by NIMS in I32. Possibly same as Poliahu hot spot
Ekhi	28.3S, 87.6W	Yes	No	No	No		No	No	Detected by SSI in one orbit (G8)
Gish Bar Patera	15.6N, 89.1W	Yes	16±4N, 89±5W	No	No	9908A?	No	No	Detected by NIMS during several orbits, including I31, I32. Possible site of outburst detected on 99/08/02 by R. Howell. Detected by Keck on 12/2001
Unnamed (NIMS I31E, Aluna Patera)	43.9N, 90.7W	Yes	44±2N, 91±2W	No	No		No	No	Detected by SSI in E15 and by NIMS in I31, I32
Unnamed	37.3S, 91.9W	No	No	No	No	39.6±5.7S, 91.2±5.5W	No	No	Detected by Keck (Marchis *et al.*, 2003)
Unnamed (NIMS 132K)	5.8N, 96.7W	No	7±1N, 95±1W	No	No		No	No	Detected by NIMS in I32
Sigurd Patera	5.9S, 97.4W	No	5±4S, 100±4W	No	No	990930I?, 991124F?	No	No	Detected by NIMS in several orbits, including I31
Itzamna	15.2S, 97.7W	No	15±3S, 97±3W	No	No	990930I?	No	No	Detected by NIMS in C10, I31, I32
Arusha Patera	39S, 100.7W	No	39±2S, 100±2W	No	No	9503A?	No	No	Possible site of outburst detected by J. Spencer in March 1995. Hot spot detected by NIMS in I31, I32
Catha Patera	53.6S, 100.9W	No	53±1S, 105±1W	No	No		No	Yes	Detected by NIMS in C30, I31, I32
Monan Patera	20.3N, 103.8W	Yes	20±1N, 103±1W	No	No		No	Yes?	Detected by NIMS in several orbits, including I31, I32. Detected by SSI in E15. Plume possibly detected by SSI in E4. SSI images suggest 3 main active areas

Unnamed (“Ah Peku Patera”)	10.3N, 106.3W	Yes	9±1N, 105±1W	No	No		No	No	Detected by SSI in orbit E15, by NIMS in I32
Unnamed (NIMS 131D)	Possibly part of Monan Patera complex	No	20±2N, 106±2W	No	No	No	No		Detected by NIMS in I31, near Monan
Altjirra Patera	34.3S, 108.4W	No	35±2S, 108±2W	No	Yes-same as Malik?		No	Yes	Bright red deposits. Detected by NIMS in several orbits, including I31, I32
Unnamed (NIMS I32G)	47.1S, 108.1W	No	48±2S, 109±2W	No	No	No	No	No	Detected by NIMS in orbit I32
Unnamed (NIMS I32F)	69.1S, 108.3W	No	69±2S, 109±2W	No	No	No	No	No	Detected by NIMS in orbit I32
Unnamed (NIMS C30B)	24N, 109W	No	24±1N, 109±1W	No	No	No	No	No	Detected by NIMS in orbit C30
Unnamed (NIMS I27E, NW of Amirani)	31.1N, 115.9W	No	31±0.5N, 117±0.5W	No	No	No	No	No	Detected by NIMS in I27, I31, I32
Amirani	23.2N, 116.3W (location of caldera)	Yes	27±4N, 112±4W (very extended)	No	Yes	Yes	V, G	Yes	Bright red deposits. NIMS detects thermal emission along whole flow. Persistent hot spot detected by NIMS and SSI in several orbits, including NIMS in I31, I32. Detected from Keck in 12/2001
Unnamed (NIMS I31J, in Tvashtar Catena)	59.5N, 117.9W	No	59±1N, 117±1W	No	No	No	No	No	Detected by NIMS in I31. Activity in SW corner of caldera located to the SE of Tvashtar lava fountain site
Dusurra	37.1N, 118.5W	No	39±7N, 125±7W	No	No	No	No	No	Detected by NIMS in orbits C21, I25, I27, I31, I32
Unnamed (NIMS I32M)	40N, 118.6W	No	37±2N, 118±2W	No	No	No	No	No	Detected by NIMS in I31 (fainter), I32
Emakong	3S, 120W	No	3±1S, 119±1W	No	No	No	No	No	Detected by NIMS in orbits I25, I27, I32

(*continued*)

Table A.1. Active volcanic centers on Io (*cont.*).

Volcanic center	Location of candidate surface feature, if known	Detected by *Galileo* SSI?	Detected by *Galileo* NIMS?	Detected by *Galileo* PPR?	Detected by *Voyager* IRIS?	Detected from ground or HST NICMOS?	Plume detected? (*Galileo* = G *Voyager* = V *Cassini* = C)	Surface change detected?	Notes
Tvashtar Catena (Lava fountain site)	61.5N, 120.2W, 62N, 123W	Yes	62±1N, 123±1W	No	No	9911A	No	Yes	Detected by NIMS in I25, I27, G29, I31, I32. Detected by SSI in I25 and G7. Lava fountain seen in I25. Possible site of 990930A and of outbursts in 11/13/00 and 12/16/00
Unnamed (NIMS I31K, in Tvashtar Catena)	60.5N, 120.4W	No	61±1N, 120±1W	No	No	No	No	No	Detected by NIMS in orbit I31 (I31K). Small caldera SE of Tvashtar lava fountain site
Maui Patera	16.2N, 123.8W	No	16.5±1N, 124±1W	No	Yes-same as Amirani?	No	V	Yes?	Voyager plume site was at the end of Amirani flow. Hot spot detected by NIMS in several orbits prior to I27, I31, and I32, but position uncertain
Unnamed (NIMS I31L, NE Tvashtar Catena)	67N, 125W	No	67±1N, 125±1W	No	No	No	No	No	Small caldera to the north-east of Tvashtar, detected by NIMS in I31
Tvashtar Catena (Flow site)	64.8N, 126W	Yes	65±1N, 126±1W	No	No	Yes?	G	Yes	Hot spot detected by SSI in orbits G7, I27. Hot spot detected by NIMS in orbits I27, I31, I32. Plume detected by Cassini 12/200000-01/2001. Hot regions seen in dolphin-shaped flow in caldera
Unnamed (NIMS I31H)	11S, 128W	No	11±1S, 127±1W	No	No	No	No	No	Detected by NIMS in orbits I31, I32
Malik Patera	34S, 129W	No	34±2S, 128±2W	No	Yes	No	No	No	Bright red deposits. Hot spot detected by NIMS in several orbits, including I31, I32
Unnamed (NIMS I27B, "Maju Patera")	19.5N, 131.1W	No	20±1N, 130±1W	No	No	No	No	No	Detected by NIMS in I27, I31, I32
Unnamed (NIMS I31A, "Thor")	39N, 131–135W	No	38±1N, 131±1W, 39±1N, 135±1W	No	No	0108A, Keck 12/20	G	Yes	Large outburst. Hot spot detected by NIMS in I31, I32. Active flow detected by NIMS in I31, I32. Large plume detected by SSI in I31 and I32

Yaw Patera (NIMS Camaxtli C)	9.3N, 132W	No	9.5±1N, 132±1W	No	No	No	No	No	Detected by NIMS in I25, I27, I32
Unnamed (S Seth Patera, NIMS I25B)	2S, 133W	No	5±1S, 132±1W	No	No	991124D?	No	No	Detected by NIMS in I25, I27, C30, I31, I32. Seth Patera is at 2S, 133W
Tien Mu Patera (NIMS Camaxtli east)	12N, 133.9W	No	12±1N, 134±1W	No	No	No	No	No	Detected by NIMS in I24, I27, I31, I32
Camaxtli Patera	15N, 136.4W	Yes	14.5±1N, 136±1W	No	No	No	No	No	Detected in E15 by NIMS, SSI. Detected by NIMS in I24, I27, I32
Unnamed (NIMS I31B)	35.2N, 137.2W	No	35±1N, 137±1W	No	No	No	No	No	Detected by NIMS in I31 and I32, probably related to I31A
Ruaumoko Patera (NIMS Camaxtli West)	14.5N, 139.3W	No	15±1N, 139±1W	No	No	No	No	No	Detected by NIMS in I24 and I27
Unnamed ("Chors Fluctus", NIMS I32H and I)	45S, 140W	No	45±1S, 139±1W	No	No	No	No	No	Detected by NIMS in I32
Tupan Patera	19S, 141W	No	17±1S, 141±1W	No	No	No	No	No	Bright red deposits. Persistent hot spot detected by NIMS in several orbits, including I31, I32. High-resolution NIMS and SSI observations in I32
Unnamed (N. Polar)	66N, 144W	Yes	No	No	No	No	No	No	Detected by SSI in orbit G7
Unnamed (NIMS I24A, near Surya)	22N, 145.6W	No	22±1N, 145±1W	No	No	No	No	No	Detected by NIMS in I24, I27, I31, I32
Cuchi Patera (NIMS I25A)	0.6N, 145.8W	No	2±1S, 144±1W	No	No	No	No	No	Detected by NIMS in I25, I32
Unnamed (NIMS I32C, "Thor Fluctus")	26S, 147W	No	26±1S, 147±1W	No	No	No	No	No	Detected by NIMS in I31 (faint), I32
Arinna Fluctus	32N, 147W	No	30±1N, 147±1W	No	No	No	No	Yes	Extensive, bright red deposits. Detected by NIMS in several orbits, including I31, I32

(*continued*)

Table A.1. Active volcanic centers on Io (*cont.*).

Volcanic center	Location of candidate surface feature, if known	Detected by *Galileo* SSI?	Detected by *Galileo* NIMS?	Detected by *Galileo* PPR?	Detected by *Voyager* IRIS?	Detected from ground or HST NICMOS?	Plume detected? (*Galileo* = G *Voyager* = V *Cassini* = C)	Surface change detected?	Notes
Sobo Fluctus (NIMS I24B)	14N, 150W	No	14±1N, 150±1W	No	No	No	No	No	Detected by NIMS in I24, I27, and I32. Possibly two hot spots detected in I32
Surya (NIMS I27A)	21.3N, 150.9W	No	22±1N, 152±1W	No	No	No	No	Yes	Detected by NIMS in I27. Surface change detected by SSI
Shamash Patera	35S, 152W	No	34±1S, 153±1W 36±1S, 151±1W	No	Yes-same as Malik?	No	No	No	Detected by NIMS in several orbits, including I32, when NIMS detected thermal emission from patera and flow (I31I)
Prometheus Patera	0.5N, 153W	Yes	1±3S, 155±3W	No	No	No	V, G	Yes	Bright red deposits. Volcanic activity along flow. Persistent hot spot detected by NIMS and SSI in several orbits, including I31, I32. Plume moved between *Voyager* and *Galileo*
Chaac	11.8N, 157.2W	No	10N, 157W	No	No	No	No	No	Bright green deposits on caldera floor. Hot spot detected by NIMS in I25 and I27
Radegast Patera	28S, 160W	No	27± 0.5S, 160±0.5W	No	No	No	No	No	Detected by NIMS in I32 – small caldera near Tohil
Culann Patera	19.9S, 161.5W	Yes	18±3S, 163±3W	No	No	No	G	Yes	Bright red deposits. Persistent plume and hot spot. Hot spot detected by NIMS in several orbits, including I32, and by SSI in E11
Tsui Goab Fluctus (NIMS I27D)	0.0, 163.3W	No	0, 164W	No	No	No	No	No	Detected by NIMS in I27 (I27D), I31, I32
Unnamed (NIMS I32E)	65.9S, 168.6W	No	68±1S, 166±1W	No	No	No	No	No	Detected by NIMS in orbits C30 (faint), I32

Michabo Patera (NIMS I31G)	3N, 168.8W	No	2±2S, 169±2W	No	No	No	No	No	Detected by NIMS in orbit I31
Zamama	18N, 174W	Yes	17±2N, 172±2W	No	No	Keck 12/01	G	Yes	Bright red deposits. Detected from Keck 12/2001. Persistent hot spot detected by NIMS and SSI in several orbits, including I32
Unnamed (NIMS I32D)	42S, 175W	No	45±2S, 172±2W	No	No	No	No	No	Detected by NIMS in orbit I32
Aidne Patera	2S, 178W	No	2±3S, 178±3W	No	No	No	No	Yes	Detected by NIMS in several orbits, including I27
Volund	25N, 184.3W	Yes	25±3N, 174±3W	No	Yes	No	V	Yes	Detected by NIMS and SSI. Prometheus-type plume and lava flow
Donar Fluctus	24.3N, 186.2W	Yes	No	No	No	No	No	No	Detected by SSI in E11
Haokah	20.7S, 187W	No	19±3S, 185±3W	No	No	No	No	No	Bright green deposit in SSI images. Hot spot detected by NIMS in E11, E14
Unnamed	28.1N, 192W	Yes	No	No	No	No	No	No	Detected by SSI in G1 and by NIMS in I24
Fo Patera	40.9N, 192.6W	Yes	39±3N, 191±3W	No	No	No	No	Yes	Detected by NIMS and SSI in several orbits
Sethlaus Patera	52S, 194W	No	50±3S, 195±3W	No	No	No	No	No	Red deposits. Hot spot detected by NIMS in several orbits
Unnamed	32N, 199W	No	Yes	No	No	No	No	No	Detected by NIMS in I24
Rata Patera	35.2S, 199.2W	Yes	35±3S, 199±3W	Yes	No	No	No	No	Red deposits. Detected by NIMS in several orbits, by SSI in E11, by PPR in I25, I27, I31, I32
Gabija	51S, 203W	No	52±3S, 204±3W	Yes	No	No	No	No	Hot spot detected by NIMS in E14, I24. Detected by PPR in I25, I27, I31, I32
Lei-Kung Fluctus	38N, 204W	Yes	37±3N, 206±3W	Yes (north and south Lei-Kung)	No	No	No	No	Bright red deposits. Detected by SSI and NIMS in several orbits and by PPR in I27, I31, I32
Unnamed	55S, 206W	No	No	Yes	No	No	No	No	Detected by PPR in I25, I27, I31, I32
Isum Patera-N&S	28N, 209W	32.9N, 204.7W, 30.3N, 206.8W	31±3N, 207±3W	Yes	Yes	9510A?	No	No	Bright red deposits. SSI detected two hot spots, Keck 12/2001. Activity detected by NIMS in several orbits, including I31. Detected by PPR in I27, I31, I32

(*continued*)

Table A.1. Active volcanic centers on Io (*cont.*).

Volcanic center	Location of candidate surface feature, if known	Detected by *Galileo* SSI?	Detected by *Galileo* NIMS?	Detected by *Galileo* PPR?	Detected by *Voyager* IRIS?	Detected from ground or HST NICMOS?	Plume detected? (*Galileo* = G *Voyager* = V *Cassini* = C)	Surface change detected?	Notes
Marduk	28.4S, 209.9W	Yes	27±2S, 211±2W	Yes	Yes	No	V, G	Yes	Bright red deposits. Detected by NIMS and SSI in several orbits, by PPR in I25, I27, I31, I32
Unnamed	65N, 215W	No	No	No	No	No	No	No	Detected by PPR in I25. Possible Lei-Kung source
Ot	0.9S, 217W	No	2±3S, 218±3W	Yes	No	No	No	No	Detected by NIMS in several orbits including I24. Detected by PPR in I25, I27, I31, I32
Unnamed	10.1S, 217.3W	Yes	No	No	No	No	No	No	Detected by SSI in E11
Mulungu Patera	17.2N, 217.5W	Yes	17±3N, 219±3W	Yes (with Susanoo)	No	9510A?	No	No	Detected by NIMS in several orbits, by SSI in G1. Detected by PPR in I25, I27, I31, I32
Kurdalagon Patera	50S, 218.4W	No	47±3S, 219±3W	Yes	No	No	No	No	Red deposits. Detected by NIMS and PPR in several orbits
Susanoo	22.3N, 219.3W	No	21±3N, 222±3W	Yes (with Mulungu)	No	9510A?	No	No	Hot spot detected by NIMS in E14 and I24. Detected by PPR in I25, I27, I31, I32
Unnamed (NIMS I32A)	31N, 222W	No	28±2N, 227±2W	No	No	No	No	No	Detected by NIMS in I32
Unnamed	24S, 224W	No	No	Yes	No	No	No	No	Detected by PPR in I25, I27, I31, I32
Wayland Patera	32.2S, 225.5W	No	33±2S, 223±2W	Yes	No	No	No	No	Hot spot detected by NIMS in E14. Detected by PPR in I25, I27, I31, I32. Detected by *Cassini* ISS on 01/01/01
Unnamed	4S, 233W	No	No	Yes	No	No	No	No	Detected by PPR in I27, I31, I32
Unnamed	28S, 233W	No	No	Yes	No	No	No	No	Detected by PPR in I25, I27, I31, I32
Reiden Patera	13S, 236W	Yes	11±2S, 234±2W	Yes	No	No	No	No	Detected by SSI in G1, by NIMS in I24 and I32, by PPR in I25, I27, I31, I32
Unnamed	49S, 236W	No	No	Yes	No	No	No	No	Detected by PPR in I25, I27, I31, I32
Girru	22.6N, 239.3W	Yes	22±3N, 238±3W	Yes	No	No	No	No	Detected by NIMS in several orbits, by SSI in E11. Detected by PPR in I27, I31, I32

Llew	12.1N, 241.8W	No	10±2N, 240±2W	Yes	No	No	No	No	Detected by NIMS in I32. Detected by PPR in I27, I31, I32
Unnamed	35.6S, 242.5W	Yes	No	No	No	No	No	No	Detected by SSI in E11
Pillan Patera	12S, 244W	9.5S, 242.7W, 11.5S, 242.2W	13±3S, 244±3W	Yes	No	Keck 12/2001	G	Yes	Major eruption in 1997. Plume detected by SSI and HST. Persistent hot spot detected by NIMS since 1996 (G2). Caldera, fissure vent, lava flows identified by SSI
Chors Patera	68.5N, 249.9W	No	No	Yes	No	No	No	No	Detected by PPR in I27, I31, I32
Pyerun Patera	55.4S, 251.1W	No	No	No	yes-same as Mithra?	No	No	No	*Voyager 1* detection
Pele	18.4S, 255.7W	Yes	20±3S, 255±3W	Yes	Yes	No	V, G	Yes	Large, bright red deposits. Plume detected also by HST. Very persistent hot spot detected by NIMS, SSI, and PPR numerous times
Unnamed	37N, 261W	No	No	Yes	No	No	No	No	Detected by PPR in I27, I31, I32
Unnamed	53N, 264W	No	No	Yes	No	No	No	No	Detected by PPR in I27, I31, I32
Svarog Patera	48S, 265.5W	Yes	42±5S, 269±5W	Yes	Yes	Keck, 12/2001	No	No	Detected by NIMS, SSI, and PPR in several orbits
Shakuru Patera	23.1N, 266W	No	No	Yes	Yes-same as Daedalus?	No	No	No	Very low albedo. Detected by PPR in I27, I31, I32
Mithra Patera	58.6S, 266.7W	54.3S, 268.6W	No	Yes	Yes-same as Pyerun?	No	No	No	Red deposits. SSI detected hot spot north of patera. Detected by PPR in I25, I27, I31, I32
Babbar Patera	39.4S, 271.8W	No	37±4S, 283±8W	Yes	Yes	No	No	No	Detected by NIMS in several orbits, by PPR in I25, I27, I31, I32
Daedalus Patera	19N, 274.4W	No	18±3N, 273±3W	Yes	Yes	990929E?, 991030C?, 991125A?, 980905B?, 0112G?	No	Yes	Red deposits. Detected numerous times from ground. Detected as a hot spot by PPR in I25, I27, I31, I32
Unnamed	7S, 277W	No	No	Yes	No	No	No	No	Detected by PPR in I27, I31, I32
Unnamed	13S, 278W	No	No	Yes	No	No	No	No	Detected by PPR in I27, I31, I32
Atar Patera	31N, 278W	No	No	Yes	No	No	No	No	Detected by PPR in I27, I31, I32
Unnamed	49.9N, 278.6	No	No	No	No	Yes, Keck12/2001	No	No	Observed by Keck on 12/2001
Viracocha Patera	61.4S, 281W	No	No	No	Yes	No	No	No	Detected by *Voyager*

(*continued*)

Table A.1. Active volcanic centers on Io (*cont.*).

Volcanic center	Location of candidate surface feature, if known	Detected by *Galileo* SSI?	Detected by *Galileo* NIMS?	Detected by *Galileo* PPR?	Detected by *Voyager* IRIS?	Detected from ground or HST NICMOS?	Plume detected? (*Galileo* = G *Voyager* = V *Cassini* = C)	Surface change detected?	Notes
Ulgen Patera	40.4S, 287.7W	No	41±9S, 291±9W	Yes	Yes	N6?, D?, Keck (12/2001)	No	No	Very low albedo, detected by NIMS in C22. Detected by Keck 12/2001. Detected by PPR in I25, I27, I31, I32
Hephaestus Patera	1.9N, 290.1W	No	No	Yes	No	Keck	No	No	Detected By PPR in I27, I31, I32. Detected from Keck on 12/2001
Lerna Regio	62S, 292W	No	No	Yes	No	No	No	No	Detected by PPR in I25, I27, I31, I32
Vivasvant Patera	75.1N, 295W	No	No	Yes	No	No	No	No	Detected by *Galileo* PPR in I27, I31, I32
Gibil Patera	15S, 295W	No	No	Yes	No	No	No	No	Detected by PPR in I27, I31, I32
Dazhbog Patera	54.3N, 301.1W	No	No	Yes	No	N13, Keck 12/2001	No	Yes	Detected by NICMOS (66.4±8 N, 310.6±14W). Red plume deposits observed by SSI in I31, I32. Hot spot detected by PPR in I25, I27, I31, I32
Rarog	41.4S, 304.9W	No	No	Yes	No	44±1S, 302±2W (Unnamed Keck "I")	No	No	Detected from Keck (12/2001; de Pater *et al.*, 2003). Large patera. Detected by PPR in I25, I27, I31, I32
Sengen Patera	32.5S, 304W	No	No	Yes	No	9506J?, N6?, D?, Keck (12/2001)	No	Yes	Detected by PPR in I25, I27, I31, I32
Unnamed (Keck "M")		No	No	No	No	61±2S, 305±2W	No	No	Detected from Keck (12/2001, de Pater *et al.*, 2003)
Mihr Patera	16.2S, 305.7W	Yes	No	Yes	No	Keck (12/2001)	No	No	Detected by SSI in orbits C9, E11. Detected by PPR in I27, I31, I32
Amaterasu Patera	36.3N, 306.2W	No	40±4N, 309±4W	Yes	Yes	Maybe	No	Yes	Detected by NIMS in several orbits, by PPR in I25, I27, I31, I32
Loki Patera	12.7N, 308.8W	Yes	9±7N, 309±7W	Yes	Yes	Numerous ground-based observations, N1	V	Yes	Detected multiple times from ground and by NIMS. Two plumes observed to the north of caldera by *Voyager*. Hot regions in caldera observed by NIMS and PPR at high resolution (I24, I27, I31 (PPR only), I32)

Aten Patera	48.2S, 310.5W	No	No	Yes	Yes	N9, D?	No	Yes	Pele-type plume deposits, reddish. Detected by PPR in I25, I27, I31, I32
Kinich Ahau	50.4N, 311W	No	No	No	No	N11	No	No	Detected by NICMOS (50.3±5N, 318.8±8W)
Heno Patera	57S, 311W	No	No	Yes	No	No	No	No	Detected by PPR in I25, I27, I31, I32
Mazda Catena	9.4S, 314.9W	No	No	Yes	Yes	9606H?N7?, D?	No	No	Red deposits. Detected by PPR in I27, I31, I32
Nemea	78S, 320W	No	No	No	Yes	No	No	No	
Manua Patera	35.2N, 321.6W	Yes	No	No	No	06/1997?	No	No	Detected by SSI in orbit E6 and by UH AO on 06/97
Argos Planum	47S, 322W	No	No	Yes	No	No	No	No	Detected by PPR in I25, I27, I31, I32
Tol-Ava Patera	2N, 322W	No	No	Yes	No	No	No	No	Detected by PPR in I27, I31, I32
Ra Patera	8.3S, 325.2W	No	No	Yes	No	No	G	Yes	Major brightening and surface change observed by HST between 3/1994 and 3/1995 (Spencer *et al.*, 1997). Plume detected by SSI in orbit G1, E4. Detected by PPR in I25, I27, I31, I32
Unnamed (Keck "L")	Possibly Fuchi or Manua?	No	No	No	No	34±1N, 326±1W	No	No	Detected from Keck (12/2001; de Pater *et al.*, 2003)
Unnamed	40.5S, 326.3W	Yes	36±9S, 324±9W	No	No	9606G?	No?	No	Detected by NIMS in C22. NIMS hot spot could also be from feature at 40.5S, 326.3W
Fuchi Patera	28.3N, 327.7W	Yes	No	Yes	No	9606G?, N4, D, Keck 12/2001	No	No	Red deposits, hot spot detected by SSI in several orbits. Detected by PPR in I27, I31, I32
Huo Shen Patera	15S, 329W	No	No	Yes	No	No	No	Yes	HST changes (Spencer *et al.*, 1997). Detected by PPR in I27, I31, I32
Dongo Patera	16.6N, 332W	Yes	No	No	No	No	No	No	Detected by SSI in orbits C9, E11
Acala Fluctus	11N, 337W	Yes	No	Yes	Yes	N3, D	G	Yes	Detected by SSI in E14, PPR in I27, I31, I32
Surt	44.9N, 337.1W	No	No	No	No	9606E?, N12, 0102A, Keck 12/2001	No	Yes	Pele-type plume deposits observed by *Voyager 2*. Outbursts observed on 02/2001
Creidne Patera	52.4S, 343.2W	No	No	No	Yes	N8?	No	Yes	Tentative identification of hot spot location

(*continued*)

Table A.1. Active volcanic centers on Io (*cont.*).

Volcanic center	Location of candidate surface feature, if known	Detected by *Galileo* SSI?	Detected by *Galileo* NIMS?	Detected by *Galileo* PPR?	Detected by *Voyager* IRIS?	Detected from ground or HST NICMOS?	Plume detected? (*Galileo* = G *Voyager* = V *Cassini* = C)	Surface change detected?	Notes
Unnamed	3.1N, 350.4W	Yes	No	No	No	No	No	No	Detected by SSI in several orbits
Tiermes Patera	22.2N, 350.4W	No	No	Yes	No	9507A	No	No	Detected by PPR in I25, I27, I31, I32
Euboea Fluctus	45S, 352W	No	No	No	No	9606F?, N8?, D?, Keck 12/2001	No	Yes	Pele-type plume deposits, bright red
Unnamed (Keck "R")	Possibly Mama Patera at 10.6S, 356.5W	No	No	No	No	7±1S, 353±3W	No	No	Detected from Keck (12/2001, de Pater et al., 2004)
Unnamed	4.8N, 356.1W	Yes	No	No	No	No	No	No	Detected by SSI in several orbits
Fjorgynn Fluctus	12N, 358W	Maybe (16.0N, 3.8W)	No	No	No	9606D?, N10, D, Keck "N" (9±1N, 1±1W)	No	Yes	Possibly detected by SSI in orbit E15. Detected from Keck (12/2001; de Pater *et al.*, 2004)

Table A.2. Identification of possibly active volcanic centers.

Volcanic center	Location of candidate surface feature, if known	Galileo SSI?NIMS Tentative detection?	Ground-observed? HST NICMOS?	Surface change?	Notes
Unnamed	15.3N, 4.7W	No	9606D?	No	
Cataquil Patera	23.5S, 18.2W	No	9906A?	No	Tentative identification of ground-observed hot spot
Ukko Patera	32N, 20W	No	9508A?	Yes	Surface changes indicate activity
Unnamed	19.4N, 23.3W	No	0011A?	No	Tentative identification of ground-observed hot spot
Unnamed	13.5S, 23.9W	SSI	9606C?	No	Faint spot in SSI G8, E15 images
Lei-Zi Fluctus	14N, 45W	No	No	Yes	New plume deposits detected by SSI in orbit C9
NIMS I32		NIMS at 39±1N, 69±1W	No	No	Possibly detected by NIMS in I32, very faint
Wabasso Patera	55N, 73.8W	No	0011B?	No	Dark patera. May be same hot spot as above
"Poliahu"	19.4S, 81.8W	No	Yes	No	Reported at 22±5S, 79±5W by Goguen *et al.* (1988) as very bright eruption in 1986. Same as I32J?
Shango	31.7N, 99.7W	Yes	No	No	Faint spot in SSI eclipse image
NIMS C30	53S, 148W	NIMS	No	No	Possibly detected by NIMS in C30, very faint
Unnamed	25.7S, 168.2W	SSI at 22S, 168W	No	No	Faint spot detected by SSI in E11
Namarrkun	10.1N, 175.7W	SSI	No	No	Identification based on SSI data
Kami-Nari Patera	8S, 234W		No	Yes	Pillan-type plume deposits detected by SSI in C21, I24
NIMS I32		NIMS at 23±3N, 248±3W	No	No	Possibly detected by NIMS in I32, very faint
Unnamed	38S, 291W	No	No	No	Low albedo and bright red materials
Khalla Patera	5.7N, 303.4W	No	Yes	No	Probably site of hot spots observed by University of Hawaii AO 06/1997
Unnamed	2S, 352W	Yes	Yes?	No	Faint spot in SSI G8 eclipse image. Possibly same as hot spot detected by C. Dumas on 6/3/98 at 6±3S, 358±3W and by Keck (Keck "R")

Appendix 2: Ionian mountains identified to date

Elizabeth P. Turtle, Windy L. Jaeger, and Paul M. Schenk

List of the 135 Ionian mountains positively identified to date, documenting locations, heights, geomorphic classification (tectonic or volcanic), and proximity to paterae (compiled by re-examining and attempting to minimize discrepancies between the lists published in Schenk *et al*., 2001, and Jaeger, 2005). The geographic positions of adjacent paterae are also noted.

Table A.3. Ionian mountains.

Feature name	Mountain position		Height (km)	Tectonic/volcanic (T/V)	Number of paterae in contact with mountain	Patera(e) position(s) (latitude (°), longitude (°))
	Latitude (°)	Longitude (°West)				
	38.2	2.8	4.2	T		
	30.4	7.3	4.8	T	0	
	86.0	8.0	6.1			
	36.6	10.1	8.2	T	1	34.9, 11.9
	−12.5	14.7	9.5	T	0	
	31.2	24.7	6.1			
	−24.0	25.0	6.5	T	1	−21.8, 24.3
	−35.4	25.7	3.0	T		
	−84.9	28.9	1.6			
	−10.4	29.1	3.8	T	1	−13.5, 23.9
Ethiopia Planum	−44.1	30.0	3.0–4.5	T	0	
	35.0	30.1	>8.0	T		
	30.1	31.8	3.9	T	1 (or 2)	29.4, 22.3 (31.5, 34.6)
	−27.2	33.8	3.5–5.0	T		
Pan Mensa	−50.2	34.4	5.0	T	1 (or 2)	−47.5, 37.8 (−51.9, 32.2)
	70.0	36.0	10.7	T		
	−87.4	36.4	1.0–2.9			
	38.7	40.5	3.5	T	0	
	18.3	43.5	5.9	T	0	
	−25.4	43.7	3.5–5.5	T		
	−65.0	43.8			0	
	12.8	46.2	3.9	T		
Haemus Montes	−69.7	47.7	8.4–10.8	T	1	−68.5, 58.2
	69.9	50.6	3.8	T		
	−11.9	55.8			0	
	42.0	57.0	11.2	T	0	

	22.9	59.5	1.8			
	−15.8	60.8	>5.1	T	0	
	63.3	60.9				
	47.8	62.7			0	
	−6.7	63.1	>2.9	T	1	−9.8, 63.6
Mongibello Mons	22.6	66.6	8.6	T	0	
	15.5	67.2	>1.5		0	
	−25.6	68.9				
	39.3	69.8	1.4		0	
Shamshu Mons	−11.3	71.7	2.9	T	0	
Zal Montes	33.8	72.2	7.4	T	1	40.5, 74.9
Hi′iaka Montes	−7.4	78.7	4.3	T	1	−3.1, 79.8
Zal Montes	40.5	79.6	2.5	T	1	40.5, 74.9
Hi′iaka Montes	−9.4	81.6	4.5	T	0	
Hi′iaka Montes	−2.1	82.3	11.1	T	2	−3.1, 79.8; −6.3, 84.1
	25.0	83.3	6.2–6.4	T	0	
	14.2	84.7	3.1–4.0	T	0	
	17.6	86.8	2.4	T	1	15.7, 89.8
Gish Bar Mons	18.9	87.2	9.7–11.0	T	2	21.2, 86.9; 15.6, 89.1
	33.4	91.9			0	
	39.3	93.7	8.2	T	1	38.7, 24.9
Skythia Mons	25.7	98.8	5.5–6.0	T	0	
Monan Mons	15.4	104.0	6.5	T	2	20.3, 103.8; 10.3, 106.3
	−20.4	107.8	4.5	T	0	
	−10.3	113.2	6.0–6.5	T	0	
Tvashtar Mensae	62.1	116.6	2.0	T	1	61.5, 120.2
	54.2	120.0	3.0	T	0	
Telegonus Mensae	−63.8	120.9	2.7–4.0	T	0	
Capaneus Mensa	−16.5	121.1	9.2–9.5	T	0	
Tvashtar Mensae	58.8	122.4	6.0–6.6	T	2	61.5, 120.2; 64.8, 126.0
	−13.0	124.2	5.0	T	0	
	−26.3	124.5	3.9–6.0	T	0	
	45.6	125.9	5.0–7.2	T	1	47.9, 123.5

(*continued*)

Table A.3. Ionian mountains (*cont.*).

Feature name	Mountain position		Height (km)	Tectonic/volcanic (T/V)	Number of paterae in contact with mountain	Patera(e) position(s) (latitude (°), longitude (°))
	Latitude (°)	Longitude (°West)				
Euxine Mons	26.5	126.2	6.0–7.7	T	2	25.6, 124.3; 23.3, 125.1
	14.5	127.2	3.0–3.3	T	1	16.3, 126.1
	−42.5	129.7	3.2–4.5	T	1	−41.6, 137.5
Seth Mons	−10.3	134.0	7.0–7.5	T	0	
	−19.4	148.6	2.0	T	1	−18.7, 150.7
	−37.0	148.7	>3.0	T	1	−35.0, 152.0
	−64.2	157.2	1.7		0	
	28.9	159.5	3.0	T	2	27.5, 157.9; 31.6, 159.1
	−68.2	159.5	1.9–4.8		0	
Tohil Mons	−28.9	160.3	9.0–9.4	T	3	−35, 152; −27, 158; −28, 160
	−60.8	161.6	1.1–2.2			
	47.0	162.0	2.2–5.5	T	0	
Thomagata	25.2	165.5		V	1	25.2, 165.5
	−23.9	171.9	3.9–4.0	T	0	
	16.8	173.7	1.5	V	1	16.8, 173.7
	18.7	174.4	1.5	V	0	
	64.5	174.8	3.5	T		
	−77.7	179.0	2.7	T		
	20.7	188.7	2.4–5.5	T	0	
Dorian Montes	−21.5	193.0	8.5–9.2	T	2	−23.0, 193.9; −20, 194
	59.2	195.5	8.6–11.0	T	1	59.4, 198.6
	−73.1	196.8	7.0–7.3	T		
	73.8	200.5	7.0	T		
	−52.0	200.9	1.7		1	−51, 203
Rata Mons	−35.7	201.3	7.0–8.1	T	1	−35.2, 199.2

Dorian Montes	−26.8	201.8	7.7	T	0	
	−57.1	203.9	1.8		1	−55, 207
	53.0	206.8	9.0	T	0	
	−35.1	210.3	4.5	T	1	−36, 208
	9.2	212.7	>3.3	T	0	
Ot Mons	4.1	215.5	3.6	T	0	
	−27.2	236.0			0	
Ionian Mons	8.6	236.1	12.7	T	0	
Caucasus Mons	−32.2	238.0	10.6	T	0	
Crimea Mons	−75.0	243.4	3.7	T	1	−74.7, 246
Pillan Mons	−7.9	245.5	5.0–5.3	T	0	
	−29.9	245.6	2.0	V	1	−29.9, 245.6
Nemea Planum	−64.8	248.2	2.8–6.0	T	2	−67.2, 242.6; −62.6, 244.4
	−69.9	248.7	1.9		0	
Nile Montes	50.2	249.2	9.0	T	0	
Nile Montes	57.5	253.4	6.5	T	0	
Danube Planum	−21.5	257.6	3.4–5.5	T	2	−18.4, 255.7; −25.2, 257.7
Egypt Mons	−40.2	258.9	10.0	T	0	
	7.8	262.0	4.0	T	0	
Boösaule Montes	−2.2	263.9	7.0	T	0	
	23.6	269.0	7.0–7.2	T	1	23.1, 266
Boösaule Montes	−2.8	269.2	8.5	T	0	
Boösaule Montes	−9.6	272.3	17.5–18.2	T	0	
Silpium Mons	−51.8	273.4	5.5	T	0	
	−31.3	273.6	4.6	T	0	
	−5.4	279.1	4.0	T	1	−6.5, 276.1
	9.2	279.3	4.0	T	0	
	37.8	283.4			0	
	7.0	284.5	4.5	T	0	
Ulgen Montes	−39.1	284.7	4.0–6.0	T	0	
	75.0	287.0	4.2–8.4	T		
	−23.3	295.2	3.9–6.7	T	0	
	−36.3	299.1	3.7	T	0	

(*continued*)

Table A.3. Ionian mountains (*cont.*).

Feature name	Mountain position		Height (km)	Tectonic/volcanic (T/V)	Number of paterae in contact with mountain	Patera(e) position(s) (latitude (°), longitude (°))
	Latitude (°)	Longitude (°West)				
Iynx Mensa	−62.1	304.0	4.5	T	0	
	−44.6	310.1	>1.7		0	
Argos Planum	−47.7	318.3	3.2	T	1	−48.6; 320.1
Carancho Montes	−5.0	318.7	8.1–8.5	T	1	1.9, 322.4
	71.0	320.8	5.4			
	60.5	324.0	4.9	T	0	
	14.8	331.7	4.9– >6.0	T	0	
Iopolis Planum	−34.9	333.1	4.1–4.5	T	0	
	43.7	334.7			1	45.0, 337.1
Euboea Montes	−48.0	336.2	10.3–13.4	T	0	
	56.0	337.0	9.6	T	0	
	1.5	341.2	7.0	T	3	−0.1, 340; 0.7, 341; 0.7, 344
	−24.7	345.1	2.5	T	1 (or 2)	−22.2, 345.4 (−26.6, 343.3)
	1.6	346.9	4.5	T	0	
Euboea Montes	−51.4	348.6	2.5	T	1	−52.4, 343.2
Apis Tholus	−10.9	348.7		V	1	−10.9, 348.7
Inachus Tholus	−15.8	348.8	1.8	V	1	−15.8, 348.8
Echo Mensa	−79.9	355.7	0.7–3.0		0	
Possible mountains	22.4	151.6	>0.8		1	21.1, 151.6
	20.3	157.3	>∼0.9		1	19.4, 158.8
	13.4	160.7			2	11.3; 155.8; 11.8, 157.2
	−1.7	183.7	>∼0.7		0	
	4.6	185.8	>∼0.8		1	6.3, 187.6

Note: Values for longitude increase to the west.

Index

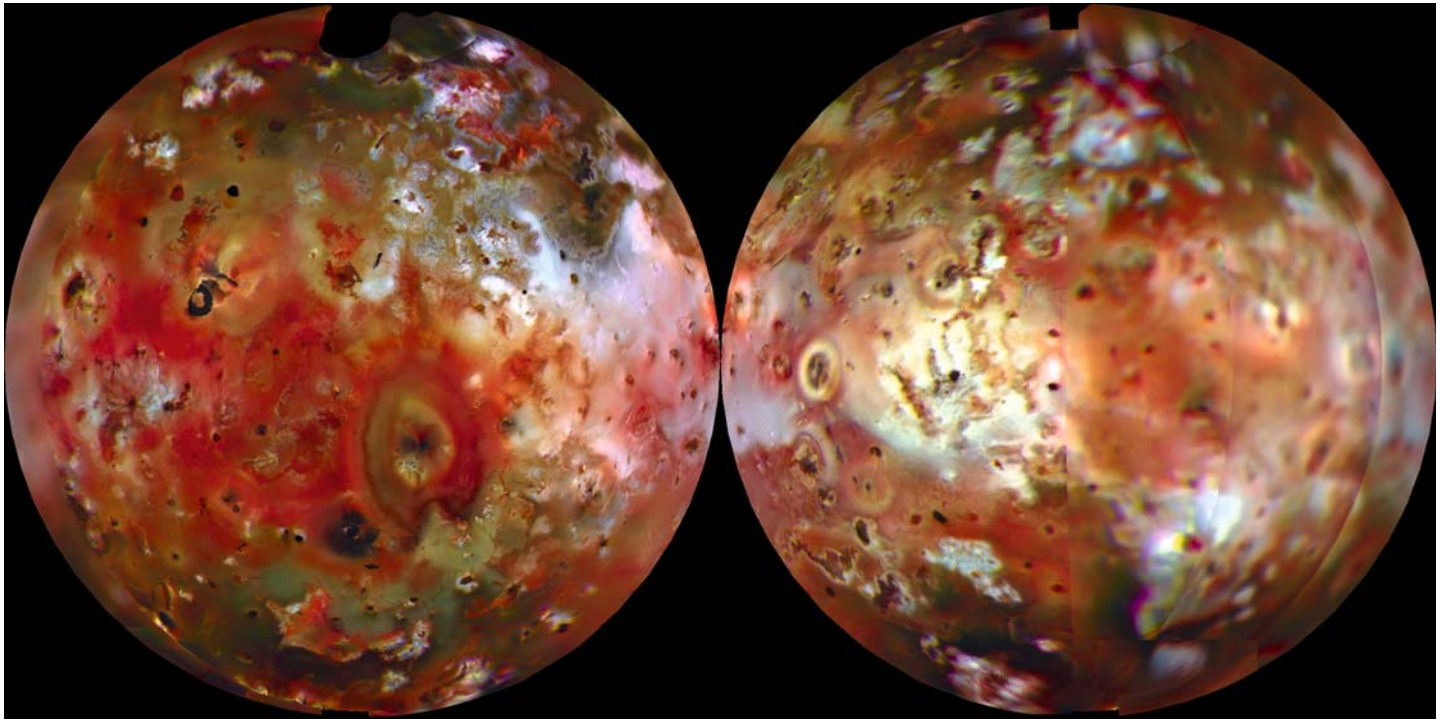

Figure 2.8. Mosaic of two hemispheres of Io from *Voyager* images. The *Voyager* images established that Io was devoid of impact craters and that Io's surface was the youngest in the Solar System. The detection of active volcanism caused a major shift in thinking regarding Io as a member of the outer Solar System of bodies. (Source: NASA Planetary Photojournal, image PIA00318.)

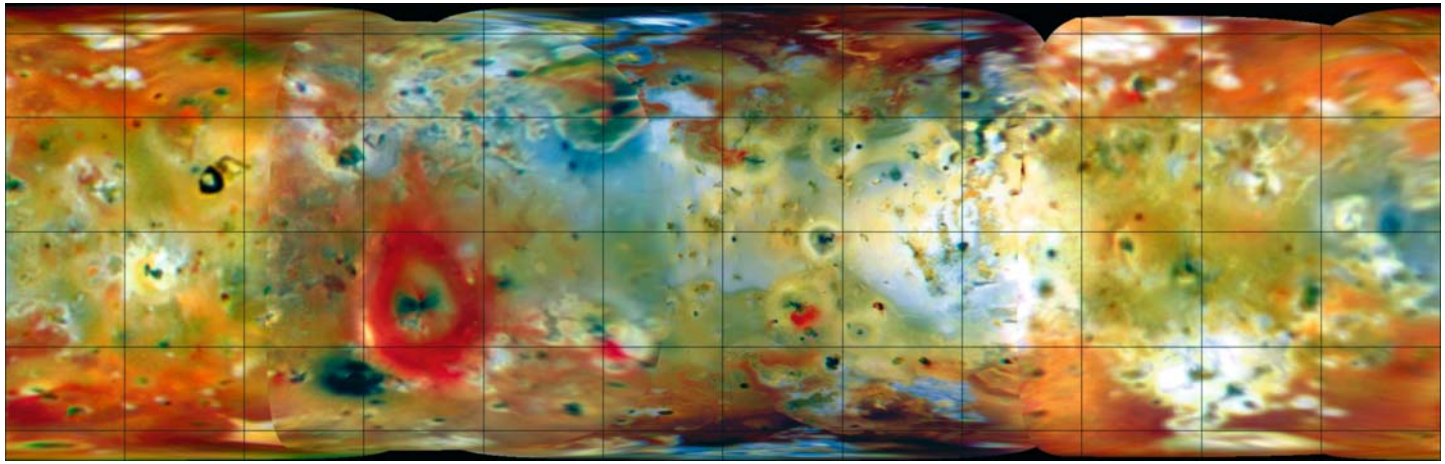

Figure 3.2. Color mosaic of images taken during the 1st and 2nd orbits during the *Galileo* nominal mission. A grid was overlain with 30° by 30° spacing. Numerous changes were observed between *Voyager* and *Galileo* but the overall pattern of volcanic centers and overall color variation was still recognizable, indicating that surface changes were limited to the area around volcanic centers that repeatedly erupted (NASA press release image PIA00585).

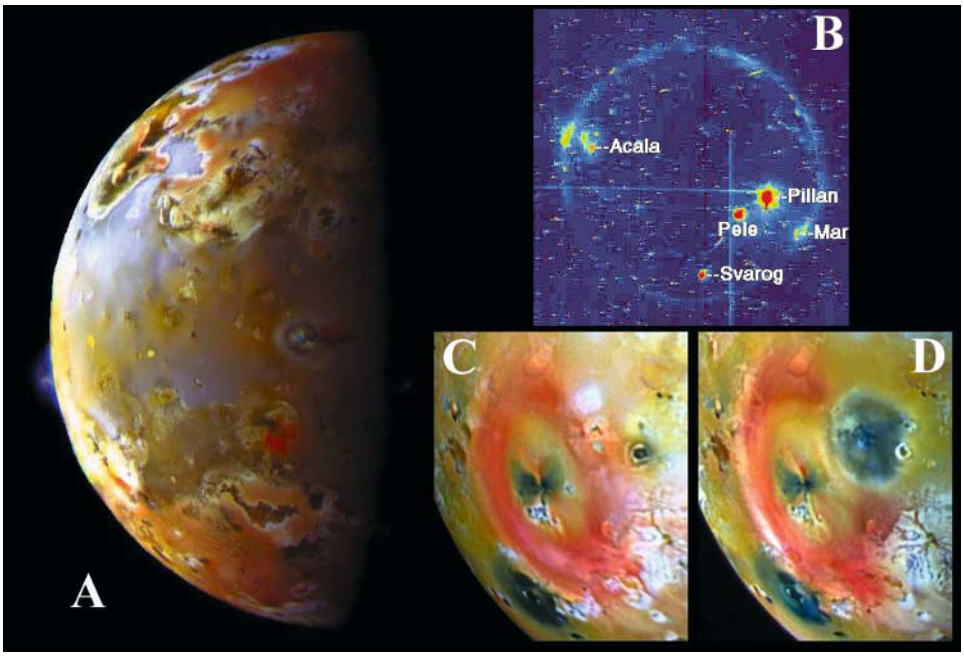

Figure 3.3. Several views of the summer 1997 eruption of Pillan Patera. North is up in all panels. (A) Shows a moderate phase angle image taken during orbit 9 (C9), showing the plume over Pillan at the limb. This observation was taken from a distance of 600,000 km and has a resolution of 6 km per pixel. (B) Shows an eclipse observations from orbit 9 showing the intensity of the Pillan eruption at the time. That observation was taken from a distance of 1.46 million kilometers and has a resolution of 14.6 km per pixel. The image has been color-coded for intensity, with red being the most intense signal. Both (C) and (D) show the aftermath of the Pillan eruption, with a new dark deposit surrounding Pillan Patera in (D). Pele and the ring that surrounds it can be seen to the south-east of Pillan. (C) Was taken during orbit 7 in April 1997 from a distance of 563,000 km, and has a resolution of 5.63 km per pixel. (D) was taken during orbit 9 in September 1997 from a distance of 506,000 km, and has a resolution of 5.06 km per pixel (NASA press release images PIA00703, PIA01635, PIA00744).

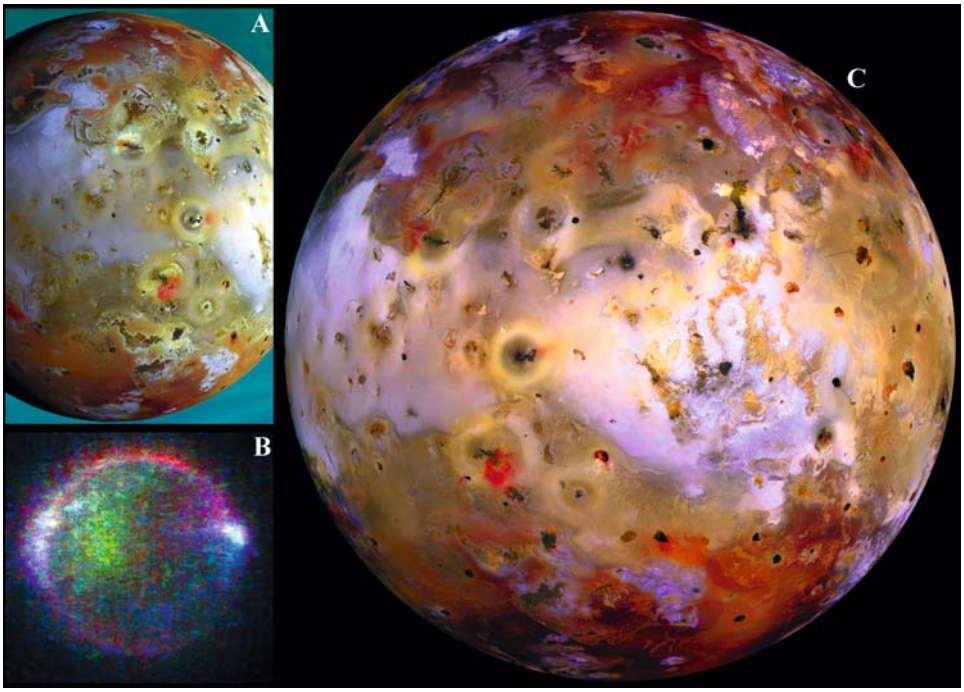

Figure 3.4. Imaging highlights from the Europa and perijove reduction phases of the GEM. (A) A mosaic of two, three-color frames showing the anti-Jovian hemisphere, taken during orbit 14 from a distance of 290,000 km with a resolution of 2.9 km per pixel. (B) A three-color observation of Io during eclipse. The faint red glows represent emissions from atomic oxygen and green glows from atomic sodium, while the bright blue emissions near the equator are likely due to electron impacts on SO_2. Image (B) was taken during orbit 15 from a distance of 1.4 million km and has a resolution of 14 km per pixel. (C) A large, three-color, 16-frame mosaic taken during orbit 21. This mosaic represents the highest resolution view of Io by *Galileo* prior to the Io-targeted encounters later in the mission. The images in this mosaic were taken from a distance of 130,000 km and have a resolution of 1.3 km per pixel (NASA press release images PIA01604, PIA01637, PIA02309).

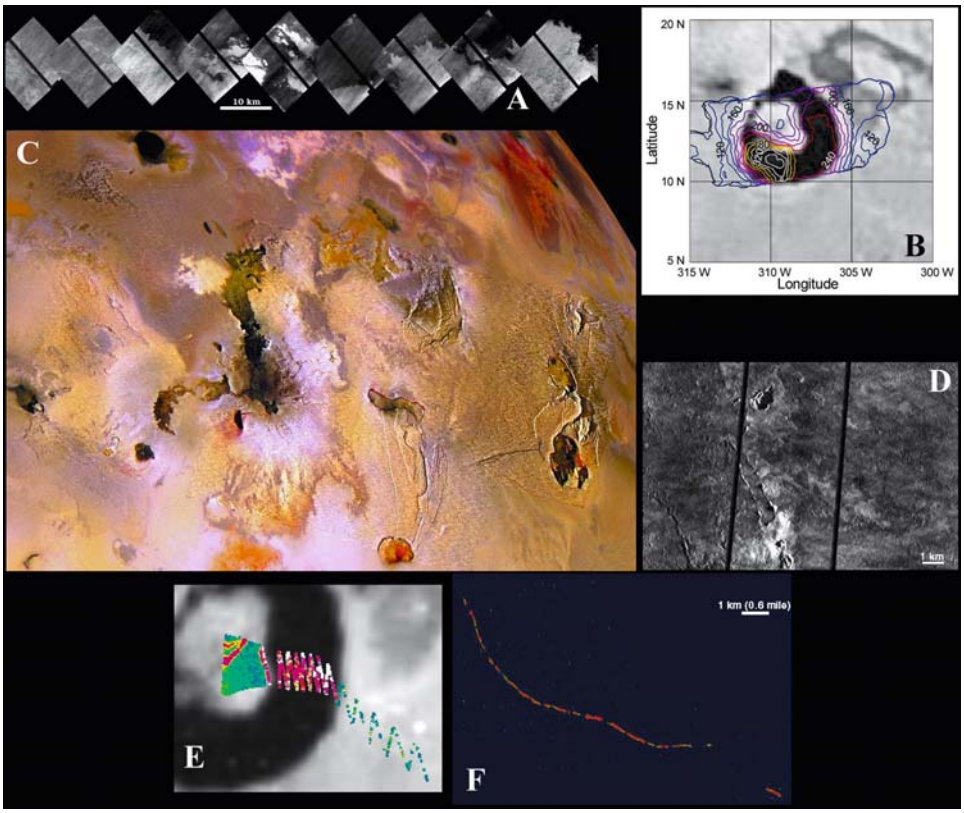

Figure 3.5. Highlights from the I24 fly-by of Io. (A) The ZAMAMA01 observation from I24. (B) Temperature map of Loki Patera taken by the PPR instrument. (C) AMSKIGI01 observation merged with color from orbit 21. (D) Portion of the PILLAN01 observation showing pits and rafted plates within the Pillan flow field. (E) NIMS observation of Loki Patera from shortly before the closest approach. (F) PELE_01 observation with a string of hot spots marking the margin of the Pele lava lake (NASA press release images PIA02537, PIA02524, PIA02526, PIA02536, PIA02514, PIA02511).

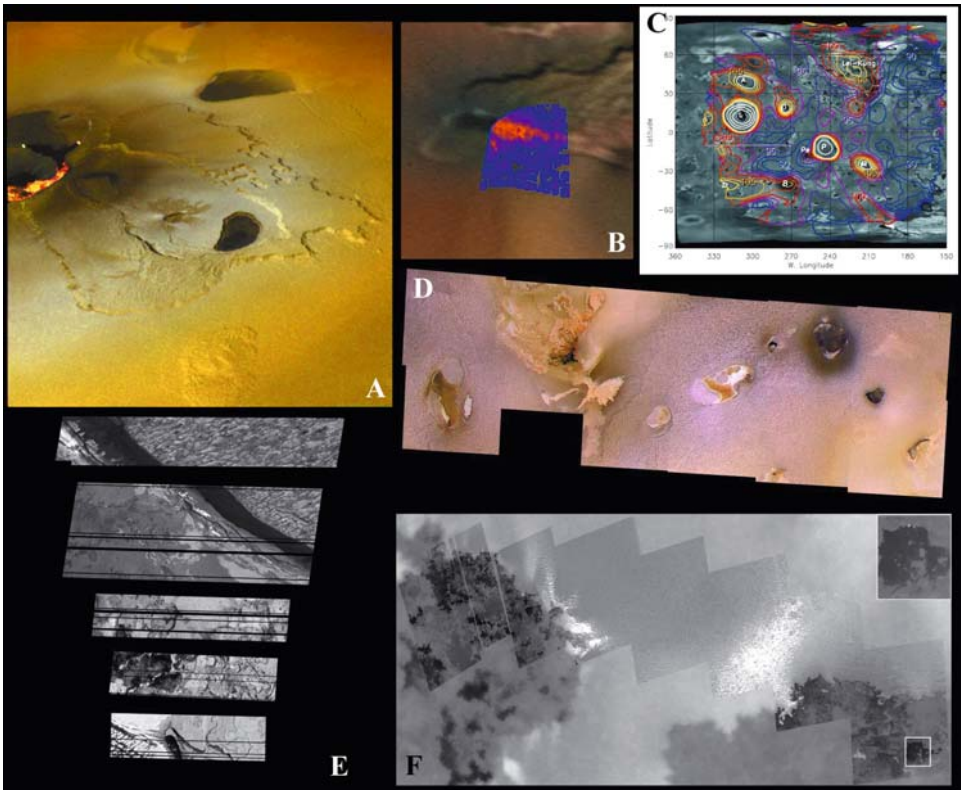

Figure 3.7. Highlights from the I27 fly-by. (A) False-color view of Tvashtar Paterae from the TVASHT01 observation. (B) NIMS observation of the Pele caldera overlain on a false-color image from *Voyager 1*. (C) Map of night-time temperatures of Io's trailing hemisphere taken by the PPR instrument. (D) CAMAXT01 observation merged with color from orbit 21. (E) Partial frames from the CHAAC01 observation. Frames showing the north-east margin of Chaac Patera are see at the top while frames showing the floor and the south-west margin are seen at the bottom. (F) PROMTH01 observation. A dark flow with two spots of incandescent lava is highlighted to the right (NASA press release images PIA02550, PIA02560, PIA02548, PIA02566, PIA02551, PIA02564).

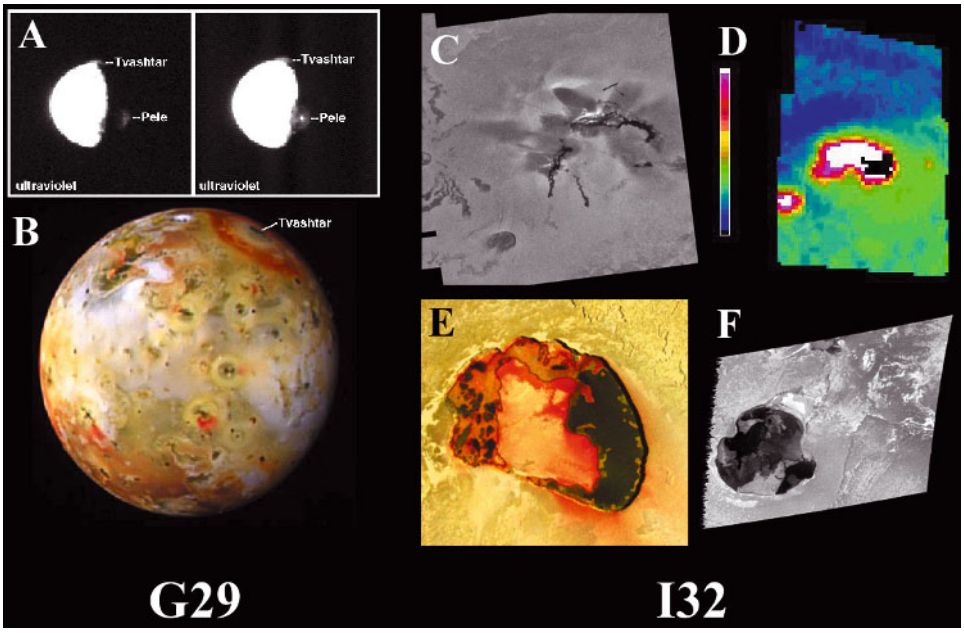

Figure 3.8. Highlights from orbit 29 and I32. Both (A) and (B) highlight a new eruption at Tvashtar observed during late 2000. The two figures in (A), enhanced images from the *Cassini* spacecraft, show a 385 km tall plume over Tvashtar as well as the plume over Pele. As seen in (B) from *Galileo*, both plumes have formed large red ring deposits. Panels (C–F) show highlights from the I32 fly-by. Both (C) and (D) show a new eruption at Thor, first seen by NIMS during I31 and in distant observations from the same orbit. Image (C) is taken from the TERMIN02 observation while (D) is a 13–16 km per pixel observation from NIMS. (E) Color observation of Tupan Patera, from the observation TUPAN_01. (F) Frame from the observation GSHBAR01, revealing fresh lava flows on its surface.

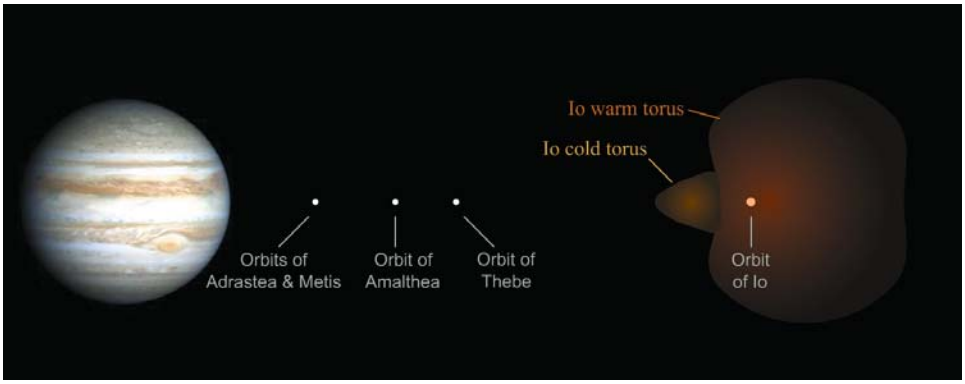

Figure 3.9. This figure illustrates both the warm and cold torus of Io. The *Galileo* spacecraft was able to sample the cold torus on the 34th orbit of Jupiter just before its final trajectory loop around Jupiter on J35. Courtesy Windows to the Universe *www.windows.ucar.edu* A34 Interactive Graphic.

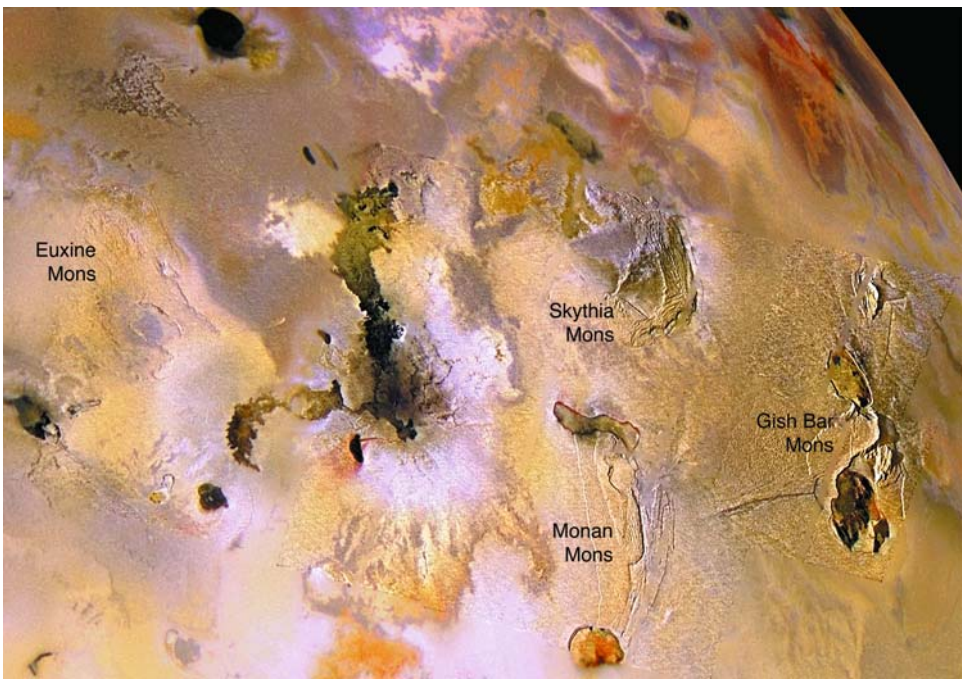

Figure 6.1. This moderate-resolution, ~500 m per pixel, regional mosaic combined with lower resolution, 1.3 km per pixel, color images acquired by *Galileo* includes several examples of Ionian mountains and volcanic centers. The mountains are isolated from each other, but a high fraction of those in this region are associated with paterae. The illumination, which is from the left, accentuates the topography and surface textures. This effect is strongest on the eastern side where the solar incidence angle is 21–28° and weakens toward the west where the Sun is higher, solar incidence angle ~37–45°: compare the visibility of ~10 km high Gish Bar Mons, between Gish Bar Patera to the south and Estan Patera to the north; ~6 km high Monan Mons, between Monan Patera to the north and Ah Peku Patera to the south; and ~7 km high Euxine Mons.

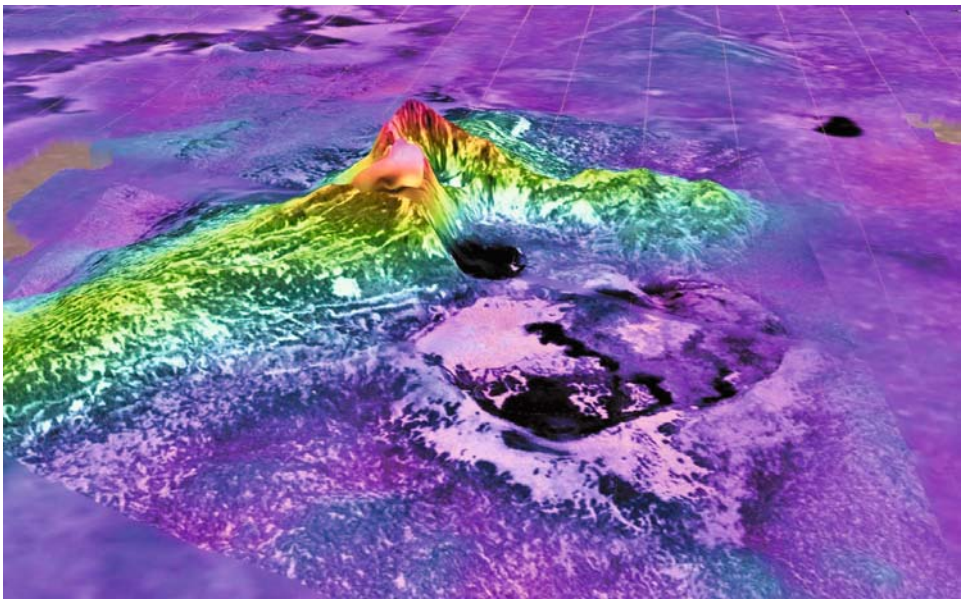

Figure 6.4. Perspective view of Tohil Mons looking south-west. Color-coding represents topography (red is high). Topography is derived from stereo analysis by P. Schenk. Tohil Mons is comprised of several parts, including a broad lineated plateau to the east (left in this view) truncated by a small dark patera (center), and a circular, faulted plateau to the north-west (right). Each plateau is 3–5 km high, and between them lies a circular amphitheater with a crest rising 8 km above the surrounding plains. Vertical exaggeration is a factor of $\sim$25.

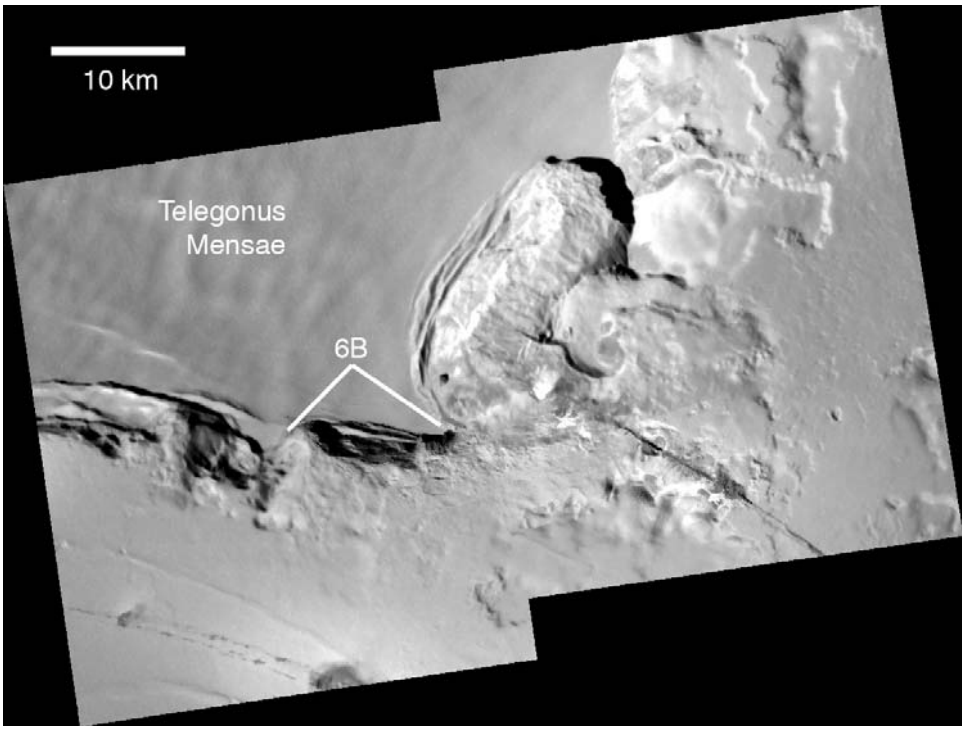

(A)

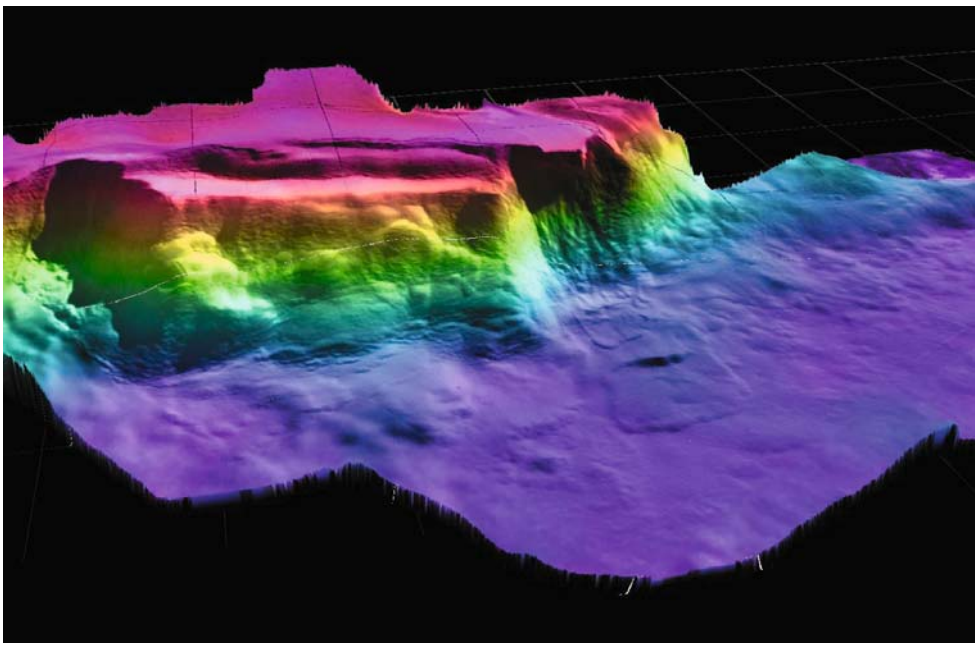

(B)

Figure 6.6. (A) High-resolution (42 m per pixel) mosaic of the south-eastern margin of Telegonus Mensae. The label 6B indicates the section of the scarp illustrated in (B). Illumination is from the upper right. (B) Perspective view of southern scarp of Telegonus Mensae looking north. Color-coding represents topography (red is high); total relief is ~1.5 km. Topography is derived from stereo analysis by P. Schenk. A small (~4 km long, ~2 km wide), low (~100 m) landslide is evident at center right. Note the wrinkled appearance of the scarp and terrace face, suggesting down-slope creep of surface material. Vertical exaggeration is a factor of ~50.

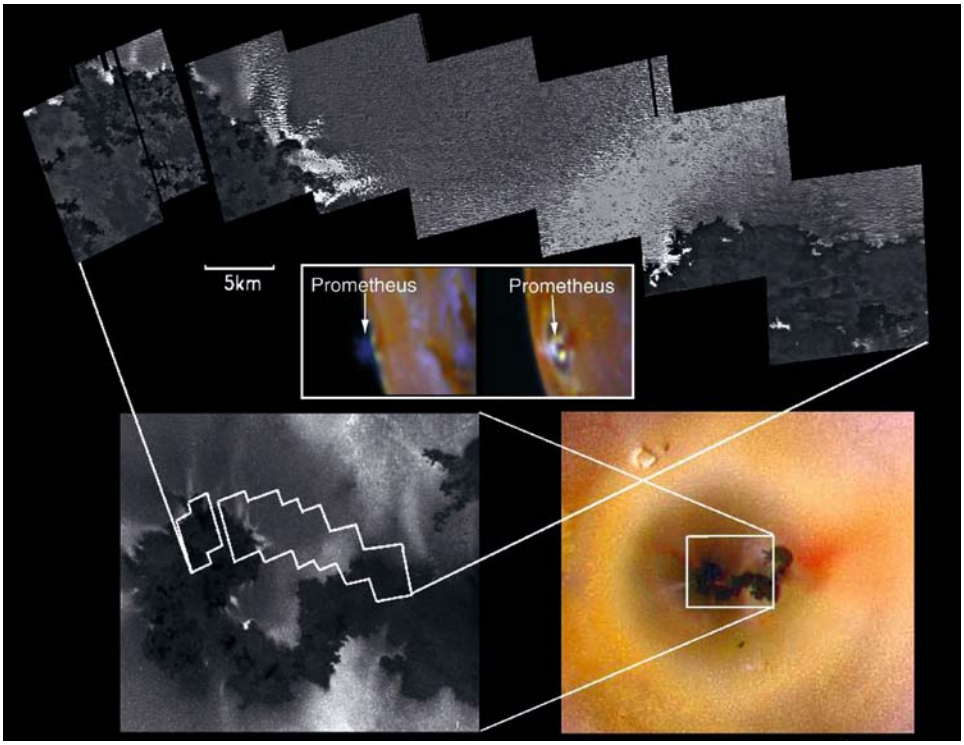

Figure 7.2. A montage of *Galileo* SSI images of the Prometheus volcano at several different resolutions, which identify various aspects of the flow-dominated eruption style. These eruptions produce compound silicate flow fields that are slowly emplaced over months to years, with measured temperatures consistent with terrestrial basaltic volcanism (Keszthelyi *et al*., 2001). Note the small dark patches in the flow field indicative of recent breakouts. Heat from advancing flows vaporizes SO_2 snow producing jet-like flow front plumes (Kieffer *et al*., 2000; Milazzo *et al*., 2001). The central inset shows examples of the Prometheus plume.

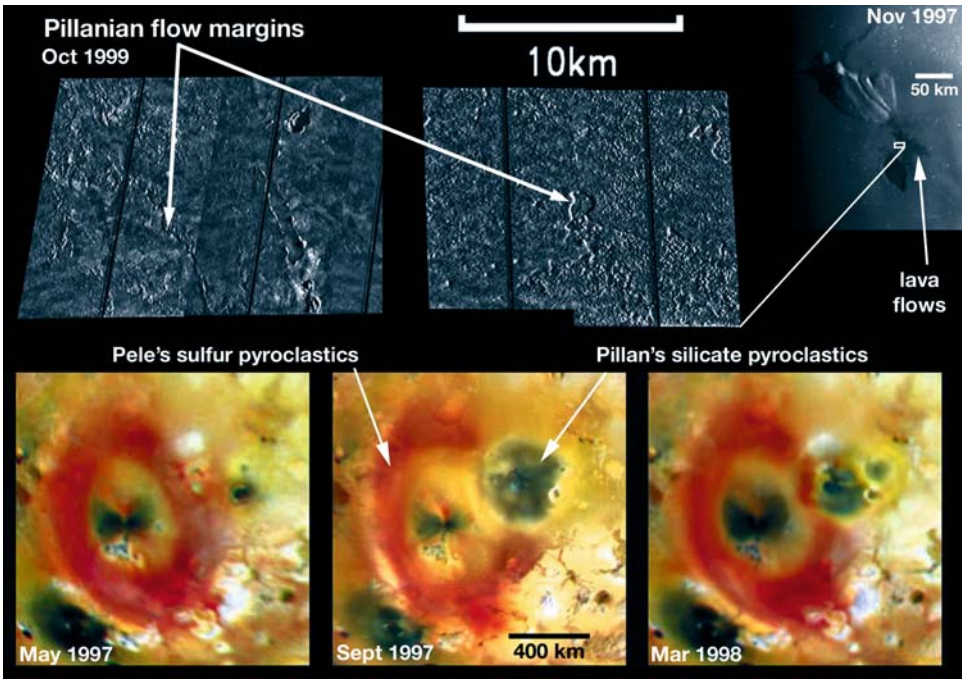

Figure 7.4. A montage of *Galileo* SSI images of the Pillan volcano at several different resolutions, which identify various aspects of an explosion-dominated (formerly Pillanian) eruption style. (*top*) The Pillan lava flow field, which emanated from fissures that fracture a mountain north of the caldera. (*bottom*) Changes to Pillan's surroundings (including Pele's red ring) due to activity at these volcanoes. These eruptions produce extensive flow fields that are rapidly emplaced over days to weeks, with measured temperatures consistent with terrestrial mafic to ultramafic volcanism (Keszthelyi *et al*., 2001).

Figure 7.5. A montage of *Galileo* SSI and *Cassini* imaging science subsystem (ISS) images showing a range of eruption styles at Tvashtar. In November 1999 Tvashtar had a possibly flow-dominated eruption, producing a lava fountain and flow field. In February 2000 an intra-patera eruption could have occurred, producing fresh material in a lava lake (or possibly just a confined lava flow). In December 2000, the *Cassini* spacecraft recorded an explosion-dominated eruption, from which *Galileo* imaged a large red ring deposit of sulfur. It remains unclear whether any new flows were emplaced (rapidly or otherwise) after the December 2000 event.

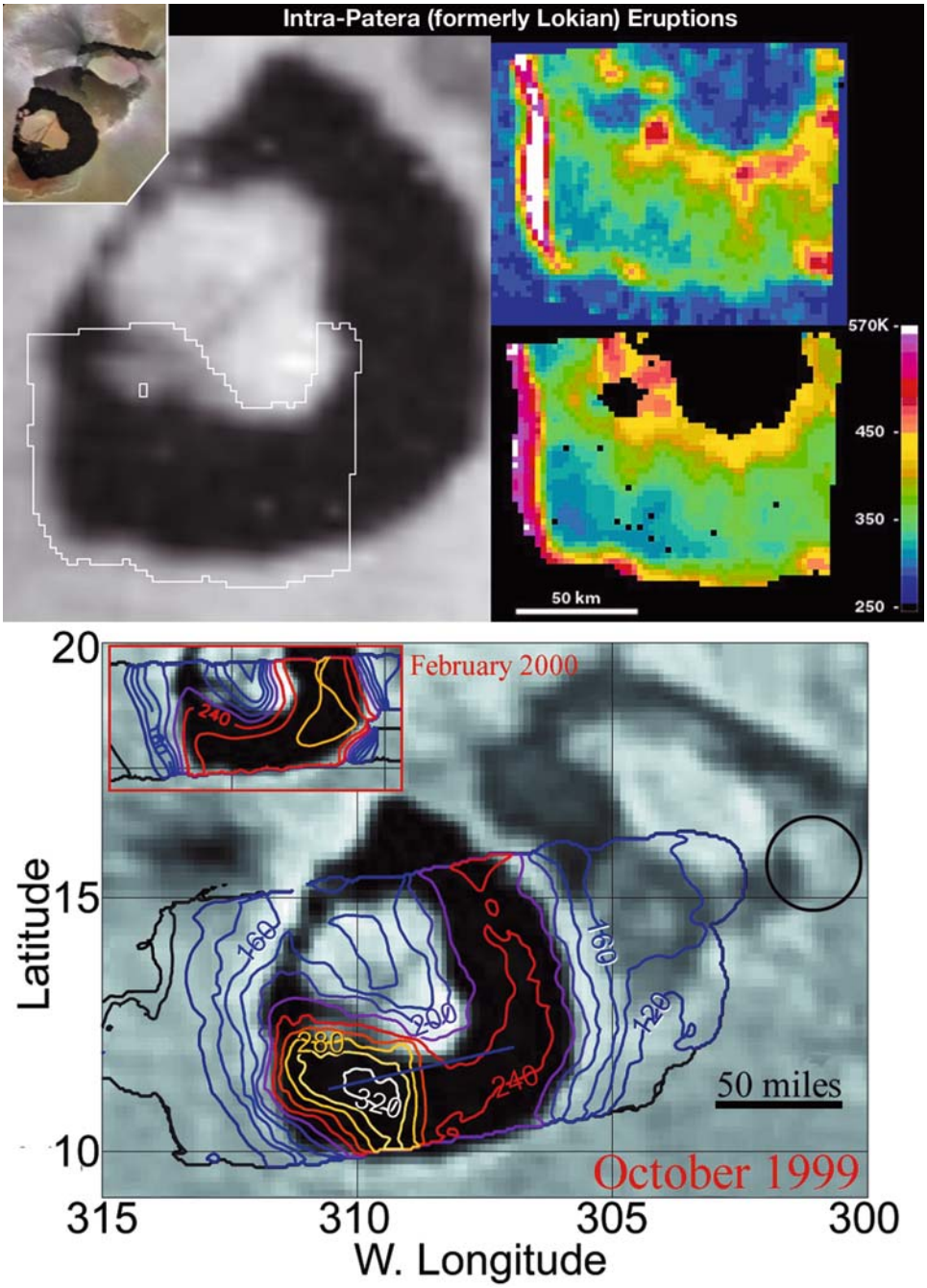

Figure 7.6. A montage of *Voyager* and *Galileo* SSI, NIMS, and PPR images of Loki volcano at several different resolutions and times, which identify various aspects of an intra-patera (formerly Lokian) eruption style. These eruptions produce lava lakes that are overturned over months to years, with measured temperatures typically consistent with terrestrial basaltic volcanism (Lopes *et al.*, 2004). The color panel at upper right is a NIMS map at 2.5 μm showing a hot edge (white: $T \sim 840$ K) at the western wall, whereas the image at lower right is a NIMS temperature map showing warmer and cooler parts of the patera floor. The bottom image shows PPR data over an image of Loki, showing the migration of the hottest part of the patera floor from west to east (from Spencer *et al.*, 2000b).

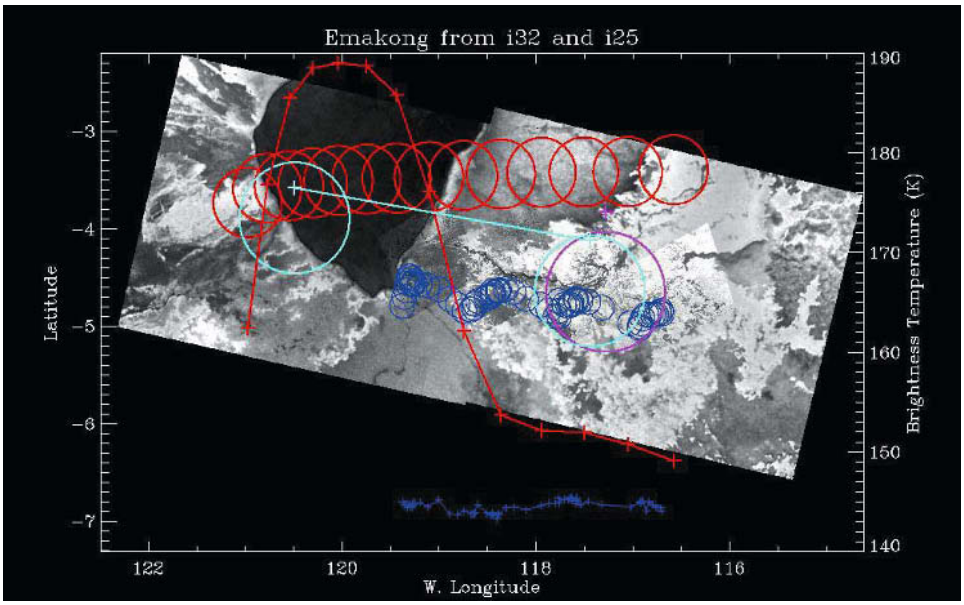

Figure 7.7. *Galileo* PPR data superposed upon SSI images of Emakong Patera. The PPR data demonstrate the very cold surface of the floor of Emakong Patera and its surrounding bright flows. NIMS data also showed that SO_2 frost is stable on parts of the patera floor, which suggests that Emakong may represent a cooled, inactive sulfur volcano (or, alternatively, a very cooled silicate volcano with silicate flows heavily mantled by sulfurous deposits: Williams *et al*., 2001b).

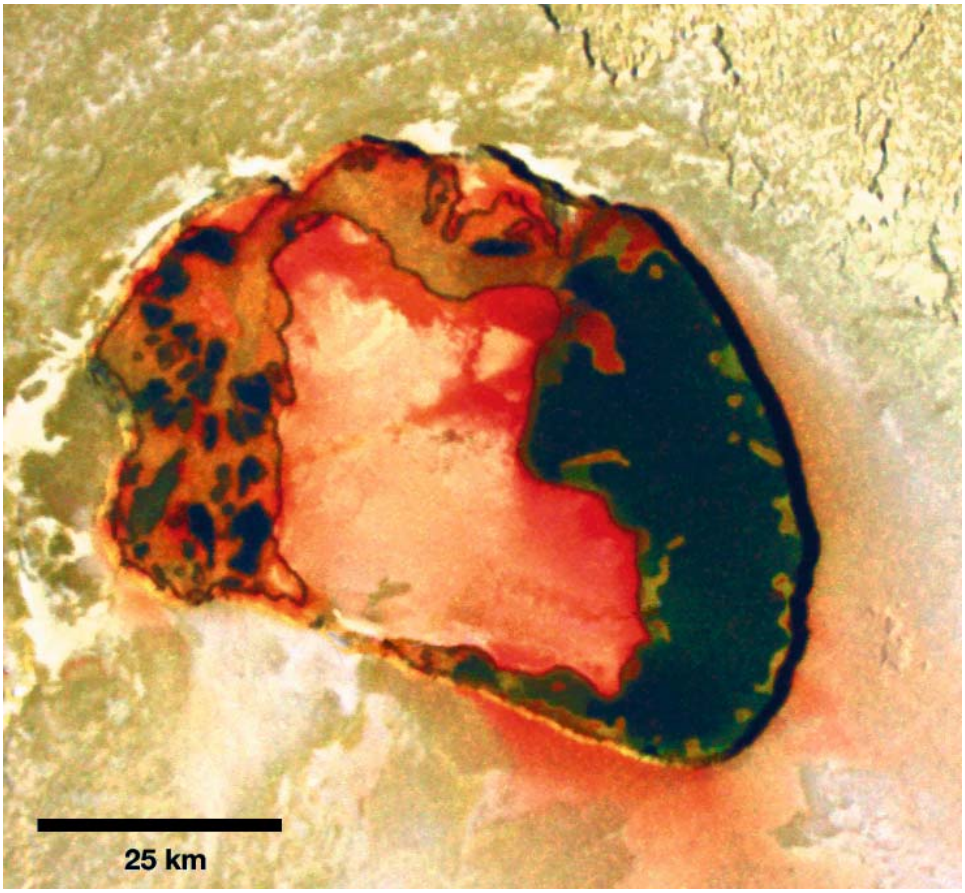

Figure 7.8. *Galileo* SSI image of Tupan Patera obtained in October 2001, another example of an intra-patera eruption style. Heat from the lava lake appears to melt bright sulfur deposits along the margins of the lake, which accumulate as bright "puddles" on the dark surface of the lake. Diffuse red deposits, presumably short-chain sulfur crystallized from S_2 gas, cover the margins of the patera and large parts of the central island. This is the highest resolution color image of Io obtained during the *Galileo* mission (132 m per pixel).

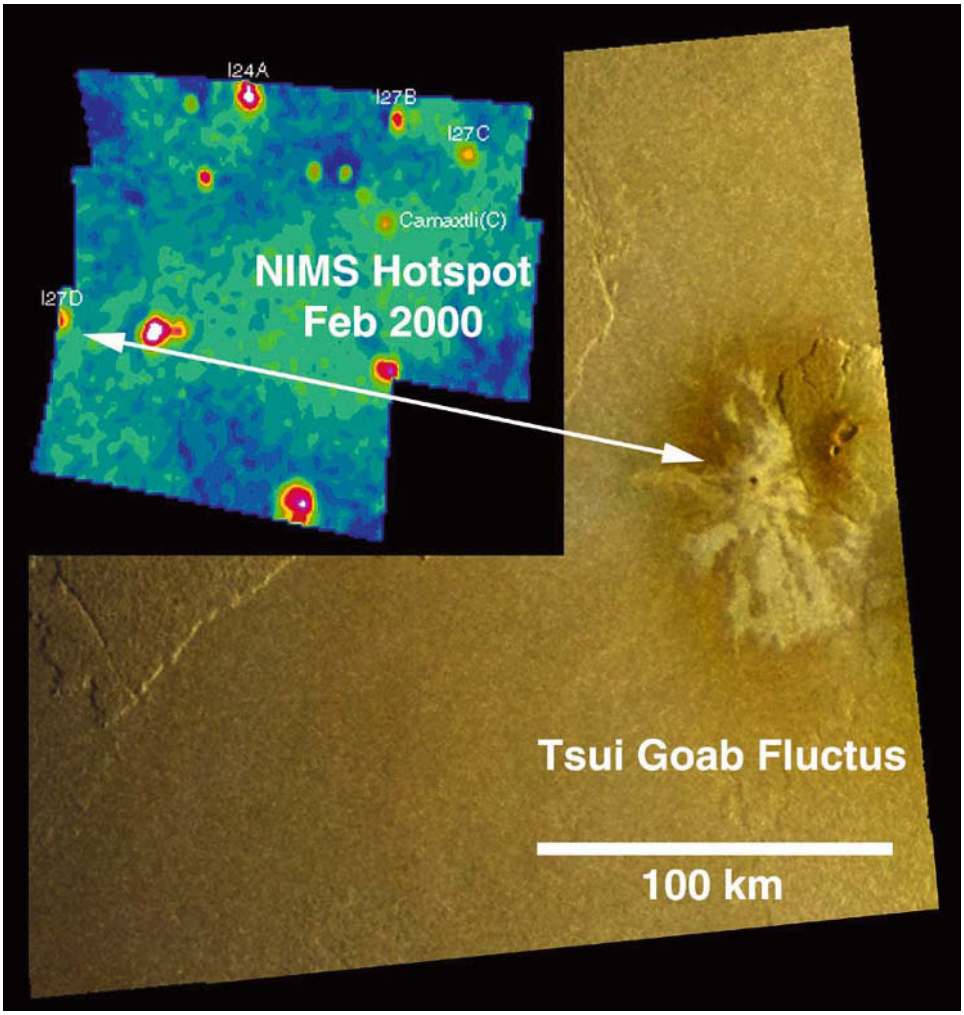

Figure 7.9. Low-resolution NIMS hot spot image (*inset*), with white arrows showing the correlation of the I27D hot spot of Lopes *et al.* (2001) with the bright flow field of Tsui Goab Fluctus in the Culann-Tohil region as imaged by the SSI during October 2001. This is the only location of potentially active, primary sulfur effusive volcanism detected during the *Galileo* mission.

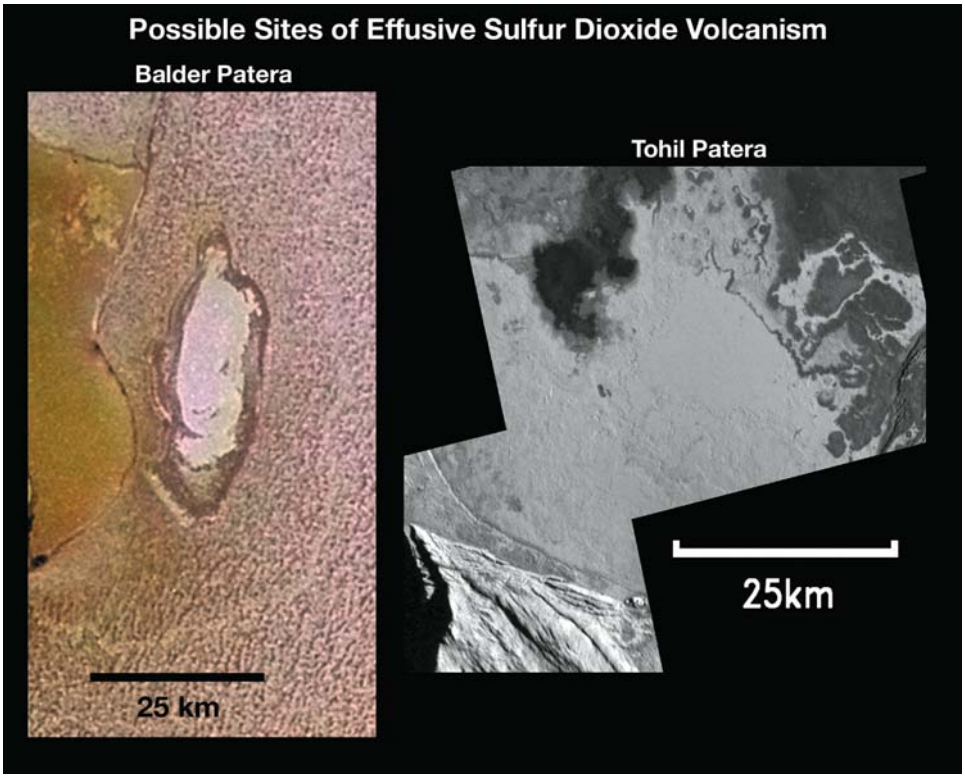

Figure 7.10. *Galileo* SSI images showing possible sites of effusive SO_2 volcanism on Io. (*left*) Balder Patera in the Chaac-Camaxtli region (Williams *et al*., 2002), site of a proposed glacial-like flow (Smythe *et al*., 2000). (*right*) Tohil Patera in the Culann-Tohil region (Williams *et al*., 2004), the south-west section of which has an enhanced SO_2 signature and flow-like margins in its interior.

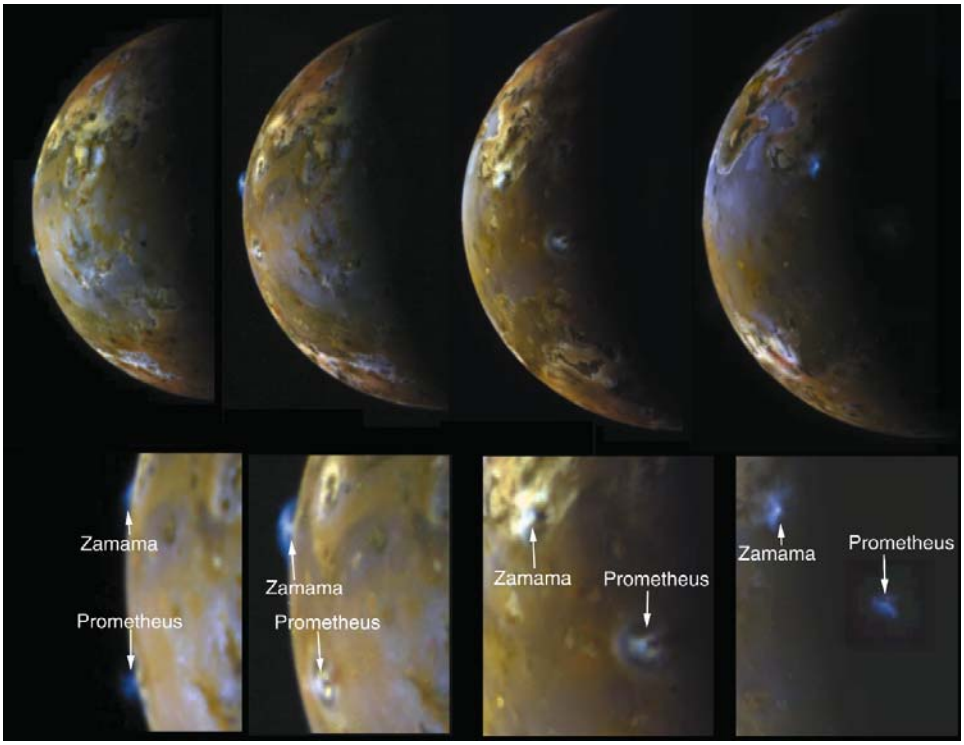

Figure 8.3. Zamama and Prometheus. This sequence of four images watches as two small plumes rotate onto the disk of Io. The blue colors of the plumes are caused by the light-scattering properties of the dust particles (NASA press release image PIA01652).

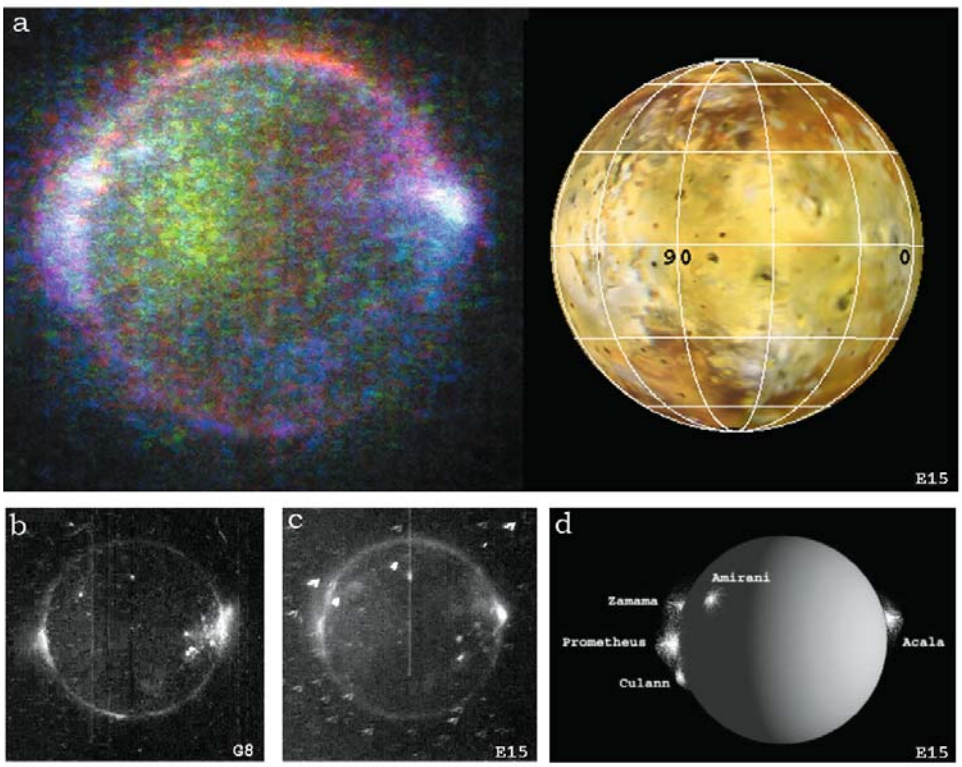

Figure 8.4. *Galileo* images of plumes in eclipse. (a) Visible-color image of atmospheric emissions during an eclipse in orbit 15 (*left*) compared with the sunlit appearance of the same hemisphere (*right*). The visible emissions are stimulated by charged particles, similar to terrestrial aurorae. The blue–white glows are produced by SO_2, and are concentrated at the locations of active plumes. The red and green glows are produced by atomic oxygen and atomic sodium, respectively (NASA press release image PIA01637). (b) Clear-filter image of the glows seen 1 year earlier, during the eclipse of orbit 8. The bright points on the disk show lava glowing by thermal emission. (c) Clear-filter image of glows seen during the eclipse of orbit 15. (d) Schematic diagram showing the locations of active plumes at the time of orbit 15 observations.

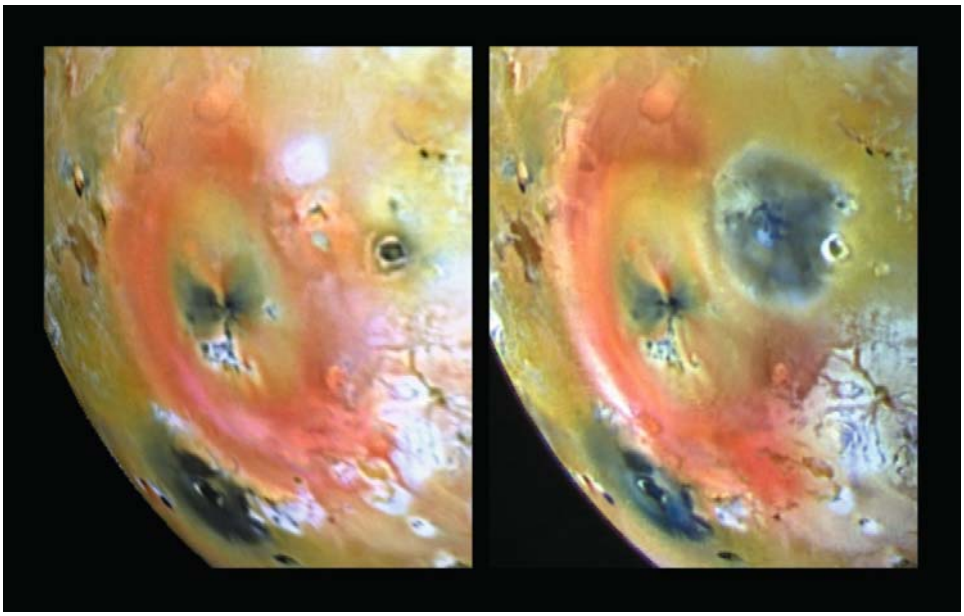

Figure 8.5. Two types of plume deposits. This pair of *Galileo* images shows the giant red ring of Pele, before (*left*) and after (*right*) the eruption of Pillan. Pele's annulus is elongated in the north–south direction, and reaches 720 km southwards from the source patera. Pillan's deposit is typical of small, SO_2-rich plumes that deposit ejecta up to 200 km from the eruption, except that it is colored by dark silicates (NASA press release image PIA00744).

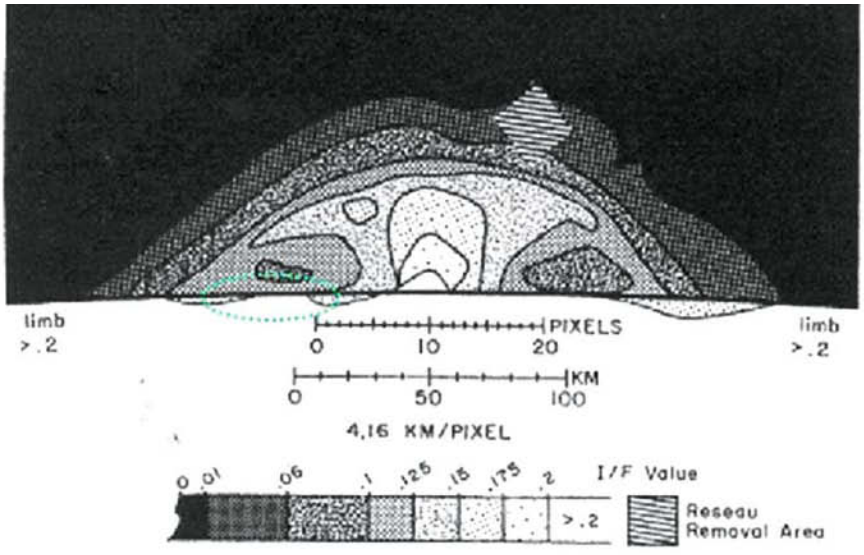

(a)

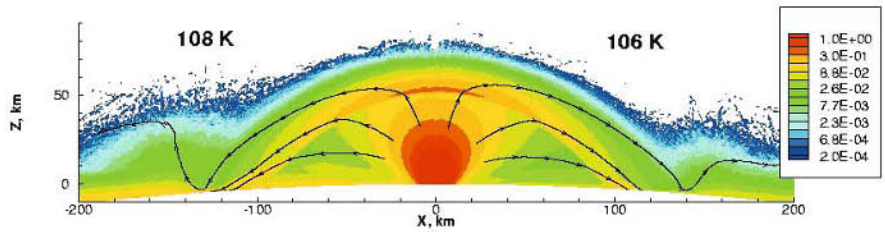

(b)

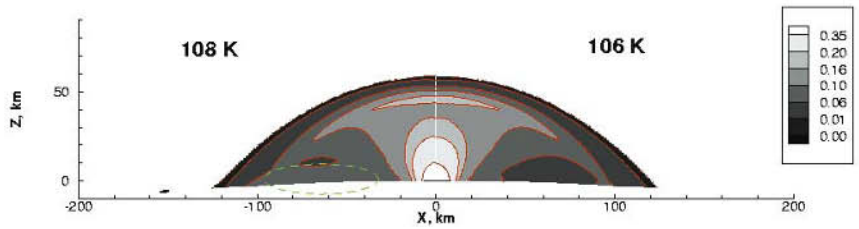

(c)

Figure 8.8. (a) *Voyager* image of the brightness of the Prometheus plume (from Strom and Schneider, 1982). Note the general sickle shape of the contours and the presence of a small signal near the surface on the left. (b) DSMC simulated number density contours (normalized by $5 \times 10^{16}\,\mathrm{m}^{-3}$) of gas with a surface temperature of 108 K on the left and 106 K on the right. Select gas flow streamlines are also shown. (c) Normalized column density contours of 1-nm particles entrained in the gas flow. Notice the low-altitude "dust cloud" circled on the left reflecting a settling time through the local atmosphere under the canopy of ~1,200 s. No cloud is seen on the right reflecting a settling time of only a couple of hundred seconds there.

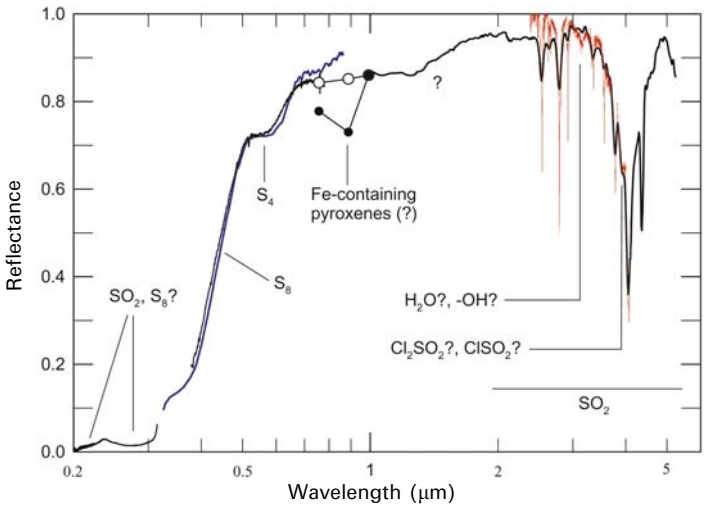

Figure 9.1. Solar reflectance spectra of Io. The ultraviolet HST measurements in the 200- to 310-nm region are from Jessup *et al*. (2002); ground-based measurements from 330–860-nm data (blue line) and from 380–780 nm (black line) are from Nelson and Hapke (1978) and Spencer *et al*. (1995), respectively. Scaled *Galileo* SSI multicolor spectrophotometry of white areas (open circles) and dark areas (filled circles) are from Geissler *et al*. (1999). Modest resolution near-infrared measurements by *Galileo* NIMS (black line) are from Carlson *et al*. (1997) while the higher resolution ISO spectrum (red line) is from Schmitt and Rodriguez (2003). Many of these spectra are summarized in the compilation by Spencer *et al*. (2004).

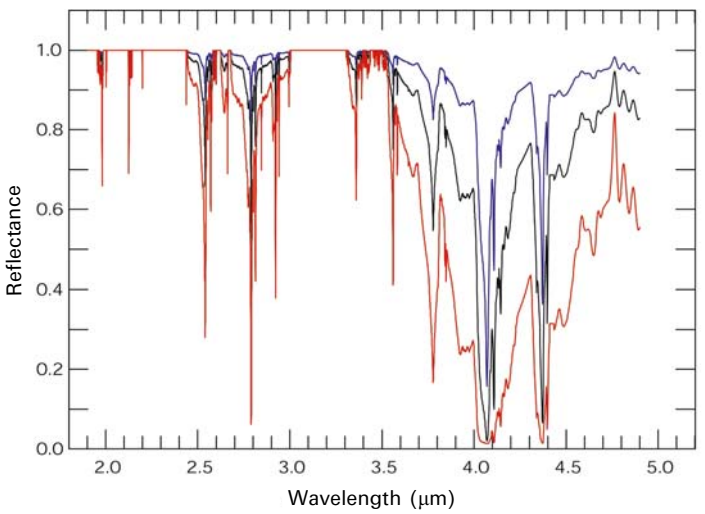

Figure 9.6. Theoretical reflectance spectra for SO_2 frost. The diffuse reflectance spectra of optically thick frosts of 10-, 100-, and 1,000-μm grains are shown as blue, black, and red lines, respectively. The optical constants of Schmitt *et al*. (1994, 1998b) were used.

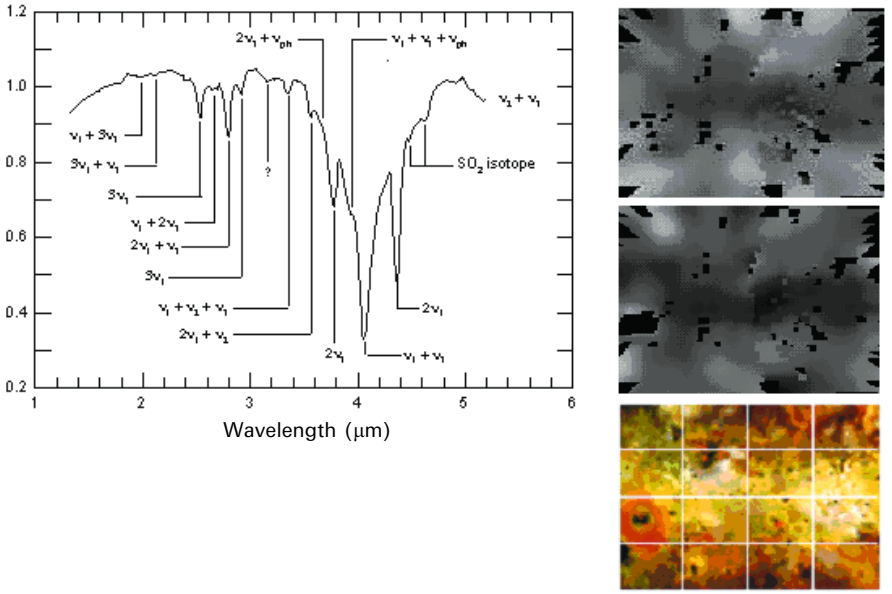

Figure 9.7. Spectrum of Io and equivalent-width maps. Maps of the absorption strength (equivalent width) of the 1.98-μm SO_2 band (*top*) and the 3.15-μm band (*middle*) are shown at the right, with black signifying more absorption. Note the strong equatorial enhancement of the unknown 3.15-μm absorber (possibly H_2O) and its correlation with both the weak, long-path-length SO_2 feature and the bright deposits in the Io reference map (*bottom*).

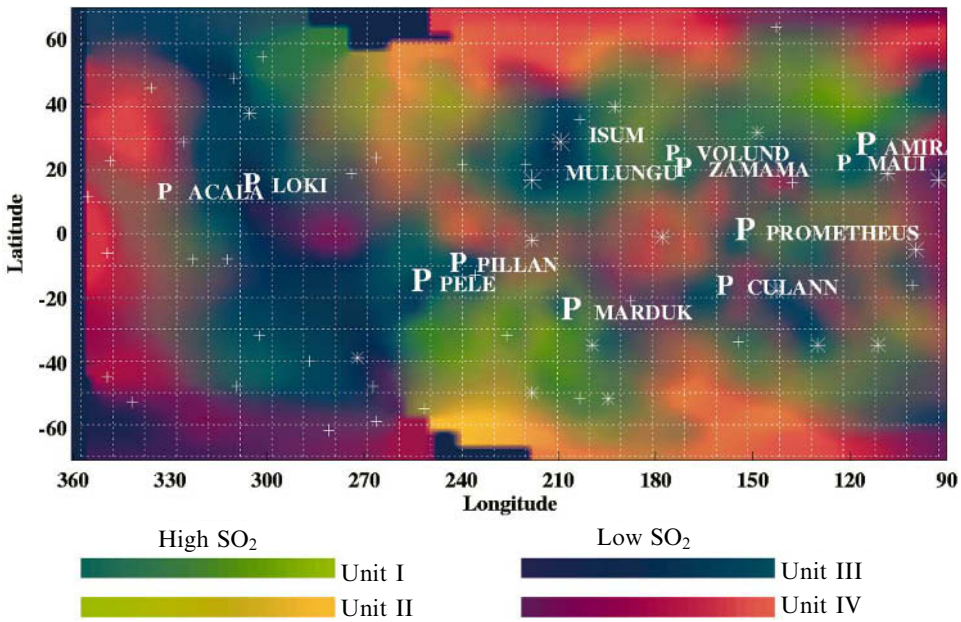

Figure 9.8. Sulfur dioxide spectral unit map. The plumes (P) are sources of fine-grained SO_2 frost (Unit I, green) deposits, generally poleward of the low-latitude plumes. Hot spot locations are denoted with stars and crosses, with stars being long-lived hot spots and crosses denoting sporadic thermal features. Metamorphosed SO_2 snowfields (Unit II) are shown as light green and yellow. SO_2-poor areas (Units III, IV) occur in the 270 to >360°W longitude region.

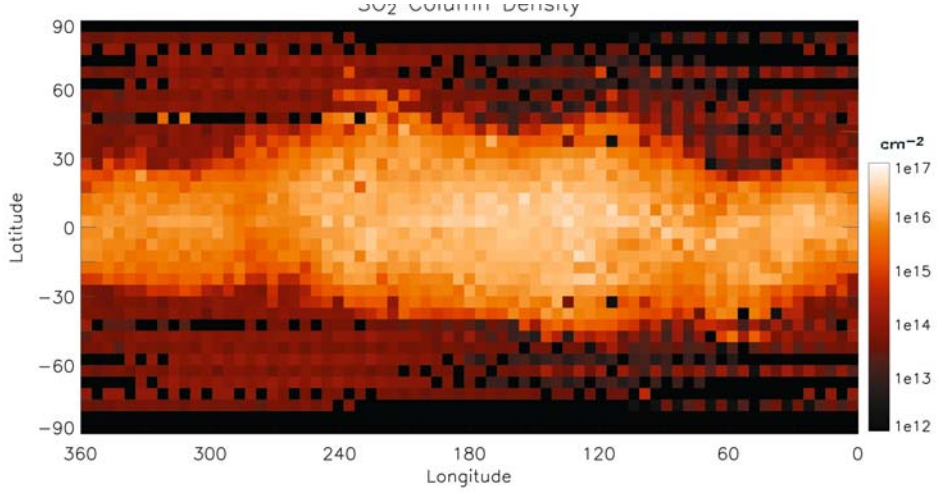

Figure 10.4. 2-D SO_2 gas distribution, as inferred from Lyα images (from Feaga *et al*., 2004a).

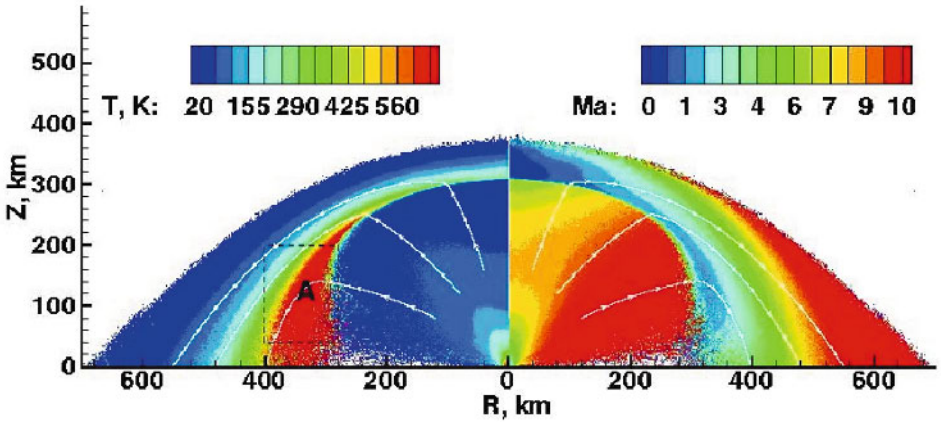

Figure 10.7. Model of an isolated Pele-type volcanic plume. Contours of the temperature and Mach number are shown (from Zhang *et al*., 2003).

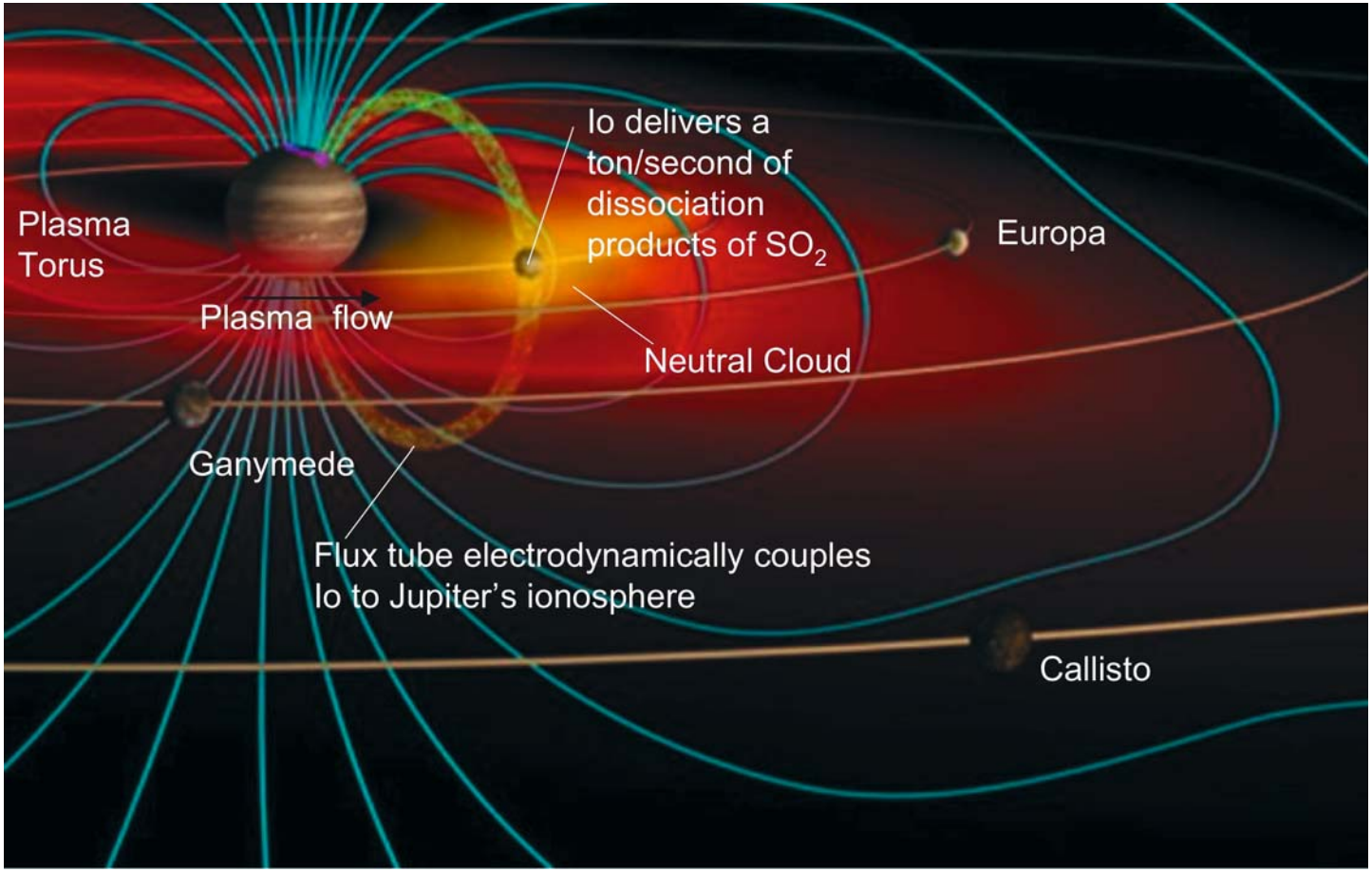

Figure 11.1. The main components of the Jupiter–Io system and their primary interactions.

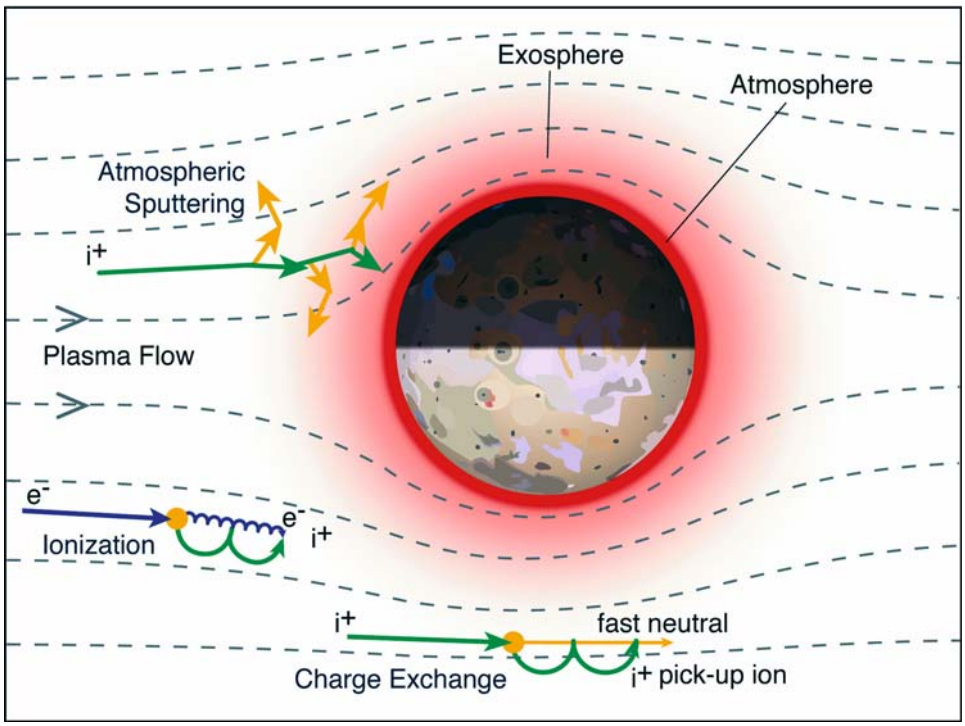

Figure 11.2. Important plasma/atmosphere interactions near Io. For simplicity the diagram shows the gyromotion for pick-up ions and electrons, but not for incident ions or electrons. The scale of the gyromotions has been greatly exaggerated: the gyroradius of a pick-up oxygen ion is 5 km, much less than Io's radius, and that of an electron is about 40,000 times smaller than the ion's.

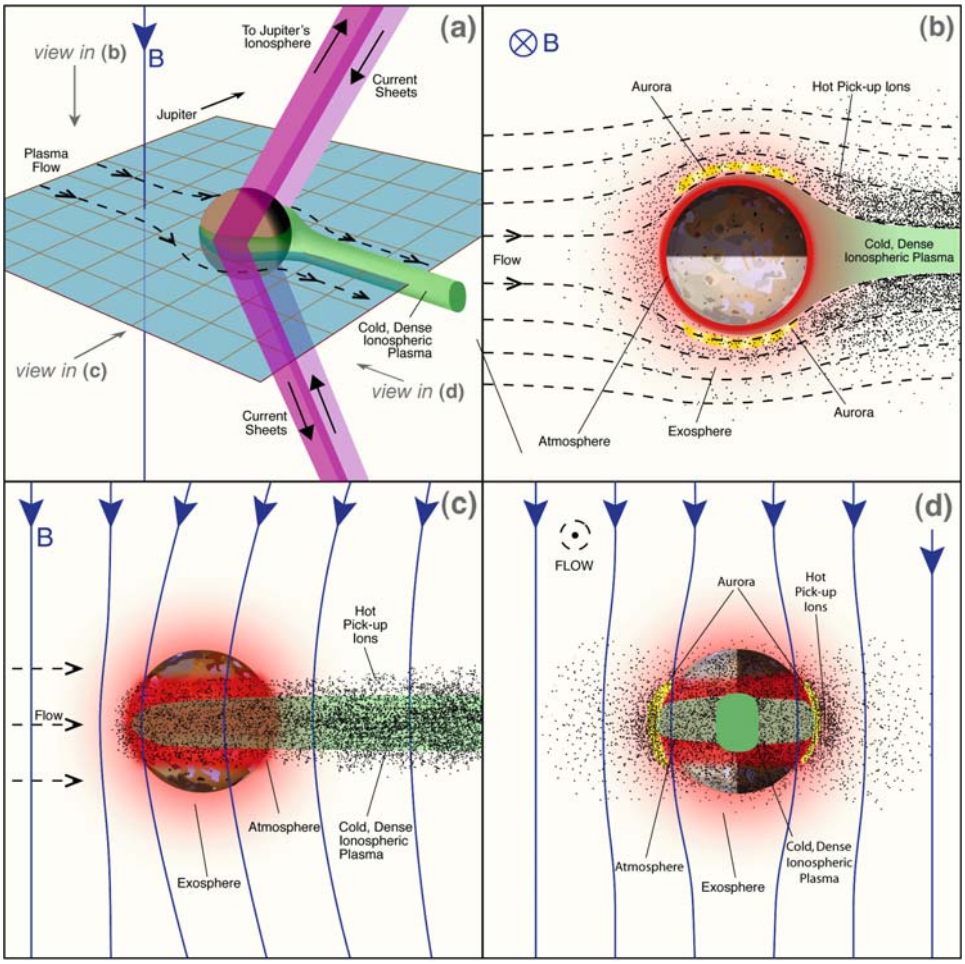

Figure 11.10. Four views of the interaction between Io and the plasma torus. (a) A 3-D view showing the current sheets that couple Io and the surrounding plasma to Jupiter's ionosphere. (b) A cross section of the interaction looking down on the north pole of Io, in the plane of Io's equator, when Io is located between the Sun and Jupiter (orbital phase 180°, local noon in magnetospheric coordinates). (c) A projected view of the Io interaction from the Sun toward Jupiter. (d) A projected view of the interaction from downstream in the flowing plasma (ahead of Io in its orbit).

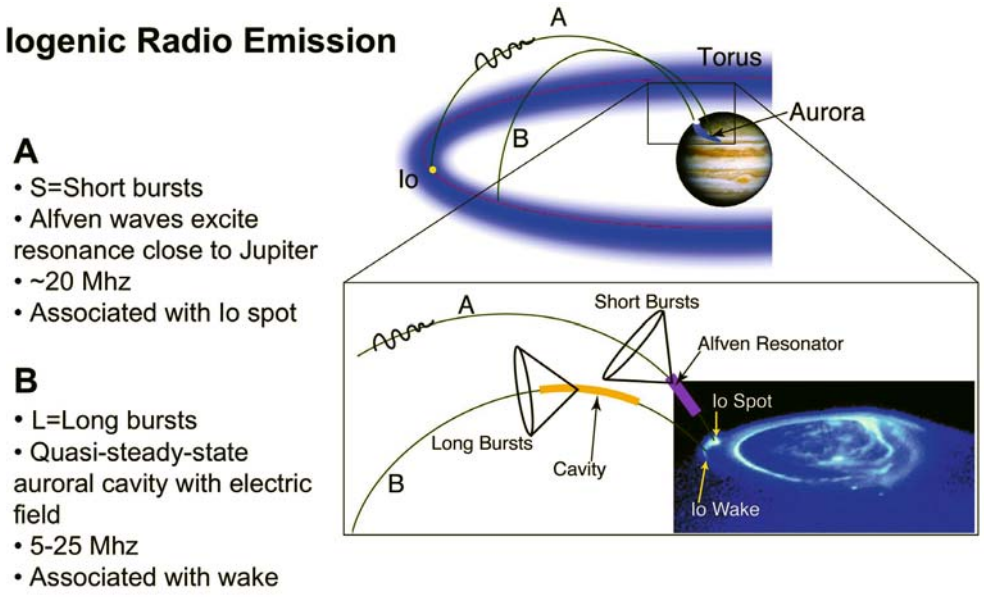

Figure 11.11. Geometry and mechanisms for Io-generated radio emissions from Jupiter's ionosphere.

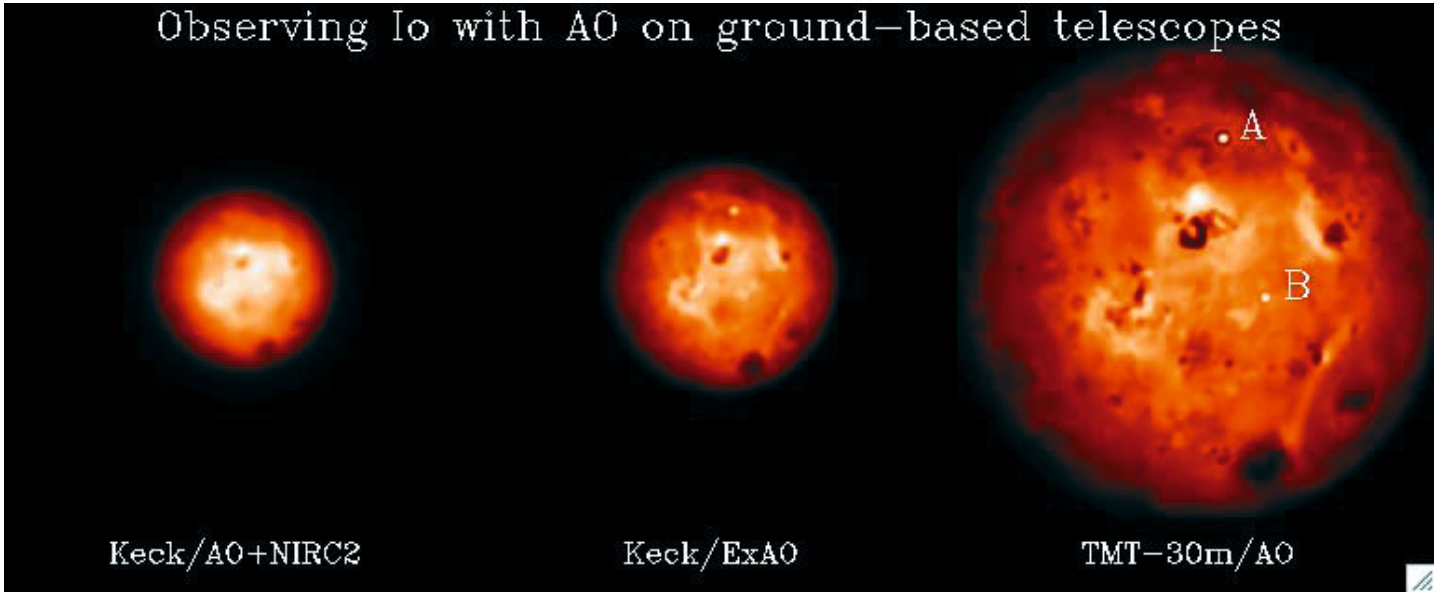

Figure 12.1. Observations of Io in H-band (1.6 μm) with several AO systems. Three AO system performances were simulated. The spatial resolution with the Keck AO is estimated to be 160 km on the center of the disk. An extreme AO system (ExAO) would provide a full correction of the wavefront for such a bright target, providing a sharper image, with a spatial resolution of 120 km on Io. Because of its larger aperture, the spatial resolution of 45 km, attainable on Io with the Thirty Meter Telescope (TMT), would be competitive with most of the global observations recorded by the *Galileo* spacecraft. On rare occasions the thermal output of hot spots is large enough at H-band to be detected in sunlit observations such as these. Thanks to the stability provided by ExAO, hot spot A is detected with this system. Hot spot B, with an intensity 12 times lower than the Keck AO limit of detection is clearly visible in the TMT simulation. More of these high-temperature eruptive centers could be studied with those new instruments helping to better constrain the composition of the magma. No *a posteriori* data processing to enhance the sharpness of the images (such as deconvolution) was applied to these simulations.

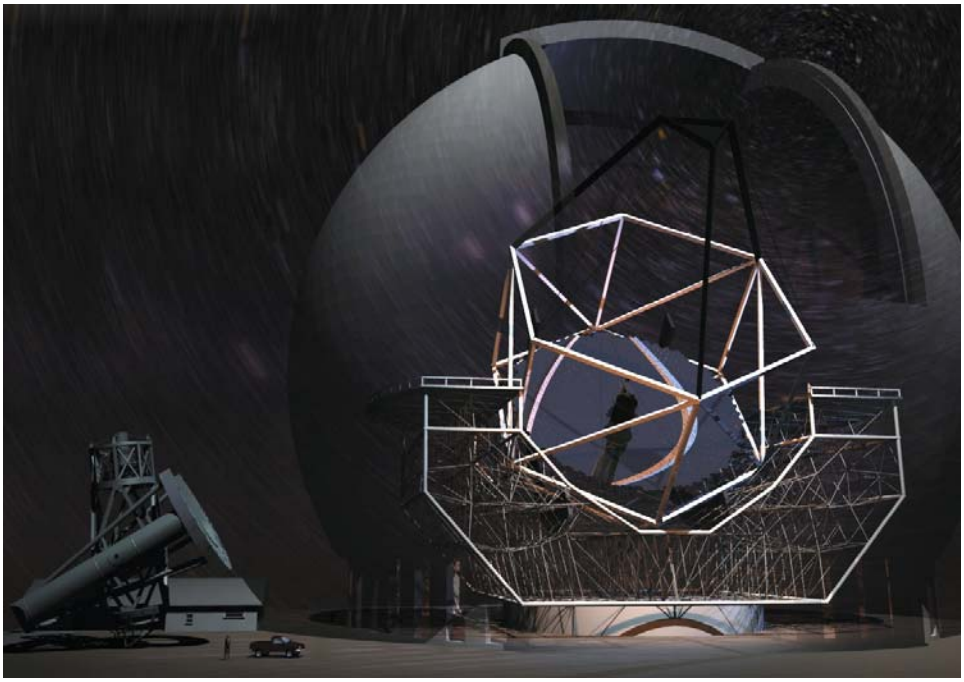

Figure 12.2. Artist's renderings of the TMT and comparison with the Palomar 5-m Hale telescope. This telescope, developed in partnership between the U.S.A. and Canadian institutes, should be available in 2014. Because of the large size of its aperture, combined with the capabilities of AO systems, it will provide an unprecedented spatial resolution of Io, better than most of the *Galileo* spacecraft infrared observations (courtesy California Institute of Technology).

Figure 12.3. Artistic vision of the Pluto-bound *New Horizons* spacecraft flying past the Jovian system at the end of February 2007. Multi-wavelength observations (from ultraviolet to near-infrared) of Io's surface, plumes, and atmosphere will be recorded.